Geochemistry of Palaeoarchaean to Palaeoproterozoic Kaapvaal Craton marine shales: Implications for sediment provenance and siderophile elements endowment

---

by

Glen Nwaila

Thesis

Submitted in fulfilment of the requirements for the degree

of

Doctor rerum naturalium (Dr. rer. nat.)

in

Geology

in the

Institute of Geography and Geology

at the

Faculty of Philosophy

Julius–Maximilians–Universität Würzburg, Germany

Supervisor: Prof. Dr. Hartwig Frimmel

Mentors: apl. Prof. Dr. Ulrich Schüssler,

PD Dr. Nikola Koglin

June 2017

Soli Deo Gloria

DECLARATION

I declare that this thesis is my own original work, conducted under the supervision of Prof. Dr. Hartwig E. Frimmel and mentorship of apl. Prof. Dr. Ulrich Schüssler and PD Dr. Nikola Koglin. It is submitted in fulfilment of the requirements for the degree of Dr. rer. nat. in Geology at the Institute of Geography and Geology at the Julius–Maximilians–Universität Würzburg, Germany. No part of this research has been submitted in the past, or is being submitted, for a degree or any examination at any other university.

Glen Nwaila **02.06.2017**

ABSTRACT

The Kaapvaal Craton hosts a number of large gold deposits (e.g. Witwatersrand Supergroup) which mining companies have exploited at certain stratigraphic positions. It also hosts the largest platinum group element (PGE) deposits (e.g. Bushveld Igneous Complex) which mining companies have exploited in different mineralised layered magmatic zones. In spite of the extensive exploration history in the Kaapvaal Craton, the origin of the Witwatersrand gold deposits and Bushveld Igneous Complex PGE deposits has remained one of the most debated topics in economic geology. The goal of this study was to identify the geochemical characteristics of marine shales in the Barberton, Witwatersrand, and Transvaal supergroups in South Africa in order to make inferences on their sediment provenance and siderophile element endowments. Understanding why some of the Archaean and Proterozoic hinterlands are heavily mineralised, compared to others with similar geological characteristics, will aid in the development of more efficient exploration models. Fresh, unmineralised marine shales from the Barberton (Fig Tree and Moodies groups), Witwatersrand (West Rand and Central Rand groups), and Transvaal (Black Reef Formation and Pretoria Group) supergroups were sampled from drill core and underground mining exposures. Analytical methods, such as X-ray powder diffraction (XRD), optical microscopy, X-ray fluorescence (XRF), inductively coupled plasma optical emission spectroscopy (ICP-OES), inductively coupled plasma mass spectrometry (ICP-MS), and electron microprobe analysis (EMPA) were applied to comprehensively characterise the shales. All of the Au and PGE assays examined the newly collected shale samples.

The Barberton Supergroup shales consist mainly of quartz, illite, chlorite, and albite, with diverse heavy minerals, including sulfides and oxides, representing the minor constituents. The regionally persistent Witwatersrand Supergroup shales consist mainly of quartz, muscovite, and chlorite, and also contain minor constituents of sulfides and oxides. The Transvaal Supergroup shales comprise quartz, chlorite, and carbonaceous material. Major, trace (including rare-earth element) concentrations were determined for shales from the above supergroups to constrain their source and post-depositional evolution. Chemical variations were observed in all the studied marine shales. Results obtained from this study revealed that post-depositional modification of shale chemistry was significant only near contacts with over- and underlying coarser-grained siliciclastic rocks and along cross-cutting faults, veins, and dykes. Away from such zones, the shale composition remained largely unaltered and can be used to draw inferences concerning sediment provenance and palaeoweathering in the source region and/or on intrabasinal erosion surfaces. Evaluation of weathering profiles through sections of the studied supergroups revealed that the shales therein are characterised by high

chemical index of alteration (CIA), chemical index of weathering (CIW), and index of compositional variability (ICV), suggesting that the source area was lithologically complex and subject to intense chemical weathering.

A progressive change in the chemical composition was identified, from a dominant ultramafic–mafic source for the Fig Tree Group to a progressively felsic–plutonic provenance for the Moodies Group. The West Rand Group of the Witwatersrand Supergroup shows a dominance of tonalite–trondhjemite–granodiorite and calcalkaline granite sources. Compositional profiles through the only major marine shale unit within the Central Rand Group indicate the progressive unroofing of a granitic source in an otherwise greenstone-dominated hinterland during the course of sedimentation. No plausible likely tectonic setting was obtained through geochemical modelling. However, the combination of the systematic shale chemistry, geochronology, and sedimentology in the Witwatersrand Supergroup supports the hypothesised passive margin setting for the >2.98 to 2.91 Ga West Rand Group, and an active continental margin source for the overlying >2.90 to 2.78 Ga Central Rand Group, along with a foreland basin setting for the latter.

Ultra-low detection limit analyses of gold and PGE concentrations revealed a variable degree of gold accumulation within pristine unmineralised shales. All the studied shales contain elevated gold and PGE contents relative to the upper continental crust, with marine shales from the Central Rand Group showing the highest Au (±9.85 ppb) enrichment. Based on this variation in the provenance of contemporaneous sediments in different parts of the Kaapvaal Craton, one can infer that the siderophile elements were sourced from a fertile hinterland, but concentrated into the marine shales by a combination of different processes. It is proposed that accumulation of siderophile elements in the studied marine shales was mainly controlled by mechanical coagulation and aggregation. These processes involved suspended sediments, fine gold particles, and other trace elements being trapped in marine environments. Mechanical coagulation and aggregation resulted in gold enrichments by 2–3 orders of magnitude, whereas some of the gold in these marine shales can be reconciled by seawater adsorption into sedimentary pyrite.

For the source of gold and PGEs in the studied marine shales in the Kaapvaal Craton, a genetic model is proposed that involves the following:

(1) A highly siderophile elements enriched upper mantle domain, herein referred to as “geochemically anomalous mantle domain”, from which the Kaapvaal crust was sourced. This mantle domain enriched in highly siderophile elements was formed

either by inhomogeneous mixing with cosmic material that was added during intense meteorite bombardment of the Hadaean to Palaeoarchaean Earth or by plume-like ascent of relics from the core–mantle boundary. In both cases, elevated siderophile elements concentrations would be expected. The geochemically anomalous mantle domain is likely the ultimate source of the Witwatersrand modified palaeoplacer gold deposits and was tapped again ca. 2.054 Ga during the emplacement of the Bushveld Igneous Complex. Therefore, I propose that there is a genetic link (i.e. common geochemically anomalous mantle source) between the Witwatersrand gold deposits and the younger Bushveld Igneous Complex PGE deposits.

(2) Scavenging of crustal gold by various surface processes such as trapping of gold from Archaean/Palaeoproterozoic river water on the surface of local photosynthesizing cyanobacterial or microbial mats, and reworking of these mats into erosion channels during flooding events.

The above two models complement each other, with model (1) providing a common geological source for the Witwatersrand gold and Bushveld Igneous Complex PGE deposits, and model (2) explaining the processes responsible for Witwatersrand-type gold pre-concentration processes. In sequences such as the Transvaal Supergroup, a less fertile hinterland and/or less reworking of older sediments led to a correspondingly lower gold endowment. These findings indicate temporal distribution of siderophile elements in the upper crust (e.g. marine shales). The overall implications of these findings are that background concentrations of gold and PGEs can be used to target potential exploration areas in other cratons of similar age. This increases the likelihood of finding other Witwatersrand-type gold or Bushveld Igneous Complex-type PGE deposits in other cratons.

CONTRIBUTION STATEMENT

The outcomes listed below are considered original contributions from this research:

1) The creation of a unique Archaean–Palaeoproterozoic marine shale mineral chemistry database, consisting of more than 100 analyses of well-known shale sequences derived from the Kaapvaal Craton.
2) The inclusion of information on siderophile elements and details of the elemental correlations between shale types and the associated carbon, as well as sulfur analyses, contributes to the uniqueness of the database.

This database also provides a frame for evaluating pre-existing datasets to determine sediment provenance and element mobility. This has permitted a comprehensive analysis of different shale compositions, provenances, and background Au and PGE concentrations. Moreover, this study suggests that the exceptional gold and PGE concentrations in the Kaapvaal Craton are not coincidental, but have a common siderophile elements enriched mantle domain. Although the geochemical models proposed in this work cannot necessarily predict the exact mineralisation content, they can assist in highlighting potential mineral deposit exploration targets. This study also demonstrates the importance of understanding the extent of mineral paragenesis and the implications of the regional geology when interpreting unmineralised shale sample results. Several mechanisms are proposed to account for differences in the siderophile element distribution. A new end-member model (referred to herein as sediment mechanical coagulation and aggregation) is proposed that helps to explain how siderophile elements were introduced into marine shales. Finally, this study illustrates geochemistry's utility as a field of research in aiding the understanding of the chemistry of marine shales.

Below is the list of peer-reviewed publications and international conference proceedings presentations of this study:

Nwaila, G., Frimmel, H.E., Minter, W.E.L., Beukes, N., 2015, Provenance and geochemical variations in shales of the Mesoarchaean Witwatersrand Supergroup. In: Andre-Mayer, A.-S. (Eds) Mineral Resources in a Sustainable World, Proc. 13th Biennial SGA Meeting, 24–27 August 2015, Nancy, Univ. de Lorraine, France.

Nwaila, G., Frimmel, H.E., 2016. Secular Au and PGE Sequestration in the Kaapvaal cratonic crust, South Africa. In: Goldfarb, R., Greyling, L., Cline, J., Simmons, S., Frimmel, H.E.

(Eds) Gold Mineralizing Systems: The Crustal Gold Cycle, Proc. 35th International Geological Congress (IGC), 27 August–4 September 2016, Cape Town, South Africa.

Nwaila, G., Frimmel, H.E., Minter, W.E.L., 2017. Provenance and geochemical variations in shales of the Mesoarchaean Witwatersrand Supergroup. The Journal of Geology, 125. In press.

Nwaila, G., Frimmel, H.E., 2017. Geochemistry of marine shales in the West Rand and Central Rand groups of the Mesoarchaean Witwatersrand Basin: implications for sedimentary gold endowment. 14th Biennial SGA Meeting, 20–23 August 2017, Quebec, Canada. In press.

PREFACE

Gold and platinum group elements are expected to continue to dominate the precious metals market, but demand for them will soon surpass their supply (O'Connor et al., 2015). I consider myself fortunate to have been given the opportunity to carry out a PhD research project on the Kaapvaal Craton, which is host to a number of world-class mineral deposits. This research provides insight into the provenance of marine shales in the Barberton, Witwatersrand, and Transvaal supergroups, and the chemistry of gold and platinum group elements. It also provides mining companies and economic mineral deposit explorers with a set of geochemical tools that can be used to target exploration areas for precious metal deposits in the future. I have been enthralled by research that involves a combination of chemistry, statistics, and geology since my undergraduate years. Working with Dr. Chris Rowan and Prof. Michiel de Kock as a laboratory assistant in the palaeomagnetism laboratories for three years, with Dr. Jens Gutzmer in the sample preparation laboratory, and enrolling in various analytical chemistry and metallurgy courses mentored by Ms. Henda Oosthuizen provided me with opportunities to innovate and explore multifaceted research. Working with Dr. Megan Becker, Prof. Jochen Petersen, and Prof. David Reid during my MSc program in chemical engineering introduced me to the applications of process engineering and applied earth science—a critical path that moved me from applied mining sciences to the academic world. A conversation with Prof. Hartwig Frimmel and an encouragement by Dr. Megan Becker motivated me to further my studies and ultimately enrol as a PhD candidate. This doctoral thesis takes a step into the giant leap towards addressing some of the most contested subjects in the sphere of the geosciences in South Africa, pertaining to the distribution of gold and platinum group elements.

References cited only in Preface

O'Connor, F.A., Lucey, B.M., Batten, J.A., Baur, D.G., 2015. The financial economics of gold – A survey. International Review of Financial Analysis. pp. 1–59.

ACKNOWLEDGEMENTS

I would like to express my sincere gratitude to Prof. Hartwig Frimmel for all his valuable constructive criticism, suggestions, insights, friendship, and patience in the course of this research project. Special thanks to Emeritus Prof. Lawrence Minter and Emeritus Prof. David Reid for all their guidance, input, and support at the Department of Geological Sciences, University of Cape Town. I thank Prof. Ulrich Schüßler and Dr. Nikola Koglin at Würzburg University for their help with sample preparation and XRF analyses. I also thank Prof. Helene Brätz at Erlangen University for LA-ICP-MS analyses.

This study was supported by a research grant from the National Research Foundation (NRF) to G. Nwaila (Grant UID: 88323). Various Witwatersrand gold mines (Sibanye Gold, Goldfields, and Anglo Gold Ashanti) provided access for sampling in both underground workings and drill cores. Prof. Axel Hofmann (University of Johannesburg) assisted in various aspects of the research, including sourcing of the Barberton Supergroup samples and advising on the Barberton post-depositional alteration processes. Sibanye Gold Limited also contributed financial and research support. The Bavarian Georesources Centre research group at the Institute of Geography and Geology, Julius–Maximilians–Universität Würzburg, and the National Research Foundation (NRF, Grant UID: 88323) of South Africa provided financial support.

Thank you to my wife, Phumzile Nwaila, for collecting and preparing samples, assisting with logistics, and supporting me throughout. I also wish to thank my parents, Daniel and Catherine Nwaila, my aunt Grace Machumele, and my friends for all their love, support, patience, and encouragement during this project, and for always believing in my abilities, especially Lebogang Phoshoko for his endless faith and support. Special thanks to Carol Simelane, Derek Rose, and David Mamba for their help in various aspects of this research. I also wish to thank my mentor, Dr. Richard Steward (Executive Vice President of Business Development at Sibanye Gold), for his continuous support and motivation. Messrs Cliff Dewey, Lancelot Madondo, Kobus Horn, Johan van Eeden, Gerhard Janse van Vuuren, and Corne Strydom afforded me time off from work to work on this research project. Mr. Leon Tolmay (Consultant Geostatistics and Evaluation at Sibanye Gold) is acknowledged for his guidance in the use of Applied Geostatistics and help in the development of an excel spreadsheet that deals with outlier effects. Messrs Stephen Tau and Christian Hedzane at Driefontein west mining complex (Geology Department) are acknowledged for their support and help during sample

collection. I thank my colleagues at Julius–Maximilians–Universität Würzburg, Stefan Höhn and Wesley Whymark, for their friendship during my frequent visits to Germany.

This work is dedicated to my children, Nkateko and Hlulani Nwaila, and to my siblings, Khumbulani, Nhlanhla, and Fumani Nwaila. The quote below is a message for them:

'When a man raises himself from the lowest conditions in society to the highest, mankind pays him the tribute of their admiration; When he accomplishes this elevation by native energy, guided by prudence and wisdom, their admiration is increased; But when his course, onward and upward, excellent in itself, furthermore proves possible what had hitherto been regarded as an impossible reform; Then he becomes a shining light on which the aged may look with gladness, the young with hope, the downtrodden, as a representative of what they themselves may become.' – James McCune Smith on Frederick Douglass

TABLE OF CONTENTS

DECLARATION ... **iii**

ABSTRACT ... **iv**

CONTRIBUTION STATEMENT ... **vii**

PREFACE ... **ix**

ACKNOWLEDGEMENTS ... **x**

TABLE OF CONTENTS ... **xii**

LIST OF FIGURES ... **xvi**

LIST OF TABLES ... **xxv**

APPPENDIX LIST OF FIGURES ... **xxvi**

APPPENDIX LIST OF TABLES ... **xxvi**

LIST OF EQUATIONS ... **xxvii**

LIST OF ABBREVIATIONS AND ACRONYMS ... **xxix**

CATIONS AND ANIONS ... **xxxi**

MINERAL NAMES AND FORMULAE ... **xxxi**

GLOSSARY ... **xxxiii**

1. INTRODUCTION ... **1**

1.1. Previous studies of Kaapvaal Craton shales ... 4

1.2. Problem statement ... 6

1.3. Overall research scope ... 7

1.3.1. Motivation and primary research objective ... 7

1.3.2. Exclusion of isotope data ... 8

1.3.3. Scope of the study ... 9

1.4. Thesis structure ... 9

2. GEOLOGICAL SETTING ... **11**

2.1. Regional geology of the Kaapvaal Craton ... 11

2.2. Local geology of the study areas on the Kaapvaal Craton ... 13

2.2.1. Barberton Supergroup ... 13

2.2.2. Witwatersrand Supergroup ... 18

2.2.3. Ventersdorp Supergroup 22
2.2.4. Transvaal Supergroup 24
2.2.5. Bushveld Igneous Complex 32
3. SEDIMENT PROVENANCE INDICATORS AND LITHOGEOCHEMISTRY ANALYTICAL METHODS 35
3.1. Sediment provenance 35
3.2. The distribution of elements and compounds as a provenance indicator in shale 36
3.3. Lithogeochemical methods commonly applied in shale, gold, and platinum group elements characterisation studies 37
4. METHODOLOGY 40
4.1. Sampling and sample preparation 40
4.2. Qualitative and semi-quantitative mineralogy 41
4.3. Bulk chemical assays: major and trace element analysis 42
4.4. Reference rock composition 43
4.5. Statistical analysis 43
4.6. Extent of post-depositional alteration 43
4.7. Chlorite chemical analysis and geothermometry 44
4.8. Highly siderophile element assays 44
4.9. Geostatistical treatment of highly siderophile elements 45
5. PETROGRAPHY AND MINERALOGY 50
5.1. Petrography 50
5.1.1. Fig Tree Group: Sheba Formation marine shales 51
5.1.2. Moodies Group: Clutha Formation marine shales 52
5.1.3. West Rand Group marine shales 52
5.1.4. Central Rand Group marine shales 53
5.1.5. Black Reef Formation marine shales 56
5.1.6. Pretoria Group: Silverton Formation marine shales 56
5.2. Mineralogy 59
5.2.1. Detailed petrographic and mineralogical descriptions of the shales 59
5.2.2. Barberton Supergroup marine shales 60

5.2.3. Witwatersrand Supergroup marine shales 61
5.2.4. Chlorite chemistry and geothermometry 66
5.2.5. Transvaal Supergroup marine shales: The Black Reef Formation 76
5.2.6. Transvaal Supergroup marine shales: Pretoria Group 78
6. MARINE SHALE GEOCHEMISTRY 81
6.1. Barberton Supergroup marine shales 82
6.1.1. Major elements 82
6.1.2. Trace elements including rare earth and highly siderophile elements 85
6.1.2.1. Distribution of trace elements and stratigraphic variations 85
6.1.2.2. Total rare earth element contents and stratigraphic variations 86
6.1.2.3. Highly siderophile elements 88
6.2. Witwatersrand Supergroup marine shales 91
6.2.1. Major elements 91
6.2.2. Trace elements including rare earth and highly siderophile elements 93
6.2.2.1. Distribution of trace elements and stratigraphic variations 93
6.2.2.2. Total rare earth element content and stratigraphic variations 95
6.2.2.3. Highly siderophile elements 96
6.3. Transvaal Supergroup marine shales: Black Reef Formation 101
6.3.1. Major elements 101
6.3.2. Trace elements including rare earth and highly siderophile elements 102
6.3.2.1. Distribution of trace elements and stratigraphic variations 102
6.3.2.2. Total rare earth element contents and stratigraphic variations 103
6.3.2.3. Highly siderophile elements 103
6.4. Transvaal Supergroup marine shales: Pretoria Group 105
6.4.1. Major elements 105
6.4.2. Trace elements including rare earth and highly siderophile elements 107
6.4.2.1. Distribution of trace elements and stratigraphic variations 107
6.4.2.2. Total rare earth element contents and stratigraphic variation 108
6.4.2.3. Highly siderophile elements 109

6.5. Summary of marine shales chemical composition with special reference to siderophile elements 111

7. DISCUSSION 123

7.1. Summary of the minerals encountered and mineral paragenesis 123

7.2. Extent of post-depositional alteration 127

7.3. Sediment provenance 134

7.4. Extent of palaeoweathering 154

7.5. Sources of siderophile elements 161

7.6. Controls on the distribution of siderophile elements 173

8. CONCLUSION 184

9. RECOMMENDATIONS 189

REFERENCES 190

APPENDICES 237

Appendix A. 1. Whole rock geochemical data 237

Appendix A. 2. Mineral chemistry of chlorite. 325

Appendix A. 3. Brief history of geostatistics and its application to unmineralised marine shales. 332

Appendix A. 4. Mass transfer calculation results for profile from upper contact into shale unit of Roodepoort Formation. Abbreviations: ΔCi/Ci0 = Gain/Loss relative to Ci0 and Δci = Gain/Loss in wt. % or ppm. 335

Appendix A. 5. Sources of Nickel in the studied marine shales. 337

LIST OF FIGURES

Figure 1: Surface and subsurface distributions of the main Archaean stratigraphic units of the Kaapvaal Craton. The Witwatersrand Basin fill comprises the West Rand and Central Rand groups; the purple line delineates traces of the Black Reef Formation at the base of the late Archaean to Palaeoproterozoic Transvaal Basin (modified after Frimmel et al., 2005a; Frimmel, 2014). BIC = Bushveld Igneous Complex (modified after Rose et al., 2011). TML = Thabazimbi–Murchison Lineament. Fm. = Formation. 2

Figure 2: Surface and subsurface distribution of Kaapvaal Craton's main Archaean stratigraphic units. The Witwatersrand Basin fill comprises the West Rand and Central Rand groups, while the purple line delineates traces of the Black Reef Quartzite Formation at the base of the Palaeoarchaean to Palaeoproterozoic Transvaal Basin (Frimmel et al., 2005; Frimmel, 2014). 12

Figure 3: Geological map of Barberton Supergroup (modified after Otto et al., 2007)..... 14

Figure 4: A. Overview of Witwatersrand Basin and extent of Kaapvaal Craton (after Guy, 2012). B. Surface and sub-surface geological map of Witwatersrand Basin with locations of major goldfields (from Frimmel et al., 2005). 18

Figure 5: Witwatersrand Supergroup stratigraphic column (modified from Frimmel et al., 2005). 21

Figure 6: Ventersdorp Supergroup stratigraphic column (after Schneiderhan et al., 2011); the lithostratigraphy of the Kameeldoorns and Bothaville Formations is illustrated in detail. The U–Pb zircon ages for Klipriviersberg lavas and the Makwassie Formation are from Armstrong et al. (1991). De Kock (2007) dated the Kameeldoorns Formation at 2.73 ± 0.003 Ga, and Poujol et al. (2005) constrained an older age for the Makwassie Formation, at 2.92 ± 0.006 Ga; the Bothaville Formation remains unconstrained in age. Fm = formation, VCR = Ventersdorp Contact Reef. 23

Figure 7: Distribution of Transvaal Supergroup in South Africa (modified from Dorland, 1999; Coetzee, 2001). 25

Figure 8: Cross-section illustrating the Black Reef facies types that incise the Witwatersrand Supergroup's underlying Kimberley Reef in the East Rand Basin (modified from Barton and Hallbauer, 1996; Fuchs et al., 2016a). 27

Figure 9: Stratigraphy of Transvaal Supergroup: the correlation between the Griqualand West and Transvaal regions (modified after Dorland, 1999; Beukes, 2010), with available radiometric ages is also indicated. GOE: Global Oxidation Event. Onset of the GOE occurred between ca. 2460 and 2426 Ma (Gumsley et al., 2017)..... 29

Figure 10: Summary of Transvaal Supergroup stratigraphy (modified after Eriksson et al., 2001). 31

Figure 11: Simplified geological map of Bushveld Igneous Complex, which includes the Rustenburg Layered Suite, Rooiberg Volcanics, and Lebowa Granite Suite (Rose et al., 2011). 33
Figure 12: Schematic flow sheet illustrating sample handling and sample preparation. 41
Figure 13: Geostatistical data processing to obtain the most accurate estimates of average Au and PGE compositions. Graphs a–c represents distribution of data with (a) negative skewness, (b) positive skewness (lognormal distribution), and (c) normal distribution or Gaussian distribution. 47
Figure 14: Geological map showing location of sampled shale sequences (black stars) and extent of Kaapvaal Craton. TML = Thabazimbi–Murchison lineament. Fm. = Formation. 51
Figure 15: A. Witwatersrand Supergroup stratigraphic column illustrating sampled formations in pink), SG = subgroup; ages as given in Frimmel et al. (2005); B. Basin assemblage and sampled formations, modified after Guy et al. (2010). 55
Figure 16: Stratigraphic profile of Transvaal Supergroup with marked sample locations (modified after Beukes et al., 2002)..... 57
Figure 17: Lithostratigraphic profile of sampled Kaapvaal Craton sequences. Ages: Barberton Supergroup and Dominion Group (Lowe and Byerly, 1999; Poujol et al., 2003; Schoene et al., 2009; Zeh et al., 2009); Witwatersrand Supergroup (Kositcin and Krapež, 2004); Ventersdorp and Transvaal Supergroup (Armstrong et al., 1991). 59
Figure 18: Photomicrographs of selected Fig Tree (A and B) and Moodies (C and D) shales demonstrating the characteristics of certain minerals under plane-polarised light. (A) Quartz intergrown with dolomite and albite. (B) Chlorite flakes surrounded by detrital quartz. (C) Graded shale with fine-grained quartz, sericite, and illite surrounded by quartz and dolomite. (D) Illite-rich shale with detrital quartz and dolomite. 60
Figure 19: Photomicrographs of selected Roodepoort Formation shales indicating the mineral phases present. (A) Chlorite- and calcite-rich shale with secondary chlorite occurring along the calcite rim. Plane-polarised light. (B) Chlorite- and calcite-rich zoned shale with secondary chlorite and pyrite. Plane-polarised light. (C) Graded shale with intergrown chlorite and calcite. Plane-polarised light. (D) Chlorite-, calcite-, and ankerite-rich shale grading into fine-grained chlorite-biotite layer. Plane-polarised light. (E) K-feldspar intergrown with chlorite surrounded by quartz, ankerite, and pyrite. (EMPA BSE image). (F) Secondary rutile surrounded by calcite and secondary chlorite. (EMPA BSE image)..... 63
Figure 20: Photomicrographs of selected Booysens Formation shales demonstrating some of the mineral phases present. (A) Chlorite grain and pyrite. Plane-polarised light. (B) Chlorite flake surrounded by quartz and muscovite matrix. Plane-polarised light. (C)

Series of microfaults filled with calcite veinlets. Plane-polarised light. (D) Greenish biotite, calcite and pyrite in chlorite matrix. Plane-polarised light. 64
Figure 21: Petrography of Witwatersrand shales showing metamorphic and hydrothermal chlorite. Abbreviations: Chl = chlorite and Py = pyrite. 67
Figure 22: Compositional diagram of Witwatersrand chlorite in Al^{IV}–Mg–Fe ternary diagram (from Zane and Weiss, 1998). 68
Figure 23: Classification of Witwatersrand chlorite via $Mg/(Mg + Fe_{total})$ versus $^{VI}R^{3+}$ (apfu) diagram (from Plissart et al., 2009). 69
Figure 24: Plot of R^{2+} versus Si (apfu) for Witwatersrand chlorite (from Wiewióra and Weiss, 1990). 70
Figure 25: Diagram of Mg versus Fe^{2+} for Witwatersrand chlorite, illustrating correlation coefficient results with limit lines. 71
Figure 26: Correlation of Al and temperatures of chlorite formation based on Al^{IV} (apfu) content (from Hiller and Velde, 1991). 75
Figure 27: Photomicrographs of selected Black Reef Formation shales demonstrating some of the mineral phases present. Plane-polarised light. (A) Elongated chlorite and concretion of siderite within black shale laminae. B) Euhedral to subhedral calcite, and elongated chlorite. (C) Rounded detrital quartz and secondary euhedral pyrite. (D) Chlorite intergrown with ankerite surrounding detrital quartz concretion and pyrrhotite. (E) Graded shale illustrating cyclicity of kerogen and coarse- and fine-grained fractions. (F) Layering along the bedding filled with kerogen surrounded by a matrix quartz-muscovite and chlorite. 77
Figure 28: Photomicrographs of selected Pretoria Group shales illustrating some of the mineral phases present. Plane-polarised light. (A) Very fine-grained secondary muscovite within the black shale laminae of the Pretoria Group. (B) A typical example of a soft-sediment deformation structure (e.g. contorted bedding). Note the kerogen along the bending. (C) Evidence of micro faulting within the shale lamina in the lower Pretoria Group shale unit's calcite veinlet. (D) Chlorite intergrown with calcite surrounding a detrital quartz concretion. 79
Figure 29: Example of Fig Tree and Moodies groups' marine shale major element data prior to geostatistical processing. 82
Figure 30: Multi-element diagram of average major element concentrations for Fig Tree and Moodies groups' shales. Coloured bands mark the range of data for the respective sample group. Normalising values after Taylor and McLennan (1985). 83
Figure 31: A. Ternary diagram of ACNK (Al_2O_3:[CaO* + Na_2O]:K_2O) (modified after Nesbitt and Young, 1984) for Fig Tree and Moodies Group shales, illustrating a wide range of palaeoweathering. Average values for the upper continental crust and PAAS values

were obtained from Taylor and McLennan (1985); B. Ternary diagram (ACF) indicating molar proportions of Al_2O_3:(CaO* + Na_2O + K_2O):Fe_2O_3 + MgO) and distinctive chemical change characteristic of alteration for some Fig Tree and Moodies Group shales. The average PAAS value was obtained from Taylor and McLennan (1985). The composition of the upper continental crust is from Rudnick and Gao (2005). 84

Figure 32: Multi-element diagram of average trace element concentrations for Fig Tree and Moodies groups' shale. Coloured bands mark the range of data for the respective sample group. Normalising values after Taylor and McLennan (1985). 86

Figure 33: Multi-element diagram of average REE concentrations for Fig Tree and Moodies groups marine shales. Coloured bands mark the range of data for the respective sample group. Normalising values after Taylor and McLennan (1985) and McLennan (2001).87

Figure 34: Chemostratigraphic plots of Au and PGE for Fig Tree Group marine shale (drill core BARBFC). 88

Figure 35: Chemostratigraphic plots of Au and PGE for Fig Tree Group marine shale (drill core BARBFD). 89

Figure 36: Chemostratigraphic plots of Au and PGE for Fig Tree Group marine shale (drill core BARBMA). 89

Figure 37: Chemostratigraphic plots of Au and PGE for Fig Tree Group marine shale (drill core BARBMB). 90

Figure 38: A. Ternary diagram of ACNK (Al_2O_3:[CaO* + Na_2O]:K_2O) (modified after Nesbitt and Young, 1984) for West Rand and Central Rand Group shales, illustrating both a wide range of palaeoweathering and source differences for the goldfields. Blue lines indicate weathering trends for felsic (right) and intermediate (left) source rocks. Average values for upper continental crust and PAAS are from Taylor and McLennan (1985). B. Ternary diagram (ACF) showing molar proportions of Al_2O_3:(CaO* + Na_2O + K_2O):Fe_2O_3 + MgO) and distinctive chemical change characteristic of alteration for some West Rand and Central Rand Group shales. Ideal mineral compositions: Amp p amphibole; Bio = biotite; Chl/chl = chlorite; Fsp = feldspars; Gib/gib = gibbsite; Ill = illite; Kao = kaolinite; Kfsp = K-feldspar; Mo = montmorillonite; Msc = muscovite; No = nontronite; PAAS = post-Archaean Australian shale; Pla = plagioclase; Pyx = pyroxene; Sa = saponite; Se = serpentine; Sm = smectite. Average value of upper continental crust and PAAS from Taylor and McLennan (1985). The composition of upper continental crust is from Rudnick and Gao (2005). 92

Figure 39: Multi-element diagram of average trace element concentrations for Roodepoort and Booysens Formations' shale. Normalising values after Taylor and McLennan (1985).94

Figure 40: A. PAAS-normalised, average REE patterns for Witwatersrand shale units. B. PAAS-normalised data from Fuller et al. (1981) and Wronkiewicz and Condie (1987). Normalising values after Taylor and McLennan (1985) and McLennan (2001). 96
Figure 41: Chemostratigraphic plots of Au and PGE for Roodepoort Formation marine shale (drill core E1E). 98
Figure 42: Chemostratigraphic plots of Au and PGE for Roodepoort Formation marine shale (drill core E1G). 98
Figure 43: Chemostratigraphic plots of Au and PGE for Roodepoort Formation marine shale (drill core D5P03463). 99
Figure 44: Chemostratigraphic plots of Au and PGE for Roodepoort Formation marine shale–MR10 33XCW (underground profile UNG). 99
Figure 45: Chemostratigraphic plots of Au and PGE for Booysens Formation marine shale–Welkom goldfield (drill core BOOYWG). 100
Figure 46: Chemostratigraphic plots of Au and PGE for Booysens Formation marine shale–Western Areas goldfield (Zuurbekom drill core Z1637). 100
Figure 47: Multi-element diagram of average major element concentrations for Black Reef Formation shale. Normalising values after Taylor and McLennan (1985). 101
Figure 48: Multi-element diagram of average trace element concentrations for Black Reef Formation shale. Normalising values after Taylor and McLennan (1985). 102
Figure 49: Multi-element diagram of Black Reef Formation shales' REE patterns. Normalising values after Taylor and McLennan (1985). 103
Figure 50: Chemostratigraphic plots of Au and PGE for Black Reef Formation marine shale (drill core E1H). 104
Figure 51: Multi-element diagram of average major element concentrations for Pretoria Group shales. Coloured bands mark the range of data for the respective sample group. Normalising values after Taylor and McLennan (1985). 105
Figure 52: A. Ternary diagram of ACNK (Al_2O_3:[CaO* + Na_2O]:K_2O) (modified after Nesbitt and Young, 1984) for Pretoria Group shales, illustrating both a wide range of palaeoweathering and differences in source rocks. Average values for upper continental crust and PAAS values are from Taylor and McLennan (1985). B. Ternary diagram (ACF) indicating molar proportions of Al_2O_3:(CaO* + Na_2O + K_2O):Fe_2O_3 + MgO and distinctive chemical change characteristic of alteration for Pretoria Group shales. The average PAAS value is from Taylor and McLennan (1985). The composition of the upper continental crust is from Rudnick and Gao (2005). 106
Figure 53: Multi-element diagram of average trace element concentrations for Pretoria Group shales; coloured bands mark the range of data for the respective sample group. Normalising values after Taylor and McLennan (1985). 108

Figure 54: Multi-element diagram of average REE for Pretoria Group shales. Coloured areas mark the range of data for the respective sample group. Normalising values after Taylor and McLennan (1985). 109
Figure 55: Chemostratigraphic plots of Au and PGE for Pretoria Group marine shale (drill core DP22). 110
Figure 56: Chemostratigraphic plots of Au and PGE for Pretoria Group marine shale (drill core DP23). 111
Figure 57: Binary plots of averaged Kaapvaal Craton shales normalised to composition of upper continental crust (Rudnick and Gao, 2005). A. Averaged Au, B. Averaged Pd, and C. Averaged Pt. 114
Figure 58: Bivariate diagrams for Barberton Supergroup marine shales showing correlations of SiO_2, MgO, TOC, and S with Au. 116
Figure 59: Bivariate diagrams for Barberton Supergroup marine shales showing correlations of SiO_2, MgO, TOC, and S with Pd. 117
Figure 60: Bivariate diagrams for Barberton Supergroup marine shales showing correlations of SiO_2, MgO, TOC, and S with Pt. 117
Figure 61: Bivariate diagrams for Witwatersrand Supergroup marine shales showing correlations of SiO_2, MgO, TOC, S, Zr, and Ni with Au. 118
Figure 62: Bivariate diagrams for Witwatersrand Supergroup marine shales showing correlations of SiO_2, MgO, TOC, S, Zr, and Ni with Pd. 119
Figure 63: Bivariate diagrams for Witwatersrand Supergroup marine shales showing correlations of SiO_2, MgO, TOC, S, Zr, and Ni with Pt. 120
Figure 64: Bivariate diagrams for Transvaal Supergroup marine shales showing correlations of SiO_2, MgO, TOC, and S with Au. 121
Figure 65: Bivariate diagrams for Transvaal Supergroup marine shales showing correlations of SiO_2, MgO, TOC, and S with Pd. 121
Figure 66: Bivariate diagrams for Transvaal Supergroup marine shales showing correlations of SiO_2, MgO, TOC, and S with Pt. 122
Figure 67: Summary of major mineralogical proportions of Barberton, Transvaal, and Witwatersrand supergroups. 125
Figure 68: Relative stabilities of selected minerals in Barberton, Transvaal, and Witwatersrand supergroups as a function of metamorphic grade (adapted from Kisch, 1987; Frey and Robinson, 1999; Klein, 2005). 126
Figure 69: Marine shale profile showing extent of post-depositional alteration. The samples were obtained from Driefontein 8 shaft, MR10 32XCW. 129

Figure 70: Isocon diagram of Roodepoort Formation shales illustrating behaviour of major oxides and selected trace element constituents. Abbreviations: CM = constant mass, CV = constant volume; calculation after Grant (2005). 131
Figure 71: Diagram of Th versus Th/U for Barberton Supergroup shales. 132
Figure 72: Diagram of Th versus Th/U illustrating syn- and post-depositional mobility in selected Witwatersrand shales. Note the differences in Th/U between different positions within the same stratigraphic unit, reflecting differences in provenance. 133
Figure 73: Ni versus total organic carbon plot for the Booysens Formation shale. .. 136
Figure 74: Geochemical model of Ni concentration in the Archaean hinterland. Lower limit lines indicate minimum required Ni derived from particulate, detrital compounds. Time scale (X-axis) indicates amount of time required to source Ni from the hinterland. Hinterland Ni (ppm) [left Y-axis] indicates hinterland concentration of Ni; % Ni from the hinterland (right Y-axis) indicates total % Ni supply to shales from the hinterland. ... 137
Figure 75: Diagram of X_{Mg} versus Ni/Co, demonstrating Kaapvaal Craton shale composition variations. 138
Figure 76: Binary plot of Ni versus Cr for Fig Tree and Moodies Group shales, illustrating change from mafic to felsic source rocks. Reference sample data are from Condie (1993). 140
Figure 77: Binary plot of Ni versus Cr for selected Witwatersrand shale units. Reference sample data are from Condie (1993). 141
Figure 78: Ni versus Cr diagram for Black Reef Formation and Pretoria Group shales, illustrating change from mafic to felsic source rocks; reference samples from Condie (1993). 142
Figure 79: Diagram of Th/Sc versus Zr/Sc for Witwatersrand shales. Source-rock compositions from Condie (1993). Low Th/Sc ratio (<1) indicates a mafic source, which is usually enriched in compatible elements (e.g. Sc), while the incompatibility of Th results in higher concentrations in well-differentiated felsic rocks (Th/Sc ± 1; Taylor and McLennan, 1985). 143
Figure 80: Diagram of Cr versus Zr for Booysens Formation shale in various goldfields, illustrating differences in source rocks; reference samples are from Condie (1993). 144
Figure 81: Down-borehole variations in Zr/Ni and CIA for Booysens Formation shale, reflecting a progressive increase in felsic/mafic source-rock proportions in the course of sedimentation, as well as a possible change in provenance. 145
Figure 82: Ternary diagrams: A, C, E. Th–Sc–Zr/10 ternary diagram with heavy mineral fraction (Zr). B, D, F. La–Th–Sc ternary diagram between light REE (La), incompatible element (Th), and compatible element (Sc). Source rock compositions are from Condie (1993). Discrimination fields of tectonic setting are after Bhatia and Crook (1986).

Abbreviations: OIA = oceanic island arc; CIA = continental island arc; ACM = active continental margin; PM = passive margin; KOM = komatiite; BAS = basalt; GRA = granite; TTG = tonalite–trondhjemite–granodiorite; AG = Archaean shale; FVO = felsic volcanic rocks. 147

Figure 83: Diagram of Th/Co versus La/Sc for Witwatersrand shales, demonstrating geochemical variations in trace element ratios (fields after Cullers, 2002)..... 148

Figure 84: A. Diagram of Ti/Zr versus La/Sc of Kaapvaal Craton shales showing geochemical variation in trace element ratios. B. Diagram of La/Th versus Hf of Kaapvaal Craton shales showing geochemical variation in trace element ratios (after Floyd and Leveridge, 1987). 149

Figure 85: Diagram of Th–Zr–Co for Witwatersrand shales of (A) Central Rand Group and (B) West Rand Group, illustrating source variations between goldfields and stratigraphic positions. Source rock compositions are from Condie (1993)..... 151

Figure 86: Estimated proportion of likely source rocks in the course of sedimentation and provenance variation indicators in Kaapvaal Craton shales, as reflected by Cr/Th ratios. Abbreviations: BLR = Black Reef Formation; SG = Subgroup. 152

Figure 87: Summary of estimated general palaeogeography and palaeocurrent directions for Witwatersrand Supergroup (adapted from Stanistreet and McCarthy, 1991; McCarthy, 2006; Guy et al., 2010)..... 153

Figure 88: A. CIA versus ICV for Barberton shale samples. B. Down-borehole variation in CIA, indicating weathering patterns with depth. C. Down-borehole variation in Zr/Ni, reflecting felsic/mafic source rock proportions in the course of sedimentation. 156

Figure 89: CIA versus ICV for Witwatersrand shale samples. 157

Figure 90: A. Bivariate plots of CIA versus ICV for Transvaal shale samples. B. Down-borehole CIA variations, indicating weathering patterns with depth for Pretoria Group shales. C. Down-borehole variations in Zr/Ni, reflecting felsic/mafic source rock proportions in the course of sedimentation for Pretoria Group shales..... 159

Figure 91: Bivariate plot of Th versus Th/U for Transvaal Supergroup. 160

Figure 92: Binary diagrams showing concentration of (a) evolution of Earth's atmospheric oxygen content through time (after Lyons et al., 2014), (b) Au content in marine shales and H_2S/SO_2 versus time. The ratios H_2S/SO_2 curve is from Frimmel (2015)..... 167

Figure 93: Binary diagrams showing (a) Pt content in marine shales and H_2S/SO_2 versus time, (b) Pd content of marine shale and H_2S/SO_2 versus time. The ratios H_2S/SO_2 curve is from Frimmel (2015). 168

Figure 94: Interpretation of likely gold sources in Booysens Formation marine shale: (A) gold versus Zr/Ni; (B) gold versus Th/Sc. Zirconium and Th in these diagrams represent felsic source rocks, whereas Ni and Sc represent mafic source rocks..... 179

Figure 95: Mechanical coagulation model possibly responsible for majority of gold formation in marine shales: (A) idealised cross-section of Archaean/Palaeoproterozoic continental and marine environments; (B) depiction of Archaean/Palaeoproterozoic hinterland and gold scavenging by mechanical coagulation processes (diagram is modified from Chamberlin and Dickey, 2007). 183

LIST OF TABLES

Table 1: Example of variance comparison using hypothesis-testing statistics. 48
Table 2: Interpretation of test results. 49
Table 3: Summary of sampled Kaapvaal Craton sequences and their respective stratigraphic location. 58
Table 4: Semi-quantitative modal mineralogy of selected Barberton Supergroup shale samples, as obtained by Rietveld analysis (in vol.%). 61
Table 5: Semi-quantitative modal mineralogy of selected Witwatersrand Supergroup shale samples, as obtained by Rietveld analysis (in vol.%). 65
Table 6: Estimation of Witwatersrand shale chlorite formation temperatures (n = 129). 76
Table 7: Semi-quantitative modal mineralogy of selected Black Reef Formation shale samples, as obtained by Rietveld analysis (in vol.%). 78
Table 8: Semi-quantitative modal mineralogy of selected Transvaal Supergroup shale samples, as obtained by Rietveld analysis (in vol.%). 80
Table 9: Selected average Kaapvaal Craton HSE concentrations, from the oldest domain to the youngest sampled sequence (values reported in ppb, ± = variance). 112
Table 10: Modelling of sedimentary pyrite gold contribution in marine shales. 177

APPPENDIX LIST OF FIGURES

Figure A. 1. Outlier calculation custom-designed spreadsheet. 333

APPPENDIX LIST OF TABLES

Table A. 1. Major element concentrations of the Fig Tree and Moodies groups' marine shales. 237
Table A. 2. Trace element concentrations of the Fig Tree and Moodies groups' marine shales. 240
Table A. 3. Major element concentrations of the Witwatersrand Supergroup marine shales. 251
Table A. 4. Trace element concentrations of the Witwatersrand Supergroup marine shales. 268
Table A. 5. Major element concentrations of the Black Reef Formation marine shales..... 311
Table A. 6. Trace element concentrations of the Black Reef Formation marine shales. 312
Table A. 7. Major element concentrations of the Pretoria Group marine shales. 314
Table A. 8. Trace element concentrations of the Pretoria Group marine shales. 317
Table A. 9. Ni in Archaean Rock Proportion Composition (Condie, 1993). 337
Table A. 10. Rock Proportions Mixture Model. 337
Table A. 11. Average Ni Composition from sediment mixture..... 337
Table A. 12. Source rock mixture model scenarios. 337
Table A. 13. Calculations parameters/assumptions..... 338
Table A. 14. Time required to accumulate Ni from source rocks. 339

LIST OF EQUATIONS

$$\bar{x} = \frac{1}{N}\sum_{i=1}^{n} x_i$$ Equation 1 45

$$S^2 = \frac{\sum\left(x - \bar{x}\right)^2}{N-1}$$ Equation 2 45

$$\gamma_1 = \frac{\sum(X-\mu)^3}{n\sigma^3}$$ Equation 3 45

$$r = \frac{n\sum xy - \sum x \sum y}{\sqrt{\left[n\sum x^2 - \left(\sum x\right)^2\right]\left[n\sum y^2 - \left(\sum y\right)^2\right]}}$$ Equation 4 46

$$2\gamma(h) = \frac{1}{N(h)} \times \sum_{n=1}^{N(h)} \left[z(u_n) - z(u_n + h)\right]^2$$ Equation 5 46

$$T\beta = \ln(Au + \beta)$$ Equation 6 46

$$\bar{x}_{Au\_PGE} = e^{\left(\overline{T\beta} + (S^2)/2\right)}$$ Equation 7 47

Test statistic = $t_{\bar{x}} = \frac{\bar{x} - u}{\frac{8}{\sqrt{n}}}$ Equation 8 48

$TCN_{85–Al^{IV}}$ (°C) = 106 * $Al^{IV}O_{28}$) + 18 Equation 9 72

$TCN_{85–Octahedral\ vacancy}$ (°C) = ((Octahedral vacancy O_{28} - 2.41) * 1000)/-8.57 Equation 10 72

$TKML_{87–Al^{IV}}$ (°C) = 106 * ($Al^{IV}O_{28}$ + 0.7 * (Fe/Fe + Mg) + 18) Equation 11 72

$TC_{88–Al^{IV}}$ (°C) = -61.92 + 160.99 * $Al^{IV}O_{28}$) Equation 12 72

$TK_{90–Si}$ (ºC) = 4833.946 – 2817.776 * ($Si^{IV}O_{14}$) + 419.858 * ($Si^{IV}O_{14}$)^2 Equation 13 73

$TJ_{91–Al^{IV}}$ (°C) = 319 (($Al^{IV}O_{14}$) + (0.1 * (Fe/Fe + Mg)) - 69 Equation 14 73

$THV_{91–Al^{IV}}$ (°C) = ($Al^{IV}O_{28}$ - 1.303546)/0.004007 Equation 15 73

$TC_{93–Octahedral\ occupancy}$ (°C) = (($_{Octahedral\ occupancy}O_{14}$) - 5.550)/0.001359 Equation 16 73

$TC_{93–Si^{IV}}$ (°C) = (($Si^{IV}O_{14}$) - 3.610)/-0.001327 if 'Al-chlorite' < 0.20 Equation 17 73

$TZF_{95–Al^{IV}}$ (°C) = 106.2 * (($Al^{IV}O_{28}$) - 0.88 * ((Fe/(Fe + Mg) - 0.34)) + 17.5 Equation 18 74

$TX_{97–Al^{IV}}$ (°C) = 160.99 * (($Al^{IV}O_{28}$) + 1.33 * (0.31 - Fe/(Fe+Mg)) - 61.92 if Fe/(Fe + Mg)) < 0.31 Equation 19 74

$TES_{00–Al^{IV}}$ (°C) = 106.2 * (($Al^{IV}O_{28}$) - 0.48 * (Fe/ (Fe + Mg) - 0.163) + 17.5 Equation 20 74

$Fv\rho s\rho pCn\ s - Cnp\ = Xn.$ Equation 21 129

X_{Mg} = [Mg/(Mg + Fe)] × 100 Equation 22 134

$CIA = [Al_2O_3/(Al_2O_3 + CaO^* + Na_2O + K_2O)] \times 100$ Equation 23 154

$CIW = [Al_2O_3/ (Al_2O_3 + Na_2O + CaO^*)] \times 100$ Equation 24 154

$ICV = (CaO + K_2O + Na_2O + Fe_2O_{3\ (tot)} + MgO + MnO + TiO_2)/Al_2O_3$ Equation 25 154

LIST OF ABBREVIATIONS AND ACRONYMS

AIPEA	Association Internationale Pour l'Étude des Argiles Nomenclature Committee
Alb	Albite
Am	Amphibole
Ank	Ankerite
Apa	Apatite
apfu,	Atoms per formula unit
BIC	Bushveld Igneous Complex
BMA	Bulk modal analysis
BSE	Back-scattered electron
Bt	Biotite
Calc	Calcite
Chl	Chlorite
CL	Cathodoluminescence imaging
Dol	Dolomite
EDS	Energy-dispersive spectroscopy
EDX	Energy Dispersive X-rays
EMPA	Electron Microprobe Analysis
f	Fugacity
FEG	Field emission gun
Fm	Formation.
Fsp	Feldspars
g/t	Grams per metric ton
GDP	Gross Domestic Product
Gi	Gibbsite
ICP	Inductively Coupled Plasma
Ill	Illite
IV	Tetrahedral site
Kao	Kaolinite
Kfsp	K-feldspar
MLA	Mineral Liberation Analyser
Mnz	Monazite
Mo	Montmorillonite
Ms	Muscovite
MSE	Mean squared error

Mt	Metric ton
No	Nontronite
OES	Optical Emission Spectrometer
P	Pressure (bar)
Po	Pyrrhotite
PSD	Particle size distribution
Py	Pyrite
Pyp	Pyrophyllite
Pyx	Pyroxene
QEMSCAN	Quantitative Evaluation of Minerals by Scanning Electron Microscopy
Qtz	Quartz
QXRD	Quantitative X-ray Diffraction
R	Gas constant (83.14 cm^3 bar K^{-1} mol^{-1})
Re–Os	Rhenium–Osmium Radiometric Dating
Rut	Rutile
Sa	Saponite
Se	Serpentine
SEI	Secondary-electron imaging
SEM/EDS	Scanning Electron Microscope and Energy Dispersive Spectrometry
Sid	Siderite
Sm	Smectite
T	Temperature
TML	Thabazimbi–Murchison lineament
Tons	Metric tonne
U–Pb	Uranium–Lead Radiometric Dating
V	Volume (cm^3)
VCR	Ventersdorp Contact Reef
VI	Octahedral site
WDS	Wavelength–dispersive spectroscopy
WDXRF	Wavelength dispersive X-ray Fluorescence
Wt.	Weight
wt.%	Weight percentage
XRD	X-ray Diffraction
XRF	X-ray Fluoresces
Zr	Zircon

ρ	Density

CATIONS AND ANIONS

Ca^{2+}	Calcium
Cu	Copper
Fe	Iron
Fe^{2+}	Ferrous iron
Fe^{3+}	Ferric iron
H^+	Hydrogen ions
H_2	Molecular hydrogen
H_2S	Hydrogen sulfide
K^+	Potassium ion
Na^+	Sodium ion
Pb	Lead
S	Sulfur
S^{2-}	Sulfide ion
SO_2	Sulfur dioxide
SO_4^{2-}	Sulfate ion

MINERAL NAMES AND FORMULAE

Apatite	$Ca_5(PO_4)_3(OH)$
Arsenopyrite	FeAsS
Biotite	$K(Mg, Fe_3^{2+})(Al, Fe^{3+})Si_3O_{10}(OH, F)_2$
Calcite	$CaCO_3$
Chalcopyrite	$CuFeS_2$
Chamosite	$[(Fe^{2+}{}_5Al)(Si_3Al)O_{10}(OH)_8]$
Chlorite	$(Mg,Fe)_3(Si,Al)_4O_{10}(OH)_2.(Mg,Fe)_3(OH)_6$
Clinochlore	$[(Mg_5Al)(Si_3Al)O_{10}(OH)_8]$
Fe oxides/hydroxides	$FeO–Fe_2O_3$
Galena	PbS

Gold (native)	Au
K-feldspar	$KAlSi_3O_8$
Muscovite	$KAl_2\ (AlSi_3O_{10})\ (OH)_2$
Pennantite	$[(Mn_5Al)(Si_3Al)O_{10}(OH)_8]$
Plagioclase Feldspar	$NaAlSi_3O_8$–$CaAl_2Si_2O_8$
Pyrite	FeS_2
Pyrophyllite	$Al_2Si_4O_{10}\ (OH)_2$
Pyrrhotite	$Fe_{1-x}S$
Quartz	SiO_2
Rutile/Ilmenite	TiO_2 – $FeTiO_3$
Sphene	$CaTiO\ (SiO_4)$
Uraniferous Minerals	$\pm UO_2\ (Ce, La, Y, Yh)\ PO_4$
Zircon	$ZrSiO_4$

GLOSSARY

The following definitions are given within the context of this study:

Archaean Craton: A segment of Archaean-age (>2.5 Ga) continental crust and, importantly, an underlying segment of genetically linked upper mantle or mantle keel (or tectosphere), where the crust–keel segment as a whole has attained and maintained long-term stability, thus allowing it to serve as a basement for accumulation of shallow-water or subaerial volcano–sedimentary sequences (or basins, following the definition below) on platforms, in large unrifted depressions or in rift valleys. Tectonic reworking is confined to the margins of the craton.

Archaean: An aeon of geological time extending from about 3.9 billion years to 2.5 billion years ago.

Aureole: A zone surrounding an igneous intrusion, in which contact metamorphism has taken place.

Banded iron formation (BIF): A sedimentary mineral deposit dominated by iron oxides, carbonates, or silicates that were deposited chemically from seawater. Most BIFs were formed between 2.5 and 3.5 billion years ago. Their formation is related to the rise of oxygen in the atmosphere.

Bedding plane: A surface separating layers of sedimentary rocks and deposits. Each bedding plane marks termination of one deposit and the beginning of another of a different character, such as a surface separating a sandstone bed from an overlying shale bed. Rock tends to break or separate readily along bedding planes.

Bedding: A collective term used to signify the presence of beds or layers, in sedimentary rocks and deposits.

Biogenic sediment: Sediments produced directly by the life processes of plants or animals.

Biogenic sedimentary rock: A sedimentary rock composed primarily of biogenic sediments.

Burial metamorphism: Takes place in an environment where pressure and temperature are barely more intense than during diagenesis, typically in a deepening sequence of sediments.

Chloritisation: A proposed mechanism for the lowering of the pH of the circulating fluid, which also causes significant loss of silica from altered rocks.

Clastic: Refers to rock or sediments made up primarily of broken fragments of pre-existing rocks or minerals.

Concretion: A compact mass of mineral matter, usually spherical or disk-like in shape and embedded in a host rock of different composition. They form by precipitation of mineral matter about a nucleus such as a leaf, or a piece of shell or bone.

Contact metamorphism: Metamorphism genetically related to the intrusion (or extrusion) of magmas and taking place in rocks at or near their contact with a body of igneous rock.

Continent: The definition of Rogers (1996) for ‘continent’ is employed. A continent consists of cratons, which are amalgamated by a network of orogens that may contain oceanic, island-arc, and continental margin rocks, as well as local fragments of older cratons. Continental lithosphere or crust, which is the segregation of SIAL from the mantle, is therefore not equivalent to a continent nor to a craton. The SIAL refers to the composition of the upper layer of the Earth's crust, namely rocks rich in silicates and aluminium minerals.

Continental crust: The part of the crust that directly underlies the continents and continental shelves. It averages about 35 km in thickness, but may be over 70 km thick under the largest mountain ranges.

Continental rise: The portion of the continental margin that lies between the abyssal plain and the continental slope. The continental rise is underlain by crustal rocks of the ocean basin.

Continental shelf: The portion of the continental margin that extends as a gently sloping surface from the shoreline seaward to a marked change in slope at the top of the continental slope. Seaward depths average about 130 m.

Cover Sequence: The term ‘cover sequence’ is used in a similar sense as ‘basin’ by the Geological Survey of Western Australia (1990). It is applied to unconformity-bound rock packages (of substantial thickness) made up of volcano-sedimentary rocks. Cover sequences possess unifying characteristics of stratigraphy and structure due to deposition during a regional episode or episodes of crustal depression. A cover sequence may be a tectonic component of a specific craton or orogen, or it may extend to and rest unconformably on adjacent cratons or orogens.

Craton: The stable portions of the continents that have escaped orogenic activity for the last 2 billion years. Made predominantly of granite and metamorphic rocks.

Detrital sedimentary rock: A sedimentary rock made up of detrital sediments.

Detrital sediments: Sediments made of fragments or mineral grains weathered from pre-existing rocks.

Diagenesis: All the physical, chemical, and biologic changes undergone by sediments from the time of their initial deposition, through their conversion to solid rock, and subsequently to the brink of metamorphism.

Geothermometer: An indicator of the temperature, or range of temperatures, at which a geological event (e.g. the crystallisation of magma or the metamorphism of pre-existing rocks) occurred.

Greenstone belt: An ancient geological structure composed of metamorphosed volcanic rocks with associated sedimentary rocks.

Metasomatism: A metamorphic process by which the chemical composition of a rock or rock portion is altered in a pervasive manner, and which involves the introduction and/or removal of chemical components as a result of the interaction of the rock with aqueous fluids (solutions). During metasomatism, the rock remains in a solid state.

Orogen: As defined by the Geological Survey of Western Australia (1990), is a tectonic belt characterised by regional metamorphism and abundant plutonic intrusion. Orogen-related rocks include deformed and reworked parts of older cratons. An orogen is the result of a distinct short-lived tectonic pulse, but may be reactivated during later tectonic episodes, as it remains a zone of weakness in the crust.

Orogenic: Mountain building.

Oxygen fugacity: An equivalent of the partial pressure of oxygen in a particular environment (e.g. atmosphere, rocks) corrected for the non-ideal character of the gas.

Petrogenesis: Origin of rocks.

Petrography: Description of rock textures.

Proterozoic: Geological time period from 1.5 billion to 542 million years before present.

1. INTRODUCTION

South Africa has a very mature mining history. For more than a century, it has enjoyed a reputation as the world's most valuable piece of mineral real estate, as the country hosts the world's largest known mineral resources. Represented are platinum group metals (PGMs), manganese, diamonds, nickel, chrome, vanadium, coal, gold, alumino-silicates, fluorspar, titanium, and zirconium minerals. These elements and minerals are hosted in various geological sequences, such as the Barberton Supergroup (which hosts gold, platinum group elements (PGEs), and base metal sulfides (Anhaeusser, 2012)), the Mesoarchaean Witwatersrand Supergroup (which hosts the world's largest gold and uranium deposits, (Frimmel, 2014)), the Transvaal Supergroup (which hosts the world's largest manganese, iron ore, and andalusite deposits), and the Bushveld Igneous Complex (which hosts the world's largest PGM, chromium, and vanadium deposits, (Cawthorn et al., 2006)). All of these sequences form part of the Kaapvaal Craton in South Africa (Figure 1), making it unique among Archaean cratons worldwide. The genesis of these deposits has been widely studied, although researchers have not yet reached a consensus regarding the craton's metallogeny. It was principally the Kaapvaal crust's unique enrichment in highly siderophile elements (HSE: Os, Ir, Ru, Rh, Pt, Pd, and Au) that motivated this study.

This project was founded on the hypothesis that the Kaapvaal Craton's exceptional gold and PGE concentrations are not coincidental and instead have a common geological origin. Gold and PGEs are HSEs, and while they are known to occur in low concentrations in the silicate portion of the Earth, they are presumably concentrated in its core (Schmidt et al., 2000). This thesis therefore proposes that the ultimate source of the gold in the Witwatersrand, and of PGEs in the Bushveld Complex, is traceable to an anomalous mantle domain that would have been tapped repeatedly, not only during the Mesoarchaean crust formation but also during the emplacement of the 2.054 Ga (U-Pb crystallization age by Scoates and Friedman, 2008) Bushveld Igneous Complex. The strong enrichment in HSEs in certain parts of the mantle could have been caused by inhomogeneous mixing with cosmic material that was added during the intense meteorite bombardment of the Hadaean to Palaeoarchaean Eras or the plume-like ascent of relics from inefficient core formation. Understanding the colloquial mineralisation in the Mesoarchaean palaeoplacer gold deposits of the Witwatersrand Supergroup and the magmatic PGE deposits of the Bushveld Igneous Complex would require monitoring the changes in the HSE distribution through the geological record, from the Kaapvaal cratonic rocks spanning the Palaeoarchaean Barberton Supergroup and Mesoarchaean Witwatersrand Supergroup, to the post-Great Oxidation Event strata of the Proterozoic Transvaal Supergroup (Figure 1).

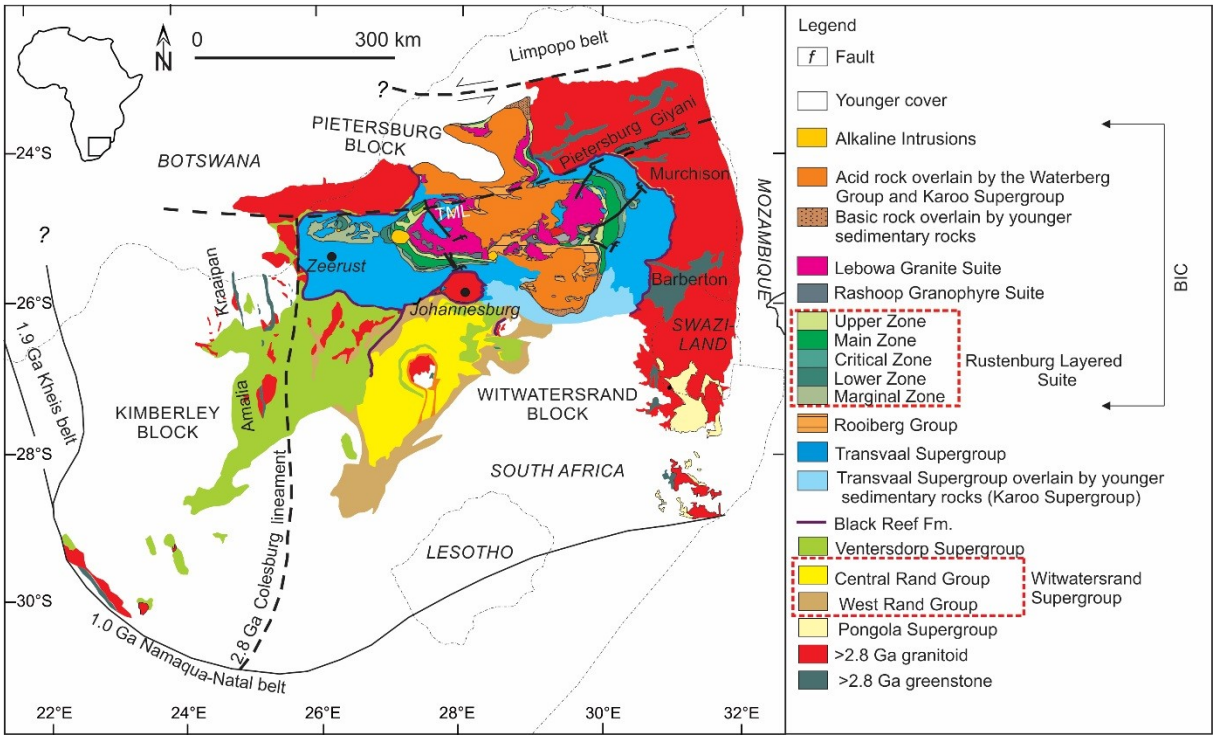

Figure 1: Surface and subsurface distributions of the main Archaean stratigraphic units of the Kaapvaal Craton. The Witwatersrand Basin fill comprises the West Rand and Central Rand groups; the purple line delineates traces of the Black Reef Formation at the base of the late Archaean to Palaeoproterozoic Transvaal Basin (modified after Frimmel et al., 2005a; Frimmel, 2014). BIC = Bushveld Igneous Complex (modified after Rose et al., 2011). TML = Thabazimbi–Murchison Lineament. Fm. = Formation.

The majority of the Palaeoarchaean Greenstone Belt gold deposits are tectonically classified as orogenic gold deposits, also referred to as lode, mesothermal, hydrothermal, shear-zone-hosted, and quartz-carbonate vein gold deposits (Groves et al., 1998; Goldfarb et al., 2001). In the Kaapvaal Craton, gold mineralisation in the Palaeoarchaean Barberton Supergroup is mesothermal in character, and its occurrence is associated with late-tectonic secondary shears and fractures. Host rocks include greenstone, greywacke, shale, banded ferruginous shale, quartzite, and a variety of chert. Alterations associated with these mineralised fractures comprise silicification, carbonatisation, sericitisation, and sulfidation (Brandl et al., 2006).

South Africa's Witwatersrand Basin is the world's largest gold province, and is estimated to have produced more than 52,000 metric tonnes of gold (40 % of global production). Moreover, it also hosts a major uranium source, which has produced 1.35×10^6 metric tonnes of uranium (Frimmel et al., 2005; Hartnady, 2009; Depiné et al., 2013). The gold in Witwatersrand Province's quartz pebble conglomerates occurs in the matrix as finely dispersed particles with a general grain size of 0.001–1.2 mm, which varies from reef to reef (Hallbauer and Joughin,

1972; Barton and Hallbauer, 1996). There is a strong association between gold and pyrite (Ramdohr, 1958), and radioactive minerals (e.g. uraninite and brannerite), which also occur in these fluvial conglomerates. Fe-oxides (predominantly magnetite) take the place of pyrite in marine sedimentary rocks, such as the shales in the West Rand Group (Frimmel, 1996). Rare earth elements (REEs) occur in the Witwatersrand reefs in different mineralogical forms. Although the REE occurrences are widespread, they are not present in economically feasible concentrations (Rasmussen et al., 2007; van der Watt and Waanders, 2012).

Sporadic palaeoplacer gold exists in the widespread Black Reef Formation, which sits at the base of the Neoarchaean to Palaeoproterozoic Transvaal Supergroup (Figure 1). The incised Black Reef Formation channels intersect the high-grade Witwatersrand reefs and Ventersdorp Contact Reef, increasing the potential for high-grade reef horizons (reworked channels, (Germs, 1982)). In addition to the palaeoplacer gold deposits, the Transvaal Supergroup is world-renowned for its gigantic deposits of iron ore, manganese, base metals, dolomite, limestone, asbestos, and andalusite (Söhnge, 1986; Meyer, 1988). It also bears a record of various significant geological events, such as the Great Oxidation Event, characterised by an increase in the concentration of atmospheric oxygen from less than 1 part per million (ppm) to 20,000 ppm by volume some 2.4 billion years ago, Gyr (Watanabe et al., 1997; Coetzee, 2001).

The concentrated PGEs in the Bushveld Igneous Complex (BIC) have been attributed to various magmatic processes (Figure 1). The BIC also contains significant amounts of chromium, vanadium, and other valuable elements (Eales and Cawthorn, 1996; Viljoen and Reimold, 2002). The world's largest known layered mafic intrusion, the BIC underlies an area of 65,000 km^2, with a maximum vertical thickness of 8 km (Kruger and Marsh, 1985; Reimold, 2002; Cawthorn et al., 2006). The BIC hosts more than 80 % of the world's PGE and chromium resources (Cawthorn, 2010). At approximately 2.054 Ga, magmas intruded the clastic sedimentary rocks of the Pretoria Group and the chemical sedimentary rocks of the Chunniespoort Group, part of the Palaeoproterozoic Transvaal Supergroup (Kinnaird et al., 2005; Scoates and Friedman, 2008). Fractional crystallisation led to the formation of Mg- and Fe-rich cumulates, followed at lower temperatures by Ca-, Al-, and Na-rich silicates (von Gruenewaldt, 1991; Vermaak, 1995). As more magma intruded and cooled, the cycle repeated itself under variable conditions, resulting in segregated layers. This segregation is recognisable on a scale ranging from the microscopic to megascopic accumulations of rock layers. The resultant layering also controlled the distribution of ore deposits. Chromite, ilmenite, and PGMs normally occur in more mafic regions, whereas magnetite, cassiterite, and zircon are generally restricted to more felsic regions. From time to time throughout this

process, the magma may have varied in composition, and layers of chromium-rich mineral (chromite) formed, yielding chromitite. Occasionally, variations in the magma's composition gave rise to a layer rich in base metal sulfides, arsenides, tellurides, and PGE alloys, forming PGMs (Kruger and Marsh, 1985; Viljoen and Hieber, 1986; Cawthorn, 1999a, 1999b).

Although a range of the above-mentioned mineral deposits are found in different stratigraphic units, rocks that can approximate their hinterland should be able to provide clues as to their HSE distribution. Marine shales are a reliable proxy for the general lithological make-up of a hinterland at deposition. Shales are also an important host for redox-sensitive metals (e.g. Mo, Ni, V, U, and Re), noble metals (e.g. Pd, Pt, Au, and Ag), and many other metals, such as Se, As, Hg, Sb, and REEs (Fan et al., 1973, Hirst, 1974; Holland, 1979; Coveney et al., 1992; Pašava, 1993; Murowchick et al., 1994; Lott et al., 1999). Therefore, selected regionally persistent marine shales of the Kaapvaal Craton appear to be the rock type that best represents both provenance and HSE distribution for any given stratigraphic unit.

1.1. Previous studies of Kaapvaal Craton shales

A significant volume of research has been done on the Barberton (Hofmann, 2005; Toulkeridis et al., 2015), Witwatersrand (Frimmel et al., 2005), and Transvaal supergroups (Eriksson et al., 2006) and the Bushveld Igneous Complex (Cawthorn et al., 2006; Rose et al., 2011) because of their economic and geological significance, as well as the availability of material for sampling. Much of this work has been published, but information is also contained in unpublished mining company reports. A large amount of geochemical data has been obtained from a number of different rock types throughout the Witwatersrand Supergroup, including mineralised conglomerates, quartzite, and banded iron formations (BIFs). Geochemical studies of the low-grade metamorphosed shales (metapelites) within the Kaapvaal Craton are limited in number and suffer from incomplete trace element datasets. Notwithstanding a regional lower greenschist–facies metamorphic overprint (Wallmach and Meyer, 1990; Frimmel, 1994; Phillips and Law, 1994; Toulkeridis et al., 1996), the sedimentary features of the various siliciclastic rock types are so well-preserved that I shall henceforth refer to those metapelitic rocks that retain their very fine, clay-sized grain size of less than 0.004 mm as 'shales'. Conversely, a more comprehensive geochemical dataset covering Kaapvaal Craton shale units may help to constrain systematic changes in the hinterland's lithology to the period of deposition, as well as to specific areas of the basin. This information should play a fundamental role in any discussion of tectonic setting and the likely origins of the various detrital components, including gold.

The shales of the Barberton Supergroup are some of the most studied in the Kaapvaal Craton, and have been used to constrain the provenances, source compositions, weathering, and diagenetic events that potentially occurred during the evolution of sedimentary sequences and tectonic episodes (e.g. McLennan, 1982; Tailor and McLennan, 1985; McLennan et al., 1993; McDaniel et al., 1994; Hemming et al., 1995; Jahn and Condie, 1995; Hofmann et al., 2003; Hofmann et al., 2013). More recently, Toulkeridis et al. (2015) used the approximately 3.5–3.1 Ga old Barberton greenstone belt shale geochemistry, along with Rb–Sr, Sm–Nd, and Pb–Pb isotopes, to constrain the sediment source materials and post-depositional evolution based on successive potential alteration impacts. The study by Toulkeridis et al. (2015) provided a more detailed account of the provenance and conditions of the post-depositional evolution, but did not discuss the HSE content of the Barberton Supergroup shales.

Fuller et al. (1981) provided the first systematic geochemical characterisation and provenance analysis of Mesoarchaean Witwatersrand Supergroup shale units. Wronkiewicz and Condie (1987) followed their lead, suggesting that the relative proportions of granite, basalt, and komatiite increased with time in the sediment source areas at the expense of tonalite, and that the Archaean granites' hydrothermally altered roof zones may have been the major source of detrital gold and uraninite in the Witwatersrand placers. This analysis was followed by a study by Watanabe et al. (1997), who concluded that the atmosphere had been oxic (i.e. $PO_2 > 1$ % PAL) since at least 3.0 Ga, and that even the rounded uraninite and pyrite grains in pre-2.4 Ga quartz pebble conglomerates were not detrital. This notion, however, is in conflict with a wealth of data, some of which is more recent, that has proven beyond doubt the detrital nature of rounded uraninite and pyrite (e.g. Frimmel, 2005; Hofmann et al., 2009; Frimmel et al., 2014).

Guy et al. (2010) employed multiple sulfur isotope ratios ($^{36}S/^{34}S/^{33}S/^{32}S$) and carbon isotope ratios ($^{13}C/^{12}C$) from non-conglomeratic metasedimentary rocks (including shales) from the Witwatersrand Supergroup to suggest that the input of crustal sulfur into the basin environment may have played a key role in Mesoarchaean glaciations (drawdown of H_2 and CH_4). Smith et al. (2013) studied the geochemistry, S isotopic composition, petrology, and sedimentology of the West Rand Group iron formations and established their depositional environments. Phillips and Powell (2014) reported additional geochemical analyses of Witwatersrand shales, emphasising post-depositional alterations. Unfortunately, they did not provide the underlying raw data, and consequently, their conclusions cannot be tested and compared with any new study. More recently, Fuchs et al. (2016b) focused on organic-rich shales within the Witwatersrand Supergroup and compared their chemistry with that of locally gold-rich hydrocarbon layers, which they interpreted as pyrobitumen. They concluded that the

Witwatersrand Supergroup's intrabasinal shale units were the source of migrating oils that ultimately led to the formation of the pyrobitumen. Although this last study provided very useful information on the conditions supporting post-depositional fluid infiltration (which caused some local mobilisation of ore components, such as gold), it was not concerned with sediment provenance. To obtain additional information on sediment provenance and the associated changes, both lateral and vertical within stratigraphic units, I thus examined chemical variations in the West and Central Rand groups' marine shale sequences. Bearing in mind the post-depositional metamorphic/hydrothermal overprint(s), I also assessed the extent of post-depositional alteration before interpreting the geochemical data on the least altered samples in terms of source rocks and the extent of palaeoweathering, whether in the Mesoarchaean hinterland or on former erosion surfaces within the Witwatersrand Supergroup.

The sedimentary succession of the Transvaal Supergroup's Palaeoproterozoic Pretoria Group represents a period of extreme environmental changes on Earth. That era fluctuated from global ice ages to periods of significant warming, thus it holds critical clues for understanding the Earth's ancient history. This succession has been studied in detail, and researchers have reconstructed the genetic stratigraphic model via integrated sequence stratigraphy, sedimentology, and geochemical analysis of shales and other sedimentary rocks (Coetzee, 2001; Coetzee et al., 2006). However, just like other Palaeoarchaean–Palaeoproterozoic Kaapvaal Craton sequences (i.e. the Barberton Supergroup, Witwatersrand Supergroup, and Black Reef Formation shales), there is no record of published geochemical data on HSEs.

1.2. Problem statement

Gold and PGEs comprise a select group of transition metals, HSEs, which are mainly concentrated in the Earth's core (McDonough and Sun, 1995; Schmidt et al., 2000, 2003). As a result, the highly evolved upper continental crust is relatively depleted in these elements. That layer thus presents a significant geochemical characterisation challenge, because of the low abundances of HSEs in the bulk continental crust (Keays and Scott, 1976; Nesbitt et al., 1987; Cameron, 1998; Cameron et al., 1992; Ravizza and Pyle, 1997; Gao et al., 1998; Webber et al., 2010). The average gold concentration in the bulk continental crust is estimated to be 1–3 parts per billion, ppb (Taylor and McLennan, 1995; Wedepohl, 1995; Terashima et al., 1994; Rudnick and Gao, 2005). The most recent study on the topic estimated that 1.5 ppb of Au, 0.5 ppb of Pt, and 0.52 ppb of Pd are finely dispersed in the average continental crust (Rudnick and Gao, 2005).

It is well known that shale is a rock type that typically represents the best mixture of continental crust at a given point in time (Taylor and McLennan, 1985; Wedepohl, 1995; Peucker-Ehrenbrink and Jahn, 2001; Park et al., 2012). Although HSEs have an affinity for sulfides and carbonaceous matter, shales enriched in these may also be more enriched in HSEs. Systematic variations in shale geochemistry, specifically with regard to HSE contents from the Palaeoarchaean to the Palaeoproterozoic Eras, offer testimony of the postulated variations in crustal HSE endowments over time. The abundance of HSEs in various crustal rocks is an important constraint on Au- and PGE-concentrating processes. The variable nature of shale source rocks results in a large range of gold concentrations, thus shale is an ideal rock for monitoring Au and PGE background concentrations (Meyers et al., 1992; Large et al., 2011, 2013; Pitcairn, 2011; Bryndzia and Braunsdorf, 2014).

Analysing HSE variations in the Kaapvaal Craton shales could thus provide significant insights into the genesis of the Witwatersrand Supergroup gold and the Bushveld Igneous Complex PGE deposits, and background concentrations can act as a proxy for the source region of Au and PGEs. Knowledge of the background concentrations of metals in different rocks has recently been used to constrain the provenance and formation mechanisms of gold deposits in New Zealand's Otago Schists, the state of Victoria in Australia, and Scotland's Dalradian metasedimentary belt (Pitcairn et al., 2006; 2010a, b).

1.3. Overall research scope

1.3.1. Motivation and primary research objective

Gold and PGE reserves are in decline in most of the world's contributing regions, including the Witwatersrand Basin (South Africa), the Bushveld Igneous Complex (South Africa), the Great Dyke (Zimbabwe), the Sudbury Igneous Complex (Canada), and the Stillwater Igneous Complex (USA) (Smith, 2016). The underlying hypothesis of this study is that the exceptional concentrations of Witwatersrand Au and Bushveld Igneous Complex PGEs (Figure 1) are not coincidental but share a common geological cause. I further build upon previous suggestions by Frimmel (2014) in that their genesis should be sought in the anomalous chemistry of the source regions of the mantle, from which the Kaapvaal crust emanated. Studies on Archaean and Proterozoic shale geochemistry are numerous, and have addressed general aspects of continental crustal evolution, regional provenances, and secular changes in the Earth's atmosphere. However, to our knowledge, none of these studies focused on the distribution of HSEs. One of the objectives of this thesis is therefore to produce reliable geochemical data

on HSEs for the Kaapvaal Craton sequences listed below (in geochronological order from youngest to oldest):

- Transvaal Supergroup (~2.6 to 2.1 Ga),
- Witwatersrand Supergroup (>2.98 to 2.78 Ga),
- Barberton Supergroup (~3.5 to 3.1 Ga).

The broader objective of this study is to improve our understanding about background values and their significance on the sequestration of Au and PGEs from the mantle into the crust over time. The genesis of these deposits has been widely researched, although scientists are not yet in agreement on the craton's metallogeny.

The study was undertaken in order to:

i. Examine chemical variations in shale sequences.

ii. Assess the extent of post-depositional alteration of the shale geochemistry prior to interpreting the geochemical data on the least-altered samples in terms of source rocks and the extent of palaeoweathering, be it in the hinterland or on erosion surfaces within the sequences, bearing in mind the post-depositional metamorphic/hydrothermal overprint(s).

iii. Provide more information on sediment provenance and associated changes in both the studied basins and stratigraphic levels.

iv. Document and evaluate Au and PGE anomalies in the Palaeoarchaean–Palaeoproterozoic shales, relative to the average continental crust.

v. Understand secular variations in Au and PGE contents that may suggest cratonic or stratigraphic controls.

vi. Evaluate the mineralogy and geochemistry of shales from the Kaapvaal Craton sequences to test whether there was an elevated Au flux into the marine depositories at the time of deposition and whether secular changes in this flux existed.

1.3.2. Exclusion of isotope data

Researchers have previously obtained important isotope composition information (e.g. C, Fe, and S isotopes) concerning the paragenesis of different mineral phases or organic matter in the Kaapvaal Craton shales (e.g. Jahn and Condie, 1995; Farquhar et al., 2000; Bekker et al., 2004; Hofmann, et al., 2009; Smith et al., 2010; Guy et al., 2010; Beukes, 2010; Marin–Carbonne, 2014). The shale isotope data (e.g. constrained Sr, Sm, Nd, U, and Pb) provide

the general age and share of juvenile material, and crustal residence times of melts from which potential source rocks might have been derived. Such information would be very useful for a cratonic provenance study, as such analyses usually reconstruct the sources of, for example, Neoproterozoic sediments from different cratons. However, this is not of concern for this study, since the source is the Kaapvaal Craton. Therefore, there is no need to seek further proof of them. What is nonetheless critical for understanding the larger debate on gold genesis is the variety of source rocks within that craton (or the lack thereof). For the isotopic characterisation of source rocks, I have referenced previous studies that dealt with isotopic compositions (e.g. Kositcin and Krapež, 2004; Frimmel et al., 2005; Koglin et al., 2010; Zeh et al., 2013).

1.3.3. Scope of the study

The field of geochemistry is extremely diverse, and this geochemical study focused on acquiring and interpreting major and trace element (including REE and HSE) background concentrations for Kaapvaal Craton shales. To that end, it characterises the chemistry, mineralogy, and texture of shales. It further discusses the genetic implications of the Au and PGE background concentrations for geochemical exploration models. The shales' mineralogy and texture were assessed via qualitative optical microscopy and semi-quantitative X-ray diffraction (XRD) using the Rietveld method. Their chemistry was studied by inductively coupled plasma mass spectrometry (ICP-MS), electron microprobe analysis (EMPA), X-ray fluorescence (XRF) spectroscopy, fire assays, and Laboratory Equipment Corporation (LECO) instruments. The information generated from this study will help to interpret the behaviour of the various major and trace elements in different geological eras within the same craton, ultimately improving the usefulness, accuracy, and reliability of background Au and PGE concentrations as signatures for valuable Archaean to Palaeoproterozoic mineral deposits. Other aspects of sedimentary geochemistry and metamorphic petrology, such as the experimental simulation of Au and PGE formation, craton HSE quantification, and fluid inclusion, are beyond the scope of this study.

1.4. Thesis structure

This thesis consists of nine chapters, and is constructed so that each chapter deals with a specific topic connected with marine shales of the Barberton, Witwatersrand, and Transvaal supergroups. Chapter 2 describes the geological setting of selected Kaapvaal Craton sequences and their relevance to this study. Chapter 3 presents aspects of sediment provenance, sedimentary geochemistry, and analytical techniques commonly applied to characterise clastic sedimentary rocks. Details of sample preparations, analytical methods, and data quantification techniques used in this study are presented in Chapter 4. The results

are then divided into two chapters: Chapter 5 provides details concerning the petrography and mineralogy of the shale samples, while Chapter 7 provides the geochemical results. Generally, the depositional environment affects the mineralogy and geochemical features of sediments, as it records information on the palaeoenvironment and its evolution. Therefore, Chapter 7 contains a complete discussion of the results, including the linkages between individual findings. Chapter 8 offers the conclusions of this study. Several recommendations for future research are presented in Chapter 9. All the results are also provided in the Appendix.

2. GEOLOGICAL SETTING

This chapter presents the geological setting of the Kaapvaal Craton, with emphasis on marine shales in the Barberton, Witwatersrand, and Transvaal supergroups. A more detailed summary of the sampled units is presented in Chapter 5. This chapter introduces the regional geological setting of the Kaapvaal Craton, followed by a more detailed summary of the stratigraphy of selected sequences. Although the study focused on the sampled marine shales, the stratigraphy of other sequences that have implications on the formulation of the research questions was included. These sequences include the following. (a) The Ventersdorp Supergroup, which is a cover sequence for the Witwatersrand Supergroup, and forms the basement of the Transvaal Supergroup. This implies that the sediment at the Base of the Transvaal Supergroup (i.e. Black Reef Formation) may have been partly sourced from the Ventersdorp Supergroup. The Ventersdorp Supergroup does not contain marine shales, thus it was not sampled. (b) The Bushveld Igneous Complex, which is the largest known preserved layered mafic intrusion in the work and hosts >80 % of the world's PGE deposits. The Bushveld Igneous Complex forms an integral part of this study as its PGE concentrations are hypothesised to originate from the mantle from which the palaeoplacer gold deposits of the Witwatersrand were sourced. It also does not contain representative marine shales, therefore the current study did not include samples from the Bushveld Igneous Complex, but I reference it in various discussions in order to explain where the PGEs were sourced. Other domains/building blocks of the Kaapvaal Craton such as the Dominion Group, various Archaean Greenstone Belts, and the Pongola Supergroup are mentioned in various discussions, but their stratigraphy is not discussed in this chapter because of the limitations of this study.

2.1. Regional geology of the Kaapvaal Craton

The Kaapvaal Craton (Figure 2) formed and consolidated over a period ranging from approximately 3.7–2.5 Ga, making it one of the oldest reasonably sized (~1.6 × 10^6 km^2) examples of an ancient continental fragment (De Wit et al., 1992). It comprises several crustal blocks that are separated from one another by major lithospheric suture zones, and can be subdivided into four main domains (Lowe and Byerly, 1999; Poujol et al., 2003; Schoene et al., 2009; Zeh et al., 2009):

(a) The eastern block, whose development ran parallel with that of the Barberton greenstone belt from approximately 3.6–3.20 Ga.

(b) The central block, the basement of which is largely made up of granitoid massifs (e.g. the exposures in the Johannesburg and Vredefort domes), followed by the deposition of the volcano–sedimentary Dominion Group and the Witwatersrand Supergroup.

(c) The northern block, comprising the Murchison (3.23–3.09 Ga), Pietersburg (2.95 Ga), and Giyani (3.20 Ga) greenstone belts.

(d) The western block, which is located west of the Colesberg magnetic anomaly and consists of the Amalia (2.75 Ga), Kraaipan (circa 3.08 Ga), and Madibe (3.10 Ga) greenstone belts, the Gaborone granite complex, and the granitoid terrane in the Kimberley region (3.25 Ga).

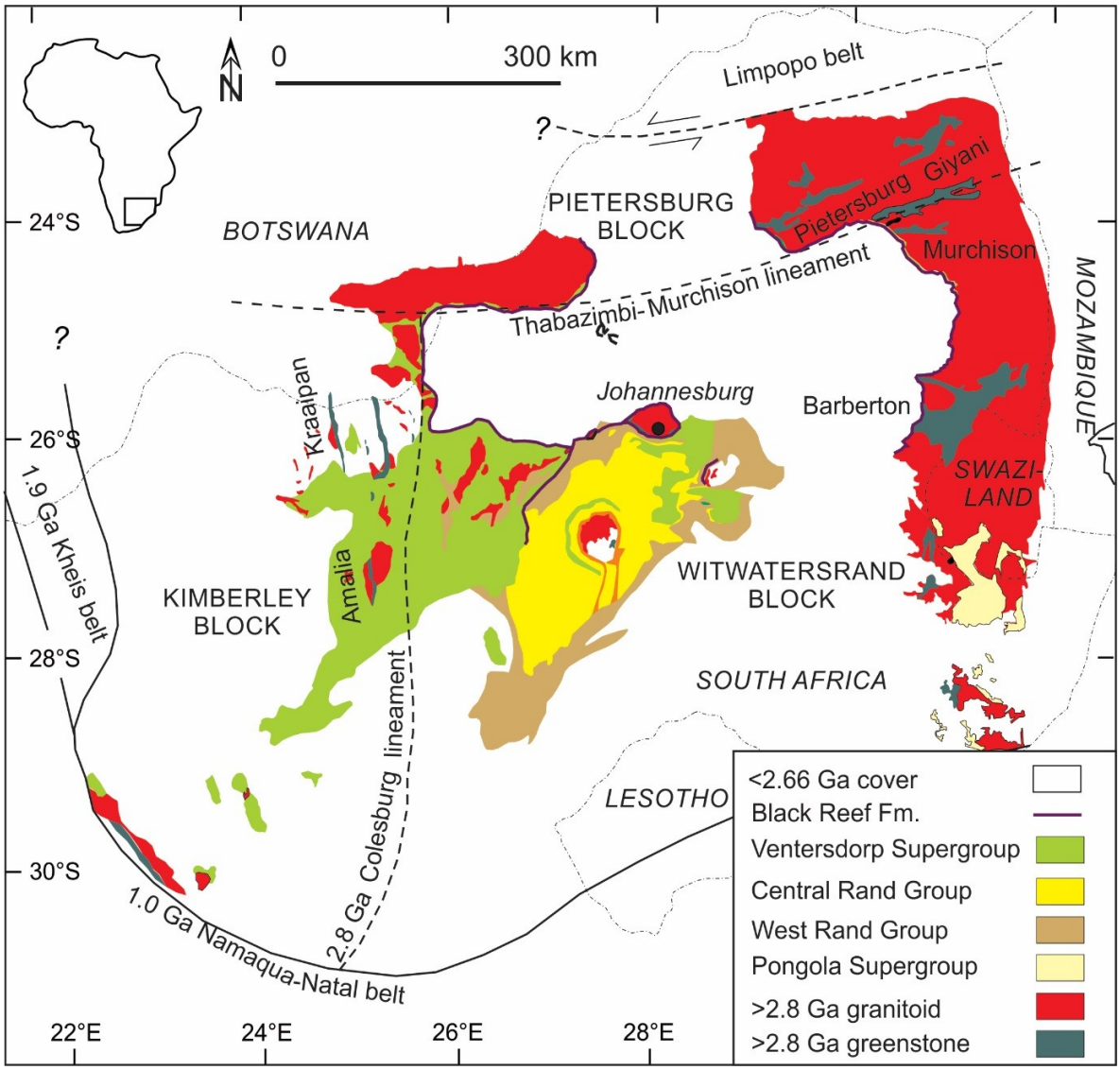

Figure 2: Surface and subsurface distribution of Kaapvaal Craton's main Archaean stratigraphic units. The Witwatersrand Basin fill comprises the West Rand and Central Rand groups, while the purple line delineates traces of the Black Reef Quartzite Formation at the base of the Palaeoarchaean to Palaeoproterozoic Transvaal Basin (Frimmel et al., 2005; Frimmel, 2014).

The Kaapvaal Craton is bordered to the north by the Limpopo Belt (Barton and Van Reenen, 1992a, 1992b; Van Reenen et al., 1987; Treloar et al., 1992). To the south, it is constrained by the ca. 1.0–1.2 Ga Namaqua-Natal metamorphic complex, and to the west by the ca. 1.8 Ga Kheis belt (Hartnady et al., 1985; Cornell et al., 2006; Bailie et al., 2007). Towards the east, the Kaapvaal Craton was rifted during the breakup of Gondwanaland. Palaeogeographical reconstructions suggest that the Grunehogha region of Antarctica was connected to the eastern side of the Kaapvaal Craton prior to the breakup (Groenewald et al., 1991).

I have selected as examples three prominent sequences. These represented (a) the oldest, best-preserved volcano-sedimentary sequences (i.e. the Barberton Supergroup), (b) a palaeoplacer gold province (i.e. the Witwatersrand Supergroup), and (c) a post-Great Oxidation Event shale sequence (i.e. the Transvaal Supergroup). These three sequences are frequently referenced in the international literature, and contain regionally persistent shales that are traceable throughout the Kaapvaal Craton. They afford geologists a unique opportunity to study the early history of the Earth, the evolution of the primitive crust, and the systematic changes between the Palaeoarchaean and Palaeoproterozoic Eras.

2.2. Local geology of the study areas on the Kaapvaal Craton

2.2.1. Barberton Supergroup

South Africa's Barberton Supergroup (Figure 3) is one of the world's best-preserved sequences of Mesoarchaean (3.5–3.1 Ga) volcanic and sedimentary rocks (Arndt, 2011). It is located in the south-east of South Africa's Mpumalanga Province. In ascending order, the Barberton Supergroup contains three stratigraphic units: (a) the Onverwacht Group, which consists of submarine ultramafic–mafic volcanic rocks and minor felsic volcanic and silicified sedimentary rocks, which form the base of the Barberton Supergroup; (b) the Fig Tree Group, which comprises shale, greywacke, and felsic volcaniclastic rocks with minor conglomerates and BIFs; (c) the Moodies Group, which consists of shallow-marine to fluvial sandstone and conglomerate with minor shale and BIFs (Hofmann, 2011). The Barberton Greenstone Belt is a north-east trending, isoclinally folded, metamorphosed volcano-sedimentary succession entirely surrounded by intrusive granitoid rocks. Although the Barberton rocks have been affected by a low-grade post-depositional metasomatic alteration (i.e. silicification, carbonatisation, and the widespread formation of secondary sericite and chlorite), they widely preserve primary volcanic and sedimentary lithology, structures, and textures (Nocita and Lowe, 1990; Lowe, 1991). This geological region underlies a mountainous zone extending in

a north-east direction for approximately 100 km. That band is up to 40 km wide and includes part of northern Swaziland (Lowe and Byerly, 2007).

In addition to being one of the world's best-preserved greenstone belts, the Barberton greenstone belt has produced more than 345 metric tonnes of gold since the discovery of that metal ca. 1883 (Anhaeusser, 2012). The bulk of the production comes from the Sheba (123.7 metric tonnes), New Consort (68.5 metric tonnes), and Fairview (63.4 metric tonnes) mines. These mines continue to produce 2.5–3 metric tonnes of gold annually at average grades of 10–12 g/t (Dirks et al., 2009). Most Archaean greenstone belt gold occurrences are tectonically classified as orogenic gold deposits, but often go by other names, including: lode gold, mesothermal gold, hydrothermal gold, shear-zone-hosted gold, and quartz-carbonate vein gold (Groves et al., 1998; Goldfarb et al., 2001). Gold mineralisation in the Barberton greenstone belt is structurally controlled, and the assemblage is similar to that of mesothermal gold ores in Western Australia's Archaean Yilgarn Craton (Dziggel et al., 2002; Dziggel et al., 2007; Vaughan and Kyin, 2004). Host rocks to the gold mineralisation range from greenstone to greywacke, and also comprise shale, banded ferruginous shale, quartzite, and a variety of chert. Wall-rock alterations associated with the mineralised fractures include silicification, carbonatisation, sericitisation, and sulfidation (Brandl et al., 2006).

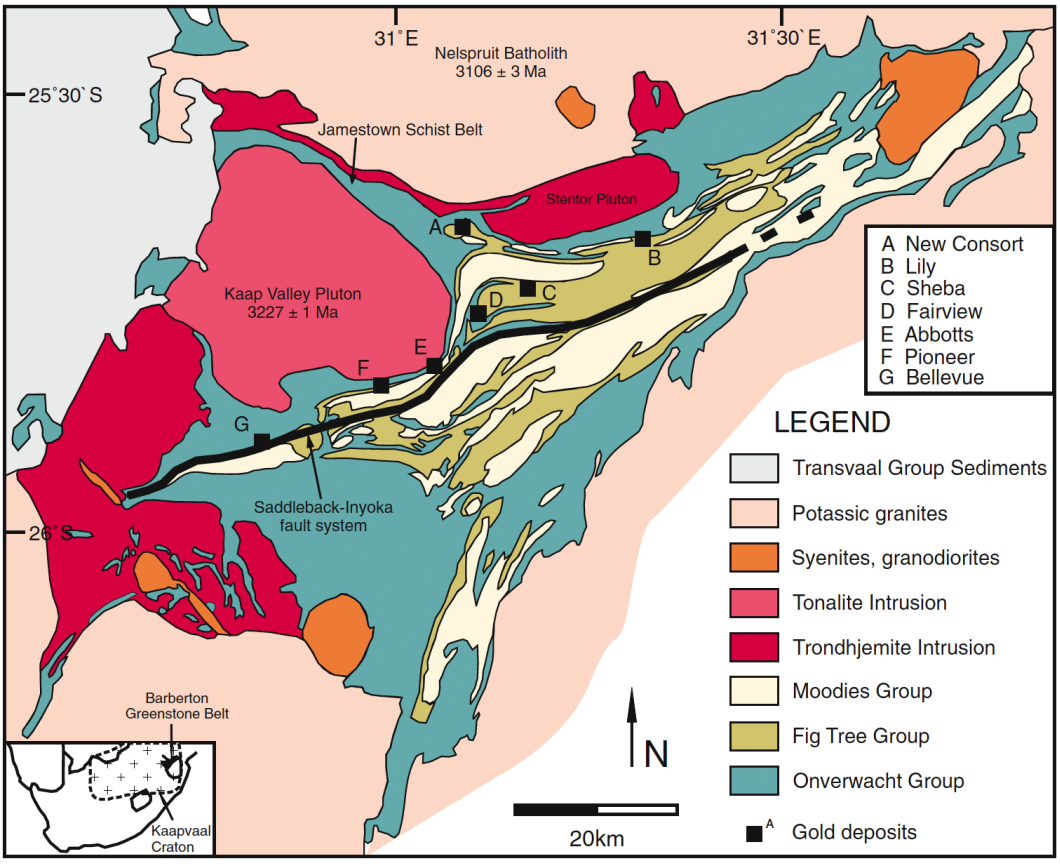

Figure 3: Geological map of Barberton Supergroup (modified after Otto et al., 2007).

2.2.1.1. Onverwacht Group

The 3.55–3.30 Ga Onverwacht Group is the base of the Barberton Supergroup, and it comprises metavolcanic basaltic mafic rocks with a predominance of komatiites of ultramafic composition (in the lower part of the group) and tholeiititic basalts of a more felsic composition (towards the top of the group; Viljoen and Viljoen, 1969; Lowe and Byerly, 1999). This group does not contain marine shales and was not sampled, but its proximity to the sampled Fig Tree and Moodies groups makes its composition relevant. The Onverwacht Group, located in the northern part of the Barberton greenstone belt, has a lithology composed of isolated extrusive and intrusive rock lenses surrounded by schist units from the north-west trending Jamestown Schist Belt (Anhaeusser et al., 1969). These rock units have been termed the Weltevreden Formation, and they are regarded as the youngest in the Onverwacht Group. The best available age constraint is a Sm–Nd isochron age of 3.29 ± 0.029 Ga (Lowe and Byerly, 1999). The Onverwacht Group is divided into six formations in the southern part of the Barberton greenstone belt. In chronological order (from oldest to youngest) these are the Sandspruit, Theespruit, Komati, Hooggenoeg, Kromberg, and Zwartkoppie Formations. A sedimentary chert unit known as the 'Middle Marker' separates the Komati and Hooggenoeg Formations (Viljoen and Viljoen, 1969), while the Hooggenoeg and Kromberg Formations are separated by a silicified unit known as the 'Buck Reef Chert'. The Mendon Formation forms the top part of the Onverwacht Group in the southern part of the belt. The overlying chert-rich Zwartkoppie Formation, which marks the group's contact with the overlying Fig Tree Group, is a separate unit (Lowe and Byerly, 1999).

2.2.1.2. Fig Tree Group

The Fig Tree Group (3.26–3.23 Ga) unconformably overlies the rocks of the Onverwacht Group (Condie et al., 1970; Eriksson et al., 1994; Kohler and Anhaeusser, 2002). The Fig Tree Group (>1500 m in thickness) is dominated by clastic sedimentary rocks, and has been divided into the northern and southern facies of the northern and southern terranes on either side of the Inyoka–Saddleback fault system. The northern facies contain deep-water sediments, whereas the southern facies are characterised by shallow-water sediments (Condie et al., 1970; Reimer, 1983; de Wit 1982; Lamb and Paris, 1988). The northern facies consist of the Ulundi, Sheba, Belvue Road, Bien Venue, and Schoongezicht Formations (Lowe and Byerly, 1999; Kohler and Anhaeusser, 2002; Brandl et al., 2006).

Marking the base of the Fig Tree Group is the Ulundi Formation, which is composed of carbonaceous and pyritic shale units, as well as banded chert layers (Hofmann, 2005). The Ulundi Formation shapes the Ulundi Syncline in the northern regions of the Barberton

greenstone belt. The Sheba Formation overlies the Ulundi Formation, and consists of turbiditic sandstone (siltstone and greywacke) with interbeds of shale and BIF units. The Belvue Road Formation overlies the Sheba Formation, with the former comprising carbonaceous shale with a few intercalations of greywacke, BIF, and dacitic, epiclastic rocks. The Bien Venue Formation overlies the Belvue Road Formation, and it contains quartz-muscovite schist, banded chert, phyllite, and biotite-chlorite schist. The Schoongezicht Formation, which consists of coarse- to fine-grained tuff, overlies the Bien Venue Formation (Condie et al., 1970; Heinrichs, 1980; Ward, 1999; Hofmann, 2005). The Schoongezicht Formation is a thinly developed unit, and is mainly composed of tuff and agglomerate accompanied by shale, grit, chert, and BIFs. It attains a maximum thickness of approximately 100 m in the area between the Eureka and Ulundi Synclines (Visser, 1956; Anhaeusser, 1976; Ward, 1999).

The Fig Tree Group in the southern facies consists of five formations: the Loenen, Ngwenya, Mapepe, Auber Villiers, and Schoongezicht Formations (Brandl et al., 2006). The Loenen Formation marks the base of the group. It is composed of laminated carbonaceous and ferruginous shales with silicified tabular sand-to-siltstone beds. The Loenen Formation is succeeded by the Ngwenya Formation, which consists of layers of jaspilitic BIFs (Hofmann, 2005). The Ngwenya Formation is succeeded by the Mapepe Formation, which is composed of conglomerate and sandstones (Nocita and Lowe, 1990). The Auber Villiers Formation, formed from dacitic volcanoclastic, ferruginous sedimentary units interlayered with conglomerate, and greywacke, overlies the Mapepe Formation (Lowe and Byerly, 1999). The Schoongezicht Formation forms the top of the Fig Tree Group and is located south of the Barberton greenstone belt (Heinrichs, 1980; Lowe and Byerly, 1999).

2.2.1.3. Moodies Group

The Moodies Group overlies the syn-orogenic Fig Tree Group, in some areas para-conformably and in others with a slight discordance. In some places, it lies directly on the Onverwacht Group. The Moodies Group is one of the best-preserved Mesoarchaean sedimentary units. It was deposited in a shallow-marine to fluvial setting, prior to the emplacement of the Kaap Valley tonalite pluton (Kamo and Davis, 1993). The Moodies Group deposition is dated as having begun at 3.22 ± 0.001 Ga, immediately following the dacitic volcanism of the Schoongezicht Formation. Moodies strata are tightly folded and juxtaposed with respect to the Kaap Valley Pluton, and intruded by post-deformation felsic rocks from ca. 3.21 Ga (Kamo and Davis, 1993). Radiometric age data and stratigraphic relationships constrain the total available deposition and deformation time for the Moodies Group to be between less than 1 million years and 14 million years. The timing is further constrained by age data obtained from felsic volcanics in the uppermost Fig Tree Group (Schoongezicht

Formation) directly underlying the Moodies basal conglomerate. These volcanics have ages of 3.22 ± 0.006 Ga (Kröner and Todt, 1988), 3.23 ± 0.003 Ga (Kröner et al., 1991), 3.23 ± 0.005 Ga (Byerly et al., 1996), 3.23 ± 0.001 Ga, and 3.22 + 0.01 Ga (Kamo and Davis, 1993). Further age data were gathered from the Moodies basal conglomerate's youngest granitic clasts, which yield zircon U–Pb ages of 3.23 ± 0.008 Ga (U–Pb sensitive high-resolution ion microprobe [SHRIMP], Sanchez-Garrido et al., 2011) and 3.22 ± 0.006 Ga (U–Pb multi-grain zircon, Tegtmeyer and Kröner, 1987) and sets of small porphyritic dykes cross-cutting the basal Moodies conglomerate. These dykes are dated from 3.21 ± 0.002 Ga ($^{207}Pb/^{206}Pb$ evaporation age on single zircons; Heubeck and Lowe, 1994b; Heights Syncline) and 3.23 ± 0.0004 Ga ($^{207}Pb/^{206}Pb$ single-zircon evaporation age; Layer et al., 1996; Eureka Syncline), indicating that sedimentation of basal Moodies strata must have been underway by that time.

The rocks of the Moodies Group occur as structurally isolated blocks bounded by faults (Lowe and Byerly, 1999). The outcrops include rocks in the Lily, Eureka, Moodies, Stolzburg, and Saddleback Synclines. The Moodies Group consists predominantly of fine- to coarse-grained, immature to mature, and dominantly quartzose sandstones deposited in alluvial, deltaic, tidal, and other shallow-marine environments. Subordinate jaspilites, shales, and siltstones represent deposition below wave-base. Along with a laterally extensive basaltic lava layer located at the approximate midsection of the Moodies Group, they exhibit a crude, regional, lithostratigraphic correlation between the tectonically separated Moodies Synclines (Anhaeusser, 1976; Heubeck and Lowe, 1994b; Lowe and Byerly, 1999; Kirstein et al., 2010; Ohnemüller et al., 2010; Heubeck et al., 2013). In most Moodies Group rock packages, a conglomerate unit marks the base of the group (Lowe and Byerly, 1999). The Eureka Syncline exposes Moodies Group rocks. The Moodies Group lithology in the Eureka Syncline has been classified into three formations. From oldest to youngest, these are the Clutha, Joe's Luck, and Baviaankop Formations.

The Moodies Group's thick sedimentation record largely consists of terrestrial and shallow-water settings, and is apparently free of major stratigraphic breaks. It preserves an excellent temporal stratigraphic resolution and offers a brief but very detailed window on Archaean surface environments and processes. Moodies strata north of the Inyoka Fault record a range of terrestrial and shallow-marine environments, including alluvial, fluvial-deltaic, shoreline, tidal, and shallow-middle shelf deposits (Eriksson, 1979, 1980a, 1980b; Heubeck and Lowe, 1994a). In contrast, the Moodies Group strata south of the Inyoka Fault are far thinner, lack marker horizons, and do not contain K-feldspar (Heubeck and Lowe, 1999a).

2.2.2. Witwatersrand Supergroup

The Witwatersrand Basin, located in the centre of the Kaapvaal Craton (Figure 4), is by far the world's richest known gold province, having contributed more than 40 % (>50,000 t) of the global gold production (Frimmel et al., 2005; Hartnady, 2009). Although widely cited in the literature, the term 'Witwatersrand Basin' is deceptive, because it refers to two different basins. These are the West Rand and the Central Rand basins, the fills of which were stacked on top of each other (Frimmel et al., 2005). Although most researchers have agreed on a foreland basin setting for most parts of the Witwatersrand Supergroup (Burke et al., 1986), the changes in the tectonic setting throughout its sedimentation history remain a matter of debate. With a total thickness of approximately 8 km, the Witwatersrand Supergroup has traditionally been subdivided into the West Rand Group (depositional age >2.98 to 2.91 Ga) and the overlying Central Rand Group (>2.90 to 2.78 Ga; SACS, 2006). The succession is the thickest along the western and northern margins, then thins towards the south and east (Pretorius, 1981, 1986).

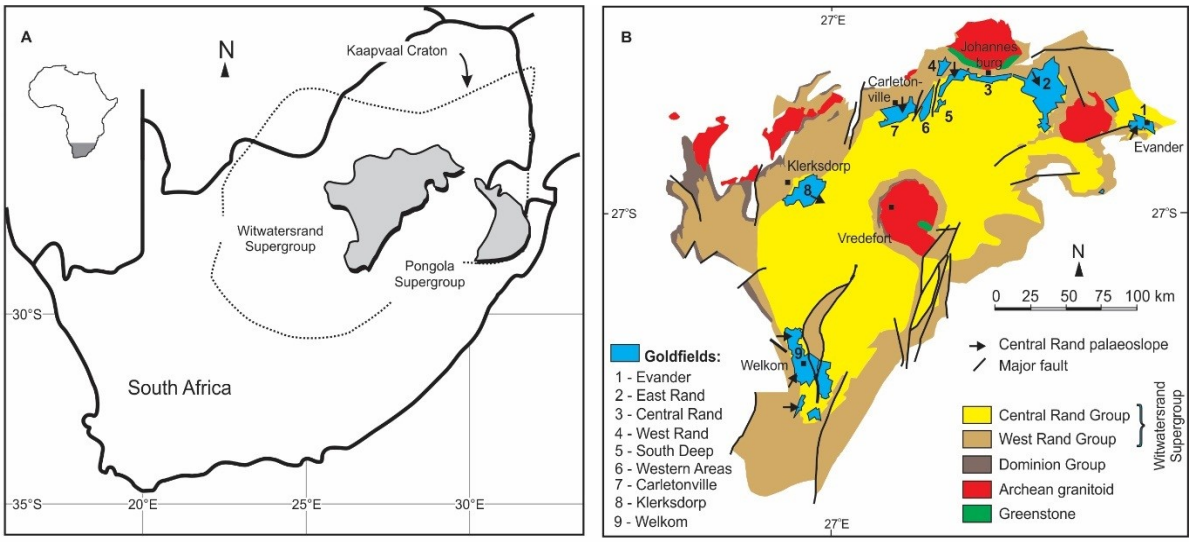

Figure 4: A. Overview of Witwatersrand Basin and extent of Kaapvaal Craton (after Guy, 2012). B. Surface and sub-surface geological map of Witwatersrand Basin with locations of major goldfields (from Frimmel et al., 2005).

The West Rand Group has contributed less than 5 % of Witwatersrand gold production, while the Central Rand Group's share is more than 80 % (Frimmel et al., 2005; Müller and Frimmel, 2011). The remainder comes from post-Witwatersrand reefs in the overlying Ventersdorp Group (e.g. the Ventersdorp Contact Reef) and, to a lesser extent, from the Black Reef Formation at the base of the Transvaal Supergroup. The genesis of the Witwatersrand gold deposits has been a topic of controversy for more than a century, with most researchers now

agreeing on a palaeoplacer model with some post-depositional hydrothermal remobilisation of ore constituents (for arguments for/against this hypothesis, see Frimmel et al., 2005). The source of the assumed detrital gold, however, remains enigmatic. In this regard, the question of sediment provenance comes to the fore.

Sedimentation of the West Rand Group, the lower portion of the Witwatersrand Supergroup, commenced after 2.985 ± 0.014 Ga (the youngest detrital zircon age in basal sandstone; Kositcin and Krapež, 2004) and comprises (in terms of pre-metamorphic protoliths) roughly similar amounts of shale and quartzwacke. Deposition of the West Rand Group primarily occurred in marine or intertidal environments in a semi-restricted basin, with only minor fluvial deposition. Intercalated magnetite-bearing shales ('magnetic shales') and iron-bearing formations are considered to have formed during the maximum transgression of an epicontinental sea, in some cases following deglaciation of the ice cover (Catuneanu, 2001; Smith et al., 2013).

The West Rand Group is subdivided into the Hospital Hill, Government, and Jeppestown Subgroups (SACS, 2006). Its minimum areal extent is approximately 42,000 km^2, and the group attains a maximum thickness of 5,150 m in the Klerksdorp goldfield. Based on consistent palaeocurrent directions from the north and north-east (in today's coordinates), the size of the basin must have been much larger than today's known extent, and most likely included the depositional area of the Pongola Supergroup further east (Frimmel and Minter, 2002; McCarthy, 2006).

The age spectra of the detrital zircon grains become less complex upsection through the West Rand Group (Kositcin and Krapež, 2004), indicating an increase in the hinterland's maturity, as can be expected for an evolving passive margin. Such a setting might appear to contradict estimates of the sedimentation rate, which total at least 60 m/million years for most of the West Rand Group. This figure is twice as high as that for Phanerozoic passive margins, but is similar to foreland basin subsidence rates. It is critical to remember, however, that sediment flux off the Archaean hinterland was most likely far more intense because of the lack of land vegetation, thus comparisons with more recent sedimentation rates are problematic. Within the Hospital Hill Subgroup, the shale/sandstone ratio decreases upsection, with the sandstone in the Hospital Hill Subgroup interpreted as subtidal quartz arenite. Higher up in the group, feldspathic sandstone and quartz wacke are more abundant, with shale and intercalated diamictite and BIFs becoming less prominent. This upward-coarsening sequence has been interpreted as reflecting the emergence of an orogenic front to the west and north-west, dividing the basin into a foreland basin in the north-west (filled by the upper West Rand Group)

and a passive margin further east (the Mozaan Group). This would have occurred after a foreland bulge separated the two (McCarthy, 2006; Smith et al., 2013).

The predominantly arenitic Central Rand Group sediments were primarily deposited in braided stream systems that formed coalescing alluvial fans, with subordinate littoral and shallow-marine deposits (Camden-Smith, 1980; Burke et al., 1986; Beukes and Nelson, 1995). Deposition of the Central Rand Group sediments ended between 2.84 ± 0.003 Ga (youngest detrital xenotime; Kositcin and Krapež, 2004) and 2.78 ± 0.003 Ga (authigenic xenotime; Kositcin et al., 2003). The Central Rand Group is subdivided into the Johannesburg and Turffontein Subgroups (SACS, 2006) and mainly consists of low-grade metamorphosed greywacke, conglomerate, and sandstone. It spans a minimum area of 10,000 km^2 and attains a maximum thickness of 2,880 m near the centre of its present distribution. The Central Rand Group's younger lithostratigraphic units were affected, at least along the basin margin, by syn-depositional folding and thrusting, attesting to syn-orogenic sedimentation with respect to collisional tectonic activity towards the north and west. The only major shale unit within the group is the Booysens Formation at the top of the Johannesburg Subgroup (Figure 5).

In contrast to the West Rand Group, the zircon age spectra within the Central Rand Group become more complex upsection, consistent with a foreland basin setting (Kositcin and Krapež, 2004). Such a tectonic setting is further supported by the palaeocurrent directions from all around the basin (Frimmel and Minter, 2002). Although this group's apparent sedimentation rates are, at 10–15 m/million years, far too low for a foreland basin, the true sedimentation rates for individual sequences must have been much higher (although unconstrained), in view of the numerous hiatuses in the deposition. Erosion and, in places, angular unconformities bear testament to these gaps.

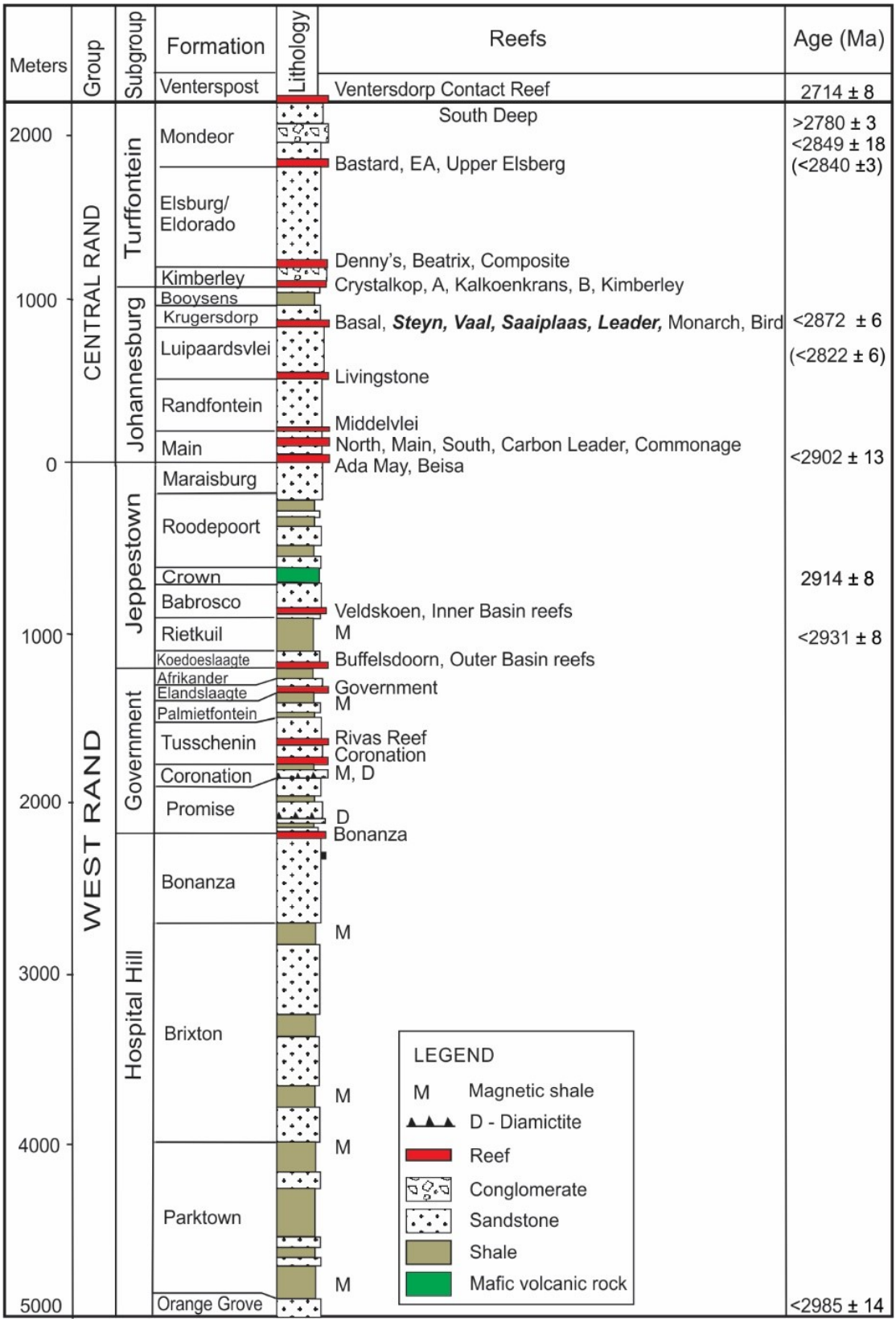

Figure 5: Witwatersrand Supergroup stratigraphic column (modified from Frimmel et al., 2005).

2.2.3. Ventersdorp Supergroup

The Neoarchaean Ventersdorp Supergroup contains the oldest uniformity-bounded sequences, and represents the largest and most extensive volcano-sedimentary sequence preserved on the Kaapvaal Craton (Cheney et al., 1996; Van der Westhuizen et al., 1991). The Ventersdorp Supergroup is preserved over approximately 200,000 km^2, extending from central South Africa into southern Botswana. The pristine nature of the sequence is demonstrated by the fact that it has subgreenschist-to-greenschist facies metamorphism (Cornell, 1978; Tyler, 1979; Crow and Condie, 1998).

The Ventersdorp Supergroup is dated at 2.729–2.665 Ga (Armstrong et al., 1991). The Klipriviersberg basalts, aged ca. 2.714 Ga, delineate the Supergroup's maximum age (Armstrong et al., 1991), which still remains to be verified, although several complications might slow that process. The Ventersdorp Supergroup is, in turn, unconformably overlain by sedimentary rocks of either the Neoarchaean to Palaeoproterozoic Transvaal Supergroup (2.64–2.2 Ga) or the Permian to Jurassic Karoo Supergroup.

The Ventersdorp Supergroup can be split into (a) the basal Klipriviersberg Group, which is limited to the Witwatersrand region and, thus, to the central Kaapvaal Craton (Figure 6; Van der Westhuizen et al., 1991), (b) the middle Platberg Group, and (c) the upper Bothaville and Allanridge Formations, which constitute the Pniel Group. In the western part of the Kaapvaal Craton, the best exposures of middle and upper Ventersdorp rocks occur between Kimberley, Ventersdorp, Mafikeng, and Vryburg (Keyser, 1998; Visser et al., 1976). The Klipriviersberg Group consists of six formations of mafic volcanic rocks (Winter, 1976).

The Platberg Group is composed of the Kameeldoorns, Makwassie, and Rietgat Formations. In turn, the Kameeldoorns Formation consists of sedimentary rocks, which are in places intercalated with Klipriviersberg Group lava close to the Platberg Group base. The base is composed of volcaniclastic diamictites. Moreover, wacke is intercalated with conglomerates, fine-grained reworked ash deposits, and carbonate-rich shales with locally developed stromatolitic textures. These are covered with rhyolites and rhyodacites of the Makwassie Formation, and these contain horizons of wacke up to 0.5 m thick. The Rietgat Formation, which is on top of the Makwassie Formation, also contains felsic lavas and locally coarse volcaniclastic diamictites (Winter 1976).

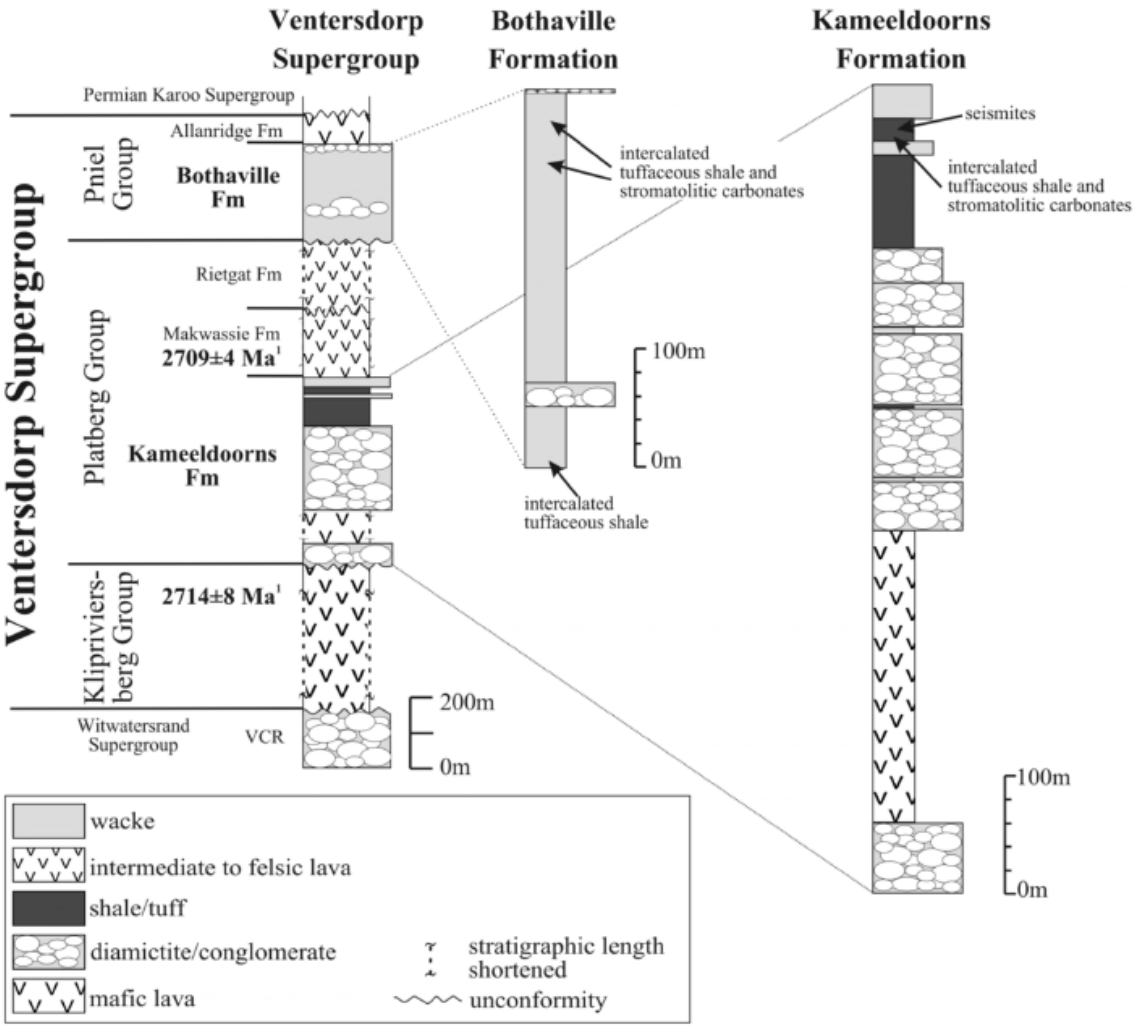

Figure 6: Ventersdorp Supergroup stratigraphic column (after Schneiderhan et al., 2011); the lithostratigraphy of the Kameeldoorns and Bothaville Formations is illustrated in detail. The U–Pb zircon ages for Klipriviersberg lavas and the Makwassie Formation are from Armstrong et al. (1991). De Kock (2007) dated the Kameeldoorns Formation at 2.73 ± 0.003 Ga, and Poujol et al. (2005) constrained an older age for the Makwassie Formation, at 2.709 ± 0.006 Ga; the Bothaville Formation remains unconstrained in age. Fm = formation, VCR = Ventersdorp Contact Reef.

The uppermost Pniel Group is subdivided into the Bothaville and Allanridge Formations, and unconformably covers the Platberg Group. The Bothaville Formation is of clastic origin, with wacke (most of which is medium sand grain-sized) framed by conglomerates at both its base and its top. The Allanridge Formation concludes the Ventersdorp Supergroup succession and is characterised by mafic lava flows that are petrographically and chemically similar to those of the Klipriviersberg Group. Provenance studies of the Supergroup's siliciclastic and volcaniclastic sequences have demonstrated that the Ventersdorp Basin was sourced from

two different regions, one with a Mesoarchaean history, and another that maintained its juvenile character at the time of deposition (Schneiderhan et al., 2011). This study did not include Ventersdorp Supergroup shale samples, but references them in places.

2.2.4. Transvaal Supergroup

After deposition of the volcano-sedimentary Ventersdorp Supergroup, the Kaapvaal Craton was subjected to large-scale erosion, resulting in a major unconformity at the contact with the overlying Neoarchaean to Paleoproterozoic Transvaal Supergroup rocks. The Transvaal Supergroup is structurally preserved in the Transvaal and Griqualand West regions (Figure 7), covering an area of at least 500,000 km^2. The Vryburg Formation, located at the base of the Transvaal Supergroup, has established the maximum age limit for the Transvaal Supergroup, 2.669 ± 0.005 Ga old (SHRIMP U–Pb ages; Gutzmer and Beukes, 1998) and 2.664 Ga (Sumner and Beukes, 2006). Its minimum age limits are a zircon SHRIMP age of 2.054 ± 0.0028 Ga, measured from the Critical Zone of the Rustenburg Layered Suite of the Bushveld Igneous Complex (Scoates and Friedman, 2008), and a 2.057 ± 0.0038 Ga zircon SHRIMP age for the Kwaggasnek Formation of the Rooiberg Group (Armstrong et al., 1991). This study sampled the shallow marine Black Reef Formation shales and shallow-to-deep marine Pretoria Group (post Oxidation Event Silverton Formation shales) in order to monitor the HSE variations and distribution in the Transvaal Supergroup. The Transvaal Supergroup is predominantly made up of siliciclastic and chemical sedimentary rocks with subordinate volcanic rocks. It attains a maximum thickness of about 12 km in the Transvaal and 8 km in Griqualand West. The basement on which the Transvaal Supergroup was deposited varies greatly. In Mpumalanga Province, it consists of Palaeoarchaean greenstone, gneiss, and granite, while in the North–West and Limpopo provinces, it consists of approximately 2.7 Ga old volcanic rocks from the Ventersdorp Supergroup. In Gauteng Province, the Transvaal Supergroup rests on a basement of Palaeoarchaean granites and greenstone, Mesoarchaean Witwatersrand sedimentary rocks, and Ventersdorp mafic rocks. The pre-Transvaal topography was rather irregular, with basement granites tending to form palaeo-highs. Below the Black Reef Formation, a palaeosol (chemically weathered basement rock) of several meters' thickness usually mantles the pre-Transvaal erosion surface (Button, 1973). The deposition of the Black Reef Formation fluvio-marine sands and shales followed a period of uplift and erosion. The Malmani Subgroup was deposited during several regressive cycles that were terminated by rapid marine transgressions (Figure 10).

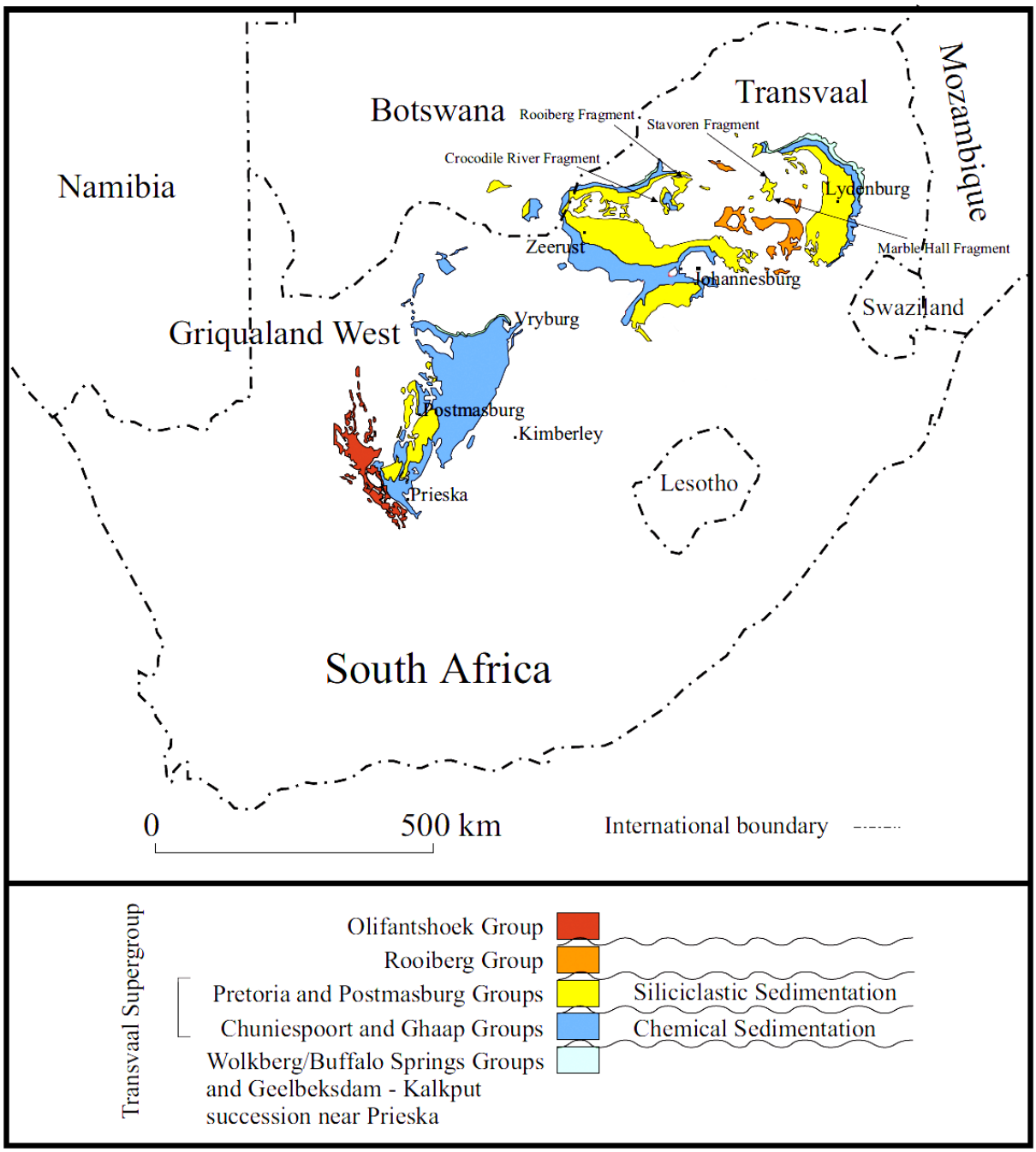

Figure 7: Distribution of Transvaal Supergroup in South Africa (modified from Dorland, 1999; Coetzee, 2001).

2.2.4.1. Black Reef Formation

The Black Reef Formation unconformably overlies the Wolkberg and Buffelsfontein groups, and is in turn conformably overlain by the Chuniespoort Group. It was previously known as the Kromdraai Quartzite, Berg, and Kantoor Sandstone (SACS, 2006). The term 'black reef' refers to the formation's dark colour, a result of the abundance of chlorite, and carbonaceous material in its rocks. On palaeo-highs, the Black Reef Formation in places rests directly on

pre-Wolkberg/Buffelsfontein basement. In contrast to the Witwatersrand Supergroup, the Black Reef Formation did not experience substantial metamorphism and deformation. Its metamorphic grade is subgreenschist facies (ca. 250–350°C and 1–2 kbar, with geothermal gradients of 30–35°C km^{-1}) which excludes the possibility of post-depositional introduction of gold by any orogenic, metamorphic fluids (Button, 1986; Frimmel, 2014).

The Black Reef Formation varies in thickness from a few meters to 50 m. It includes a mafic unit, the Serala Volcanic Member (Button, 1986), which reaches a maximum thickness of 10 m. The Black Reef Formation comprises Fe- and Mn-rich dolomite, carbonaceous shale, and quartzite (Button, 1986). The shales were deposited in the intracratonic Transvaal Basin in a shallow marine setting. They are representative of the Neoarchaean hinterland, regionally persistent, and commonly associated with carbonaceous matter. In some places, the shales comprise calcite veinlets. Towards the base of the Black Reef Formation, the shales are intercalated with silty material that sometimes hosts palaeoplacer gold. The base of the Black Reef Formation predominantly consists of quartz-pebble conglomerate intercalated with quartzite and carbonaceous shale, and contains significant concentrations of gold, uranium, and some PGEs. The poly-mineralised Black Reef Formation units are also widespread, with deeply scoured channels and gullies eroded into the underlying units (Figure 8). Exploration drilling has also indicated that multiple conglomerate beds intercalated with black shales are found in localised areas of the Black Reef Formation (Barton and Hallbauer, 1996). The conglomerates' matrix usually comprises poorly sorted siliceous quartzite, whereas the framework consists of predominantly well-rounded quartz pebbles with a diameter of 15 mm or less, along with lesser proportions of quartzite pebbles. Some localities of the Black Reef Formation horizon contain large pebbles with clasts that vary according to the underlying palaeo-surface's composition (Visser, 1989; Coetzee, 1996).

On a regional scale, the Black Reef Formation's dominant feature is the pyritic carbonaceous shales that alternate with argillaceous quartzite. Volcaniclastic conglomerates are present locally (Tyler, 1979). It is a thin but laterally extensive succession of siliciclastic rocks at the base of the Neoarchaean to Palaeoproterozoic Transvaal Supergroup. The quartz-pebble conglomerates of the Black Reef Formation contain a wide variety of ore minerals, namely, pyrite, chromite, zircon, rutile, chalcopyrite, arsenopyrite, gersdorffite, colbaltite, pyrrhotite, galena, sphalerite, uraninite, brannerite, monazite, xenotime-(Y), and native gold. (Frey, 1988; Barton and Hallbauer, 1996; Fuchs et al., 2016a). Gold occurs as discrete grains, <5 to 250 µm in diameter, and contains on average 86.6 wt.% Au and 0.53 wt.% Hg (Gauert et al., 2011). No major geological structures are associated with the Black Reef Formation, however, post-Transvaal Bushveld period faulting and the Vredefort event (2.050 Ga and 2.006 Ga,

respectively) have had an effect on the Black Reef Formation (Trieloff et al., 1994). The Black Reef Formation is the youngest gold-bearing deposit in South Africa within the context of Witwatersrand-type deposits (Frey and Germs, 1986; Els et al., 1995).

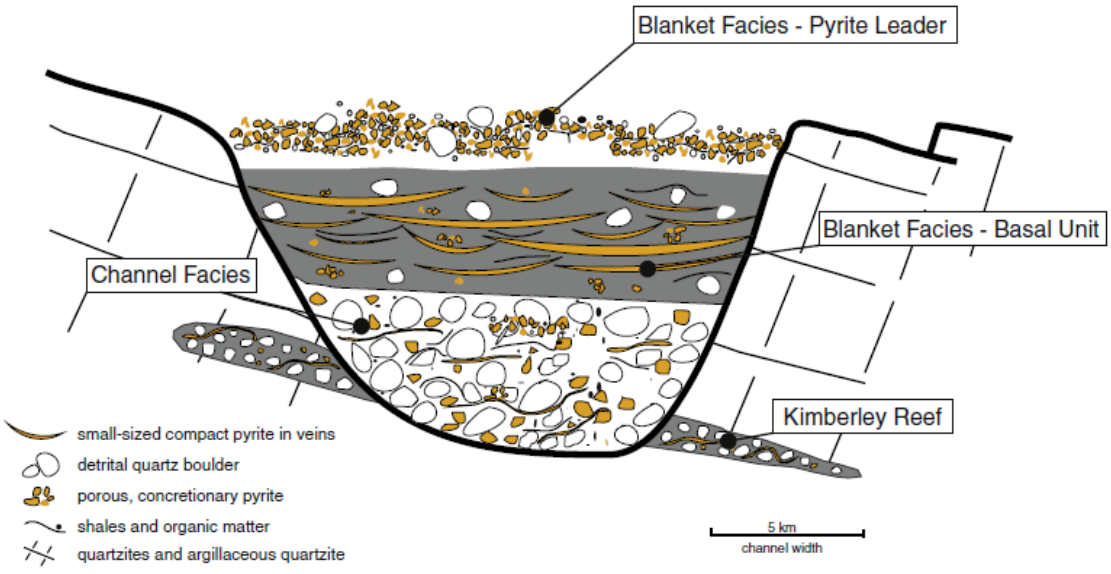

Figure 8: Cross-section illustrating the Black Reef facies types that incise the Witwatersrand Supergroup's underlying Kimberley Reef in the East Rand Basin (modified from Barton and Hallbauer, 1996; Fuchs et al., 2016a).

Over the last two decades, the Black Reef Formation has been extensively explored because of the economic potential of the West Rand and East Rand goldfields. Successful gold exploration projects on the Black Reef Formation include, but are not limited to, the Lindum Reef gold mine and Randfontein Estates gold mine in the West Rand region, as well as Mpumalanga's East Rand and Pilgrim's Rest gold mines (Meyer, 1988; de Bever, 1997). Several surface boreholes were drilled to further explore different regions of the Black Reef Formation, and most of these found the reef to contain low-grade gold deposits with erratic, medium- to high-grade tonnages and high levels of carbonaceous material from the shales. Thus, exploration companies did not consider most parts of the Black Reef Formation to be economically valuable compared to the Witwatersrand Basin gold-bearing conglomerates (i.e. the Carbon Leader, Middelvlei, and Ventersdorp Contact Reefs) in the West Wits line (de Bever, 1997; Coetzee, 1996). However, these surface boreholes clearly demonstrate that Witwatersrand-style gold mineralisation in the Black Reef Formation took place long after the deposition of the Witwatersrand sediments, and even after orogenic events that might have affected the Witwatersrand Basin fill.

2.2.4.2. Chuniespoort Group

The Chuniespoort Group (the Ghaap Group in the Griqualand West Basin is an analogous body) is subdivided into the Malmani Subgroup and the Penge and Asbesheuwels BIFs (Figure 9). This group was not sampled in this study, as it does not contain marine shales that represent the hinterland of that time. The Malmani and Campbellrand Subgroups comprises limestone and both chert-rich and chert-poor dolomite, and they reach a maximum known thickness of 2400 m. The Malmani Subgroup can be divided into the following.

(a) The Oaktree Formation, which consists of dark-coloured chert-poor dolomite, with wad and carbonaceous shale locally toward the base and occasional chert partings at the top of the formation.

(b) The Monte Christo Formation, which consists of light-coloured chert-rich recrystallised dolomite with stromatolites and basal oolitic bands.

(c) The Lyttelton Formation, which is chert-free and comprises dark brown dolomite.

(d) The Eccles Formation, which consists of chert-rich light-grey dolomite and silicified chert breccia.

(e) The Frisco Formation, which is chert-free and consists of dark-brown dolomite (SACS, 1980).

The Monte Christo Formation can be further subdivided into the Rietfontein, Tweefontein, Rietspruit, Swartkrans, and Crocodile River Members (Eriksson and Truswell, 1974). The subdivision of the Malmani Subgroup is based on the chert content, the presence or absence of stromatolite structures, and the range of such structures. An erosional unconformity separates the Malmani Subgroup from the Rooihoogte Formation.

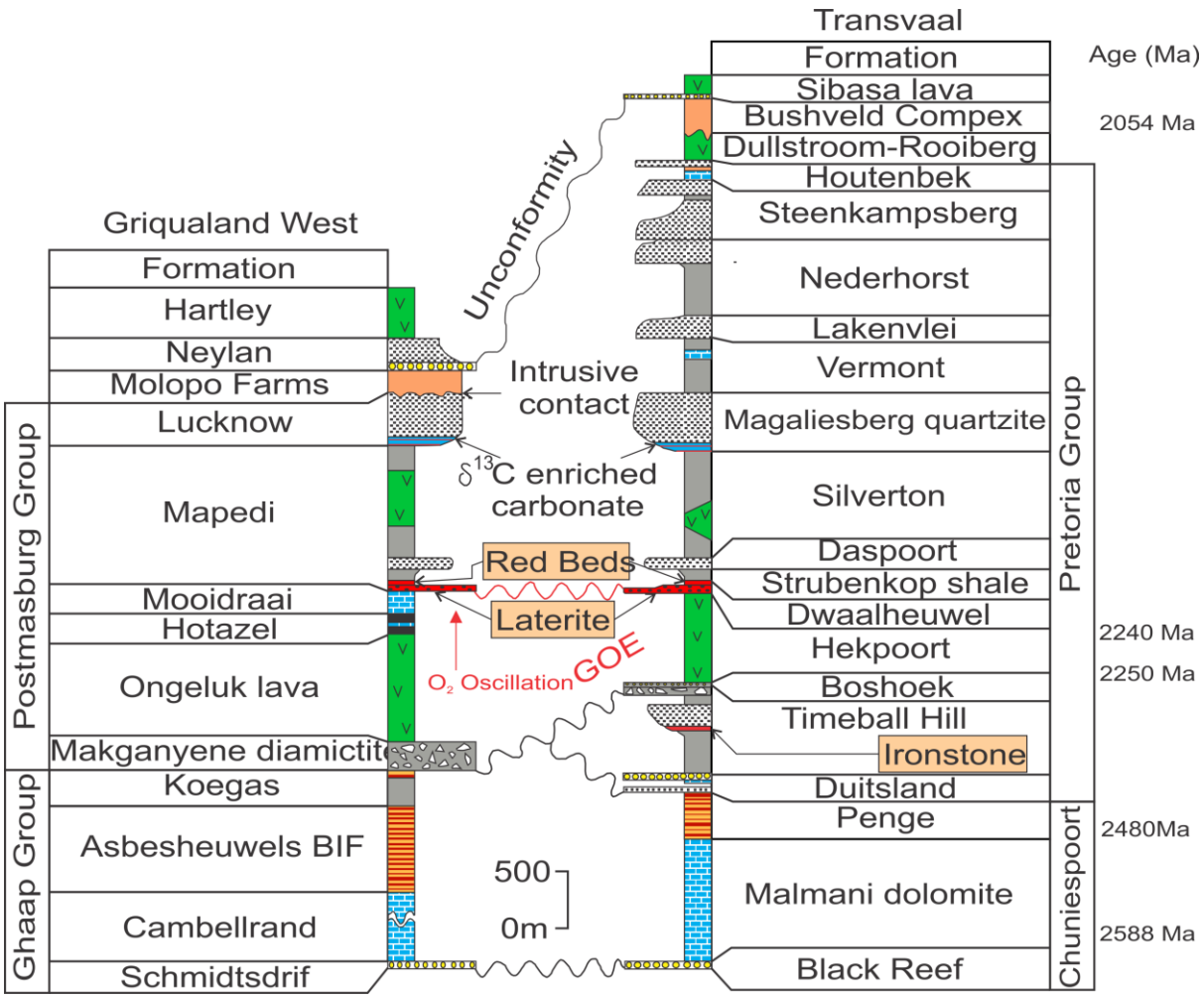

Figure 9: Stratigraphy of Transvaal Supergroup: the correlation between the Griqualand West and Transvaal regions (modified after Dorland, 1999; Beukes, 2010), with available radiometric ages is also indicated. GOE: Global Oxidation Event. Onset of the GOE occurred between ca. 2460 and 2426 Ma (Gumsley et al., 2017).

2.2.4.3. Pretoria Group

The Palaeoproterozoic sedimentary succession of the Pretoria Group (2.32–2.06 Ga) marks the transition from predominantly chemical sedimentation to clastic sedimentation from the Ghaap/Chuniespoort Group (Figure 10). Its equivalent is the Postmasburg Group in the Griqualand West Basin (Eriksson et al., 2006). The five upper formations are only preserved in the east of the Transvaal Basin, with a single western equivalent lacking any continuous outcrops (Eriksson et al., 1998; Eriksson et al., 2001). The Rooihoogte/Duitschland Formation, which consists of the lower Bevets Member (shales, siltstones, and chert) and the Pologround Member (sandstones and interbedded siltstones), is followed by an erosional contact on the Penge Iron Formation in the Transvaal region (Button, 1973; Obbes, 1995). This period represents a time of extreme environmental changes on Earth, from colder periods to

greenhouse climate states. The Pretoria Group's depositional palaeoenvironment was likely either an epeiric marine setting (Willemse, 1959; Visser, 1969; Button, 1973, 1986; Button and Vos, 1977; Eriksson et al., 2001, 2006) or an intracratonic basin with short-lived marine incursions (Crockett, 1972).

The Timeball Hill Formation is overlain by the Hekpoort Formation, which is composed of altered basaltic rocks (Engelbrecht, 1986). A well-preserved lateritic weathering profile, the Hekpoort palaeosol, caps the Hekpoort mafic rocks in the Transvaal region (Button, 1973; Dorland, 1999). The palaeosol can be traced westward from Transvaal into Botswana, where the overlying Dwaalheuwel Formation develops into a thick red-bed succession, very similar to that at the base of the Mapedi and Gamagara Formations in Griqualand West, with a marked basal erosional unconformity (Beukes et al., 2002). A major erosional unconformity at the base of the Neylan conglomerate cuts deep into the Mapedi–Lucknow succession and permits a correlation between the Mapedi–Lucknow and Dwaalheuwel–Magaliesberg strata (Van Niekerk, 2006). Intercalation of shale and quartzose sandstone characterise the volcano-sedimentary succession of the Pretoria Group (Schreiber, 1991), in which three main volcanic units have been identified. These volcanic units are, in ascending stratigraphic order, the Timeball Hill Formation's Bushy Bend Mafic Member, the Hekpoort Formation, and the Silverton Formation's Machadodorp Member (Lenhardt et al., 2012). The regionally persistent Timeball Hill Formation shales consist mainly of pyritic shales, and depending on the location within the Transvaal Bain, the shale coarsens upwards into either quartzite or oolitic ironstone. The unmineralised shales of the Timeball Hill Formation are not regionally persistent in the Transvaal area (Dorland, 1999). The Silverton Formation shales of the Palaeoproterozoic Pretoria Group provide an ideal environment to monitor changes in HSE concentrations, as they were deposited in oxidising palaeoenvironmental conditions. The Silverton Formation shale unit extends vertically for more than 500 m, making it the thickest marine shale unit in the Pretoria Group. The Silverton Formation consists of two thick units of carbonaceous shale and siltstone, separated from each other by a basaltic unit in the Potchefstroom area. The basaltic lava unit is regarded to be stratigraphically equivalent to the Machadodorp basaltic unit in the eastern Transvaal. Below the basaltic unit, the Silverton Formation contains upward-coarsening and upward-fining lithofacies sequences (Coetzee, 2001). These upward-coarsening lithofacies sequences are composed of unmineralised black shale at the base, grading into grey siltstone. The fining upwards sequences have fine-grained quartzite with contorted bedding at the base, and grade upwards into unmineralised black shales (Coetzee, 2001).

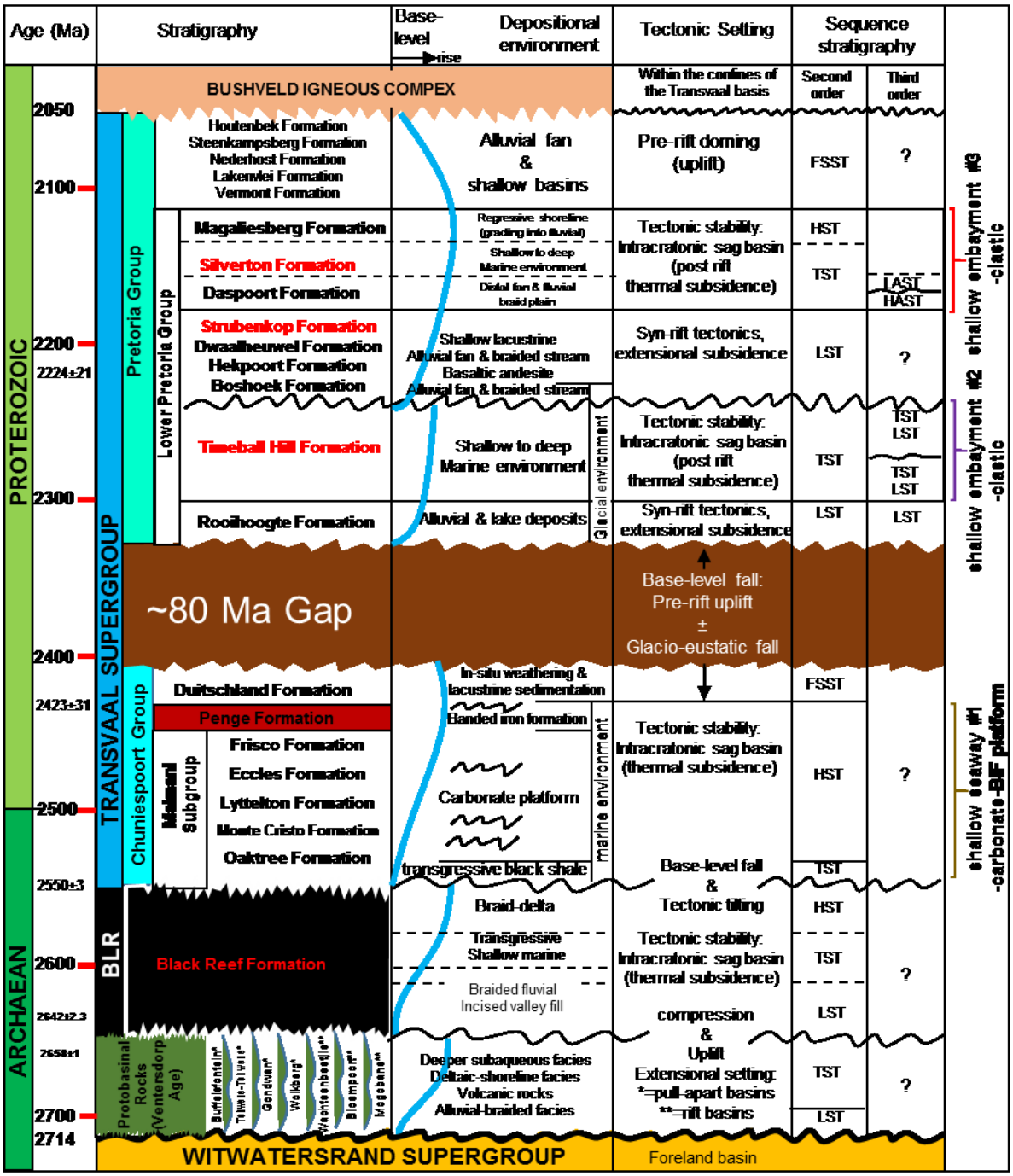

Figure 10: Summary of Transvaal Supergroup stratigraphy (modified after Eriksson et al., 2001).

2.2.5. Bushveld Igneous Complex

The ca. 2.054 Ga Palaeoproterozoic BIC of South Africa is the largest preserved layered mafic intrusion in the world (Figure 11). The BIC is estimated to host over 80 % of the world's deposits of platinum group elements (PGE) and chromium, and is also the world's largest reserve of vanadium (Cawthorn et al., 2006). The BIC has been subdivided in four rock suites, namely the (a) Rooiberg Group, (b) Rustenburg Layered Suit, (c) Rashoop Granophyre Suite, and (d) Lebowa Granite Suite (SACS, 1980; Cawthorn et al., 2006). The Rooiberg Group is mainly made up of siliceous volcanic rocks with sandstone and shale intercalations (Buchanan et al., 2002). The basal Dullstroom Formation of the Rooiberg Group is mainly basaltic andesite that becomes more felsic upwards and overlies the Pretoria Group. The Rustenburg Layered Suite has the greatest economic importance, since it hosts the PGE- and Cr-bearing units. It is preserved close to the surface in major compartments, namely the western, far western, eastern, south-eastern, and northern limbs (Cawthorn et al., 2006; Naldrett et al., 2009). Stratigraphically, it is subdivided into five zones, namely the Marginal, Lower, Critical, Main, and Upper Zones and comprises norite, gabbronorite, harzburgite, pyroxinite, chromitite, diorite, magnetite, and anorthosite. The Rashoop Granophyre Group overlies both the Rooiberg and Pretoria groups, and is subdivided on petrographic grounds into magmatic and metamorphic rocks (Walraven, 1995). The Lebowa Granite Suite occupies two semi-circular lobes in the eastern and western limbs of the BIC and comprises mainly granitic rocks. Two prominent magmatic processes have been proposed to explain the genesis of the BIC and its PGE mineralisation, commonly referred to as the 'uppers' and 'downers' models, and are summarised in Naldrett et al. (2009) and updated in Cawthorn (2011). The uppers model proposes that mineralisation was introduced by upward-migrating fluids (Lauder, 1970; Boudreau, 2008). In this model, a large amount of underlying rocks accumulated, and during the final crystallisation of the residual liquids, a water- and chlorine-rich vapour was produced. The water-rich vapour ascended, dissolving S, PGE, Cu, and Ni along the way, and as it encountered a crystal mush layer where the interstitial magma was under-saturated with water, the vapour dissolved into this magma, and its high-water content caused extensive re-melting that later crystallised the sulfides and PGM.

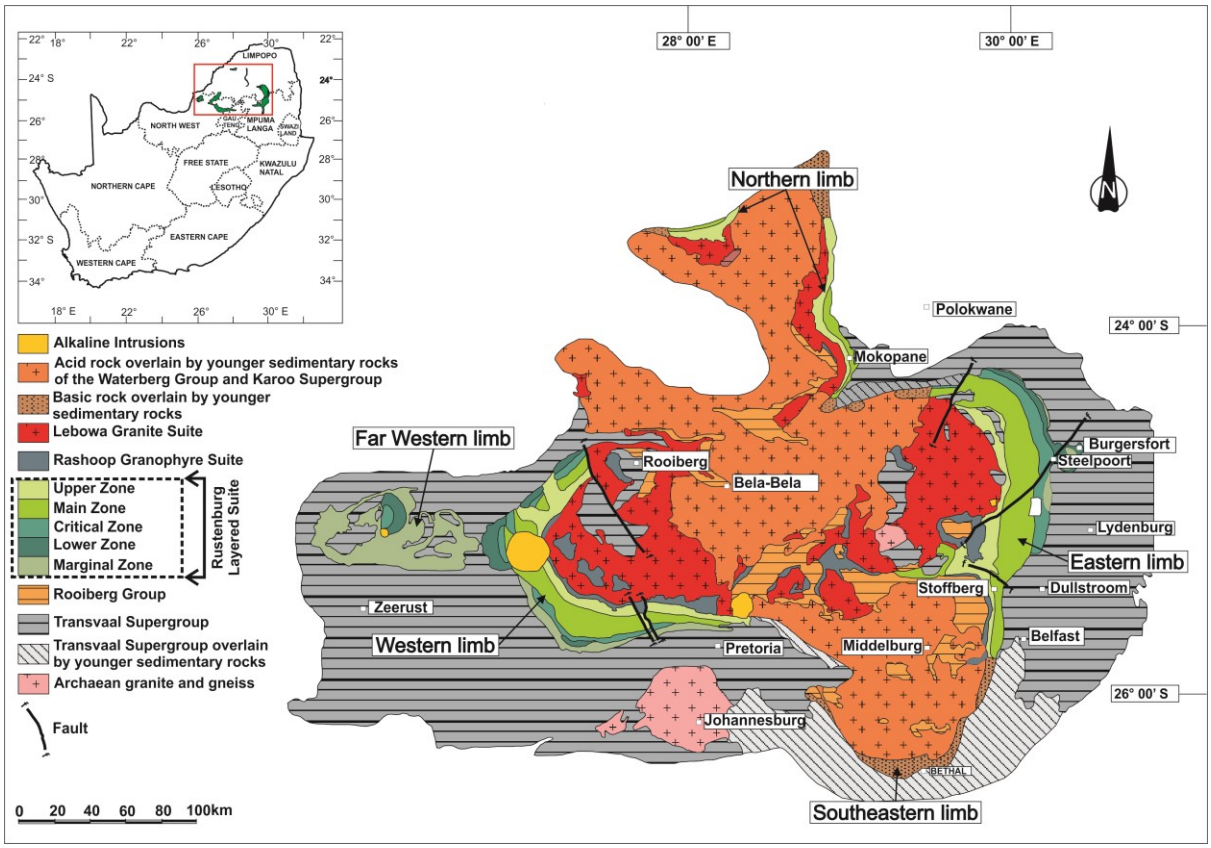

Figure 11: Simplified geological map of Bushveld Igneous Complex, which includes the Rustenburg Layered Suite, Rooiberg Volcanics, and Lebowa Granite Suite (Rose et al., 2011).

The downers model assumes that the PGE, Ni, and Cu were concentrated in an immiscible sulfide liquid that sank to the bottom of the magma chamber. In this model, two magmas are required, namely a resident magma and influx of a later magma. Pertaining to the origin of the magmas, Kruger (2002) proposes that the Lower and Critical Zone magmas were derived from a mantle source enriched in a seawater-rich subducted component, and that this dehydrated constituent was melted to form the Main Zone magmas. In one variation of this model, the newly injected magma mixed with the resident magma, which then formed an immiscible sulfide liquid (Campbell et al., 1983). This immiscible sulfide liquid progressively scavenged all the Cu, Ni, and PGE from the magma and settled to the bottom of the chamber, later crystallising as PGE-enriched base metal sulfides and PGMs. Cawthorn (2011) proposed a new variation on the downers model, stating that no magma mixing occurred, and that every layer with chromitite at its base was formed by a new injection of magma on top of the existing underlying rocks. The associated increase in pressure triggered the crystallisation of chromite and pyroxene, and also formed immiscible sulfide liquid (Cawthorn, 2005). Subsequent magma injections could have potentially completely eroded and removed the previous layer of chromite and pyroxene, or reworked it, re-melting to pegmatoidal feldspathic pyroxenite.

The final step was the injection of a denser magma of Main Zone affinity below the resident magma of Critical Zone affinity (Seabrook et al., 2005). The injection of the Main Zone magma beneath the Critical Zone magma would cause an increase in pressure that would precipitate chromite and pyroxene from the upper magma that settled into the newly injected magma, with plagioclase crystallising from the interstitial liquid in the lower magma (Seabrook et al., 2005). The PGE and sulfide mineralisation in this model is due to the pressure increase that caused chromite and pyroxene crystallisation, but the importance of chromite as a potential collector of PGE is also emphasised (Barnes and Maier, 2002; Cawthorn, 2011).

3. SEDIMENT PROVENANCE INDICATORS AND LITHOGEOCHEMISTRY ANALYTICAL METHODS

This chapter presents an overview of the available literature on the processes and factors contributing to sediment provenance and the chemistry of shales. In line with the study's objective, the geochemical tests and analytical methods commonly applied to characterise shales, Au, and PGE are discussed in detail, highlighting the gaps in the literature that were used to formulate the hypotheses and primary research objectives.

3.1. Sediment provenance

The term 'provenance' encompasses all factors related to the production of sediment or sedimentary rocks. Importantly, provenance studies identify a source area's elevation, source rocks, topographic relief, climate, tectonic setting, transport history, and diagenetic modifications (Nesbitt and Young, 1982; Bhatia and Crook, 1986; Wronkiewicz and Condie, 1987, 1989, 1990). Fine-grained sedimentary rocks, both clastic and carbonate, are believed to be the most abundant rock types making up the Earth's crust (Picard, 1971; Blatt, 1982), and have been used extensively for provenance studies. Fine-grained rocks appear to constitute somewhere in the region of 70 % (Holmes, 1937) to 80 % (Clarke, 1889, 1924) of all sediment ever produced. Of fine-grained sedimentary rocks, shale is considered to more effectively represent the average crustal composition than any other clastic sedimentary rock (McCulloch and Wasserburg, 1978). Shale is defined as a clastic sedimentary rock composed of very fine clay-sized particles (less than 0.004 mm in size), and has a low permeability.

The very fine-grained particles and inevitable diagenetic modification of clay minerals hamper the traditional petrographic approach in shale provenance studies (Taylor and McLennan, 1985). Thus, researchers have adopted other techniques based on geochemical signatures. Shales' absolute and normalised element abundances have been utilised with much success, mainly because of the seminal work of Taylor and McLennan (1985). Sediment provenance, weathering, and climatic conditions have been extensively modelled and inferred using major element abundance patterns (Nesbitt and Young, 1982). Even prevailing tectonic environments have been deduced from the major and trace element geochemical characterisation (Feng and Kerrich, 1990).

Shale geochemistry has provided an understanding of the continental crust's composition and evolution (Wronkiewicz and Condie, 1987). Chemical elements are quantitatively transferred into clastic sedimentary rocks during weathering and recycling, and are thus preserved in them (Taylor and McLennan, 1985). On the other hand, elements with a short residence time in

seawater are expected to transfer early into sedimentary rocks, so they play a significant role in recording the evolutionary history of the crust (Fedo et al., 1996). Certain incompatible to compatible elemental ratios (e.g. Ba/Co) provide an avenue for differentiating between a felsic provenance and a mafic provenance (Taylor and McLennan, 1985; Rollinson, 2007). High field strength elements (HFSEs) are generally resistant to change during weathering and alteration. As a result, their ratios are useful for characterising source rock compositions (Bhatia and Crook, 1986).

3.2. The distribution of elements and compounds as a provenance indicator in shale

Elements and compounds differ in terms of their stability and solubility in water, with factors such as free energy, mineral weathering reactions, pH, Eh, the concentration of different ions in water, and temperature all playing decisive roles. Because of stability differences, shales have an almost zero probability of hosting certain minerals, such as olivine (Rollinson, 1993; Merriman and Peacor, 1999; Deer at al., 2009).

Weathering is critical in determining the distribution of elements in shales. Depending on the nature of the parent rock and hydraulic regimes, various secondary minerals are formed as reaction products during and after weathering processes (Wronkiewicz and Condie, 1990). Silicate weathering is more important than carbonate mineral weathering as a long-term control of atmospheric CO_2 (McLennan, 1993; McLennan, 2001). Feldspars are usually transformed in upper crust conditions because of their presence in numerous igneous rocks, and their reaction products dominate the composition of many terrigenous sedimentary rocks (Taylor and McLennan, 1985).

The physical sorting of transported particles in water usually influences the composition of the primary sediment (McLennan, 1982; McLennan et al., 2006). This results in enrichment of heavy minerals, thus Th/Sc and Zr/Sc ratios are useful for tracing sedimentary recycling. The distribution of zircon in heavy minerals during recycling results in an increased Zr/Sc that is independent of changes in Th/Sc. This implies that ratios such as TiO_2/Zr are not effective provenance indicators in shales, because of the transport-related fractionation.

Better provenance indicators include La and Th, both of which are known to reside in silicic rocks. In contrast, Co, Sc, and Cr are more enriched in basic rocks (Taylor and McLennan, 1985). Therefore, La, Th, Co, Sc, and Cr are valuable indicators of source rock composition. Elements such as V and Mo are easily removed from minerals with oxidising solutions. Moreover, these elements are leached from source rocks during weathering in an oxygenated water environment, and they can precipitate from seawater under reducing conditions

(McLennan, 1982; McLennan, 2001). They are therefore expected to display a positive correlation with organic carbon. Other elements have a strong affinity for different solutions, and their distributions may provide clues on temporal and spatial emplacement. These elements include, but are not limited to, Ni, Cu, and PGE (chalcophile elements), which are known to strongly partition into a sulfide liquid that separates from magma (Pitcairn, 2011; Pašava et al., 2013; Fuchs et al., 2016b).

Indicator elements, and subsequent mineral abundances in the sediments, depend on the primary content of the indicator mineral in the source rock, the degree of post-emplacement/formation weathering of the indicator mineral's source, and the dispersion/dispersal transport mechanisms (e.g. fluvial, glacial, and aeolian). A variety of gold and PGE deposit indicator minerals exist, and are usually sampled from surficial sediments. Gold grains are considered the best indicator mineral for detecting the presence of gold deposits, although sulfides (e.g. pyrite, pyrrhotite, arsenopyrite, chalcopyrite, sphalerite, galena, pyrargyrite, proustite, and cinnabar), PGMs, tellurides, scheelite, cassiterite, barite, rutile, and secondary minerals (e.g. jarosite, limonite, goethite, and pyrolusite) may also be useful in specific regions (Schwartz, 1944; Boyle and Gleeson, 1972; Gleeson and Boyle, 1980; Barakso and Tegart, 1982; Youngson et al.,2002; Chapman et al., 2005; Scott and Radford, 2007). Similar to gold, PGEs can be the best indicator of their own deposits. However, this type of geochemical approach does not apply in most Archaean palaeosurfaces, as gold and PGM grains are extremely small (<1 μm) and occur in concentrations that are in the parts per billion. Furthermore, PGE indicators are usually partly or highly unstable in oxidised surficial sediments, and are thus not often present in those sediments in sufficient numbers to serve as useful PGE indicator minerals. For unoxidised Archaean sediments, a novel approach to assessing the background concentrations of these metals should provide clues regarding potential Au and PGE endowments.

3.3. Lithogeochemical methods commonly applied in shale, gold, and platinum group elements characterisation studies

Lithogeochemical studies of shale require a detailed geochemical characterisation of rock samples. Commonly, shale lithogeochemical studies require accurate analysis of both mobile and immobile elements (major and trace element geochemistry, including REEs and HSEs, (Meyers et al., 1992; McLennan, 2001; Hofmann, 2005; Pitcairn, 2011)). This information aids in the understanding of shale provenance and in quantifying any processes that may have affected them. This is partly because shale constituents can originate from the disintegration

and weathering of pre-existing rock systems, as well as from the precipitation of compounds from solutions with or without the assistance of biological mechanisms (Bauluz et al., 2000).

Lithogeochemical techniques are also useful for geochemical fingerprinting, measuring crystal fractionation, identifying regolith processes, and calculating stratigraphic correlations (Hofmann et al., 2013). Analytical techniques commonly used for shale geochemical studies include both fusion and acid digests with XRF, ICP-OES, and ICP-MS (Pitcairn et al., 2006; Guy et al., 2010; Fuchs et al., 2016a). Various studies have proven that acid digestion offers a 'near total' dissolution of almost all mineral species, targeting silicates not dissolved in less aggressive aqua regia digests (Nesbitt et al., 1987; Terashima, 1988; Arne et al., 2008). Prudently staged digestion phases reduce losses due to the volatilisation of some elements. Highly resistant refractory minerals (e.g. zircon, cassiterite, columbite-tantalite, ilmenite, xenotime, rutile, barite, and wolframite) require a stronger fusion digestion to guarantee complete dissolution (Arne et al., 2008).

All of these methods have the potential for accurate quantification with low detection limits, although ICP-MS methods usually produce the lowest detection limits (Hall and Bonham–Carter, 1988). Among the different sample fusion techniques, lithium borate fusion offers a relatively low-temperature and aggressive digestion that dissolves almost all geological samples while limiting losses due to volatilisation. This technique can be optimised for a wide range of element concentrations. Major element analysis can be carried out via borate fusion with either ICP-OES or XRF. Nonetheless, XRF is the more precise option, although highly mineralised samples may be more amenable to an ICP-OES (Caporali et al., 2010). Additional elements may be analysed via ICP-OES and/or ICP-MS. Upper and lower limits may vary with the instrument type and sample matrix. Lithium borate fusions are not a suitable technique when the sulfur and copper content of the sample exceeds 2 % and 1 %, respectively. Likewise, XRF is not a suitable method for borate fusions in which the total REE oxide content exceeds 1 % (Lötter, 2014).

There are several well-developed methods for analysing Au and PGE in low-concentration materials, and these usually involve the dissolution of Au and PGE from the geological material, followed by pre-concentration and quantification of the precious metals (Van Loon and Barefoot, 1991; Terashima, 1988; Pitcairn et al., 2006). Aqua Regia digestion, for example, has been proven to produce low recoveries of Au compared to fire assay and complete acid digestion methods (Hall et al., 1989). Precious metals are best analysed by fire assay, with lead collection used to analyse Au, Pt, and Pd. In contrast, nickel sulfide collection is applicable for the full suite of PGEs (Ely et al., 1999; Pitcairn et al., 2006, 2010). Other commonly used quantification methods include neutron activation analysis (Tilling et al., 1973;

Keays and Scott, 1976; Nesbitt et al., 1987) and atomic adsorption spectroscopy (Terashima et al., 1994; Zentilli et al., 1985).

In the last two decades, PGE analysis has primarily relied on neutron activation. This method has been particularly effective for Ir, which can be analysed by instrumental neutron activation analysis (INAA) without dissolving the sample and applying radiochemical separation procedures. The other PGEs are more than 10 times less sensitive to INAA (Palme, 2008). Their analysis requires lengthy radiochemical procedures. With the increasingly popular use of ICP-MS, INAA has lost ground. It is also worth noting that fire assay flux recipes have been carefully formulated over a century to optimise precious metal recovery in diverse mineralogical matrices (Van Loon and Barefoot, 1989). Further flux modification and reductions in the charge weight can be used to improve recoveries in difficult sample matrices, such as shale.

A significant problem in accurately quantifying certain elements (e.g. Au) in unmineralised rocks is their heterogeneous distribution, i.e. the nugget effect (Van Loon and Barefoot, 1989). However, Pitcairn et al. (2006) demonstrated that analyses of large sample aliquots (e.g. 10 g) or multiple smaller aliquots from the same sample provide more representative concentrations (e.g. Pitcairn et al., 2006). Carbon and sulfur analyses are possible via a variety of spectroscopic or gravimetric methods, with the possibility of using pre-treatments to target specific forms of the analysed element (Gazulla et al., 2012).

4. METHODOLOGY

This chapter presents the experimental methods carried out in this study. Related tasks included sample preparation, characterisation of the sample for mineralogy, and definition of the chemical and geostatistical methods used to average the data without compromising their integrity. This chapter also explains the different test methods used to characterise the studied shales.

4.1. Sampling and sample preparation

A total of 307 unmineralised, partly silty shale samples, free of hydrothermal overprint (such as quartz and/or carbonate veins) from Kaapvaal Craton sequences, i.e. the Transvaal Supergroup (~2.6 to 2.1 Ga], Witwatersrand Supergroup (>2.98 to 2.78 Ga), and Barberton Supergroup (~3.5 to 3.1 Ga), were collected for this study. Particular emphasis was placed on only collecting samples from well-constrained stratigraphic intervals with a well-understood alteration history or no well-understood alteration history. Errors introduced into the final results because of the use of redundant, biased sampling techniques cannot be offset by via statistical manipulation of the data. Sampling for geochemical analysis was limited to drill cores, underground chip samples, and near-surface samples (Figure 12) from different sequences of the Kaapvaal Craton to avoid the effects of surface weathering.

Once the samples were selected, the sample position within the core (top–bottom), together with the rock type, was noted on the core tray and in a notebook. The information was later transferred to electronic format and captured in Datamine, DHLogger, and Fusion Database, with backups stored in customised databases. Samples were cut in half down the orientated centre line across the bedding. One half was retained in the core tray as a record of the core, while the other half was cut again to yield quarter-core samples.

All samples were carefully washed with distilled water, dried, and then visually examined. Samples that did not contain veins or evidence of mineralisation were crushed into coarse particles (3–10 mm) using a jaw-crusher. These were subsequently picked to remove fragments containing the original drill core surface. Picked particles were further washed with distilled deionized water (several times, to remove attached dust), dried, and pulverised in an agate mill. Between each milling run, coarse quartz sand was milled to minimise cross-contamination between the samples, and duplicate control samples were also processed.

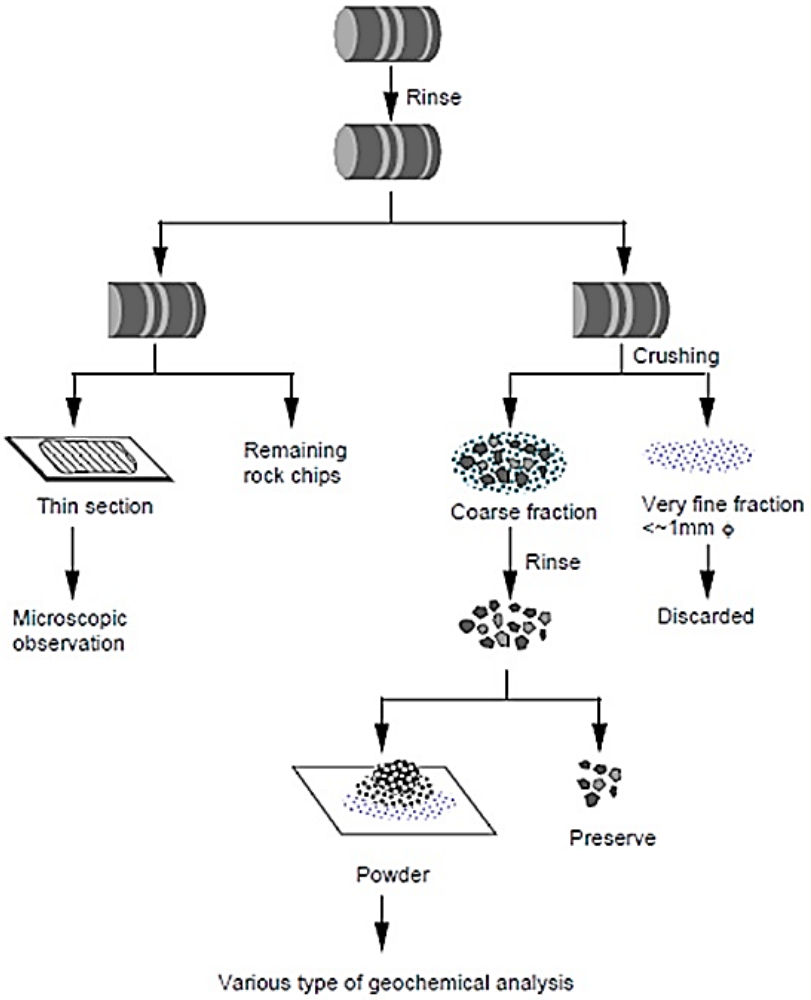

Figure 12: Schematic flow sheet illustrating sample handling and sample preparation.

4.2. Qualitative and semi-quantitative mineralogy

Mineralogical analysis was conducted with a standard petrographic light microscope and X-ray powder diffraction (XRD) at XRD Analytical & Consulting and at the Geodynamics and Geomaterials Research Department at the University of Würzburg. Modal mineral abundances were obtained using the Rietveld method, which is a full-pattern fit technique. The measured profile and a profile calculated from crystal structure data were compared in terms of their differences in a number of parameters, and the dissimilarities between the two profiles were minimized. The quantification procedures followed those described in Young (1995, 2000). The lower detection limit of this method is typically between 0.5–2 wt.%, depending on the minerals and the complexity of the sample.

The normative mineralogy of the analysed samples was calculated using a SEDMIN-Microsoft Excel™ spreadsheet for calculating fine-grained sedimentary rock mineralogy from the bulk geochemical analysis, as developed by Kackstaetter (2014). The mineralogical data obtained

via SEDMIN was only used to evaluate the general composition of the shales prior to further inspection through XRD and optical microscopy. Such data are not reliable because of modelling challenges related to variable depositional environments, particle hydraulics, and sedimentary source systems.

4.3. Bulk chemical assays: major and trace element analysis

Major and trace element concentrations were obtained by conventional X-ray fluorescence (XRF) spectrometry and laser ablation inductively coupled plasma mass spectrometry (LA-ICP-MS). Procedural blanks and several standard reference materials were used to monitor data quality. Loss on ignition was determined after heating previously dried powders to a temperature of 950°C. Major elements and some trace elements were analysed on lithium borate fused glass beads and pressed powder pellets, respectively, at the Department of Geological Sciences, University of Cape Town. The techniques followed those described in Willis (1999), which have also been covered in detail by Willis and Duncan (2008). In addition, a PANalytical MINPAL4 X-ray fluorescence spectrometer at the Geodynamics and Geomaterials Research Department in Würzburg was used to determine the major element concentrations. The instrument is equipped with a side-window Rh-tube with max 30 kV, max 1 mA, and max 9W, and an energy-dispersive Si drift detector. The sample chamber was flushed with He to lower the detection limits and reduce analytical errors. The analytical errors for most elements were less than 0.1 % (relative), except for MgO (0.5 %) and Na_2O (3.4 %). For more details, see:

http://www.geographie.uni–wuerzburg.de/geodynamik_und_geomaterialforschung/analytische_ausstattung/

An Agilent 7700× quadrupole ICP-MS equipped with a Photon-Machines Analyte 193 excimer laser ablation system and a Helex two-volume ablation cell at the GeoZentrum Nordbayern, University of Erlangen, was used to identify the trace element concentrations. Helium was used as the carrier gas. The analyses were performed at a laser repetition rate of 10 Hz, a laser pulse energy of ~4 $J \cdot cm^{-2}$, and spot diameters from ranging from 34–63 µm, depending on the nature of the sample. Continuous line-scan analyses were conducted with a pre-ablation step, 5 µm/s scanning speed, and beam size of 25 µm. Samples were assessed in cycles of approximately 15 analyses, and these were bracketed by analyses of each standard. The GLITTER™ software package (Griffin et al., 2008) was used for the offline selective integration of time-resolved signal intensities and to calculate the element concentrations, detection limits, and 1σ uncertainties. The detection limit for major elements was 0.001 wt.%, 0.5 ppm for trace elements (excluding Cr = 20 ppm, Sr = 0.2 ppm, Sc and V = 10 ppm,

respectively, and Sn, W, Zn, and Zr = 1 ppm), and 0.1 ppm for REEs. Replicate analyses of the samples indicated that absolute precision for the major elements were better than 1 %, whereas the precision for trace elements was >95 %. The Fe_2O_3 content represented the total Fe content. Total organic carbon (TOC) and sulfur (S) were analysed using CS-2000 LECO analysers with a detection limit of 0.01 % at Intertek Laboratory in Perth, Australia.

4.4. Reference rock composition

Ideally, the Barberton, Witwatersrand, and Transvaal Supergroup shale data should be compared with worldwide Archaean crustal rock compositions. However, available average global Archaean crustal composition data, such as those provided by Condie (1993), are incomplete, with several elements missing. Thus, Taylor and McLennan's (1985) Post-Archaean Australian Shale composite (PAAS) was used to normalise the data. The HFSEs (elements that are incompatible with low partition coefficients and residence times in seawater) were transferred almost quantitatively to the sediment, and they closely reflected the composition of the continental crust (Taylor and McLennan, 1985). The REE data were normalised relative to the chondrite composition provided by Taylor and McLennan (1985). The subscript N indicates chondrite-normalised values and Eu* represents the interpolated value of Eu (i.e. $Eu/Eu^* = Eu_N/[(Sm_N)\ (Gd_N)]^{1/2}$). The symbols $\bar{x}$ and ± indicate the mean and standard deviation, respectively.

4.5. Statistical analysis

The inter-element relationships among the major and trace element contents were evaluated through correlation analysis. Pearson's correlation coefficient (r), also known as the Pearson product-moment correlation, measures the strength of the linear relationships between two quantitative variables, and helps to reveal relevant differences regarding alteration and provenance. It is commonly defined as the ratio of the covariance of two variables representing a set of numerical data, normalised to the square root of their variances (Cowan, 1998).

4.6. Extent of post-depositional alteration

The extent of post-depositional alteration of the Witwatersrand shales was assessed by means of chemical mass balance modelling between (a) the macroscopically and microscopically least altered samples and (b) the most altered samples from zones of macroscopically evident fluid flow. Many methods are used for calculation of mass loss or gain in mineral deposits, including methods such as volume factor (Gresens, 1967), immobile elements (MacLean and Kranidiotis, 1987; MacLean, 1990; Nesbitt and Markovics, 1997), and isocons (Grant, 1986). The applied modelling calculations were based on Gresens (1967) who postulated a

relationship between the volume, composition, and density changes between an altered rock and its protolith. When the protolith of the alteration product is known, the relationship is regionally applicable to all alteration processes. In this study, the calculations followed the modified equations of Grant (1986, 2005), who proposed a revamped version of Gresens' mass balance equation, where volume and density are substituted with mass, allowing for a direct comparison of the mass transfer to the composition of the protolith and of the altered rock through an isocon diagram. Grant (1986) made it possible for the variations in elements and oxides to be illustrated in the isocon diagram.

4.7. Chlorite chemical analysis and geothermometry

Chlorite chemical analysis on standard-size polished thin sections with a 25 µm carbon coating was conducted using an electron micro probe analyser (EPMA) equipped with four wavelength-dispersive spectroscopes (WDS). An array of imaging detectors was used, including secondary electron imaging (SEI) and back-scattered electron imaging (BSE). Analytical conditions were as follows: 15 kV accelerated voltage, 20 nA beam current, 20 s peak and background per element counting times, and 1 µm beam spot size. For measurements, the Kα (alpha) lines were taken. For calibration, the following standards were used: Albite for Na, MgO for Mg, almandine for Si, and Al_2O_3 for Al (TAP crystal), orthoclase for K, andradite for Ca, $MnTiO_3$ for Ti, and Cr_2O_3 for Cr (PET crystal), haematite for Fe, and $MnTiO_3$ for Mn (LIF crystal). An atomic number effects/ZAF matrix correction was also introduced. Using these measurement conditions, the detection limit was about 0.05 wt.%. The analytical error was below 1 % relative to all major elements, except Na (<2 % relative), but it rose to 10 % relative to the trace elements. The acquired oxide elemental data were then recalculated as chlorite mineral structural formulae based on stoichiometric principles. Quantitative temperature estimates were determined from chlorite using various calibrations (see Chapter 5). Determining the temperature of the mineral assemblage is fraught with uncertainties, and it is thus important to utilise as many geothermometers as possible to validate the estimates (Azor et al., 1997).

4.8. Highly siderophile element assays

The split of each shale sample was milled using an agate mill such that 95 % of the sample mass passes 75 µm at Genalysis Laboratory Services in Johannesburg, South Africa. The subsamples were then sent to Intertek Laboratory in Perth, Australia for PGE (Pt, Pd, Rh, Ru, Ir, and Os) and Au analysis. The PGE and Au content was obtained by ICP-MS following nickel sulfide collection fire assay. The detection limit used in this procedure was 1 ppb for Au and 0.5 ppb for Pt, Pd, Rh, Ru, Ir, and Os with a >95 % confidence limit. Certified reference

materials (AMIS and OREAS series standards) were used to ensure optimum quality, and duplicates assessed to check the repeatability of the results.

4.9. Geostatistical treatment of highly siderophile elements

Several past studies have reported that Au and PGE values do not usually follow the normal (or Gaussian) distribution. However, the logarithms of the values might be more normally distributed (Koch and Link, 1970; Dowd, 1982; Cheeney, 1983). This phenomenon is frequently observable in ore deposits and in unmineralised rocks with low concentrations (Appendix A.3). To calculate the average Au and PGE composition within each stratigraphic unit, so as to identify outliers, a three-parameter logarithmic distribution (Beta = β) was introduced to create a standardised moment. Outliers were further assessed using the interquartile range (iqr). Any value deviating more than 1.5 times the iqr from the median was regarded as an outlier. Below are the equations and variables applied to calculate the estimated mean composition of Au and PGE in the different stratigraphic units:

Sample mean = $\bar{x}$:

$$\bar{x} = \frac{1}{N}\sum_{i=1}^{n} x_i \qquad \textbf{Equation 1}$$

where

x_i = the current value of the variable,

N = the number of observations in the population.

The sample variance (S) was calculated as follows:

$$S^2 = \frac{\sum\left(x - \bar{x}\right)^2}{N-1} \qquad \textbf{Equation 2}$$

Sample skewness (γ_1) was defined with respect to the third moment about the mean:

$$\gamma_1 = \frac{\sum(X-\mu)^3}{n\sigma^3} \qquad \textbf{Equation 3}$$

where *X* is the random variable, *μ* is the mean, *σ* is the standard deviation, and *n* is the number of samples.

Skewness measured in this way is sometimes referred to as ‘Fisher’s skewness’.

The correlation coefficient (r) was calculated according to the following formula:

$$r = \frac{n\sum xy - \sum x \sum y}{\sqrt{\left[n\sum x^2 - \left(\sum x\right)^2\right]\left[n\sum y^2 - \left(\sum y\right)^2\right]}}$$

Equation 4

where *x, y,* and *z* are known covariance variables.

Variogram = $2\gamma(h)$:

A variogram is a description of the spatial continuity of the data. The experimental variogram is a discrete function calculated using a measure of variability between pairs of points at various distances. In this study, variograms were only modelled to assess the spatial continuity of marine shales chemical composition for the purpose of making inferences on lateral and vertical variability. The variogram is described by equation 5:

$$2\gamma(h) = \frac{1}{N(h)} \times \sum_{n=1}^{N(h)} \left[z(u_n) - z(u_n + h)\right]^2$$

Equation 5

where:

N (h) = number of data pairs at distance *h* (inside the searching neighbourhood area)

z (u_n) = the value at location u_n

z (u_n+*h*) = the value at location u_n + *h*

Transformation of variables = $T\beta$:

Transformation of variables in the context of this study involves adding a third parameter in order to cater for outliers and thus best estimating the mean of the data through simulating a normal distribution.

$$T\beta = \ln(Au + \beta)$$

Equation 6

The beta value was calculated in Microsoft Excel by setting the skewness equal to zero. This was achieved by changing the third parameter of the natural logarithm.

Estimation mean:

$$\bar{x}_{Au\_PGE} = e^{\left(\overline{T\beta}+(S^2)/2\right)}$$ **Equation 7**

Where:

e^x = Napier's constant (2.718281828)

x = the power value of the exponent *e*.

These geostatistical equations were employed to resolves outliers, a process that yielded the best Au and PGE averages in the data (Figure 13)

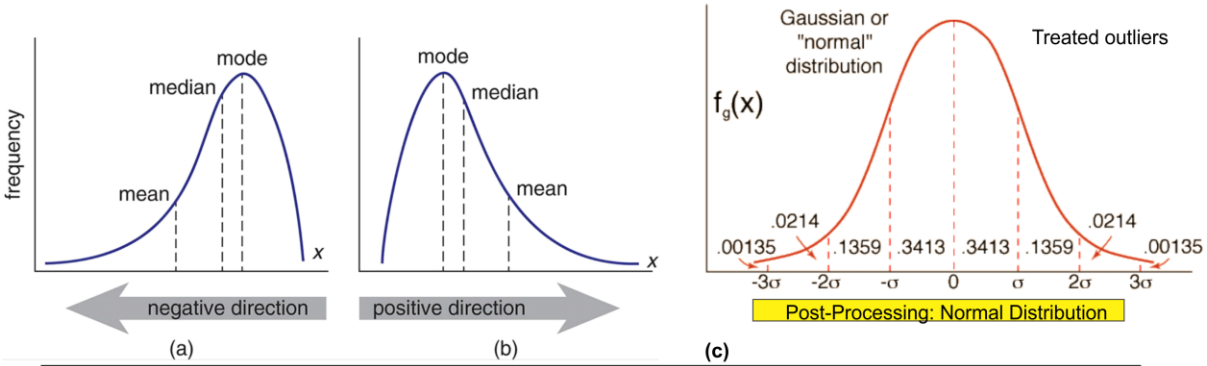

Sample No.	Au	Ln(Au+Beta)	Skewness		Beta
D5P03463-048	0.5	-1.17	0.00		-0.19
D5P03463-032	0.5	-1.17	Transformed Mean	Variance	Estimated Mean (ppb)
D5P03463-035	0.5	-1.17	1.00	1.76	6.57
D5P03463-036	0.5	-1.17			
D5P03463-045	0.5	-1.17			
D5P03463-038	2	0.59			Arithmetic Mean (ppb)
D5P03463-049	2	0.59			6.61
D5P03463-013	2	0.59			
D5P03463-046	3	1.03			
D5P03463-020	4	1.34			

Figure 13: Geostatistical data processing to obtain the most accurate estimates of average Au and PGE compositions. Graphs a–c represents distribution of data with (a) negative skewness, (b) positive skewness (lognormal distribution), and (c) normal distribution or Gaussian distribution.

Evaluation of statistical relationships

Various F-test null hypothesis statistics tests can be used to examine the variance in statistical relationships. Each test type has its own hypothesis. The paragraphs below introduce three common types of F-test statistics: two-tailed tests, right-tailed tests, and left-tailed tests.

→ Two-tailed test

- Hypothesis: H_0: $\sigma_1 = \sigma_2$ or H_a: $\sigma_1 \neq \sigma_2$

  where: Null hypothesis: H_0 (always =); Alternative hypothesis: Ha (>, <, ≠).

When F < F (critical one-tail), I cannot reject the null hypothesis. In such instances, there are similarities between two different variances, implying related statistical distribution patterns.

→ Right-tailed test

- Hypothesis: H_0: $\sigma_1 = \sigma_2$ or H_a: $\sigma_1 > \sigma_2$

→ Left-tailed test

- Hypothesis: H_0: $\sigma_1 = \sigma_2$ or H_a: $\sigma_1 < \sigma_2$

This study employed a two-tailed test, as it compared two variances of different PGE variables.

- Notation:

Test statistic = $t_{\bar{x}} = \dfrac{\bar{x} - u}{\dfrac{8}{\sqrt{n}}}$ **Equation 8**

where: *t* is the test statistic, *μ* is the mean, and *n* is the number of variables.

→ Significance level = *α* (in decimal form). The *α* level in this study was 0.005 (confidence level of 95 %).

→ Critical values = t_{α} or $\pm t_{\alpha/2}$

→ Degrees of freedom (df) = n – 1

Table 1 illustrates hypothesis testing for the final outputs. This study employed Microsoft Excel's data analysis tool to complete a two-tailed test. Table 2 indicates how to interpret the results.

Table 1: Example of variance comparison using hypothesis-testing statistics.

F-Test Two-Sample for Variances		
	A	*B*
Mean	4.50	4.09
Variance	0.32	0.25
Observations	64	64
df	63	63
F	1.30	
P(F<=f) one-tail	0.15	
F Critical one-tail	1.52	

Table 2: Interpretation of test results.

Hypothesis Test	Compare	Result
Classical Method	test statistic > critical value (i.e. F > F crit)	Reject the null hypothesis
Classical Method	test statistic < critical value (i.e. F < F crit)	Cannot Reject the null hypothesis
p value Method	p value < a	Reject the null hypothesis
p value Method	p value > a	Cannot Reject the null hypothesis

5. PETROGRAPHY AND MINERALOGY

Since the majority of samples required to fulfil the objectives of this project were almost entirely concealed beneath later cover sequences, conventional geological mapping and surface sampling were rendered impractical. However, several drill core samples with pertinent core logs and relatively unaltered underground samples from mines were obtained. This chapter provides descriptions of the samples studied in order to fulfil the objectives of this study.

5.1. Petrography

A total of 307 samples of were collected from drill cores/chips for this study (Appendix A.1). Most of these samples were collected from the Witwatersrand Supergroup. In addition to the historical and largely unpublished geochemical data, new data were obtained from 307 samples (Barberton Supergroup [n = 26], Witwatersrand Supergroup [n = 248], Black Reef Formation [n = 4], and Transvaal Supergroup [n = 29]) collected from different Kaapvaal Craton sequences (Figure 14 and Table 3). Supplementary data came from Wronkiewicz and Condie (1987) and Fuller et al. (1981). The samples were collected from the following areas: the Barberton, Carletonville, Welkom, Klerksdorp, Krugersdorp, Central, Evander, East Rand, and Western Areas goldfields (Table 3). The main objective of the sampling strategy was to collect shales that lacked evidence of significant post-depositional mass transfers. This aspect was assessed with the help of sample profiles ranging from zones of alteration to seemingly unaltered shale units. Samples were collected from laterally equivalent distal positions across different Kaapvaal Craton stratigraphic units, so they focused on regionally persistent marine shales. Sampling intervals averaged 30–50 cm for pristine shales and 30–50 m for intervals containing extensive quartzite–siltstone–shale sequences (i.e. Roodepoort Formation [Carletonville goldfield], Booysens Formation [Western Areas goldfield], and Pretoria Group [South Deep mine]).

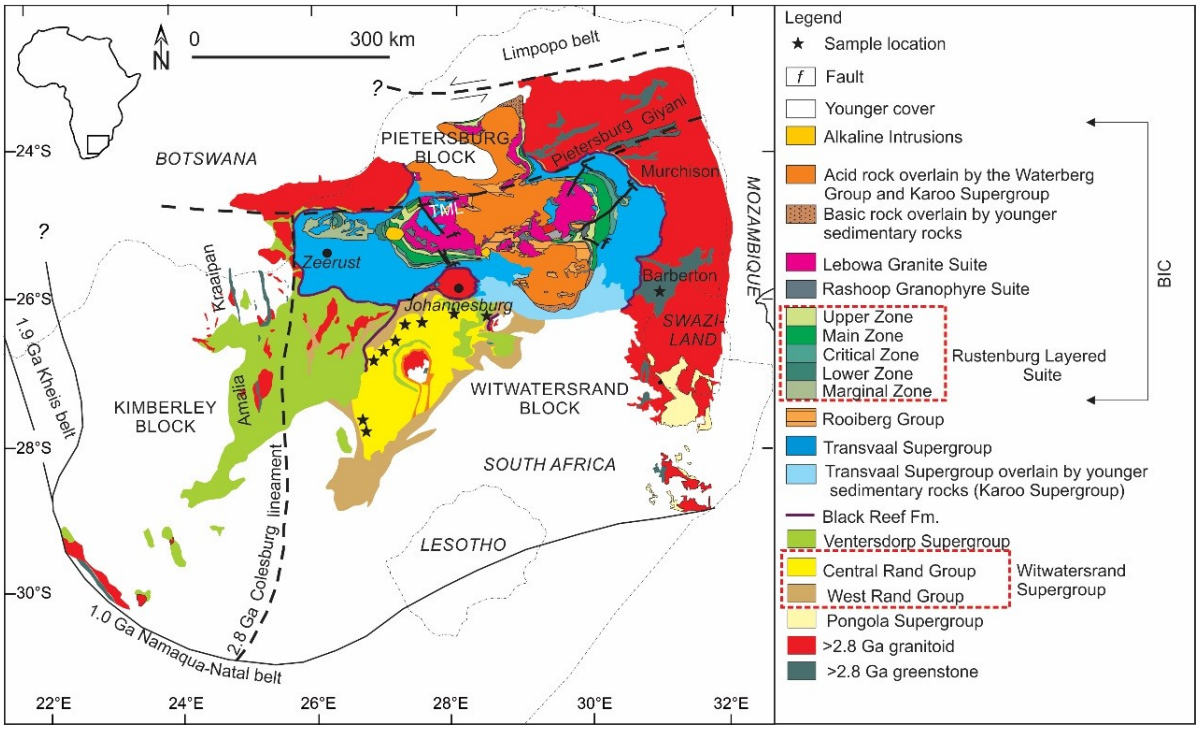

Figure 14: Geological map showing location of sampled shale sequences (black stars) and extent of Kaapvaal Craton. TML = Thabazimbi–Murchison lineament. Fm. = Formation.

5.1.1. Fig Tree Group: Sheba Formation marine shales

The Fig Tree Group shales were sampled in the Barberton area, Mpumalanga Province (Table 3). The Sheba Formation of the Fig Tree Group overlies the Zwartkoppie Formation, and has an average calculated thickness of 700 m (Condie et al., 1970). The Sheba Formation is a succession of greywacke, shale, and thin chert bands. The greywacke mainly consists of angular and sub–angular fragments (average 1 mm) of quartz, chert, feldspar, black shale, and muscovite. The shales in this formation are usually grey–black in colour. The sedimentary rocks display characteristics of turbidite deposition, with features such as graded bedding, sole marks, flute casts, slide marks, load casts, and flame structures. The nature of the Fig Tree Group's sedimentary rocks and sedimentary structures suggests that the deposition took place rapidly in a relatively deep-water environment (Visser et al., 1956; Kuenen, 1963; van Vuuren, 1964; Anhaeusser et al., 1968, 1969). Shale forms a considerable proportion of the Sheba Formation. It varies in colour, ranging from dark grey to greenish grey in more siliceous portions, to reddish and greyish brown in the ferruginous types.

5.1.2. Moodies Group: Clutha Formation marine shales

The Clutha Formation consists of a basal conglomerate, calcareous quartzite, feldspathic quartzite, shale, and jaspilitic iron formation, and is overlain by the Joe's Luck Formation. The shale sequence overlies the feldspathic quartzite unit and consists of sub-greywacke, sandy shale, finely laminated shale, and dark shaley quartzite. Mud cracks also occur in the shales. There is a magnetic shale and jaspilitic iron formation band near the base, and it forms a persistent marker band through most of the Eureka Syncline, except in the area of the Clutha gold mine. The ferruginous shale units of the Clutha Formation continue above the iron formation marker, developing the latter and eventually becoming partly arenaceous near the top. At that point, subgreywackes and lenses of impure quartzite are developed below the basal quartzite unit of the Joe's Luck Formation.

5.1.3. West Rand Group marine shales

In the Hospital Hill Subgroup of the West Rand Group, two formations were sampled, namely, the Parktown and Brixton Formations. The Parktown Formation occurs near the base of the Hospital Hill Subgroup (Figure 15 A and B). In the western part of the West Rand Basin, near the Klerksdorp goldfield, sedimentary rocks of the Parktown Formation onlap directly onto Dominion Group mafic rocks (Watchthorn, 1981). The Parktown Formation reaches a maximum thickness of approximately 1000 m near the Carletonville goldfield, and thins in southerly and south-easterly directions. In terms of pre-metamorphic protoliths, the lower Parktown Formation comprises lenticular-laminated siltstone-shale, black carbonaceous shale, magnetic shale, meso-banded, oxide-carbonate facies, and BIFs. The upper Parktown Formation starts with a black magnetic shale that grades into Fe-rich carbonate-bearing non-magnetic shale and green pyrite-bearing non-magnetic shale. In turn, that shale is overlain with a sharp contact by a micro-banded BIF that is approximately 10 m thick (Contorted Bed Member).

The Brixton Formation constitutes the middle part of the Hospital Hill Subgroup. It reaches a maximum thickness of approximately 1600 m near the Carletonville and Klerksdorp goldfields (Camden-Smith, 1980), and thins in easterly, southerly, and south-easterly directions (SACS, 2006). It comprises grey- to green-coloured magnetic shale that grades into light-grey interlaminated siltstone-shale, and then into mature quartz arenite. The arenite beds display trough cross-bedding and contain thin interbeds of carbonaceous shale.

Two formations were sampled in the Government Subgroup of the West Rand Group, namely, the Promise and Palmietfontein Formations. The Promise Formation forms the base of the Government Subgroup and rests with an angular unconformity on top of the Bonanza

Formation. On the eastern side of the basin, the Bonanza Formation was removed prior to Government Subgroup deposition, causing the Promise Formation to rest directly on the Brixton Formation (Guy et al., 2010). The Promise Formation thickens gradually in a south-easterly direction, ranging from 250 m near Vredefort to 400 m near the East Rand goldfield, Heidelberg (SACS, 2006). Its lithology includes diamictite, sandstone, laminated siltstone-shale, and carbonaceous shale. The Palmietfontein Formation occurs in the central part of the Government Subgroup and reaches a stratigraphic thickness of approximately 250 m in the north-western, northern, and central parts of the basin, with its thickness decreasing towards the East Rand goldfield. It is characterised by symmetrical cycles of magnetic and non-magnetic shale. Arenite sequences are also present, as are intercalated diabase sills. The Palmietfontein Formation is truncated by the basin-wide disconformity of the Government Reef.

The Roodepoort Formation, which belongs to the Jeppestown Subgroup, was sampled in the Carletonville goldfield. The Roodepoort Formation is stratigraphically the highest major marine shale unit in the relatively gold-poor West Rand Group. It reaches a maximum thickness of approximately 500 m in the Klerksdorp and Welkom goldfields but thins in an easterly direction towards the East Rand goldfield, where it is less than 150 m thick. The lower Roodepoort Formation has a distinct east–west lithofacies variation comprised of graded wackestone and ripple cross-laminated siltstone in the west, and magnetic shale in the east. Its lithology includes stripy sandstone from the lower quartzite unit, overlain by massive grey sandstone, wackestone, non-magnetic siltstone-shale, and magnetic siltstone-shale. Unlike many other magnetic shale units of the West Rand Group, this unit is composed of black, green, and white bands, which represent laminae composed of black magnetic shale, green non-magnetic shale, and white quartz-epidote sand lenses. A dolerite sill occurs in the upper half of the Roodepoort Formation.

5.1.4. Central Rand Group marine shales

The only unit that consists predominantly of laterally extensive marine shale within the Central Rand Group is the Booysens Formation of the Johannesburg Subgroup in the middle of the Central Rand Group. It represents an initially upward-coarsening, then upward-fining sequence, and was sampled at various localities (Table 3). It is thickest in the Western Areas (West Rand Region) and Carletonville goldfields (~300 m) but decreases in thickness in westerly, southerly, and easterly directions to <100 m. At the base, coarse-grained and cross-laminated sandstone of the Krugersdorp Formation grades into sandstone and wackestone of the Booysens Formation. Higher up, the proportion of carbonaceous shale bands increases towards the central shale unit.

Arenaceous intercalations persist into the main shale unit, albeit at a lower frequency. The change in colour from dark grey to light brown in the central shale unit may reflect carbonate alteration. The transition from the main shale unit into the overlying Kimberley Formation corresponds to a decrease in the number of shale bands and an increase in abundance of siltstone and sandstone laminae (Tweedie, 1968). The Kimberley Formation of the Turffontein Subgroup also contains shale ('K8 shale') with siltstone and fluvial sandstone intercalations. Geochemical data on it were taken from Wronkiewicz and Condie (1987) and Phillips (1986).

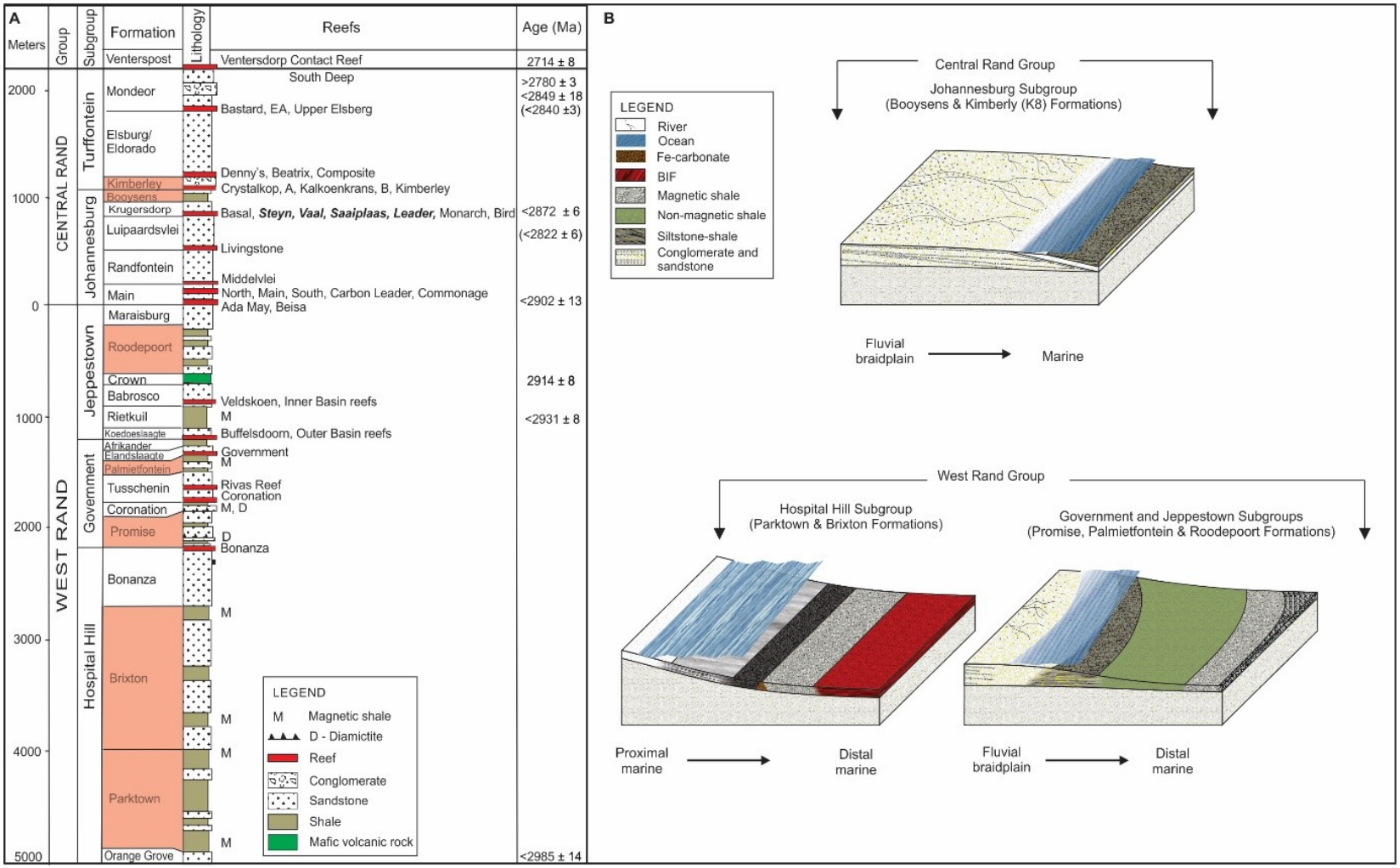

Figure 15: A. Witwatersrand Supergroup stratigraphic column illustrating sampled formations in pink), SG = subgroup; ages as given in Frimmel et al. (2005); B. Basin assemblage and sampled formations, modified after Guy et al. (2010).

5.1.5. Black Reef Formation marine shales

The Black Reef Formation lies at the base of the Transvaal Supergroup, and is conformably overlain by the carbonates of the Chuniespoort Group (Figure 16). The interbedded shale unit is characterised by penetrative cleavage. Thin bedding-parallel quartz veins are common in the interbedded shale unit, and are characterised by quartz-fibre lineation. There is a sharp, non-erosional contact between the Black Reef shale and quartzite. The shale is horizontally laminated and has small quartzite grains at the bottom, and small-scale soft-sediment deformation structures. These suggest a rapid transition from a high-energy environment to a low-energy environment, due to transgression (Frey et al., 1991). The black, horizontally laminated shale formed under low-energy conditions in a reducing environment subject to restricted circulation (Eriksson, 1972). The shale content increases upward. The sampled shale units are finely laminated and carbonaceous. The shales are overlain by dark-brown sub-tidal dolomite, which is characterised by megadomal stromatolites.

5.1.6. Pretoria Group: Silverton Formation marine shales

Shales from the Silverton Formation, which belongs to the Pretoria Group, were sampled within the South Deep mining-right area using surface exploration boreholes (Figure 16). The South Deep mine is underlain by outliers of Karoo Supergroup shales, and sandstones, followed by the Pretoria Group and Chuniespoort Group. The Chuniespoort Group overlies the Klipriviersberg Group volcanic rocks, which are in turn underlain by the Central Rand Group's gold-bearing conglomerate (reefs). The lithofacies of the sampled Pretoria Group shales is mainly black–grey carbonaceous shale of the Silverton Formation. These shales are mostly massive in texture, with concretions of carbonate, and parallel lamination in places. The upper shale units are composed of monotonously alternating laminae of siltstone and shale, with siltstone laminae increasing in abundance towards the top. Secondary pyrite specks and blobs are common in most of the carbonaceous beds near the base of the upper shale unit. The lower shale unit consists of monotonous alternating laminae of black shale and dark grey siltstone. Towards the base of each unit, the shale is highly carbonaceous and silt-poor. Carbonate concretions are common throughout the Pretoria Group shales. Although calcite veins and veinlets crosscut the succession, they are not very abundant.

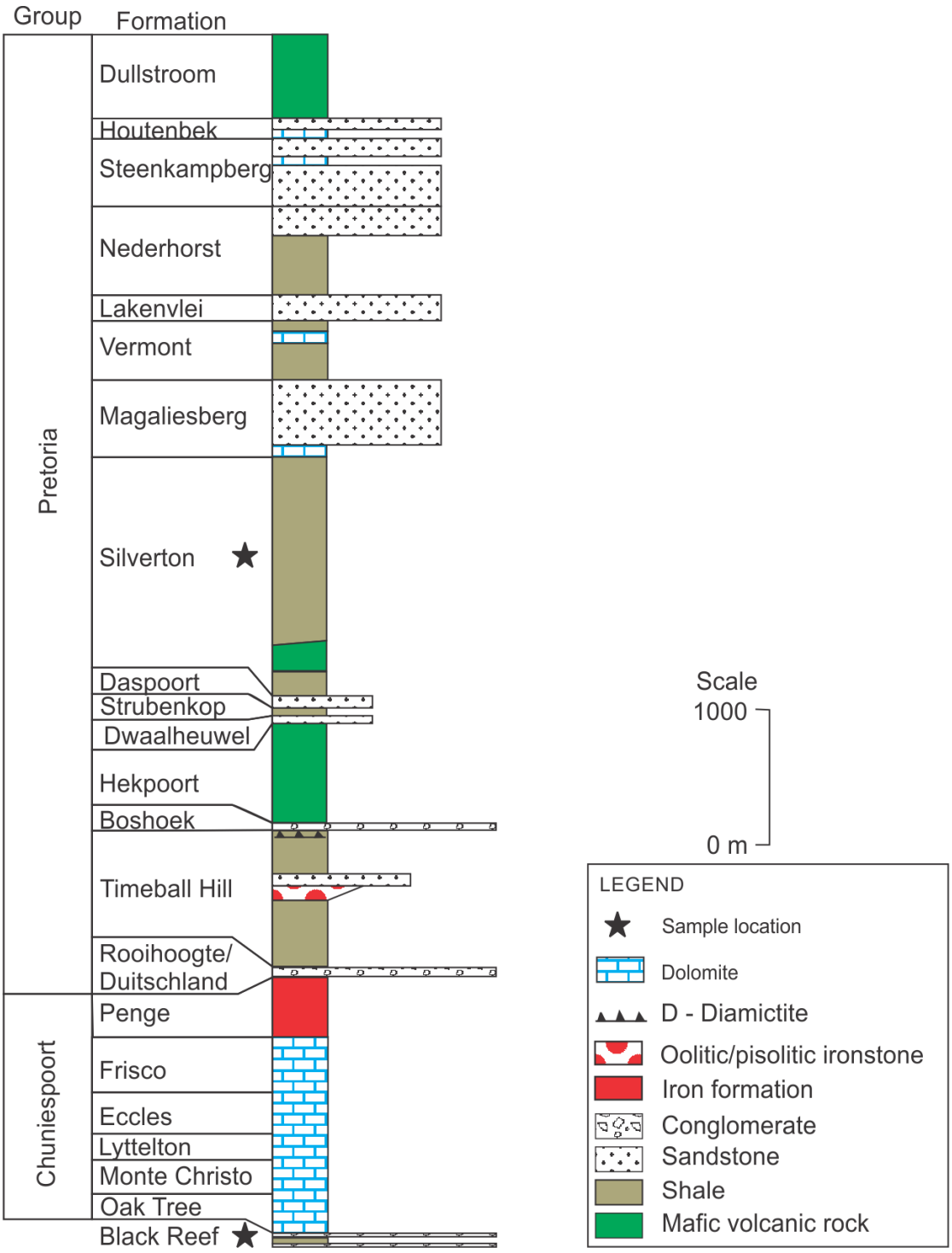

Figure 16: Stratigraphic profile of Transvaal Supergroup with marked sample locations (modified after Beukes et al., 2002).

A summary of the sampled shale units is provided in Table 3 and whole rock geochemistry is given in Appendix A.1.

Table 3: Summary of sampled Kaapvaal Craton sequences and their respective stratigraphic location.

Supergroup	Group	Shale Unit Sampled	Location	Nearest Town
Transvaal	Pretoria	Silverton Formation	South Deep Mine	Westonaria
		Black Reef Formation	Carletonville Goldfield	Carletonville
Witwatersrand	Central Rand	Johannesburg Subgroup, Booysens Formation	Klerksdorp Goldfield	Klerksdorp
		Johannesburg Subgroup, Booysens Formation-Vaal Reefs mine		Strathmore
		Johannesburg Subgroup, Booysens Formation-Klerksdorp		
		Johannesburg Subgroup, Booysens Formation-Welkom division of Western Holdings	Welkom Goldfield	Dagbreek
		Johannesburg Subgroup, Booysens Formation-Geduld mine		
		Johannesburg Subgroup, Booysens Formation-Saaiplaas mine		
		Johannesburg Subgroup, Booysens Formation-Cooke section	Western Areas Goldfield	Zuurbekom
		Johannesburg Subgroup, Booysens Formation-Beatrix mine	Welkom Goldfield	Welkom
	West Rand	Jeppestown Subgroup, Roodepoort Formation-Driefontein surface borehole	Carletonville Goldfield	Carletonville
		Jeppestown Subgroup, Roodepoort Formation-Driefontein surface borehole		
		Jeppestown Subgroup, Roodepoort Formation-East Driefontein mine		
		Jeppestown Subgroup, Roodepoort Formation-West Driefontein mine		
		Jeppestown Subgroup, Roodepoort Formation	Central Rand and East Rand Goldfield	Marievale
		Jeppestown Subgroup, Roodepoort Formation	Klerksdorp Goldfield	Klerksdorp
		Jeppestown Subgroup, Roodepoort Formation	East Rand Goldfield	Heidelberg
		Government Subgroup, Promise Formation		
		Government Subgroup, Palmietfontein Formation		
		Hospital Hill Subgroup, Parktown and Brixton Formations	East Rand Goldfield	Heidelberg
Barberton	Moodies	Clutha Formation	Sheba Mine	Barberton
	Fig Tree	Sheba Formation	Sheba Mine	Barberton

5.2. Mineralogy

Petrographic and mineralogical analyses were conducted on marine shales from the Kaapvaal Craton sequences, namely, the Barberton, Witwatersrand, and Transvaal supergroups (Figure 17). This section further investigates whether the distribution of minerals in shales varies in terms of the stratigraphic profile both with and across depository systems.

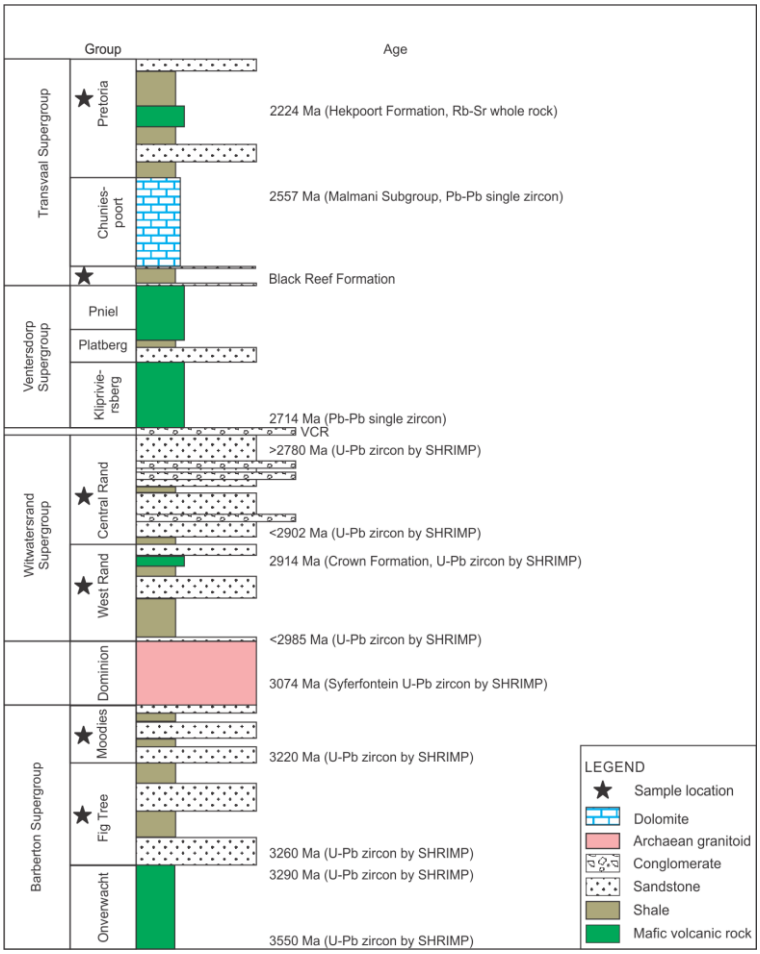

Figure 17: Lithostratigraphic profile of sampled Kaapvaal Craton sequences. Ages: Barberton Supergroup and Dominion Group (Lowe and Byerly, 1999; Poujol et al., 2003; Schoene et al., 2009; Zeh et al., 2009); Witwatersrand Supergroup (Kositcin and Krapež, 2004); Ventersdorp and Transvaal Supergroup (Armstrong et al., 1991).

5.2.1. Detailed petrographic and mineralogical descriptions of the shales

Petrographic and mineralogical studies were performed on 100 thin sections, and 20 polished sections were selected based on their visible chlorite grains for chlorite chemistry examination. The following sections describe the mineralogical and textural characteristics of the shales. In this study, shale sections (both thin and polished) were studied in detail using both conventional optical microscopy and various mineralogical analytical techniques. The goal

was to evaluate significant mineralogical assemblages, textural transitions, and the presence of clastic micaceous minerals and their crystallinity.

5.2.2. Barberton Supergroup marine shales

Regionally persistent shales of the Fig Tree and Moodies groups are grey to black in colour, with a greenish shimmer. They comprise quartz, illite, dolomite, chlorite, albite, and K-feldspar (Table 4). Accessory minerals included monazite, apatite, Cr-spinel, zircon, and sphene. A variety of other heavy minerals are minor constituents, including sulfides and oxides. The illite content of the <2 µm fraction of the Fig Tree shales ranges from 13–20 vol.%, averaging 17 vol.%, with the remainder being chlorite (Figure 18 A and B). The Moodies Group shales contain 8–19 vol.% illite, with an average of 14 vol.%, some detrital and some of authigenic origin. The remainder is chlorite (Figure 18 C and D). Chlorite makes up as much as 27 vol.%, of the Fig Tree shales, but reaches 40 vol.%, in the Moodies Group shale.

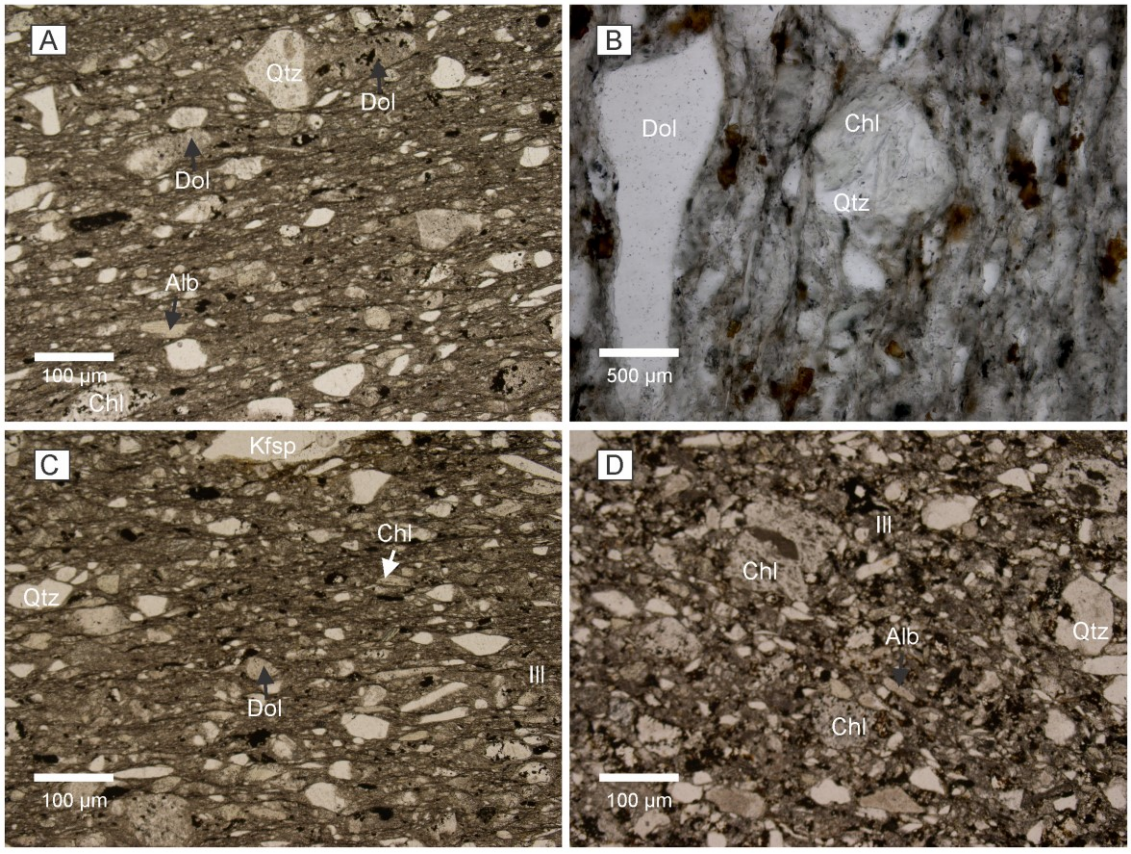

Figure 18: Photomicrographs of selected Fig Tree (A and B) and Moodies (C and D) clastic sedimentary rocks demonstrating the characteristics of certain minerals under plane-polarised light. (A) Quartz intergrown with dolomite and albite. (B) Chlorite flakes surrounded by detrital quartz. (C) Graded shale-siltstone with fine-grained quartz, sericite, and illite surrounded by quartz and dolomite. (D) Illite-rich shale-siltstone with detrital quartz and dolomite.

Table 4: Semi-quantitative modal mineralogy of selected Barberton Supergroup shale samples, as obtained by Rietveld analysis (in vol.%).

Sample ID	Quartz	Illite	Dolomite	Plagioclase	K-feldspar	Chlorite	Siderite
Fig Tree Group							
BARBFC–001	56	18	5	5	2	14	
BARBFC–002	53	19	9	4	2	13	
BARBFC–003	52	15	7	6	2	17	
BARBFC–004	58	15	4	4	1	18	
BARBFD–001	48	20	0	6	2	25	
BARBFD–003	45	20	0	6	3	25	
BARBFD–005	52	13	0	6	2	27	
BARBFD–007	49	16	0	6	3	26	
Moodies Group							
BARBMA–001	44	8	24	5	2	13	2
BARBMA–002	41	17	0	5	1	36	
BARBMA–003	40	14	0	4	1	40	
BARBMA–004	40	18	0	5	1	36	
BARBMA–005	41	19	0	5	2	33	
BARBMA–006	52	11	14	5	2	16	
BARBMB–001	47	7	19	8	2	17	
BARBMB–002	53	12	9	6	2	15	3
BARBMB–003	53	10	7	6	3	18	3
BARBMB–004	43	14	9	5	2	26	
BARBMB–005	48	14	6	5	2	25	
BARBMB–006	45	12	14	5	2	22	
BARBMB–008	51	12	11	3	1	22	
BARBMB–009	47	12	12	5	2	20	1

5.2.3. Witwatersrand Supergroup marine shales

Regionally persistent (low-grade metamorphosed) shales of the West Rand Group are composed of quartz, magnetite, amphibole, chlorite, ankerite, muscovite, and biotite. Those from the Central Rand Group are composed of quartz, chlorite–muscovite mixtures, pyrite, carbonate, rutile, pyrophyllite, and chloritoid (Table 5). These mineralogical assemblages are similar to those reported by Wronkiewicz and Condie (1987), Guy et al. (2010), and Phillips and Powell (2014). Various heavy minerals, including sulfides and oxides, are also present in

minor amounts. All of the studied shale samples appeared homogenous at hand-specimen scale but revealed laminations by thin alternating siltstone and shale intercalations when assessed microscopically.

Shale belonging to the Parktown Formation consist of quartz ($\bar{x}$ = 46 vol.%), chlorite ($\bar{x}$ = 20 vol.%), and muscovite ($\bar{x}$ = 14 vol.%), with minor albite and accessory biotite, zircon, rutile, ilmenite, monazite, allanite, apatite, and ankerite. The Brixton Formation shale comprises quartz ($\bar{x}$ = 53 vol.%), chlorite ($\bar{x}$ = 16 vol.%), and muscovite ($\bar{x}$ = 11 vol.%), with accessory ankerite, rutile, and zircon. The Promise and Palmietfontein Formations are composed of quartz ($\bar{x}$ = 48 vol.%), chlorite ($\bar{x}$ = 17 vol.%), muscovite ($\bar{x}$ = 13 vol.%), and albite ($\bar{x}$ = 2 vol.%), with accessory pyrite, pyrrhotite, biotite, rutile, titanite, zircon, apatite, monazite, allanite, and/or calcite. The studied Roodepoort Formation shale is made up of quartz ($\bar{x}$ = 54 vol.%), Fe-rich chlorite ($\bar{x}$ = 12 vol.%), muscovite ($\bar{x}$ = 12 vol.%), and minor detrital biotite, K-rich feldspar, and authigenic carbonates. Accessory minerals included pyrite, zircon, calcite, apatite, and titanite. A distinct feature observed in the Roodepoort Formation shales (Carletonville goldfield) is the occurrence of syn-sedimentary carbonate overgrown by secondary (hydrothermal) chlorite of a distinctly different composition than the syn-metamorphic matrix chlorite (Figure 19).

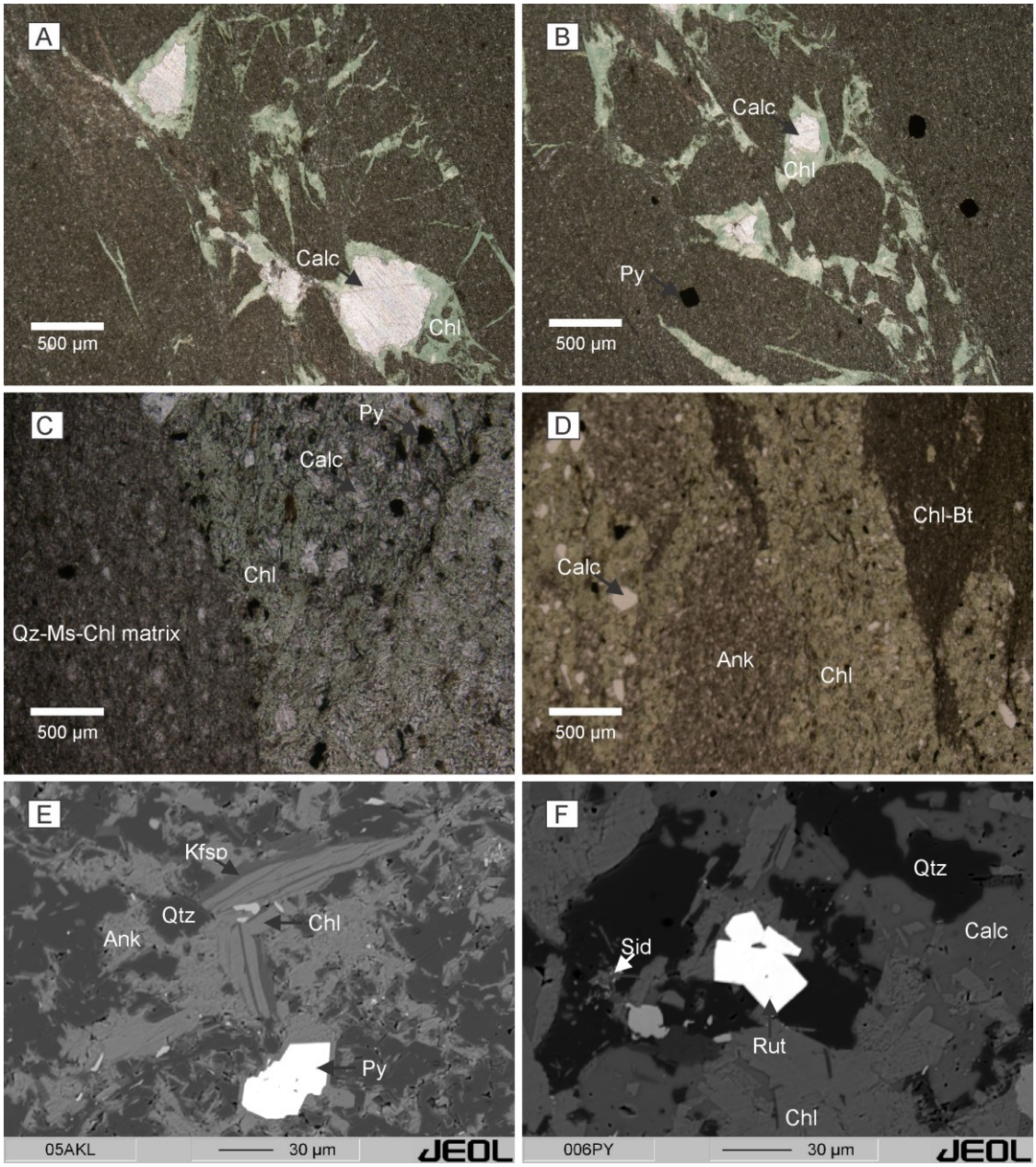

Figure 19: Photomicrographs of selected Roodepoort Formation shales indicating the mineral phases present. (A) Chlorite- and calcite-rich shale with secondary chlorite occurring along the calcite rim. Plane-polarised light. (B) Chlorite- and calcite-rich zoned shale with secondary chlorite and pyrite. Plane-polarised light. (C) Graded shale with intergrown chlorite and calcite. Plane-polarised light. (D) Chlorite-, calcite-, and ankerite-rich shale grading into fine-grained chlorite-biotite layer. Plane-polarised light. (E) K-feldspar intergrown with chlorite surrounded by quartz, ankerite, and pyrite. (EMPA BSE image). (F) Secondary rutile surrounded by calcite and secondary chlorite. (EMPA BSE image).

The Booysens Formation shale consists of quartz ($\bar{x}$ = 46 vol.%), chlorite ($\bar{x}$ = 18 vol.%), muscovite ($\bar{x}$ = 32 vol.%), and minor albite and epidote. Accessory minerals included pyrite, pyrrhotite, biotite, apatite, calcite, zircon, and titanite. The Kimberley Formation shale comprises quartz ($\bar{x}$ = 60 vol.%), chlorite ($\bar{x}$ = 11 vol.%), muscovite ($\bar{x}$ = 4 vol.%), albite ($\bar{x}$ = 2 vol.%), and minor epidote. Accessory minerals included pyrite, pyrrhotite, biotite, apatite, calcite, zircon, and titanite. An upward-coarsening sequence (siltstone–shale intercalation) is noticeably characterised by the presence of hydrothermal pyrite grains in both the Roodepoort and Booysens Formation sequences. Some samples from both of these formations are transacted by thin (0.5–3 mm) veins of quartz and pyrite. The dominant alteration processes observable in the Roodepoort and Booysens Formation shales are sericitisation and chloritisation. The analysed rocks did not undergo metamorphic overprint higher than the lower greenschist facies, as evident from the presence of chlorite, syn-metamorphic white mica, pyrophyllite, and/or chloritoid, and the absence of metamorphic biotite further supports that conclusion. Although carbonates were observed, they generally occur in only very minor amounts in the studied shale samples (Figure 20).

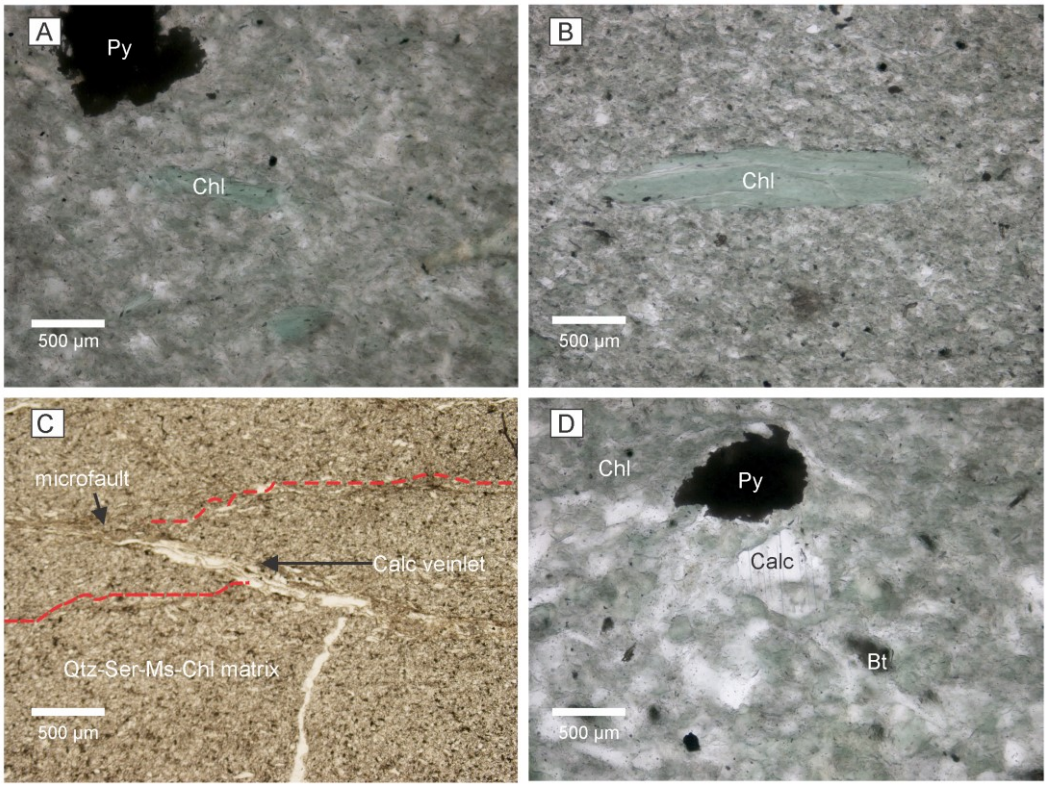

Figure 20: Photomicrographs of selected Booysens Formation shales demonstrating some of the mineral phases present. (A) Chlorite grain and pyrite. Plane-polarised light. (B) Chlorite flake surrounded by quartz and muscovite matrix. Plane-polarised light. (C) Series of microfaults filled with calcite veinlets. Plane-polarised light. (D) Greenish biotite, calcite and pyrite in chlorite matrix. Plane-polarised light.

Table 5: Semi-quantitative modal mineralogy of selected Witwatersrand Supergroup shale samples, as obtained by Rietveld analysis (in vol.%).

Sample ID	Quartz	Muscovite	Albite	Calcite	Pyrophyllite	K-feldspar	Chlorite
Roodepoort Formation							
D5P03463–001	50	23	1	1			24
D5P03463–010	59	8		2		1	30
D5P03463–016	53	8	1	7		2	29
D5P03463–029	57	11	1			2	29
D5P03463–031	59	10	1	2		1	28
D5P03463–039	53	15	1	5		1	26
D5P03463–041	49	10	1	9		2	29
D5P03463–049	52	11	1	8		1	28
Booysens Formation							
BOOYWG_11	46	47	1		4	1	2
BOOYWG_12	37	53			5	1	3
BOOYWG_13	26	2					71
BOOYWG_14	40	51	1		3	1	4
BOOYWG_15	47	47	1		4	1	
BOOYWG_16	48	5	1	15		1	30
BOOYWG_17	56	37			2		4
BOOYWG_19	61	24					15
BOOYWG_20	56	26				1	18

Overall, the West Rand and Central Rand shales comprise convoluted–laminated, dark-grey to black shale, with the latter interstratified with layers of carbonate in many places. Most of the samples are also well-laminated on a thin-section scale. In places, silty and muddy layers are interlaminated. The silt-size fraction comprises quartz, microcline, and, very rarely, plagioclase. Pyrite is the most abundant sulfide and occurs in various forms, including detrital, syngenetic, diagenetic, and epigenetic types. The abundance of pyrite varies with respect to the stratigraphic position, but is generally low in these marine deposits. In addition, XRD analysis revealed that hydromuscovite and magnesian chlorite are the principal sheet silicates. No free gold particles were observed.

5.2.4. Chlorite chemistry and geothermometry

Chlorite is a hydrous phyllosilicate with a structure of recurring, alternating tetrahedral–octahedral 2:1 layers and interlayer octahedral cations (De Caritat et al., 1993; Vidal et al., 2001; Krivovichev et al., 2004; Deer et al., 2009). It is one of the most studied rock-forming minerals, and it forms in a variety of rocks and geological environments, including sedimentary, low-grade metamorphic and hydrothermally altered rocks. This section examines the samples' chlorite chemistry to determine the chlorite type, assess differences in the chlorite population, and estimate the crystallisation temperature in the Witwatersrand Supergroup. Both primary (matrix) and secondary chlorites were studied using EPMA (See Appendix A.2. for full chlorite mineral chemistry).

In order to classify the chlorite type and estimate chlorite formation temperature, the observed textural characteristics of chlorites and corresponding chemical compositions were first screened. Textural requirement was that all the measured chlorites must be classified as either hydrothermal or metamorphic. Matrix chlorites were classified as 'metamorphic chlorites', whereas those that showed evidence of secondary origin were classified as 'hydrothermal chlorites' (Figure 21). Metamorphic chlorite grains were dominant in all the studied samples. They occur as both basal matrix and as authigenic grains. Texturally, they are coarse grained and well preserved. They generally have one set of fine micaceous cleavages, and lamellar twinning. Hydrothermal chlorite grains were characterised by colour zoning and other altered minerals. These chlorites were also found with pyrite grains. Texturally, the hydrothermal chlorites are fine grained and consist of haloes. The dominant colour for both metamorphic and hydrothermal chlorite is light green, although some light brown chlorites were also observed. Because these are low-temperature chlorites, only geothermometers calibrated at a temperature range of 50–500°C were considered. The input into the geothermometers also followed the metamorphic and hydrothermal classification. The Al saturation was fulfilled by ensuring that Al-bearing minerals are present in the studied marine shale samples. To this end, the dominant Al-bearing minerals observed are muscovite and sericite, with some of the samples containing K-feldspar. Only muscovite-sericite-bearing samples were considered as a measure of chlorite analysis quality assurance. When these first criteria were met, two additional chemical criteria were applied to exclude contaminated analyses or those that could not be expressed as a linear combination of end members. These are as follows:

- $K_2O + Na_2O + CaO < 1$ wt.%
- $Al^{IV}(+Fe^{3++VI}\text{-}Al^{IV}) = \text{vacancies} \times 2$

As a result, a total of 129 analyses were retained for formation temperature calculations.

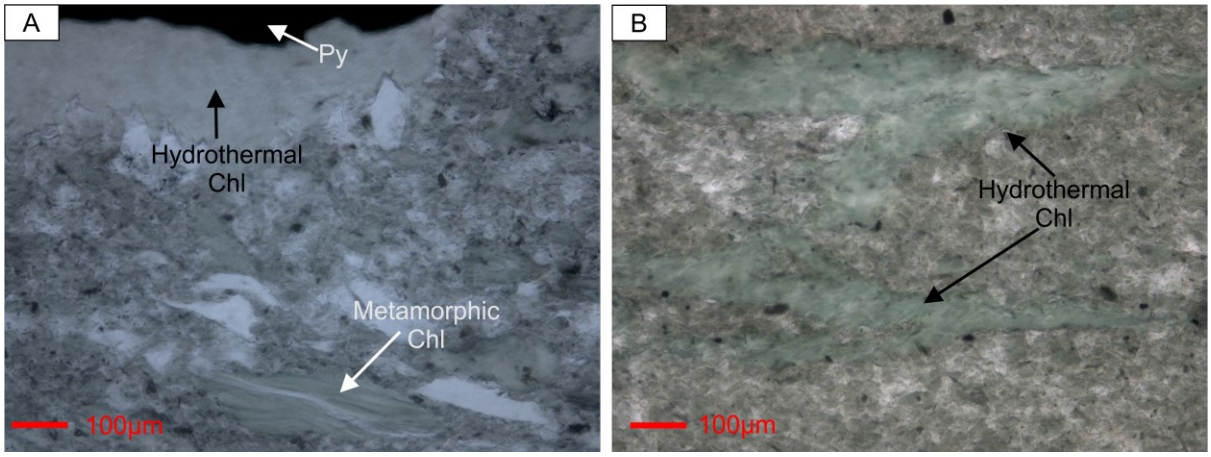

Figure 21: Petrography of Witwatersrand shales showing metamorphic and hydrothermal chlorite. Abbreviations: Chl = chlorite and Py = pyrite.

Chlorite structural formulae were calculated using the current Association Internationale Pour l'Étude des Argiles (AIPEA) nomenclature from Guggenheim et al. (2006). The calculations included classifying the chlorite data based on 18 anions (i.e. $O_{10}[OH]_8$ = 14 oxygen equivalents), as this approach is the commonly employed normalisation procedure for chlorite calculation. It estimates the Fe^{2+}, Fe^{3+}, and H_2O content from electron-microprobe analysis based on stoichiometric criteria, shares out the recalculated cations at different tetrahedral, octahedral, and interlayer sites, then calculates various empirical chlorite geothermometers. The chlorite mineral groups that occur in diverse geological conditions have a low Fe^{3+} content, typically <15 % of Fe_{tot}, suggesting that the Fe^{3+} content in chlorite is controlled by crystallochemical constraints rather than by fO_2 conditions (Dyar et al., 1992; Zane et al., 1998).

Schemes for classifying chlorite group minerals are numerous. The Witwatersrand shale data was plotted on in Figure 22, which takes into account the Mg, Fe, and Al atoms-per-formula-unit (apfu) content in determining whether the chlorites are Type I (i.e. $X_{Mg} + X_{Fe} \geq X_{Al} + X_{Vacancy}$) or Type II (i.e. $X_{Mg} + X_{Fe} < X_{Al} + X_{Vacancy}$) chlorites. This plot revealed that the analysed Witwatersrand chlorites are Type-I trioctahedral chlorites (Figure 22). Furthermore, Figure 23 assigns names to these different chlorite types (i.e. Mg-chlorite, Fe-chlorite, and Al-chlorite) according to the dominant cation in the octahedral site. Based on this classification, the studied chlorites are of the Fe-rich type.

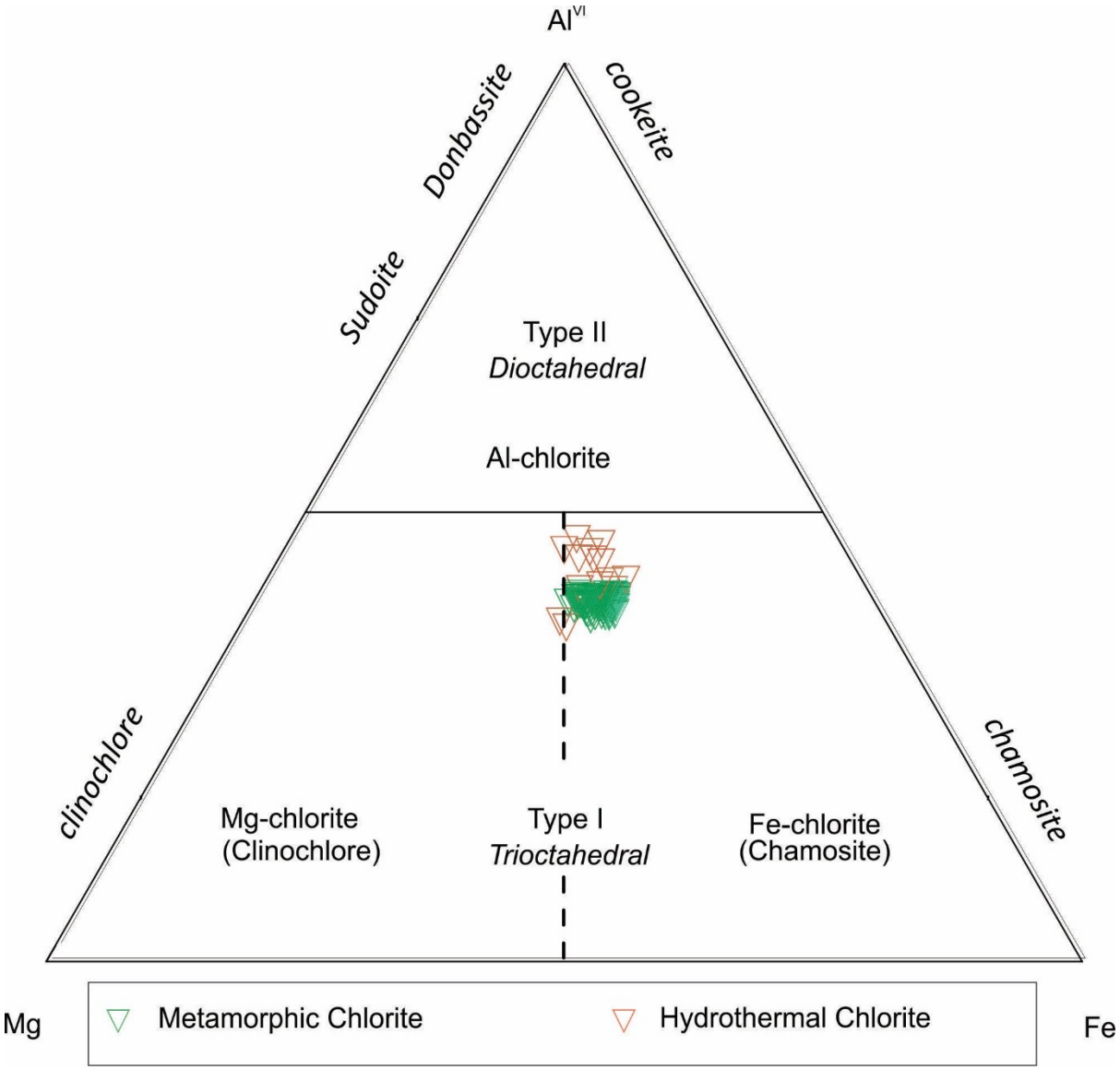

Figure 22: Compositional diagram of Witwatersrand chlorite in Al^{IV}–Mg–Fe ternary diagram (from Zane and Weiss, 1998).

To validate the Type-I chlorite identification obtained via the diagram pictured in Figure 22, the same data were graphically plotted on an X_{Mg} versus $^{VI}R^{3+}$ diagram (Figure 23; Plissart et al., 2009) with the end-member compositions. This diagram classifies chlorite as trioctahedral, tri-dioctahedral, or dioctahedral, and it is generally more accurate, since it considers both chlorite-discriminating factors (Mg–Fe and site occupancy). The plot confirms that the studied chlorites are trioctahedral and Fe-rich, although they are of different generations (i.e. metamorphic and hydrothermal).

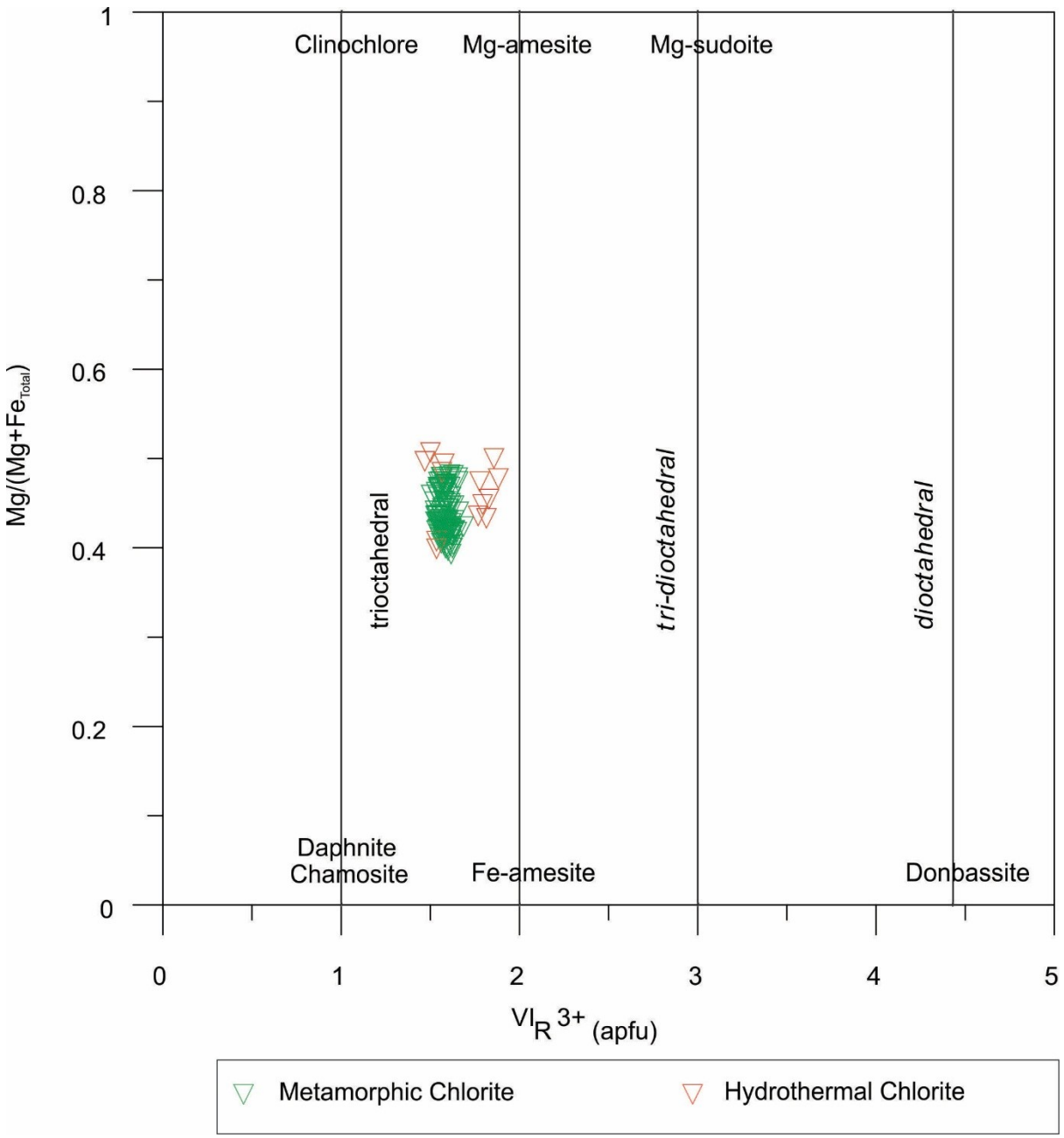

Figure 23: Classification of Witwatersrand chlorite via Mg/(Mg + Fe_{total}) versus $^{VI}R^{3+}$ (apfu) diagram (from Plissart et al., 2009).

The unified system of projection of chemical composition, adapted from Wiewióra and Weiss (1990), was used to validate the chlorite group mineral identification. Figure 24 demonstrates that the dominant phase of this Fe-chlorite is between ripidolite and chamosite. Several other classification plots were also assessed, and yield similar results as those depicted in Figures 22 and 23 (e.g. Hey, 1954; Foster, 1962; Deer et al., 1962; Velde, 1973, 1985; Curtis et al., 1985; Buurman et al., 1988; Jiang et al., 1994; Chabu, 1995; Árkai and Ghabrial, 1997; Martínez-Serrano and Dubois, 1998; Moazzen, 2004; Ruiz Cruz and NIieto, 2006; Fagereng and Cooper, 2010).

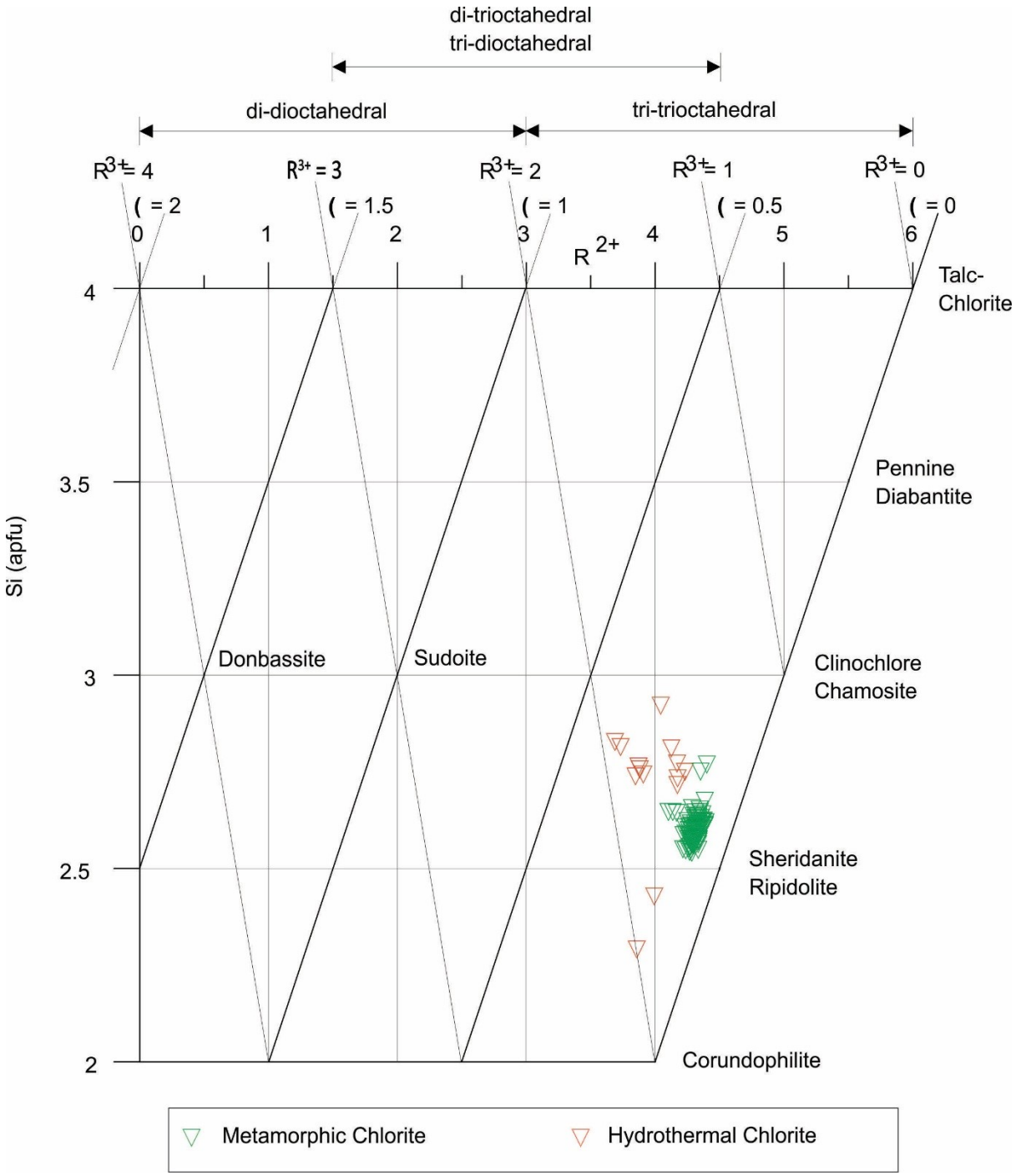

Figure 24: Plot of R^{2+} versus Si (apfu) for Witwatersrand chlorite (from Wiewióra and Weiss, 1990).

Chemical variations in the Witwatersrand chlorite were examined using a graphical representation of the recalculated Mg versus Fe^{2+} constituents, and this plot thus measured their polynomial correlation coefficient. The graphical representation also included the upper and lower limit lines to measure deviations from the polynomial regression line (Figure 25). The results indicate a strong negative correlation between Mg and Fe, although it is far from perfect (Figure 25). The vast majority of the chlorite group mineral data plots within the 10 %

regression limit lines. A total of 6 % (n = 8 out of n = 129) of the data points were observed texturally and compositionally to be hydrothermal in nature and contaminated with other minerals. This yields a composition with the characteristics of chlorite-muscovite, and Mg and Fe are thus dispersed beyond the established 10 % limit lines. Overall, the Witwatersrand chlorite grains revealed little variation in both metamorphic and hydrothermal chlorite (i.e. <10 %), as indicated by their Mg versus Fe polynomial correlation coefficient (Figure 25).

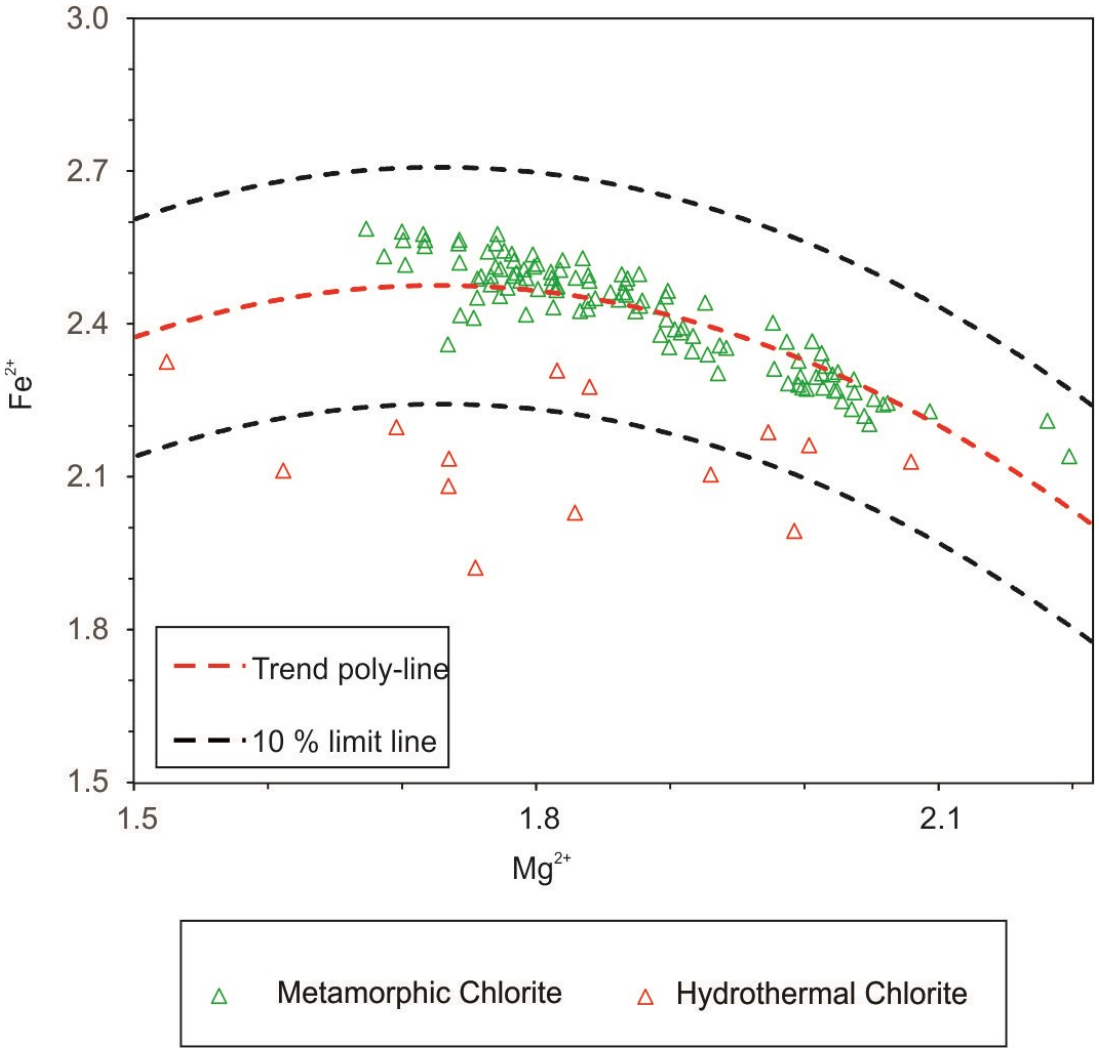

Figure 25: Diagram of Mg versus Fe^{2+} for Witwatersrand chlorite, illustrating correlation coefficient results with limit lines.

Chlorite geothermometers that obtain temperature values via empirical approaches might not provide accurate formation temperatures, as such estimation methods do not take into account the influence of the bulk-rock composition (e.g. De Caritat et al., 1993; Bourdelle et al., 2013). This is further complicated by the fact that the chlorite analyses used in the calibration equations can be contaminated by other Al-rich mineral phases (e.g. Cathelineau and Nivea, 1985; Cathelineau, 1988). Although several tentative correction factors were implemented in

various chlorite geothermometers to reduce the effect of bulk-rock composition, the empirical geothermometers are applicable only to chlorite from restricted geological environments. The upper Witwatersrand shales (i.e. Roodepoort Formation) are regionally persistent and provided an ideal case for the estimation of chlorite formation temperature. A total of 12 empirical geothermometers employing different compositional chlorite parameters were used to model specific chlorite formation temperature conditions. These chlorite geothermometers are as follows:

a) $TCN_{85-Al^{IV}}$ f, taken from Cathelineau and Nieva (1985), which is based on the Al^{IV} (apfu) content,

$TCN_{85-Al^{IV}}$ (°C) = 106 * $Al^{IV}O_{28}$) + 18 **Equation 9**

Specifically, $Al^{IV}{}_{O28}$ and $Al^{IV}{}_{O14}$ denote the tetrahedral aluminium content of trioctahedral chlorite analyses calculated based on 28 oxygen and 14 oxygen, respectively.

b) $TCN_{85-Octahedral\ vacancy}$, also from Cathelineau and Nieva (1985), which, as the name suggests, is based on the octahedral vacancy:

$TCN_{85-Octahedral\ vacancy}$ (°C) = ((Octahedral vacancy O_{28} - 2.41) * 1000)/-8.57 Equation 10

c) $TKML_{87-Al^{IV}}$, as described in Kranidiotis and MacLean (1987), is based on the Al^{IV} (apfu) content with the Fe/(Fe + Mg) correction factor:

$TKML_{87-Al^{IV}}$ (°C) = 106 * ($Al^{IV}O_{28}$ + 0.7 * (Fe/Fe + Mg) + 18) **Equation 11**

d) $TC_{88-Al^{IV}}$ (Cathelineau,1988) is based on the AlIV (apfu) content:

$TC_{88-Al^{IV}}$ (°C) = -61.92 + 160.99 * $Al^{IV}O_{28}$) **Equation 12**

e) TK_{90-Si} (Kavalieris et al., 1990) is based on the tetrahedral Si (apfu) content:

TK_{90-Si} (ºC) = 4833.946 – 2817.776 * ($Si^{IV}O_{14}$) + 419.858 * ($Si^{IV}O_{14}$)^2 **Equation 13**

f) $TJ_{91-Al}{}^{IV}$, from Jowett (1991), is based on the Al^{IV} (apfu) content with the Fe/(Fe + Mg) correction factor:

$TJ_{91-Al}{}^{IV}$ (°C) = 319 (($Al^{IV}O_{14}$) + (0.1 * (Fe/Fe + Mg)) - 69 **Equation 14**

g) $THV_{91-Al}{}^{IV}$ (Hiller and Velde, 1991) is based on the Al^{IV} (apfu) content:

$THV_{91-Al}{}^{IV}$ (°C) = ($Al^{IV}O_{28}$ - 1.303546)/0.004007 **Equation 15**

h) $TC_{93-\text{Octahedral occupancy}}$, as described in De Caritat et al. (1993), is based on the octahedral occupancy:

$TC_{93-\text{Octahedral occupancy}}$ (°C) = (($_{\text{Octahedral occupancy}}O_{14}$) - 5.550)/0.001359 **Equation 16**

i) $TC_{93-Si}{}^{IV}$ (De Caritat et al., 1993) is based on the tetrahedral Si (apfu) content:

$TC_{93-Si}{}^{IV}$ (°C) = (($Si^{IV}O_{14}$) - 3.610)/-0.001327 if 'Al-chlorite' < 0.20 **Equation 17**

$TC_{93-Si}{}^{IV}$ (°C) = ((($Si^{IV}O_{14}$) - 3.233)/-0.001327 if 0.24 > 'Al–chlorite' > 0.20

$TC_{93-Si}{}^{IV}$ (°C) = (($Si^{IV}O_{14}$) - 2.792)/-0.000486 if 'Al–chlorite' > 0.24

j) $TZF_{95-Al}{}^{IV}$, from Zang and Fyfe (1995), is based on the Al^{IV} (apfu) content with the Fe/(Fe + Mg) correction factor:

TZF_{95-Al}^{IV} (°C) = 106.2 * ((Al^{IV} O_{28}) - 0.88 * ((Fe/(Fe + Mg) - 0.34)) + 17.5 Equation 18

k) TX_{97-Al}^{IV} (Xie et al., 1997) is based on the AlIV (apfu) content with the Fe/(Fe + Mg) correction factor,

TX_{97-Al}^{IV} (°C) = 160.99 * ((Al^{IV} O_{28}) + 1.33 * (0.31 - Fe/(Fe+Mg)) - 61.92 if Fe/(Fe + Mg)) < 0.31 Equation 19

TX_{97-Al}^{IV} (°C) = 160.99 * ((Al^{IV} O_{28}) - 1.33 * (Fe/(Fe + Mg) - 0.31) - 61.92 if Fe/(Fe + Mg)) > 0.31

l) TES_{00-Al}^{IV}, from El-Sharkawy (2000), is based on the AlIV (apfu) content with the Fe/(Fe + Mg) correction factor:

TES_{00-Al}^{IV} (°C) = 106.2 * ((Al^{IV} O_{28}) - 0.48 * (Fe/ (Fe + Mg) - 0.163) + 17.5 Equation 20

This study utilised all of the above geothermometers, and tested each one graphically (e.g. Figure 26). The results obtained from these geothermometers are presented in Table 6. The estimated chlorite formation temperatures ranged between 250 and 422°C. Several of the applied geothermometers yield relatively similar chlorite formation temperatures. An average chlorite formation temperature of 325°C ± 26°C was obtained in this study by calculating the arithmetic mean of the 12 geothermometers (Table 6). This average temperature is similar to the one obtained by Frimmel (1994) and Phillips and Law (1994) (i.e. 350°C ± 50°C). The exception is the immediate vicinity of the Vredefort dome. In that area, the lower parts of the basin fill that experienced medium- to high-grade thermal metamorphism during the Bushveld event were subsequently upturned during the Vredefort impact event (Gibson and Wallmach, 1995; Frimmel, 1997). The TK_{90-Si} geothermometer also uses more than one factor in the form of a quadratic equation, and is thus able to more accurately approximate temperatures.

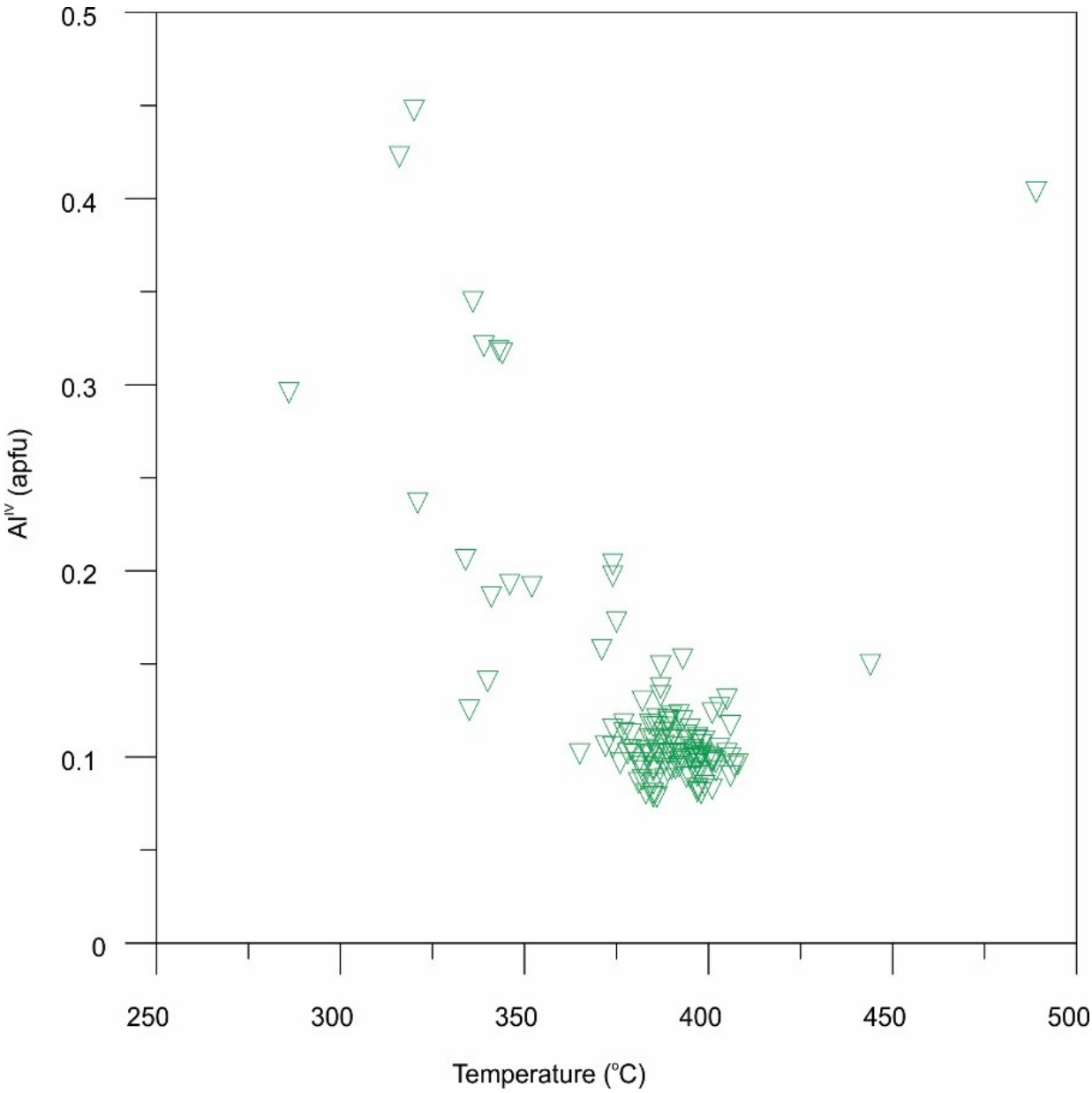

Figure 26: Correlation of Al and temperatures of chlorite formation based on Al^{IV} (apfu) content (from Hiller and Velde, 1991).

Table 6: Estimation of Witwatersrand shale chlorite formation temperatures (n = 129).

	Geothermometer	Temperature (°C)
1	TCN_{85-Al}^{IV}	308 ± 15
2	$TCN_{85-Octahedral\ Vacancy}$	252 ± 16
3	$TKML_{87-Al}^{IV}$	356 ± 16
4	TC_{88-Al}^{IV}	385 ± 23
5	TK_{90-Si}	341 ± 44
6	TJ_{91-Al}^{IV}	393 ± 23
7	THV_{91-Al}^{IV}	368 ± 36
8	$TC_{93-Octahedral\ Occupancy}$	250 ± 20
9	TC_{93-Si}^{IV}	422 ± 65
10	TZF_{95-Al}^{IV}	290 ± 15
11	TX_{97-Al}^{IV}	268 ± 22
12	TES_{00-Al}^{IV}	269 ± 15

5.2.5. Transvaal Supergroup marine shales: The Black Reef Formation

The carbonaceous Black Reef Formation shales from the base of the Transvaal sequence are almost opaque in thin sections, because of the abundant carbonaceous material. The mineralogical assemblage is quartz ($\bar{x}$ = 53 vol.%), muscovite ($\bar{x}$ = 29 vol.%), chlorite ($\bar{x}$ = 13 vol.%), and K-feldspar ($\bar{x}$ = 1 vol.%; Table 7). Carbonates (calcite, siderite, and ankerite, $\bar{x}$ = 4 vol.%), along with quartz, are among the major mineral phases. Kerogen and chlorite demonstrate a well-laminated parallel orientation in the bedding (Figure 27 A and B). The detrital quartz is usually rounded, whereas the quartz that occurs along the laminae appears elongated (Figure 27 C and D). Kerogen occurs along the laminae and often appears bent because of compaction (Figure 27 E and F).

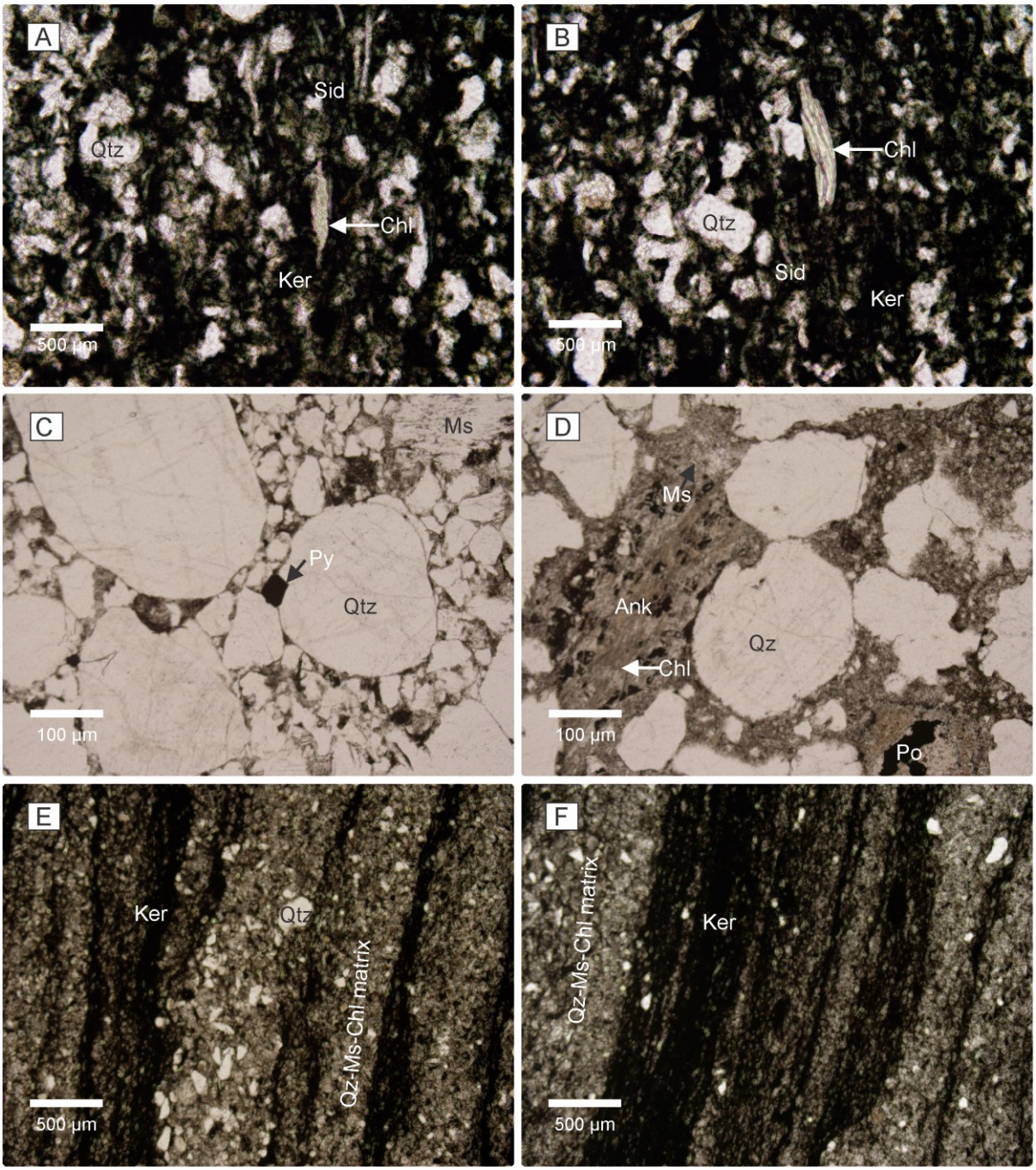

Figure 27: Photomicrographs of selected Black Reef Formation clastic sedimentary rocks demonstrating some of the mineral phases present. Plane-polarised light. (A) Elongated chlorite and concretion of siderite within black shale laminae. B) Euhedral to subhedral calcite, and elongated chlorite. (C) Rounded detrital quartz and secondary euhedral pyrite. (D) Chlorite intergrown with ankerite surrounding detrital quartz concretion and pyrrhotite. (E) Graded shale illustrating cyclicity of kerogen and coarse- and fine-grained fractions. (F) Layering along the bedding filled with kerogen surrounded by a matrix quartz-muscovite and chlorite.

Chlorite in the Black Reef Formation shales generally takes the form of flaky to tabular crystals or a matrix intergrown with quartz and muscovite. Chlorite, siderite, and muscovite are generally fine-grained (5–30 µm width) but reach 500 µm in length in places. Sulfides (i.e. pyrite and pyrrhotite) are finely disseminated, occur between quartz grains, or appear as concretions in the shale matrix (Figure 27 C and D). Muscovite and pyrite occur in minor to trace amounts.

Table 7: Semi-quantitative modal mineralogy of selected Black Reef Formation shale samples, as obtained by Rietveld analysis (in vol.%).

Sample ID	Quartz	Muscovite	K-feldspar	Chlorite	Carbon
E1H–000001	47	36	1	13	3
E1H–000002	57	25	1	11	6
E1H–000003	51	32	1	14	2
E1H–000004	58	26	1	12	3

5.2.6. Transvaal Supergroup marine shales: Pretoria Group

The Pretoria Group black shale lithofacies is composed of alternating black shale and siltstone laminae with wavy, lenticular, and flat (parallel) lamination. The laminae and bed thickness varies between 1–5 cm. The shale laminae and beds are black and highly carbonaceous. Moreover, minute carbonate and pyrite nodules occasionally occur in the shale laminae. These nodules or micro-concretions are ellipsoidal in shape, and the laminae appear compacted around them, indicating an early diagenetic origin for the concretions. The shales are composed of quartz ($\bar{x}$ = 34 vol.%), muscovite ($\bar{x}$ = 40 vol.%), dolomite ($\bar{x}$ = 1 vol.%), albite ($\bar{x}$ = 5 vol.%), chlorite ($\bar{x}$ = 32 vol.%), K-feldspar ($\bar{x}$ = 2 vol.%), and siderite ($\bar{x}$ = 1 vol.%, Table 8). Muscovite flakes often appear bent by compaction around larger quartz grains. Secondary muscovite, intergrown with chlorite, is also present (Figure 28 C). Other secondary minerals include pyrite and calcite. This mineralogical assemblage is common in both the upper (Figure 28 A and B) and lower (Figure 28 C and D) shale units of the Pretoria Group. In some shale units, soft-sediment deformation structures, like contorted bedding and load structures, are well-preserved (Figure 28 B). Brittle deformation structures are also present, and these include microfaults with a displacement of not more than a few millimeters (Figure 28 C).

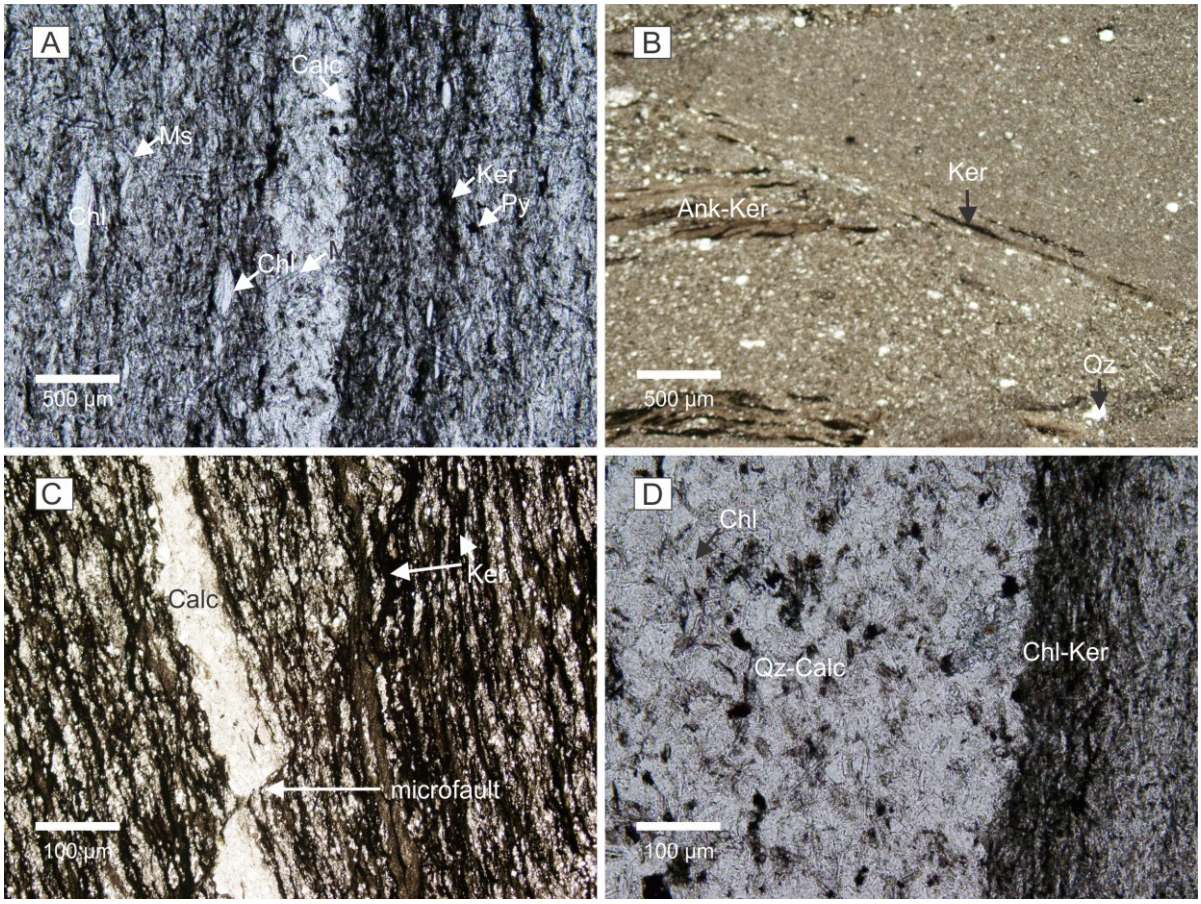

Figure 28: Photomicrographs of selected Pretoria Group shales illustrating some of the mineral phases present. Plane-polarised light. (A) Very fine-grained secondary muscovite within the black shale laminae of the Pretoria Group. (B) A typical example of a soft-sediment deformation structure (e.g. contorted bedding). Note the kerogen along the bending. (C) Evidence of micro faulting within the shale lamina in the lower Pretoria Group shale unit's calcite veinlet. (D) Chlorite intergrown with calcite surrounding a detrital quartz concretion.

Table 8: Semi-quantitative modal mineralogy of selected Transvaal Supergroup shale samples, as obtained by Rietveld analysis (in vol.%).

Sample ID	Quartz	Muscovite	Dolomite	Albite	K-feldspar	Chlorite	Siderite
Pretoria Group							
DP22–012	43	37	1	4	1	15	
DP22–013	20	48	1	8	4	19	
DP22–014	21	45	1	12	3	18	
DP22–015	23	44	1	9	4	20	
DP23–001	40	42		1		16	
DP23–009	45	43		1	1	10	1
DP23–014	43	29		1	1	25	1
DP23–015	40	30		1	1	28	1

6. MARINE SHALE GEOCHEMISTRY

Major and trace element (including REE and HSE) geochemical analyses have been used to characterise marine shales in the Barberton, Witwatersrand, and Transvaal supergroups (See Appendix A.1 for full dataset). Thus, this chapter defines the key geochemical indicators, discusses their distribution, and provides the Kaapvaal Craton sequences' background Au and PGE concentrations. Chemostratigraphic diagrams are presented to illustrate the inter-element behaviour of Au and PGE with regard to lithology and stratigraphy. Furthermore, this chapter offers crucial evidence of siderophile element endowment in the hinterland. The detailed geochemical dataset is given in Appendix A.1.

All the major and trace element (including REE) concentrations were normalised against the post-Archaean Australian shale (PAAS) values (Taylor and McLennan, 1985). The PAAS normalisation also serves to illustrate which elements were gained (enrichment) and which elements were lost (depletion) relative to the reference values. It can be expected that the sample elemental and compound values in a regional stratigraphy (i.e. samples from various geographic locations within the Fig Tree Group) will be subject to a larger relative variation than those in close proximity to the same stratigraphic unit. This implies that samples taken close to each other are more likely to have similar values than those taken farther apart. It is therefore important to monitor and reduce conditional biases that may be introduced by systematic under- and over-valuation of compositional mean estimates in different stratigraphic units or within the same stratigraphic unit. In this study, sampling covered large and varied geographic locations and vertical profiles (Figure 29). Element concentrations with distinct differences between their arithmetic and geometric mean values indicate that the data are log-normally distributed. In this case, data were averaged using geostatistical mean such as Napier's constant inverse log, adding a standardised moment as described in Chapter 4, Section 4.9. Therefore, data presented in this Chapter represent averaged values of different samples with some stratigraphic units having over 100 samples (Appendix A.1). Three groups of trace elements that are classified on the basis of their behaviour were used to characterise the trace element data, namely: (i) large ion lithophile elements (LILEs), including Mn, Rb, Ba, Sr, Pb, Cs, Th, and U; (ii) transition elements (TEs), including Co, Cr, Cu, Ni, V, Sc, and Zn; (iii) HFSEs, including Ga, Ge, Zr, Nb, Hf, Ta, and Ti. The REEs (La to Lu) can be divided into light REEs (LREEs, La to Nd), middle REEs (MREEs, Sm to Dy), and heavy REEs (HREEs, Ho to Lu).

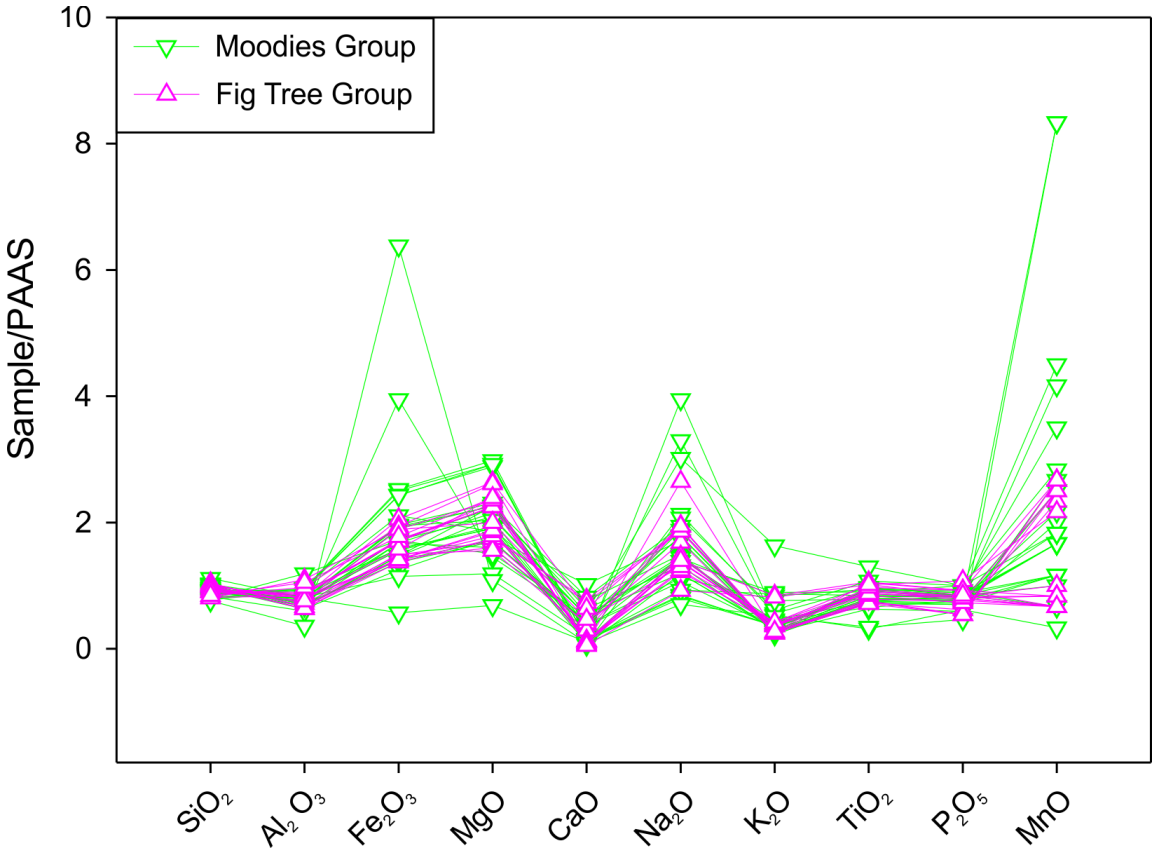

Figure 29: Example of Fig Tree and Moodies groups' marine shale major element data prior to geostatistical processing.

6.1. Barberton Supergroup marine shales

6.1.1. Major elements

This analysis examined two Barberton Supergroup shale formations, namely, the Sheba Formation of the Fig Tree Group, and the Clutha Formation of the Moodies Group. These two formations were chosen as the most representative units of marine shale deposits in the Fig Tree and Moodies groups, respectively. Chemical variations of the samples are visible in the major element contents, as also observed by Toulkeridis et al. (2015). The SiO_2 content of the Fig Tree shales ranges from 58.29 to 67.28 wt.%, averaging 63 wt.%. This figure is slightly higher than that for the Moodies shales, where the SiO_2 content ranges from 50.03 to 66.77 wt.%, averaging 58.81 wt.%. Toulkeridis et al. (2015) observed that the SiO_2 contents of the Fig Tree Group shales range from 50.2 to 58.9 wt.%, with an average of 54.4 wt.%. This is lower than the SiO_2 contents of the Moodies Group shales, which range from 55.5 to 63.1 wt.%, with an average of 60.4 wt.%. The sampled Moodies shales have a higher Al_2O_3, Fe_2O_3, MgO, and CaO content and lower K_2O and Na_2O content relative to PAAS data. Data from Toulkeridis et al. (2015) show that the Fig Tree Group shales have higher TiO_2, Fe_2O_3, MnO,

MgO, and P_2O_5 contents, lower K_2O and Na_2O contents, and a higher loss of ignition (LOI) than the Moodies Group shales. Both the Fig Tree and Moodies groups marine shales yield lower SiO_2, TiO_2, and CaO contents relative to PAAS values (Figure 30). The Fig Tree and Moodies groups' shale yield lower K_2O/Na_2O ratios ($\overline{x}$ = 0.78 and $\overline{x}$ = 0.87, respectively), both of which are below the PAAS benchmark (3.48). The Fig Tree and Moodies Group shales' K_2O/Na_2O ratios are similar to values obtained in previous studies of the Archaean shales, with a range of 0.7–1.5 (Taylor et al., 1986; Wronkiewicz and Condie, 1989). The Fig Tree Group shales' SiO_2/Al_2O_3 ratio ($\overline{x}$ = 4.98 ± 0.86) is slightly lower than that of the Moodies Group shales ($\overline{x}$ = 4.58 ± 0.99), although both ranged within the known level of variation for Archaean greenstone shales (from approximately 3 to 5, Taylor et al., 1986). The chemical variations between shales from this current study and those of Toulkeridis et al. (2015) are attributed to the differences in sampling points. Toulkeridis et al.'s (2015) samples were taken from two localities that are in close proximity to Fairview gold mine (Fig Tree Group shales) and Agnes gold mine (Moodies Group samples). This increases the geochemical differences with stratigraphic range, and widens the potential depositional differences.

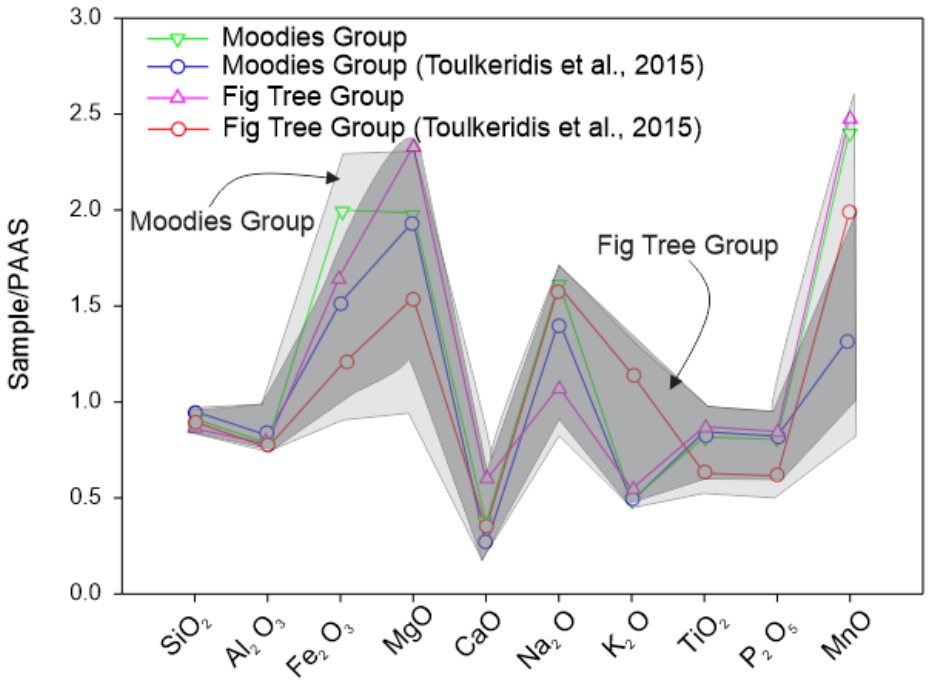

Figure 30: Multi-element diagram of average major element concentrations for Fig Tree and Moodies groups' shales. Coloured bands mark the range of data for the respective sample group. Normalising values after Taylor and McLennan (1985).

There are positive correlations between Al_2O_3–TiO_2 (r = 0.7), Fe_2O_3–MgO (r = 0.96), Fe_2O_3–TiO_2 (r = 0.95), SiO_2–C (r = 0.93), MgO–TiO_2 (r = 0.95), CaO–MnO (r = 0.87), CaO–S (r =

0.90), and MnO–S (r = 0.70) in the Fig Tree Group. Moreover, there are positive correlations between Al_2O_3–TiO_2 (r = 0.8), Al_2O_3–P_2O_5 (r = 0.78), Fe_2O_3–MnO (r = 0.72), Fe_2O_3–S (r = 0.82), MnO–S (r = 0.75), TiO_2–P_2O_5 (r = 0.89), and total organic carbon–sulfur (r = 0.87) in the Moodies Group. The positive Al_2O_3–TiO_2 correlation corroborates the assumption that heavy minerals such as titanite and illmenite, are the main carriers of Ti, and that they are intimately mixed with the clay particles in the <2 µm fraction (Toulkeridis et al., 2015). Figure 31 A and B illustrates the abundance of minerals present, including biotite and hornblende (representing mafic source rocks), felsic and clay minerals (e.g. K-feldspar), muscovite, and quartz.

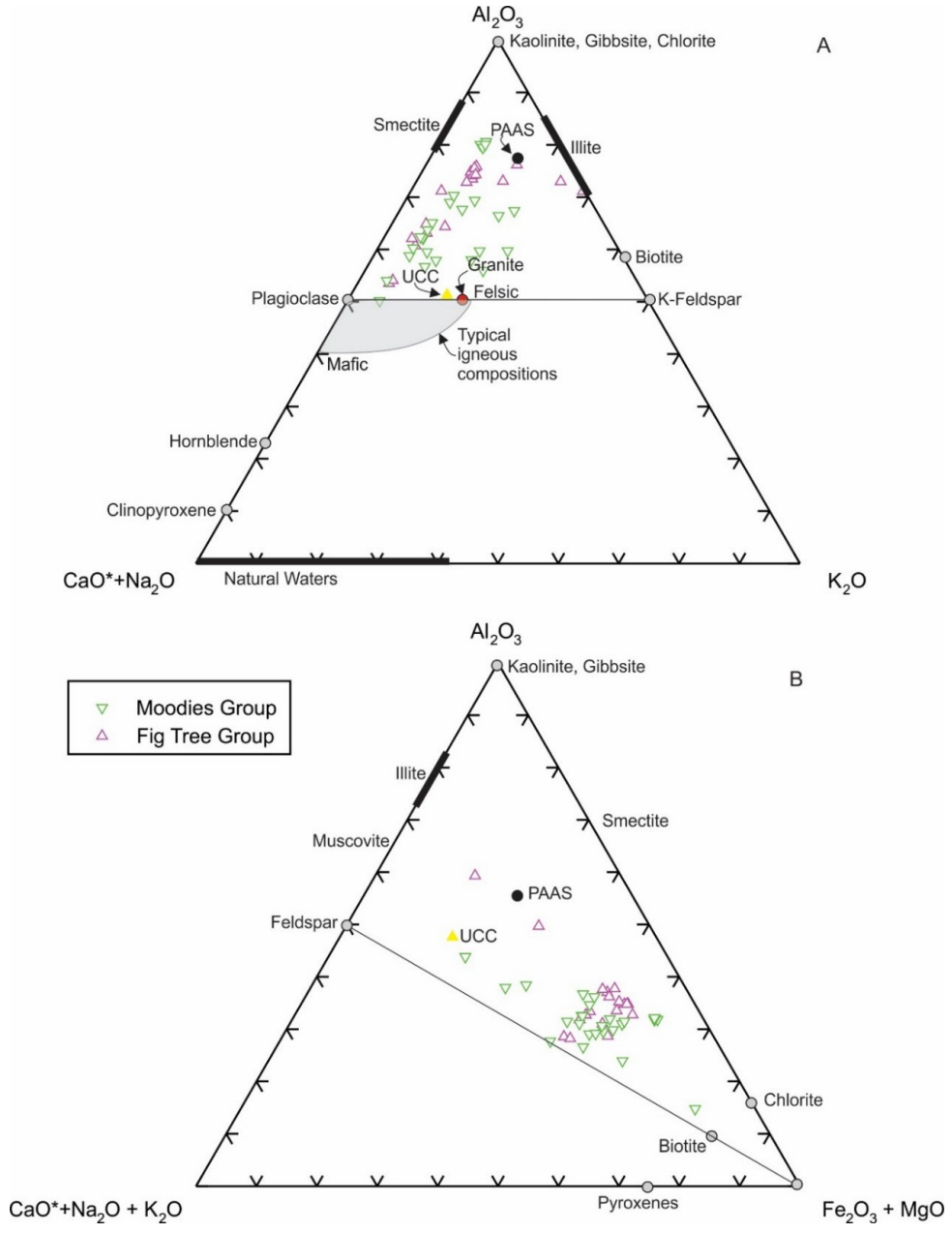

Figure 31: A. Ternary diagram of ACNK (Al_2O_3:[CaO* + Na_2O]:K_2O) (modified after Nesbitt and Young, 1984) for Fig Tree and Moodies Group shales, illustrating a wide

range of palaeoweathering. Average values for the upper continental crust and PAAS values were obtained from Taylor and McLennan (1985); B. Ternary diagram (ACF) indicating molar proportions of Al_2O_3:($CaO^* + Na_2O + K_2O$):$Fe_2O_3 + MgO$) and distinctive chemical change characteristic of alteration for some Fig Tree and Moodies Group shales. The average PAAS value was obtained from Taylor and McLennan (1985). The composition of the upper continental crust is from Rudnick and Gao (2005).

6.1.2. Trace elements including rare earth and highly siderophile elements

6.1.2.1. Distribution of trace elements and stratigraphic variations

Large ion lithophile element geochemistry: The Fig Tree shales are depleted in Rb ($\overline{x}$ = 55 ppm), Sr ($\overline{x}$ = 56 ppm), Ba ($\overline{x}$ = 255 ppm), and U (1.43 ppm) relative to the PAAS reference, and the same trend was observed in the Moodies shales. Both the Fig Tree (Rb = 28.70–78 ppm) and Moodies (Rb = 30.18–54.30 ppm) groups are highly variable in their Rb content. The Th contents of both the Fig Tree and Moodies shales are also depleted relative to PAAS (Figure 32). Data from Toulkeridis et al. (2015) also show that the Fig Tree Group shales have lower Rb, Sr, Cs, U, and Th contents than the Moodies Group shales.

High-field strength element and transition metal geochemistry: The Fig Tree and Moodies Group shales yield lower Hf, Zr, Nb, Ta, and Y contents than the PAAS reference. Compared to the Moodies Group shales, the Fig Tree Group shales contain less Zr and Y, but have similar amounts of Hf, Nb, and Ta. The Fig Tree Group shales revealed slightly higher Zr/Y ratios, whereas the Zr/Nb ratio is similar to those of Moodies Group shales. There are strong positive correlations between Ta–Nb (r = 0.95), Y–Nb (r = 0.91), and Zr–Hf (r = 0.99) in the Fig Tree Group shales. The Moodies Group shales also display positive correlations for Ta–Nb (r = 0.85) and Zr–Hf (r = 0.97). A reliable positive correlation is also observed between U–Th (r = 0.99), U–Zr (+0.9), and Th–Zr (r = 0.7) in the Fig Tree Group shales and between Th–Zr (r = 0.9), U–Th (0.87), and U–Zr (r = 0.8) in the Moodies Group shales. High Cr and Ni concentrations were noted by Danchin (1967), and later by McLennan et al. (1983), in the Barberton Supergroup shales. In this study, the Fig Tree and Moodies groups yield Cr contents of 874 ppm and 861 ppm, respectively, distinctly above the PAAS reference value (110 ppm). The Ni content is also higher compared to that of PAAS (23), averaging 343 ppm for the Fig Tree Group shales and 351 ppm for the Moodies Group shales. Compared to the Fig Tree Group, trace element contents of the Moodies Group shales are similar to those of PAAS in the Toulkeridis et al. (2015) data. Although the absolute abundances differ, the Cr/Ni ratio

(~3) is similar for the Fig Tree and Moodies groups, and higher than the Cr/Ni ratio of komatiites (~1.6, Condie, 1993, 1994). A positive correlation exists between Cr and Ni on the one hand, and MgO, Sc, and V, on the other hand, in both groups of samples. The Fig Tree group yields an average Co content of 80 ppm, a figure lower than that observed for the Moodies Group (Co = 103 ppm) but higher than the PAAS value (Co = 23).

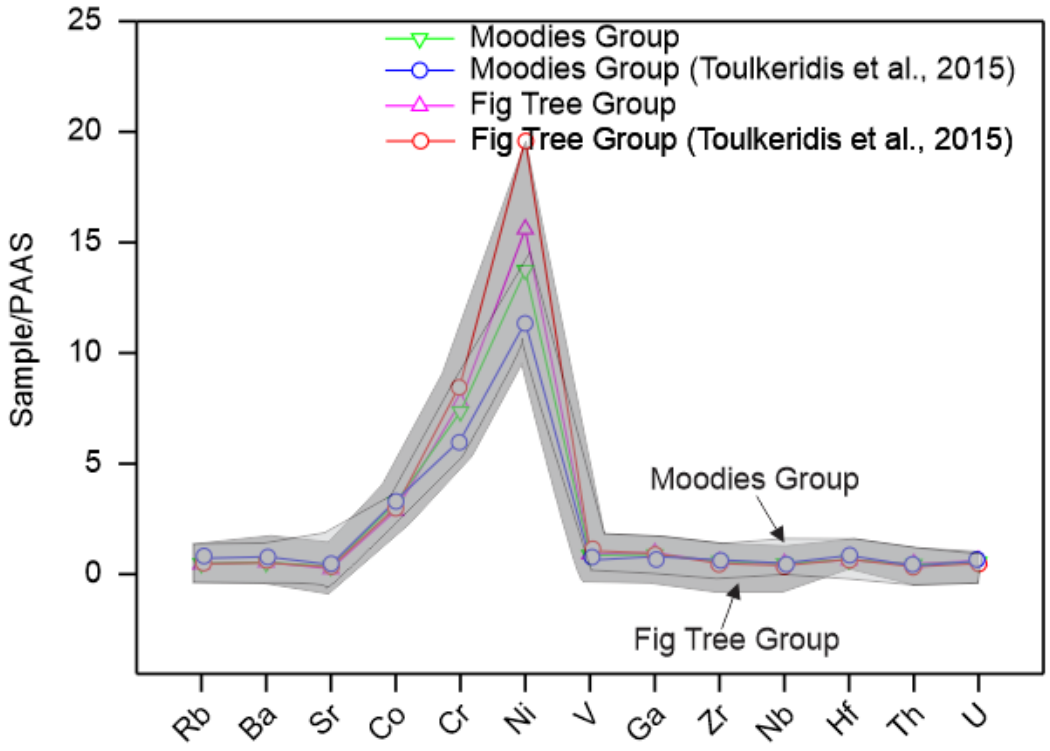

Figure 32: Multi-element diagram of average trace element concentrations for Fig Tree and Moodies groups' shale. Coloured bands mark the range of data for the respective sample group. Normalising values after Taylor and McLennan (1985).

6.1.2.2. Total rare earth element contents and stratigraphic variations

The REEs are known to be reliable provenance indicators (e.g. Taylor and McLennan, 1985), because they tend to be transferred without significant fractionation from the source material to the site of deposition. For that reason, they reflect the average REE composition of the source (Cullers et al., 1979; McLennan et al., 1980). This assumption, however, does not seem to be universal (Chaudhuri et al., 1992; Honty et al., 2008). Moreover, although the REE concentrations are variable, the PAAS-normalised patterns are very similar for both groups (Figure 33). Shales from the Fig Tree and Moodies groups are depleted in REE relative to PAAS. The apparent depletion of REEs is most likely because some of the samples are actually silty and thus have a higher quartz content, which would have diluted the total REE.

This conclusion is in line with a study by McLennan et al. (1983), which noted that the low abundances of many of the trace elements (e.g. total REE, LILE, and ferromagnesian elements) are due to dilution with quartz. In this study, quartz dilution is illustrated by a SiO_2 content that is much higher (SiO_2 = 77.24 wt.%) in some samples than in PAAS (SiO_2 = 64.8 wt.%). Furthermore, REE fractionation can occur during diagenesis or low-grade metamorphism (Awwiller and Mack, 1991; Schaltegger et al., 1994; Awwiller, 1993, 1994; and references therein). The total REE concentration in the Fig Tree Group is similar to that of the Moodies Group. In the Fig Tree Group, the total average LREE content is 77 ppm, the total average MREE content is 12 ppm, the total average HREE content is 5 ppm, and the total average Y content is 17 ppm. In the Moodies Group, the total LREE content is 82 ppm, the total MREE content is 12 ppm, and the total HREE content is 5 ppm. In both groups, the LREE/MREE, LREE/HREE, and MREE/HREE ratios are similar, although the individual samples vary. Overall, the Barberton Supergroup shales reveal fairly uniform REE patterns, with low total REE and La_N/Yb_N, and positive Eu anomalies relative to PAAS. The same patterns were observed by Toulkeridis et al. (2015).

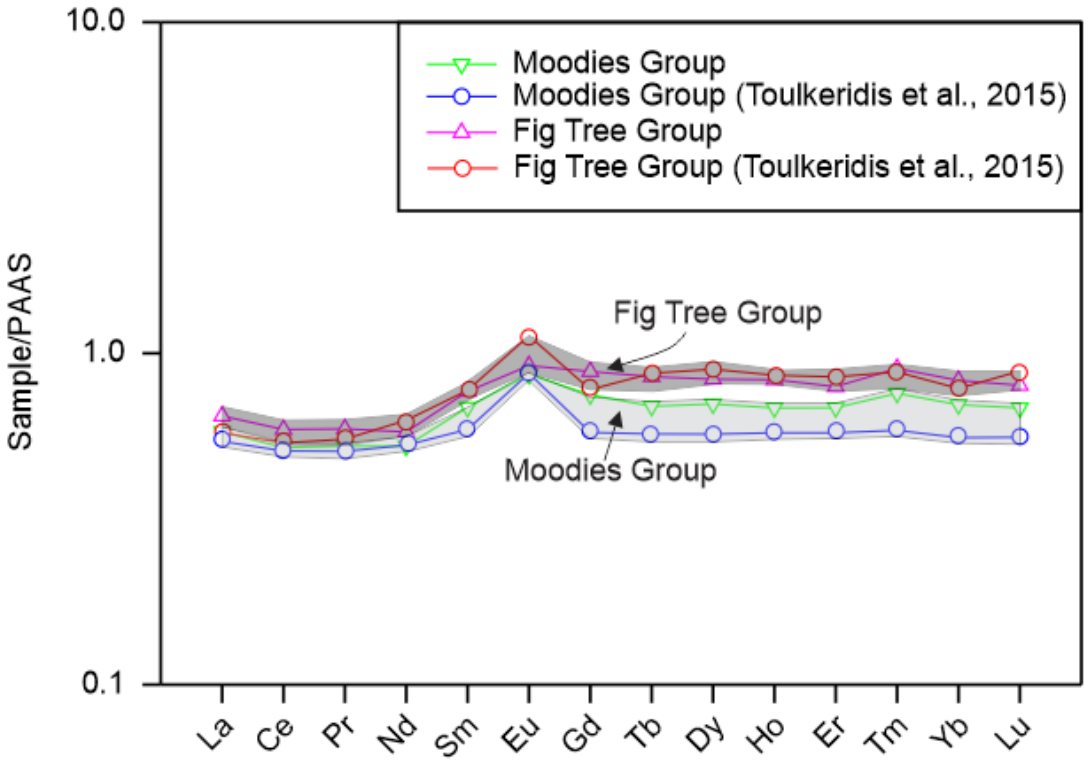

Figure 33: Multi-element diagram of average REE concentrations for Fig Tree and Moodies groups marine shales. Coloured bands mark the range of data for the respective sample group. Normalising values after Taylor and McLennan (1985) and McLennan (2001).

6.1.2.3. Highly siderophile elements

The Au content of the Fig Tree Group shales ranges from 2–18 ppb (Figure 34 and 35). Moreover, the Au content of some of the drill cores is highly variable and characterised by outliers. The Pd concentrations in the Fig Tree Group shales range from 2–4 ppb. Generally, the Pd content does not exhibit much variation or systematic changes. The Pt concentrations in the Fig Tree Group shales also range from 2 to 4 ppb. In contrast to the Pd concentrations, the Pt content is more variable, although its distribution is slightly different. Other PGEs (e.g. Ir, Os, and Rh) in the Barberton Supergroup shales have concentrations below the detection limits, while the Ru yields fall within a very narrow range (1–3 ppb). The Fig Tree Group shales yield maximum Ru concentrations of 2 ppb, whereas this figure is 3 ppb for the Moodies Group shales. The Au content of the Moodies Group shales ranges from 2 to 5 ppb (Figure 36 and 37). In contrast, its PGE content is less variable, with no significant outliers. The Pd concentrations of the Moodies Group shales also range from 2 to 5 ppb, but do not demonstrate a high level of variance or systematic changes. The Pt concentration of the Moodies Group shales ranges from 2 to 6 ppb. In most Moodies Group samples, the Pt content mimics the Pd curve, although slight variations arise in places, within the same stratigraphic profile. In general, with the exception of the Au outliers, the Moodies Group shales display similar Au and PGE compositional patterns, similar to the Fig Tree Group shales.

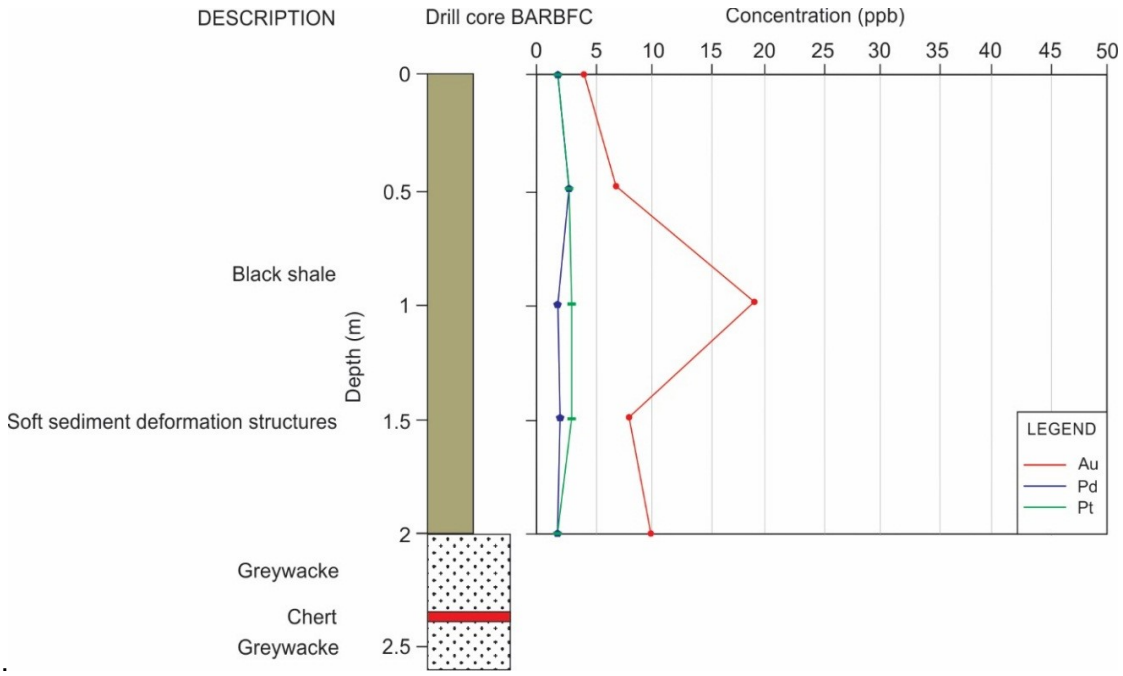

Figure 34: Chemostratigraphic plots of Au and PGE for Fig Tree Group marine shale (drill core BARBFC).

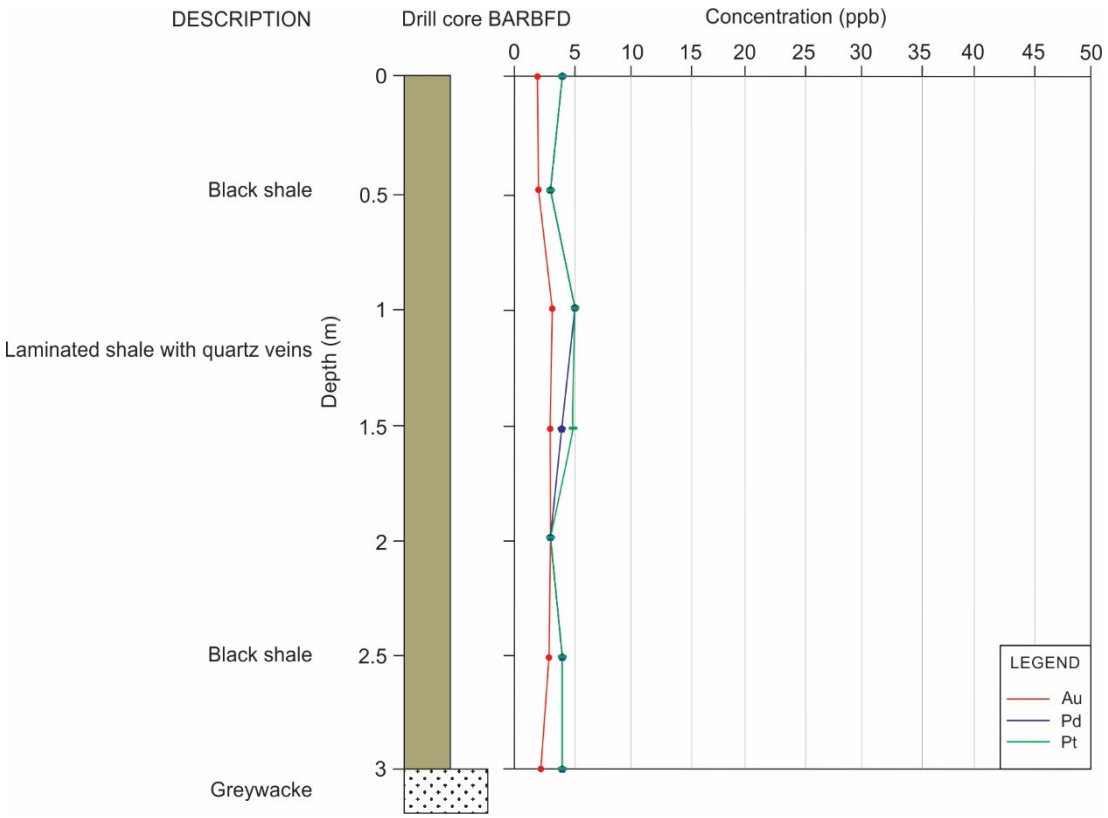

Figure 35: Chemostratigraphic plots of Au and PGE for Fig Tree Group marine shale (drill core BARBFD).

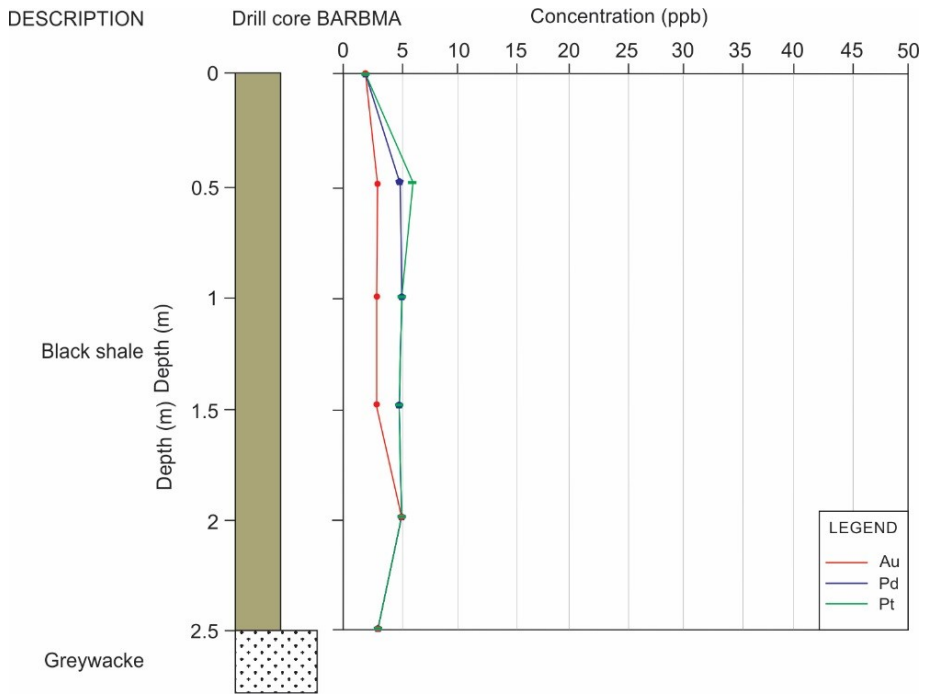

Figure 36: Chemostratigraphic plots of Au and PGE for Fig Tree Group marine shale (drill core BARBMA).

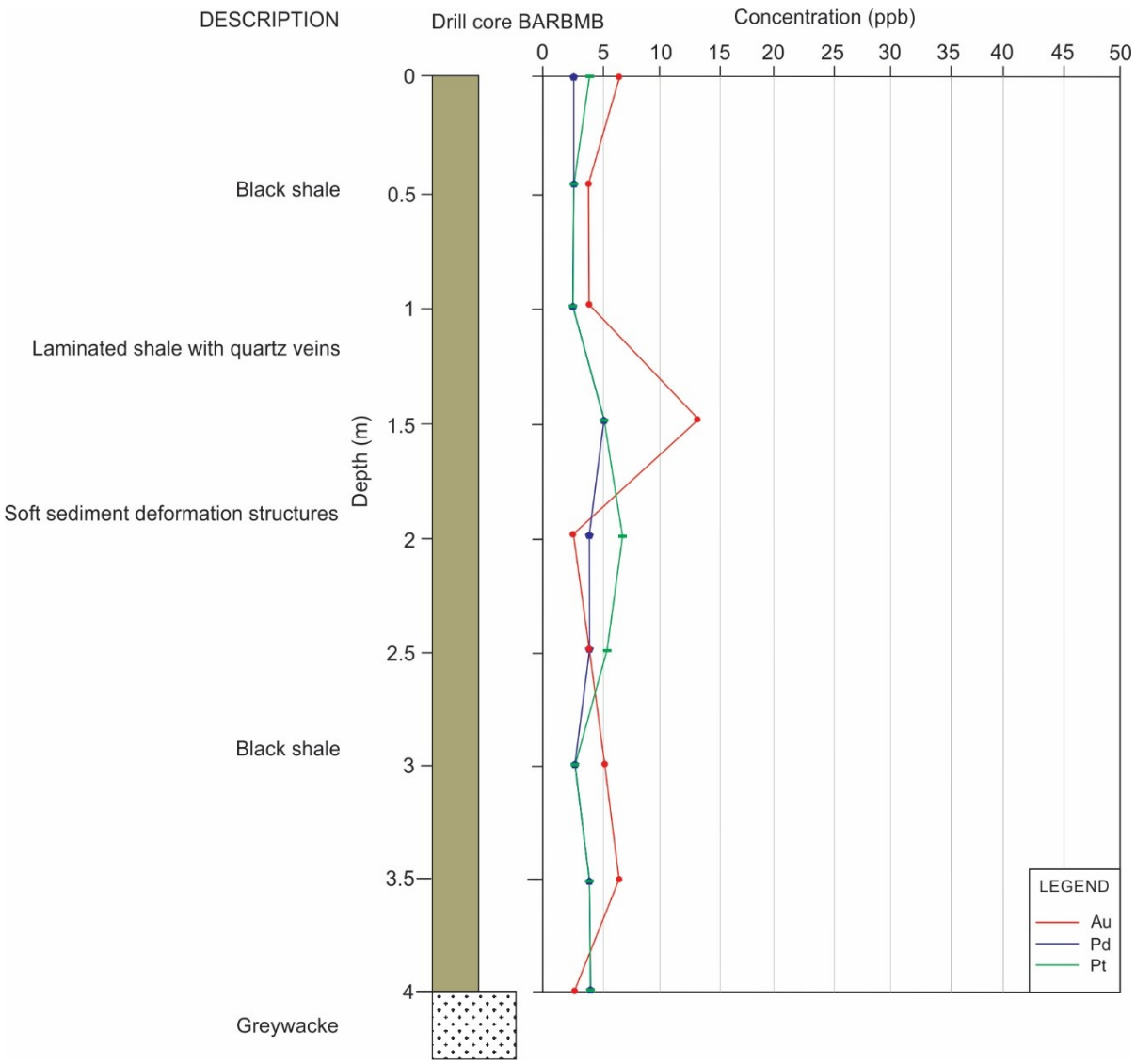

Figure 37: Chemostratigraphic plots of Au and PGE for Fig Tree Group marine shale (drill core BARBMB).

6.2. Witwatersrand Supergroup marine shales

6.2.1. Major elements

The main Witwatersrand shale components are SiO_2, Al_2O_3, Fe_2O_3 (representing total Fe content), MgO, and K_2O, and they show significant variations in concentration among individual stratigraphic units. The shale composition changes both with stratigraphic height and laterally within a given stratigraphic unit. The SiO_2/Al_2O_3 ratio is generally high, with considerable stratigraphic variation (e.g. 1.9–6.6 in the Hospital Hill Formation, 4.4–5.2 in the Government Formation, 3.4–5.1 in the Roodepoort Formation, and 2.4–7.7 in the Booysens Formation shale). The analysed shales have highly variable TiO_2 concentrations that range from 0.01 to 1.9 wt.%. Differences in TiO_2 content within a single shale unit can be as much as ±1.3 wt.%, as in the Booysens Formation shale in the Welkom goldfield. The concentration of Al_2O_3 is inversely proportional to that of SiO_2, reflecting a higher abundance of clay minerals (e.g. kaolinite and illite) than in the coarser, more quartz-dominated fraction. The negative correlation coefficient reiterates the quartz/clay antagonism. The Pearson correlation coefficient of TiO_2–Al_2O_3 in the Roodepoort Formation is r = 0.4, whereas in the Booysens Formation it is as high as r = 0.95. Most West Rand Group and Central Rand Group shales show a strong positive correlation between Al_2O_3–K_2O (r = 0.80) in the Roodepoort Formation and in the Booysens Formation (r = 0.91), with a K_2O/Al_2O_3 ratio (0.3) close to the upper limit of the clay mineral range. This suggests that the principal host minerals of these components are chlorite and muscovite, which is supported by the petrographic modelling (Figure 38 A). The West Rand Group shales contain, on average, 0.12 wt.% total organic carbon, and 0.42 wt.% sulfur. Likewise, those from the Central Rand Group contain, on average, 0.2 wt.% total organic carbon, and 0.09 wt.% sulfur.

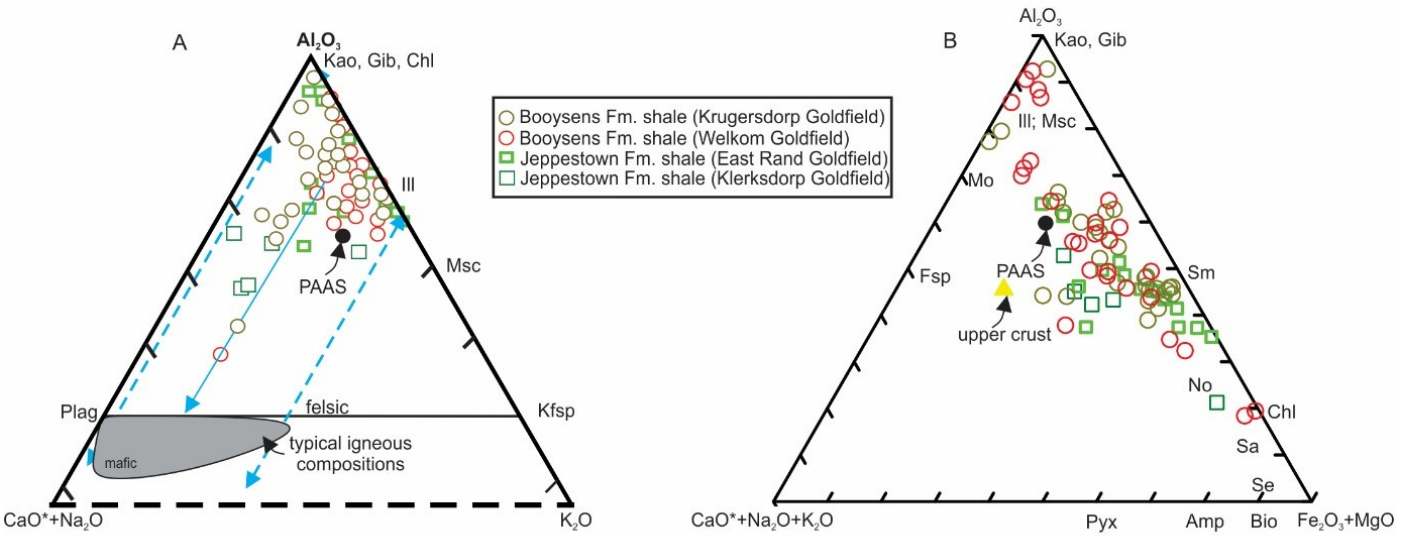

Figure 38: A. Ternary diagram of ACNK (Al_2O_3:[CaO* + Na_2O]:K_2O) (modified after Nesbitt and Young, 1984) for West Rand and Central Rand Group shales, illustrating both a wide range of palaeoweathering and source differences for the goldfields. Blue lines indicate weathering trends for felsic (right) and intermediate (left) source rocks. Average values for upper continental crust and PAAS are from Taylor and McLennan (1985). B. Ternary diagram (ACF) showing molar proportions of Al_2O_3:(CaO* + Na_2O + K_2O):Fe_2O_3 + MgO) and distinctive chemical change characteristic of alteration for some West Rand and Central Rand Group shales. Ideal mineral compositions: Amp p amphibole; Bio = biotite; Chl/chl = chlorite; Fsp = feldspars; Gib/gib = gibbsite; Ill = illite; Kao = kaolinite; Kfsp = K-feldspar; Mo = montmorillonite; Msc = muscovite; No = nontronite; PAAS = post-Archaean Australian shale; Pla = plagioclase; Pyx = pyroxene; Sa = saponite; Se = serpentine; Sm = smectite. Average value of upper continental crust and PAAS from Taylor and McLennan (1985). The composition of upper continental crust is from Rudnick and Gao (2005).

As the ACF ternary plot (Figure 38 B) illustrates, the shale compositions reflect a wide range of mixtures of chlorite (derived from ferromagnesian minerals in mafic source rocks), illite, kaolinite, and feldspars (derived from felsic minerals in granitic source rocks). Most of the West Rand Group shales are enriched in Fe, as are some of the Central Rand Group shales (e.g. the Booysens Formation shales). In general, the Central Rand Group shales are more aluminous. Almost all of the analysed samples have a low CaO and P_2O_5 content. The depletion of CaO and P_2O_5 is reflected by the low proportion of phosphorous accessory phases, such as apatite and monazite, compared to average post-Archaean shale composites (e.g. PAAS). Significant variations in Na_2O, K_2O, and CaO are observed in the Central Rand Group shales, such as the Booysens Formation shales in the Krugersdorp, Klerksdorp, and Welkom goldfields.

An ACF ternary plot illustrates the relative abundance of ferromagnesian minerals, such as biotite and hornblende (representing mafic source rocks), and felsic minerals, such as K-feldspar, muscovite, and quartz (Figure 38 B). Note that some of the Fe is related to chemical sedimentation of Fe-oxide/silicate especially in the West Rand Group shales which are rich in magnetite that is not detrital. Almost all of the samples have a low CaO and P_2O_5 content. The depletion of CaO and P_2O_5 is reflected by the low proportion of phosphorous accessory phases, such as apatite and monazite, compared to PAAS.

6.2.2. Trace elements including rare earth and highly siderophile elements

6.2.2.1. Distribution of trace elements and stratigraphic variations

The Roodepoort Formation shales (Figure 39) are depleted in large ion lithophile elements (LILE) relative to PAAS, particularly in Rb (15.5 to 135 ppm, $\overline{x}$ = 48.25 ppm), Sr (10.2 to 213 ppm, $\overline{x}$ = 64 ppm), Ba (131.8 to 833.8 ppm, $\overline{x}$ = 412 ppm), and U (0.98 to 1.4 ppm, $\overline{x}$ = 1.14 ppm). The same trend was observed in the Parktown-Brixton Formation and the Promise Formation. The Mn concentration of the West Rand Group shales is higher (>0.06 ppm) than PAAS and varies with depth. The Booysens Formation shale is enriched in Ba (711 to 761 ppm, $\overline{x}$ = 742 ppm) relative to PAAS, depleted in Rb and Sr, and its U content varies with stratigraphy and geographic location. In the Kimberley (K8) Formation, Ba concentrations are low. The shales from the K8 Formation are enriched in K, Sr, and Pb, relative to other formations of the Witwatersrand.

Transition elements are compatible and tend to be concentrated in mafic rather than felsic rocks. In the Roodepoort Formation, V ($\overline{x}$ = 105 ppm) concentrations are lower compared to PAAS (150 ppm), and the Co, Cr, and Ni contents ($\overline{x}$ = 81, 633, 245 ppm, respectively) are

considerably higher relative to PAAS. Conversely, in the Booysens Formation, Co, Cr, Ni concentrations ($\bar{x}$ = 124, 580, 114 ppm, respectively) are elevated relative to PAAS but lower than in West Rand Group shales. Central Rand Group shales are enriched in V ($\bar{x}$ = 143 ppm) compared to West Rand Group shales but have a lower concentration than PAAS. In the K8 Formation, the V content ($\bar{x}$ = 179 ppm) is higher than that in PAAS.

High-field strength elements are, because of their incompatible behaviour, preferentially concentrated in felsic rocks. Their relatively immobile behaviour during alteration makes them useful for provenance studies (Taylor and McLennan, 1985). The concentrations of the HFSE in the West Rand Group shales are lower than in PAAS. Comparison of PAAS, West Rand Group, and Central Rand Group shales shows that concentrations of Ga, Hf, Zr, Ta, and Ti are higher in the Central Rand Group. The Nb concentration (15.6–18.5 ppm) is similar to that in PAAS (19 ppm). The Cs concentration is also low (<9 ppm) in almost all of the Witwatersrand Supergroup marine shales.

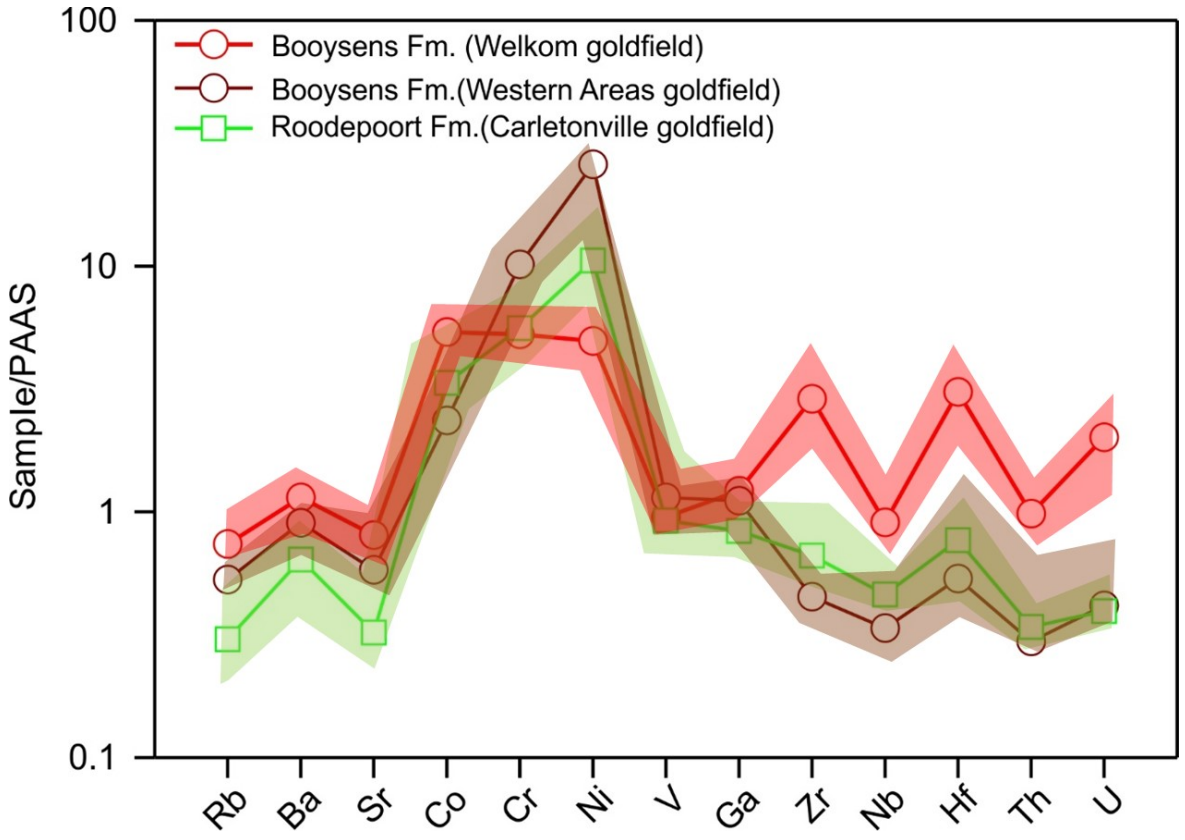

Figure 39: Multi-element diagram of average trace element concentrations for Roodepoort and Booysens Formations' shale. Normalising values after Taylor and McLennan (1985).

For the Roodepoort Formation, the Pearson correlation coefficients for trace element concentrations reveal a strong positive correlation between the following elements: Nb–Co (r = 0.63), Ni–Cr (r = 0.84), Ba–Rb (r = 0.76), Hf–Sc (r = 0.68), Hf–Th (r = 0.82), Hf–Zr (r = 0.9), and Th–Zr (r = 0.86). The Cr/V ratios of the Witwatersrand shales are significantly higher than those of PAAS (0.73), and the Y/Ni ratios in most cases are lower (<0.09) than those of PAAS (0.49). The V/Ni ratios are also low (<1), whereas the Ni/Co (9.9) and Cr/Co (20.4) ratios are much higher than those in PAAS (Ni/Co = 2.4 and Cr/Co = 4.8). The Nb/Cr (0.01 to 0.71), Nb/Zr (0.03 to 0.13), and Nb/Y (0.21 to <1) ratios are similar to those of PAAS. A most striking feature is the vertical chemical variation within an individual shale unit (i.e. Booysens Formation shale, as evident from data from borehole DN–2).

6.2.2.2. Total rare earth element content and stratigraphic variations

Significant absolute concentration variations in REE content were found to exist between various stratigraphic units of the Witwatersrand and within individual formations. In a PAAS-normalised REE plot (Figure 40), the shale samples from the Witwatersrand Supergroup show similar patterns (relative concentrations) for all formations. Shales of the Orange Grove and Kimberley Formations are slightly enriched in all REEs relative to PAAS. Those of the Parktown, Brixton, and Promise Formations are depleted in REEs. Total REE contents range from 70 to 175 ppm, $\overline{x}$ = 113 ppm (Roodepoort Formation) and 174 to 186 ppm, $\overline{x}$ = 181 ppm (Booysens Formation). In the Roodepoort Formation, the total average of light REE (LREE, i.e. La to Nd) ($\overline{x}$ = 90.9 ppm) content gradually increases from the bottom to the top of the shale unit. The total average content of middle REEs (MREE, i.e. Sm to Dy) ($\overline{x}$ = 15.2 ppm) and heavy REEs (HREE, i.e. Ho to Lu) ($\overline{x}$ = 7.1 ppm) and Y ($\overline{x}$ = 24 ppm) in the Rooderpoort Formation shale fluctuates with changes in depth. In the Booysens Formation shale, the average LREE ($\overline{x}$ = 155 ppm), MREE ($\overline{x}$ = 18 ppm) and HREE ($\overline{x}$ = 8.7 ppm), Y ($\overline{x}$ = 26.4 ppm) content is highly variable. The shales from the Central Rand Group are enriched in REEs, analogous to LILE, HFSEs, and transition metals, relative to shales from the West Rand Group. A slight positive Eu anomaly is noted for all Witwatersrand shales relative to PAAS (Eu* = 1.24), which most likely reflects the overall more reducing conditions of sedimentation during Archaean times compared to later, post-GOE (‘Great Oxidation Event’) times.

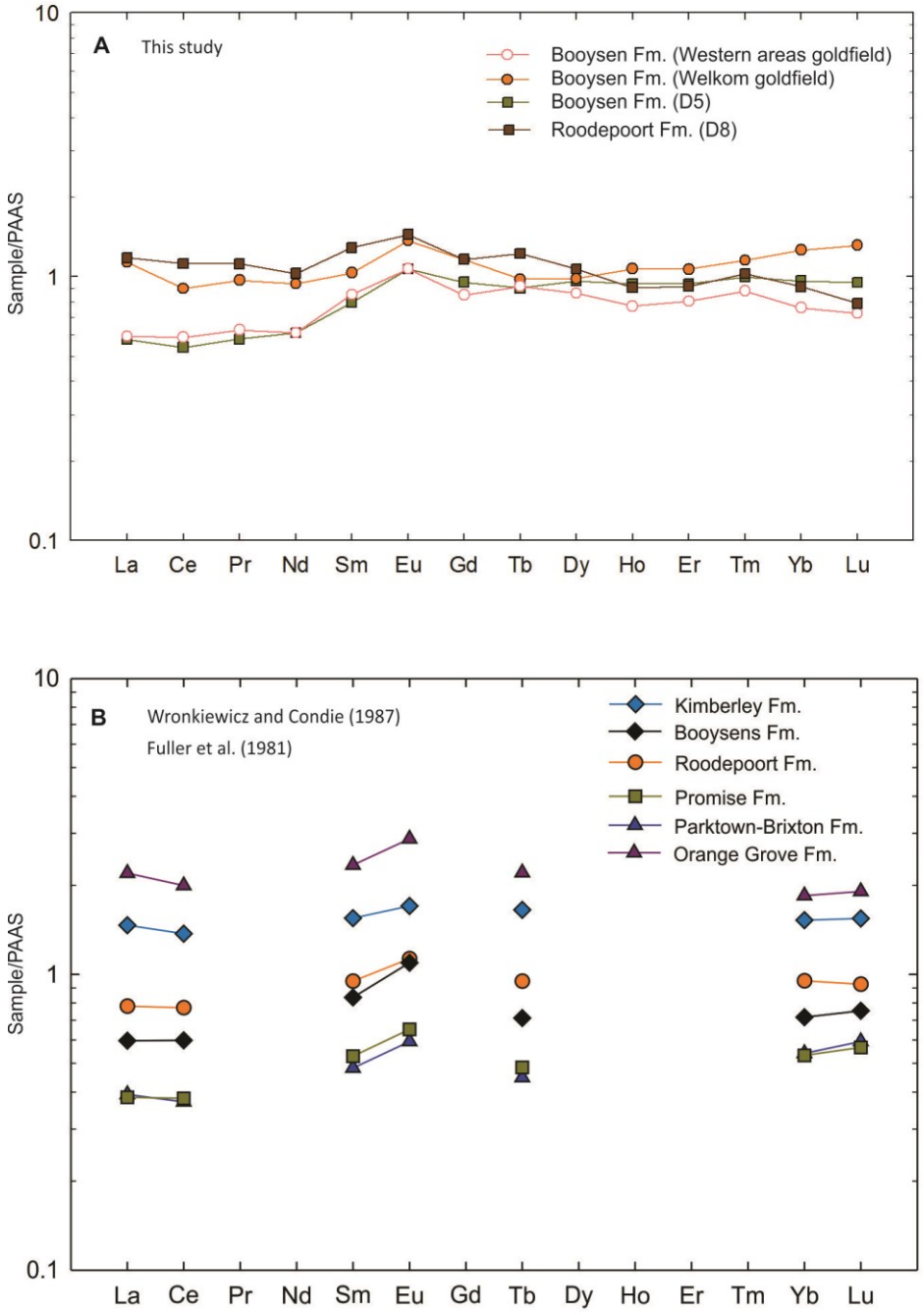

Figure 40: A. PAAS-normalised, average REE patterns for Witwatersrand shale units. B. PAAS-normalised data from Fuller et al. (1981) and Wronkiewicz and Condie (1987). Normalising values after Taylor and McLennan (1985) and McLennan (2001).

6.2.2.3. Highly siderophile elements

The Au content of the Roodepoort Formation shales varies significantly, both vertically and laterally, and averages 6.57 ± 1.76 ppb. The Pd and Pt concentrations in the same samples

average 4.2 ± 0.02 and 3.97 ± 0.02 ppb, respectively, being less variable, both vertically and laterally. Moreover, Au positive outliers are common in both pristine and altered Roodepoort Formation shales. A detailed stratigraphic Au concentration profile for the Roodepoort Formation is provided by drill core D5P03463 (Figure 43). As the figure indicates, the Au concentration appears uniform in most of the Roodepoort Formation shale units, with major Au positive outliers occurring in specific zones. This trend is also observed in drill cores E1E (Figure 41) and E1G (Figure 42). The alteration profile (UNG, Figure 44) yields relatively higher Au values (>20 ppb) and lower PGE values (>10 ppb). Generally, the Au content ranges from 3 to 7 ppb, with part of the sample population falling below the 1 ppb detection limit. The Pd concentrations range from 2 to 8 ppb in all sampled Roodepoort Formation shale units.

The Pd concentrations are lower in concentration and less variable than those of Au. No noteworthy Pd positive outliers are observed in the sampled units, including those observed to be altered. The Pt concentrations for the Roodepoort Formation range from 2 to 7 ppb. These concentrations display similar compositional patterns to those for Pd, but are less variable, both vertically and laterally. No progressive increase or decrease in Pd is observed, aside from highly localised fluctuations of less than 2 ppb.

In general, the Roodepoort Formation is characterised by high Au concentrations relative to Pt and Pd concentrations. The Booysens Formation shales were sampled in both the Welkom (Figure 45) and Western Areas goldfields (Figure 46). The Au content of the Booysens Formation shale ranges from 6 to 26 ppb in the Welkom goldfield, and <1 to 5 ppb in the Western Areas goldfield. The Pt content in the Welkom and Western Areas goldfields is similar to the Pd content both in range, of 3 to 5 ppb and 6 to 13 ppb, respectively, and in distribution pattern. Highly siderophile elements such as Ir, Os, and Rh in the Witwatersrand Supergroup shales yield concentrations below detection limits. Although largely constant concentrations of Ru (1–2 ppb) were observed across all assayed Witwatersrand shales, positive outliers reaching a maximum of 4 ppb were observed. No positive correlation between total organic carbon, sulfur, and gold in the studied samples was observed.

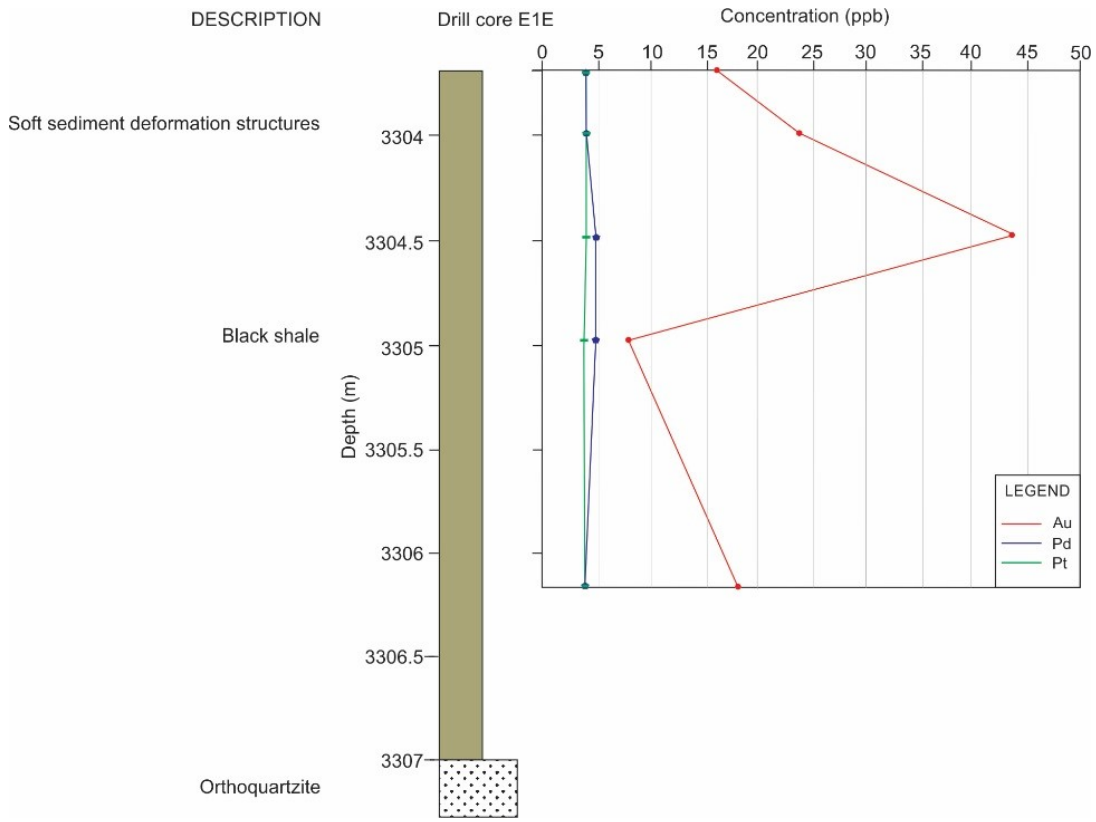

Figure 41: Chemostratigraphic plots of Au and PGE for Roodepoort Formation marine shale (drill core E1E).

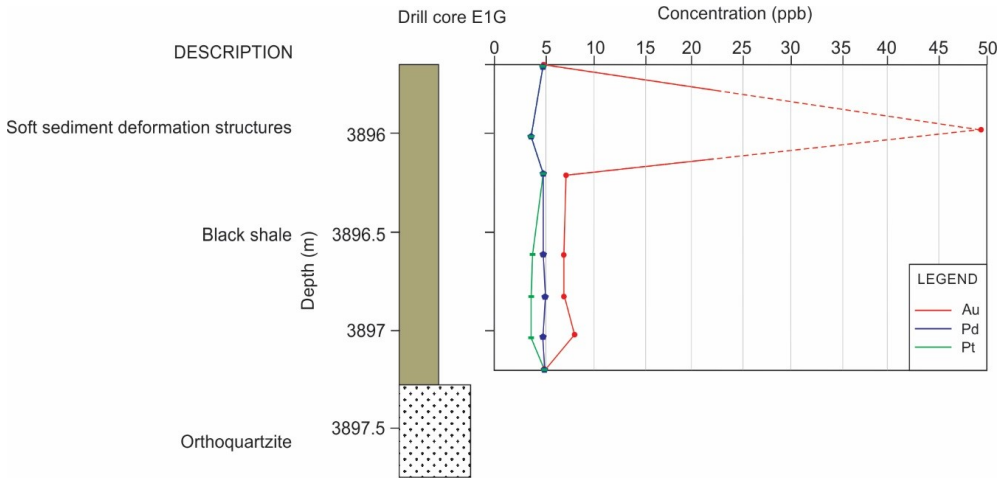

Figure 42: Chemostratigraphic plots of Au and PGE for Roodepoort Formation marine shale (drill core E1G).

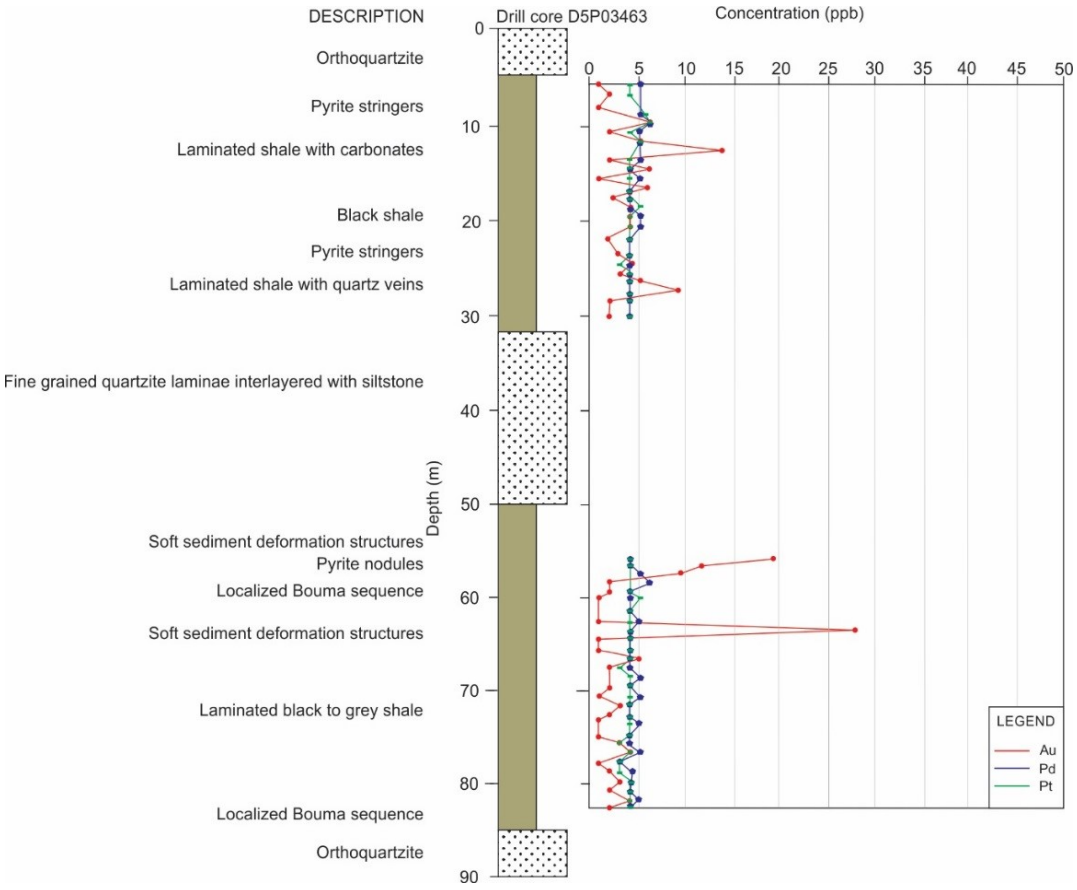

Figure 43: Chemostratigraphic plots of Au and PGE for Roodepoort Formation marine shale (drill core D5P03463).

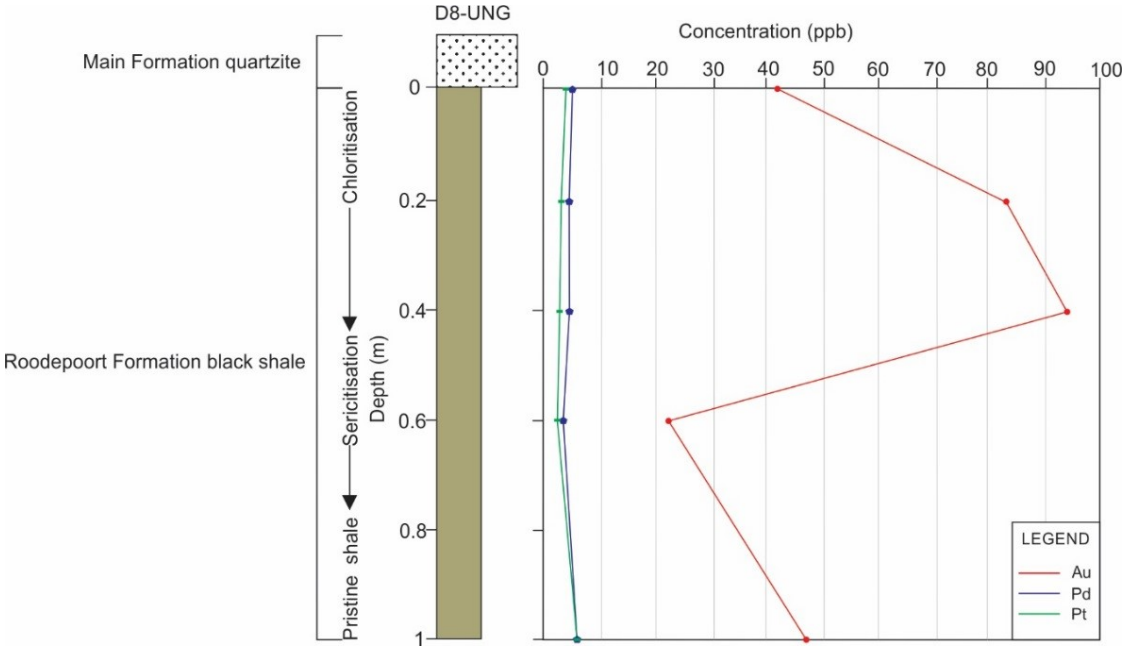

Figure 44: Chemostratigraphic plots of Au and PGE for Roodepoort Formation marine shale–MR10 33XCW (underground profile UNG).

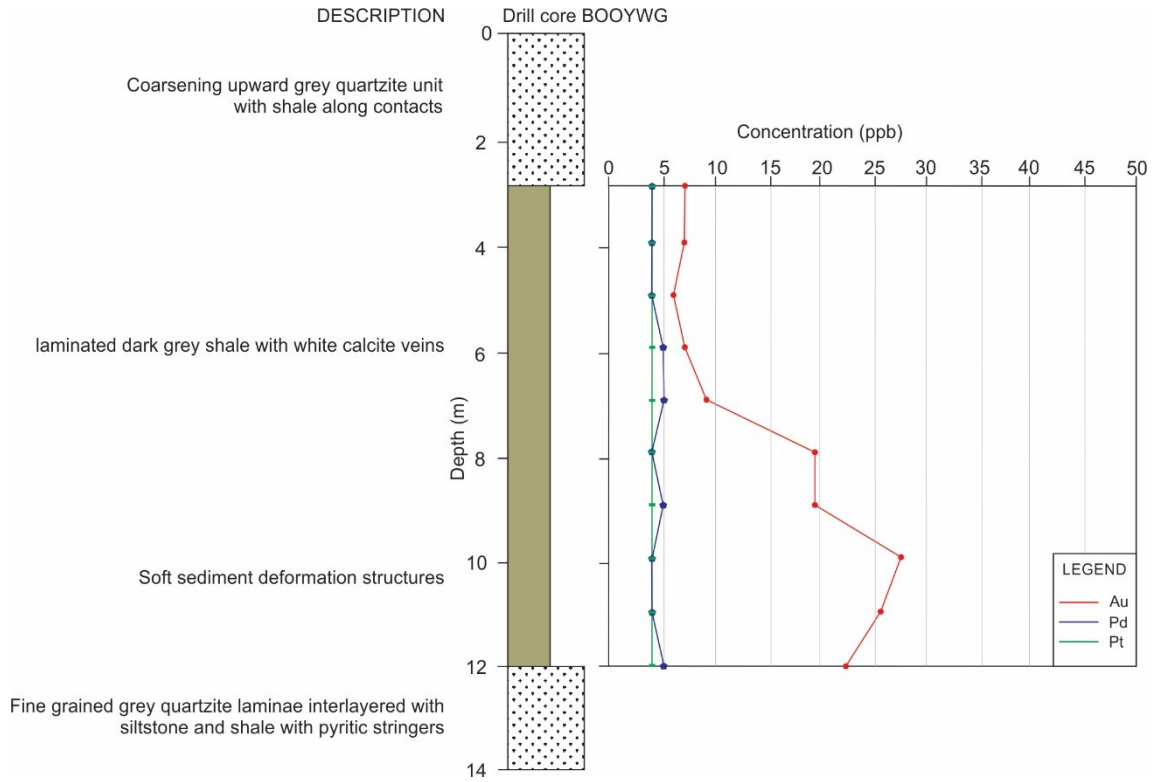

Figure 45: Chemostratigraphic plots of Au and PGE for Booysens Formation marine shale–Welkom goldfield (drill core BOOYWG).

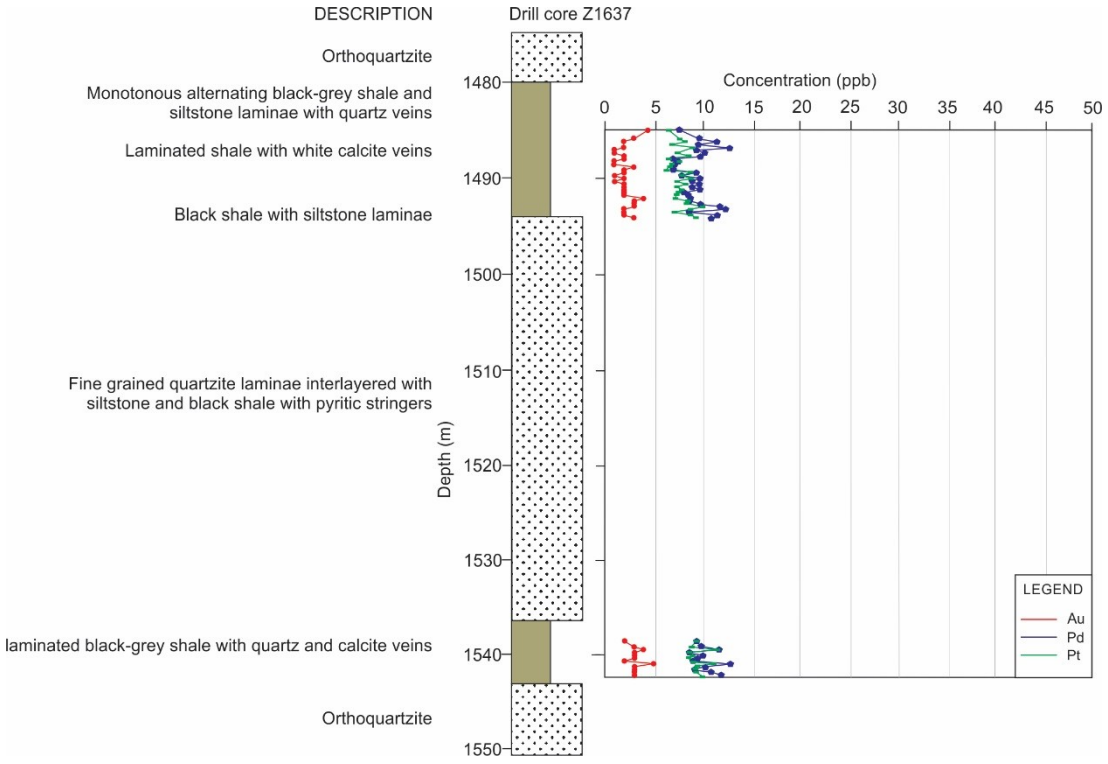

Figure 46: Chemostratigraphic plots of Au and PGE for Booysens Formation marine shale–Western Areas goldfield (Zuurbekom drill core Z1637).

6.3. Transvaal Supergroup marine shales: Black Reef Formation

6.3.1. Major elements

The Black Reef Formation shales are highly variable in their SiO_2 content (60.93–70.64 wt.%, $\bar{x}$ = 66.57 wt.%) and the SiO_2 content is negatively correlated with the Al_2O_3, Fe_2O_3, and MgO content. Moreover, Al_2O_3 has a strong and positive correlation with TiO_2, Fe_2O_3, MgO, MnO, CaO, and K_2O, suggesting that these elements reside in the clay minerals. There is also a positive correlation between TiO_2 and Fe_2O_3, MgO, MnO, and CaO, while CaO is also positively correlated with Fe_2O_3, MgO, and MnO. Compared to PAAS, the Black Reef Formation shales are depleted in P_2O_5, Na_2O, and CaO but enriched in Fe and Mg (Figure 47).

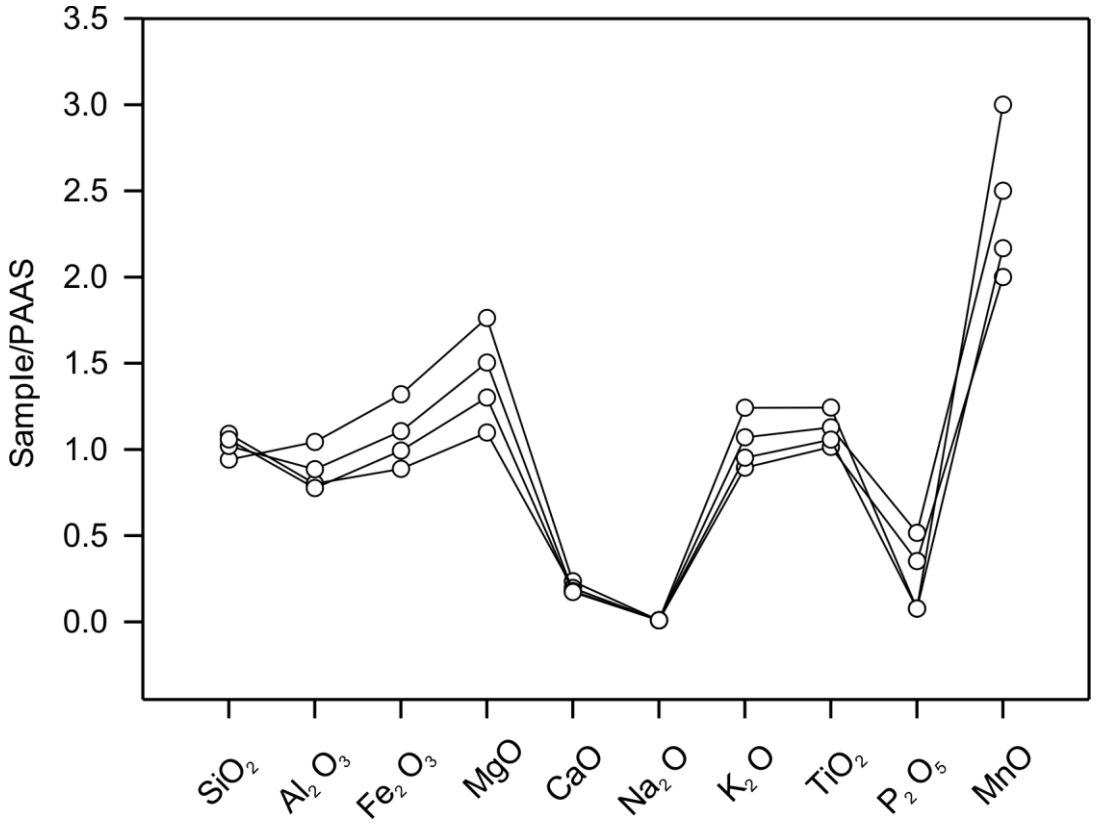

Figure 47: Multi-element diagram of average major element concentrations for Black Reef Formation shale. Normalising values after Taylor and McLennan (1985).

The Black Reef Formation shales have relatively low Al_2O_3 (14.81 wt.%) values compared to PAAS (16.90 wt.%), indicative of the samples' elevated silt content and higher SiO_2 content. Figure 52 A and B illustrate the abundance of minerals present in the Black Reef Formation shales.

6.3.2. Trace elements including rare earth and highly siderophile elements

6.3.2.1. Distribution of trace elements and stratigraphic variations

Large ion lithophile element geochemistry: Figure 48 illustrates depletion in Ba, and especially Sr, and enrichment in Co, Cr, and Ni relative to PAAS, whereas all the other element contents are similar to PAAS.

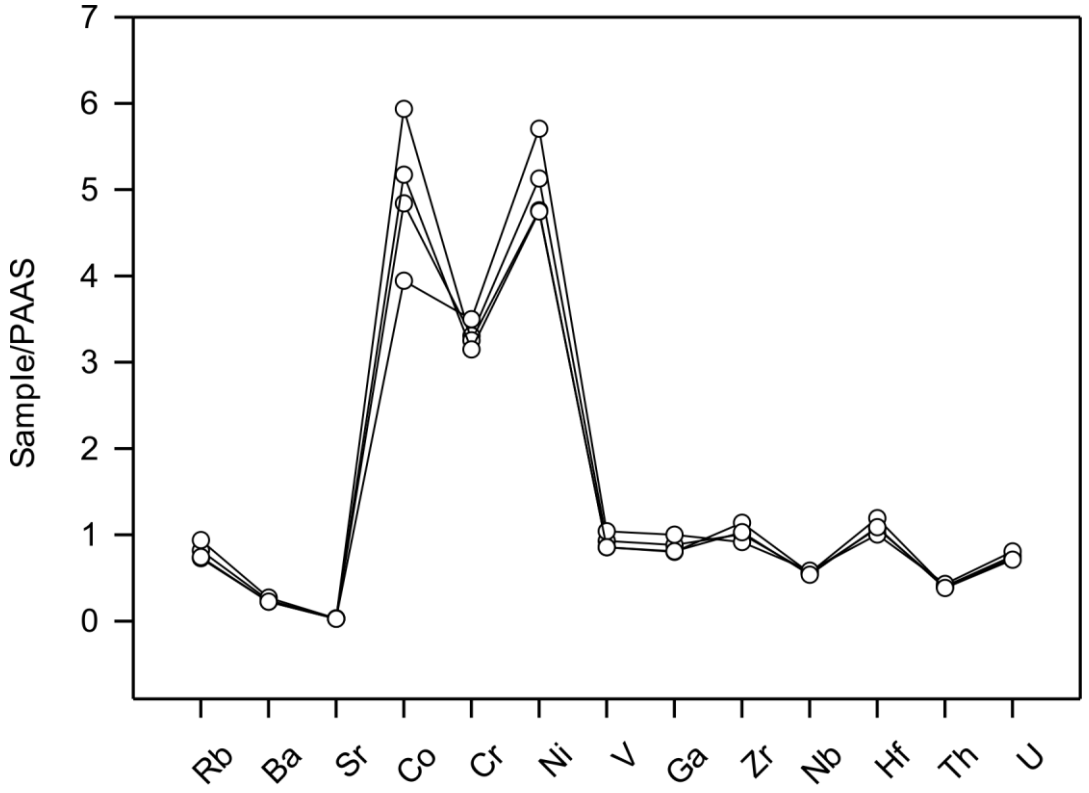

Figure 48: Multi-element diagram of average trace element concentrations for Black Reef Formation shale. Normalising values after Taylor and McLennan (1985).

The Black Reef Formation shales have slightly higher Zr/Y ($\bar{x}$ = 10.45 ppm) and Zr/Nb ($\bar{x}$ = 20 ppm) ratios than the PAAS reference. Moreover, a relatively strong positive correlation exists between the following pairs: Ta–Nb (r = 0.97), Y–Nb (r = 0.88), and Zr–Hf (r = 1). The Black Reef Formation shales have a Cr content averaging 363 ppm, a figure higher than that for PAAS (110 ppm). The Ni ($\bar{x}$ = 117 ppm) content is also higher in the Black Reef Formation than in PAAS (23), and the Cr/Ni ratio is 3.1. The Black Reef Formation shales yield an average Co content of 8 ppm, lower than the analogous PAAS value (Co = 23). Moreover, there is a strong positive correlation between Zr and Co (r = 0.99).

6.3.2.2. Total rare earth element contents and stratigraphic variations

The Black Reef Formation shales have low REE levels relative to PAAS (Figure 47), probably due to its dilution with quartz and the effects of sorting. The concentration of total REEs in the Black Reef Formation shales is 104.71 ppm. The Y (20.79 ppm) concentration is lower in that formation than in PAAS (27 ppm). The LREE (85.34 ppm), MREE (12.63 ppm), and HREE (6.73 ppm) contents are all lower than the respective PAAS values, and the REE ratios vary significantly (LREE/MREE = 6.74, LREE/HREE = 12.63, and MREE/HREE = 1.87). The Black Reef Formation shales yields an Eu/Eu* anomaly of 1.57. Furthermore, these shales have a Y/Ho ratio of 26 indicating, that the two elements are tightly coupled in many geochemical processes, leading to a steady Y/Ho ratio in common igneous rocks and clastic sediments (Y/Ho ratio circa 28; Bau, 1996).

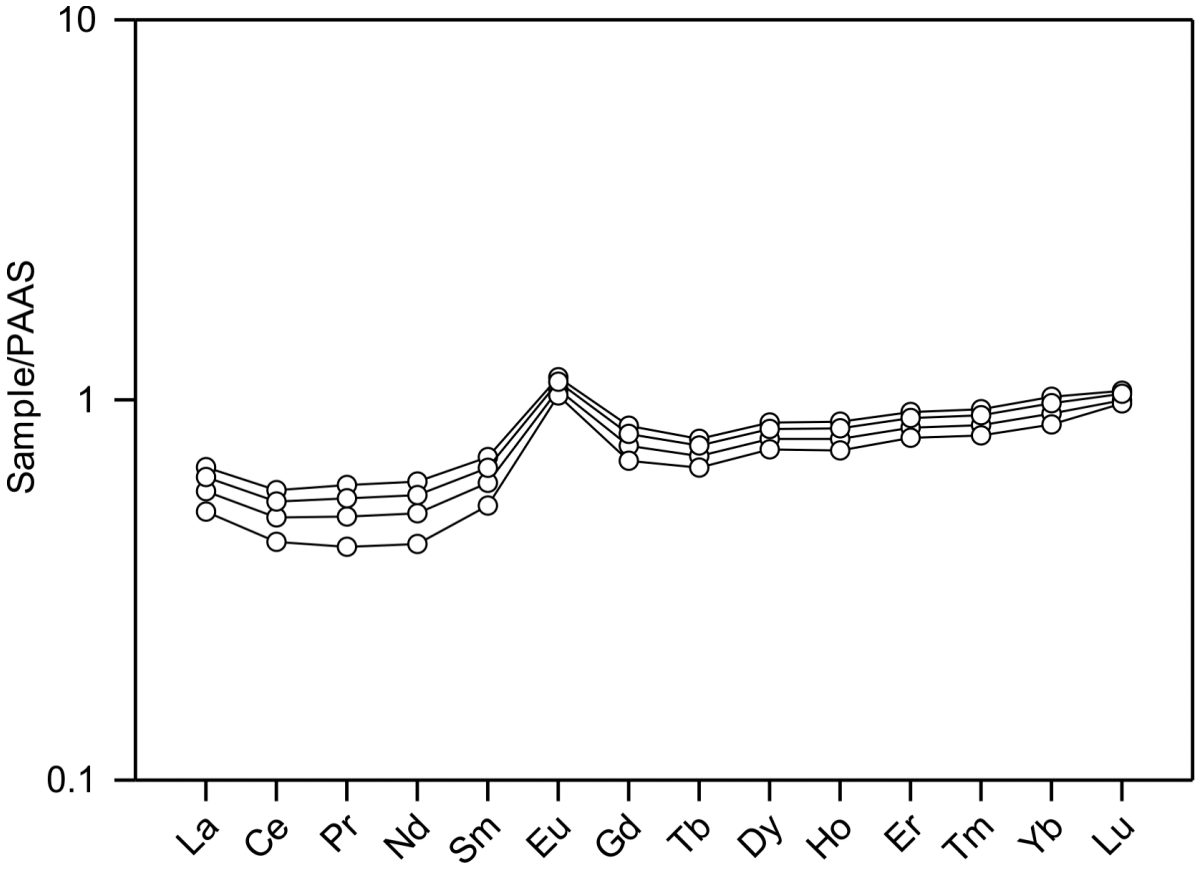

Figure 49: Multi-element diagram of Black Reef Formation shales' REE patterns. Normalising values after Taylor and McLennan (1985).

6.3.2.3. Highly siderophile elements

The Au content of the Black Reef Formation shales ranges from 2 to 5.5 ppb. The Pd concentrations of those shales range from 9 to 10 ppb, with the higher values toward the

bottom of the shale–siltstone–quartzite beds. This trend is also observable for Au. The Pd content is constant in the sampled Black Reef Formation shales. Throughout the Black Reef Formation shales, Pt concentrations range from 5 to 6 ppb. Other Black Reef PGEs (e.g. Ir, Os, and Rh) fall below the detection limits, while the Ru values are within a very narrow range of concentrations (1–2 ppb). In general, the Black Reef Formation shales are more abundant in Pt and Pd than in Au, although Pt and Pd patterns differ significantly (drill core E1H, Figure 50).

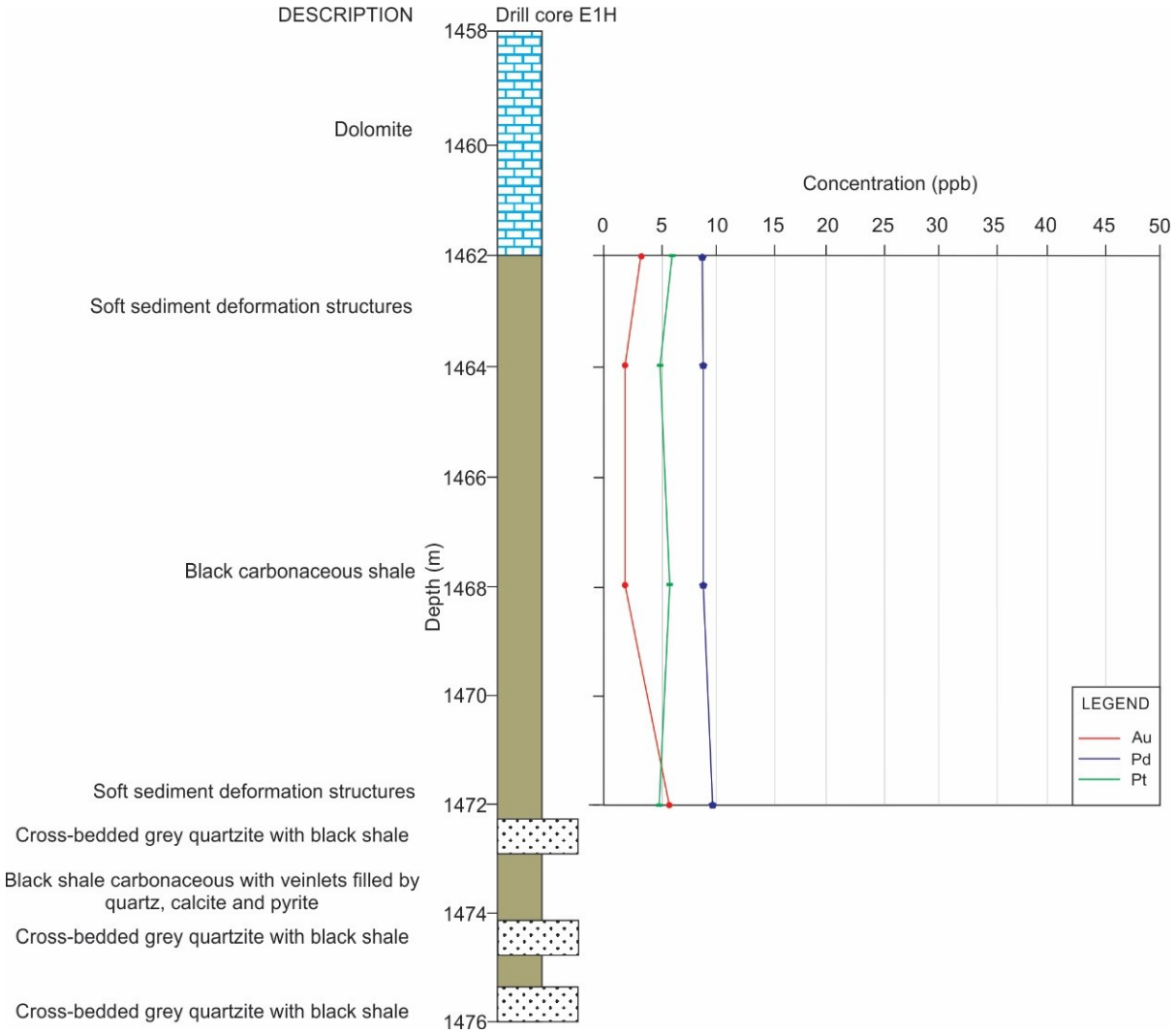

Figure 50: Chemostratigraphic plots of Au and PGE for Black Reef Formation marine shale (drill core E1H).

6.4. Transvaal Supergroup marine shales: Pretoria Group

6.4.1. Major elements

The Pretoria Group shales are divided into two subtypes based on depth: the upper shale unit (0–300 m) and lower shale unit (301–750 m). The shales' SiO_2 content ranges between 50.9 and 61.77 wt.%, averaging 57.45 wt.%. The SiO_2 content increases slightly from the lower shale unit ($\bar{x}$ = 57.34 wt.%) to the upper shale unit ($\bar{x}$ = 57.56 wt.%). The upper shale unit shows a progressive decrease in SiO_2 content from the bottom (60.55 wt.%) to the top (56.58 wt.%) of the unit. The Al_2O_3 content mirrors the SiO_2 content almost exactly. In particular, the Al_2O_3 content declines markedly upward from the bottom of the upper shale unit (21.87 wt.%), to the top of that unit (19.73 wt.%). Figure 51 shows the Transvaal Supergroup shales' major elements normalised against the PAAS reference.

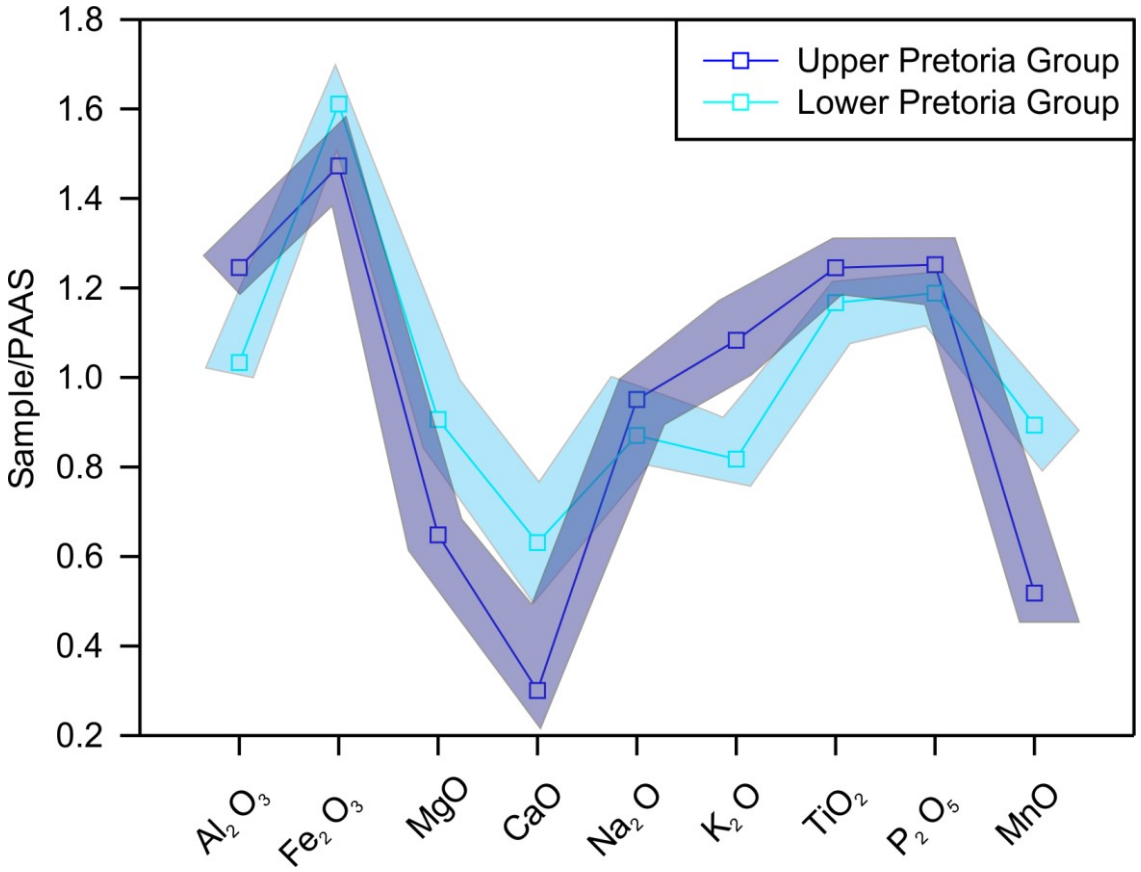

Figure 51: Multi-element diagram of average major element concentrations for Pretoria Group shales. Coloured bands mark the range of data for the respective sample group. Normalising values after Taylor and McLennan (1985).

Concentrations of both MgO ($\bar{x}$ = 2.59 wt.%) and CaO ($\bar{x}$ = 2.12 wt.%) are higher for the lower shale unit than for the upper ([MgO] $\bar{x}$ =1.85 wt.% and [CaO] $\bar{x}$ = 1.01 wt.%, respectively) shale

unit. In contrast, Na_2O content increases slightly upwards, shifting from an average of 0.99 wt.% in the lower shale unit to an average of 1.08 wt.% in the upper shale unit. The K_2O content follows the same pattern, rising from an average of 3.25 wt.% in the lower shale unit, to an average of 4.3 wt.% in the upper shale unit. The average Fe_2O_3 content of the Pretoria Group is higher than that of PAAS (5.66 wt.%). The Pretoria Group's TiO_2 ($\bar{x}$ = 0.84) content is similar to that of the Black Reef Formation shales ($\bar{x}$ = 0.78 wt.%), with the Pretoria Group slightly enriched in TiO_2 compared to PAAS (0.70 wt.%).

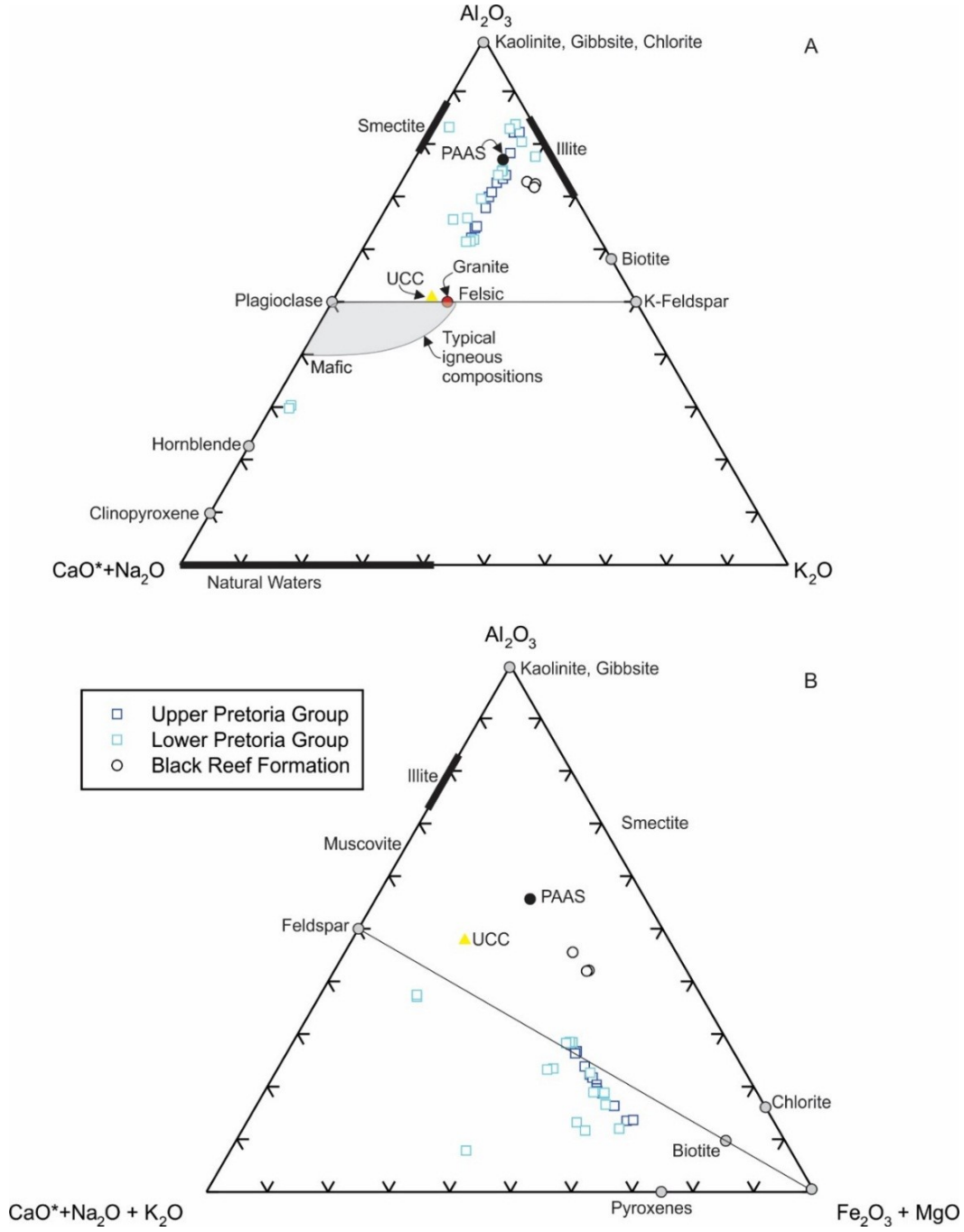

Figure 52: A. Ternary diagram of ACNK (Al_2O_3:[CaO* + Na_2O]:K_2O) (modified after Nesbitt and Young, 1984) for Pretoria Group shales, illustrating both a wide range of

palaeoweathering and differences in source rocks. Average values for upper continental crust and PAAS values are from Taylor and McLennan (1985). B. Ternary diagram (ACF) indicating molar proportions of Al_2O_3:(CaO^* + Na_2O + K_2O):Fe_2O_3 + MgO and distinctive chemical change characteristic of alteration for Pretoria Group shales. The average PAAS value is from Taylor and McLennan (1985). The composition of the upper continental crust is from Rudnick and Gao (2005).

6.4.2. Trace elements including rare earth and highly siderophile elements

6.4.2.1. Distribution of trace elements and stratigraphic variations

Large ion lithophile element geochemistry: Figure 53 illustrates depletion in Ba, and especially Sr, and enrichment in Co relative to PAAS, whereas all the other element contents are similar to the PAAS reference. Transition elements: the average Sc content is 22.1 ppm, with the average for the lower shale unit at 23.51 ppm and the average for the upper shale unit at 20.24 ppm. No concentration trends are observable for Sc, V ($\overline{x}$ = 135 ppm), Cr ($\overline{x}$ = 180 ppm), Co ($\overline{x}$ = 93 ppm), and Ni ($\overline{x}$ = 51 ppm). Nonetheless, the Cr, Co, and Ni contents are higher in the Pretoria Group shales than in PAAS (Figure 53). There is a strong positive correlation between Sc and V (r = 0.84), as well as between Cr and Ni (r = 0.97), while Co and Co (r = –0.01) are negatively correlated. High-field strength elements: concentrations of most of the HFSEs (Ga, Hf, and Zr) in the Pretoria Group shales are higher than in PAAS (Figure 53). An exception is the Pretoria Group's Nb ($\overline{x}$ =17.88 ppm) concentration, which is lower than that of PAAS (19 ppm). For the Pretoria Group, the Pearson's correlation coefficients for trace element concentrations reveal a strong positive correlation between the following pairs of elements: Nb–Ga [r = 0.89], Nb–Hf [r = 0.7], Zr–Ga [r = 0.69], Zr–Hf [r = 1], Zr–Nb [r = 0.68], Ta–Ga [r = 0.84], and Ta–Nb [r = 0.94]). The Ti/Zr and Zr/Hf ratios are lower in the Pretoria Group samples than in PAAS, whereas the Zr/Nb (13.15) ratio is higher.

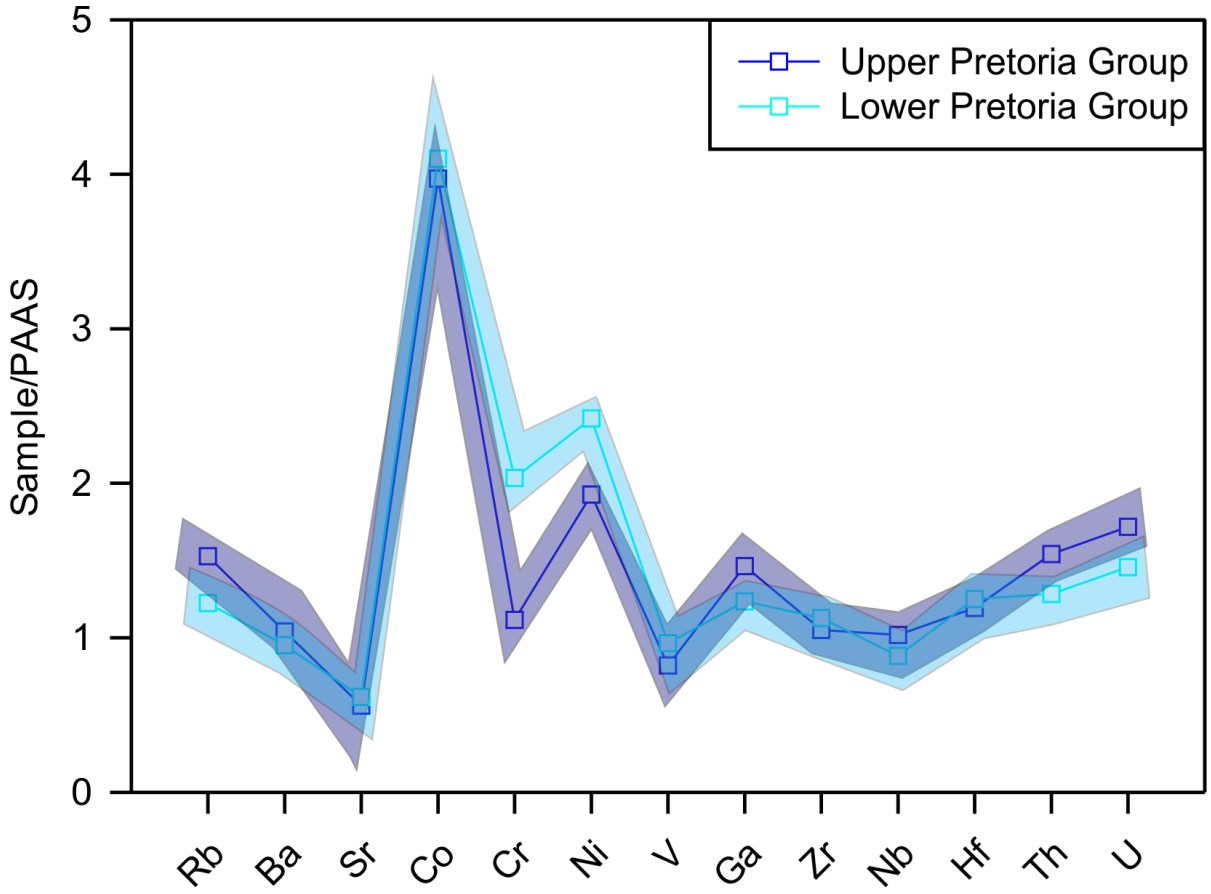

Figure 53: Multi-element diagram of average trace element concentrations for Pretoria Group shales; coloured bands mark the range of data for the respective sample group. Normalising values after Taylor and McLennan (1985).

6.4.2.2. Total rare earth element contents and stratigraphic variation

The Pretoria Group shales are enriched in REEs relative to PAAS (Figure 54). The total REE concentration in the Pretoria Group is 226 ppm. The Pretoria Group has a higher Y content ($\overline{x}$ = 32.5 ppm) than PAAS (27 ppm). The LREE (193 ppm), MREE (22.8 ppm), and HREE (9.65 ppm) concentrations are all higher than in PAAS, and the REE ratios vary significantly (LREE/MREE = 8.56, LREE/HREE = 21.08 and MREE/HREE = 2.45). The Pretoria Group yields an Eu/Eu* anomaly of 0.99.

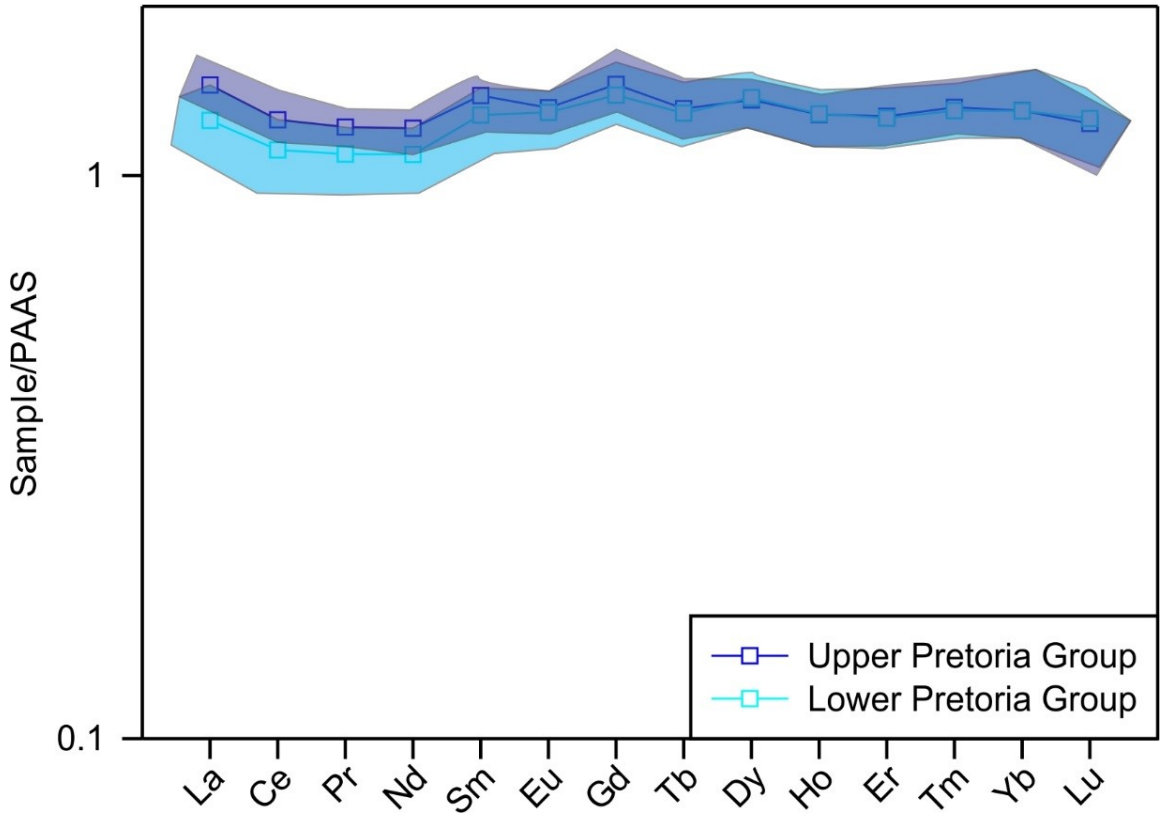

Figure 54: Multi-element diagram of average REE for Pretoria Group shales. Coloured areas mark the range of data for the respective sample group. Normalising values after Taylor and McLennan (1985).

6.4.2.3. Highly siderophile elements

The Au content of the upper Pretoria Group marine shales ranges from 1 to 5 ppb. In the lower shale unit, the Au content is between 1 and 3 ppb, with an outlier reaching 7 ppb in drill core DP22. The Au outlier occurs close to a quartzite, siltstone, and shale transition contact. Although the Pretoria Group sequence is thick, a systematic increase in Au is observable between the lower shale unit and the upper shale unit. Moreover, the Pd concentrations in the upper Pretoria Group shales range from 1 to 3 ppb. For the lower shale unit, the Pd content is highly variable, ranging from <1 to 8.5 ppb, with the widest range present in drill core DP23. Irregular sampling was done for drill core DP23 in order to objectively sample the pristine portions of the drill core. Both Au and Pd outliers are present between 500 and 650 m in drill cores DP22 and DP23 (Figure 55 and 56). Drill core DP22 indicates the presence of Pd concentrations ranging between 1 and 2 ppb in a more constant composition. Generally, the Pd content did not display regional systematic changes, although clustered, systematic increases and decreases are observable throughout the DP22 and DP23 drill cores. The Pt concentrations of the upper Pretoria Group marine shales range from 1 to 3 ppb (Figure 55).

The Pt content of the lower shale unit is uniform in drill core DP22 (Pd = 1 ppb) but variable in drill core DP23 where it spans from <1 to 4 ppb. An elevated Pt content is seen at depths similar to those of the Au and Pd outliers (i.e. 500 m and 650 m, respectively). Drill core DP22 exhibits a progressive increase in Pt from the lower shale unit to the upper shale unit. In contrast, drill core DP23 displays a repetitive cycle of localised Pt increases and decreases from the lower shale unit to the upper shale unit. Other PGEs (e.g. Ir, Os, and Rh) in the Transvaal Supergroup shales yield concentrations below the detection limits, while the Ru content remains within a very narrow range (1–2 ppb). Localised Ru outliers reach 4 ppb in the lower shale unit and 3 ppb in the upper shale unit.

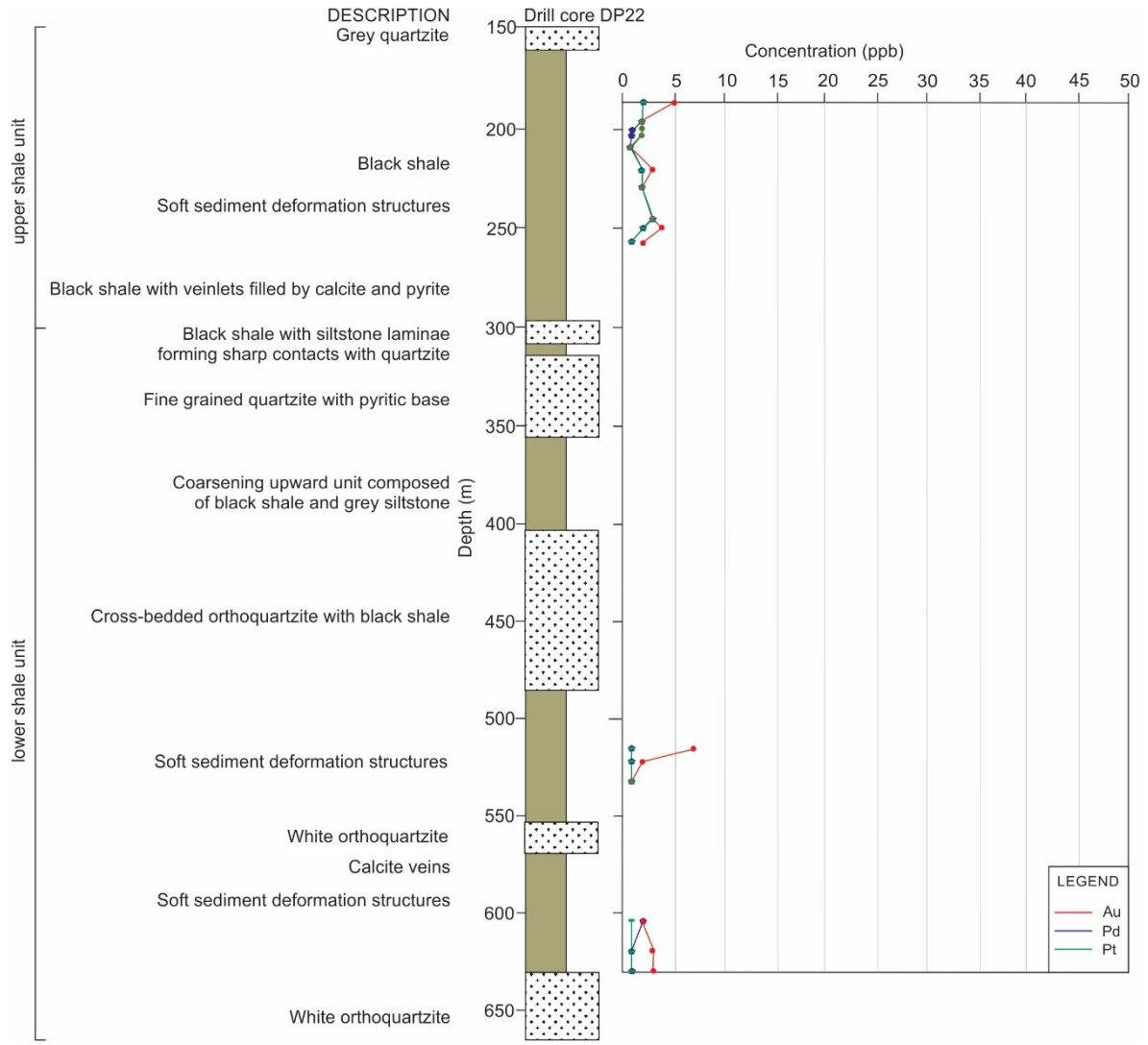

Figure 55: Chemostratigraphic plots of Au and PGE for Pretoria Group marine shale (drill core DP22).

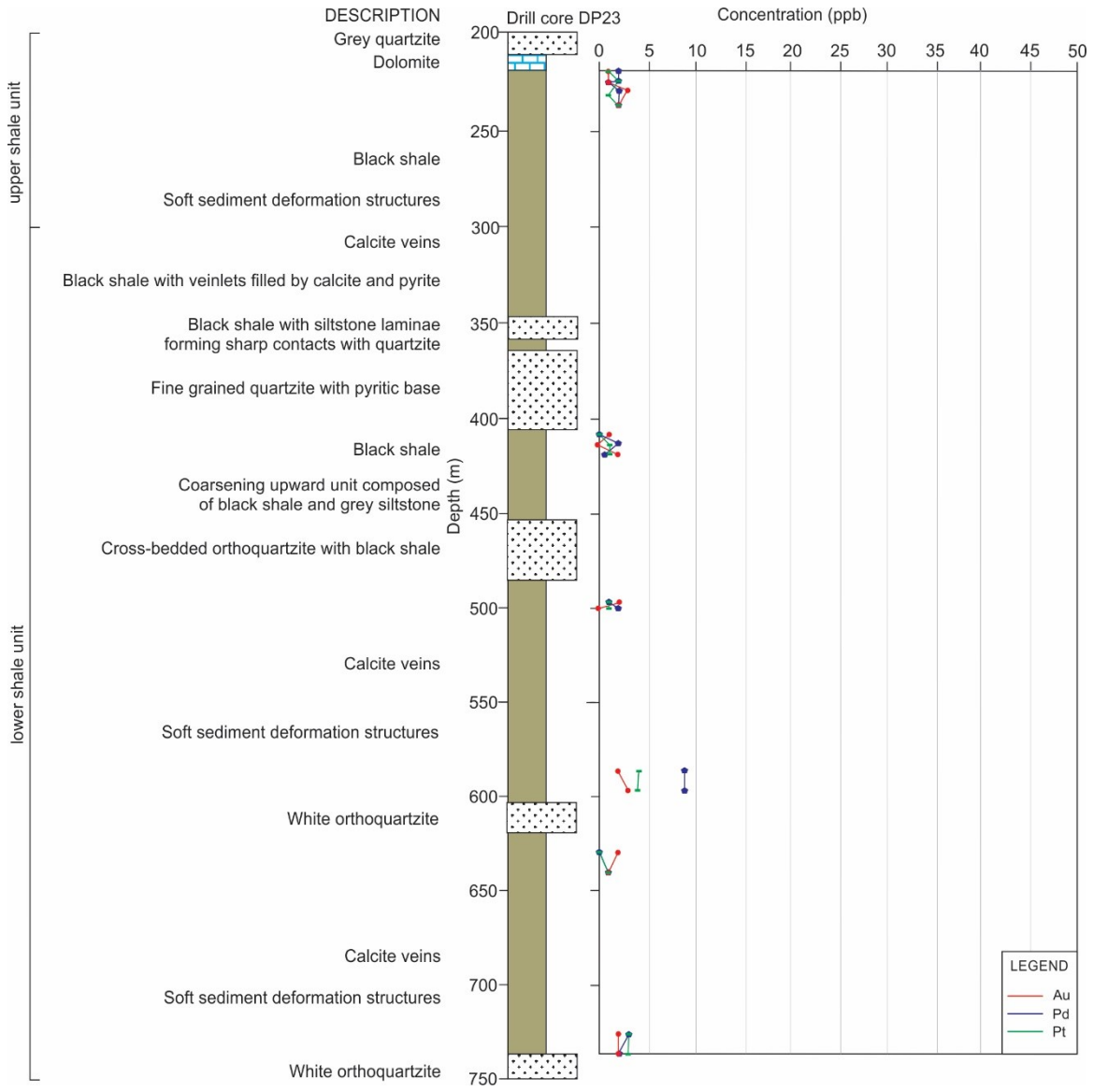

Figure 56: Chemostratigraphic plots of Au and PGE for Pretoria Group marine shale (drill core DP23).

6.5. Summary of marine shales chemical composition with special reference to siderophile elements

The shales predominantly reveal an igneous and metamorphic inheritance of conservative elements (Ti, Al, REE, Sc, Co). TiO_2 correlates with the mafic-affiliated elements Fe_2O_3, Co, and Sc. Thorium correlates with the incompatible elements Hf and LREE. On the other hand, SiO_2 correlates with felsic-affiliated Th and LREEs. Abundances of HSEs in the upper continental crust are poorly constrained, with published values varying by up to an order of magnitude. Highly siderophile element concentrations are difficult to estimate because of high variability in grade distribution. This is especially true in the upper continental crust, which is

the most accessible part of the Earth and has long been the target of geochemical investigations (Clarke, 1889). In general, the continental crust comprises highly diverse rock types, thus making the estimation of HSE distributions more complex. Many HSE variables have sample distributions that are positively skewed. For that reason, the variance declines, and a significant deskewing of the histogram occurs when shifting from an individual sample to a regional domain.

The distribution and abundance of HSE in marine shales of the Barberton, Witwatersrand, and Transvaal supergroups are variable, even within the same stratigraphic profile (Table 9). In the Barberton Supergroup, the Fig Tree Group appears to have a higher HSE content than the Moodies Group, although their Pt concentrations do not differ significantly. In some of the sequences, the Au values are higher than the Pd and Pt values (e.g. Booysens Formation–Welkom goldfield). Elsewhere in the same formation (e.g. Western Areas goldfield), however, Pd and Pt concentrations are higher than Au concentrations. In general, the Witwatersrand Supergroup shales have the highest HSE concentrations. In comparison to those shales, the Black Reef appears to have a lower Au content but higher PGE content. That said, the Witwatersrand shales contain much higher HSE concentrations than the Transvaal Supergroup marine shales.

Table 9: Selected average Kaapvaal Craton HSE concentrations, from the oldest domain to the youngest sampled sequence (values reported in ppb, ± = variance).

Sample	Au	Pd	Pt
Fig Tree Group	4.61 ± 2.11	5.64 ± 0.03	6.63 ± 0.02
Moodies Group	2.23 ± 0.70	2.32 ± 0.32	5.5 ± 0.06
Roodepoort Formation–Carletonville goldfield	6.57 ± 1.76	4.2 ± 0.02	3.97 ± 0.02
Booysens Formation–Welkom goldfield	9.85 ± 1.29	4.16 ± 0.02	3.89 ± 0.2
Booysens Formation– Western Areas goldfield	5.18 ± 0.03	10.7 ± 0.02	6.12 ± 0.04
Black Reef Formation	3.25 ± 3.58	9.13 ± 0.2	5.50 ± 0.33
Pretoria Group	2.65 ± 0.23	2.0 ± 0.58	2.06 ± 0.21

Estimating the anomalies and determining the average HSE composition of the Kaapvaal Craton shales requires large–scale sampling of pristine shales (unbiased). This permits the averaging of the various shale sequences, resulting in greater analytical quality (Table 9 and methods section). It is critical to use reliable, high-quality data to draw conclusions regarding anomalous HSE depletion and/or enrichment, and this is especially true at the craton scale.

Rudnick and Gao (2005 and references therein*)* have provided an updated best estimate for the upper continental crust's chemical composition. Because of its comprehensive range of analysed elements, that reference constitutes the most suitable source for normalising the Kaapvaal Craton shale HSE data. Figure 57 depicts HSE concentrations in shale units normalised against their respective concentrations in the upper continental crust. This diagram makes it clear that the Kaapvaal Craton at the time of sedimentation of the studied shale samples must have been enriched in HSE relative to the average upper continental crust. Compared to Au, Pd and Pt concentrations occur in higher abundances across most of the studied Kaapvaal Craton sequences.

A stratigraphy-based classification yields the following Au anomalies, ranked from highest to lowest: the Booysens Formation shales (Welkom goldfield), the Roodepoort Formation, the Booysens Formation shales (Western Areas goldfield), the Fig Tree Group, the Black Reef Formation, the Transvaal Supergroup, and the Moodies Group. Post-depositional alteration assessment of the least and most altered samples in the Jeppestown Subgroup revealed that there were no significant changes in elemental mobility during alteration, thus no additional Au enrichment is expected in the studied marine shales (see Section 8.2 for a detailed discussion). The samples used to investigate the extent of post-depositional alteration yield uniform Au concentrations confirming that there was no additional gold input during alteration. The Pd enrichment, in order from highest to lowest, are: the Booysens Formation shales (Western Areas goldfield), the Black Reef Formation, the Fig Tree Group, the Roodepoort Formation, the Booysens Formation shales (Welkom goldfield), the Moodies Group, and the Transvaal Supergroup.

The Pt anomalies, ranked from highest to lowest, are: the Fig Tree Group, the Booysens Formation shales (Western Areas Goldfield), the Black Reef Formation, the Moodies Group, the Roodepoort Formation, the Booysens Formation shales (Welkom goldfield), and the Transvaal Supergroup. The altered samples from the Roodepoort Formation follow similar Pd and Pt compositional patterns as the pristine marine shales. In the Kaapvaal Craton shales, HSE (e.g. Ir, Os, Rh, and Ru) concentrations are predominantly below the detection limits, although Os and Ru positive outliers are observable across all sampled sequences. Although the majority of the Ir, Os, Rh, and Ru concentrations are below the detection limit, the few samples above that limit yield concentrations above the average upper continental crust composition (i.e. Ir = 0.022, Os = 0.031, Rh = 0.018 ppb, and Ru = 0.34 ppb; Rudnick and Gao, 2005; Park et al., 2012).

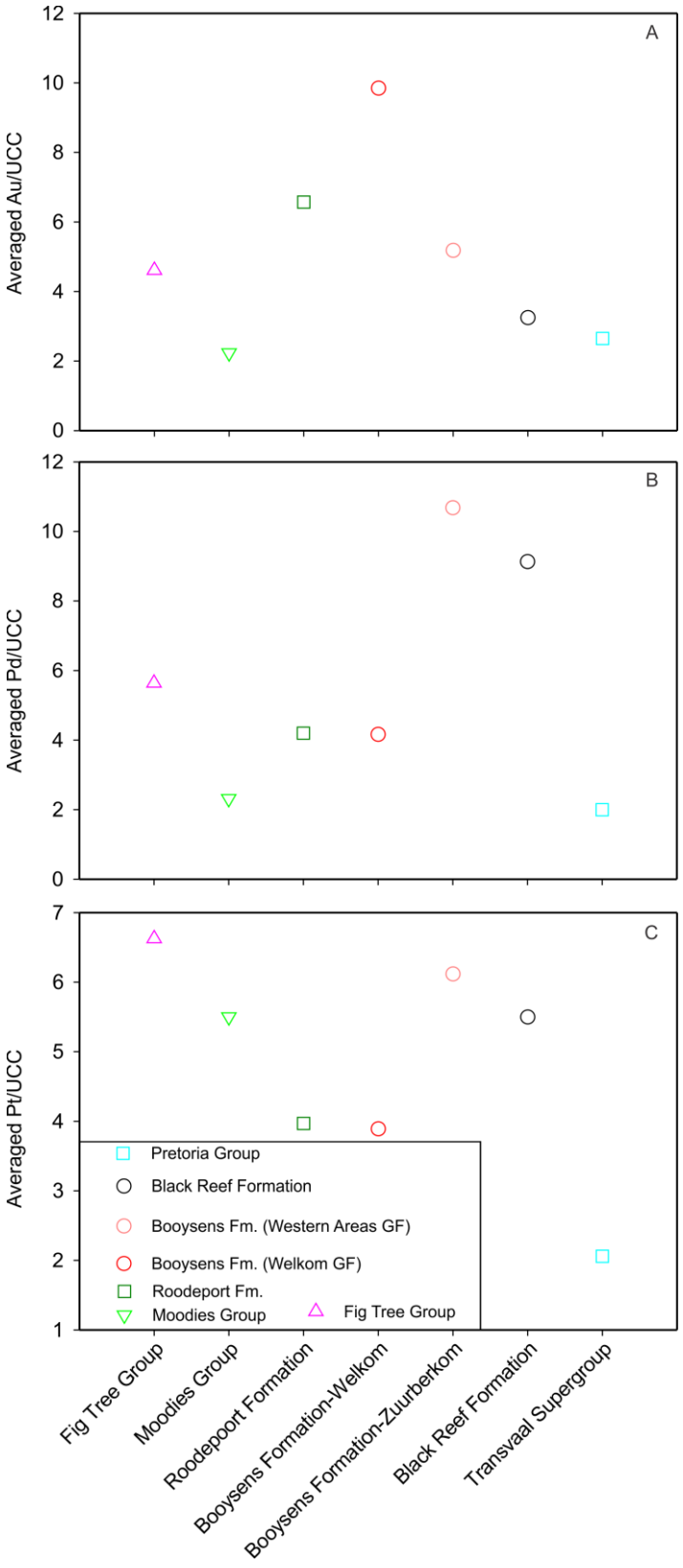

Figure 57: Binary plots of averaged Kaapvaal Craton shales normalised to composition of upper continental crust (Rudnick and Gao, 2005). A. Averaged Au, B. Averaged Pd, and C. Averaged Pt.

Average Au and PGE abundances are poorly constrained in the upper continental crust, with published values varying by up to an order of magnitude. Gold and PGE belong to a group of metals whose concentrations are difficult to quantify because of the high variability in concentration, especially in the upper continental crust (Taylor and McLennan, 1995; Rudnick and Gao, 2005). In general, the continental crust comprises highly diverse rock types, thus adding to the complexity of Au and PGE distributions. Most Au and PGE concentrations have statistical sample distributions that are very positively skewed. In recent years, interest in the geochemistry of Au and PGE has increased considerably because it complements the information about the Earth's accretion, core–mantle differentiation, mantle evolution, and magma genesis that can be derived from lithophilic incompatible elements (e.g. Brandon et al., 1998, 1999; Puchtel and Humayun, 2000). Variations in the Au and PGE content of low-sulfur rocks are very sensitive indicators, attesting to the presence or absence of sulfide liquid saturation during the evolution of a magma series, owing to the extremely high partition coefficients of PGEs into sulfides (Fleet et al., 1991). There is no plausible correlation trend between Au and PGE when plotted against carbon and sulfur for the Fig Tree and Moodies shales (Figure 58–60). The same was observed in the Black Reef Formation and Pretoria Group shales, with the exception of the Black Reef showing a positive correlation between Au and S (Figure 64–66). In the present study, the Au and PGE contents define distinctly different behaviours for high-Mg shales (mafic source rocks) and low-Mg shales (felsic source rocks) (e.g. Figure 58–66). Both Pd and Pt increase noticeably with MgO and Ni in the Barberton Supergroup, although this is not related to Au (Figure 59–60). In general, the distribution and abundance of Au and PGE in marine shales of the Barberton, Witwatersrand, and Transvaal supergroups are compositionally variable, even within similar sequences in the Barberton Supergroup. The Fig Tree Group is richer in HSE relative to the Moodies Group, although the Pt concentration does not differ much between the two. In some of the sequences (e.g. the Booysens Formation), the Au values are higher than the Pt and Pd values in one area (e.g. the Welkom goldfield, Figure 61–63), while the opposite is true in another area (e.g. the Western Areas goldfield, Figure 61–63). In general, the Witwatersrand Supergroup shales (Figure 61–63) have higher HSE concentrations than the Barberton Supergroup shales (Figure 58–60). The Black Reef has a low Au content compared to the Witwatersrand Supergroup, but a higher PGE content (Figure 64–66). Estimating HSE anomalies and determining the HSE average composition of the Kaapvaal Craton shales requires large-scale sampling of pristine shales and high-quality analysis. Rudnick and Gao's (2005; and references therein) updated best estimate of the chemical composition of the average continental crust employs different methods that rely on the elements' solubility. Relative to

the average continental crust, Au and PGE occur in higher concentrations in all of the studied marine shales.

Other PGEs (e.g. Ir, Os, Rh, and Ru) in the studied marine shales largely have concentrations that are below detection limits, although Os and Ru positive outliers were observed in all the sampled units. In this regard, Ir, Os, Rh, and Ru concentrations below or near detection limits do not permit conclusive findings. Even though the majority of Ir, Os, Rh, and Ru concentrations are below detection limits, the few samples above those limits yield concentrations higher than the average upper continental crust composition (i.e. the average upper continental crust has the following composition: Ir = 0.022 ppb, Os = 0.031 ppb, Rh = 0.018 ppb, and Ru = 0.34 ppb; Rudnick and Gao, 2005; Park et al., 2012). The Os content, and initial $^{187}Os/^{188}Os$ ratio of 0.108 in the Mesoarchaean Witwatersrand gold (Kirk et al., 2001) have been interpreted as being most compatible with mantle magmatic sources. Generally, the introduction of Os and Re into crustal rocks has been linked to a higher level of radiogenic heat production and to partial melting in the mantle (Pollack, 1997; Babeyko et al., 2002; Slagstad, 2008; Lay et al., 2008).

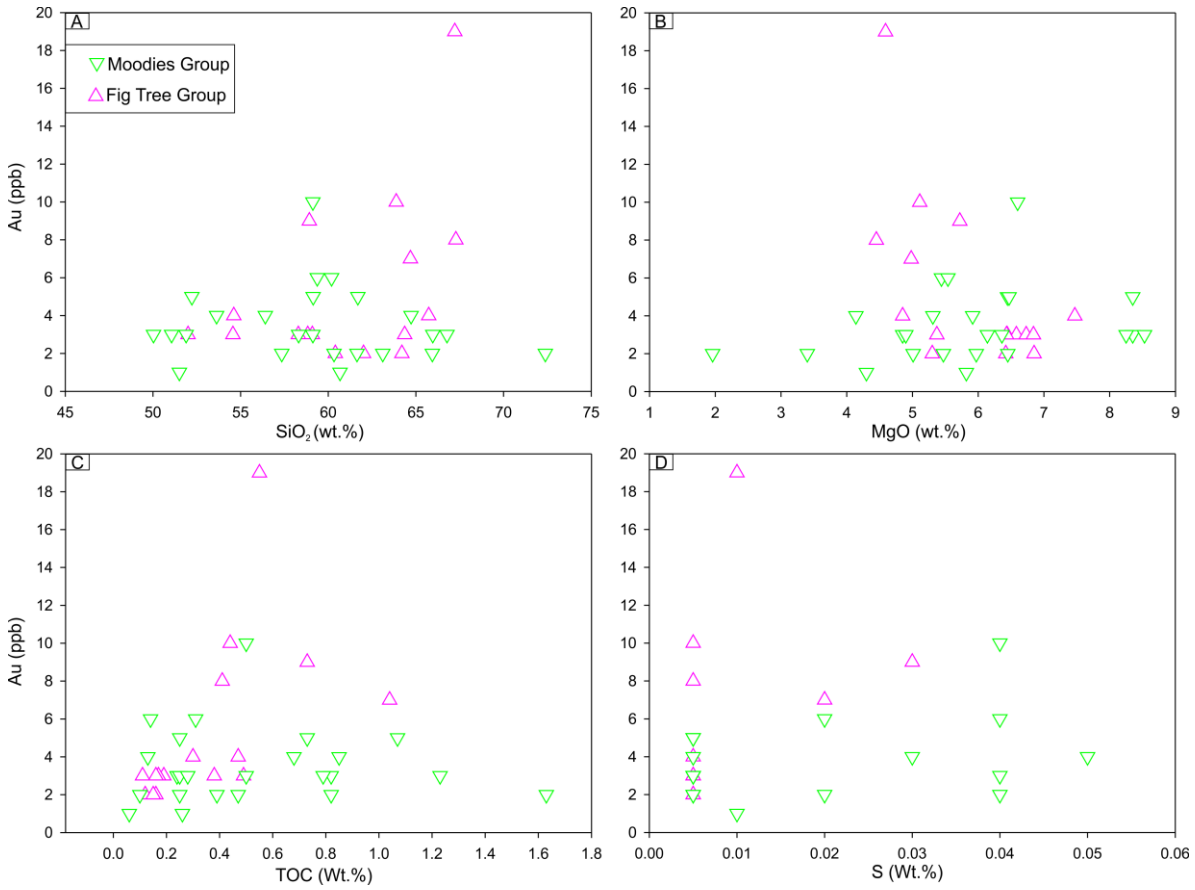

Figure 58: Bivariate diagrams for Barberton Supergroup marine shales showing correlations of SiO_2, MgO, TOC, and S with Au.

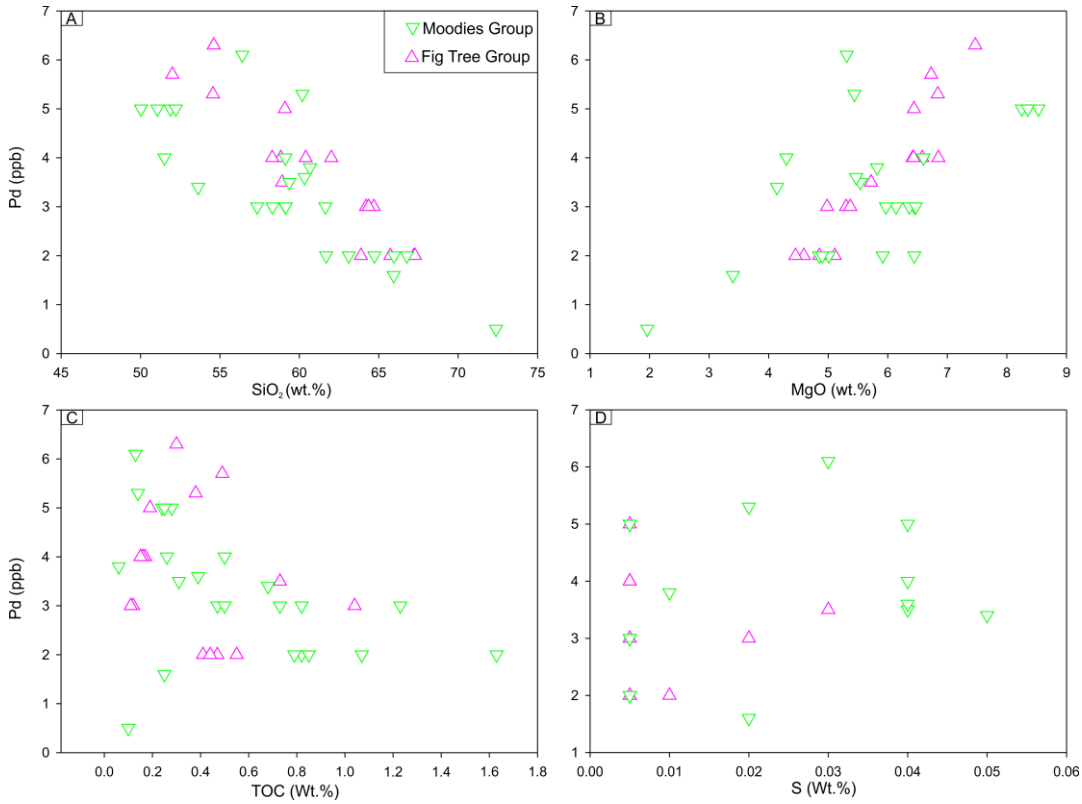

Figure 59: Bivariate diagrams for Barberton Supergroup marine shales showing correlations of SiO_2, MgO, TOC, and S with Pd.

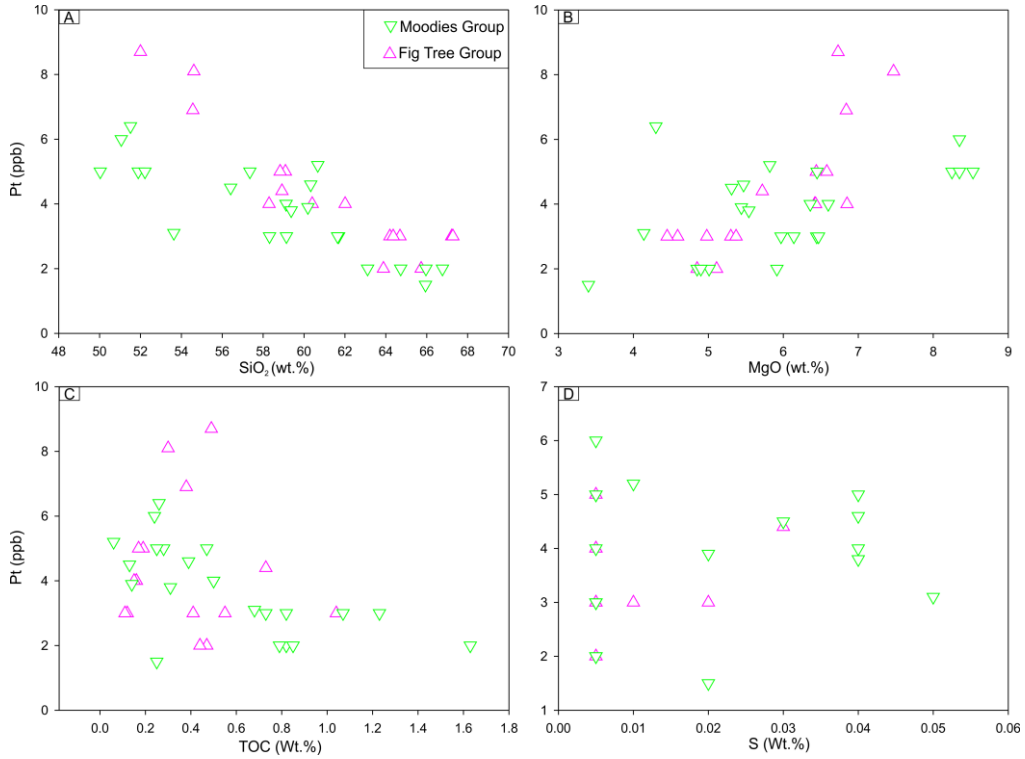

Figure 60: Bivariate diagrams for Barberton Supergroup marine shales showing correlations of SiO_2, MgO, TOC, and S with Pt.

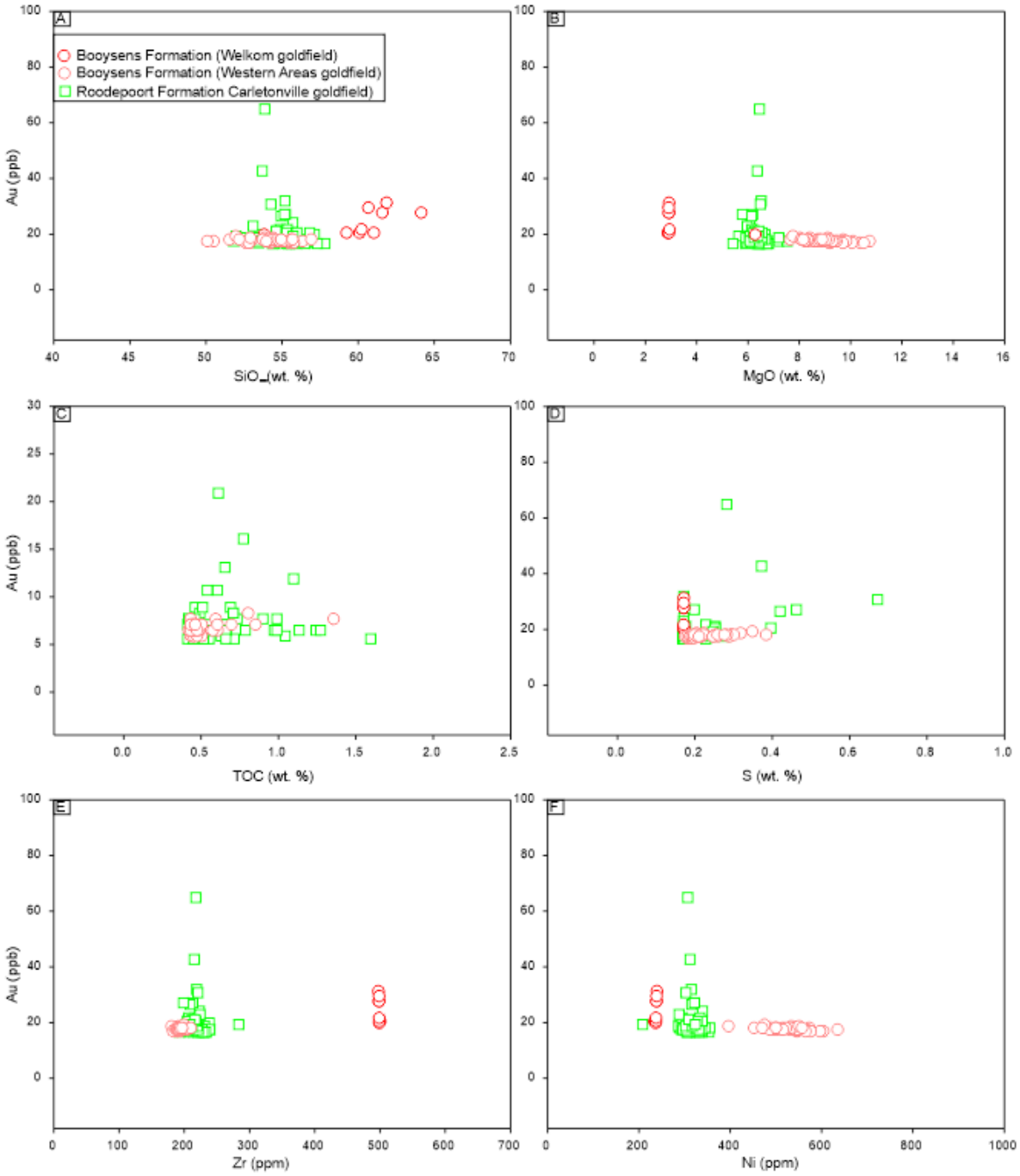

Figure 61: Bivariate diagrams for Witwatersrand Supergroup marine shales showing correlations of SiO_2, MgO, TOC, S, Zr, and Ni with Au.

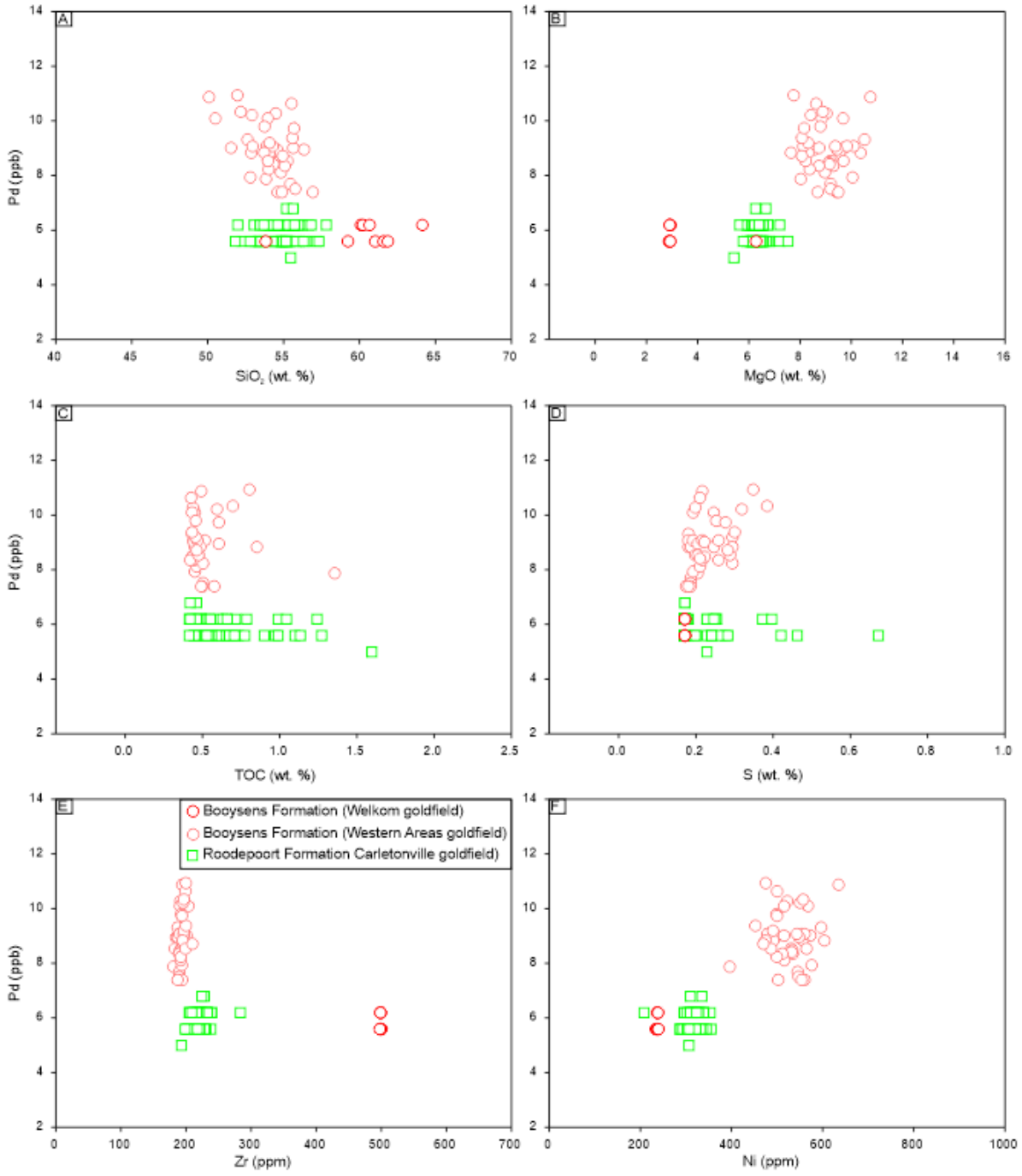

Figure 62: Bivariate diagrams for Witwatersrand Supergroup marine shales showing correlations of SiO_2, MgO, TOC, S, Zr, and Ni with Pd.

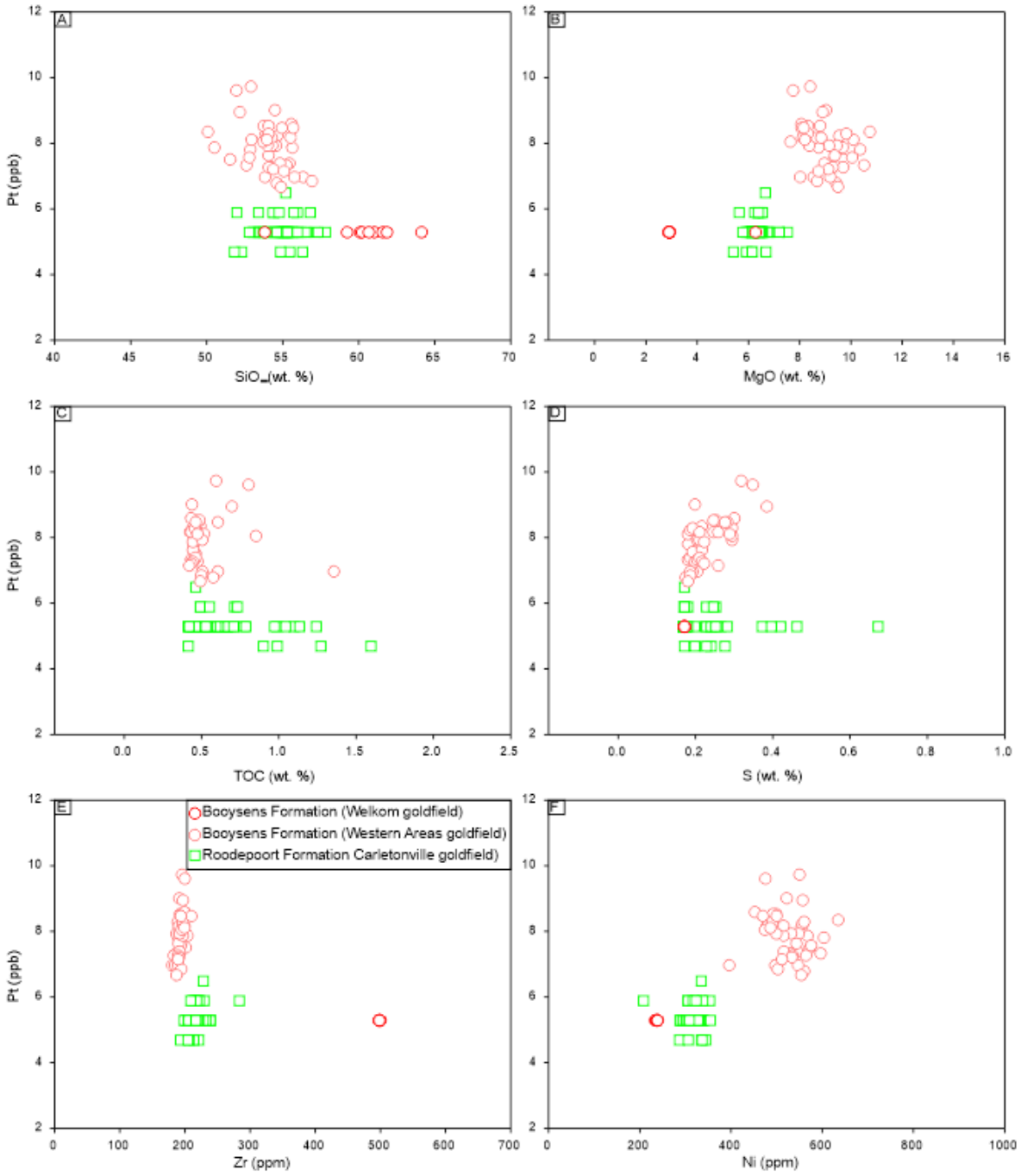

Figure 63: Bivariate diagrams for Witwatersrand Supergroup marine shales showing correlations of SiO_2, MgO, TOC, S, Zr, and Ni with Pt.

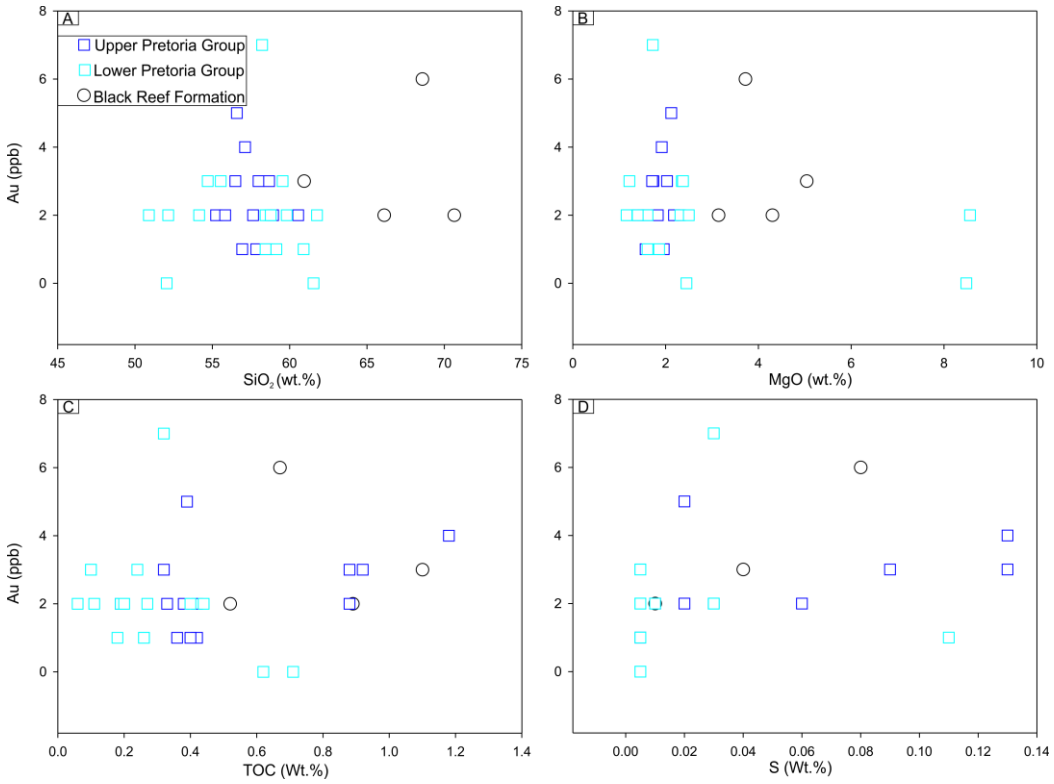

Figure 64: Bivariate diagrams for Transvaal Supergroup marine shales showing correlations of SiO_2, MgO, TOC, and S with Au.

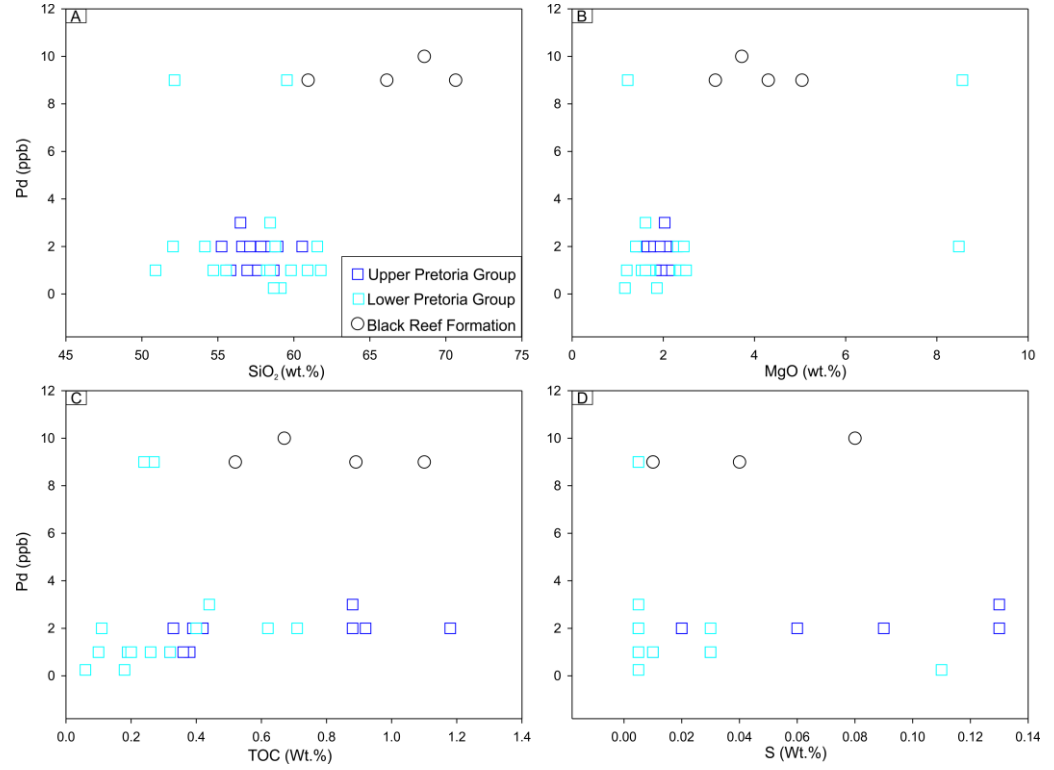

Figure 65: Bivariate diagrams for Transvaal Supergroup marine shales showing correlations of SiO_2, MgO, TOC, and S with Pd.

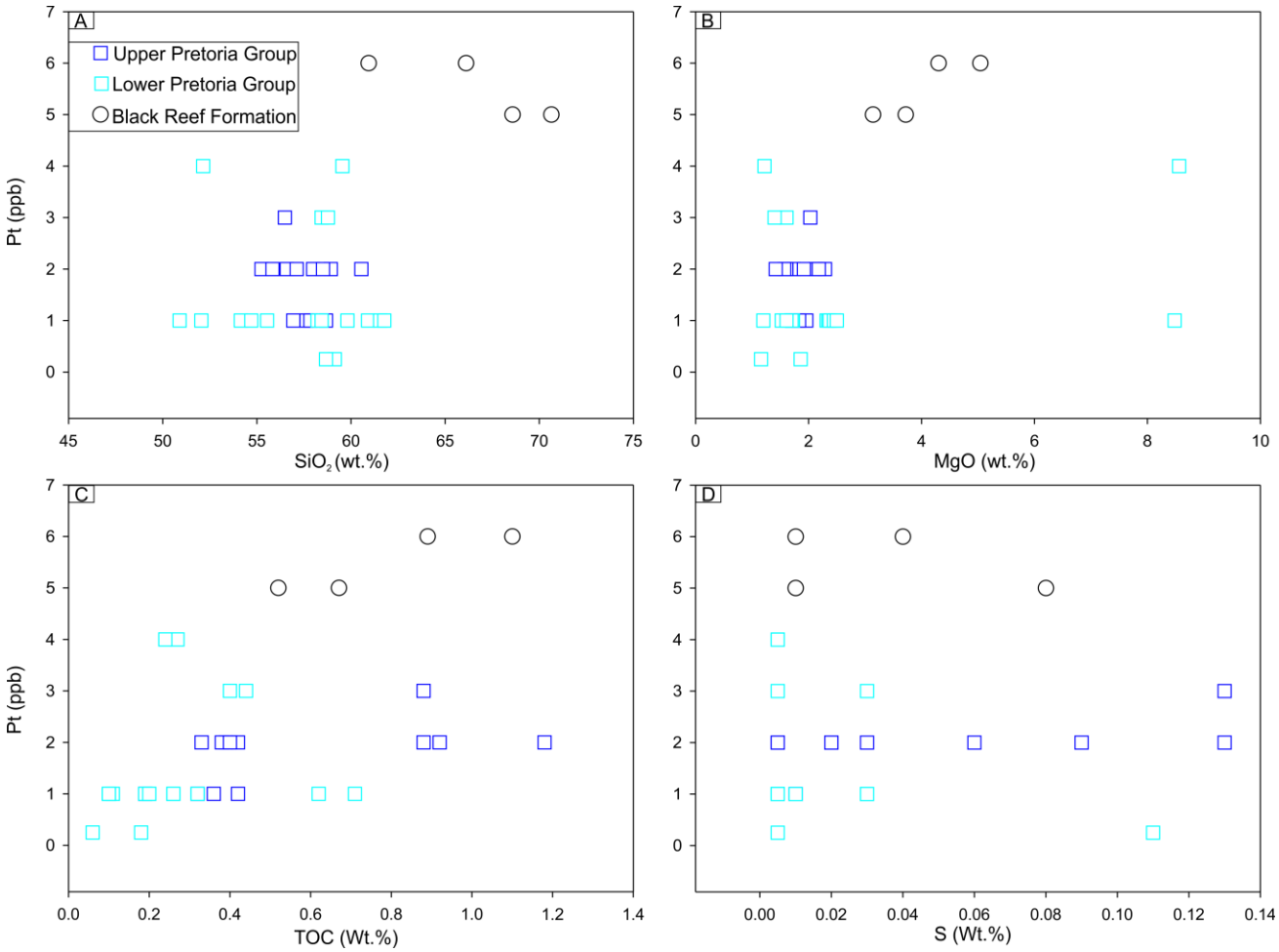

Figure 66: Bivariate diagrams for Transvaal Supergroup marine shales showing correlations of SiO_2, MgO, TOC, and S with Pt.

7. DISCUSSION

Compared to other cratons, the Kaapvaal Craton sequences host large, world-class mineral deposits. The petrography and mineralogy of the sampled marine shales (Chapter 5), along with geochemical results (Chapter 6), helped to identify potential predictive indicators of the mineralogical and elemental abundances and HSE distributions. However, to assess the extent to which these characteristics translate into post-depositional alteration, provenance, and palaeoweathering, the results are further assessed and compiled in this chapter. This chapter is subdivided into sections, each of which addresses one of the primary objectives proposed in Section 1.3. Once the relationship between shale petrography, mineralogy, and geochemistry has been investigated, some final implications of this relationship are used to explain the potential sources of siderophile elements.

7.1. Summary of the minerals encountered and mineral paragenesis

In many rocks, including shales, phase transformations begin shortly after sedimentation and continue to take place with increased burial. Thus, distinguishing the transition between diagenesis and metamorphism is largely arbitrary (Coombs, 1961; Pettijohn, 1957). The temperature separating the diagenetic from the metamorphic realm is thought to be ~200°C (Schulz-Rojahn and Phillips, 1989). At temperatures below 300°C, clay minerals are still very sensitive to changes in both temperature and pressure, resulting in a series of compositional and micro-textural transformations (Merriman and Peacor, 1999). Dioctahedral and trioctahedral clays transform from smectite into muscovite and chlorite, respectively, during late diagenesis. The formation of Illite, which is the intermediate phase between muscovite and smectite, results from mixed-layer illite/smectite transformation (Morad et al., 2000). This conversion occurs because of the reaction between smectite and potassium, which also releases connate water into permeable horizons (e.g. Si, Mg, Fe, Na, and Ca ions into solution).

The abundance of sericite appears to reflect both the abundance of feldspar that was originally present in the sample, and the degree of alteration that the samples underwent. In most of the studied samples, sericite occurs as fine grains, replacing feldspar and micas. Chlorite is common in the Kaapvaal Craton shales. It occurs as flakes amongst quartz grains. Some flakes are bent around quartz grains, potentially indicating compaction. In most cases, the chlorite grains form part of the matrix, suggesting a metamorphic origin for them. An overgrowth of secondary chlorite on the metamorphic chlorite grain margins is present in some instances. Quartz appears to be consumed during the reaction in which the authigenic chlorite

was formed. The second generation of chlorite could be attributed to either the epigenetic growth of chlorite on the existing grain or Mg-replacement with iron via hydrothermal fluids. In the case of the feldspar, XRD analysis indicates that the plagioclase feldspar is mostly Na-rich, and approaches the composition of albite. This finding is consistent with the feldspar compositions measured by Watchthorn (1981) and Holdsworth (1996). Monomineralic quartz grains are common in all the studied shales, and occur in a variety of sizes and shapes. Overall, the Barberton, Transvaal, and Witwatersrand Supergroup mineralogical assemblages appear similar, aside from the stratigraphic variants in proportion. Thus, the reactions below represent some of the mineral formations within the studied shales:

- Chlorite + K-feldspar → biotite + quartz + H_2O
- Ferrihydrite + Fe^{2+}–hydroxide → magnetite + H_2O
- Kaolinite + quartz → pyrophyllite + H_2O
- Muscovite + quartz + ankerite + H_2O → biotite + calcite + chlorite + CO_2
- Pyrite + organic matter + H_2O → pyrrhotite + H_2S + CO_2
- Siderite + ferrihydrite → magnetite + CO_2 + $3H_2O$
- Smectite → mixed-layer smectite/corrensite/chlorite (S/Co, Co/C) → chlorite
- Smectite → mixed-layer illite/smectite (I/S) → illite → muscovite

In summary, the studied shales mineral composition is fairly standard and is characterised by quartz, illite, chlorite, albite (Figure 67), and minor heavy minerals. Furthermore, the rocks seem to contain several generations of minerals, with reference to the clay minerals. The silty fractions of the shales contain various sulfides, mainly pyrite. This is expected for an interstitial mineral whose size is determined by its grain size and the dimensions of the primary silicate filling the interstitial spaces of the silty sections. Sulfides comprise a large proportion of the authigenic minerals, and are dominated by pyrite. Post-diagenetic subhedral pyritic overgrowths are the most common pyrites present in the studied shales, especially in the Witwatersrand shales. Calcite is a fairly common mineral in the Jeppestown shales. It occurs as large anhedral grains, and probably has its genesis in the release of Ca during albitisation. Provided that calcite is related to Ca release during albitisation, it is more likely metamorphic. Figure 68 summarises the relative stabilities of selected minerals present in Kaapvaal Craton shales.

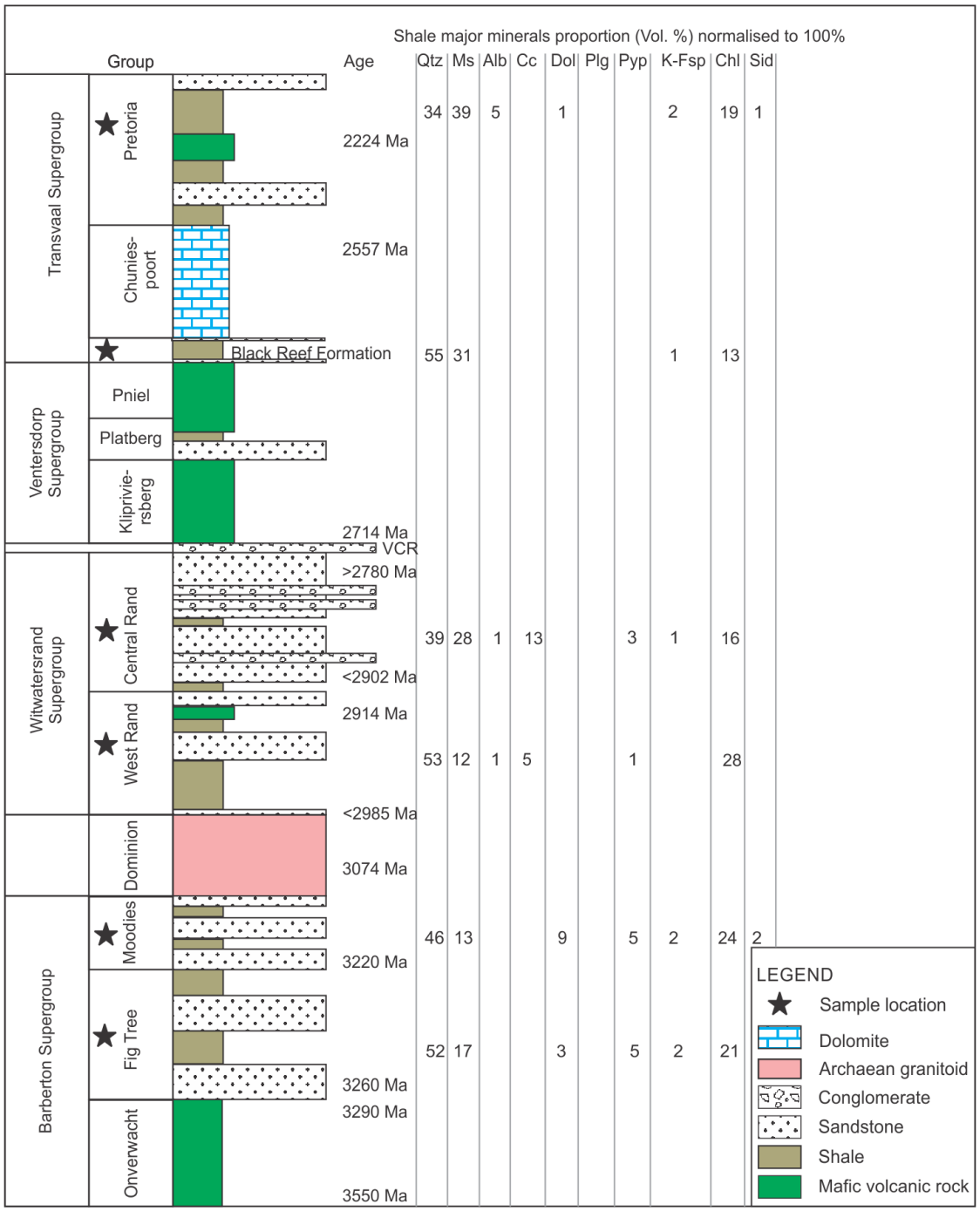

Figure 67: Summary of major mineralogical proportions of Barberton, Transvaal, and Witwatersrand supergroups.

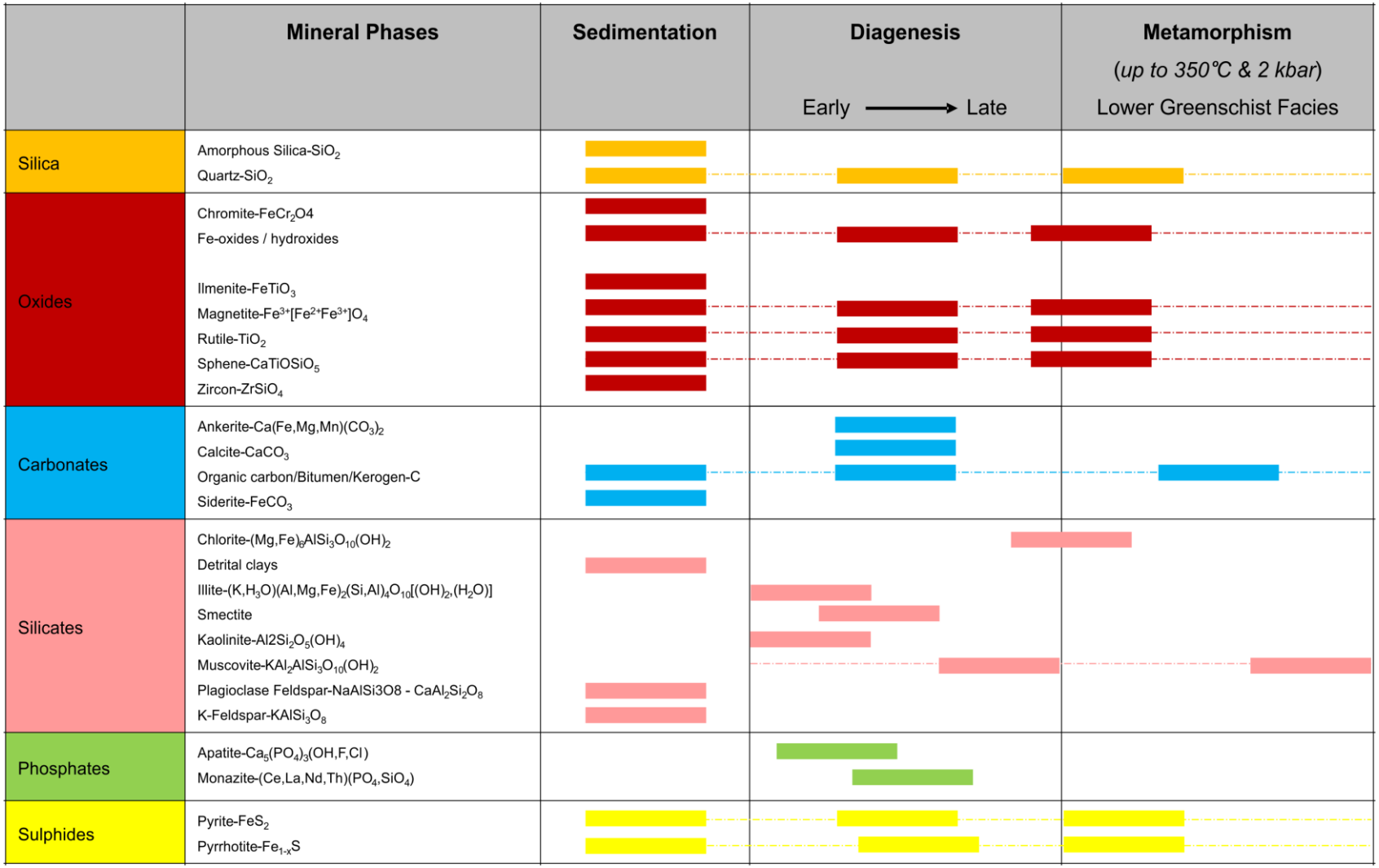

Figure 68: Relative stabilities of selected minerals in Barberton, Transvaal, and Witwatersrand supergroups as a function of metamorphic grade (adapted from Kisch, 1987; Frey and Robinson, 1999; Klein, 2005).

Rutile occurs as an accessory mineral in the Barberton and Witwatersrand supergroups. The transformation of pyrite to pyrrhotite most likely involved the release of CO_2, which was later used to form some of the calcite (Tweedie, 1968). The Transvaal Supergroup contains calcite and pyrrhotite, most of which occurs in carbonaceous shale. These findings confirm observations reported in previous studies, although these minerals usually appear in shales along with epidote. Under increasing grades of metamorphism, metamorphic fluids from hydrous phyllosilicate minerals are expelled during dehydration reactions (i.e. clay minerals can contain up to 14 vol.% water in their structures prior to greenschist facies metamorphism, Deer et al., 1983). Therefore, the late diagenetic assemblage of quartz–chlorite–illite in the studied shales evolved into quartz–chlorite–muscovite, as the illite transformed into muscovite, because of changes in its crystallinity related to the fluid pressure, temperature, and stress. Pyrophyllite was not observed during petrographic examination, but was observed with XRD analysis in the Barberton and Witwatersrand supergroups. The diagenetic assemblage in the Central Rand Group thus would have evolved from quartz–kaolinite–illite to quartz–muscovite–chlorite during metasomatism and greenschist facies metamorphism (Feather and Koen, 1975; Winkler, 1979; Phillips et al., 1990). The phyllosilicate transformations that occurred during late diagenesis and low-grade metamorphism include an increase in crystal size, a decrease in lattice defect densities, a decrease in the proportion of clay minerals and mixed layering, and the formation of more uniform phyllosilicates (Merriman and Peacor, 1999). As indicated earlier in Chapter 5, the general mineral assemblage of studied shales comprises quartz, muscovite, calcite, chlorite, and pyrophyllite with the phyllosilicates confirming a lower greenschist facies metamorphic grade based on the computed chlorite formation temperatures. Petrographic studies reveal two generations of chlorites, namely metamorphic and hydrothermal chlorite. Their presence constitutes the most likely explanation for the variable formation temperatures, as calculated via the range of geothermometers. The occurrence of different generations of chlorite in the fresh, unmineralised shales implies that their chemistry is only minimally, if at all, affected by modern weathering. Although the chlorite represents different generations, their chemical composition is similar.

7.2. Extent of post-depositional alteration

Although shales generally have low permeability, depending on the extent of fracturing, the Witwatersrand shales were subjected to various degrees of post-depositional alteration in the course of diagenesis, low-grade metamorphism, and shattering by the 2.020 ± 0.005 Ga (Kamo et al., 1996) Vredefort impact event. Thus, it is important to distinguish between post-

depositional alteration and mixing of sediment from different sources, or sedimentary sorting, to account for the variations in whole-rock shale chemistry. Whether the low-grade metamorphic overprint evident in all Witwatersrand units was isochemical has been a question of debate. While some authors have argued for widespread H^+-metasomatism to explain the common occurrence of pyrophyllite (Phillips and Law, 1994; Barnicoat et al., 1997), others emphasised the strong stratigraphic control on the chemistry and mineralogy of Witwatersrand arenites, and concluded that metamorphism was essentially isochemical with the exception of K (Sutton et al., 1990). The noted loss of K in the coarser-grained siliciclastic facies could be ascribed to acid leaching by post-depositional fluids, as suggested by Barnicoat et al. (1997) and more recently by Phillips and Powell (2014), but also to acid rain on old erosion surfaces, followed by more or less isochemical metamorphism of kaolinite-rich deeply weathered sediment (Wallmach and Meyer, 1990; Frimmel, 1994). The former, post-depositional fluid-induced alteration should follow fluid pathways and display zonation patterns that reflect dispersion from the fluid pathway into the country rocks. Since, in that hypothesis, the main fluid pathways are believed to follow arenite beds, dispersive alteration haloes should be found in both the corresponding underlying and overlying units. The pebble fraction certainly reduces the total porosity, but the permeability is controlled by the interstitial sand grain fraction. Maximum weathering should be in the immediate underlying conglomeratic reef units where the contact between both represents a palaeo-erosion surface. If the loss of K is due to leaching by meteoric waters on ancient erosion surfaces, only the upper parts of the corresponding footwall should be affected. Available geochemical data on conglomerates and arenites reveal that large-scale alteration, marked by a very high chemical index of alteration values, is indeed most intense in the arenitic rocks immediately underlying the conglomerate-covered palaeo-erosion surfaces, gradually decreasing with depth over tens of metres, and absent in the arenites above the conglomerates (Frimmel and Minter, 2002). Dispersion haloes into both the underlying and overlying beds due to bedding-parallel fluid flow along the conglomerated beds are spatially limited to <1 m (Frimmel and Minter, 2002) and involved little externally derived fluid (Gartz and Frimmel, 1999). These findings strongly indicate that most of the H^+-alteration is an effect of palaeo-weathering, and that post-depositional fluid-induced alteration is volumetrically far less significant.

The most intensely altered zones typically occur along and near structural boundaries (i.e. faults) and mafic dykes. In most cases, this alteration led to the chloritisation of the country rocks, irrespective of whether they are conglomerates (e.g. Frimmel, 1997) or shales (e.g. Phillips and Powell, 2014). For the purpose of this study, such zones were generally avoided when taking samples. To assess the possible influence of post-depositional alteration on the

overall shale chemistry, five fresh samples were taken from an underground exposure of the Roodepoort Formation shale at Driefontein 8 Shaft (MR10 32 XCW), representing a profile from the upper contact of the shale unit, where it appears altered along the contact, into less altered shale (Figure 69).

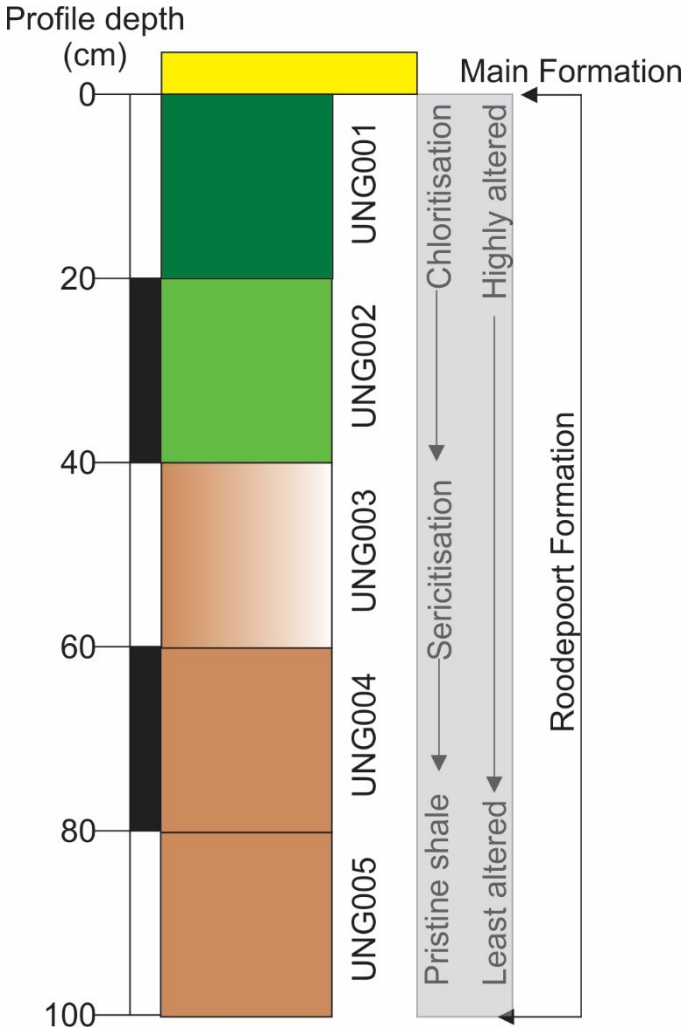

Figure 69: Marine shale profile showing extent of post-depositional alteration. The samples were obtained from Driefontein 8 shaft, MR10 32XCW.

The samples' alteration indices were determined using the Isocon technique described by Grant (1986, 2005). The method is based on Gresens' (1967) chemical mass balance equation:

$$Fv\left(\frac{\rho^s}{\rho^p}\right)C_n^s - C_n^p = X_n \qquad \textbf{Equation 21}$$

where the superscripts *p* and *s* refer to protolith (primary) and altered (secondary) rock, respectively; C_n^s and C_n^p are the fractional concentrations of element *n* in altered and unaltered rocks, respectively; X_n or ΔC is the amount of mass change (gained or lost) in element *n*; Fv is the overall volume factor (i.e. the ratio of the volume of altered rock to the volume of unaltered protolith; Fv = V^s/V^p).

Results from the geochemical mass balance modelling show that even the most altered sample does not result in any gain or loss (% change in concentration, ΔC) of >20 % with regard to any major and trace element. There was, however, a considerable gain of K relative to the least altered reference sample, illustrated by a systematic change of K_2O (ΔK_2O = +0.82, +1.08, and +0.16) in the altered samples. Absolute mobility of elements such as Cr, V, and Ba indicates that there was significant systematic mass transfer of >10 %. Calculations of volume change assuming net gain/loss of 0 for relatively immobile elements (i.e. ΔTiO_2 = 0) yield a volume factor of 1 (i.e. altered sample UNG001 versus unaltered sample UNG005), further demonstrating the insignificant elemental net transfer.

The mass transfer results obtained (Appendix A.4) might suggest that at this test site generally mobile components, such as K, behaved as if immobile and normally immobile components, such as Cr, behaved as if mobile. This apparent contradiction is likely an artefact of two different types of alteration that were superimposed onto each other along the same contact of the shale unit, although over different distances from that contact. An earlier K-metasomatism in the form of sericitisation affected the shale along its upper contact over a wide (1 m) space. This was followed by chloritisation (and thus the loss of K), which was limited to the immediate contact between the shale and the overlying coarser-grained quartzite and conglomerate of the main formation. This superposition of two chemically different alteration events is analogous to that described for the Ventersdorp Contact Reef, which has been regarded by many as the most intensely altered reef in the Witwatersrand (Frimmel and Gartz, 1997; Gartz and Frimmel, 1999). Numerous field observations in the current study suggest that this seems to be common throughout most of the Witwatersrand goldfields.

Considering that most studies on post-depositional alteration have been conducted on the coarser-grained fractions, essentially conglomerates, the extent of post-depositional fluid flow through the intervening shale units should have been even smaller because of their generally much lower permeability. This is supported by our data on REE, Al, and Ti, all of which remained immobile in the studied test profile across the Roodepoort Formation shale towards its altered upper contact (Figure 70).

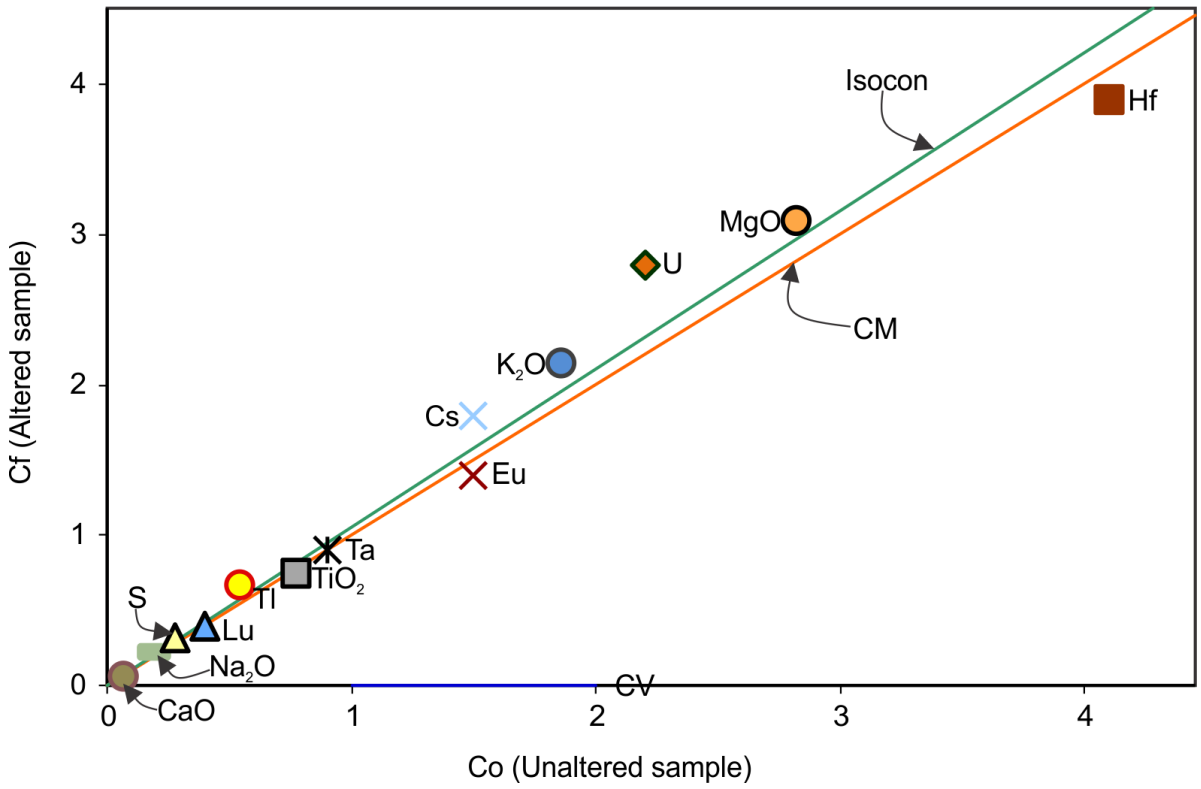

Figure 70: Isocon diagram of Roodepoort Formation shales illustrating behaviour of major oxides and selected trace element constituents. Abbreviations: CM = constant mass, CV = constant volume; calculation after Grant (2005).

As shown below, ratios of various trace elements (e.g. Ni, Cr, Co, Sc, Zr, Hf, and Th) in the analysed shale samples conform to those typical of specific source rock types, thus precluding major post-depositional mobilisation. The REE patterns observed in the Witwatersrand shales (Wronkiewicz and Condie, 1987) are uniform across stratigraphic units and conform to those typical of unaltered shale elsewhere. Even U mobility was seemingly limited, as evident from the relatively uniform Th/U ratios across most of the shale units. Wronkiewicz and Condie's (1987) shale data also displayed similar patterns for the Promise Formation (Th/U $\bar{x}$ = 5.36 ± 0.69) and K8 Formation (Th/U $\bar{x}$ = 2.33 ± 0.45); however, a slightly higher deviation was observed in the Parktown and Brixton Formations (Th/U: $\bar{x}$ = 3.15 ± 1.38). These features are typical for Archaean sedimentary rocks and match those found for other sequences (e.g. the Barberton Supergroup, Figure 71).

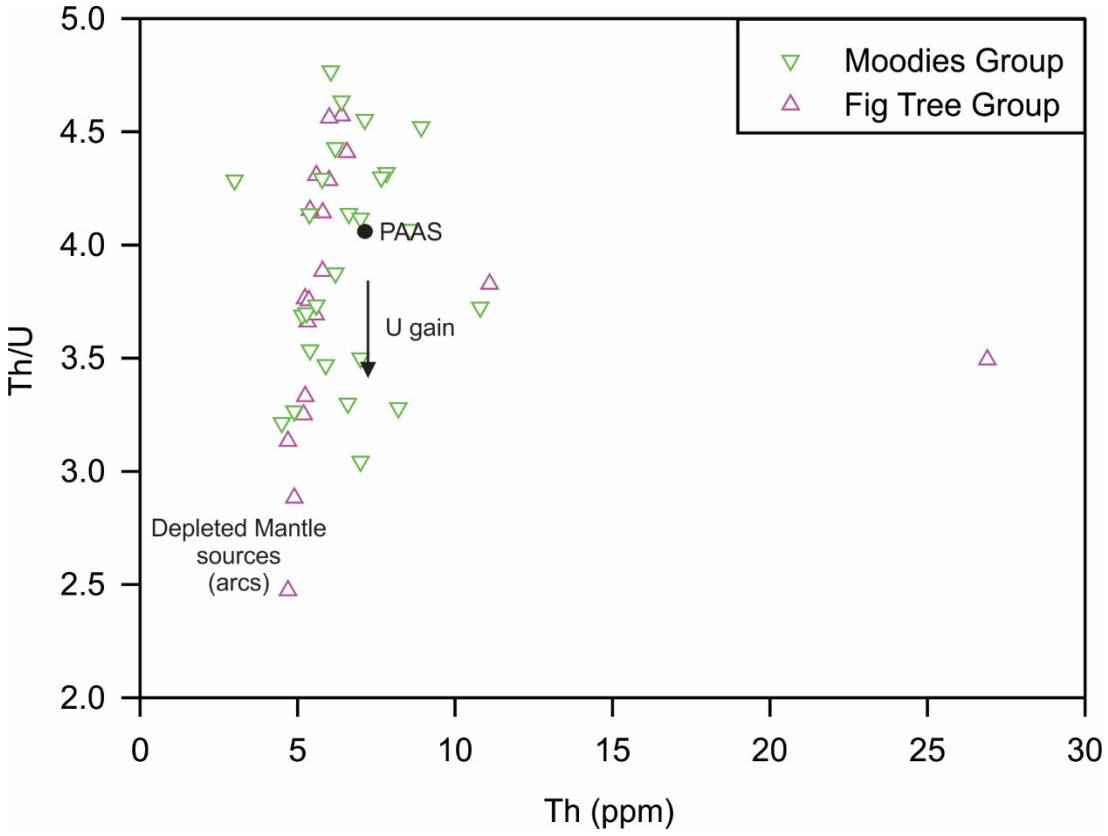

Figure 71: Diagram of Th versus Th/U for Barberton Supergroup shales.

The chief uranium-bearing minerals in the Witwatersrand conglomerates are uraninite ($U^{4+}O_2$ to $U[^{4+}, ^{6+}]_3O_8$) and brannerite ($[U, Ca, Ce][Ti, Fe]_2O_6$), whereas the Th-bearing minerals are thorite ($ThSiO_4$) and thorianite (ThO_2), with significant amounts of Th also occurring in uraninite, monazite, and zircon (Sebola, 2014; Depiné et al., 2013; Frimmel et al., 2014). The uranium content and its mobility in aqueous systems are mainly controlled by the pH, reduction oxidation (redox) potential, and type of complexing agents present (e.g. carbonates, phosphates, and silicates (Langmuir, 1997)).

Uranium has been largely mobile in post-Archaean times after the 'Great Oxidation Event' at approximately 2.4–2.2 Ga (Kumar et al., 2011). In the Archaean environment, however, U mobility should, have been very limited because of the overall reducing conditions and thus the stability of detrital uraninite (Frimmel, 2005). This can be tested by means of Th–U correlation. If U transportation was mainly in the form of dissolved U (uranyl ion, UO_2^{+2}), its concentration should be only weakly or not at all correlated with that of Th. However, if Th and U were exclusively hosted by the above minerals in detrital form and mechanically disintegrated during sediment transport and hydraulic sorting into finely discrete particles, a perfect positive correlation between U and Th should be expected. A positive correlation can be noted in most of the Witwatersrand shales, but it is far from perfect with the exception of a

few localities (i.e. the base of the Booysens Formation shale in the Welkom Goldfield, r = 0.95).

Any deviation from ideal Th/U-versus-U correlation can be ascribed to dispersion of U (Figure 72), which has been far more mobile during post-depositional alteration than Th (Schidlowski, 1981; Oberthür, 1987; Depiné et al., 2013). Post-depositional U mobility, be it by hydrothermal fluid circulation or metamorphic dehydration, is particularly evident in the Booysens Formation shale in the Strathmore area. In contrast, shales from the same formation located in the Krugersdorp and Welkom goldfields display a fairly strong Th–U correlation, implying only limited U mobility. Thus, it can be inferred that U mobility in the Witwatersrand shales is significant in some places but less so in others.

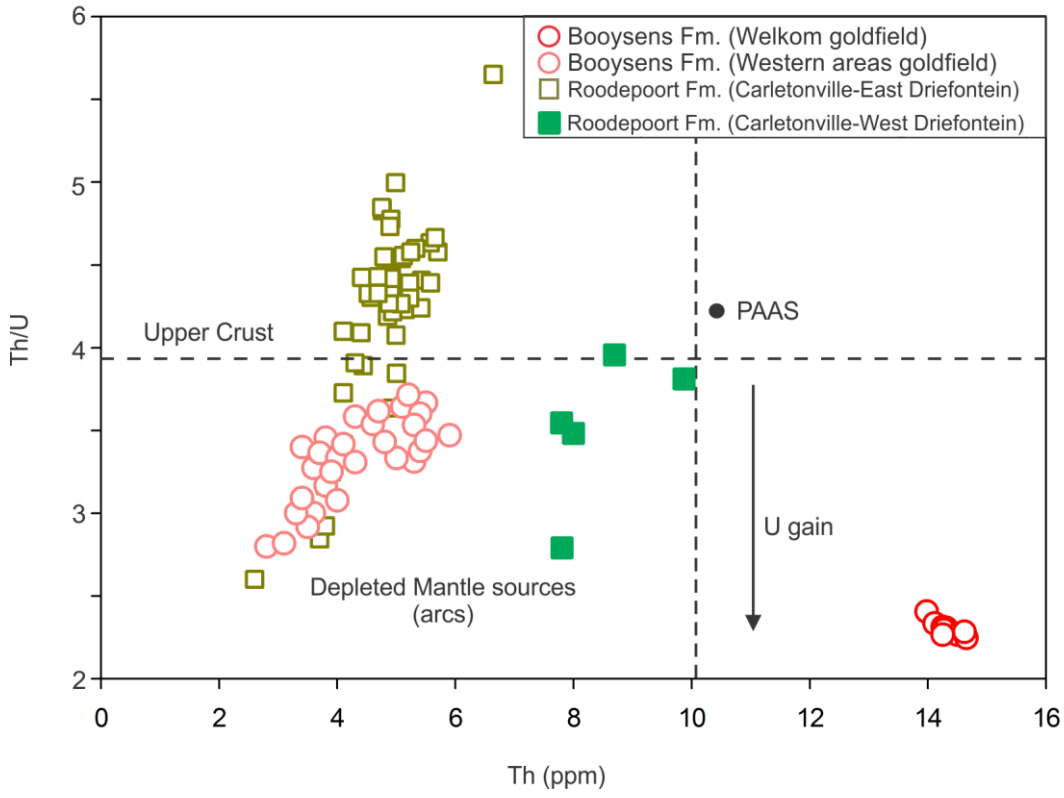

Figure 72: Diagram of Th versus Th/U illustrating syn- and post-depositional mobility in selected Witwatersrand shales. Note the differences in Th/U between different positions within the same stratigraphic unit, reflecting differences in provenance.

Further evidence against significant post-depositional alteration of the shale units comes from S isotope studies (Farquhar and Wing, 2003; Bekker et al., 2008; Ono et al., 2009). Witwatersrand Supergroup shales have uniformly negative $\Delta^{33}S_{In}$ values and largely negative $\delta^{34}S$ values. This rare combination is inherited from photochemically produced, reduced-S species, such as elemental S, implying that the shales are not significantly modified by

hydrothermal fluid circulation (Ono et al., 2009; Farquhar et al., 2013). The uniformly negative $\Delta^{33}S_{In}$ values suggest that atmospheric sulfur preserved in terrestrial environments was preferentially derived via the aerosol sulfate pathway rather than via the elemental sulfur (S_8) pathway (Hofmann et al., 2009; Guy et al., 2010). Sulfate from aerosols could have been fixed in the palaeosols through either biological or thermochemical mechanisms (Maynard et al., 2013).

The Witwatersrand sulfur isotope data do not support a large role for hydrothermal fluids moving preferentially along the gold-bearing conglomerate units, except for in the Ventersdorp Contact Reef (Sutton and Maynard, 1993; Zhao et al., 1999). Results from Witwatersrand diamictites reveal sulfur with a relatively narrow range of isotopic values ($\Delta^{33}S_{In}$ values = -0.17–0.07 ‰; Maynard et al., 2013). The sulfur present in the Witwatersrand palaeosols is a mixture of remobilised inherited S (with $\Delta^{33}S_{In}$ in the +0.1 % to -0.1 ‰ range), along with atmospheric S (with $\Delta^{33}S_{In}$ in the -0.3 % to -0.6 ‰ range; Hofmann et al., 2009; Guy et al., 2010; Maynard et al., 2013). Overall, post-depositional alteration was minor, except along contacts with different overlying and underlying rock types and along those with fractures, faults, and dykes. Thus, the chemistry of the shales from undisturbed, least-altered domains is taken to represent the original sediment composition, and is consequently useful for reconstructing the provenance and pre-/syn-depositional palaeoweathering.

7.3. Sediment provenance

Knowing the nature of source rocks that contributed to the formation of the studied marine shales is crucial to understanding the composition of the hinterland, basin architecture, and preservation of relatively immobile elements. Immobile elements are mainly transferred as suspended material to mud deposition sites. This is supported by the fact that REE, HFSE, and transition metal concentrations are significantly higher in the suspended load than in the dissolved load in major rivers of the world (Goldstein and Jacobsen, 1988; Dupré et al., 1996). The X_{Mg} ratio can serve as a proxy for the proportion of mafic or ultramafic rocks in the source area (equation 22):

$$\mathbf{X_{Mg} = [Mg/(Mg + Fe)] \times 100} \qquad \textbf{Equation 22}$$

This equation computes what is generally known as the ‘magnesium number’, which has been widely applied in igneous and metamorphic petrology (Rollinson, 1993, 2007). It should be low in shales derived from felsic source rocks and high in those from mafic and ultramafic sources.

In the modern ocean, a large proportion of Ni is complexed with organic ligands (Sunda, 2014). Degradation of organic matter invariably leads to the release of Ni from organometallic complexes and its concentration in carbonaceous shales, be it by adsorption onto, or substitution in, clay-sized particles or in early diagenetic pyrite (Bekker et al., 2009; Steadman et al., 2015). The supply of Ni is interpreted as having changed significantly through the Archaean–Proterozoic, and this affect the abundance of Ni in sediments that were deposited in these eras. Three main sources of Ni in the Archaean lithosphere and hydrosphere can be distinguished: (i) hotter Archaean mantle that produced abundant Ni-rich rocks such as komatiite (Jaun and Thauer, 2007), (ii) palaeo-seawater sequestration through organic matter adsorption (Konhauser et al., 2009), and (iii) scavenging of Ni from a fertile hinterland. There are various ways to evaluate the potential sources of Ni in Archaean marine shales without using experimentally derived partition coefficients. This can be done by examining the fractionation variation between Ni and Cr ratio of the Archaean shales and comparing it with post-Archaean shales Ni/Cr ratio. In this study, I examined the Ni/Cr ratio in shales from the Barberton Supergroup, the Witwatersrand Supergroup, and PAAS. The Ni/Cr ratios of the Barberton Supergroup (Ni/Cr = 0.4) and Witwatersrand Supergroup (Ni/Cr = 0.42) shales are not very different from that of PAAS (Ni/Cr = 0.21). An alternative method involves examining the scaling between Ni and total organic carbon in the shale record. In so doing, it becomes apparent that there is a negative correlation ($r = -0.65$) between Ni and total organic carbon (Figure 73). This speaks against a palaeo-seawater origin of Ni in the shale. If the total organic carbon was the primary source of Ni in the shales, Ni abundance should mirror the total organic carbon abundance in Archaean rocks. For such postulated syngenetic origin of Ni sourced from seawater, one would expect a positive correlation between Ni and total organic carbon, which is not the case in this study. Furthermore, Konhauser et al., (2009, 2015) estimated the highest palaeomarine Ni concentration to be approximately 400 nM (0.0023 ppm). Mass balance calculations using this concentration of dissolved Ni demonstrate that the time required to scavenge Ni into the shales/marine mud to reach an average of 221 ppm (Condie, 1993) by 2.7 Ga would require more dissolved Ni than the oceans could provide. This rule out the seawater sequestration model.

.

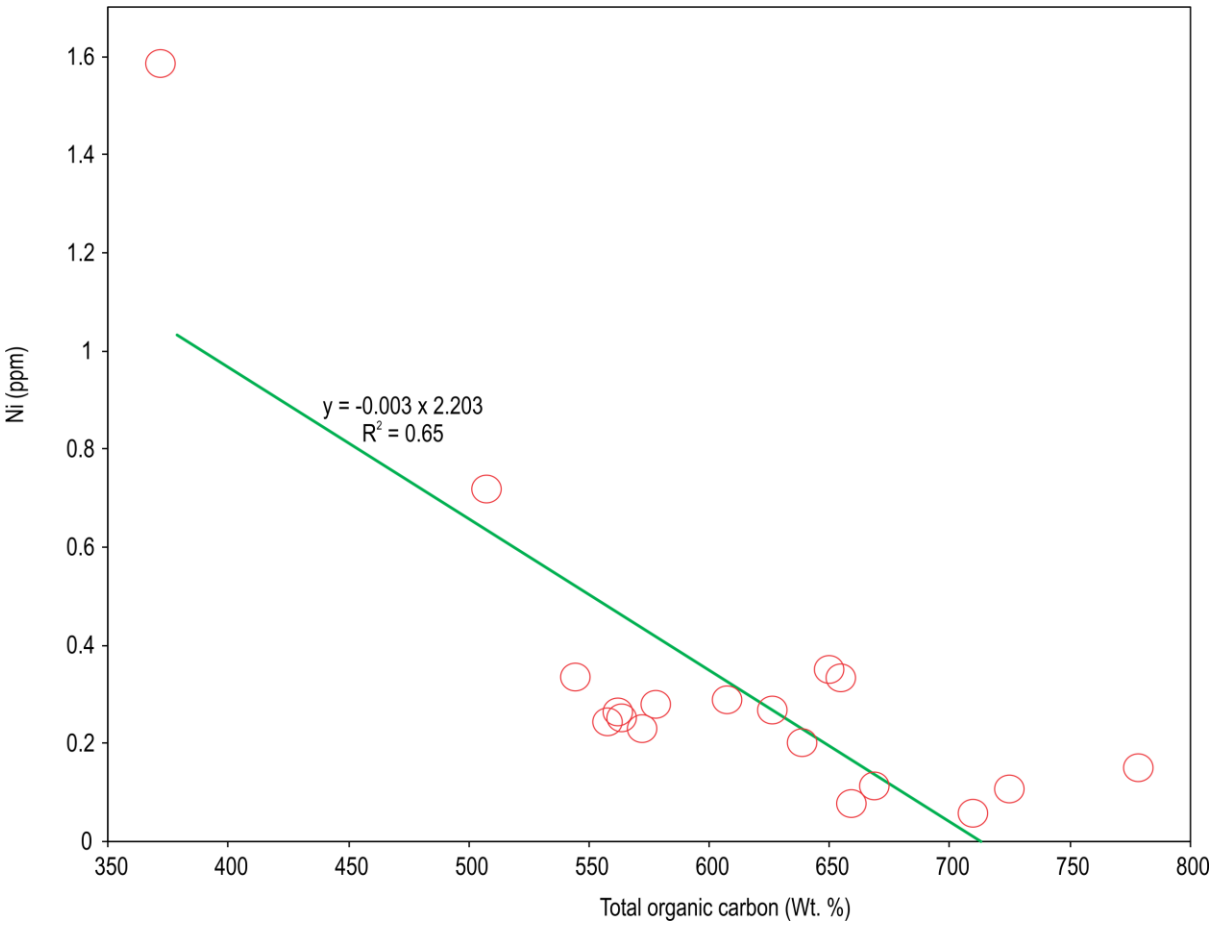

Figure 73: Ni versus total organic carbon plot for the Booysens Formation shale.

Another approach to examine the source of Ni in Archaean shales is through modelling of the shale's source sediments (proportion of rock types in the hinterland). This was achieved by reconstructing the lithological make-up of the Archaean and estimating the potential source-rock proportions (Appendix A.5). Following this step, various sediment mixing models were constructed using Ni concentrations in the respective source rocks multiplied by their proportion. This results in Ni concentrations that indicate a hinterland enriched in Ni (Figure 74**;** Appendix A.5) to an extent that suggests that most Ni in the shales is derived from particulate, detrital compounds. Consequently, I suggest that the Ni/Cr ratio is a good approximation of the sediment's provenance.

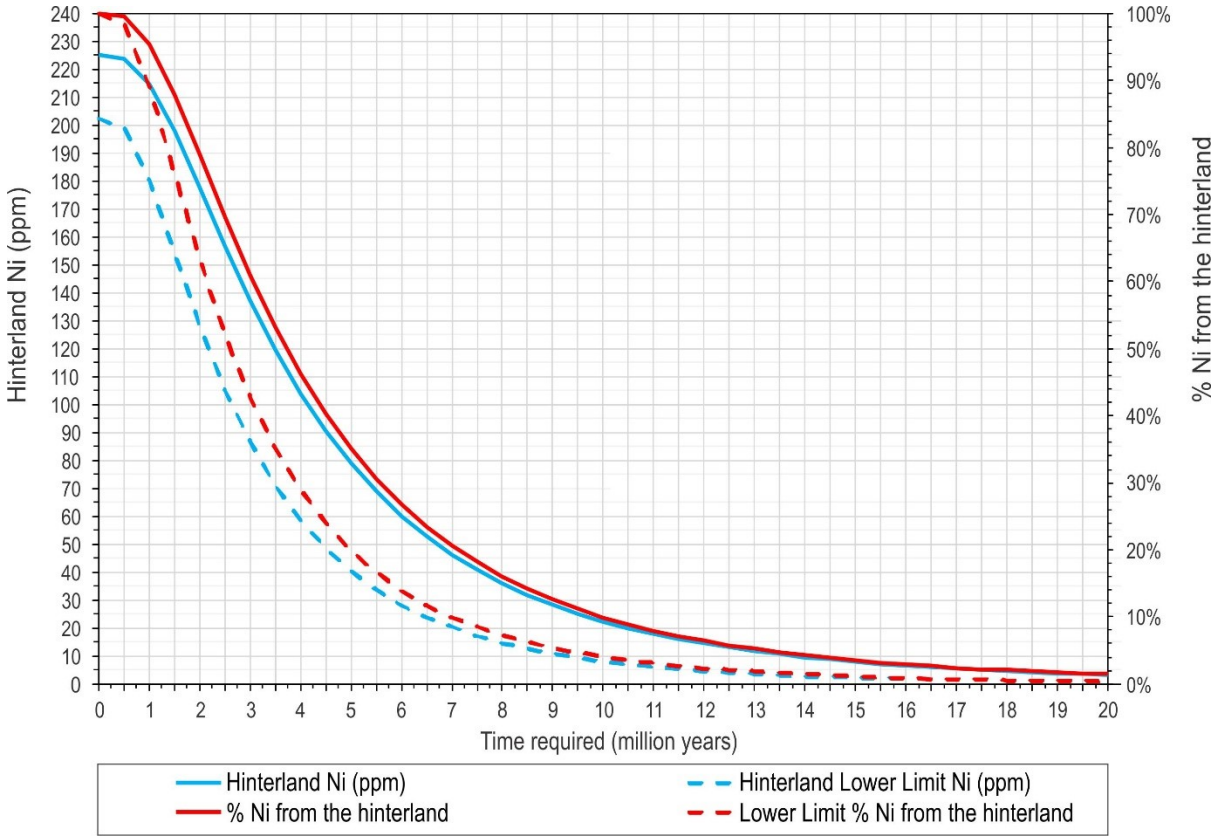

Figure 74: Geochemical model of Ni concentration in the Archaean hinterland. Lower limit lines indicate minimum required Ni derived from particulate, detrital compounds. Time scale (X-axis) indicates amount of time required to source Ni from the hinterland. Hinterland Ni (ppm) [left Y-axis] indicates hinterland concentration of Ni; % Ni from the hinterland (right Y-axis) indicates total % Ni supply to shales from the hinterland.

As Figure 75 demonstrates, the X_{Mg} is less variable in the Barberton Supergroup shales, but is highly variable in the Witwatersrand shales, where it ranges from 0.1 to nearly 0.6. The latter end of this range indicates a large proportion of mafic and ultramafic rocks in the hinterland, as would be expected for a typical Archaean greenstone terrane.

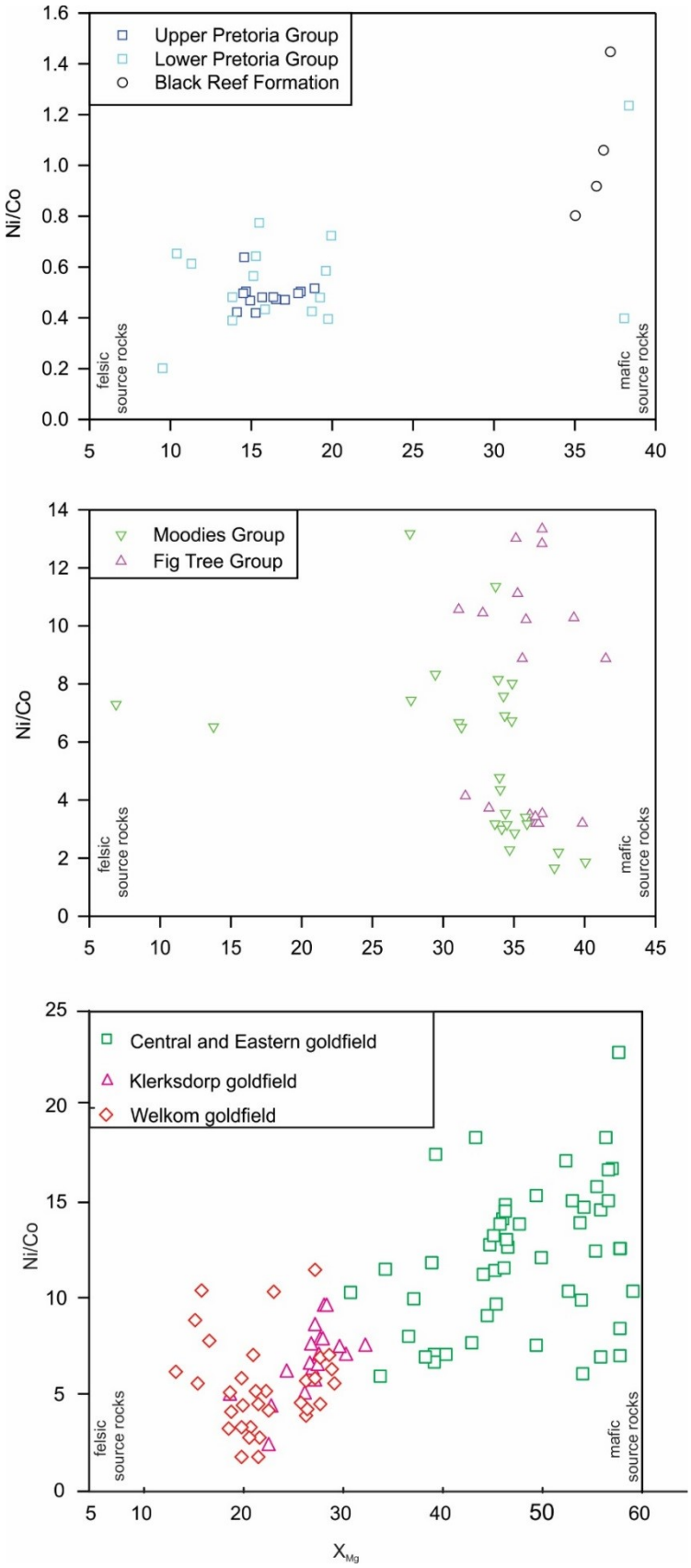

Figure 75: Diagram of X_{Mg} versus Ni/Co, demonstrating Kaapvaal Craton shale composition variations.

Particularly noteworthy is the clustering of data within the same stratigraphic unit based on stratigraphic location. The Booysens Formation shale units in the central and eastern goldfields are distinctly more magnesian than those in the north-western and western goldfields. This is interpreted as a primary provenance signal, because it is mirrored by another provenance indicator, the Ni/Co ratio, which is typically higher in more mafic and ultramafic source rocks (Figure 76). The Black Reef Formation exhibits a rather high XMg value relative to the Pretoria Group shales. Thus, the results imply that the Pretoria Group's source rocks are predominantly felsic.

In the absence of biological Ni transfer in the ocean, Ni and Cr abundances should mirror the proportion of (ultra)mafic source rocks, if neither of the two elements was subjected to post-depositional mobility. If the Ni and Cr in the shales were derived entirely from a mafic Archaean source, their Ni/Cr ratio should correspond to that of typical Archaean basalt or komatiite. As evident from Figure 76–78, this is indeed the case for the studied Kaapvaal Craton shales.

Among elements that exhibit chalcophile characteristics in the studied shales, the Ni and Cr abundances are abnormally high in both the Fig Tree (Ni = 59–593 ppm; Cr = 23–1277 ppm) and Moodies groups (Ni = 68–543 ppm and Cr = 55–1549 ppm) (Figure 76). This suggests that the preferential enrichment in Cr and Ni relative to other ferromagnesian elements present in the Fig Tree Group (FeO = 8.2 ppm and MgO = 5.5 ppm) also holds true for the Moodies Group (FeO = 11.3 ppm and MgO = 5.7 ppm). These values are among the highest recorded for Archaean shales, and can be attributed to the high abundances of ultramafic source rocks and the scavenging of the transition elements by clay-sized particles (Danchin, 1967; McLennan et al., 1983; Toulkeridis et al., 1999). These Ni and Cr concentrations represent values several times as high as those found in Phanerozoic shales (Condie, 1993).

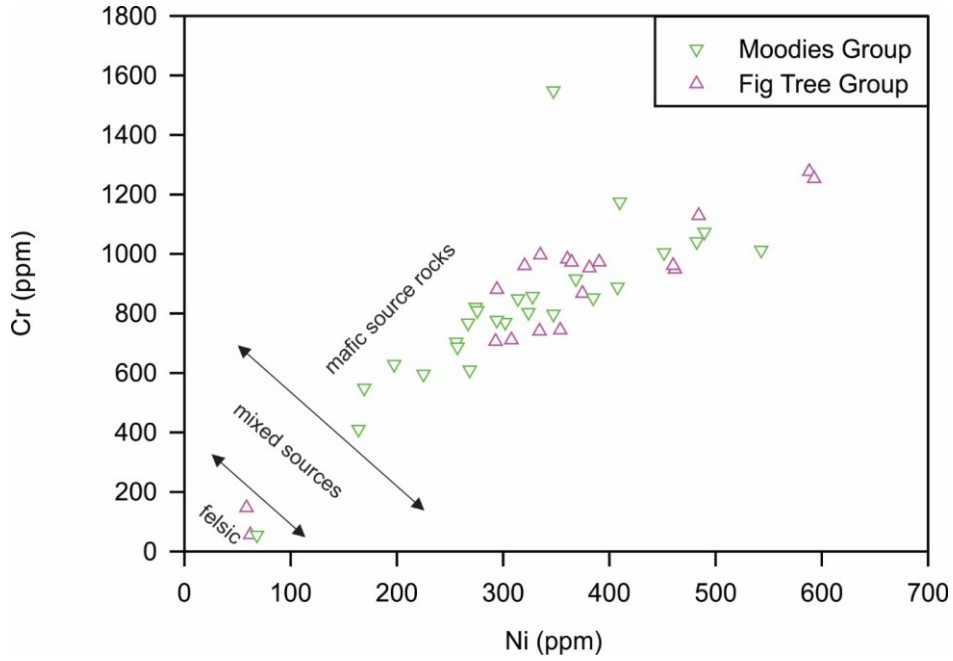

Figure 76: Binary plot of Ni versus Cr for Fig Tree and Moodies Group shales, illustrating change from mafic to felsic source rocks. Reference sample data are from Condie (1993).

As expected, Ni is negatively correlated with SiO_2 and positively correlated with MgO in both the Fig Tree and Moodies groups. Although the absolute abundances differ, the shales' Cr/Ni ratios fall within a narrow span (2.36 ± 0.47 and 2.57 ± 0.62), which is within the range of Cr/Ni ratios for komatiite-type rocks (Condie, 1993). The Cr/Ni ratio therefore recorded the source material's geochemical signal without significant fractionation (Garver et al., 1996). This resulted in high Cr/V and Ni/Co ratios and low V/Ni ratios for both the Fig Tree and Moodies groups. In addition, both Cr and Ni are positively correlated with MgO, Sc, and V.

The Roodepoort Formation shales indicate a significant input from mafic source rocks (Figure 77), with a strong positive correlation between Ni and Cr (r = 0.84). This suggests that the two elements remained relatively immobile after sediment deposition. A similarly positive Ni–Cr correlation of r = 0.91 was found for the Booysens Formation shales in various goldfields.

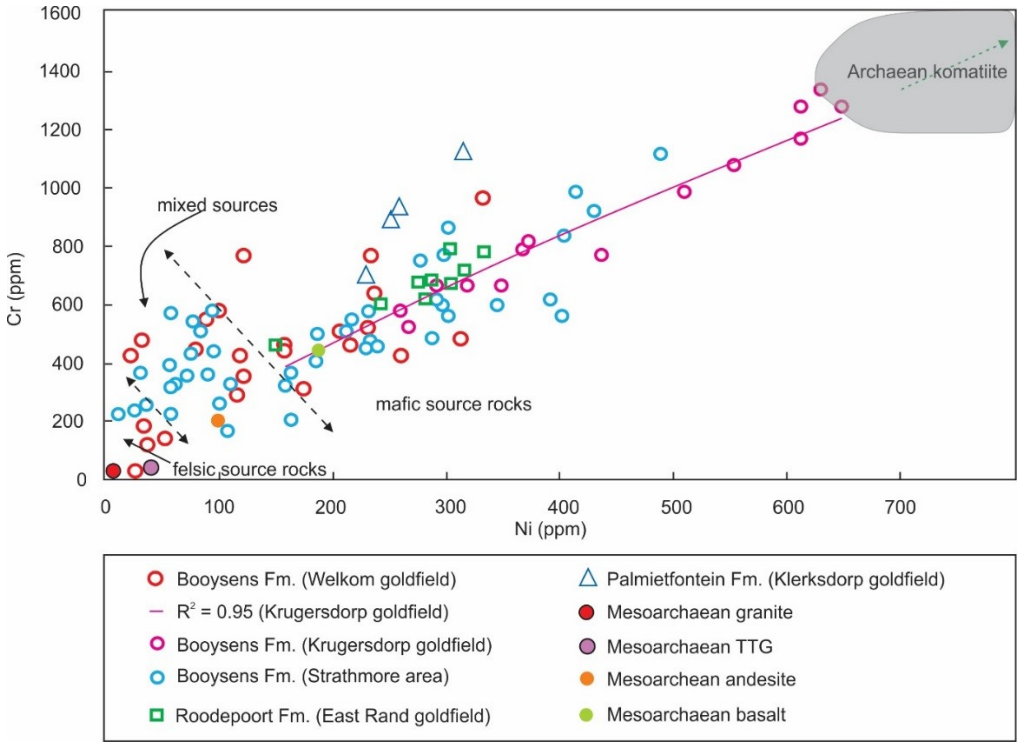

Figure 77: Binary plot of Ni versus Cr for selected Witwatersrand shale units. Reference sample data are from Condie (1993).

Several of the samples have very low Cr and Ni concentrations, which is due to the correspondingly high proportion of sediment from felsic source rocks. Any deviation from the ideal positive correlation line in Figure 77 would indicate either the post-depositional mobility of one (or both) of the two elements or biological Ni transfer. There is little evidence of either the latter or post-depositional Ni mobility. Consequently, Ni/Co can be used as a provenance indicator, and its strong correlation with X_{Mg} constitutes a reliable indication that the sediment sources have variable proportions of felsic and (ultra)mafic rocks, with a predominantly felsic hinterland for the Klerksdorp and Welkom depositories and chiefly mafic and ultramafic sources for the detritus in the goldfields further east.

Too few Black Reef Formation analyses exist, but they all show sediment input from mixed source rocks. That formation's Ni content ranges from 105 to 135 ppm, while its Cr content ranges from 304 to 390 ppm (Figure 78). The Pretoria Group has relatively low abundances of Ni and Cr, with not many samples revealing higher levels of Cr enrichment (Figure 78). The Black Reef Formation X_{Mg} values show a narrow range (34.5–37.5 %), and are thus less variable than those found for the Pretoria Group (5–40 %).

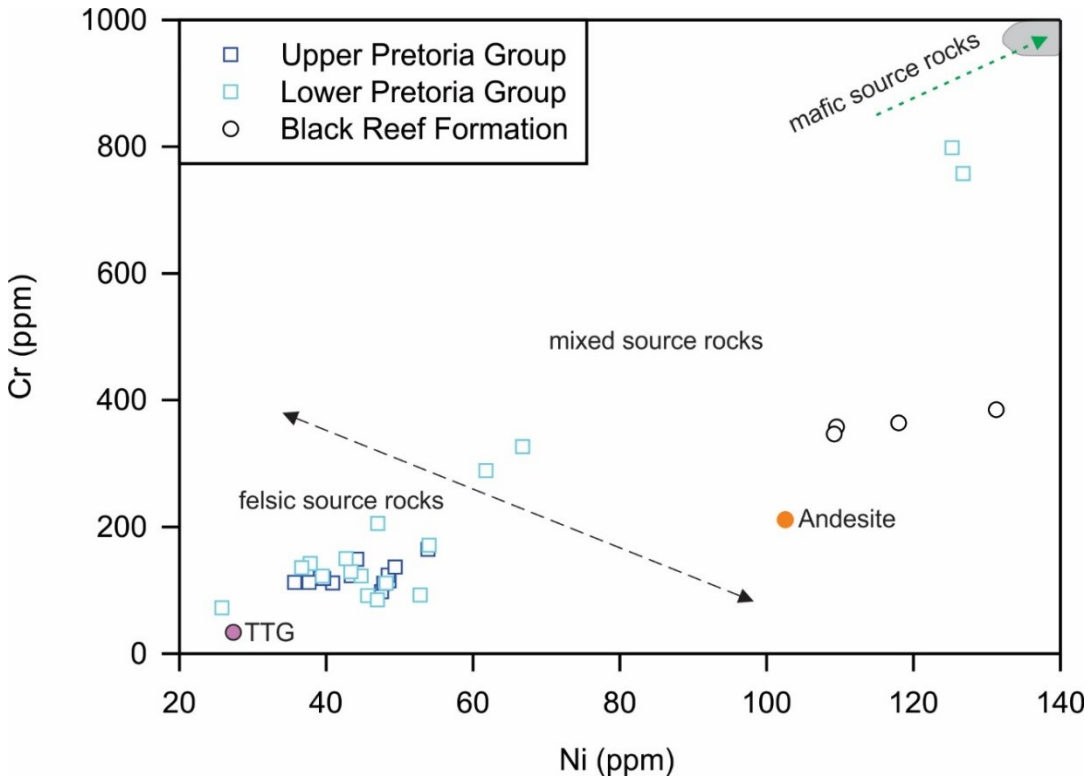

Figure 78: Ni versus Cr diagram for Black Reef Formation and Pretoria Group shales, illustrating change from mafic to felsic source rocks; reference samples from Condie (1993).

The mafic and felsic source rocks could also be differentiated from each other using numerous other trace element ratios. The Zr/Cr and Zr/Ni ratios can be used to distinguish between felsic- and mafic-dominated source rocks because Zr chiefly occurs in zircon, and is thus mainly derived from felsic sources. Similarly, Th/Sc can serve the same purpose, because of felsic rocks' enrichment in Th-bearing minerals and Sc's affinity for mafic compositions (Figure 79). The Th/Sc ratio is an effective indicator of igneous chemical differentiation processes, and the Zr/Sc ratio is a useful index of zircon enrichment (McLennan et al., 1993). Therefore, the Th/Sc versus Zr/Sc plot can be used to both evaluate the source rock composition, and to assess the degree of sedimentary sorting and recycling. The Barberton Supergroup shales exhibit a linear relationship between the two ratios, with greater dispersion of shales towards higher Th/Sc and Zr/Sc ratios. This trend indicates a consistent provenance and compositional variation without zircon enrichment, suggesting that the studied Fig Tree and Moodies groups marine shales did not undergo intra-basin recycling but they went through igneous differentiation. In contrast, the Pretoria Group shales display strong evidence of localised intra-basin recycling.

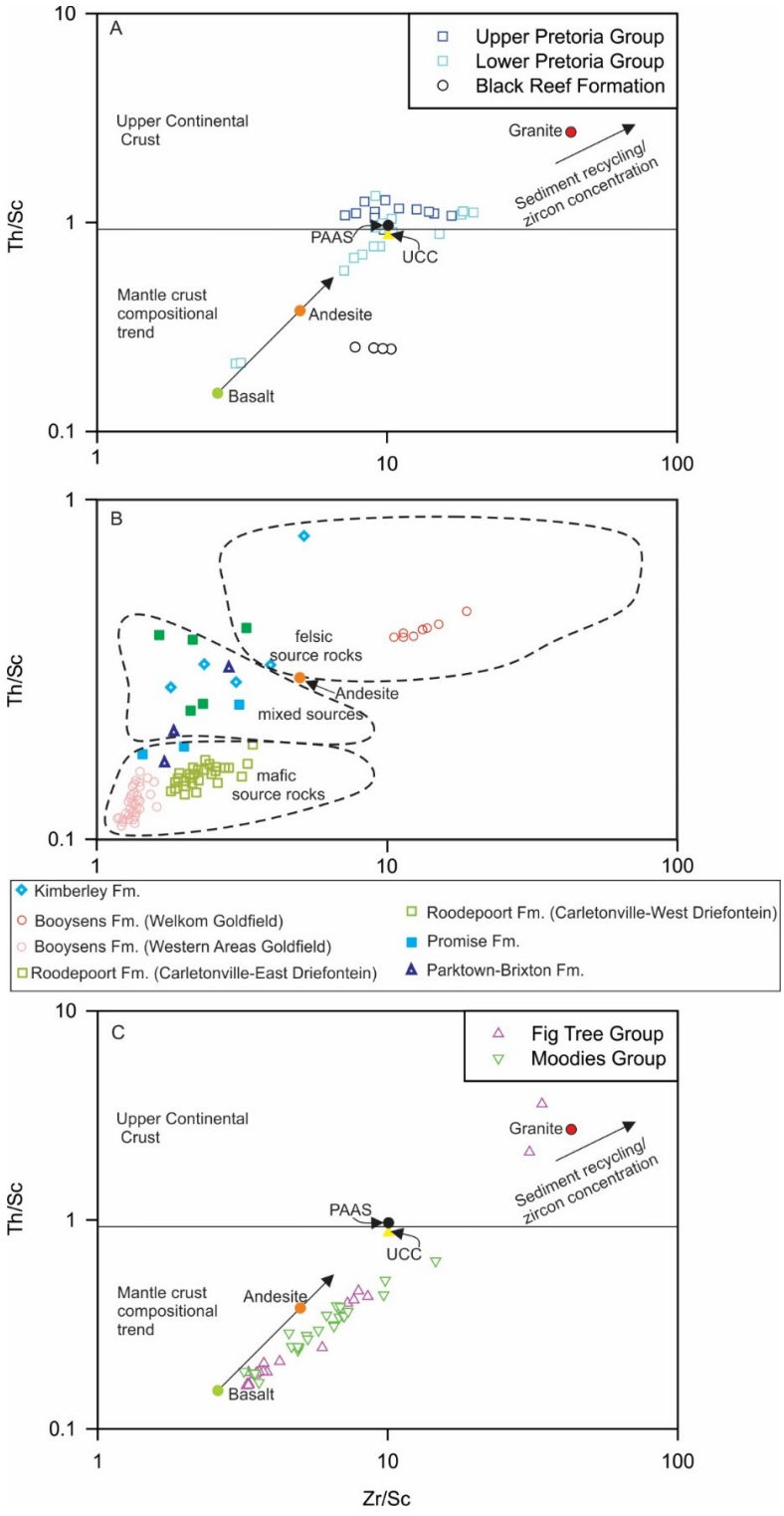

Figure 79: Diagram of Th/Sc versus Zr/Sc for Witwatersrand shales. Source-rock compositions from Condie (1993). Low Th/Sc ratio (<1) indicates a mafic source, which is usually enriched in compatible elements (e.g. Sc), while the incompatibility of Th results in higher concentrations in well-differentiated felsic rocks (Th/Sc ± 1; Taylor and McLennan, 1985).

The shale samples display a wide range of Th/Sc ratios (0.1–2), reflecting highly variable proportions of felsic rocks versus mafic rocks in the source area, a phenomenon mirrored by the strong variation in Zr/Cr, both within a given stratigraphic unit and across goldfields (Figure 80). In such a Zr–Cr space, shale from a specific stratigraphic unit (in particular, the Booysens Formation) in the western part of the basin (Welkom goldfield) has a composition pointing to predominantly felsic sources. On the other hand, in the central and eastern parts (Central and East Rand goldfields), mafic sources are dominant. The Booysens Formation shales in the Klerksdorp goldfield have an intermediate position, with both felsic and mafic sources contributing to the argillic sediment budget to variable extents.

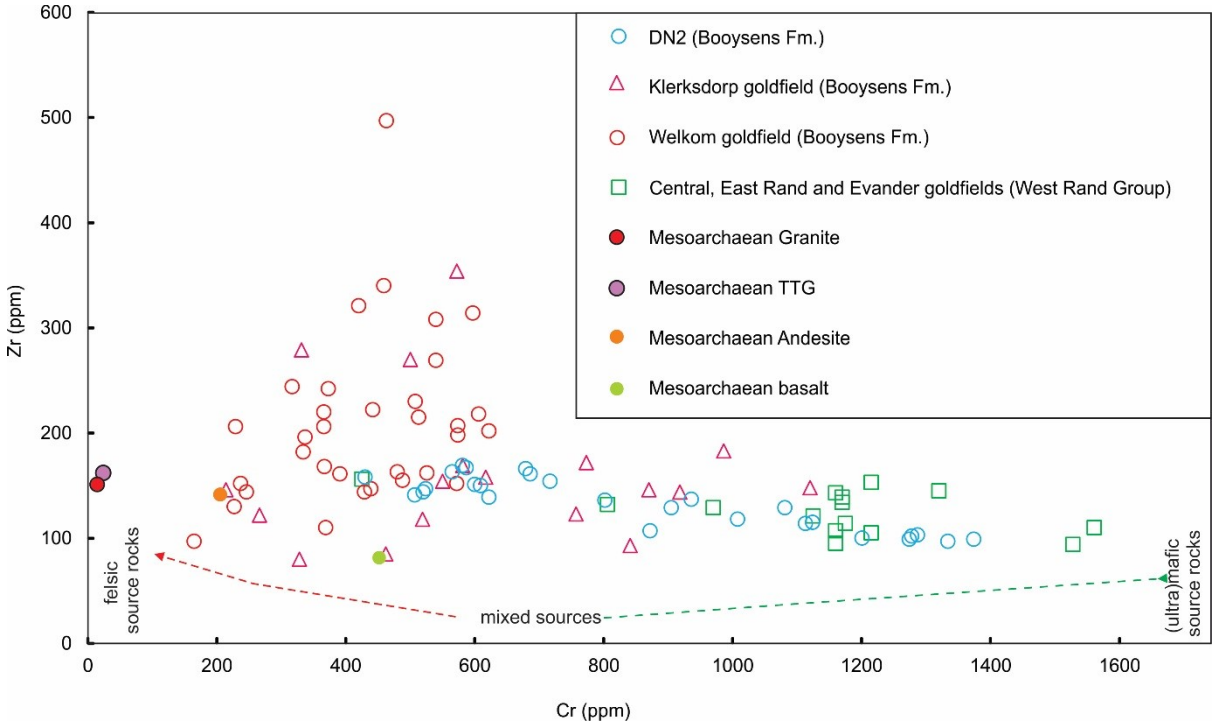

Figure 80: Diagram of Cr versus Zr for Booysens Formation shale in various goldfields, illustrating differences in source rocks; reference samples are from Condie (1993).

There are, however, chemical variations not only between different (palaeo-) geographic regions but also across stratigraphic levels within a given shale unit, as exemplified by the Booysens Formation. Bulk compositional variations with the stratigraphic position are not limited to the Witwatersrand shales, but are also common in coarse-grained rocks (i.e. Witwatersrand quartzite units; Sutton et al., 1990). Data from borehole DN–2, which intersected the entire Booysens Formation, illustrates a systematic increase in the Zr/Ni ratio (a proxy for felsic/mafic source rocks) from top to bottom (Figure 81). Thus, at a single given locality, the dominant hinterland lithology gradually changes from mafic to felsic.

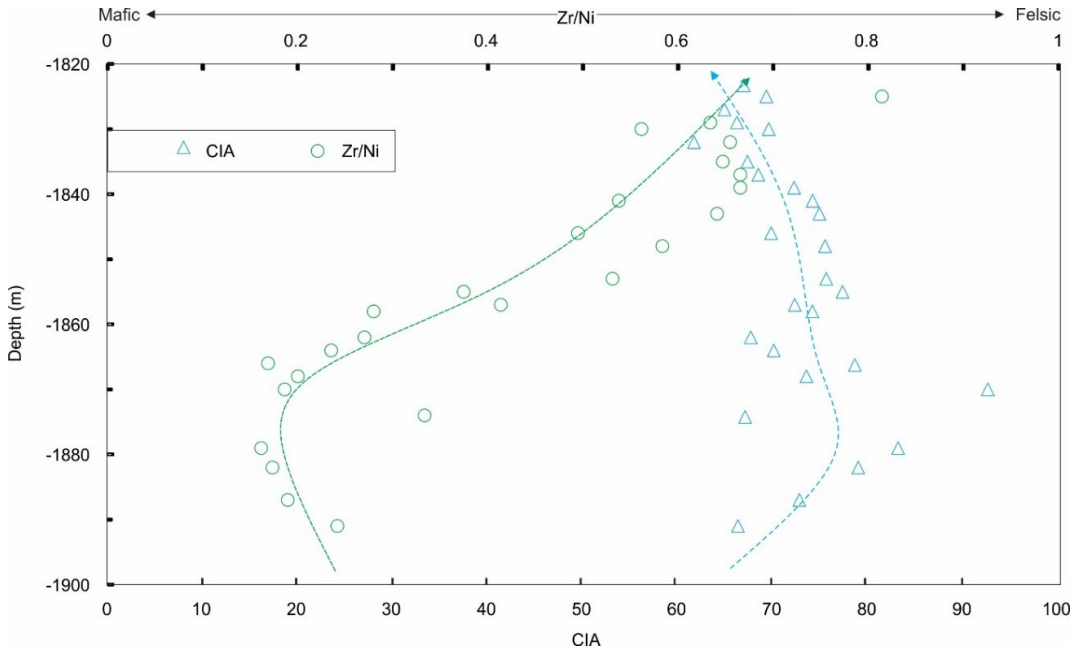

Figure 81: Down-borehole variations in Zr/Ni and CIA for Booysens Formation shale, reflecting a progressive increase in felsic/mafic source-rock proportions in the course of sedimentation, as well as a possible change in provenance.

Trace elements in the Archaean and Proterozoic sedimentary rocks have previously provided important information on the tectonic evolution of cratonic rocks (Bhatia and Crook, 1986; Roser and Korsch, 1986; Hayashi et al., 1997; Zhang et al., 1998). The Archaean–Proterozoic boundary is regarded as a time of diachronous change in the evolution of the Earth's crust, in terms of both tectonic style and geochemical composition (Windley, 1984; Taylor and McLennan, 1985; Diener et al., 2005; Moyen et al., 2006; McLennan et al., 2006). Studies by Bhatia (1983, 1985) and Bhatia and Crook (1986) identified discrimination factors, based on major element and trace element data, for siliciclastic sediments derived from different tectonic settings.

These researchers' diagrams have been widely used by sedimentary geochemists to constrain the likely provenance of siliciclastic sediments, and it is tempting to employ them to characterise the Barberton, Witwatersrand, and Transvaal shales as well. Figure 82 shows a wide scattering of data points, which could mean that the various rocks are derived from a great variety of sources. When assessing such discrimination diagrams, one must keep in mind that the reference fields are obtained for much younger sedimentary rocks (i.e. Palaeozoic Era) and for coarser grain sizes (i.e. greywackes). The results obtained in this study illustrate the limitations of such discrimination diagrams for Archaean shales, which is explicable by the fact that Archaean continental crust evolved under different magmatic and

tectonic regimes than the Proterozoic and Phanerozoic crust. The challenge of modelling Archaean tectonics has also been encountered in other Archaean environments such as the Barberton Supergoup (Toulkeridis et al., 1996; 2015). Nevertheless, the diagrams effectively reflect the same finding as obtained from other major and trace element ratios above, that is, a differentiation between a mafic-to-ultramafic and a felsic source.

A sequence stratigraphy and petrographical assessment by Lowe and Nocita (1999) suggested that both the Fig Tree and Moodies groups' sediments were deposited in foreland basins, although the original size, nature, and tectonic setting of such basins are topics of considerable debate (Artemieva and Meissner, 2012). The geochemical distribution patterns of some of the elemental ratios (i.e. La/Sc, La/Th, Th/Sc, Ti/Zr, and Hf; Figure 83 and 84) reflect the nature of variable source rocks.

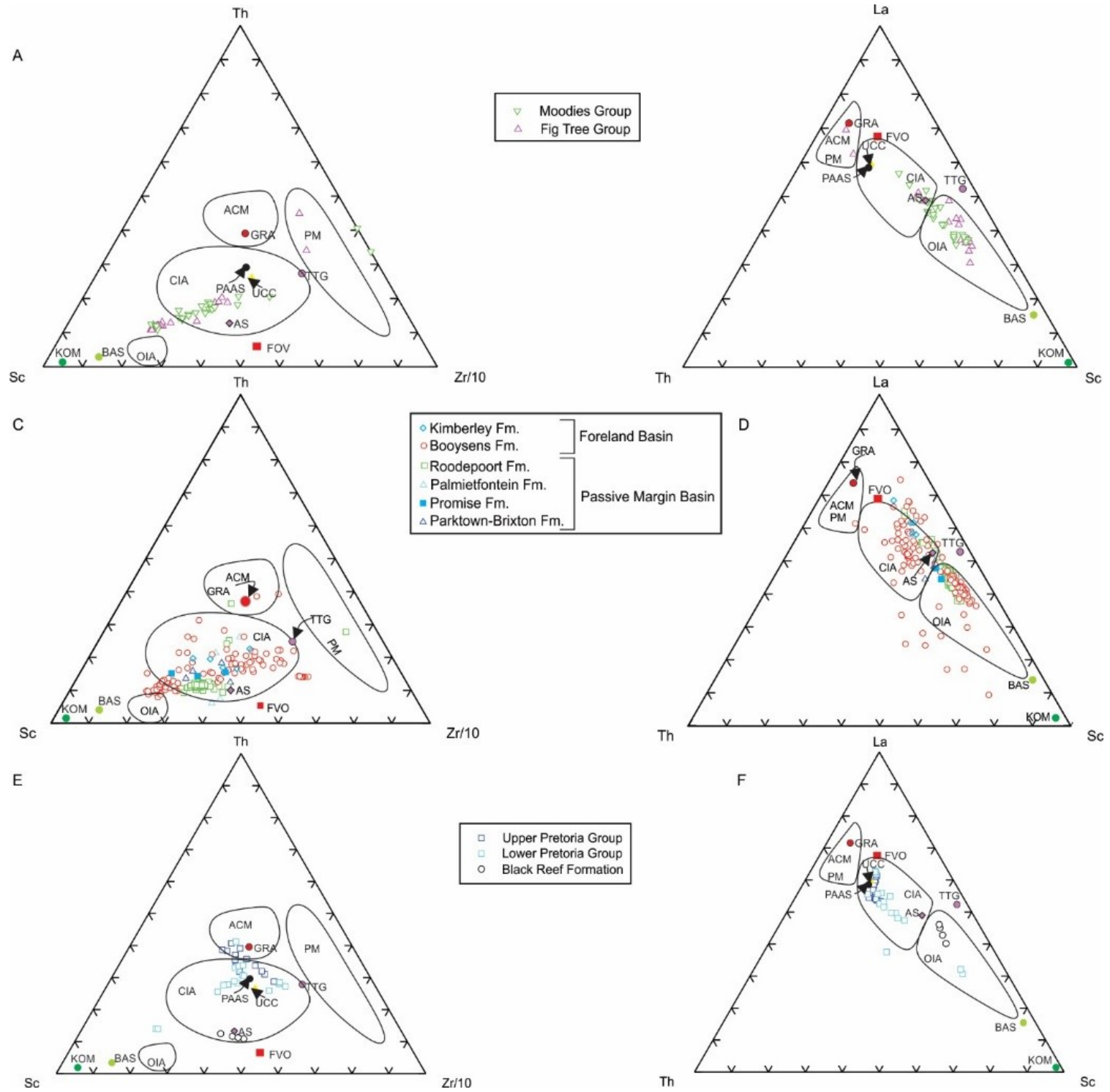

Figure 82: Ternary diagrams: A, C, E. Th–Sc–Zr/10 ternary diagram with heavy mineral fraction (Zr). B, D, F. La–Th–Sc ternary diagram between light REE (La), incompatible element (Th), and compatible element (Sc). Source rock compositions are from Condie (1993). Discrimination fields of tectonic setting are after Bhatia and Crook (1986). Abbreviations: OIA = oceanic island arc; CIA = continental island arc; ACM = active continental margin; PM = passive margin; KOM = komatiite; BAS = basalt; GRA = granite; TTG = tonalite–trondhjemite–granodiorite; AG = Archaean shale; FVO = felsic volcanic rocks.

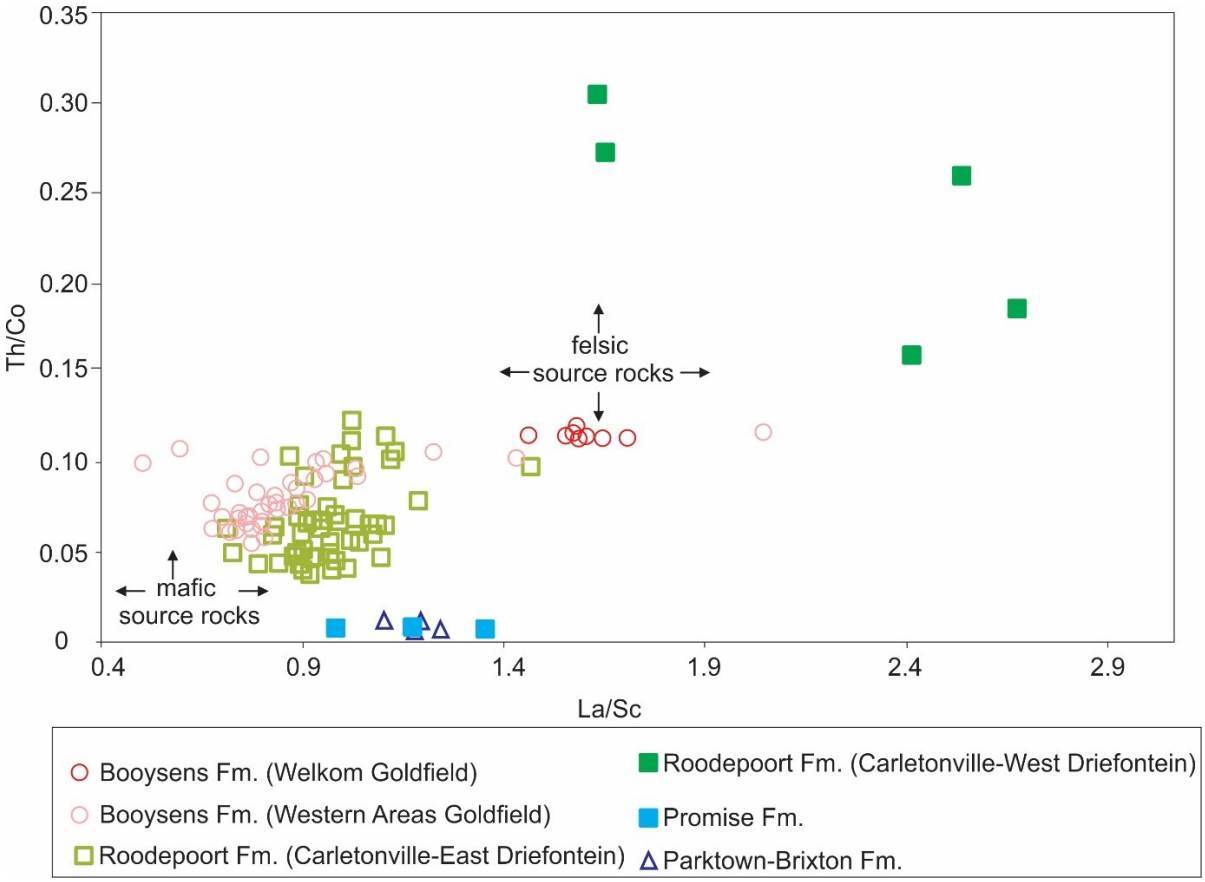

Figure 83: **Diagram of Th/Co versus La/Sc for Witwatersrand shales, demonstrating geochemical variations in trace element ratios (fields after Cullers, 2002).**

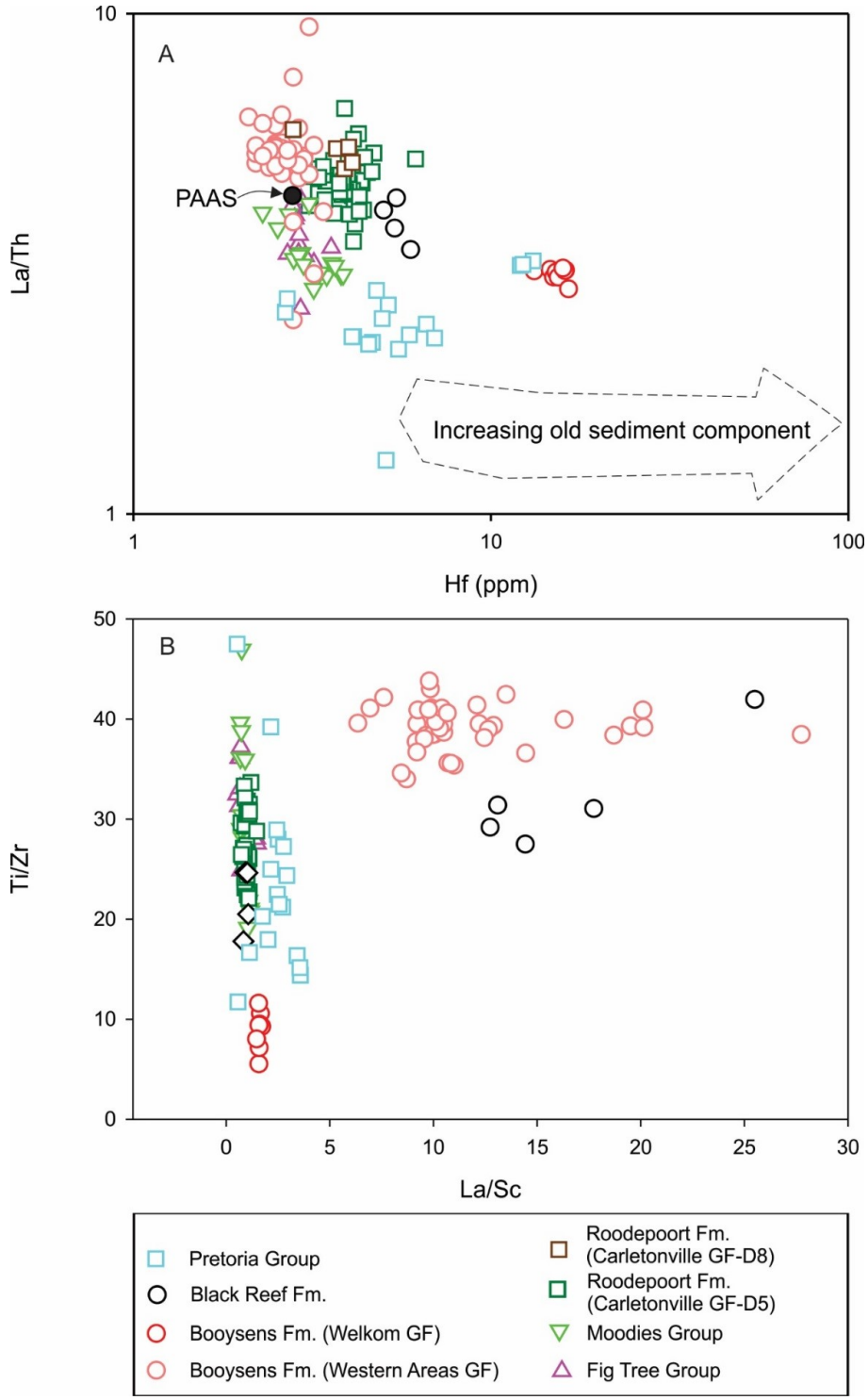

Figure 84: A. Diagram of Ti/Zr versus La/Sc of Kaapvaal Craton shales showing geochemical variation in trace element ratios. B. Diagram of La/Th versus Hf of Kaapvaal Craton shales showing geochemical variation in trace element ratios (after Floyd and Leveridge, 1987).

However, the above ratios exhibit significant variations laterally within a given stratigraphic unit, depending on geographic location, as well as vertically along the stratigraphic profiles (i.e. the Booysens Formation samples covers a wide range of Zr/Sc ratios). This observation supports the presence of active plate tectonics processes in the Central Rand Basin's hinterland, confirming previous predictions of a foreland basin setting, such as those put forward by Burke et al. (1986), Myers et al. (1990), and Coward et al. (1995). In the Transvaal Supergroup, this data suggest that some sedimentary recycling has taken place, and that there is a significant granitic contribution. Whereas almost all of the samples in this study are true shales, some effect of grain size on the geochemical signature becomes evident when comparing the results for the Roodepoort Formation in two adjacent areas, the East and West Driefontein mines. While the samples from East Driefontein cover about 100 m of stratigraphic height across the lower part of the formation, those from West Driefontein represent the immediate underlying units up to 1 m below the Carbon Leader Reef, and also contain some silty laminations. The higher La and Th content in the latter most likely reflects a higher proportion of corresponding detrital minerals (e.g. uraninite, thorite, and xenotime). The Roodepoort Formation's Th/Sc ratio differs systemically between East Driefontein (lower Rooderpoort Formation) and West Driefontein (upper Roodepoort Formation) because of potential post-depositional alteration in the West Driefontein profile close to the Carbon Leader Reef.

The significant differences between the West and Central Rand Basins, as demonstrated by the age spectra of the detrital zircon grains (Kositcin and Krapež, 2004), reflect a major change in provenance between those two basins. Overall, the age spectra of the detrital zircon (Kositcin and Krapež, 2004) support a passive margin setting for the West Rand Group and an active continental margin source for the overlying Central Rand Group.

In the studied shale samples, Nb and Ta ($r = 0.99$) are positively correlated, as are Hf and Zr ($r = 0.98$), as these pairs exhibit similar geochemical behaviours. Differences are evident in the hinterland lithology of the various parts of the basin, especially at the time of the Booysens Formation deposition (Figure 85 A). Most of the West Rand Group shales are derived from a mixture of typical Archaean tonalite–trondhjemite–granodiorite (TTG) and Archaean greenstone compositions, with the exception of the lower Hospital Hill Subgroup, which has a strong granitic affinity (Figure 85 B).

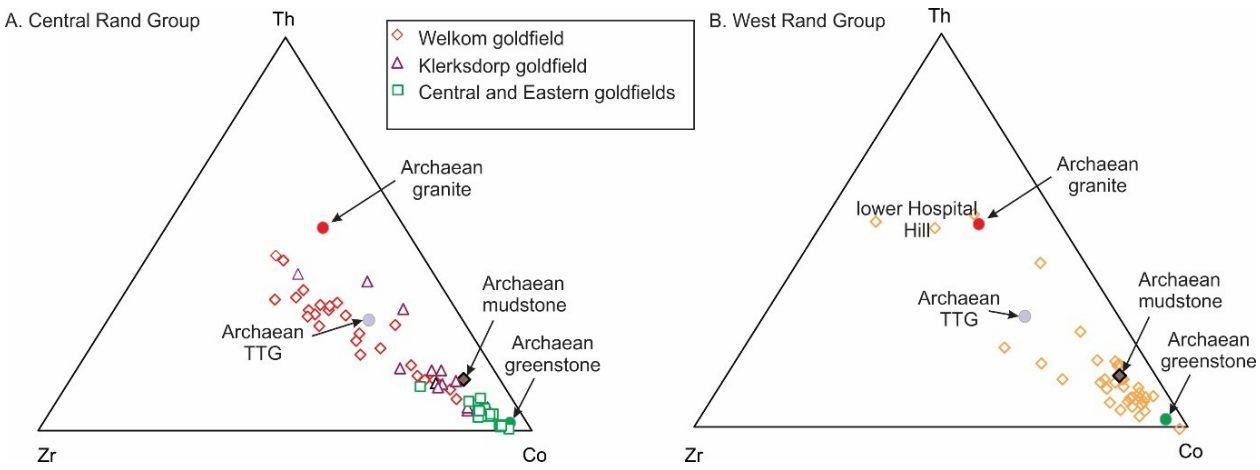

Figure 85: Diagram of Th–Zr–Co for Witwatersrand shales of (A) Central Rand Group and (B) West Rand Group, illustrating source variations between goldfields and stratigraphic positions. Source rock compositions are from Condie (1993).

In the Transvaal Supergroup, shales from both the Black Reef Formation and Pretoria Group plot within oceanic island arc, continental island arc, and active continental margin settings. A few samples overlap into the continental island arc margins because of relative Sc enrichment, while a relative Th enrichment at both sites cause some shale samples to plot outside of the defined tectonic boundaries.

Relying on all of the above shale provenance constraints, in combination with the known geological make-up of the currently exposed Archaean granitoid–greenstone terranes in the Kaapvaal Craton, the relative proportions of principal source rock types in the respective hinterlands are modelled using the ratios of relatively immobile elements (Figure 86). The relative proportions were calculated by averaging the percentage of a given geochemical shale population for each stratigraphic unit. In addition to the mass balance calculations, the Cr/Th ratio, which is controlled most by the effects of local provenance and local tectonics (e.g. Wronkiewicz and Condie, 1989) was calculated for the studied marine shales. In this study, the two elements (Cr and Th) were first plotted against some of the relatively immobile elements such as Sc and Th, and correlated well with these elements, suggesting that they are dominantly controlled by provenance. The Cr/Th ratios in Figure 86 appear to monitor provenance changes with time.

The Barberton Supergroup (i.e. Fig Tree and Moodies groups) reflects variation in mafic and felsic source rocks characterised by higher Cr/Th ratios. Accordingly, the West Rand Group shales are mainly derived from TTG and calcalkaline granites. A shift towards more mafic source rocks began during the deposition of the Jeppestown Subgroup in the upper West

Rand Group and peaked in the middle Central Rand Group time. Towards the end of the Johannesburg Subgroup deposition, when the Booysens Formation shale was laid down, this trend was reversed, and granitic rocks became progressively unroofed in the hinterland (Figure 86). The Turffontein Subgroup (i.e. K8 Formation) reflects a derivation from fractionated and evolved crustal sources. The Black Reef Formation contains significant contributions from basalt–komatiite sources. The Pretoria Group is derived from the most fractionated and fully evolved upper continental crust on the Kaapvaal Craton (i.e. evolved granitic sources). The lower Cr/Th ratios further support that conclusion (Figure 86).

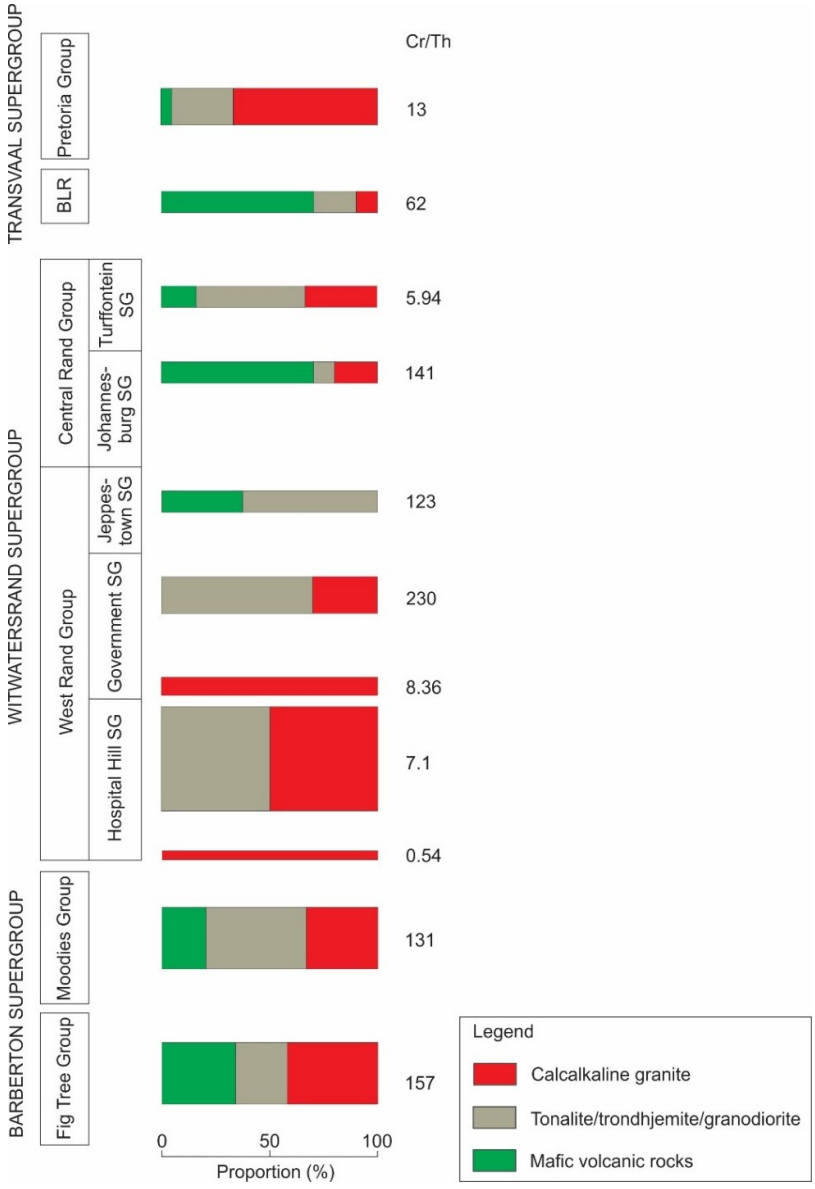

Figure 86: Estimated proportion of likely source rocks in the course of sedimentation and provenance variation indicators in Kaapvaal Craton shales, as reflected by Cr/Th ratios. Abbreviations: BLR = Black Reef Formation; SG = Subgroup.

Another factor that affects provenance is palaeogeography. For example, the significant variation in the Witwatersrand shale provenance evidenced in this study is consistent with the conclusions of multiple previous analyses (e.g. Tweedie, 1968; Minter, 1978; Bailey et al., 1989) that characterised the palaeocurrent direction and demonstrated the existence of systematic changes in the Mesoarchaean Witwatersrand palaeogeography. The estimated general palaeogeography and palaeocurrent directions of the West and Central Rand Basins are shown in Figure 87. Note that the illustrative boundary between the marine (continental shelf) and open ocean (pelagic zone) regions reflects the distribution of the different facies in the two basins, as well as their stacking patterns, and the orientation of their clinoforms (Minter, 1978; Smith and Minter, 1979; Watchthorn, 1981; Guy et al., 2010; Smith et al., 2013).

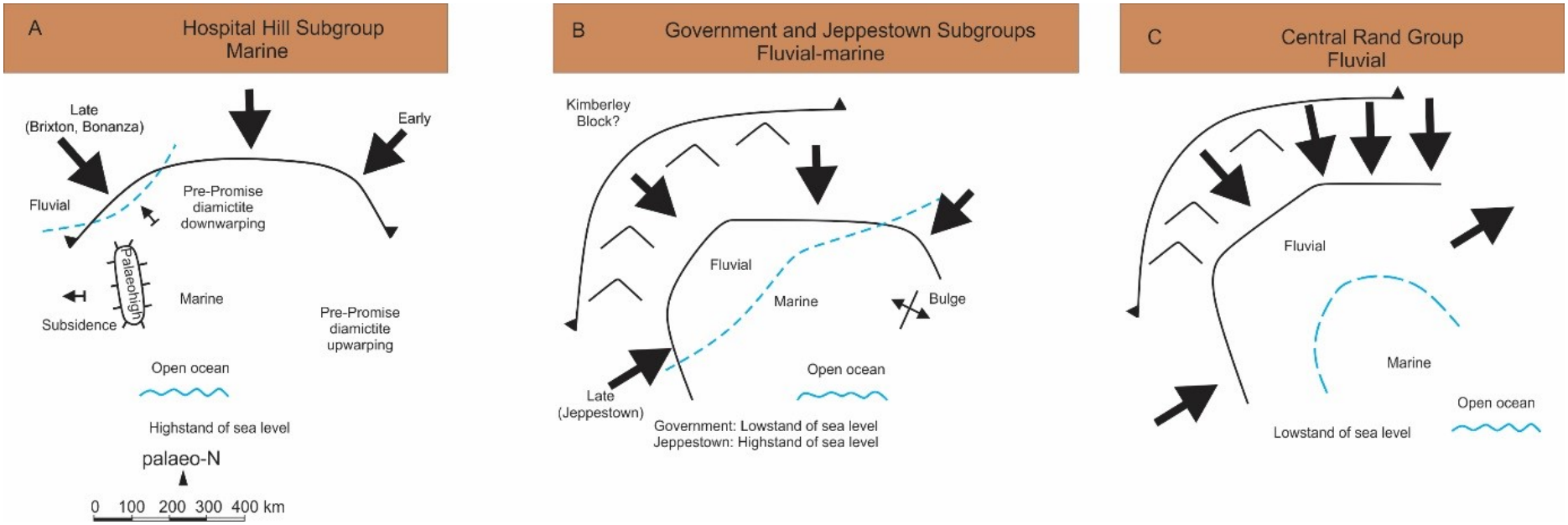

Figure 87: Summary of estimated general palaeogeography and palaeocurrent directions for Witwatersrand Supergroup (adapted from Stanistreet and McCarthy, 1991; McCarthy, 2006; Guy et al., 2010).

7.4. Extent of palaeoweathering

The weathering of igneous and metamorphic rocks generally induces a depletion in alkali and alkali earth elements, and a corresponding enrichment in Al_2O_3 in the resulting materials, thus providing a means of examining the weathering history of clastic sedimentary rocks (Nesbitt and Young, 1982, 1984). The dataset used to estimate the extent of palaeoweathering was first screened to eliminate samples that were significantly affected by post-depositional alteration. Most of the analysed samples demonstrate uniform LOI values and low CaO concentrations, such that the presence of significant amounts of carbonates can be effectively ruled out. Nesbitt and Young's (1982) chemical index of alteration (CIA) quantitatively expresses the degree of weathering of feldspars to clays:

$$\mathbf{CIA = [Al_2O_3/(Al_2O_3 + CaO^* + Na_2O + K_2O)] \times 100} \qquad \textbf{Equation 23}$$

where CaO* only refers to the CaO in silicates. In general, CIA values are typically less than 40 for unweathered igneous and metamorphic rocks, and 100 for pure alumina-silicate weathering products (i.e. kaolinite; Taylor and McLennan 1985; McLennan et al., 1983). This index is complemented by the chemical index of weathering (CIW; Harnois, 1988):

$$\mathbf{CIW = [Al_2O_3/ (Al_2O_3 + Na_2O + CaO^*)] \times 100} \qquad \textbf{Equation 24}$$

The relationship between the degree of weathering (i.e. CIA) and the original source composition can be assessed by combining the CIA with the index of compositional variability (ICV; Cox et al., 1995; Potter et al., 2005). The ICV discriminates between source rock types based on major element concentrations in shales:

$$\mathbf{ICV = (CaO + K_2O + Na_2O + Fe_2O_{3\,(tot)} + MgO + MnO + TiO_2)/Al_2O_3} \qquad \textbf{Equation 25}$$

In this equation, CaO includes all sources of Ca, including detrital carbonate. A high ICV value indicates complex/variable source rocks rich in non-clay silicate minerals, whereas low values represent compositionally less variable source rocks. As weathering progresses, the ICV decreases because of the conversion of feldspars to clays. Thus, ICV variability might be due to variations in the source rock composition and/or differences in weathering (Cox et al., 1995; Potter et al., 2005).

The CIA values for the Fig Tree Group shales average 69 ± 7.29 %, while the CIA values for the Moodies Group shales average 65 ± 8.33 % (Figure 88). The CIW values are 77 ± 11.88 % for the Fig Tree Group shales and 72 ± 9.39 % for the Moodies Group shales. The Fig Tree Group CIA and CIW values range from 54 to 76 % and from 57 to 99 %, respectively, while

Moodies Group CIA and CIW values range from 50 to 81 % and from 53 to 87 %, respectively, indicative of a moderate degree of weathering compared to the PAAS reference (CIA = 70–75 %; Taylor and McLennan, 1985). Thus, the results imply a moderate degree of weathering of the source components as compared to post-Archaean times.

The variables used to characterise the extent of palaeoweathering in both the Fig Tree and Moodies groups suggest increasing Al and K content and decreasing Ca and Na content. These compositional trends could not have resulted from the simple removal of alkali/alkali-earth elements via the weathering of a homogeneous source. The relative Al_2O_3 content in the Fig Tree and Moodies groups overlaps with typical igneous compositions, and is also close to that of PAAS, again suggesting that the source materials may have undergone minor alteration. The ICV of the Fig Tree (1.4 ± 0.31) and Moodies (1.86 ± 1.14) groups is probably a record of the variable source rock composition and of the chemical changes that occurred in the shales after deposition and compaction (e.g. the crystallisation of authigenic minerals, mostly of clay type). This also applies to the alteration of detrital minerals of igneous origin. Toulkeridis et al.'s (2015) findings further support that interpretation.

The CIA values for the Witwatersrand Supergroup shales range from 40 to 98 %, with large variations within individual shale units (Figure 89). This implies that in some instances, palaeoweathering has proceeded to the stage at which alkali and alkali earth elements have been completely removed (this is demonstrated well by the Booysens Formation shales' stratigraphic variation). The following explanations could explain the elevated CIA and CIW levels: (a) chemical weathering over the course of a given depositional cycle, (b) chemical weathering in the source region of the sediments in a given unit, or (c) post-depositional chemical weathering from the top, e.g. an old erosion surface, downwards. The wide range in CIA and CIW, reflecting in parts increased rates of chemical weathering, mirrors an observation also noted in Witwatersrand Supergroup quartzites (Sutton et al., 1990).

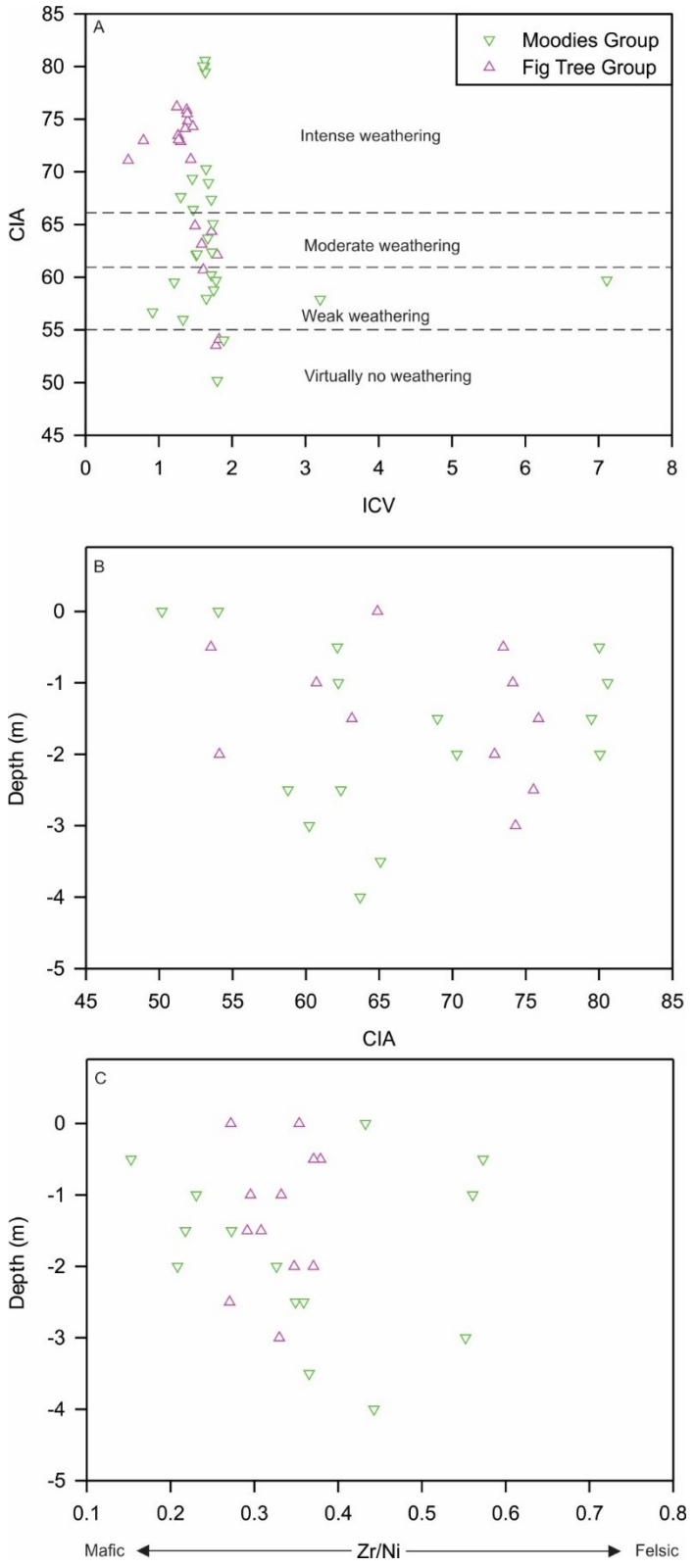

Figure 88: A. CIA versus ICV for Barberton shale samples. B. Down-borehole variation in CIA, indicating weathering patterns with depth. C. Down-borehole variation in Zr/Ni, reflecting felsic/mafic source rock proportions in the course of sedimentation.

Compared with smaller cations (e.g. Na and Ca), larger cations (e.g. K, Cs, and Rb) are preferentially immobilised by exchange and adsorption processes onto the clays' mineral surface during source rock weathering (Nesbitt et al., 1980; Bauluz et al., 2000). The scattering in the ICV reflects a geologically complex and variable hinterland, whereas clustering reflects a geologically uniform source provenance. The West Rand Group's higher K_2O/Na_2O ratios relative to those of the Central Rand Group could be interpreted as reflecting more intense chemical weathering in the source region, because Na is preferentially removed from the source rock because of the decomposition of plagioclase prior to K removal from alkali feldspars and micas. The generally high CIA values noted for these shales seem to support that conclusion. Changes in the CIW/CIA ratios of two different rock series may then indicate differences in their mineral compositions, dissimilarities that are not necessarily related to rock weathering and/or tectono-thermal alteration, but to selective transport from the source area to the deposition site.

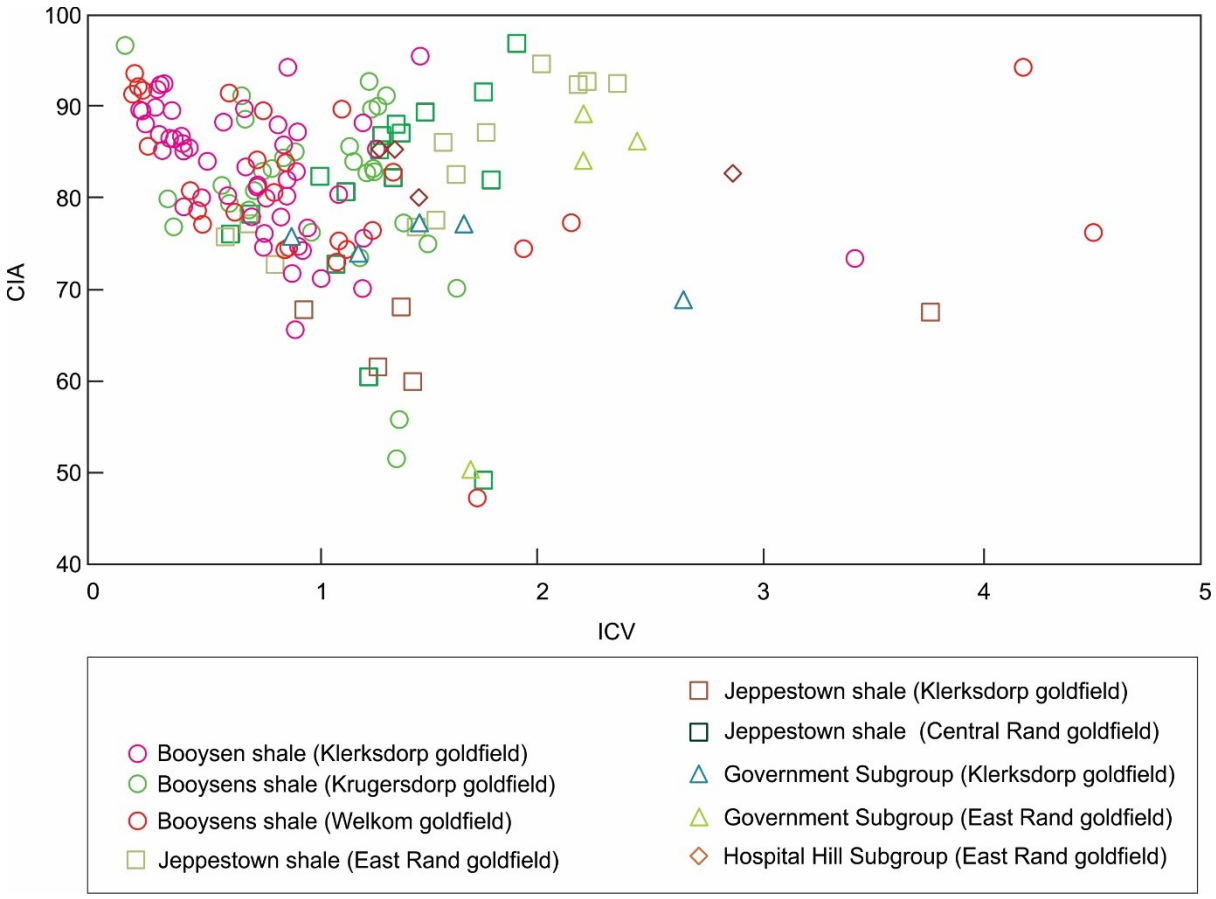

Figure 89: CIA versus ICV for Witwatersrand shale samples.

The Booysens Formation shale data provide evidence of both a progressive increase in felsic to mafic sources in the hinterland and CIA variations, with a noticeable change in the lower

half of the formation (as illustrated by chemical changes between a depth of approximately -1880 and -1860 m in borehole DN–2, Figure 81). Based on this observation, one can infer that the dominantly mafic hinterland indicated for the lower Booysens Formation was subjected to progressive chemical weathering, resulting in CIA values as high as 95. The decrease in CIA further upsection, combined with the drastic increase in Zr/Ni ratio (Figure 81), can then be explained by the progressive unroofing of young granites that had not experienced prolonged periods of chemical weathering.

The CIA values (Figure 90) for the Black Reef Formation shales average 72 ± 0.43 %, while the value for the Pretoria Group is 70 ± 13.06 %. The CIW values for these groups are 92 ± 0.55 % and 82 ± 15.91 %, respectively. The Black Reef Formation's CIA and CIW values span from 72 to 73 % and from 92 to 93 %, respectively. The Pretoria Group's CIA and CIW values ranged from 30 to 84 % and from 31 to 97 % respectively, indicating a higher weathering degree than that of the PAAS reference (CIA = 70–75 %; Taylor and McLennan, 1985). The Pretoria Group's minimum CIA of 31 % is found in two samples from that group.

The CIA values for the Transvaal Supergroup samples suggest a moderate-to-intense degree of chemical weathering, possibly reflecting high-temperature palaeoclimatic conditions under which physical disaggregation was the primary influence on the sediments. Rock decomposition reaction rates generally increase with temperature. If the higher temperature is because of a location in lower latitudes, the climate is likely to be humid and tropical, which also accelerates hydration. Silicate weathering tends to consume atmospheric CO_2, mainly because of the release of Ca^{2+} and other divalent cations.

The relative Al_2O_3 content of the Black Reef Formation and Pretoria Group overlap with typical igneous compositions, and are close to those of PAAS. The ICV values (Figure 90) for the Black Reef Formation (1.07 ± 0.06) and Pretoria Group (1.07 ± 0.69) suggest the presence of source rocks of varying composition in the provenance, and of variable palaeogeomorphological and palaeoclimatic conditions (which may induce different degrees of source rock weathering). The ICV ratios tend to be the highest in pyroxenes and amphiboles, decline in alkali feldspars and montmorillonite, and are lowest in kaolinite group minerals (Cox et al., 1995). The Pretoria Group serves as a classic example of ICV values decreasing as weathering progresses, as a result of the conversion of feldspars to Al-bearing clays (Figure 90). Generally, shales with ICV values of less than one tend to form under intense weathering and minimal tectonic uplift, as evidenced by the Pretoria Group shales.

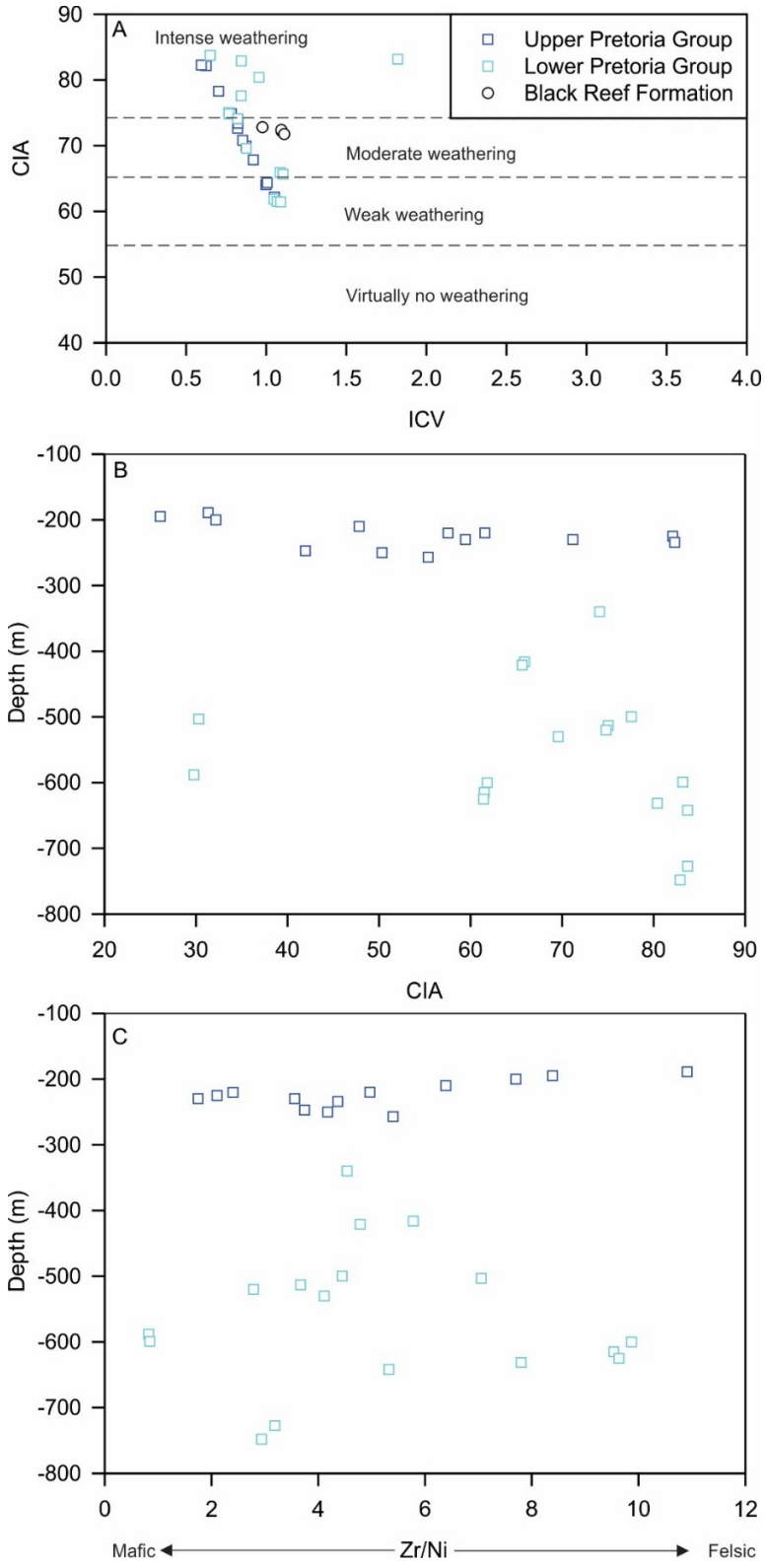

Figure 90: A. Bivariate plots of CIA versus ICV for Transvaal shale samples. B. Down-borehole CIA variations, indicating weathering patterns with depth for Pretoria Group shales. C. Down-borehole variations in Zr/Ni, reflecting felsic/mafic source rock proportions in the course of sedimentation for Pretoria Group shales.

Despite the fact that U^{4+} is insoluble and consequently equally immobile in reducing environments, U can be readily removed (U^{4+} is oxidised to U^{6+}) by weathering under oxidising conditions. On the other hand, Th is relatively immobile under most conditions. Therefore, weathering and redeposition can result in an elevated Th/U ratio, which is considered to be a solid indicator of weathering and sedimentary recycling (McLennan et al., 1993). The Th/U ratios for the Black Reef Formation shales range from 2.51 to 2.54, averaging 2.53. In contrast, the Th/U ratios for the upper Pretoria Group shales range from 3.72 to 5.31, averaging 4.31, while the lower group's range is 2.45–10.19, averaging 4.52. These figures are higher than that of the UCC (3.89), and comparable to PAAS (4.71; Rudnick and Gao, 2005), indicating overall sedimentary recycling under oxidising conditions (Figure 91). This finding supports an O_2-poor, CO_2-rich atmosphere that became rapidly oxygenated in the period between 2.25 and 2.05 Ga, as hypothesised by Cloud (1973), Kasting (1987), Holland and Beukes (1990), and Holland (1999).

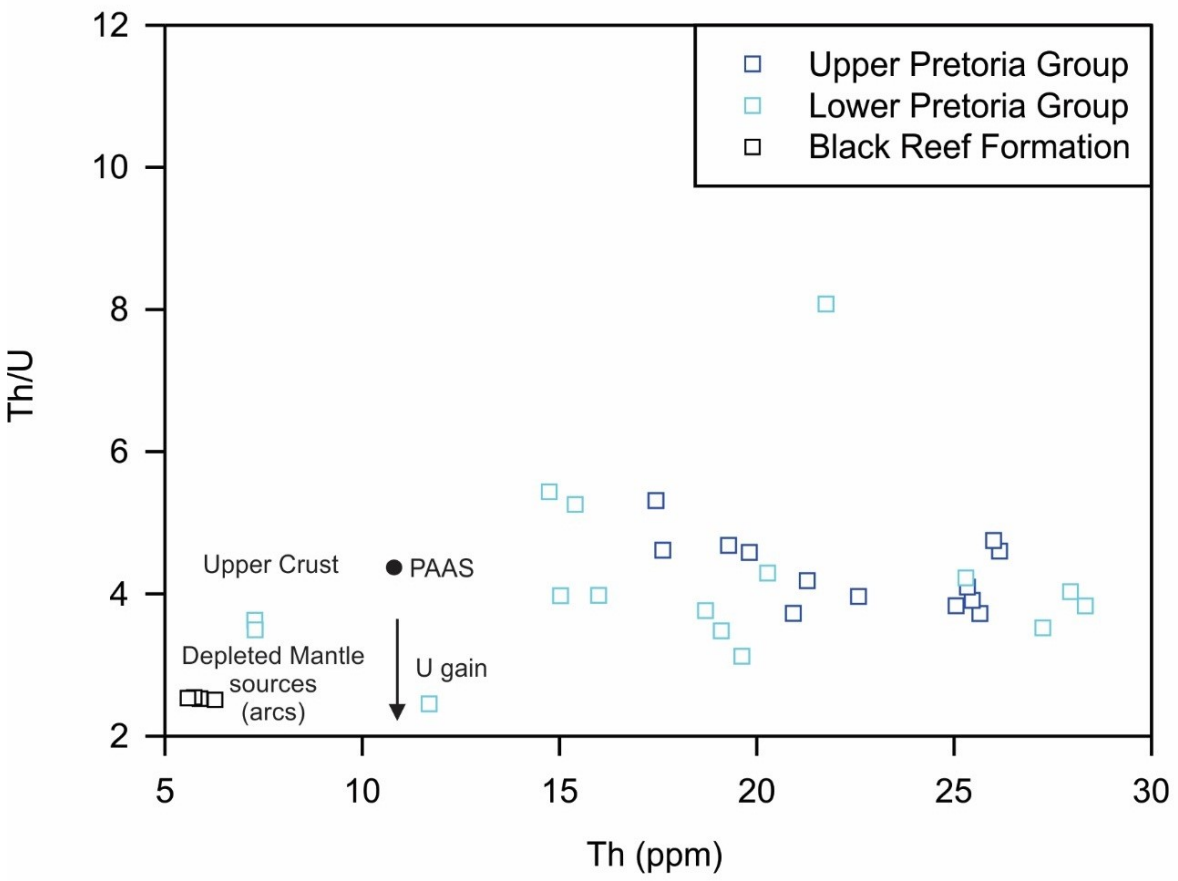

Figure 91: Bivariate plot of Th versus Th/U for Transvaal Supergroup.

The Archaean palaeoenvironment was characterised by vigorous volcanic activity in both sub-aerial and subaqueous settings (Cloud, 1988; Lowe, 1994; Gaillard et al., 2011). Volcanic activity introduced inorganic compounds (H_2, CO_2, CH_4, SO_2, H_2S) degassing into an essentially oxygen-free atmosphere (i.e. reducing atmosphere; Canfield and Raiswell, 1999). The clouds in this type of atmosphere would have produced acid rain with pH < 4 (Krupp et al., 1994). Geochemical evidence of the prevailing palaeoclimatic conditions during the Archaean also lies in the evolution of the sulfur cycle, which is preserved in various sedimentary rocks, including shales. This has been studied extensively through the use of isotopes (i.e. $\delta^{34}S$: $\delta^{32}S$) in order to monitor sulfur fractionation, and as a tool for palaeoclimatic modelling, including thermodynamic modelling of acid rain (Kasting, 1993; Ohmoto et al., 1993; Ono et al., 2003).

More importantly, provided that the acid rain precipitated on a fairly hot land surface, this must have resulted in very intense chemical weathering as documented in the Witwatersrand palaeo-surfaces (Frimmel and Minter, 2002; Frimmel, 2014). This phenomenon is supported by a number of geochemical studies (Kasting, 1993; Farquhar et al., 2000; Frimmel and Minter, 2002; Catling and Claire, 2005; Holland, 2009; Guy et al., 2010). Given that the Archaean land surface predominantly comprised silicates (e.g. feldspar) and little or no carbonates, the acid rain resulted in the dissolution of feldspathic rocks, converting them to kaolinite. The feldspar alteration reactions resulted in near-neutral pH surface waters (Frimmel, 2014). The H_2S fugacity was, presumably, also very high (Frimmel, 2014; Heinrich, 2015), and this is evident from the syn-depositional growth of pyrite in the Witwatersrand Supergroup (Hofmann et al., 2009; Guy et al., 2010; Frimmel 2014). Under these chemical conditions, thermodynamic calculations (Frimmel, 2014) predict high solubility of Au-sulfide complexes in shallow seawater and meteoric waters.

7.5. Sources of siderophile elements

Determining the source of Au and PGEs assists in unravelling the past geological record of the earth and has great economic significance, especially for mineral deposit exploration. The Barberton and Witwatersrand Supergroup gold deposits, Bushveld Igneous Complex PGE deposits, and other known Au–PGE deposits are continuously being explored. Their genetic models are also re-evaluated in the process, with the aim of acquiring additional data that can be used to discover new deposits. The Barberton Supergroup hosts the oldest recognised orogenic gold deposits. Economically significant gold-bearing quartz veins of the Barberton Supergroup are recognised as having formed at 3.08 and 3.04 Ga (Dziggel et al., 2010). The Barberton goldfields have long reached their exploration maturity and there is not much debate

about their genetic models. Our knowledge of the Hadaean–Archaean gold endowment, however, is far from complete, limited by the fact that less attention has been paid to the sedimentary record that tracks the overall endowment from the hinterland. The Mesoarchaean Witwatersrand Basin in South Africa is one of the most comprehensively studied Archaean sedimentary sequences, mainly because of the basin's enormous gold endowment and mature exploration properties. The genesis of the Witwatersrand gold has been contested for more than a century. Detailed descriptions of the many Witwatersrand metallogenic models are not repeated here, as these have been described in several review papers such as those by Robb and Robb (1998), Phillips and Law (2000), Frimmel and Minter (2002), and Frimmel et al. (2005). Supporters of the modified palaeoplacer model suggest that the gold was introduced as fluvially transported particulates into the Witwatersrand Basin from a fertile Archaean hinterland, and were subjected to local hydrothermal remobilisation after burial (Kirk et al., 2001; Frimmel and Minter, 2002; Minter, 2006; Frimmel, 2005). Conversely, suggestions of auriferous post-depositional hydrothermal fluids infiltrating the coarser clastic sediments such as the Witwatersrand sandstones and fluvio-deltaic conglomerates have been raised (Barnicoat et al., 1997; Phillips and Law, 2000; Phillips and Powell, 2011).

The 2.054 Ga Bushveld Igneous Complex in South Africa had a great thermal effect on the central Kaapvaal Craton, including the Witwatersrand Supergroup (Gibson and Wallmach, 1995; Frimmel, 1997). It intruded into the Archaean granite-gneiss basement, Mesoarchaean Witwatersrand Supergroup and Palaeoproterozoic (2.7–2.1 Ga) sediments of the Transvaal Supergroup (McDonald, 2017). Like many known Au- and PGE-rich magmatic suites, the Bushveld Igneous Complex has also been a subject of various geological studies (e.g. Naldrett et al., 2009; Cawthorn, 2011), but its siderophile element source has never been linked to an upper mantle domain from which the Witwatersrand Supergroup gold was sourced. This discussion section utilises shale geochemistry to make inferences on the potential sources of highly siderophile elements in the Kaapvaal Craton.

The extent of gold and PGE distribution, and variations in regionally persistent unmineralised marine shales (i.e. Barberton, Witwatersrand, and Transvaal supergroups) can be traced both temporally (from the Palaeoarchaean to the Palaeoproterozoic) and spatially. Many studies of marine shales focused on Au and PGE enrichment in black/carbonaceous shales that are younger than 2.8 Ga (e.g. Lehmann et al., 2007; Large et al., 2011; Pitcairn, 2011; Fuchs et al., 2016b), and concluded that the Au and PGE enrichment in most black shales is a function of a geochemical redox trap. Gold from sedimentary rocks, particularly black shales, has lately been considered a viable alternative source in Au-rich provinces (Pitcairn et al., 2006; Large et al., 2007; Tomkins, 2013). The advantage of this current study is that the samples under

investigation are not black shales, and represent different geological time frames. Knowing the composition and amount of gold in the Archaean and Proterozoic hinterland is crucial to understanding the early geodynamics of our planet and early Earth surficial processes. These samples, therefore, provide insight to the overall siderophile element endowment of the Mesoarchaean hinterland. In this study, two potential source end-member models which complement each other are proposed, namely:

(1) Highly siderophile elements enriched mantle referred to herein as anomalous mantle: an anomalous mantle domain is the ultimate source, strongly enriched in siderophile elements caused by inhomogeneous mixing with cosmic material that was added during intense meteorite bombardment of the Hadaean to Palaeoarchaean Earth. Archaean geodynamic conditions are also presented with this model in order to assess whether elevated gold extraction into juvenile crust occurred when the upper mantle temperature reached its maximum during the Mesoarchaean Eon. This model makes inferences on the possibility of a similar enriched mantle source between the Witwatersrand gold deposits and the younger Bushveld Igneous Complex PGE deposits.
(2) No anomalous mantle: other processes concentrated Au near the surface, without any pre-enrichment in the source areas. In this end-member model, various possible surficial processes are assessed, such as: (a) several orders of magnitude more runoff of gold from the Mesoarchaean land surface due to intense weathering under an aggressive, reducing atmosphere and high gold solubility in coeval river water, (b) precipitation of gold from river water on the surface of local photosynthesizing microbial (cyanobacterial) mats, and (c) reworking of these mats into erosion channels during flooding events and redeposition of gold as placer particles.

The foundation of these models was laid by Frimmel (2014), although his study only focused on Witwatersrand-type gold deposits. Whether Au and PGE endowment were a global phenomenon or limited to the Kaapvaal Craton is a question that can only be answered through study of other cratons of similar ages. In order to test the proposed models, Au and PGE concentrations in marine shales of some selected time windows (Palaeoarchaean to Palaeoproterozoic) were evaluated relative to the redox conditions that most likely prevailed during the deposition of the studied marine shales and associated geological events (Figure 92 and 93). In developing the Kaapvaal Craton siderophile elements database, an attempt was made to acquire unmineralised marine samples through the Palaeoarchaean to the Palaeoproterozoic. This was achieved in this study; thus, the samples represent first-order

trends in the time series curve for Au and PGEs. Peak Au concentrations are recorded in the Mesoarchaean Witwatersrand Supergroup, where arithmetic and geostatistical estimation mean values exceed 9.5 ppb Au in the marine shales. The elevated Au in the Archaean is followed by a generally decreasing first-order trend through the Paleoproterozoic, reaching a minimum of less than 3 ppb around 2.2 Ga (Pretoria Group, (Figure 92).

With regard to the proposed end-member models, the mantle origin model assumes that an anomalous mantle (Au and PGE–rich mantle domain) was located below the Kaapvaal cratonic crust during the Mesoarchaean, remained undisturbed for more than 1 billion years, and was tapped again during the Proterozoic Era. In the mantle origin model, gold and PGE ascended with magma that was released from an anomalous mantle domain. Kirk et al. (2001) used osmium isotope and rhenium–osmium concentrations in gold, and found that the low $^{187}Os/^{188}Os$ ratio of the Mesoarchaean Witwatersrand gold is similar to the Mesoarchaean upper mantle ratio, thus supporting the mantle origin hypothesis proposed in this study. A study by Schaefer et al. (2010) revealed that the low initial Os isotope ratio of broadly isochronous minerals suggests that gold and noble metals were originally extracted by magmatic processes from the upper mantle at 3.0–3.1 Ga. The upper mantle temperature during the Mesoarchaean was probably >1400°C (Abbott et al., 1994), thus permitting voluminous upwelling of Au and PGE-rich magma. High mantle temperatures are inferred from the occurrence of very magnesian komatiitic lavas that are widespread in most Archaean greenstone belts, but rarely found after the Archaean–Proterozoic transition at 2.7 Gyr. The higher temperatures of the Archaean Earth can be attributed to the release of greater amounts of energy from the accretion of solar system material, subsequent differentiation into core and mantle, and greater concentrations of heat-producing radiogenic elements (Leitch, 2004). Mantle dynamics studies predict that when the upper mantle temperature is in the region of 1430–1500°C (Abbott et al., 1994), it results in a higher percentage of mantle melting (Loyd et al., 2007; Herzberg et al., 2010). This implies that more gold could go into the melt. The degree of partial melting in the upper mantle would have been at its maximum, which would have favoured production of sulfur-under saturated melts. Melts formed under these conditions are known to be richer in Au than sulfur-saturated ones, as proven by Au-enrichment in komatiites (Pitcairn, 2011). Provided that oceanic subduction already occurred in the Archaean, its geodynamic signature was significantly different from modern subduction (Abbott and Hoffman, 1984) as (a) in contrast to steep post-Archaean subduction, Archaean subduction was buoyant, flat, and shallow and (b) melting occurred in the slab wedge rather than in the mantle wedge as in post-Archaean tectonics (Artemieva and Meissner, 2012). However, in the case of high upper-mantle temperatures (>1400°C) in the Archaean, no

oceanic subduction existed on the Palaeoarchaean Earth, and the transition from 'no subduction' to 'pre-subduction' tectonics probably started between 3.2 and 2.5 Ga (Artemieva and Meissner, 2012). In the case of the Barberton Supergroup, de Ronde and de Wit (1994) indicate present-day-type accretion and subduction events from about 3.230–3.080 Ma, followed by a change to trans-tensional tectonics, which is coeval with gold vein formation. Thus, the palaeo-Earth geodynamic tectonics most likely contributed to the voluminous upwelling of magma during the Mesoarchaean. When the magma reached the Mesoarchaean ocean floor, volcanism resulted in the release of CO_2 into an oxygen-free atmosphere, from which siderophile elements were released with by volcanic degassing. Thermodynamic modelling suggests that in near-shore environments and areas proximal to volcanic activity, particulate gold may have been a significant component (Vlassopoulos and Wood, 1990; Rickard and Luther III, 2006).

The extra-terrestrial Au and PGE addition revolves around a domain that was marked by heavy meteor bombardment during Hadaean and Archaean times. These meteorites were presumably rich in noble metals and were scattered throughout the planet within a protracted period (ca. 4.5–3.8 Ga, Chapman et al., 2007). This indicates that Au and PGE were reintroduced to the upper mantle by the continued meteor bombardment. The chondrite origin of Au and PGE has been questioned during the past few decades. In particular, studies of upper mantle rocks yield Os isotopic compositions consistent with that of the chondrites (Chou, 1978; Morgan, 1986; O'Neill, 1991; 1996). A rebuttal to these interpretations was presented by Snow and Schmidt (1998) who found Ru/Ir, Rh/Ir, Pt/Ir and Pd/Ir ratios about 40 % higher than those of the CI chondrites in abyssal peridotites. The variations in Au and PGE content with the presumed meteoritic source can be attributed to upper mantle contamination. This implies that late-accreting materials with Au and PGE distributions were different from primitive meteorites or were contaminated by mixing of heterogeneous mantle melts.

Protracted meteorite bombardment combined with magmatism might also have triggered the return flow of the mantle near palaeo-slab edges, which would result in additional Au and PGE transfer from the lower mantle to the ascending upper-mantle plumes. Maier et al. (2009) suggested that contamination of the mantle with HSEs commenced at 3.2 Ga and was largely completed by 2.9 Ga, thus overlapping in time with the postulated Mesoarchaean giant gold episode. This could be the reason for the elevated contents of siderophile elements in Archaean hinterlands that were later pre-concentrated/reworked by lithospheric and hydrospheric processes. This is supported by an increase in the PGE contents of komatiites from the Palaeoarchaean to the Neoarchaean and Proterozoic (Maier et al., 2009). For voluminous magmatism to be repeated during the emplacement of layered igneous provinces

such as the Bushveld Igneous Complex, a secular shift in geodynamics would be required, characterised by the generation of either new or episodic magmatism from the mantle domain enriched in siderophile elements. This would then result in large, layered, igneous province-related mantle plumes enriched in Au and PGE. This implies that it is probably not a coincidence that the Kaapvaal Craton is also host to the world's largest concentration of PGEs in the form of the Bushveld Igneous Complex.

Despite the fact that the Bushveld Igneous Complex is a layered intrusive complex and considerably younger (ca. 2.054 Ga) than the Witwatersrand Supergoup (<2.9–2.7 Ga), the ultrabasic and basic melts of the Bushveld Igneous Complex might have tapped a similar mantle domain as the earlier komatiitic melts in the Mesoarchaean. The Bushveld Igneous Complex has been quoted as having been formed by rapid decompression melting at the foremost edge of a mantle plume, activated by the impact of a large iron bolide (e.g. Elston, 1992). Dating of the Vredefort dome ruled out the likelihood of this suggestion (Gibson et al., 2000). In contrast, Kruger (2002) proposes a back-arc, subduction-related setting for magmatism, whereas Gibson and Stevens (1998) advocate that during the Bushveld event the Kaapvaal Craton experienced extensional and strike-slip renaissance of Archaean structures, thus tapping the same mantle domain from which the Witwatersrand gold was sourced.

In spite of the differences in the mantle-domain siderophile element-enrichment (i.e. intense meteorite bombardment of the Hadaean to Palaeoarchaean Earth, plume-like ascent of relics from inefficient core formation, or plumes from the core–mantle boundary), the end result is large magma flare-ups during the Palaeoarchaean and Proterozoic, driven by mantle upwelling. Gibson and Stevens (1998) reported that the volume of magma estimated to have been involved in the formation of the Bushveld Igneous Complex suggest that optimum conditions for such an event involve the interaction of a mantle plume with a lithosphere that has been thinned to between 110 and 50 km. In either case, an elevated content of siderophile elements would be expected. The Au and PGE-rich mantle domain was most likely the source region for the melts that eventually led to the source rocks of the Witwatersrand gold as well as, at a later stage, for the Bushveld Igneous Complex. These models are supported by major mantle overturning in the hotter palaeo-Earth which has been reported in Condie (2004, 2005), and Artemieva and Meissner (2012), with associated plumes causing extreme heating at the base of the crust. This is consistent with the timing of the formation of the juvenile crust, especially during the Mesoarchaean.

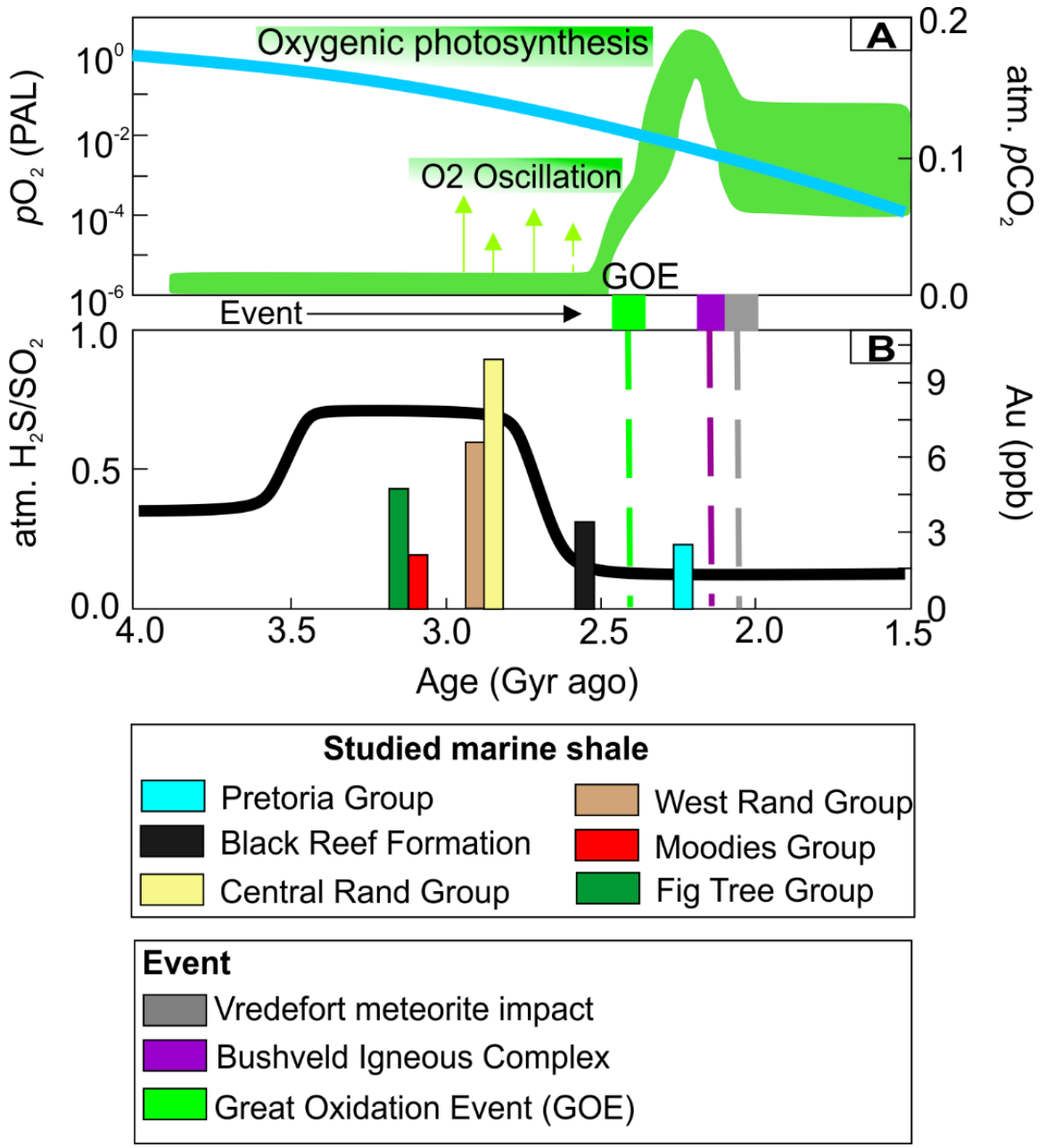

Figure 92: Binary diagrams showing concentration of (a) evolution of Earth's atmospheric oxygen content through time (after Lyons et al., 2014), (b) Au content in marine shales and H_2S/SO_2 versus time. The ratios H_2S/SO_2 curve is from Frimmel (2015).

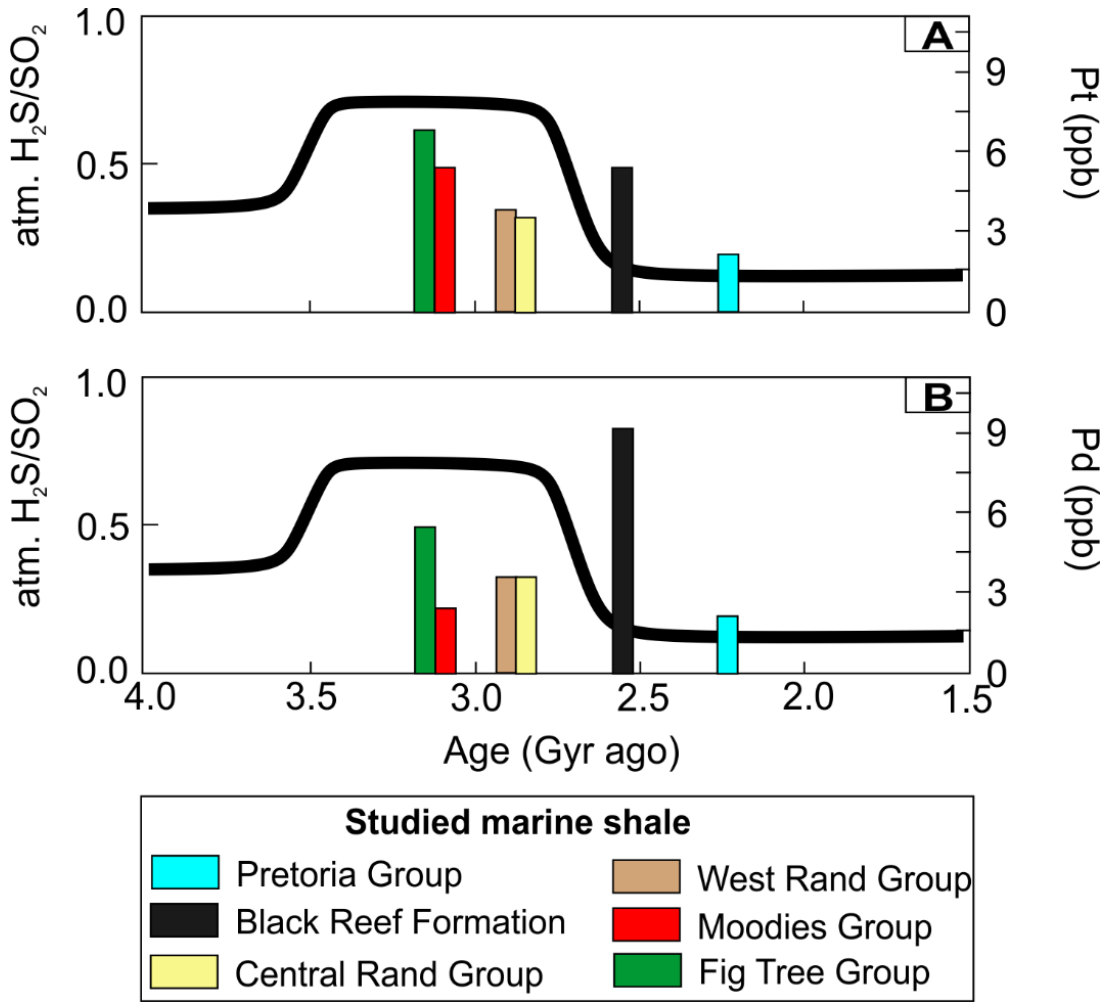

Figure 93: Binary diagrams showing (a) Pt content in marine shales and H_2S/SO_2 versus time, (b) Pd content of marine shale and H_2S/SO_2 versus time. The ratios H_2S/SO_2 curve is from Frimmel (2015).

The second end-member model, referred to as 'no anomalous mantle', complements the mantle-origin model, although it revolves around scavenging of gold from either the hinterland or other surficial sources (e.g. seawater). The intuitively most likely source will be that the Kaapvaal Craton has a number of greenstone belts that contain gold and are in the vicinity of, and beneath, the Witwatersrand Supergroup. This led various authors (de Ronde et al., 1991; Abraham et al., 1994; Goldfarb et al., 2001) to allude that if the Witwatersrand gold deposits are of placer-origin, then it is possible that an exceptional Mesoarchaean orogenic-gold-lode system existed in the Kaapvaal Craton at one time, for which the age (3.08 and 3.04 Ga; Dziggel et al., 2010) is in agreement with the most likely age of the Witwatersrand gold and associated heavy minerals. This school of thought has several shortfalls, such as (a) the lack of larger nuggets and gold-bearing quartz pebbles in the Witwatersrand (Frimmel, 2014), (b) the Barberton gold contains orders of magnitude less Os (Frimmel et al., 2005; Frimmel,

2014), and (c) the total amount of gold required to make up the content of the Witwatersrand gold (Robb and Meyer, 1990).

Another school of thought prescribes that hydrothermally altered granites of suitable age in the hinterland exhibited elevated Au content, and that erosion of these 3.1 to 2.9 Ga granites provided the main source of the gold (Hallbauer and Barton, 1987; Robb et al., 1992). Following this hypothesis, Klemd (1999) provided evidence that the low-temperature alteration in these granites is most likely related to basinal fluids that are younger than Witwatersrand sediment deposition. An alternative to granitic sources was provided by Hutchinson and Viljoen (1987), who proposed syn-sedimentary pyritic exhalites along the basin margin as the dominant gold source. This school of thought is dubious in principle because no direct evidence of gold concentration by such exhalative activity has ever been recorded, and it does not take into account the differences in mineralisation times and amenability of exhalative activities.

These schools of thought, based on the assumption that the hinterland must have contained elevated Au contents, did not gain favour following the work of Loen (1992), who calculated that an average background gold value typical of Archaean granite–greenstone terranes ranges from 0.4–6.8 ppb, thus concluding that the Au content would be sufficient to explain the world's largest accumulation of gold. An alternative to these models is that the Witwatersrand deposits are epigenetic, and that the source of the Au is within metamorphosed rocks beneath the reefs. Two principal source regions have been proposed in this regard, namely: (a) Au mineralisation was brought by the dissolution of background Au (at the ~2 ppb level) in the course of progressive devolatilisation reactions during greenschist-to-amphibolite facies metamorphism of underlying greenstone belts (Phillips and Powell, 2011), (b) the detrital pyrite is of intrabasinal origin and sourced from the West Rand Group or lower Central Rand Group, and the gold was introduced in two stages, first by sedimentary reworking of older sediments within the Central Rand Basin, then by organic-rich basinal brines whose circulation was triggered by the Bushveld event (Large et al., 2013). The study of pyritic shales by Large et al. (2013) is only limited to the Carbon Leader Reef, thus limiting its applicability to all Witwatersrand gold deposits. Another shortcoming of this model is that the trigger is thought to be the 2.504 Ga Bushveld magmatic event. This is highly unlikely to have triggered major basinal fluid flow because the Bushveld event occurred several hundred million years after sediment deposition and diagenesis, long after peak metamorphic conditions had been attained; therefore, it would have affected a Witwatersrand basin fill that was already relatively dry with very little, if any, basinal fluid preserved (Frimmel et al., 2014). The differences in age are reflected by the lack of Bushveld-event ages in post-depositional xenotime age spectra

from the Witwatersrand strata (Kositcin et al., 2003). Detailed discussions of these epigenetic schools of thought are provided in Frimmel (2014).

A study by Fuchs et al. (2016b) of the Carbon Leader Reef suggested that the relative proportions of trace elements in pyrobitumen seams and nodules are, in large part, similar to those of organic-rich shales located within the sedimentary succession. They proposed that intrabasinal shale units of the Witwatersrand Supergroup were the source for the pyrobitumen in the Carbon Leader Reef. This led them to the conclusion that the hydrocarbon liquids that formed the pyrobitumen seams in the Carbon Leader Reef played an essential role in the remobilisation and redeposition of gold in the Witwatersrand Supergroup (Fuchs et al., 2016b). The study by Fuchs et al. (2016b) also has limitations in its scope and does not represent other Witwatersrand gold-bearing reefs.

A syngenetic origin of gold in the absence of a particular source has been proposed by Frimmel (2014), and Frimmel and Hennigh (2015). This model suggests that the lack of proper nuggets in these older deposits is significant, as it eliminates the requirement for the presence of discrete gold deposits in the hinterland and, instead, allows for input of Au during sedimentation, either in colloidal form and/or dissolved in meteoric surface waters. This is predicted by the current understanding of the Archaean environment, complimented by thermodynamic modelling (Frimmel, 2014; Heinrich, 2015). This study adds to this hypothesis using both existing thermodynamics models and marine sedimentation processes. The composition of the prevailing Archaean atmosphere included various gases such as H_2, CH_4, SO_2, and H_2S as explained in Section 8.4, resulting in acid rain precipitation. In this type of environment, two recent studies, Frimmel (2014) and Heinrich (2015), used thermodynamics to model the likely mechanism for gold mobilisation. This model assumes that gold was transported from a fertile hinterland by Archaean rivers and streams into the oceans in the form of AuHS(aq) or $Au(HS)_{2^-}$. This is supported by thermodynamic modelling that suggests that dissolved Au in natural Archaean waters was predominantly $Au(HS)_{2^-}$ species, whereas in the more oxygenated Phanerozoic ocean, the most stable species was $Au(OH)(H_2O)$ (Rickard and Luther III, 2006). This implies that the Fig Tree and Moodies groups' shales should theoretically have an elevated Au content, given that they were deposited in marine environments with presumably dissolved Au complexes. Not much is known regarding the Fig Tree Basin architecture because of structural complexities, aside from sequence stratigraphy and field interpretations by Lowe and Nocita (1999), which suggest that the oldest example of a possible foreland basin (retroarc-type) is in the southern facies of the Fig Tree Group. Petrographic and stratigraphic evidence suggests that the Moodies Group was deposited in a foreland basin formed by thrust faulting and uplift of the greenstone belt in the south-east

(Heubeck and Lowe, 1994; Lowe and Nocita, 1999). The depositional basin deepened to the north, which is where the studied shales were sampled. From Figure 92 and 93, it is clear that there are contrasting concentrations of not only Au, but also of PGEs in the Fig Tree and Moodies Group. Since the studied Barberton Supergroup marine shales represent shallow-to-deep marine sediments in the vicinity of major fault lines, they tend to be prone to seafloor alteration, mainly silicification (e.g. Hofmann et al., 2017). During seafloor alteration processes gold tends to be very mobile, and in environments where there are carbonaceous marine sediments overlying alteration zones, gold tends to be incorporated into the carbonaceous material. This phenomenon has been documented in various black shale geochemical studies (Lehmann et al., 2007; Pašava et al., 2013). The low Au concentration in the Palaeoarchaean shales may be due to dilution caused by silicification.

Furthermore, in the Palaeo- and Mesoarchaean reducing atmosphere gold may have been washed off from the hinterland and transferred into the oceans. This finding is anchored by the findings of Hofmann et al. (2017), who reported the mobility of gold during silicification of mafic/ultramafic rocks, and its transfer to the Archaean ocean. The Mesoarchaean Witwatersrand Supergroup formed under different geological conditions, which include but are not limited to the atmosphere or seawater composition, and different depositional settings. These conditions were characterised by the presence of fluvial processes, deposition of sediments into the oceans, and prevailing microbial gold fixation processes. This facilitated the precipitation of gold from the $AuHS_{(aq)}$ or $Au(HS)_{2^-}$ complex (Frimmel, 2014). Sedimentary reworking of the gold-enriched microbial mats most likely took place immediately after their formation, resulting in the formation of the Witwatersrand deposits and other Witwatersrand-type gold deposits in the Kaapvaal Craton, such as the Ventersdorp Contact Reef and the Black Reef Formation.

Studies that dealt with the thermal history of the earth have found that as upper mantle radiogenic heat sources decay with time, convection transfers less heat, the preferred mantle viscosity gradually increases, and the mantle undergoes secular cooling (Schubert, 2001; Artemieva and Meissner, 2012). The gradual decrease in upper mantle temperature with time during the Proterozoic is attributed to rapid convection underneath the oceans and volatile dependent rheology (Schubert, 2001). Herzberg et al. (2010) suggest that the Archaean upper mantle was hotter than the Proterozoic upper mantle and cooled by ~100 K/Gyr, as evidenced by liquidus temperatures and MgO contents of basaltic lavas through time. If the upper mantle temperature declines with time, the upper mantle temperature would have been <1400°C during Pretoria Group marine sedimentation. Therefore, only small portions of the anomalous mantle domain could be sought, thus explaining the low Au abundances in the hinterland. This

hypothesis is supported by low Au abundances in some of the younger granite–greenstone terranes (Goldfarb et al., 2001). This implies that the distribution of gold in the Transvaal Supergroup was governed by multiple factors that included the prevailing redox conditions, availability of traps, and Proterozoic hinterland gold budget. Tectonic events that occurred between Neoarchaean and Palaeoproterozoic times mobilised hydrothermal fluids from the continental crust, and this has been used as one of the theories on the hydrothermal origin of Witwatersrand gold (Phillips and Myers, 1989; Barnicoat et al., 1997; Phillips and Powell, 2011). The crustal rocks have a high $^{187}Os/^{188}Os$ ratio (Kirk et al., 2001, 2002) compared to the low $^{187}Os/^{188}Os$ ratio in the Mesoarchaean upper mantle and Witwatersrand-type gold in the Kaapvaal Craton. This could explain that as much as the gold was concentrated by surficial processes, its origin was not derived from crustal sources. Based on the proposed end-member models (i.e. anomalous mantle and other processes), there is strong evidence that the ore-forming material is a mixture of crustal and mantle sources. The Witwatersrand gold deposits can be formed from an upper mantle source from which the Bushveld PGEs were also sourced, or they can be formed solely by scavenging of crustal gold from a fertile hinterland without an input of anomalous mantle material.

7.6. Controls on the distribution of siderophile elements

The studied marine shales reveal variable Au and PGE distributions, with several orders of magnitude higher Au enrichment in the Witwatersrand shales relative to the Barberton and Transvaal supergroups (Figure 92 and 93). These variations reflect an interplay between different geological processes. The changes in the hydrosphere–atmosphere system composition and mantle dynamics played an important role in determining the secular evolution of the Au and PGEs in the Kaapvaal Craton, as reflected in the economic deposits of Witwatersrand gold and Bushveld Igneous Complex PGEs. Siderophile element enrichment in the studied marine shales implies that a fertile hinterland existed during the Archaean. This indicates that the cycling of metals (e.g. reworking of metals by surficial processes) in the continental crust may have buffered the composition of background Au and PGE concentrations in the studied marine shales. Many published marine shale siderophile element content averages are based on black shales that are generally enriched in different metals, including siderophile elements. To this end, Ketris and Yudovich (2009) suggested a global average gold concentration in black shales of 7 ± 1 ppb, which is much higher relative to other sedimentary rocks such as sandstone and siltstone. Although this average is based on approximately 9,120 analyses and first-order statistics, the majority of the samples are post-Archaean and most of them are metal-rich carbonaceous shales. This average reflects the fact that black shales are, in general, enriched in most metals, thus it cannot be used as a representative average for Archaean–Proterozoic non-black shales such as the ones investigated in this study.

Unlike some of the mineralised Phanerozoic metal-rich black marine shales (e.g. the Zunyi region in China, Canada's Yukon, and some areas of Poland; Pašava, 1993; Pašava et al., 2013) that host economically significant Au and PGE concentrations, the studied unmineralised Palaeoarchaean–Palaeoproterozoic marine shales are, in this regard, considered to represent the hinterland of the aforementioned time window in the Kaapvaal Craton. In most instances, the post-Archaean marine black shales have been reported as a possible source of epigenetic gold mineralisation (Glasson, 1975) and recently, the case has been made for a seawater origin for these metals, including Au (Lehmann et al., 2007; Large et al., 2015). The higher concentrations of Au and PGE in black shales is thought to be due to the organic complexation of Au and PGE from seawater in anoxic organic-rich mud, which is eventually incorporated into diagenetic sulfide minerals (Helz et al., 1996). In post-Archaean times, when the ocean chemistry began to approximate modern compositions, logic would suggest that any marine deposit rich in organic carbon would have an elevated Au content. At the same time, continental margins are expected to have higher Au concentrations in seawater

because of the largely detrital flux of Au in modern oceans, in conjunction with Au's extremely low solubility in modern seawater (Nekrasov, 1996; Henderson, 1985; Anoshin, 1997). The residence time of Au in the oceans is estimated to be 1000 years (Falkner and Edmond, 1990), which is less than most other redox-sensitive trace elements such as Mo (760,000 years), As (39,000 years), Se (26,000 years), and Cu (5000 years). The Au residence time in oceans is higher than that of trace elements such as Co (340 years), Hg (350 years), and Te (100 years). Since the Au residence time is on the same order as the mixing time of the ocean (Large et al., 2015), it is intuitive to expect an equitable, homogeneous distribution of Au throughout the open ocean. However, Au concentrations of up to an order of magnitude higher have been measured in seawater close to continental margins and source river systems, compared to open ocean values (Nekrasov, 1996). Nonetheless, it remains to be established exactly how Au (and PGEs) were introduced into marine shales. Previous studies of the Kaapvaal Craton have estimated the average concentration of Au in unmineralised rocks such as granites to be approximately 2 ppb (Saager and Meyer, 1984). This figure is lower than some of the background values obtained from the Barberton and Witwatersrand supergroups. As stated in Section 7.5, syngenetic models of Witwatersrand mineralisation have been a matter of debate, as anomalous background gold concentrations would be required, or a particular Archaean basement rock would have to be well-endowed with Au for the unusual interplay of sedimentological processes that could form the giant Witwatersrand gold deposits (Minter et al., 1993; Loen, 1992; Robb and Meyer, 1995; Frimmel, 2008; Kirk et al., 2002; Frimmel et al., 2005; Frimmel, 2014).

The studied Witwatersrand marine shales across the Mesoarchaean land surface are geochemically anomalous (i.e. elevated concentrations of background Au and other metals, including PGE, relative to the average continental crust). To account for the Witwatersrand gold deposits, a fertile hinterland is required, or the dissolved Au in Archaean oceans should be elevated by several orders of magnitude. Although Au is assumed to be present predominantly as dissolved complex ions in hydrothermal ore-forming fluids (Seward, 1989), it may be present in seawater as a mixture of dissolved complexes, colloids, nano-particles, aqueous clusters, absorbed onto detrital clays, and as Au organic complexes (Vlassopoulos and Wood, 1990; Large et al., 2011). In the modern oceans, rivers draining Au mining provinces have the highest concentrations of Au being transported as suspended particles and deposited into the ocean, thus increasing the Au content (Falkner and Edmond, 1990). In the distal marine sediments of the Mesoarchaean Witwatersrand, magnetite was the principal Fe phase, the total sulfur concentrations were much lower, and the low Au and PGE solubility levels were probably low relative to the proximal marine sites. Evolution of oxygen in the

atmosphere and hydrosphere suggests that episodic oxygen oscillation in the Archaean may have commenced during the period 3.2–2.5 Ga, prior to the Great Oxidation Event (e.g. Anbar et al., 2007; Large et al., 2014; Gregory et al., 2015). Oxygen oscillation pulses may have been short-lived, but appear to have been of sufficient duration to affect chemical processes in the oceans. Large et al. (2015) suggest that parts of the Archaean oceans underwent periods of oxidation, and the reduced aqueous iron species were oxidized, creating the conditions necessary for the persistence of aqueous dissolved Au. Oxygen oscillation in the Achaean atmosphere may also have led to increased oxidative scavenging of Au from the hinterland, resulting in increased levels of dissolved Au contributed to the Mesoarchaean oceans. However, this will require a minimum 10^{-3} pO_2 (PAL). A systematic variation in Au and PGE concentrations was observed between the studied marine shales. The renewed interest in how siderophile elements were introduced into marine shales has resulted in various hypotheses, some of which are presented below.

(a) Discrete gold was transported and deposited in particulate form (Pitcairn, 2011).
(b) Siderophile elements were adsorbed from seawater and organic matter and became incorporated into sedimentary pyrite (Large et al., 2015).
(c) Silicification of komatiites during the Palaeoarchaean led to low concentrations of gold in non-carbonaceous shales (Hofmann et al., 2017).
(d) Siderophile elements were enriched in residual palaeosols before mechanical erosion and transport (Siebert et al., 2005).
(e) Gold precipitated from aqueous-carbonic, sulfur-bearing hydrothermal fluids (Phillips and Evans, 2004).
(f) Gold was introduced during sedimentary pyrite growth, such as sedimentary pyrite, that have the ability to carry discrete Au and PGEs (Agangi et al., 2015).

The above processes illustrate that there are various surficial and magmatic sources of Au and PGE, and that the processes controlling their distribution cannot be reconciled by a single enrichment model. Syngenetic pyrite (e.g. rounded, concentrically laminated, and porous pyrite rich in inclusions) is relatively common in the Archaean and Palaeoproterozoic marine shales. Sedimentary pyrite is not only common in marine shales, but has been observed in various rock units, including quartzites and auriferous conglomerates of the Witwatersrand Supergroup e.g. Carbon Leader Reef, Elsburg Reef, Basal Reef, and most commonly, in the Ventersdorp Contact Reef (Schweigart and von Rahden, 1965; Hallbauer, 1986; England et al., 2002; Frimmel, 2005; Fuchs et al., 2016b). It is usually coarse-grained and can reach up to 10 mm in size. Sedimentary pyrite is known to contain appreciable amounts of gold (up to

several tens of ppm of Au; Hallbauer, 1986; Guy et al., 2010; Koglin et al., 2010; Large et al., 2015; Agangi et al., 2013, 2015). In the Witwatersrand Supergroup, gold in sedimentary pyrite was initially regarded as secondary and due to infiltration of Au-bearing metamorphic fluids (Saager, 1970; Koppel and Saager, 1974). However, a review of the pyrite paragenetic sequence led some researchers to suggest that the Au is primary and formed by detrital grains derived from altered granites (Hallbauer and Barton, 1987; Robb et al., 1990). More recently, Large et al. (2013, 2015) proposed that the gold in sedimentary pyrite is primary and formed by adsorption from seawater during sedimentary pyrite growth in an anoxic environment. In some Witwatersrand gold-bearing reefs, high concentrations of Au are associated with thin (mm to cm scale) but laterally continuous layers of carbonaceous matter. Although the carbonaceous matter is ultimately of biogenic origin, as indicated by carbon isotopes (Spangenberg and Frimmel, 2001), different schools of thought exist regarding its indigeneity, with some suggesting that the 'carbon' seams represent solidified bitumen derived from migrating oils (Gray et al., 1998; Drennan and Robb, 2006) or in-situ former microbial mats (Hallbauer, 1975; Mossman et al., 2008; Frimmel, 2014). The latter authors provided an extensive list of observations that strongly support an indigenous origin of the carbon seams. The observations included carbon-draped foreset beds in a planar cross-bedded pebbly sandbar, truncation of carbon seams by palaeo-erosion channels, presence of heavy mineral grains interstitially to columns of carbon, re-sedimented clasts of carbon seams, and the stromatolite-like columnar structure of the carbon seams. Frimmel (2014) reported thin film kerogen draping desiccation cracks on the bottom contact of the Vaal Reef, which indicate that kerogen lining delicate sedimentary structures cannot be easily reconciled with the introduction of hydrocarbons by post-depositional oils.

Despite the fact that the presence of carbon seams is affiliated with higher gold contents, the majority of the gold is independent of such carbon seams, but sedimentary pyrite is common to most gold-bearing units. This has led several researchers to suggest that gold in various provinces, including the Witwatersrand Supergroup, was mainly introduced by pyrite (Agangi et al., 2015; Large et al., 2013). In this study, examination of Kaapvaal Craton marine shales (i.e. Au versus total organic carbon and S) demonstrates that there is no correlation between Au and total organic carbon, or Au and S. Therefore, field observations (i.e. rock volume percentage ratio of pyrite:shale) and a literature review (on sedimentary pyrite average Au concentrations) were utilised to evaluate the relative contribution of pyrite in the marine shale Au budget. For this quantification, a block volume (i.e. 100,000 m^3) of the Booysens Formation marine shales (Welkom goldfield) was used as an example because this shale unit has an

elevated Au content. The average sedimentary pyrite Au content was calculated from data given in Large et al. (2015), Table 10.

Table 10: Modelling of sedimentary pyrite gold contribution in marine shales.

Variable	Vol.%	Gold (ppb) [n = 2620]	Block volume (m^3)
Sedimentary pyrite	0.03	90	3,000
Marine shale	99.97	0	99,970
Total	100	90	100,000
Ratio–pyrite:shale	0.0003		0.03
Gold in shales from sedimentary pyrite		2.7	

Modelling of the volumetric ratio (i.e. pyrite:shale) indicates that the total amount of gold in sedimentary pyrite is 90 ppb, and this translates to 2.7 ppb in the overall marine shale rock volume, which is in turn much lower relative to the average background Au concentration obtained in this study. Results from modelling pyrite contributions show that although sedimentary pyrite contributed to the overall gold content in marine shales, and is relatively widespread, its volume is too small to solely account for the total background gold content in the Booysens Formation marine shale or the Fig Tree and Moodies groups marine shales. However, this average is sufficient to account for the overall gold content in the Palaeoproterozoic Transvaal Supergroup marine shales (Pretoria Group marine shale Au = 2.65 ppb). In order to account for the missing fraction, which is 2–3 orders of magnitude higher than that supplied by sedimentary pyrite, a new model on how gold was introduced is proposed in this study. The premise of this model is based on mechanical coagulation and aggregation of sediments in marine environments. The function of coagulation is to overcome the factors that promote the stability of a given system, while aggregation bonds particles together. In practice, coagulation is accelerated by the use of inorganic chemicals, usually sulfate salts, generally referred to as coagulant agents, or through mechanical destabilisation, where coagulation occurs due to the nature of the sediments (Tzoupanos and Zouboulis, 2008). Marine sediments originate from a variety of sources, including continental and oceanic crust, volcanoes, microbes, chemical processes, and cosmic dust.

The first prerequisite for this model is that there has to be an Au-fertile hinterland that will supply gold either from mantle sources or scavenging of crustal gold. Although sediments may be altered from their original condition by any of a number of physical, chemical, and biological

transformations that take place after deposition, assessment of the extent of post-depositional alteration proves that some elements remain relatively immobile (Section 7.2). In order to fulfil the first prerequisite, the Au content of the Booysens Formation marine shale was correlated with relatively immobile element ratios (Zr/Ni and Th/Sc) that were used to infer sediment provenance in Section 7.3. Correlation of these features with Au is very useful, especially for determining the type of source rock that likely supplied gold to marine shales. Results from these correlations show that there is a strong negative correlation between gold and Zr/Ni and Th/Sc. This implies that Au was mainly supplied by greenstones (Figure 94) from the hinterland, regardless of the fact that the dominant potential source rocks in the Booysens Formation marine shales (Welkom goldfield) were mainly felsic in composition.

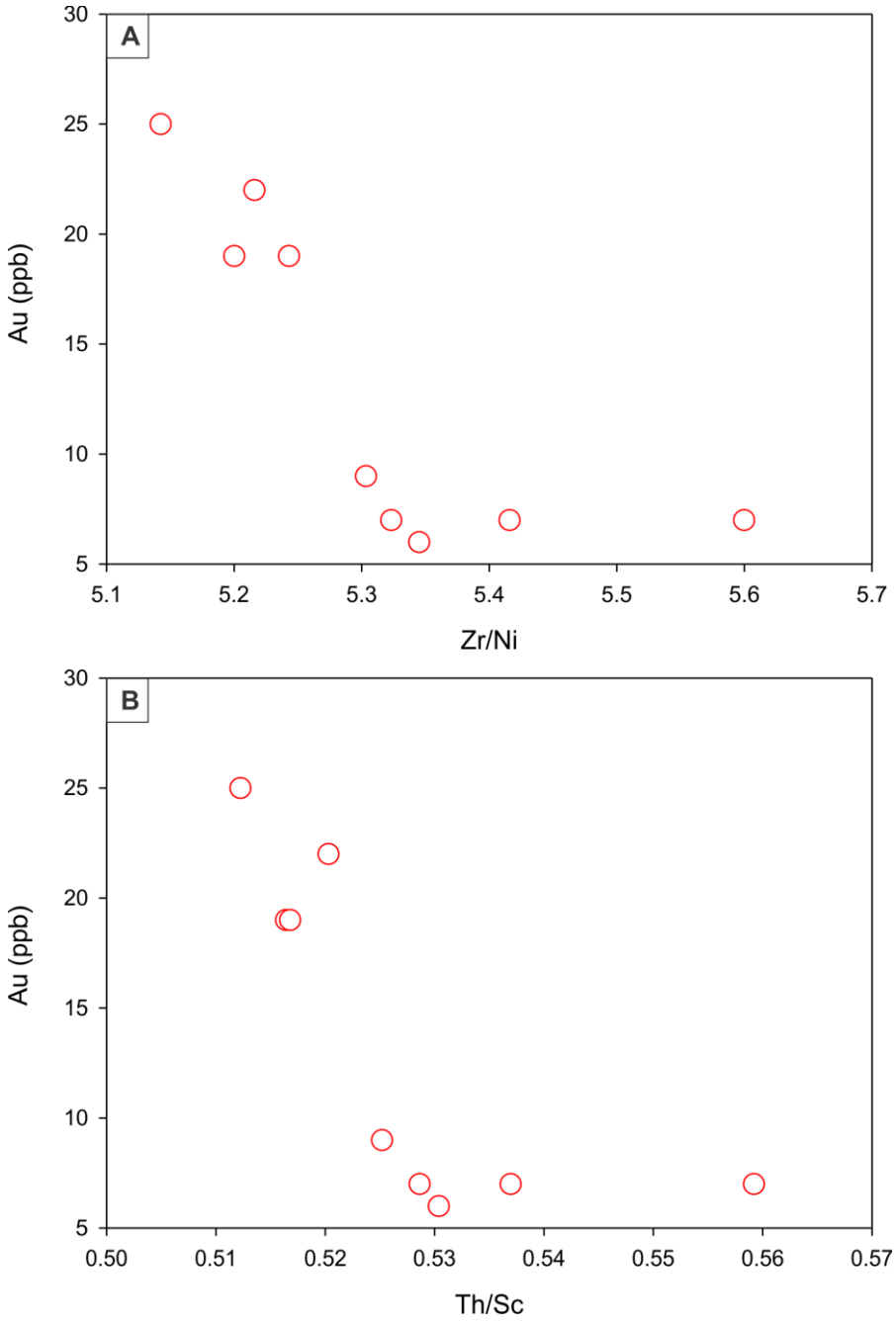

Figure 94: Interpretation of likely gold sources in Booysens Formation marine shale: (A) gold versus Zr/Ni; (B) gold versus Th/Sc. Zirconium and Th in these diagrams represent felsic source rocks, whereas Ni and Sc represent mafic source rocks.

A second prerequisite is that the gold has to be fine grained to allow transportation by various physical processes, e.g. terrestrial, and aeolian, and biogenic. In the Witwatersrand Supergroup, most of the gold is native and has been reported to occur as discrete micro-nuggets of typically toroidal to spheroidal shape, rarely reaching 1 mm in size (Hallbauer, 1986; Minter et al., 1993; Large et al., 2013; Frimmel, 2014). This observation indicates that

gold was transported from a particular place, thus producing fine-grained gold. With the aid of Figure 95, it is interpreted in this study that as gold moves downstream, it is gradually freed from the accompanying rock and flattened by the incessant pounding of gravel. Eventually, it becomes flakes and tiny particles as the flattened pieces break up, thus fulfilling the second requirement. With regard to PGEs, the grains of platinum group minerals described in situ in the Witwatersrand rocks or in production concentrates are invariably small, typical sizes being in the range from ~70 μm (Feather and Koen, 1975; Oberthür, 1983) to ~120 μm (Young, 1907). Ru-Os-Ir-Pd and Pt nuggets are mainly hosted by osmium, ruthenium, rutheniridosmine, and Pt-Ir-Os alloys and in some instances the PGEs are hosted by sudburyite, sperrylite, laurite, and cooperate (Malitch and Merkle, 2004).

The last requirement is that fine sediments/dust containing finely dispersed gold particles floating in shallow and deep marine environment have to mechanically coalesce and coagulate, thus aggregating to form clay-sized sediments that eventually sink and settle on the seafloor. In areas with sufficient natural flocculants such as organic carbon or sulfate, this is achievable within times less than gold residence times (<1000 years). This type of approach has been applied both experimentally and practically to extract gold in metallurgical plants (e.g. carbon in pulp or carbon in leach processes; Wadnerkar et al., 2015) or to remove mud and its organic and inorganic compounds in water treatment plants (coagulation and flocculation processes; Tzoupanos and Zouboulis, 2008). In Archaean marine environments, the predominant fluid was ocean water with lower viscosity, as evident from the relative scarcity of ripple marks in thick sequences, which play an important role during sediment suspension and settling (Fralick and Carter, 2011). Marine sediment trap studies revealed that small-sized grains such as dust are easier to move and suspend in marine water than large-sized grains such as cobbles, and this follows Stoke's Law (Baldock et al., 2004). Similarly, more energetic flows (e.g. fast-moving winds and currents) move larger grains, whereas less energetic flows (e.g. slow-moving winds and currents) move only small-grained sediments. Sediment suspension and sedimentation rates of particles are not only governed by particle size, but depend on other parameters such as acceleration due to gravity, particle density, particle diameter, fluid density, and fluid viscosity. This means that fine particles may remain suspended in marine water, and are carried much farther from their site of origin than large particles. The rate of sinking of fine particles (<0.01 mm) is described mathematically by Stoke's law (Baldock et al., 2004). Sediment trap experiments have been used in the past to test aggregation and sinking rates of clay-sized particles, and have since suggested that for sediments to sink, they have to first coalesce and bond in less turbulent marine environments (Gardner, 1980). Furthermore, sediment trap experiments have proven highly useful for

understanding processes that affect the flux of carbon and other elements in the deep sea (Revel et al., 2015). Therefore, a marine setting provides an ideal environment for finely dispersed gold particles and clay-sized sediments to undergo mechanical coagulation and aggregation prior to sinking, and subsequent settling. The proposed mechanical coagulation and aggregation model (Figure 95) entails that during marine sedimentation, the clastic sediment load that carries fine gold was most likely held in suspension for a longer time than the actual sedimentation rate. This allowed a build-up of fine particulate gold and PGEs bonded to clay-size sediments. Mechanical aggregation is facilitated by either perikinetic flocculation (involving variables relating to the probability of cohesion during collisions with other bodies), in which particles aggregation is brought by the thermal motion of fluid molecules, or orthokinetic flocculation (involving the kinetic energy imparted by collisions with other bodies), in which particle aggregation is brought by inducing velocity gradients and mixing in the suspension. The subsequent sinking and sedimentation processes are thus chiefly governed by marine water flow velocity changes, friction between bonded sediments, periodic flooding events, and changes in particle fluid density.

Figure 91 illustrates the processes that concentrated gold in marine shales. In this model, gold and other siderophile elements were sourced from an anomalous mantle domain and brought to the near-surface continental environment during magma flare-ups, and to the surface by volcanism. This resulted in the emplacement of granitoids/greenstones. Volcanism also resulted in CO_2 degassing. An oxygen-free atmosphere during the Archaean released gases such as H_2S and SO_2. Archaean meteoritic waters facilitated the dissolution of gold from the hinterland and flux off Archaean/Proterozoic land surfaces via channelised river systems. Gold precipitated during microbial fixation at or near the water interface (Frimmel, 2014). Photo-dissociation of SO_2 gas produced SO_4^{2-} and S_0, thus forming separate sulfur reservoirs. Sedimentary pyrite most likely formed from these reservoirs at the water–sediment interface, thus scavenging sediments containing organic matter and gold particles. Elemental sulfur would have sunk and been included in the sediment, thus later reacting with partially oxidised Fe^{2+} or sulfidation of Fe^{3+} species from banded iron formations, forming inclusion-rich pyrite (Whitehouse and Fedo, 2007; Agangi et al., 2015). Sedimentary reworking facilitated the formation of fine gold particles that would later coagulate and floc with sediments. Sedimentation of the gold-bearing mud yields about 2–3 orders of magnitude of gold enrichments. The remaining gold that accounts for the Au content in marine shales was most likely sourced through seawater adsorption by sedimentary pyrite (Large et al., 2013). The majority of the gold concentration in the studied marine shales shows a lognormal distribution, which is common for gold sourced from mechanically sorted sediments.

Overall, a gold-fertile hinterland plays a major role in controlling the distribution of gold in marine shales. This model helps to explain why certain stratigraphic units (e.g. the Roodepoort Formation) have relatively lower sedimentary gold compared to other units (e.g. the Booysens Formation marine shales). Although pre-concentration processes such as the proposed mechanical coagulation and aggregation help to scavenge the majority of finely dispersed gold, a number of other processes (e.g. post-depositional alteration and metamorphism) may occur after sedimentation and diagenesis, and this may result in gold dilution in certain stratiform zones. In other units, such as the Black Reef Formation marine shales, the Au content reflects the possibility of sulfur-related Au scavenging, as the Au correlates positively with sulfur. The Black Reef Formation marine shales anomalous Pt and Pd compositional patterns observed in this study are similar to the circa 2.7 Ga Belingwe greenstone belt in Zimbabwe (Siebert et al., 2005). The controls on the Black Reef Formation siderophile element distribution are in agreement with Crusius et al. (1996), who noted that PGE concentrations in Proterozoic marine sediments are highly variable because of their redox-dependent solubility and the subsequent scavenging of the dissolved species under marine-reducing conditions. Organic matter may have been introduced into the Transvaal Supergroup's Black Reef Formation from an external source during gold mineralisation. Most of the carbon in the Black Reef Formation was most likely precipitated from the mineralising hydrothermal fluids. Based on the composition of the studied marine shales, it is clear that the siderophile element content in the hinterland changed significantly with time. Multiple processes such as mechanical coagulation and aggregation, and reworking of sedimentary pyrite, controlled the distribution of sedimentary gold. The variation in the oxygenation of the atmosphere–ocean system during the Archaean/Palaeoproterozoic was one of the controlling factors in the distribution of Au and PGE.

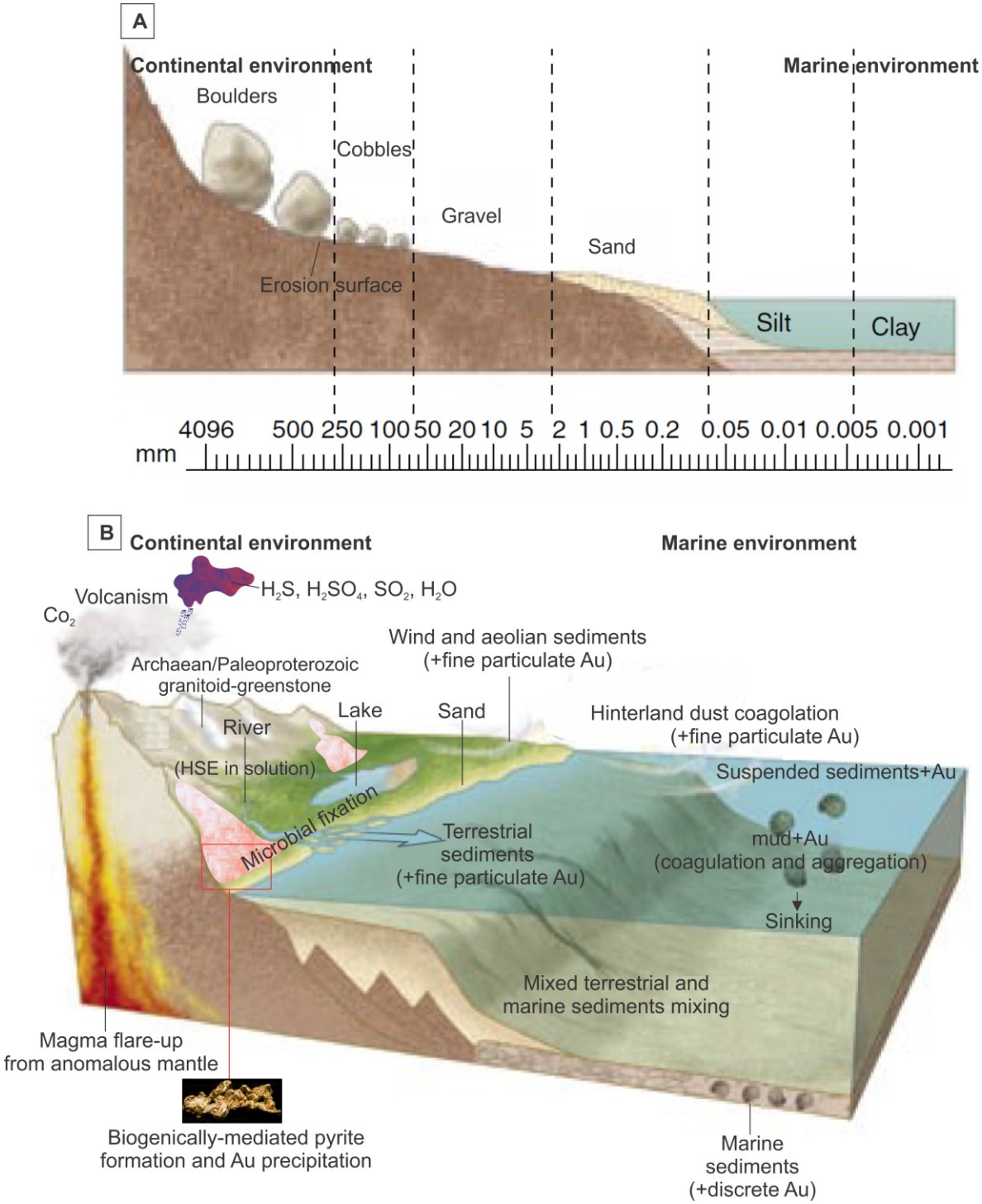

Figure 95: Mechanical coagulation model possibly responsible for majority of gold formation in marine shales: (A) idealised cross-section of Archaean/Palaeoproterozoic continental and marine environments; (B) depiction of Archaean/Palaeoproterozoic hinterland and gold scavenging by mechanical coagulation processes (diagram is modified from Chamberlin and Dickey, 2007).

8. CONCLUSION

The use of geochemical indicators to identify the siderophile element distribution is crucial for both mineral deposit exploration and regional metallogeny. However, no single geochemical test is capable of providing reliable information on the siderophile element endowment. It is, therefore, usual practice to conduct more than one geochemical test and cross-check the results via an assessment of mineralogical composition to ensure that the appropriate conclusions are drawn. Doing so improves the reliability of these tests. In cases where the results of various geochemical analyses do not match, one must consider the representativeness of the samples, as well as the element mobility assumptions used in certain test methods. A clear understanding of the behaviour of diagnostic and indicator elements under different geological conditions allows them to be used in an appropriate manner, thus improving the overall reliability of these geochemical tests.

The differences between the potential sources and distribution patterns of siderophile elements in shale units have been described. This was done through the examination of the mineralogy, geochemical variations, provenance, and the extent of post-depositional alteration and palaeoweathering. The siderophile elements evaluated in this study point to an anomalous mantle domain strongly enriched in siderophile elements, caused by inhomogeneous mixing with cosmic material that was added during intense meteorite bombardment of the Hadaean to Palaeoarchaean earth or incomplete core/mantle separation, as the causes of elevated background Au and PGE content in the hinterland. The same anomalous mantle domain is interpreted here to have been tapped again during the emplacement of the younger (2.054 Ga) Bushveld Igneous Complex. Magma flare-ups have differed during the Mesoarchaean and Proterozoic times. Volcanism is suggested to have dominated during the Palaeoarchaean to the Mesoarchaean times, whereas, during the emplacement of the Bushveld Igneous Complex, an anomalous mantle plume at the base of the Kaapvaal lithosphere led to partial melting of the crust and crystallisation of mantle melts in the upper crust. The contamination of magma occurred during the interaction of a mantle plume with the lithosphere. In the Mesoarchaean Witwatersrand Supergroup, the above findings are complemented by surficial processes that concentrated the gold from the hinterland. Such processes included fluvial transportation of dissolved gold complexes and microbial mediated precipitation of native gold. Geochemical modelling indicate that the majority of the gold and PGEs were introduced into the marine shales by mechanical processes. One such dominating process involved mechanical coagulation and aggregation where finely dispersed particulate gold is interpreted to have been sourced from a fertile hinterland, and later bonded with

suspended sediments in marine environments. According to this model, particulate gold and PGEs flocculated with mud prior to deposition. In hinterlands that had less gold (e.g. Palaeoproterozoic Transvaal Supergroup), the proposed mechanical coagulation and aggregation process occurred with a reduced amount of gold being entrapped, thus marine shales from such hinterlands are not as rich in gold and PGEs when compared to the well-endowed hinterlands for the Central Rand Group marine shales.

Based on the examination of the geochemical and provenance characteristics, it was argued that marine shales of the Barberton, Witwatersrand, and Transvaal supergroups confirm the well-established notion, derived from similar analyses of arenitic units and heavy mineral populations in conglomerate beds, of a granitoid-greenstone-dominated provenance. Geochemical variations based on the stratigraphic position and geographical locations within the craton are evident. It was argued that the higher Fe and Mg content in most of the studied samples is probably due to the shales' enrichment in clay minerals that were ultimately derived from labile igneous and metamorphic minerals such as olivine, amphibole, pyroxene, biotite, and chlorite. The depletion of Ca and Na might be due to the greater effects of weathering, or to leaching during diagenesis. The weak correlation in some of the shales between Na_2O and K_2O on the one hand, and Al_2O_3 on the other hand, is likely because sericite grains primarily formed at the expense of feldspar. In general, the Barberton and Witwatersrand Supergroup shales were found to have a low U concentration, as expected for an Archaean sediment laid down under an O_2-free atmosphere, although the figure is still higher than for other shales of similar geological age. Geochemical parameters, such as the Zr/Cr, Th/U, and Ni/Co ratios strongly imply that the studied marine shales were deposited in variable environments and were sourced from different basement rock types. Trace element concentrations were generally high across all studied shale units because of their incorporation within aluminosilicates. Rubidium and Ba increases in the shales were due to their concurrence within K-bearing minerals. Within the shales, compositional dilution by quartz, with its inherently low trace element content, was the controlling factor in the rare earth elements chemistry. Although their Au and PGE abundances are different, the trace element compositions of the Archaean shales (e.g. those in the Barberton and Witwatersrand supergroups) distinguish them from Proterozoic shales (e.g. those found in the Transvaal Supergroup).

The variable major element geochemistry reflects the differences in the major mineral assemblages. The observed secondary minerals were formed as precipitates or as alteration products of interactions between ions generated during the metamorphic/hydrothermal dissolution of sulfides, carbonates, and aluminosilicates. The shales' mineral paragenesis

indicates that various minerals had different reaction potencies, and most likely reacted under different geological conditions. For example, carbonates have a higher neutralisation potential relative to other minerals because of their fast dissolution rates, even at a near-neutral pH, unlike the silicates that only dissolve under acidic conditions. Therefore, their preservation depends on the prevailing palaeoenvironmental conditions. A change in the trace element characteristics of the Kaapvaal Craton shales appears to have occurred, and is especially associated with the approximate Archaean/Proterozoic boundary.

Trace-element geochemical signatures also demonstrate that the Archaean upper crust was more mafic than the post-Archaean upper crust in the source areas of the studied shale sediments. An evaluation of the likely tectonic setting using immobile element data indicates that the source area for the West Rand Group sediments did not undergo much tectonic rejuvenation, thus confirming a passive margin setting. In contrast, the sediments of the Central Rand Group were derived from a variety of sources, even within a single stratigraphic unit. Their chemical composition indicates major changes in the basin geometry and shifts in provenance from greenstone-dominated to granite-dominated, as syn-depositional granitoids were progressively unroofed during syn-depositional uplift and the erosion of the hinterland.

Although marine shales of the Barberton, Witwatersrand, and Transvaal supergroups have been virtually affected by low-grade metamorphism and hydrothermal alteration involving silicification, carbonatisation, and widespread formation of secondary sericite and chlorite, they widely preserve their primary structures and textures. The indexes of chemical variability and weathering for the studied marine shales are indicative of clay-rich mature sediments related either to intracratonic environments, which are characterised by the recycling of older sediments, or to sediment derivation from an intensely weathered magmatic/metamorphic basement. This study's geochemical shale data suggest a high rate of chemical weathering in the hinterland and on intrabasinal erosion surfaces. Evidence of intrabasinal erosion surfaces is still persevered in some of the shale units such as the Roodepoort Formation marine shale below the Carbon Leader Reef. This provides further support for the notion that rain from Mesoarchaean clouds was acidic, a finding with important implications for mass transfers from the Archaean land surface into the contemporaneous ocean, including the flux of gold from Mesoarchaean continents. As the analysed shale units do not contain interformational unconformities, chemical weathering on syn-depositional erosion surfaces are less likely.

The overall results of the analyses of Au and PGE in marine shales of the Barberton, Witwatersrand, and Transvaal supergroups indicate a preferential partitioning of PGEs and gold. Variations in Pt and Pd content reflect the decoupling of these two metals in the upper

continental crust. The background siderophile element concentrations in the studied marine shales reveal elevated Au and PGE background values during the Archaean era. Certain units, such as the Black Reef Formation, are enriched in PGEs, and others, such as the Witwatersrand Supergroup and Fig Tree Group, are enriched in both Au and PGEs. The enriched PGEs in the Black Reef Formation are attributed to the fact that this shale unit is rich in organic matter and has the highest sulfur content. It is likely that an Au- and PGE-enriched reservoir existed in the envisaged anomalous source mantle since at least the Palaeoarchaean. Both Au and PGEs most likely originated from the geochemically anomalous mantle domain from which the Kaapvaal cratonic crust was sourced in the course of its Archaean evolution. The anomalous mantle domain might be a remnant of a domain that experienced incomplete core–mantle differentiation in the early stages of Earth's history, or it might reflect a domain marked by extra-terrestrial additions during the heavy meteoroid bombardment stage. In either case, elevated Au and PGE background concentrations are to be expected. Other surficial processes such as scavenging of gold from the hinterland also played a major role in pre-concentrating gold that was later deposited into the Witwatersrand Basin.

In this study, Barberton, Witwatersrand, and Transvaal marine shales served as an archetypal example of how secular geological processes coincided in a particular space to produce the world's largest gold and PGE deposits. From a geochemical perspective, understanding of the background Au and PGE content in Palaeoarchaean to Palaeoproterozoic shales, and efficient forecasting concentration mechanisms/traps are likely to be the most important tools for targeting exploration areas. Whether it is a Primitive mantle-derived feature or seawater-derived Au-and PGE sources, the studied marine shales show evidence that a fertile hinterland existed during the Archaean. The concept of derivation from mantle sources provides a better starting point to explain:

(1) the potential link between the Witwatersrand gold deposits and the Bushveld Igneous Complex PGEs,
(2) the systematic fractionation of siderophile elements and their amenability to crustal concentrating processes, and
(3) the compatible behaviour of some PGEs (e.g. Pt and Pd) in the upper crust.

Based upon the proposed sediment mechanical coagulation and aggregation model, it was argued that although regional geographic variations in Au and PGE contents were observed, certain units such as the Booysens Formation are more enriched in background Au and PGE than the Roodepoort Formation shale. Inter-element correlations suggest that carbon and

sulfur did not play a major role in hosting significant concentrations of siderophile elements in the studied marine shales. There is weak correlation between the siderophile elements, suggesting that their distribution is not solely determined by their siderophile affinity e.g. gold does not correlate with any of the PGEs.

The lack of particulate gold in the studied shales is due to the grain size as defined for a shale. Gold accumulation is mainly controlled by mechanical sedimentary processes, which involve breaking down gold particles into finer discrete particles. Assuming that most of the gold was dissolved in Mesoarchaean meteoric waters, precipitation of gold that was later mechanically disintegrated could have been triggered by redox reactions with hydrocarbons. In terms of the regional scale and implications for sedimentary gold endowment, the Central Rand Basin architecture provided a sufficient catchment area and efficient sedimentary (i.e. fluvial) processes for gold accumulation in embayments such as estuaries, thus explaining why the rich goldfields are located along the edge of the basin. Potentially, an essential conclusion that can be drawn from this study is the possible link between the source of Witwatersrand gold deposits and the Bushveld igneous Complex PGE deposits. This in turn has major implications regarding future exploration strategies for discovering new Witwatersrand-type gold deposits and Bushveld-type PGE deposits on other cratons.

9. RECOMMENDATIONS

In light of the findings of this thesis, several recommendations for future research are given below.

— There are many test methods and techniques for characterising unmineralised geological samples in terms of their mineral deposit potential. Each test method is best suited for a certain type of rock and element, and can only provide meaningful results in certain contexts. The next logical step towards identifying reliable Au and PGE signatures is developing a working knowledge of the suitable rock types (e.g. marine sandstones and Archaean greenstones) that can be used for assessing background metal concentrations in places where there are no marine shales.

— Further investigation of the element partitioning mechanism in marine shales, particularly for PGEs, is recommended.

— Quantitative analysis of siderophile inclusions in fine-grained pyrite with laser ablation ICP-MS should be conducted in order to determine whether there is a relationship between pyrite-type and siderophile element content.

— Validation of the proposed sediment mechanical coagulation and aggregation using sediment trap experiments and fine gold should be performed to establish sedimentation rates that can be routinely used to estimate potential backroad siderophile element concentrations in Archaean/Palaeoproterozoic sediments.

— Further geochemical and isotopic investigations on the mantle beneath the Kaapvaal Craton in order acquire more evidence regarding the potential link between the Witwatersrand Supergroup gold deposits and the Bushveld Igneous Complex PGE deposits is recommended.

— Key ideas from this research project should be extended and applied to shale geochemistry analyses in other cratons (e.g. the Superior Craton in Canada, Dharwar Craton in India, Pilbara Craton in Australia, São Francisco Craton in South America, West African Craton) in order to assess whether the Au and PGE anomaly is a secular variation in earth history or a geographic phenomenon specific to the Kaapvaal Craton.

REFERENCES

Abbott, D.H., Hoffman, S.E., 1984. Archaean plate tectonics revisited 1: Heat flow, spreading rate, and the age of subducting oceanic lithosphere, and their effects on the origin and evolution of continents. Tectonics 3, 429–448.

Abbott, D., Burgess, L., Longhi, J., Smith, W.H.F., 1994. An empirical thermal history of the earth's upper mantle. J. Geophys. Res. 99, 13835–13850.

Abraham, A.P.G., Davis, D.W., Kamo, S.L., Spooner, E.T.C., 1994. Geochronological constraints on late Archaean magmatism, deformation and gold–quartz vein mineralization in the northwestern Anialik River greenstone belt and igneous complex, Slave Province, N.W.T. Can. J. Earth Sci. 31, 1365–1383.

Agangi, A., Hofmann, A., Wohlgemuth–Ueberwasser, C.C., 2013. Pyrite zoning as a record of mineralization in the Ventersdorp Contact Reef, Witwatersrand Basin, South Africa. Econ. Geol. 108, 1243–1272.

Agangi, A., Hofmann, A., Rollion–Bard, C., Marin–Carbonne, J., Cavalazzi, B., Large, R., Meffre, S., 2015. Gold accumulation in the Archaean Witwatersrand Basin, South Africa — Evidence from concentrically laminated pyrite. Earth–Science Reviews 140, 27–53.

Anbar, A.D., Duan, Y., Lyons, T.W., Arnold, G.L., Kendall, B., Creaser, R.A., Kaufman, A.J., Gordon, G.W., Scott, C., Garvin, J., Buick, R., 2007. A whiff of oxygen before the Great Oxidation Event? Science 317, 1903-–906

Anhaeusser, C.R., 1976. The nature and distribution of Archaean gold mineralisation in southern Africa. Miner. Eng. 8, 46–84.

Anhaeusser, C.R., 2012. The history of mining in the Barberton Greenstone Belt, South Africa, with an emphasis on gold (1868–2012). In: Paper from the Proceedings of the International Mining History Congress April 2012, pp. 1–29.

Anhaeusser, C.R., Roering, C., Viljoen, M.J., Viljoen, R., 1968. The Barberton Mountain Land: a model of the elements and evolution of an Archaean fold belt. Geol. Soc. South Africa, Trans. 71, 225–254.

Anhaeusser, C.R., Mason, R., Viljoen, M.J., Viljoen, R., 1969. A reappraisal of some aspects of Precambrian shield geology. Bull. Geol. Soc. Am. 80, 2175–2200.

Anoshin, G.N., 1977. Gold in magmatic ore deposits: Nauka, Novosibirsk, pp. 206.

Árkai, P., Ghabrial, D., 1997. Chlorite crystallinity as an indicator of metamorphic grade of low–temperature meta–igneous rocks: a case study from the Bükk Mountains, northeast Hungary. Clay Miner. 32, 205–222.

Armstrong, R.A., Compston, W., De Wit, M.J., Williams, I.S., Welke, H., 1991. Zircon ion microprobe studies bearing on the age and evolution of the Witwatersrand Triad. Precambrian Res. 53, 243–266.

Arndt, N., 2011. Scientific drilling in the Barberton Greenstone Belt, South Africa. American Geophysical Union. In: American Geophysical Union, Fall Meeting 2011, Abstract #V44B–0.

Arne, D.C., House, E., Lisitsin, V., 2008. Lithogeochemical haloes surrounding central Victorian deposits: Part 1–Primary alteration systems. In: Geoscience Victoria Gold Undercover Report 4. Department of Primary Industries, Victoria.

Artemieva, I.M., Meissner, R., 2012. Crustal thickness controlled by plate tectonics: A review of crust–mantle interaction processes illustrated by European examples. Tectonophysics 530–531, 18–49.

Awwiller, D., 1993. Illite/smectite formation and potassium mass transfer during burial diagenesis of mudrocks: a study from the Texas Gulf Coast Palaeocene–Eocene. J. Sediment. Petrol. 63, 501–512.

Awwiller, D., 1994. Geochronology and mass transfer in Gulf Coast mudrocks (south–central Texas, U.S.A.): Rb–Sr, Sm–Nd and REE systematics. Chem. Geol. 116, 61–84.

Awwiller, D.N., Mack, L., 1991. Diagenetic modification of S–Nd model ages in Tertiary sandstones and shales, Texas Gulf Coast. J. Geol. 19, 311–314.

Azor, A., Fernando Simancas, J., Exposito, I., Gonzalez Lodeiro, F., Martinez Poyatos, D., 1997. Deformation of garnets in a low–grade shear zone. J. Struct. Geol. 19, 1137–1148.

Babeyko, A., Yu., Sobolev, S.V., Trumbull, R.B., Oncken, O., Lavier, L., 2002. Numerical models of crustal scale convection and partial melting beneath the Altiplano–Puna plateau. Earth Planet. Sci. Lett. 199, 373–388.

Bailey, A.C., Law, J.D.M., Cadle, A.B., Phillips, G., 1989. The Zandfontein Quartzite Formation, a marine deposit in the Central Rand Group, Witwatersrand Supergroup. Univ. Witwatersrand, Econ. Geol. Res. Unit, Inf. Circ. 212, 1–16.

Bailie, R., Armstrong, R., Reid, D.L., 2007. The Bushmanland Group supracrustal succession, Aggeneys, Bushmanland, South Africa: Provenance, age of deposition and metamorphism. South African J. Geol. 110, 59–86.

Baldock, T.E., Tomkins, M.R., Nielsen, P., Hughes, M.G., 2004. Settling velocity of sediments at high concentrations. Coastal Engineering 51, 91–100.

Barakso, J.J., Tegart, P., 1982. Revised stream sediment geochemistry at selected precious metal deposits in British Columbia, Western Minerals, pp. 53–65.

Barnes, S.–J., Maier, W.D., 2002. Platinum group elements and microstructures of normal Merensky Reef from Impala Platinum Mines, Bushveld Complex. J. Pet. 43, 103–128.

Barnicoat, A.C., Henderson, I.H.C., Knipe, R.J., Yardley, B.W.D., Napier, R.W., Fox, N.P.C., Kenyon, A.K., Muntingh, D.J., Strydom, D., Winkler, K.S., Lawrence, S.R., Cornford, C., 1997. Hydrothermal gold mineralisation in the Witwatersrand basin. Nature 386, 820–824.

Barton, E.S., Hallbauer, D., 1996. Trace–element and U–Pb isotope compositions of pyrite types in the Proterozoic Black Reef, Transvaal Sequence, South Africa. Chem. Geol. 133, 173–199.

Barton, J.M. Jr., Van Reenen, D.D, 1992a. When was the Limpopo Orogeny? Precambrian Res. 55, 7–16.

Barton, J.M. Jr., Van Reenen, D.D., 1992b. The significance of Rb–Sr ages of biotite and phlogopite for the thermal history of the Central and Southern Marginal Zones of the Limpopo Belt of southern Africa and the adjacent portions of the Kaapvaal Craton. Precambrian Res. 55, 17–31.

Bau, M., 1996. Controls on the fractionation of isovalent trace elements in magmatic and aqueous systems: evidence from Y/Ho, Zr/Hf, and lanthanide tetrad effect. Contrib. to Mineral. Petrol. 123, 323–333.

Bauluz, B., Mayayo, M.J., Fernandez–Nieto, C., Gonzalez Lopez, J., 2000. Geochemistry of Precambrian and Palaeozoic siliciclastic rocks from the Iberian Range (NE Spain): Implications for source–area weathering, sorting, provenance, and tectonic setting. Chem. Geol. 168, 135–150.

Bekker, A., Holland, H.D., Wang, P.L., Rumble, D., Stein, H.J., Hannah, J.L., Coetzee, L.L., Beukes, N., 2004. Dating the rise of atmospheric oxygen. Nature 427, 117–120.

Bekker, A., Hofmann, A., Rumble, D., Rouxel, O., 2008. Sulfidic organic–rich shales in the Archaean low–sulfate ocean: evidence for transient oxygenated conditions, enhanced volcanism, or low sedimentation rates? Geochim. Cosmochim. Acta 72, A69.

Beresford, S.W., 2009. Atmospheric sulfur in Archaean komatiite–hosted nickel deposits. Science, 326, pp. 1086–1089.

Beukes, N.J., 2010. Fe, C, and O isotope compositions of banded iron formation carbonates demonstrate a major role for dissimilatory iron reduction in ~2.5 Ga marine environments. Earth Planet. Sci. Lett. 294, 8–18.

Beukes, N. J., Nelson, J.P., 1995. Sea–level fluctuation and basin subsidence controls on the setting of auriferous palaeoplacers in the Archaean Witwatersrand Supergroup: a genetic and sequence stratigraphic approach. In: Extended Abstract, South African Geocongress, pp. 860–863.

Beukes, N.J., Dorland, H., Gutzmer, J., Nedachi, M., Ohmoto, H., 2002. Tropical laterites, life on land, and the history of atmospheric oxygen in the Palaeoproterozoic. J. Geol. 30, 491–494.

Bhatia, M., 1983. Plate tectonics and geochemical composition of sandstones. J. Geol. 91, 611–627.

Bhatia, M., 1985. Rare earth element geochemistry of Australian Palaeozoic graywackes and mudrocks: provenance and tectonic control. Sediment. Geol. 45, 97–113.

Bhatia, M.R., Crook, K.A., 1986. Trace element characteristics of graywackes and tectonic setting discrimination of sedimentary basins. Contrib. to Mineral. Petrol. 92, 181–193.

Blatt, H., Middleton, G., Murray, R., 1980. Origin of sedimentary rocks, 2nd ed. Prentice Hall, Englewood Cliffs, New Jersey.

Boudreau, A.E., 2008. Modelling the Merensky Reef, Bushveld Complex, Republic of South Africa. Contrib. to Mineral. Petrol. 156, 431–437.

Bourdelle, F., Parra, T., Chopin, C., Beyssac, C., 2013. A new chlorite geothermometer for diagenetic to low–grade metamorphic conditions. Contrib. to Mineral. Petrol. 165, 723–735.

Boyle, R.W., Gleeson, C., 1972. Gold in heavy mineral concentrates of stream sediments, Keno Hill area, Yukon Territory. Geol. Surv. Canada 71–51.

Brandl, G.M., Cloete, M., Anhaeusser, C., 2006. Archaean greenstone belts. In: Johnson MR, Anhaeusser CR, T.R. (Eds) The Geology of South Africa. Geological Society of South Africa and Council of Geoscience, Pretoria, pp. 9–56.

Brandon, A. D., Walker, R. J., Morgan, J. W., Norman, M. D., Prichard, H.M., 1998. Coupled ^{186}Os and ^{187}Os evidence for core–mantle interaction. Science 280, 1570–1473.

Brandon, A. D., Norman M. D., Walker R. J., M.J.W., 1999. ^{186}Os–^{187}Os systematics of Hawaiian picrites. Earth Planet. Sci. Lett. 174, 25–42.

Bryndzia, L.T., Braunsdorf, N.R., 2014. From source rock to reservoir: The evolution of self–sourced unconventional resource plays. Elements 10, 271–276.

Buchanan, P.C., Reimold, W.U., Koeberl, C., Kruger, F., 2002. Geochemistry of immediate to siliceous volcanic rocks of the Rooiberg Group, Bushveld Magmatic Province, South Africa. Contrib. to Mineral. Petrol. 144, 131–143.

Burke, K., Kidd, W.S.F., Kusky, T.M., 1986. Archaean foreland basin tectonics in the Witwatersrand, South Africa. Tectonics 5, 439–456.

Button, A., 1973. A regional study of the stratigraphy and development of the Transvaal Basin in the eastern and north eastern Transvaal. University of the Witwatersrand.

Button, A., 1986. The Transvaal sub–basin of the Transvaal sequence. In: Anhaeusser, C.R., Maske, S. (Eds) Mineral Deposits of Southern Africa. Geological Society of South Africa, Pretoria, pp. 811–817.

Button, A., Vos, R., 1977. Subtidal and intertidal clastic and carbonate sedimentation in a macrotidal environment: an example from the lower Proterozoic of South Africa. Sediment. Geol. 18, 175–200.

Buurman, P., Meijer, E.L., Van Wijck, J., 1988. Weathering of chlorite and vermiculite in ultramafic rocks of Cabo Ortegal, north eastern Spain. Clays Clay Miner. 36, 263–269.

Byerly, G.R., Kroner, A., Lowe, D.R., Todt, W., Walsh, M., 1996. Prolonged magmatism and time constraints for sediment deposition in the early Archaean Barberton greenstone belt: evidence from the Upper Onverwacht and Fig Tree groups. Precambrian Res. 78, 125–138.

Cairncross, B., 2001. An overview of the Permian (Karoo) coal deposits of southern Africa. J. African Earth Sci. 33, 529–562.

Camden–Smith, P., 1980. The sedimentology, geochemistry and diagenesis of the West Rand Group sediments in the Heidelberg area, Transvaal. University of Cape Town.

Cameron, E.M., 1988. Archaean gold: relation to granulite formation and redox zoning in the crust. Geology 16, 109–112.

Cameron, K.L., Robinson, J. V., Niemeyer, S., Nimz G, J., Kuentz, D.C., Harmon, R.S., Bohlen, S.R., Collerson, K.D., 1992. Contrasting styles of pre–Cenozoic and mid–Tertiary crustal evolution in northern Mexico: evidence from deep crustal xenoliths from La Olivina. J. Geophys. Res. 97, 17353–17376.

Campbell, I.H., Naldrett, A.J., Barnes, S.J. 1983. A model for origin of platinum–rich sulfide horizons in the Bushveld and Stillwater Complexes. J. Petrol. 24, 133–165.

Canfield, D.E., Raiswell, R., 1999. The evolution of the sulfur cycle. American Journal of Science 299, 697–723.

Caporali, S., Bellandi, S., Innocenti, M., Lopilato, O., Romualdi, L., Pezzatini, G., 2010. Determination of gold in alloys via potentiometric titration; an alternative to the fire assay. Gold Bull. 43, 122–130.

Cathelineau, M., Nieva, D., 1985. A chlorite solid solution geothermometer. The Los Azufrez (Mexico) geothermal system. Contrib. to Mineral. Petrol. 91, 235–244.

Cathelineau, M., 1988. Cation site occupancy in Chlorite and Illites as a function of temperature. Clay Miner. 23, 471–485.

Catling, D.C., Claire, M.W., 2005. How Earth's atmosphere evolved to an oxic state: a status report. Earth and Planetary Science Letters 237 (1–2), 1–20.

Catuneanu, O., 2001. Flexural partitioning of the Late Archaean Witwatersrand foreland system, South Africa. Sediment. Geol. 141–142, 95–112.

Cawthorn, R.G., 1999a. Platinum–group element mineralisation in the Bushveld Igneous Complex – a critical reassessment of geochemical models. South African J. Geol. 102, 268–281.

Cawthorn, R.G., 1999b. The platinum and palladium resources of the Bushveld Complex. S. Afr. J. Sci. 95, 481–489.

Cawthorn, R.G. 2005. Stratiform platinum–group element deposits in layered intrusions. In Exploration for platinum–group element deposits. In: Mungall, J.E. (Eds) Mineralogical Association of Canada. 57–73.

Cawthorn, R., 2010. The Platinum Group Element deposits of the Bushveld Igneous Complex in South Africa. Platin. Met. Rev. 54, 205.

Cawthorn, R., 2011.Geological investigations from the PGE distribution in the Bushveld Merensky and UG2 chromite reefs. S. Afr. J. Min. Met. 111, 67–479.

Cawthorn, R.G., Merkle, R.K.W., Viljoen, M., 2002. Platinum–group element deposits in the Bushveld Complex, South Africa. In: Cabri, L. (Eds) The geology, geochemistry, mineralogy, and mineral beneficiation of Platinum–Group Elements. Canadian Institute of Mining, Metallurgy and Petroleum Special Volume, pp. 389–429

Cawthorn, R.G., Eales, H., Walraven, F., Uken, R., Watkeys, M., 2006. The Bushveld Complex. Geol. South Africa 691, 261–281.

Chabu, M., 1995. The Geochemistry of phlogopite and chlorite from the Kipushi Zn–Pb–Cu deposit, Shaba, Zaire. Can. Mineral. 33, 547–558.

Chamberlin, W.S., Dickey, T.D., 2007. Exploring the world ocean. McGraw–Hill Global Education Holdings, pp. 250–416.

Chapman, C.R., Shaw, M.H., Leake, R.C., Jackson, B., 2005. Gold in central Ochil Hills, Scotland. Earth Planet. Sci. Lett. 114, 53–64.

Chapman, C.R., Cohen, B.A., Grinspoon, D.H., 2007. What are the real constraints on the existence and magnitude of the late heavy bombardment? Icarus 189, 233–245.

Chaudhuri, S., Stille, P., Clauer, N., 1992. Sm–Nd isotopes in fine–grained clastic sedimentary materials: clues to sedimentary processes and recycling growth of the continental crust. In: Chaudhuri, N.C. (Eds) Isotopic Signatures and Sedimentary Records. Springer Verlag, Berlin, pp. 287–319.

Cheeney, R., 1983. Statistical methods in geology for field and laboratory decisions. Alien and Unwin, London, pp. 17–59.

Cheney, E.S., 1996. Sequence stratigraphy and plate tectonic significance of the Transvaal succession of southern Africa and its equivalent in Western Australia. Precambrian Res. 79, 3–24.

Chou, C. L., 1978. Fractionation of siderophile elements in the earth's upper mantle. Proceedings of the 9th Lunar and Planetary Science Conference. Geochimica et Cosmochimica Acta Supplement 219–230.

Clarke, F.W., 1889. The relative abundance of the chemical elements. Philos. Soc. Washingt. Bull. X 1, 131–142.

Clarke, F.W., Washington, H., 1924. The composition of the earth's crust. USGS 127.

Cloud, P.E., 1973. Palaeoecological significance of banded iron–formation. Econ. Geol. 68, 1135–1143.

Cloud, P. E., 1988, Oasis in space, Earth history from the beginning. New York, W. W. Norton, 508.

Coetzee, H.P., 1996. The stratigraphy and sedimentology of the Black Reef Quartzite Formation, Transvaal sequence, in the area of Carletonville and West Rand goldfields. University of North West.

Coetzee, L.L., 2001. Genetic stratigraphy of the Palaeoproterozoic Pretoria Group in the Western Transvaal. University of Johannesburg.

Coetzee, L.L., Beukes, N.J., Gutzmer, J., Kakegawa, T., 2006. Links of organic carbon cycling and burial to depositional depth gradients and establishment of a snowball Earth at 2.3Ga. Evidence from the Timeball Hill Formation, Transvaal Supergroup, South Africa. South African J. Geol. 109, 109–122.

Condie, K.C., 1993. Chemical composition and evolution of the upper continental crust: Contrasting results from surface samples and shales. Chem. Geol. 104, 1–37.

Condie, K.C., 1994. Greenstones through time. In: Condie, K.C. (Eds) Archaean crustal evolution – developments in Precambrian geology. Elsevier Science, Amsterdam, pp.85–120, chap. 3.

Condie, K.C., 2004. Supercontinents and super plume events: distinguishing signals in the geologic record. Physics of the Earth and Planetary Interiors 146, 319–332.

Condie, K.C., 2005. Earth as an evolving planetary system. Elsevier, Amsterdam, p.574.

Condie, K., Macke, J., Reimer, T.O., 1970. Petrology and geochemistry of Early Precambrian greywacke from the Fig Tree Group, South Africa. Geol. Soc. Am. Bull. 81, 2759–2776.

Connors, K.A., Noble, D.C., Bussey, S.D., Weiss, S.I., 1993. Initial gold contents of silicic volcanic rocks: bearing on the behaviour of gold in magmatic systems. Geology 21, 937–940.

Coombs, D.S., 1961. Some recent work on lower grades of metamorphism. Aust. J. Sci. 24, 203–215.

Cornell, D., 1978. Petrologic studies at T'Kulp: evidence for metamorphism and alteration of volcanic formations beneath the Transvaal volcano–sedimentary pile. Trans. Geol. Soc. South Africa 81, 261–270.

Cornell, D.H., Thomas, R.J., Moen, H.F.G., Reid, D.L., Moore, J.M., Gibson, R., 2006. The Namaqua–Natal Province. In: Johnson, M.R., Anhaeusser, C.R., Thomas, R. (Eds) The

geology of South Africa. Geological Society of South Africa and Council of Geoscience, Pretoria, pp. 325–379.

Coveney, R.M., Murowchick, J.B., Grauch, R.I., Glascock, M.D., Denison, J.R., 1992. Gold and platinum in shales with evidence against extra–terrestrial sources of metals. Chem. Geol. 99, 101–114.

Cowan, G., 1998. Statistical data analysis. Oxford University Press, London, pp. 104–115.

Coward, M.P., Spencer, R.M., Spencer, C.E., 1995. Development of the Witwatersrand Basin, South Africa. In: Coward, M. P., Ries, A.C. (Eds) Early Precambrian processes. Geological Society of London Special Publications, London, pp. 243–269.

Cox, R., Lowe, D.R., Cullers, R.L., 1995. The influence of sediment recycling and basement composition on evolution of mud rock chemistry in south–western United States. Geochemica Cosmochem. Acta 59, 2919–2940.

Crockett, R.N., 1972. The Transvaal System in Botswana: its geotectonic and depositional environment and special problems. Trans. Geol. Soc. South Africa 75, 275–292.

Crow, C., Condie, K., 1988. Geochemistry and origin of late Archaean volcanic rocks from the Rhenosterhoek Formation, Dominion Group, South Africa. Precambrian Res. 42, 19–37.

Crusius, J., Calvert, S., Pedersen, T., Sage, D., 1996. Rhenium and molybdenum enrichments in sediments as indicators of oxic, suboxic and sulfidic conditions of deposition. Earth Planet. Sci. Lett. 145, 65–78.

Cullers, R.L., 2002. Implications of elemental concentrations for provenance, redox conditions, and metamorphic studies of shales and limestones near Pueblo, CO, USA. Chem. Geol. 191, 305–327.

Cullers, R.L., Kilbane, N., Koch, R., 1979. Rare–earth in size fractions and sedimentary rocks of Pennsylvanian–Permian age from the mid–continent of the USA. Geochim. Cosmochim. Acta 43, 1285–1301.

Curtis, C.D., Hughes, C.R., Whiteman, J.A., Whittle, C.K., 1985. Compositional variation within some sedimentary chlorite and some comments on their origin. Mineral. Mag. 49, 375–386.

Danchin, R., 1967. Chromium and nickel in the Fig Trees shale from South Africa. Science 156, 261–262.

Day, J.M.D., Pearson, D.G., Hulbert, L.J., 2008. Rhenium–Osmium isotope and platinum–group element constraints on the origin and evolution of the 1.27 Ga Muskox layered intrusion. J. Petrol. 49, 1255–1295.

de Bever, N., 1997. An overview of the early – Proterozoic, auriferous Black Reef placer in the Transvaal Basin. Rhodes University.

de Caritat, P., Hutcheon, I., Walshe, J.L., 1993. Chlorite geothermometry: A review. Clay Miner. 41, 219–239.

de Kock, M., 2007. Palaeomagnetism of selected Neoarchaean–Palaeoproterozoic cover sequences on the Kaapvaal craton and implications for Vaalbara. University of Johannesburg.

de Ronde, C.E.J., de Wit, M.J., 1994. The tectonothermal evolution of the Barberton Greenstone Belt, South Africa: 490 million years of crustal evolution. Tectonics 13, 983–1005.

de Ronde, C.E.J., Kamo, S.L., Davis, D.W., de Wit, M.J., Spooner, E.T.C., 1991. Field, geochemical, and U–Pb isotopic constraints from hypabyssal felsic intrusion within the Barberton Greenstone Belt, South Africa: implications for tectonics and the timing of gold mineralization. Precambrian Res. 49, 261–280.

de Wit, M.J., 1982. Gliding and over–thrust nappe tectonics in the Barberton Greenstone Belt. J. Struct. Geol. 4, 117–136.

de Wit, M., 1992. Formation of an Archaean continent. Nature 357, 553–562.

Deer, W.A., Howie, R.A., Zussman, Z., 1962. Rock–Forming Minerals: Ortho– and Ring Silicates, 1st edition. Longman, pp. 11–270.

Deer, W.A., Howie, R.A., Zussman, J., 1983. Introduction to rock forming minerals. Wiley and Sons, New York, pp. 17–40.

Deer, W.A., Howie, R.A., Zussman, J., 2009. Layered silicates excluding micas and clay minerals. Geol. Soc. London, pp. 3–314.

Depiné, M., Frimmel, H.E., Emsbo, P., Koenig, A.E., Kern, M., 2013. Trace element distribution in uraninite from Mesoarchaean Witwatersrand conglomerates (South Africa) supports placer model and magmatogenic source. Miner. Depos. 48, 423–435.

Diener, J.F.A., Stevens, G., Kisters, A.F.M., Poujol, M., 2005. Metamorphism and exhumation of the basal parts of the Barberton Greenstone Belt, South Africa: Constraining the rates of Mesoarchaean tectonism. Precambrian Res. 143, 87–112.

Dirks, P.H.G.M., Charlesworth, E.G., Munyai, M.R., 2009. Cratonic extension and Archaean gold mineralisation in the Sheba–Fairview mine, Barberton Greenstone Belt, South Africa. South African J. Geol. 112, 291–316.

Dorland, H., 1999. Palaeoproterozoic laterite, red beds and ironstone of the Pretoria Group with reference to the history of atmospheric oxygen. University of Johannesburg.

Dowd, P.A., 1982. Lognormal Kriging – The General Case. Math. Geol. 14, 475–495.

Drennan, G.R., Robb, L.J., 2006. The nature of hydrocarbons and related fluids in the Witwatersrand basin, South Africa: Their role in metal redistribution: Geological Society of America Special Papers, 405, 353−385.

Dupré, B., Gaillardet. J, Rousseau, D., Allégre, C., 1996. Major and trace elements of river–borne material: The Congo basin. Geochemica Cosmochem. Acta 60, 1301–1321.

Dyar, M.D., Guidotti, C. V, Harper, G.D., McKibben, M.A., Saccocia, P.J., 1992. Controls on ferric iron in chlorite. Geol. Soc. Am. Bull. 24, 130.

Dziggel, A., Stevens, G., Poujol, M., Anhaeusser, C.R., Armstrong, R.A., 2002. Metamorphism of the granite–greenstone terrane south of the Barberton Greenstone Belt, South Africa: An insight into the tectono–thermal evolution of the ‘lower’ portions of the Onverwacht Group. Precambrian Res. 114, 221–247.

Dziggel, A., Otto, A., Kisters, A.F.M., Meyer, F.M., 2007. Tectonometamorphic controls on Archaean gold mineralisation in the Barberton Greenstone Belt, South Africa: An example from the New Consort Gold Mine. In: van Kranendonk, M.J., Smithies, R.H., Vickie, C. (Eds) Developments in Precambrian Geology. Earth’s Oldest Rocks. Development in Precambrian Geology, pp. 699–727.

Dziggel, A., Poujol, M., Otto, A., Kisters, A.F.M., Trieloff, M., Schwarz, W.H., Meyer, F.M., 2010. New U–Pb and 40Ar/39Ar ages from the northern margin of the Barberton Greenstone Belt, South Africa: Implications for the formation of Mesoarchaean gold deposits: Precambrian Research, 179, 206−220.

Eales, H. V., Cawthorn, R., 1996. The Bushveld Complex. In: Layered intrusions. Elsevier, Amsterdam, pp. 181–229.

Els, B.G., van den Berg, W.A., Mayer, J.J., 1995. The Black Reef Quartzite Formation in the western Transvaal: sedimentological and economic aspects, and significance for basin evolution. Miner. Depos. 30, 112–123.

Elston, W.E., 1992. Does the Bushveld-Vredefort system (South Africa) record the largest known terrestrial impact catastrophe? [abs.] In: Abstracts submitted to the International Conference on Large Meteorite Impacts and Planetary Evolution, Lunar and Planetary Institute Contribution 790, 23–24

Ely, J.C., Neal, C.R., O'Neill, J.A., Jain, J.C., 1999. Quantifying the platinum group elements (PGEs) and gold in geological samples using cation exchange pre–treatment and ultrasonic nebulisation inductively coupled plasma–mass spectrometry (USN–ICP–MS). Chem. Geol. 157, 219–234.

Engelbrecht, J.., 1986. Die Bosveld Kompleks en sy vloergesteentes in die omgewing van Nietverdiend, Wes–Transvaal. University of Pretoria, South Africa.

England, G.L., Rasmussen, B., Krapež, B., Groves, D.I., 2002. Palaeoenvironmental significance of rounded pyrite in siliciclastic sequences of the Late Archaean Witwatersrand basin: Oxygen–deficient atmosphere or hydrothermal evolution: Sedimentology 49, 1122−1156.

Eriksson, K.A., 1972. Cyclic sedimentation in the Malmani Dolomite, Potchefstroom Synclinorium. Trans. Geol. Soc. South Africa 75, 85–97.

Eriksson, K.A., 1979. Marginal marine depositional processes from the Archaean Moodies Group, Barberton Mountain Land, South Africa: Evidence and significance. Precambrian Res. 8, 153–182.

Eriksson, K.A., 1980a. Hydrodynamic and palaeogeographic interpretation of turbidite deposits from the Archaean Fig Tree Group of the Barberton Mountain Land, South Africa. Bull. Geol. Soc. Am. 91, 21–26.

Eriksson, K.A., 1980b. Transitional sedimentation styles in the Moodies and Fig Tree groups, Barberton Mountain Land, South Africa: Evidence favouring an Archaean continental margin. Precambrian Res. 12, 141–160.

Eriksson, K.A., Truswell, J., 1974. Stratotypes from the Malmani Subgroup north–west of Johannesburg, South Africa. Trans. Geol. Soc. South Africa 77, 211–222.

Eriksson, K. A., Turner, B. R., Vos, R.G., 1981. Evidence of tidal processes from the lower part of the Witwatersrand Supergroup, South Africa. Sediment. Geol. 29, 309–325.

Eriksson, P.G., Van Der Merwe, R., Bumby, A.J., 1998. The Palaeoproterozoic Woodlands Formation of eastern Botswana–north–western South Africa: Lithostratigraphy and relationship with Transvaal Basin inversion structures. J. African Earth Sci. 27, 349–358.

Eriksson, P.G., Altermann, W., Catuneanu, O., Van der Merwe, R., Bumby, A.J., 2001. Major influences on the evolution of the 2.67–2.1 Ga Transvaal basin, Kaapvaal craton. Sediment. Geol. 141–142, 205–231.

Eriksson, P.G., Altermann, W., Hartzer, F., 2006. The Transvaal Supergroup and its precursors. In: Johnson, M.R., Anhaeusser, C.R., Thomas, R. (Eds) The Geology of South Africa. Geological Society of South Africa and Council of Geoscience, Pretoria, pp. 237–260.

Fagereng, Å., Cooper, A.F., 2010. The metamorphic history of rocks buried, accreted and exhumed in an accretionary prism: an example from the Otago Schist, New Zealand. J. Metamorph. Geol. 28, 935–954.

Falkner, K.K., Edmond, J.M., 1990. Gold in seawater. Earth Planet. Sci. Lett.98, 208–221.

Fan, D., Yang, X., Wang, Y., Chen, N., 1973. Petrological and geochemical characteristics of a nickel–molybdenum multi-element bearing Lower Cambrian black shale from a certain district in south China. Geochemica Cosmochem. Acta 3, 143–163.

Farquhar, J., Wing, B.A., 2003. Multiple sulfur isotopes and the evolution of the atmosphere. Earth Planet. Sci. Lett. 213, 1–13.

Farquhar, J., Bao, H., Thiemens, M., 2000. Atmospheric Influence of Earth's Earliest Sulfur Cycle. Science 289, 756–758.

Farquhar, J., Cliff, J., Zerkle, A.L., Kamyshny, A., Poulton, S.W., Claire, M., Adams, D., Harms, B., 2013. Pathways for Neoarchaean pyrite formation constrained by mass–independent sulfur isotopes. Proc. Natl. Acad. Sci. 110, 17638–17643.

Feather, C.E., Koen, G.M., 1975. Mineralogy of the Witwatersrand Reefs. Miner. Sci. Eng. 7, 198–224.

Fedo, C.M., Eriksson, K.A., Krogstad, E.J., 1996. Geochemistry of shales from the Archaean (~3.0 Ga) Buhwa Greenstone Belt, Zimbabwe: Implications for provenance and source–area weathering. Geochim. Cosmochim. Acta 60, 1751–1763.

Feng, R., Kerrich, R., 1990. Geochemistry of fine grained clastic sediments in the Archaean Abitibi Greenstone Belt, Canada. Implication for provenance and tectonic setting. Geochemica Cosmochem. Acta 54, 1061–1081.

Fleet, M.E., Tronnes, R.G., Stone, W.E., 1991. Partitioning of platinum group elements in the Fe–O–S system to 11 GPA and their fractionation in the mantle and meteorites. J. Geophys. Res. Solid Earth 96, 21949–21958.

Floyd, P.A., Leveridge, B.E., 1987. Tectonic environment of the Devonian Gramscatho basin, south Cornwall: framework, mode and geochemical evidence from turbiditic sandstones. J. Geol. Soc. London. 144, 531–542.

Foster, M., 1962. Interpretation of the composition and a classification of the chlorite. Geol. Surv. Canada 414.

Fralich, P., Carter, J.E., 2011. Neoarchaean deep marine palaeo–temperature: evidence from turbidite successions. Precambrian Research 191, 78– 84.

Frey, M., 1988. On the metallogenesis of gold–uranium palaeoplacers in the Black Reef Formation of the Transvaal Supergroup, South Africa. University of Cologne.

Frey, M., Germs, G.J., 1986. Some sedimentological and mineralogical observations on the conglomerates of the Black Reef Formation–Transvaal Supergroup, South Africa. In: Geocongress '86. University of the Witwatersrand, Johannesburg, pp. 993–995.

Frey, M., Germs, G.J.B., Oberthür, T., Saager, R., 1991. Textural and compositional characteristics of gold, sulfides and tourmaline in the Black Reef palaeoplacer, Transvaal sequence, South Africa, Internal Research Report. Cologne.

Frey, M., Robinson, D., 1999. Low–grade metamorphism. Blackwell science, London.

Frimmel, H.E., 1994. Metamorphism of Witwatersrand gold. Explore. Min. Geol. 357–370.

Frimmel, H.E., 1996. Witwatersrand iron formations and their significance to gold genesis and the composition limits of orthoamphibole. Mineral. Petrol. 56, 273–295.

Frimmel, H.E., 1997. Chlorite Thermometry in the Witwatersrand Basin: constraints on the Palaeoproterozoic geotherm in the Kaapvaal Craton, South Africa. J. Geol. 105, 601–616.

Frimmel, H.E., 2005. Archaean atmospheric evolution: Evidence from the Witwatersrand goldfields, South Africa. Earth–Science Rev. 70, 1–46.

Frimmel, H.E., 2008. Earth's continental crustal gold endowment. Earth Planet. Sci. Lett. 267, 45–55.

Frimmel, H.E., 2014. A giant Mesoarchaean crustal gold–enrichment episode: Possible causes and consequences for exploration. Soc. Econ. Geol. Spec. Publ. 18, 209–234.

Frimmel, H.E., 2015. Onset of crustal gold cycle triggered by first oxygenic photosynthesis. In: Andre-Mayer, A.-S. (Eds) Mineral Resources in a Sustainable World, Proc. 13th Biennial SGA Meeting, 24–27 August 2015, Nancy, Univ. de Lorraine, France.

Frimmel, H.E., Gartz, V.H., 1997. Witwatersrand gold particle chemistry matches model of metamorphosed, hydrothermally altered placer deposits. Miner. Depos. 32, 523–530.

Frimmel, H. E., Minter, W.E., 2002. Recent developments concerning the geological history and genesis of the Witwatersrand gold deposits, South Africa. In: Goldfarb, R. J., Nielsen, R.L. (Eds) Integrated methods for discovery: global exploration in the twenty first century, Society of Economic Geologists Special Publication. Littleton, Society of Economic Geologists, pp. 17–45.

Frimmel, H.E., Hennigh, Q., 2015. First whiffs of atmospheric oxygen triggered onset of crustal gold cycle. Miner. Depos. 50, 5–23.

Frimmel, H.E., Hallbauer, D.K., Gartz, V.H., 1999. Gold mobilizing fluids in the Witwatersrand basin: composition and possible sources. Mineral. Petrol. 66, 55–81.

Frimmel, H.E., Groves, D.I., Kirk, J., Ruiz, J., Chesley, J., Minter, W.E.L., 2005. The formation and preservation of the Witwatersrand goldfields, the largest gold province in the world. In: Hedenquist, J.W., Thomson, J.F.H., Goldfarb, R.J. (Eds) Economic Geology 100th Anniversary Volume. Society of Economic Geologists, Littleton, Colorado, USA, pp. 769–797.

Frimmel, H.E., Zeh, A., Lehmann, B., Hallbauer, D., Frank, W., 2009. Geochemical and geochronological constraints on the nature of the immediate basement next to the Mesoarchaean auriferous Witwatersrand basin, South Africa. J. Petrol. 50, 2187–2220.

Frimmel, H.E., Schedel, S., Brätz, H., 2014. Uraninite chemistry as forensic tool for provenance analysis. Appl. Geochemistry 48, 104–121.

Fuchs, S., Williams–Jones, A.E., Jackson, S.E., Przybylowicz, W.J., 2016b. Metal distribution in pyrobitumen of the Carbon Leader Reef, Witwatersrand Supergroup, South Africa: Evidence for liquid hydrocarbon ore fluids. Chem. Geol. 426, 45–59.

Fuchs, S., Williams–Jones, A.E., Przybylowicz, W.J., 2016a. The origin of the gold and uranium ores of the Black Reef Formation, Transvaal Supergroup, South Africa. Ore Geol. Rev. 72, 149–164.

Fuller, A.O., Camden–Smith, P., Sprague, A.R.G., Waters, D.J., Willis, J., 1981. Geochemical signature of shales from the Witwatersrand Supergroup. S. Afr. J. Sci. 77, 379–381.

Gaillard, F., Scaillet, B., Arndt, N. T. 2011. Atmospheric oxygenation caused by a change in volcanic degassing pressure. Nature 478, 229–232.

Gao, S., Luo, T.C., Zhang, B., Zhang, H., Han, Y., Zhao, Z., Hu, Y.K., 1998. Chemical composition of the continental crust as revealed by studies in East China. Geochim. Cosmochim. Acta 62, 1959–1975.

Gardner, W.D., 1980. Sediment trap dynamics and calibration: a laboratory evaluation. Journal of Marine Research 38, 17–39.

Gartz, V.H., Frimmel, H.E., 1999. Complex metasomatism of an Archaean placer in the Witwatersrand basin, South Africa: The Ventersdorp contact reef – A hydrothermal aquifer? Econ. Geol. 94, 689–706.

Garver, J.I., Royce, P.R., Smick, T.A., 1996. Chromium and nickel in shale of the Taconic foreland; a case study for the provenance of fine–grained sediments with an ultramafic source. J. Sediment. Res. 66, 100–106.

Gauert, C.D.K., Brauns, M., Batchelor, D., Simon, R., 2011. Gold provenance of the Black Reef conglomerate, West and East Rand, South Africa. In Barra, F., Reich, M., Campos, E., Tornos, F. (Eds) Proceedings of the 11th Biennial SGA Meeting: Let's Talk Ore Deposits: Antofagasta, Ediciones Universidad Católica del Norte, 1, 232−234.

Gazulla, M.F., Rodrigo, M., Orduna, M., Gomez, C.M., 2012. Determination of carbon, hydrogen, nitrogen and sulfur in geological materials using elemental analysers. Geostand. Geoanalytical Res. 36, 201–217.

Germs, G.J.B., 1982. A Palaeogeographical study of the Black Reef Formation of the Transvaal Supergroup in the Ventersdorp–Balfour area. J.C.I. — Company Report No. 136.

Gibson, R. L., Wallmach, T., 1995. Low pressure–high temperature metamorphism in the Vredefort dome, South Africa: Anticlockwise pressure–temperature path followed by rapid decompression. J. Geol. 30, 319–331.

Gibson, R. L., Stevens, G., 1998. Regional metamorphism due to anorogenic intracratonic magmatism. What drives Metamorphism and metamorphic Reactions? P.J.O.B. Treloar, P.J. London, Geological Society of London, 121–135.

Gibson R. L., Reimold W. U., Phillips D., and Layer P. W. 2000. $^{40}Ar/^{39}Ar$ constraints on the age of metamorphism in the Witwatersrand Supergroup, Vredefort dome (South Africa). South African J. Geol. 103,157–190.

Glasson, M.J., 1975. Gold distribution and foliation development in lower Proterozoic rocks in central Victoria: bearing on gold mineralisation. University of Melbourne.

Gleeson, C.F., Boyle, R., 1980. Minor and trace element distribution in the heavy minerals of rivers and streams of the Keno Hill District, Yukon Territory. Geol. Surv. Canada 76.

Goldfarb, R.J., Groves, D.I., Gardoll, S.J., 2001. Orogenic gold and geologic time: a global synthesis. Ore Geol. Rev. 18, 1–75.

Goldstein, S.J., Jacobsen, S., 1988. Rare earth elements in river waters. Earth Planet. Sci. Lett. 89, 35–47.

Grant, J.A., 1986. The isocon diagram–a simple solution to Gresens' equation for metasomatic alteration. Econ. Geol. 81, 1976–1982.

Grant, J.A., 2005. Isocon analysis: A brief review of the method and applications. Phys. Chem. Earth, Parts A/B/C 30, 997–1004.

Gray, D.J., Lintern, M.J., Longman, G.D., 1998. Chemistry of gold–humic interactions. Cooperative Research Centre for Landscape Evolution & Mineral Exploration Open File Report, pp. 32.

Gresens, R.L., 1967. Composition–volume relationships of metasomatism. Chem. Geol. 2, 47–65.

Griffin, W.L., Powell, W.J., Pearson, N.J., O'Reilly, S., 2008. Glitter: Data reduction software for laser ablation ICP–MS. In: Sylvester, P. (Eds) Laser Ablation ICP–MS in the Earth Sciences: Current practices and outstanding issue. Mineralogical Association of Canada Short Course Series, Short Course 4, Vancouver, pp. 308–311.

Groenewald, P.B., Grantham, G.H., Watkeys, M.K., 1991. Geological evidence for a Proterozoic to Mesozoic link between south–eastern Africa and Dronning Maud Land, Antarctica. J. Geol. Soc. London. 148, 1115–1123.

Gromet, L.P., Dymek, R.F., Haskin, L.A., Korotev, R., 1984. The North American Shale Composite: its compilation, major and trace element characteristics. Geochemica Cosmochem. Acta 48, 2469–2482.

Groves, D.I., Goldfarb, R.J., Gebre–Mariam, M., Hagemann, S.G., Robert, F., 1998. Orogenic gold deposits: a proposed classification in the context of their crustal distribution and relationship to other gold deposit types. Ore Geol. Rev. 13, 7–27.

Groves, D.I., Condie, K.C., Goldfarb, R.J., Hronsky, J.M.A., Vielreicher, R., 2005. Secular changes in global tectonic processes and their influence on the temporal distribution of gold–bearing mineral deposits. Econ. Geol. 100, 203–224.

Gumsley, A.P., Chamberlain, K.R., Bleeker, W., Söderlund, U., de Kock, M.O., Larsson, E.R., Bekker, A., 2017. Timing and tempo of the Great Oxidation Event. PNAS. 114, 1811–1816.

Gutzmer, J., Beukes, N.J., 1998. Earliest laterites and possible evidence for terrestrial vegetation in the Early Proterozoic. Geology 26, 263–266.

Guy, B., 2012. Pyrite in the Mesoarchaean Witwatersrand Supergroup, South Africa. PhD thesis, University of Johannesburg, Johannesburg, South Africa.

Guy, B.M., Beukes, N.J., Gutzmer, J., 2010. Palaeoenvironmental controls on the texture and chemical composition of pyrite from non–conglomeratic sedimentary rocks of the Mesoarchaean Witwatersrand Supergroup, South Africa. South African J. Geol. 113, 195–228.

Hall, G.E.M., Bonham–Carter, G.F., 1988. Review of methods to determine gold, platinum and palladium in production–oriented geochemical laboratories, with application of a statistical procedure to test for bias. J. Geochemical Explor. 30, 255–286.

Hall, G.E.M., Vaive, J.E., Coope, J.A., Weiland, E.F., 1989. Bias in the analysis of geological materials for gold using current methods. J. Geochemical Explor. 34, 157–171.

Hallbauer, D.K., 1975. The plant origin of Witwatersrand carbon: Minerals Science and Engineering 7, 111−131.

Hallbauer, D.K., 1986. The mineralogy and geochemistry of the Witwatersrand pyrite, gold, uraninite and carbonaceous matter. In: Anhaeusser, C.R., Maske, S. (Eds) Mineral deposits of southern Africa. Geological Society of South Africa, pp. 731–752.

Hallbauer, D.K., Joughin, N., 1972. An investigation into the distribution, size and shape of gold particles in some Witwatersrand reefs and their effects on sampling procedures. Chamb. mines 43.

Hallbauer, D., Barton, J., 1987. The fossil gold placers of the Witwatersrand. Gold Bull. 20, 68–79.

Harnois, L., 1988. The CIW index: A new chemical index of weathering. Sediment. Geol. 55, 319–322.

Hartnady, C.J.H., Joubert, P., Stowe, C., 1985. Proterozoic crustal evolution in south–western Africa. Episodes 8, 236–244.

Hartnady, C.J.H., 2009. South Africa's gold production and reserves. S. Afr. J. Sci. 105, 328–329.

Heinrich, C.A., 2015. Witwatersrand gold deposits formed by volcanic rain, anoxic rivers and Archaean life. Nat. Geosci. 8, 206–209.

Heinrichs, T., 1980. Lithostratigraphic investigations in the Fig Tree group of the Barberton Greenstone Belt between Umsoli and Lomati, South Africa. Gottinger Arb. Geol., Pal'dontol 22, 118.

Helz, G.R., Miller C.V., Charnock, J.M., Mosselmans, J.F.W., Patrick, R.A.D., Garner, C.D., Vaughan, D., 1996. Mechanisms of molybdenum removal from the sea and its concentration in black shales: EXAFS evidence. Geochim. Cosmochim. Acta 60, 3631–3642.

Hemming, S.R., McLennan, S.M., Hanson, G.N., 1995. Geochemical and Nd/Pb isotopic evidence for the provenance of the Early Proterozoic Virginia Formation, Minnesota. Implications for the tectonic setting of the Animikie Basin. J. Geol. 103, 147–168.

Henderson, P., 1985. Inorganic geochemistry. Moscow, Mir 277.

Herzberg, C., Condie, K., Korenaga, J., 2010. Thermal history of the Earth and its petrological expression. Earth Planet. Sci. Lett. 292, 79–89.

Heubeck, C., Lowe, D.R., 1994a. Late syndepositional deformation and detachment tectonics in the Barberton Greenstone Belt, South Africa. Tectonics 13, 1514–1536.

Heubeck, C., Lowe, D.R., 1994b. Depositional and tectonic setting of the Archaean Moodies Group, Barberton Greenstone Belt, South Africa. Precambrian Res. 68, 257–290.

Heubeck, C., Engelhardt, J., Byerly, G.R., Zeh, A., Sell, B., Luber, T., Lowe, D.R., 2013. Timing of deposition and deformation of the Moodies Group (Barberton Greenstone Belt, South Africa): Very–high–resolution of Archaean surface processes. Precambrian Res. 231, 236–262.

Hey, M.H., 1954. A new review of the chlorite. Mineral. Mag. 30, 277–292.

Hillier, S., Velde, A.B., 1991. Octahedral occupancy and the chemical composition of diagenetic (low–temperature) chlorite. Clay Miner. 26, 149–168.

Hirst, D.M., 1974. Geochemistry of sediments from eleven Black Sea cores. In: Degens, E.T., Ross, D. (Eds) The Black Sea: Geology, Chemistry, and Biology. American Association of Petroleum Geologists Memoir, Tulsa, Oklahoma, pp. 430–455.

Hofmann, A., 2005. The geochemistry of sedimentary rocks from the Fig Tree Group, Barberton Greenstone Belt: Implications for tectonic, hydrothermal and surface processes during mid–Archaean times. Precambrian Res. 143, 23–49.

Hofmann, A., 2011. Archaean hydrothermal systems in the Barberton Greenstone Belt and their significance as a habitat for early life. In: Golding, S., Glikson, M. (Eds) Earliest life on Earth: Habitats, Environments and Methods of Detection. Springer Verlag, Berlin, pp. 51–78.

Hofmann, A., Bolhar, R., Dirks, P., Jelsma, H., 2003. The Geochemistry of Archaean shales derived from a mafic volcanic sequence, Belingwe Greenstone Belt, Zimbabwe: Provenance, source area unroofing and submarine versus subaerial weathering. Geochim. Cosmochim. Acta 67, 421–440.

Hofmann, A., Bekker, A., Rouxel, O., Rumble, D., Master, S., 2009. Multiple sulfur and iron isotope composition of detrital pyrite in Archaean sedimentary rocks: A new tool for provenance analysis. Earth Planet. Sci. Lett. 286, 436–445.

Hofmann, A., Bolhar, R., Orberger, B., Foucher, F., 2013. Cherts of the Barberton Greenstone Belt, South Africa: Petrology and trace–element geochemistry of 3.5 to 3.3 Ga old silicified volcaniclastic sediments. South African J. Geol. 116, 297–322.

Hofmann, A., Pitcairn, I., Wilson, A., 2017. Gold mobility during Palaeoarchaean submarine alteration. Earth Planet. Sci. Lett. 462, 47–54.

Holdsworth, R., 1996. The petrology, mineralogy and geochemistry of the upper West Rand Group in the Krugersdorp area. Bull. Geol. Surv. South Africa 119, 1–62.

Holland, H.D., 1979. Metals in black shales–a reassessment. Econ. Geol. 74, 1676–1680.

Holland, H.D., 1999. When did the earth's atmosphere become oxic? A reply. Geochemical News 100, 20–22.

Holland, H. D., 2009. Why the atmosphere became oxygenated: A proposal. Geochim. Cosmochim. Acta 73, 5241–5255.

Holland, H.D., Beukes, N.J., 1990. A palaeoweathering profile from Griqualand West, South Africa: evidence for a dramatic rise in atmospheric oxygen between 2.2 and 1.9 Ga. Am. J. Sci. 290 A, 1–34.

Holmes, A., 1937. The Age of the Earth, 3rd ed. Nelson, London.

Honty, M., Clauer, N., Šucha, V., 2008. Rare–earth elemental systematics of mixed–layered illite–smectite from sedimentary and hydrothermal environments of the Western Carpathians (Slovakia). Chem. Geol. 249, 167–190.

Hutchinson, R.W., Viljoen, R.P., 1987. Re–evaluation of gold source in Witwatersrand ores: South African Journal of Geology, 91, 157−173.

Jahn, B.M., Condie, K.C., 1995. Evolution of the Kaapvaal Craton as viewed from geochemical and Sm–Nd isotopic analyses of intracratonic pelites. Geochim. Cosmochim. Acta 59,

Jaun, B., Thauer, R. K., 2007. Nickel and its Surprising Impact in Nature. In: Sigel, A., Sigel, H., Sigel, R.K.O., Metal ions in life sciences. Wiley & Sons, 2, 323–356.

Jiang, W.T., Peacor, D.R., Buseck, P.R., 1994. Chlorite geothermometry? Contamination and apparent octahedral vacancies. Clays Clay Miner. 42, 593–605.

Jowett, E., 1991. Fitting iron and magnesium into the hydrothermal chlorite geothermometer. In: Proceedings of the Program with Abstracts, Geological Association of Canada – Mineralogical Association of Canada, Society of Economic Geologists. p. 62.

Kackstaetter, U., 2014. SEDMIN – Microsoft ExcelTM spreadsheet for calculating fine–grained sedimentary rock mineralogy from bulk geochemical analysis. Cent. Eur. J. Geosci. 6, 170–181.

Kamo, S.L., Davis, D.W., 1994. Reassessment of Archaean crustal development in the Barberton Mountain Land, South Africa, based on U-Pb dating. Tectonics 13, 167–192.

Kamo, S.L., Reimold, W.U., Krogh, T.E., Colliston, W.P., 1996. A 2.023 Ga age for the Vredefort impact event and a first report of shock metamorphosed zircons in pseudotachylitic breccias and granophyre. Earth Planet. Sci. Lett. 144, 369–387.

Kasting, J.F., 1987. Theoretical constraints on oxygen and carbon dioxide concentrations in the Precambrian atmosphere. Precambrian Res. 34, 205–229.

Kasting, J.F., 1993. Earth's early atmosphere. Science 259, 920–926.

Kavalieris, I., Walshe, J.L., Halley, S., Harrold, B.P., 1990. Dome–related gold mineralisation in the Pani Volcanic Complex, north Sulawesi, Indonesia: a study of geologic relations, fluid inclusions, and chlorite compositions. Econ. Geol. 85, 1208–1225.

Keays, R.R., Scott, R.B., 1976. Precious metals in ocean–ridge Basalts: implications for basalts as source rocks for gold mineralisation. Econ. Geol. 71, 705–720.

Ketris, M.P., Yudovich, Y., 2009. Estimations of Clarkes for carbonaceous bioliths: world averages for trace element contents in black shales and coals. Int. J. Coal Geol. 78, 135–148.

Keyser, N., 1998. The Geology and geochemistry of the Ventersdorp Supergroup in the area between Vryburg, Ottosdal and Mafikeng. Geol. Surv. South Africa, 9–33.

Kinloch, E., 1982. Regional trends in the platinum–group mineralogy of the Critical Zone of the Bushveld Complex, South Africa. Econ. Geol. 85, 1328–1347.

Kinnaird, J.A., Hutchinson, D., Schurmann, L., Nex, P.A.M., de Lange, R., 2005. Petrology and mineralisation of the southern Platreef: northern limb of the Bushveld Complex, South Africa. Miner. Depos. 40, 576–597.

Kirk, J., Ruiz, J., Chesley, J., Titley, S., Walshe, J., 2001. A detrital model for the origin of gold and sulfides in the Witwatersrand basin based on Re–Os isotopes: Geochimica et Cosmochimica Acta, v. 65, p. 2149−2159.

Kirk, J., Ruiz, J., Chesley, J., Walshe, J., England, G., 2002. A major Archaean gold and crust–forming event in the Kaapvaal craton, South Africa: Science, 297, 1856−1858.

Kirstein, J., Heubeck, C., Lippold, W., 2010. Incipient basin inversion of the Mesoarchaean Archaean Moodies Basin, Barberton Supergroup, Barberton Greenstone Belt, South Africa. Geophys. Res. Abstr. 12, 545.

Kisch, H., 1987. Correlation between indicators of very low–grade metamorphism. In Frey, M. In: Frey, M. (Eds) Low temperature metamorphism. Blackie, pp. 227–300.

Klein, C., 2005. Some Precambrian banded iron–formations (BIFs) from around the world: their age, geologic setting, mineralogy, metamorphism, geochemistry, and origin. Geol. setting, Mineral. Metamorph. Geochemistry, Orig. American Mineralogist 90, 1473–1499.

Klemd, R., 1999, A comparison of fluids causing post–depositional hydrothermal alteration in Archaean basement granitoids and the Witwatersrand basin: Miner. Pet. 66, 111−122.

Koch, G.S. Jr., Link, R., 1970. Statistical analysis of geological data. John Wiley, New York.

Koglin, N, Frimmel, H. E., Minter, W. E.L., Brätz, H., 2010. Trace element characteristics of different pyrite types in Mesoarchaean to Palaeoproterozoic placer deposits. Miner. Depos. 45, 259–280.

Kohler, E.A., Anhaeusser, C.R., 2002. Geology and geodynamic setting of Archaean silicic metavolcaniclastic rocks of the Bien Venue Formation, Fig Tree Group, north–east Barberton Greenstone Belt, South Africa. Precambrian Res. 116, 199–235.

Konhauser, K.O., Pecoits, E., Lalonde, S.V., Papineau, D., Nisbet, E.G., Barley, M., Arndt, N.T., Zahnle, K., Kamber, B.S., 2009. Oceanic nickel depletion and methanogen famine before the Great Oxidation Event. Nature 458 (7239), 750–754.

Konhauser, K.O., Robbins, L.J., Pecoits, E., Peacock, C., Kappler, A., Lalonde, S.V., 2015. The Archaean nickel famine revisited. Astrobiology 15(10), 804–815.

Koppel, V.H., Saager, R., 1974. Lead isotope evidence on the detrital origin of Witwatersrand pyrites and its bearing on the provenance of the Witwatersrand gold. Econ. Geol. 69, 318–331.

Kositcin, N., Krapež, B., 2004. SHRIMP U–Pb detrital zircon geochronology of the Late Archaean Witwatersrand Basin of South Africa: relation between zircon provenance age spectra and basin evolution. Precambrian Res. 129, 141–168.

Kositcin, N., McNaughton, N.J., Griffin, B.J., Fletcher, I.R., Groves, D.I., Rasmussen, B., 2003. Textural and geochemical discrimination between xenotime of different origin in the Archaean Witwatersrand Basin, South Africa. Geochim. Cosmochim. Acta 67, 709–731.

Kranidiotis, P., MacLean, W., 1987. Systematic of chlorite alteration in the Phelps Dodge massive sulfide deposit, Matagami, Quebec. Econ. Geol. 82, 1898–1911.

Krivovichev, S. V., Armbruster, T., Organova, N.I., Burns, P.C., Seredkin, M. V., Chukanov, N. V., 2004. Incorporation of sodium into the chlorite structure: The crystal structure of glagolevite, $Na(Mg,Al)_6[Si_3AlO_{10}](OH,O)_8$. Am. Mineral. 89, 1138–1141.

Kröner, A., Todt, W., 1988. Single zircon dating constraining the maximum age of the Barberton greenstone belt, southern Africa. J. Geophys. Res. 93, 15329–15337.

Kröner, A., Byerly, G., Lowe, D., 1991. Chronology of early Archaean granite–greenstone evolution in the Barberton Mountain Land, South Africa, based on precise dating by single zircon evaporation. Earth Planet. Sci. Lett. 103, 41–54.

Kruger, F.J., Marsh, J.S., 1985. The mineralogy, petrology, and origin of the Merensky cyclic unit in the western Bushveld Complex. Econ. Geol. 80, 958–974.

Kruger, F.J. 2002. Isotopic constraints on the origin of the Bushveld Complex magmas in a back-arc environment. Geochimica et Cosmochimica Acta 66 (15A): A420-A420 Suppl.1 AUG 2002

Kuenen, P., 1963. Turbidites in South Africa. Trans. Geol. Soc. South Africa 66, 191–195.

Kumar, A., Rout, S., Narayanan, U., Mishra, M.K., Tripathi, R.M., Singh, J., Kumar, S., Kushwaha, H.S., 2011. Geochemical modelling of uranium speciation in the subsurface aquatic environment of Punjab State in India. J. Geol. Min. Res. 3, 137–146.

Lamb, S.H., Paris, I., 1988. Post–Onverwacht Group stratigraphy in the south–east part of the Archaean Barberton greenstone belt. J. African Earth Sci. 7, 285–306.

Langmuir, D., 1997. Aqueous environmental geochemistry, Eos, Transactions American Geophysical Union. Prentice Hall, New Jersey.

Large, R.R., Maslennikov, V.V., Robert, F., Danyushevsky, L.V., Chang, Z., 2007. Multistage sedimentary and metamorphic origin of pyrite and gold in the Giant Sukhoi Log deposit, Lena Gold Province, Russia. Econ. Geol.102, 1233–1267.

Large, R.R., Bull, S.W., Maslennikov, V., 2011. A carbonaceous sedimentary source rock model for Carlin–type and orogenic gold deposits. Econ. Geol. 106, 331–358.

Large, R.R., Meffre, S., Burnett, R., Guy, B., Bull, S., Gilbert, S., Goemann, K., Danyushevsky, L., 2013. Evidence for an intrabasinal source and multiple concentration processes in the

formation of the carbon leader reef, Witwatersrand Supergroup, South Africa. Econ. Geol.108, 1215–1241.

Large, R.R., Halpin, J.A., Danyushevsky, L.V., Maslennikov, V.V., Bull, S.W., Long, J.A., Gregory, D.D., Lounejeva, E., Lyons, T.W., Sack, P.J., McGoldrick, P.J., Calver, C.R., 2014. Trace element content of sedimentary pyrite as a new proxy for deep–time ocean–atmosphere evolution. Earth Planet. Sci. Lett. 389, 209–220.

Large, R.R., Gregory, D.D., Steadman, J.A., Tomkins, A.G., Lounejeva, E., Danyushevsky, L.V., Halpin, J.A., Maslennikov, V., Sack, P.J., Mukherjee, I., Berry, R., Hickman, A., 2015. Gold in the oceans through time. Earth Planet. Sci. Lett. 428, 139–150.

Lauder, W.R., 1970. The formation of the Merensky Reef. Nature 227, 365–366.

Lay, T., Hernlund, J., Buffett, B.A., 2009. Core–mantle boundary heat flow. Nat. Geosci. 1, 25–32.

Layer, P., Kroner, A., McWilliams, M., 1996. An Archaean Geomagnetic Reversal in the Kaap Valley Pluton, South Africa. Science (80). 273, 943–946.

Lehmann, B., Nägler, T.F., Holland, H.D., Wille, M., Mao, J., Pan, J., Ma, D., Dulski, P., 2007. Highly metalliferous carbonaceous shale and Early Cambrian seawater. Geology 35, 403–406.

Leitch, A.M., 2004. Archaean Plate Tectonics. American Geophysical Union Spring Meeting.

Lenhardt, N., Eriksson, P.G., Catuneanu, O., Bumby, A.J., 2012. Nature of and controls on volcanism in the ca. 2.32–2.06 Ga Pretoria Group, Transvaal Supergroup, Kaapvaal Craton, South Africa. Precambrian Res. 214–215, 106–123.

Lepage, L.D., 2003. ILMAT: An Excel worksheet for ilmenite–magnetite geothermometry and geobarometry. Comput. Geosci. 29, 673–678.

Loen, J., 1992. Mass balance constraints on gold placers: possible solutions to ‘source area problems’. Econ. Geol. 87, 1624–1634.

Lott, D.A., Coveney, R.M., Jr., Murowchick, J., 1999. Sedimentary exhalative nickel–molybdenum ores in South China. Econ. Geol. 94, 1051–1066.

Lötter, S., 2014. Analysis of zirconium–containing materials using multiple digestion and spectrometric techniques. University of Free State, pp. 1–239.

Lowe, D.R., 1991. Geology of the Barberton Greenstone Belt: An Overview, In Two cratons and an orogen– excursion guidebook and review articles for a field workshop through selected Archaean terranes of Swaziland, South Africa, and Zimbabwe. In: IGCP Project 280, Dept. of Geology, Univ. Witwatersrand, Johannesburg, South Africa, pp. 47–58.

Lowe, D.R., 1994. Early environments: Constraints and opportunities for early evolution: In Bengtson, S. (Eds) Early Life on Earth, Nobel Symposium 84. New York, Columbia University Press, 24–35.

Lowe, D.R., Byerly, G.R., 1999. Stratigraphy of the west–central part of the Barberton Greenstone Belt, South Africa. In: Geological Society of America Special Paper 329, Boulder, Colorado, pp. 1–36.

Lowe, D.R., Nocita, B.W., 1999. Foreland basin sedimentation in the Mapepe Formation, southern–facies Fig Tree Group: In: Lowe, D.R., Byerly, G.R (Eds) Geologic Evolution of the Barberton Greenstone Belt, South Africa: Geological Society of America Special Paper, 329, 233–258.

Lowe, D.R., Byerly, G.R., 2007. An overview of the geology of the Barberton Greenstone Belt and vicinity: Implications for early crustal development. In: van Kranendonk, M.J., Smithies, R.H., Vickie, C. (Eds) Earth's oldest rocks. Developments in Precambrian Geology, pp. 481–526.

Loyd, S.J., Becker, T.W., Conrad, C.P., Lithgow–Bertelloni, C., Corsetti, F.A., 2007. Time variability in Cenozoic reconstructions of mantle heat flow: plate tectonic cycles and implications for Earth's thermal evolution. Proc. Natl. Acad. Sci. U.S.A. 104, 14, 266–271.

Lyons, T.W., Reinhard, C.T., Planavsky, N., 2014. The rise of oxygen in Earth's early ocean and atmosphere. Nature 506, 307–15.

Malitch, K.N., Merkle, R.K.W., 2004. Ru–Os–Ir–Pt AND Pt–Fe alloys from the Evander goldfield, Witwatersrand Basin, South Africa: Detrital origin inferred from compositional and Osmium-isotope data. The Canadian Mineralogist 42, 631–650.

Marin–Carbonne, J., Rollion–Bard, C., Bekker, A., Rouxel, O., Agangi, A., Cavalazzi, B., Wohlgemuth–Ueberwasser, C.C., Hofmann, A., McKeegan, K., 2014. Couple Fe and Ws isotope variations in pyrite nodules from Archaean shale. Earth Planet. Sci. Lett. 392, 67–79.

Martínez–Serrano, R.G., Dubois, M., 1998. Chemical variation in chlorite at the Los Humeros geothermal system, Mexico. Clay Miner. 46, 615–628.

Maynard, J.B., Sutton, S.J., Rumble, D., Bekker, A., 2013. Mass–independently fractionated sulfur in Archaean palaeosols: A large reservoir of negative $\Delta^{33}S$ anomaly on the early Earth. Chem. Geol. 362, 74–81.

McCarthy, T.S., 2006. The Witwatersrand Supergroup. In: Johnson, M. R., Anhaeusser, C. R., Thomas, R.J. (Eds) The Geology of South Africa. Geological Society of South Africa and Council of Geoscience, Pretoria, pp. 155–186.

McCulloch, M.T., Wasserburg, G.J., 1978. Sm–Nd and Rb–Sr chronology of continental crust formation – time of addition to continents of chemically fractionated mantle–derived materials are determined. Science 200, 1003–1011.

McDaniel, D.K., Hemming, S.R., McLennan, S.M., Hanson, G., 1994. Petrographic, geochemical, and isotopic constraints on the provenance of the early Proterozoic Chelmsford Formation, Sudbury basin, Ontario. J. Sediment. Res. 64, 362–372.

McDonald, I., Harmer, R.E., Holwel., D.A., Hughes, H.S.R., Boyce, A.J., Cu–Ni–PGE mineralisation at the Aurora Project and potential for a new PGE province in the Northern Bushveld Main Zone. Ore Geol. Rev. 80, 1135–1159.

McDonough, W.F., Sun, S., 1995. The composition of the earth. Chem. Geol. 120, 223–253.

McLennan, S.M., 1982. On the geochemical evolution of sedimentary–rocks. Chem. Geol. 37, 335–350.

McLennan, S.M., 1993. Weathering and global denudation. J. Geol. 101, 295–303.

McLennan, S.M., 2001. Relationships between the trace element composition of sedimentary rocks and upper continental crust. Geochemistry, Geophys. Geosystems 2, 1021.

McLennan, S.M., Taylor, S.R., 1982. Geochemical constraints on the growth of the continental crust. J. Geol. 90, 347–361.

McLennan, S.M., Nance, W.B., Taylor, S.R., 1980. Rare earth element–thorium correlations in sedimentary rocks, and the composition of the continental crust. Geochim. Cosmochim. Acta 44, 1833–1839.

McLennan, S.M., Taylor, S.R., Kroner, A., 1983. Geochemical evolution of Archaean shales from South Africa, I. The Swaziland and Pongola supergroups. Precambrian Res. 22, 92–124.

McLennan, S.M., Taylor, S.R., Hemming, S.R., 2006. Composition, differentiation, and evolution of continental crust: constraints from sedimentary rocks and heat flow. In: Brown, M., Rushmer, T. (Eds) Evolution and Differentiation of the continental crust. Cambridge University Press, pp. 92–134.

Meibom, A., Sleep, N.H., Chamberlain, C.P., Coleman, R.G., Frei, R., Hren, M.T., Wooden, J.L., 2002. Re–Os isotopic evidence for long–lived heterogeneity and equilibration processes in the earth's upper mantle. Nature 419, 705–708.

Merriman, R.J., Peacor, D., 1999. Very low–grade metapelites; mineralogy, microfabrics and measuring reaction. In: Frey, M., Robinson, D. (Eds) Low grade metamorphism. Blackwell Sciences Ltd, Oxford, pp. 10–60.

Meyer, M., 1988. Environment of ore formation in the Sabie–Pilgrim's Rest goldfield, South Africa. In: Geocongress '88: Durban. Geological Society of South Africa, pp. 535–540.

Meyer, M., Saager, R., 1985. The gold content of some Archaean rocks and their possible relationship to epigenetic gold–quartz vein deposits. Miner. Depos. 20, 284–289.

Meyers, P.A., Pratt, L.M., Nagy, B., 1992. Introduction to geochemistry of metalliferous black shales. Chem. Geol. 99.

Milodowski, A.E., Zalaskiewics, J., 1991. Redistribution of rare earth elements during diagenesis of turbidite/hemipelagite mudrock sequences of Llandovery age from Central Wales. In: Morton, A.C., et al. (Eds) Developments in Sedimentary provenance studies. Geological Society of London Special Publications, pp. 101–125.

Minter, W.E.L., 1978. A sedimentological synthesis of placer gold, uranium and pyrite concentrations in Proterozoic Witwatersrand sediments. In: Miall, A. (Eds) Fluvial sedimentology. Canadian Society of Petroleum Geologists, pp. 801–829.

Minter, W.E.L., 2006. The sedimentary setting of Witwatersrand placer mineral deposits in an Archaean atmosphere. In: Kessler, S.E, Ohmoto, H. (Eds) Evolution of early earth's atmosphere, hydrosphere and biosphere—Constraints from ore deposits: Geological Society of America, Boulder, Colorado. Memoir 198, p. 105–119.

Minter, W.E.L., Goedhart, M., Knight, J., Frimmel, H.E., 1993. Morphology of Witwatersrand gold grains from the Basal Reef: Evidence for their detrital origin. Econ. Geol. 88, 237–248.

Moazzen, M., 2004. Chlorite–chloritoid–garnet equilibria and geothermometry in the Sanandaj–Sirjan metamorphic belt, southern Iran. Iran. Trans. J. Sci. Technol. 28, 65–78.

Morad, S., Ketzer, J.M., De Ros, L.R., 2000. Spatial and temporal distribution of diagenetic alterations in siliciclastic rocks: Implications for mass transfer in sedimentary basins. Sedimentology 47, 95–120.

Morgan, J. W., 1986. Ultramafic xenoliths; clue to the earth's late accretionary history. Journal of Geophysical Research 91, 12375–12387.

Mossman, D.J., Minter, W.E.L., Dutkiewicz, A., Hallbauer, D.K., George, S.C., Hennigh, Q., Reimer, T.O., Horscroft, F.D., 2008. The indigenous origin of Witwatersrand "carbon": Precambrian Research, 164, 173–186.

Moyen, J.F., Stevens, G., Kisters, A., 2006. Record of mid–Archaean subduction from metamorphism in the Barberton terrain, South Africa. Nature 442, 559–562.

Müller, J., Frimmel, H., 2011. Abscissa–transforming second–order polynomial functions to approximate the unknown historic production of non–renewable resources. Math. Geol. 43, 625–634.

Murowchick, J.B., Coveney, R.M., Jr., Grauch, R.I., Eldridge, C.S., Shelton, K., 1994. Cyclic variations of sulfur isotopes in Cambrian stratabound Ni–Mo–(PGE–Au) ores of southern China. Geochemica Cosmochem. Acta 58, 1813–1823.

Myers, R.E., McCarthy, T.S., Stanistreet, I.G., 1990. A tectono–sedimentary reconstruction of the development and evolution of the Witwatersrand Basin, with particular emphasis on the Central Rand Group. South African J. Geol. 93, 180–201.

Naldrett, A.J., Wilson, A., Kinnaird, J., Chunnett, G., 2009. PGE tenor and metal ratios within and below the Merensky Reef, Bushveld Complex: Implications for its genesis. J. Petrol. 50, 625–659.

Nekrasov, I.Y., 1996. Geochemistry, mineralogy and genesis of gold deposits. Geochemistry, Mineral. Genes. Gold Depos.

Nesbitt, H.W., Young, G.M., 1982. Early Proterozoic climates and plate motions inferred from major element chemistry of lutites. Nature 299, 715–717.

Nesbitt, H.W., Young, G., 1984. Prediction of some weathering trends of plutonic and volcanic rocks based on thermodynamic and kinetic considerations. Geochemica Cosmochem. Acta 48, 1523–1534.

Nesbitt, H.W., Markovics, G., Price, R.G., 1980. Chemical processes affecting alkalis and alkaline earth during continental weathering. Geochim. Cosmochim. Acta 44, 1659–1666.

Nesbitt, B.E., St. Louis, R.M., Muehlenbachs, K., 1987. Distribution of gold in altered basalts of DSDP hole 504B. Can. J. Earth Sci. 24, 201–209.

Nocita, B.W., Lowe, D.R., 1990. Fan–delta sequence in the Archaean Fig Tree Group, Barberton Greenstone Belt, South Africa. Precambrian Res. 48, 375–393.

Nwaila, G., Frimmel, H.E., Minter, W.E.L., 2017. Provenance and geochemical variations in shales of the Mesoarchaean Witwatersrand Supergroup. J. Geol. Accepted.

O'Neill, H. St. C., 1991. The origin and the early history of the Earth—a chemical model. Part 2: The Earth. Geochimica et Cosmochimica Acta 55, 1159–1172.

Obbes, A., 1995. The structure, stratigraphy and sedimentology of the Black Reef–Malmani–Rooihoogte succession of the Transvaal Supergroup, south—west of Pretoria. In: Bulletin No 127. Council for Geoscience. p. 89.

Oberthür, T., 1983. Metallogenetische Überlegungen zur Bildung des Carbon Leader Reef, Carletonville Goldfield, Witwatersrand, Südafrika. Dr. rer. nat. thesis, Universität Köln, Köln, Germany.

Oberthür, T., 1987. Mineralogy and geochemistry of phosphate minerals and brannerite from the Proterozoic Carbon Leader Reef gold and uranium deposit, Witwatersrand, South Africa. Monogr. Ser. Miner. Depos. 27, 129–142.

Ohmoto, H., Kakegawa, T., Lowe, D. R., 1993. 3.4 billion-year-old biogenic pyrites from Barberton, South Africa: Sulfur isotope evidence. Science 262, 555–557.

Ohnemüller, F., Heubeck, C., Kirstein, J., Gamper, A., 2010. A basin on an unstable ground: correlation of the Middle Archaean Moodies Basin, Barberton Greenstone Belt, South Africa. Geophys. Res. Abstr. 12, 5267.

Ono, S., Eigenbrode, J., Pavlov, A.A., Kharecha, P., Rubbmble III, D., Kasting, J.F., Freeman, K.H., 2003. New insights into Archaean sulfur cycle from mass–independent sulfur isotope records. Earth and Planetary Science Letters 213, 15–30.

Ono, S., Beukes, N.J., Rumble, D., 2009. Origin of two distinct multiple–sulfur isotope compositions of pyrite in the 2.5 Ga Klein Naute Formation, Griqualand West Basin, South Africa. Precambrian Res. 169, 48–57.

Otto, A., Dziggel, A., Kisters, A.F.M., Meyer, F.M., 2007. The New Consort Gold Mine, Barberton Greenstone Belt, South Africa: Orogenic gold mineralisation in a condensed metamorphic profile. Miner. Depos. 42, 715–735.

Palme, H., 2008. Platinum–group elements in cosmochemistry. Elements 4, 233–238.

Park, J.W., Hu, Z., Gao, S., Campbell, I.H., Gong, H., 2012. Platinum group element abundances in the upper continental crust revisited– new constraints from analyses of Chinese loess. Geochim. Cosmochim. Acta 93, 63–76.

Pašava, J., 1993. Anoxic sediments – an important environment for PGE; An overview. Ore Geol. Rev. 8, 425–445.

Pašava, J., Zaccarini, F., Aiglsperger, T., Vymazalová, A., 2013. Platinum–group elements (PGE) and their principal carriers in metal–rich black shales: An overview with new data

from Mo–Ni–PGE black shales (Zunyi region, Guizhou Province, south China). J. Geosci. 58, 213–220.

Pettijohn, F., 1957. Sedimentary Rocks (2nd ed). Harper and Brothers, New York.

Peucker–Ehrenbrink, B., Jahn, B.M., 2001. Rhenium–osmium isotope systematics and platinum group element concentrations: Loess and the upper continental crust. Geochemistry, Geophys. Geosystems 2.

Phillips, G., 1986. Metamorphism of shales in the Witwatersrand goldfields. Univ. Witwatersrand, Econ. Geol. Res. Unit, Inf. Circ. 192, 1–25.

Phillips, G.N., Myers, R.E., 1989, Witwatersrand goldfields. Part II. An origin for Witwatersrand gold during metamorphism and associated alteration: Econ. Geol. Monograph 6, 598−608.

Phillips, N.G., Law, J.D.M., 1994. Metamorphism of the Witwatersrand gold fields: A review. Ore Geol. Rev. 9, 1–31.

Phillips, G.N., Evans, K., 2004. Role of CO2 in the formation of gold deposits. Nature 429, 860–863.

Phillips, G.N., Powell, R., 2011. Origin of Witwatersrand gold: A metamorphic devolatilisation–hydrothermal replacement model. Transactions of the Institution of Mining and Metallurgy. Appl. Earth Sci. 120, 112–129.

Phillips, G.N., Powell, R., 2014. Hydrothermal alteration in the Witwatersrand goldfields. Ore Geol. Rev. 65, 245–273.

Phillips, G.N., Law, J.D.M., Myers, R., 1990. The role of fluids in the evolution of the Witwatersrand Basin. South African J. Geol. 93, 54–69.

Picard, M., 1971. Classification of fine–grained sedimentary rocks. J. Sediment. Petrol. 41, 179–195.

Pitcairn, I.K., 2010. Source area processes and the distribution of orogenic gold deposits. In: Proc. Goldschmidt Conf., Knoxville, TN, USA, June, the University of Tennessee and Oak Ridge National Laboratory.

Pitcairn, I.K., 2011. Background concentrations of gold in different rock types. Appl. Earth Sci. 120, 31–38.

Pitcairn, I.K., Teagle, D.A.H., Craw, D., Olivo, G.R., Kerrich, R., Brewer, T.S., 2006. Sources of metals and fluids in orogenic gold deposits: Insights from the Otago and Alpine schists, New Zealand. Econ. Geol. 101, 1525–1546.

Pitcairn, I.K., Olivo, G.R., Teagle, D.A.H., Craw, D., 2010. Sulfide evolution during prograde metamorphism of the Otago and Alpine schists, New Zealand. Can. Mineral. 48, 1267–1295.

Plissart, G., Femenias, O., Maruntiu, M., Diot, H., Demaiffe, D., 2009. Mineralogy and geo–thermometry of gabbro–derived listevenites in the Tisovita–Iutu ophiolite, Southwestern Romania. Can. Mineral. 47, 81–105.

Pollack, H.N., 1997. Thermal characteristics of the Archaean. In: de Wit, M.J., Ashwal, M. (Eds) Greenstone Belts. Clarendon Press, Oxford, pp. 223–232.

Potter, P.E., Maynard, J.B., Depetris, P., 2005. Mud and mudstone: Introduction and overview. Springer Verlag, Berlin.

Poujol, M., Robb, L.J., Anhaeusser, C.R., Gericke, B., 2003. A review of the geochronological constraints on the evolution of the Kaapvaal Craton, South Africa. Precambrian Res. 127, 181–213.

Poujol, M., Kiefer, R., Robb, L.J., Anhaeusser, C.R., Armstrong, R.A., 2005. New U–Pb data on zircons from the Amalia Greenstone Belt Southern Africa: Insights into the Neoarchaean evolution of the Kaapvaal Craton. South African J. Geol. 108, 317–332.

Pretorius, D.A., 1981. Gold and uranium in quartz–pebble conglomerates. 75th Anniv. Vol. Econ. Geol. 117–138.

Pretorius, D.A., 1986. The goldfields of the Witwatersrand Basin. In: Anhaeusser, C.R., Maske, S. (Eds) Mineral deposits of southern Africa. Geological Society of South Africa, Johannesburg, pp. 1019–1020.

Puchtel, I., Humayun, M., 2000. Platinum group elements in Kostomuksha komatiites and basalts: implications for oceanic crust recycling and core–mantle interaction. Geochim. Cosmochim. Acta 64, 4227–4242.

Ramdohr, P., 1958. New observations on the ores of Witwatersrand in South Africa and their genetic significance. Transvaal Geol. Soc. South Africa, Annex. 61, 1–50.

Rasmussen, B., Fletcher, I.R., Muhling, J.R., Mueller, A.G., Hall, G.C., 2007. Bushveld–aged fluid flow, peak metamorphism, and gold mobilisation in the Witwatersrand basin, South Africa: constraints from in situ SHRIMP U–Pb dating of monazite and xenotime. Geology 35, 931–934.

Ravizza, G., Pyle, D., 1997. PGE and Os isotopic analyses of single sample aliquots with NiS fire assay preconcentration. Chem. Geol. 141, 251–268.

Reichhardt, F.J., 1994. The Molopo Farms Complex, Botswana: history, stratigraphy, petrography, petrochemistry and Ni–Cu–PGE mineralisation. Explor. Min. Geol. 3, 263–284.

Reimer, T., 1983. Accretionary lapilli and other spherical rocks from the Archaean Swaziland Supergroup, Barberton Mountain Land, South Africa. In: Peryt, T. (Eds) Coated Grains. Springer Verlag, Berlin, pp. 619–634.

Reimold, W., 2002. Mineralisation associated with impact structures, with special reference to the Vredefort–Witwatersrand system. In: Presidential Address, Geocongress 2002 and 11th Quadriennial Meeting of the International Association for the Genesis of Ore Deposits, Windhoek, Namibia, July 2002, CD–ROM. pp. 2–3.

Revel, M.E., Ducassou, E., Skonieczny, C., Colin, C., Bastian, L., Bosch, D., Migeon, S., Mascle, J., 2015. 20,000 years of Nile River dynamics and environmental changes in the Nile catchment area as inferred from Nile upper continental slope sediments. Quat. Sci. Rev. 130, 200–221.

Rickard, A., Luther III, G.W., 2006. Metal sulfide complexes and clusters. In: Vaughan, D.J. (Eds) Sulfide Mineralogy and Geochemistry. Rev. Min., 61, 421–504.

Robb, L.J., Meyer, F.M., 1990. The nature of the Witwatersrand hinterland: conjectures on the source area problem. Econ. Geol. 85, 511–536.

Robb, L.J., Meyer, F.M., 1995. The Witwatersrand Basin, South Africa: Geological framework and mineralisation processes. Ore Geol. Rev. 10, 67–94.

Robb, L.J., Meyer, F.M., Ferraz, M.F., Drennan, G.K., 1990. The distribution of radioelements in Archaean granites of the Kaapvaal Craton, with implications for the source of uranium in the Witwatersrand Basin. S. Afr. J. Geol. 93, 5–40.

Robb, L.J., Davis, D., Kamo, S.L., Meyer, F.M., 1992. Ages of altered granites adjoining the Witwatersrand basin with implications for the origin of gold and uranium. Nature, 357, 677−680.

Robb, L.J., Robb, V.M., 1998. Gold in the Witwatersrand basin. In: Wilson, M.G.C., Anhaeusser, C.R. (Eds) The mineral resources of South Africa, 16: Pretoria, Council for Geoscience, 294−349.

Rollinson, H.., 1993. Using geochemical data: Evaluation, presentation, interpretation. Longman, London.

Rollinson, H.R., 2007. Early Earth System: A geochemical approach. Blackwell Publishing.

Rose, D., Viljoen, F., Knoper, M., Rajesh, H., 2011. Detailed assessment of platinum group minerals associated with chromitite stringers in the Merensky Reef of the eastern Bushveld Complex, South Africa. Can. Mineral. 49, 1385–1396.

Rudnick, R.L., Gao, S., 2005. 3.01 – Composition of the continental crust. In: Rudnick, R. (Eds) Treatise on Geochemistry. Elsevier, Amsterdam, pp. 1–64.

Ruiz Cruz, M.D., Nieto, J.M., 2006. Chemical and structural evolution of “metamorphic vermiculite” in metaclastic rocks of the Betic Cordillera, Ma´ laga, Spain: A synthesis. Can. Mineral. 44, 249–265.

Saager, R., 1970. Structures in pyrite from the Basal Reef in the Orange Free State goldfield. Trans. Geol. Soc. S. Afr. 73, 29–46.

Saager, R., Meyer, M., 1984. Gold distribution in Archaean granitoids and supracrustal rocks from South Africa: a comparison. In: Foster, R.P. (Eds) Gold. Geol. Soc. Zimbabwe Spec. Pub. 1, Rotterdam, Balkema, pp. 53–70.

SACS (South African Committee for Stratigraphy), 1980. Stratigraphy of South Africa. Pt. 1 (Comp. L.E. Kent), Lithostratigraphy of South Africa, South West Africa/Namibia and the Republics of Boputhatswana, Transkei and Venda. Geol. Surv. South Africa 8, 690.

SACS (South African Committee for Stratigraphy), 2006. A revised stratigraphic framework for the Witwatersrand Supergroup. Counc. Geosci. Lithostratigr. Ser. 42, 1–7.

Sanchez–Garrido, C.J.M.G., Stevens, G., Armstrong, R.A., Moyen, J.F., Martin, H., Doucelance, R., 2011. Diversity in earth's early felsic crust: Palaeoarchaean peraluminous granites of the Barberton Greenstone Belt. Geology 39, 963–966.

Schaefer, B.F., Pearson, D.G., Rogers, N.W., Barnicoat, A.C., 2010. Re–Os isotope and PGE constraints on the timing and origin of gold mineralisation in the Witwatersrand basin. Chem. Geol. 276, 88−94.

Schaltegger, U., 1993. Nd, Sr and Ar isotopic dating of diagenesis and low–grade metamorphism of argillaceous sediments. GSA Abstr. 25, A34.

Schidlowski, M., 1981. Uraniferous constituents of the Witwatersrand conglomerates: Ore–microscopic observations and implications for the Witwatersrand metallogeny. U.S. Geol. Surv. Prof. Pap. 1161–N, 1–23.

Schmidt, G., Palme, H., Kratz, K.L., Kurat, G., 2000. Are highly siderophile elements (PGE, Re and Au) fractionated in the upper mantle of the earth? New results on peridotites from Zabargad. Chem. Geol. 163, 167–188.

Schmidt, G., Witt–Eickschen, G., Palme, H., Seck, H., Spettel, B., Kratz, K.L., 2003. Highly siderophile elements (PGE, Re and Au) in mantle xenoliths from the West Eifel volcanic field (Germany). Chem. Geol. 196, 77–105.

Schneiderhan, E., Zimmermann, U., Gutzmer, J., Mezger, K., Armstrong, R., 2011. Sedimentary Provenance of the Neoarchaean Ventersdorp Supergroup, Southern Africa: Shedding light on the Evolution of the Kaapvaal Craton during the Neoarchaean. J. Geol. 119, 575–596.

Schoene, B., Dudas, F.O.L., Bowring, S.A., de Wit, M., 2009. Sm–Nd isotopic mapping of lithospheric growth and stabilisation in the eastern Kaapvaal craton. Terra Nov. 21, 219–228.

Schreiber, U.M., 1991. A palaeoenvironmental study of the Pretoria Group in the eastern Transvaal. University of Pretoria.

Schreiber, U.M., Eriksson, P.G., Snyman, C.P., 1991. A provenance study of the sandstones of the Pretoria Group, Transvaal Sequence (South Africa): petrography, geochemistry, and palaeocurrent directions. South African J. Geol. 94, 288–298.

Schubert, G., Turcotte, D.L., Olson, P., 2001. Mantle convection in the earth and planets. Cambridge University Press, Cambridge, 940.

Schulz–Rojahn, J.P., Phillips, S.E., 1989. Diagenetic alteration of Permian reservoir sandstones in the Nappamerri Trough and adjacent areas, southern Cooper Basin. Aust. Pet. Explor. Assoc. J. 29, 629–646.

Schwartz, G.M., 1944. The host minerals of native gold. Econ. Geol. 39, 371–411.

Schweigart, H., von Rahden, H.O., 1965. Oolithische strukturen in pyriten des Ventersdorp Contact Reef, Südafrika. Geol. Rundsch. 54, 1143–1148.

Scoates, J.S., Friedman, R.M., 2008. Precise age of the platiniferous Merensky Reef, Bushveld Complex, South Africa, by the U–Pb zircon chemical abrasion ID–TIMS technique. Econ. Geol. 103, 465–471.

Scott, K.M., Radford, N.W., 2007. Rutile compositions at the Big Bell Au deposit as a guide for exploration. Geochemistry Explor. Environ. Anal. 7, 353–361.

Seabrook, C.L., Cawthorn, R.G., Kruger, F.J., 2005. The Merensky Reef, Bushveld Complex: mixing of minerals not mixing of magmas. Econ. Geol. 100, 1191–1206.

Sebola, P., 2014. Characterisation of Uranium–Mineral–Bearing Samples in the Vaal Reef of the Klerksdorp goldfield. MSc thesis, University of Witwatersrand, Johannesburg, South Africa.

Shenberger, D.M., Barnes, H.L., 1989. Solubility of gold in aqueous sulfide solutions from 150 to 350 °C. Geochimica et Cosmochimica Acta 53, 269–278.

Siebert, C., Kramers, J.D., Meisel, T., Morel, P., Nägler, T.F., 2005. PGE, Re–Os, and Mo isotope systematics in Archaean and early Proterozoic sedimentary systems as proxies for redox conditions of the early earth. Geochim. Cosmochim. Acta 69, 1787–1801.

Slagstad, T., 2008. Radiogenic heat production of Archaean to Permian geological provinces in Norway. Nor. Geol. Tidsskr. 88, 149–166.

Smith, A.J.B., 2014. The geometallurgical characterization of the Merensky Reef at Bafokeng Rasimone Platinum Mine, South Africa. PhD thesis, University of Johannesburg, Johannesburg, South Africa.

Smith, A.J.B., Beukes, N.J., Gutzmer, J., 2010. Lithostratigraphic correlation of the iron–rich sedimentary rocks in the Archaean Witwatersrand–Mozaan succession: Implications for early depositional environments on Earth. South African J. Sci. Technol. 29, 161–163.

Smith, A.J.B., Beukes, N.J., Gutzmer, J., 2013. The composition and depositional environments of Mesoarchaean iron formations of the West Rand Group of the Witwatersrand Supergroup, South Africa. Econ. Geol. 108, 111–134.

Smith, N.D., Minter, W.E., 1979. Sedimentological control of gold and uranium in local developments of the Leader Reef, Welkom goldfield, and Elsburg No. 5 Reef, Klerksdorp goldfield, Witwatersrand Basin. Univ. Witwatersrand, Econ. Geol. Res. Unit, Inf. Circ. 137, 1–17.

Snow, J. E., Schmidt, G., 1998. Constraints on earth accretion deduced from noble metals in the oceanic mantle. Nature 391, 166–169.

Söhnge, A.P., 1986. Mineral provinces of Southern Africa. In: Anhaeusser, C. (Eds) Mineral Deposits of Southern Africa. Geological Society of South Africa, Pretoria, pp. 1–23.

Spangenberg, J.E., Frimmel, H.E., 2001. Basin–internal derivation of hydrocarbons in the Witwatersrand Basin, South Africa: evidence from bulk and molecular δ13C data. Chem. Geol. 173, 339–355.

Stanistreet, I.G., McCarthy, T.S., 1991. Changing tectono–sedimentary scenarios relevant to the development of the Late Archaean Witwatersrand Basin. J. African Earth Sci. 13, 65–81.

Steadman, J., Large, R.R., Meffre, S., Olin, P.H., Danyushevsky, L.V., Gregory, D.D., Belousov, I., Lounejeva, V., Ireland, T.R., Holden, P., 2015. Syn–sedimentary to early diagenetic gold in black shale–hosted pyrite nodules at the Golden Mile deposit, Kalgoorlie, Western Australia. Econ. Geol. 110, 1157–1191.

Stone, W.E., Crocket, J.H., Fleet, M.E., 1990. Partitioning of palladium, iridium, platinum, and gold between sulfide liquid and basalt melt at 1200??C. Geochim. Cosmochim. Acta 54, 2341–2344.

Sun, W., Bennett, V.C., Kamenetsky, V.S., 2004. The mechanism of Re enrichment in arc magmas: Evidence from Lau Basin basaltic glasses and primitive melt inclusions. Earth Planet. Sci. Lett. 222, 101–114.

Sunda, G., 2014. Trace element nutrients. In: Steele, J., Thorpe, S.A., Turekian, K.K. (Eds) Marine Chemistry and Geochemistry: A Derivative of Encyclopaedia of Ocean Sciences. Elsevier, Amsterdam, pp. 17–28.

Sutton, S.J., Maynard, J., 1993. Sediment– and basalt–hosted regoliths in the Huronian Supergroup: role of parent lithology in Middle Precambrian weathering profiles. Can. J. Earth Sci. 30, 60–76.

Sutton, S.J., Ritger, S.D., Maynard, J.B., 1990. Stratigraphic control of chemistry and mineralogy in metamorphosed Witwatersrand quartzites. J. Geol.

Taylor, S.R., McLennan, S., 1985. The continental crust: its composition and evolution. Blackwell Sciences Ltd, Oxford.

Taylor, S.R., McLennan, S.M., 1995. The geochemical evolution of the continental crust. Rev. Geophys. 33, 241–265.

Taylor, S.R., Rudnick, R.L., McLennan, S.M., Eriksson, K.A., 1986. Rare earth element patterns in Archaean high–grade metasediments and their tectonic significance. Geochim. Cosmochim. Acta 50, 2267–2279.

Tegtmeyer, A.R., Kröner, A., 1987. U–Pb Zircon ages bearing on the nature of early Archaean greenstone belt evolution, Barberton Mountain Land, South Africa. Precambrian Res. 36, 1–20.

Terashima, S., 1988. Determination of gold in sixty geochemical reference samples by flameless atomic absorption spectrometry. Geostand. Newsl. 1, 57–60.

Terashima, S., Yuasa, M., Nohara, M., 1994. Gold content of submarine volcanic rocks from the Izu–Ogasawara (Bonin) Arc. Resour. Geol. 44, 241–247.

Tilling, R.I., Gottfried, D., Rowe, J.J., 1973. Gold abundance in igneous rocks: bearing on gold mineralisation. Econ. Geol. 68, 168–186.

Tomkins, A.G., 2013. A biogeochemical influence on the secular distribution of orogenic gold. Econ. Geol.108, 193–197.

Toulkeridis, T., Clauer, N., Kröner, A., 1996. Chemical variations in clay minerals of the Archaean Barberton Greenstone Belt (South Africa). Precambrian Res. 79, 195–207.

Toulkeridis, T., Clauer, N., Kröner, A., Reimer, T., Todt, W., 1999. Characterisation, provenance, and tectonic setting of Fig Tree greywackes from the Archaean Barberton Greenstone Belt, South Africa. Sediment. Geol. 124, 113–129.

Toulkeridis, T., Clauer, N., Kröner, A., Todt, W., 2015. A mineralogical, chemical and isotopic investigation of shales from the Barberton Greenstone Belt, South Africa, to constrain source materials and post–deposition evolution. South African J. Geol. 118, 389–410.

Treloar, P.J., Coward, M.P., Harris, N., 1992. Himalayan–Tibetan analogies for the evolution of the Zimbabwe craton and Limpopo belt. Precambrian Res. 55, 571–587.

Trieloff, M., Reimold, W.U., Kunz, J., Boer, R.H., Jessberger, E.K., 1994. 40Ar–39Ar thermochronology of Pseudotachylite at the Ventersdorp Contact Reef, Witwatersrand Basin. South African J. Geol. 97, 365–384.

Tweedie, K.A., 1968. The stratigraphy and sedimentary structures of the Kimberley Shales in the Evander goldfield, Eastern Transvaal, South Africa. Trans. Geol. Soc. South Africa 71, 235–256.

Tyler, N., 1979. Stratigraphy, origin, and correlation of the Kanye Volcanic Group in west–central Transvaal. Trans. Geol. Soc. South Africa 82, 215–226.

Tzoupanos, N.D., Zouboulis, A.I., 2008. Coagulation–flocculation processes in water/wastewater treatment: the application of new generation of chemical reagents. 6th IASME/WSEAS International conference on heat transfer, thermal engineering and environment (hte'08) Rhodes, Greece, August 20–22.

Van Der Watt, J.G., Waanders, F.B., 2012. Leaching of rare earth elements from bentonite clay. J. South. African Inst. Min. Metall. 112, 281–285.

Van der Westhuizen, W.A., De Bruiyn, H., Meintjes, P.G., 1991. The Ventersdorp Supergroup: an overview. J. African Earth Sci. 13, 83–105.

Van Loon, J.C., Barefoot, R.R., 1991. Determination of the Precious Metals: selected instrumental methods. Wiley and Sons, Chichester.

van Niekerk, H.S., 2006. The origin of the Kheis Terrane and its relationship with the Archaean Kaapvaal Craton and the Grenvillian Namaqua Province in southern Africa. University of Johannesburg.

Van Reenen, D.D., Barton, J.M., Roering, C., Smith, C.A., Van Schalkwyk, J.F., 1987. Deep crustal response to continental collision: The Limpopo belt of Southern Afric. Geology 15, 11–14.

van Vuuren, C.J., 1964. The geology of portion of the Ulundi syncline between Hislop's Creek and Fig Tree Creek, Barberton Mountain Land. Univ. Witwatersrand, Econ. Geol. Res. Unit, Inf. Circ.

Vaughan, J.P., Kyin, A., 2004. Refractory gold ores in Archaean greenstones, Western Australia: mineralogy, gold paragenesis, metallurgical characterisation and classification. Mineral. Mag. 68, 255–277.

Velde, B., 1973. Phase equilibria in the system $MgO–Al_2O_3–SiO_2–H_2O$: chlorite and associated minerals. Mineral. Mag. 39, 297–312.

Velde, B., 1995. Clay minerals: a physico–chemical explanation of their occurrence. Elsevier, Amsterdam.

Vermaak, C., 1995. The platinum–group metals – A global perspective. Mintek, Randburg, South Africa.

Vidal, O., Parra, T., Trotet, F., 2001. A thermodynamic model for Fe–Mg aluminous chlorite using data from phase equilibrium experiments and natural pelitic assemblages in the 100° to 600°C, 1 to 25 kb range. Am. J. Sci. 301, 557–592.

Viljoen, M.J., Viljoen, R.P., 1969. The geology and geochemistry of the lower ultramafic unit of the Onverwacht Group and a proposed new class of igneous rocks. Geol. Soc. South Africa Spec. Publ. 2, 55–95.

Viljoen, M.J., Reimold, W., 2002. An Introduction to South Africa's geological and mining heritage. Geol. Soc. South Africa Mintek 1.

Viljoen, M.J., Theron, J., Underwood, B., Waters, B.M., Weaver, J., Peyerl, W., 1986. The Amandelbult section of Rustenburg Platinum Mines Limited, with reference to the Merensky Reef. In: Anhaeusser, C.R., Maske, S. (Eds) Mineral deposits of southern Africa. Geological Society of South Africa, Johannesburg, pp. 1041–1060.

Visser, D.J.L. (comp.), van Eden, O.R., Joubert, G.K., Sohnge, A.P.G., van Zyl, J.S., Rossow, P.J., Taljaard, J., 1956. The geology of the Barberton area. Spec. Publ. Geol. Surv. South Africa 15, 242.

Visser, J.N.J., 1969. 'n Sedimentologiese studie van die Serie Pretoria in Transvaal. University of Orange Free State.

Visser, J.N.J., Grobler, N.J., Joubert, C.W., Putgietor, C.D., Potgieter, G.J.A., McLaren, C.H., Liebenberg, J., 1976. The Ventersdorp Group between Taung and Britstown, Northern Cape Province. Geol. Surv. South Africa 11, 15–28.

Visser, W.J., 1989. Sedimentology study of the Black Reef Quartzite Formation in the Far–West Rand. Carletonville.

Vlassopoulos, D., Wood, S.A., 1990. Gold speciation in natural waters: I. Solubility and hydrolysis reactions of gold in aqueous solution. Geochim. Cosmochim. Acta 54, 3–12.

von Gruenewaldt, G., 1991. The Bushveld Complex. Platin. Met. Rev. 35, 96.

Wadnerkar, D., Pareek, V.K., Utikar, R.P., 2015. CFD Modelling of flow and solids distribution in carbon–in–leach tanks. Metals 5, 1997–2020.

Wallmach, T., Meyer, F., 1990. A petrogenetic grid for metamorphosed aluminous Witwatersrand shales. South African J. Geol. 93, 93–102.

Walraven, F., Martini, J., 1995. Zircon Pb–evaporation age determination of the Oak Transvaal sequence: implications for Transvaal–Griqualand West basin correlations. South African J. Geol. 98, 58–67.

Ward, J.H.W., 1999. Metallogenic Map of the Barberton Greenstone Belt, South Africa and Swaziland. Counc. Geosci. South Africa Mem. 86, 108.

Watanabe, Y., Naraoka, H., Wronkiewicz, D.J., Condie, K.C., Ohmoto, H., 1997. Carbon, nitrogen, and sulfur geochemistry of Archaean and Proterozoic shales from the Kaapvaal Craton, South Africa. Geochim. Cosmochim. Acta 61, 3441–3459.

Watchthorn, M.B., 1981. Sedimentological controls on strata bound placer mineralisation on the lower Witwatersrand West Rand Group, South Africa. Univ. Witwatersrand, Econ. Geol. Res. Unit, Inf. Circ. 153, 1–4.

Webber, A., Roberts, S., Taylor, R., Pitcairn, I., 2010. Enrichment of gold in oceanic crust by the Iceland mantle plume: constraints from the Reykjanes Ridge. In: Proc. Goldschmidt Conf., Knoxville, TN, USA, June, the University of Tennessee and Oak Ridge National Laboratory.

Wedepohl, H., 1986. Chapter 5: The composition of the continental crust. Int. Geophys. Volume 34, 213–241.

Whitehouse, M.J., Fedo, C.M., 2007. Microscale heterogeneity of Fe isotopes in N3.71 Ga banded iron formation from the Isua Greenstone Belt, south–west Greenland. Geology 35, 719–722.

Wiewióra, a., 1990. Crystallochemical classifications of phyllosilicates based on the Unified System of Projection of Chemical Composition: III. The Serpentine–Kaolin Group. Clay Miner. 25, 93–98.

Willemse, J., 1959. The floor of the Bushveld Igneous Complex and its relationships with special reference to the eastern Transvaal. Trans. Geol. Soc. South Africa 82, 21–80.

Willis, J., 1999. Instrumental parameters and data quality for routine major and trace element determination by WDXRFS. Cape T. Univ. Cape T.

Willis, J., Duncan, A., 2008. Understanding XRF spectrometry. A training course in XRF Spectrometry. PANalytical B.V., Netherlands 9.

Windley, B., 1984. The evolving continents, 2nd ed. John Wiley and Sons, New York.

Winkler, H.G., 1979. Petrogenesis of metamorphic rocks. Springer Verlag, Berlin.

Winter, H., de la, R., 1976. A lithostratigraphic classification of the Ventersdorp succession. Trans. Geol. Soc. South Africa 79, 31–48.

Wronkiewicz, D.J., Condie, K.C., 1987. Archaean shales from the Witwatersrand Supergoup, South Africa: Source area weathering and provenance. Geochim. Cosmochim. Acta 51, 2401–2416.

Wronkiewicz, D.J., Kent, C., 1989. Geochemistry and provenance of sediments from the Pongola Supergroup, South Africa: Evidence for a 3.0–Ga–old continental craton. Geochim. Cosmochim. Acta 53, 1537–1549.

Wronkiewicz, D.J., Condie, K.C., 1990. Geochemistry and mineralogy of sediments from the Ventersdorp and Transvaal supergroups, South Africa: Cratonic evolution during the early Proterozoic. Geochim. Cosmochim. Acta 54, 343–354.

Xie, X., Byerly, G.R., Ferrell, R.., 1997. IIb trioctahedral chlorite from the Barberton Greenstone Belt: crystal structure and rock composition constraints with implications for geothermometry. Contrib. to Mineral. Petrol. 126, 275–291.

Young, R.A., 2000. The Rietveld Method. IUCr Publ. 3.

Young, R.A, 2002. The Rietveld Method. International Union of Crystallography, Oxford University Press, New York.

Young, R.A., Sakthivel, A., Moss, T.S., Paiva–Santos, C.O., 1995. DBWS–9411 – an upgrade of the DBWS*. * Programs for Rietveld refinement with PC and mainframe computers. J. Appl. Crystallogr. 28, 366–367.

Young, R.B., 1907. Notes on the auriferous conglomerates of the Witwatersrand. Trans. Geol. Soc. S. Afr. 10, 17-30.

Youngson, J., Wopereis, P., Kerr, L., Craw, D., 2002. Au–Ag–Hg and Au–Ag alloys in Nokomai and Nevis valley placers, northern Southland and Central Otago, New Zealand, and their implications for placer–source relationships. New Zeal. J. Geol. Geophys. 45, 53–69.

Zane, A., Sassi, R., Guidotti, C. V., 1998. New data on metamorphic chlorite as a petrogenetic indicator mineral, with special regard to greenschist–facies rocks. Can. Mineral. 36, 713–726.

Zane, A., Weiss, Z., 1998. A procedure for classifying rock–forming chlorite based on microprobe data. Rend. Lincei 56, 51–56.

Zang, W., Fyfe, W.., 1995. Chloritisation of the hydrothermally altered bedrock at Igarap gold deposits, Carajás, Brazil. Miner. Depos. 30, 30–38.

Zeh, A., Gerdes, A., Barton, J.M., 2009. Archaean accretion and crustal evolution of the Kalahari Craton – The zircon age and Hf isotope record of granitic rocks from Barberton/Swaziland to the Francistown arc. J. Petrol. 50, 933–966.

Zeh, A., Gerdes, A., Heubeck, C., 2013. U–Pb and Hf isotope data of detrital zircons from the Barberton Greenstone Belt: constraints on provenance and Archaean crustal evolution. J. Geol. Soc. London. 170, 215–223.

Zentilli, M., Brooks, R.R., Helgason, J., Ryan, D.E., Zhang, H., 1985. The distribution of gold in volcanic rocks of eastern Iceland. Chem. Geol. 48, 17–28.

Zhao, B., Clauer, N., Robb, L.J., Zwingmann, H., Toulkeridis, T., Meyer, F.M., 1999. K–Ar dating of white micas from the Ventersdorp Contact Reef of the Witwatersrand Basin, South Africa: Timing of post–depositional alteration. Mineral. Petrol. 66, 149–170.

APPENDICES

Appendix A. 1. Whole rock geochemical data

Table A. 1. Major element concentrations of the Fig Tree and Moodies groups' marine shales.

Group	Formation	Collar Coordinates (Latitude; Longitude)	Sample No.	Depth (m)	SiO_2 (wt.%)	Al_2O_3	Fe_2O_3 total	MgO	CaO	Na_2O	K_2O	TiO_2	P_2O_5	MnO	Cr_2O_3	LOI	TOC	S	Total
Fig Tree	Sheba	25° 42' 52.308" S; 31° 8' 18.276" E	BARBFC-001	0	65.7	12.13	8.4	4.85	1.29	1.92	0.98	0.55	0.1	0.15	0.13	4.57	0.47	0.01	101.27
			BARBFC-002	0.5	64.7	10.75	7.77	4.98	2.62	2.14	0.97	0.51	0.08	0.14	0.1	6.1	1.04	0.02	101.91
			BARBFC-003	1	67.2	11.2	8.11	4.59	1.37	2.22	1.02	0.52	0.07	0.16	0.11	4.48	0.55	0.01	101.63
			BARBFC-004	1.5	67.3	11.32	8.5	4.45	0.98	2.21	1.1	0.53	0.07	0.16	0.11	4.05	0.41	0.01	101.17
			BARBFC-005	2	63.9	10.67	8.09	5.11	2.46	2.12	1.01	0.5	0.07	0.15	0.1	6.04	0.44	0.01	100.65
			BARBFD-001	0	60.4	14.59	9.79	6.42	0.41	1.57	1.46	0.64	0.1	0.04	0.14	4.47	0.16	0.01	100.2
			BARBFD-002	0.5	64.2	13.82	7.98	5.3	0.4	1.56	1.57	0.62	0.1	0.04	0.14	3.8	0.12	0.01	99.66
			BARBFD-003	1	59.1	15.08	9.64	6.44	0.44	1.63	1.65	0.66	0.11	0.06	0.14	4.59	0.19	0.01	99.73
			BARBFD-004	1.5	58.8	14.65	9.66	6.58	0.4	1.39	1.52	0.64	0.11	0.05	0.14	4.51	0.17	0.01	98.65
			BARBFD-005	2	64.4	13.44	7.97	5.37	0.39	1.67	1.43	0.59	0.09	0.04	0.13	3.76	0.11	0.01	99.36
			BARBFD-006	2.5	58.3	14.45	9.64	6.43	0.41	1.42	1.48	0.64	0.1	0.04	0.14	4.33	0.16	0.01	97.54
			BARBFD-007	3	62.01	13.49	8.92	6.85	0.22	1.58	1.54	0.61	0.1	0.05	0.15	4.08	0.15	0.01	99.76

Group	Formation	Collar Coordinates (Latitude; Longitude)	Sample No.	Depth (m)	SiO_2 (wt.%)	Al_2O_3	Fe_2O_3 total	MgO	CaO	Na_2O	K_2O	TiO_2	P_2O_5	MnO	Cr_2O_3	LOI	TOC	S	Total
		25°44'00.2"S; 31°04'26.4"E	FS1		77.2	10.97	2.59	2.13	0.24	0.02	3.32	0.36	0.23	0.02		2.65	0.33	0.06	100.16
			FS3		64.4	19.15	2.11	1.58	0.02	0.04	7.1	0.29	0.08	0.01		3.54	0.42	0.01	98.74
			FS15		52.9	14.1	11.63	7.54	2.14	2.21	0.99	0.68	0.12	0.16		7.46	0.98		100.86
			FS16		58.9	12.76	10.69	5.72	1.56	1.48	1.66	0.71	0.14	0.13		6.01	0.73	0.03	100.54
			FS17		54.6	16.42	10.97	7.47	0.28	3.02	1.08	0.73	0.12	0.04		5.14	0.3		100.18
			FS18		52	18.5	10.71	6.73	0.32	1.59	3.35	0.74	0.12	0.05		5.7	0.49		100.3
			FS19		54.6	17.73	10.05	6.84	0.17	1.05	3.24	0.71	0.11	0.04		5.32	0.38		100.2
Moodies Group	Clutha	25° 42' 23.4" S; 31° 9' 56.592" E	BARBMA-001		63.1	10.63	7.09	5.01	3.42	1.95	1.04	0.44	0.08	0.16	0.09	7.3	1.63	0.01	101.95
			BARBMA-002	0.5	51.1	16.07	14.16	8.35	0.2	1.35	1.32	0.65	0.11	0.04	0.15	5.49	0.24	0.01	99.19
			BARBMA-003	1	51.9	16.15	14.29	8.53	0.46	0.91	1.44	0.67	0.12	0.04	0.15	5.78	0.25	0.01	100.68
			BARBMA-004	1.5	50.03	15.72	13.79	8.25	0.51	0.97	1.42	0.65	0.11	0.07	0.15	5.63	0.28	0.04	97.62
			BARBMA-005	2	52.2	16.05	13.73	8.35	0.47	0.95	1.46	0.66	0.12	0.07	0.16	5.56	0.25	0.01	100.05
			BARBMA-006	2.5	58.3	12.39	9.49	6.14	2.55	1.7	1.16	0.5	0.09	0.12	0.11	6.71	1.23	0.01	100.51
			BARMB-001		61.7	11.3	8.32	6.45	2.76	2.22	0.89	0.52	0.09	0.15	0.1	6.12	1.07	0.01	101.67
			BARMB-002	0.5	66.8	11.79	7.75	4.85	1.42	2.04	1.15	0.53	0.09	0.07	0.11	4.74	0.82	0.01	102.14
			BARMB-003	1	65.96	11.9	7.95	4.9	1.36	2.14	1.14	0.54	0.1	0.07	0.12	4.67	0.79	0.01	101.65
			BARMB-004		59.1	13.39	11.1	6.6	1.01	1.65	1.36	0.63	0.11	0.1	0.12	5.29	0.5	0.04	101.02

Group	Formation	Collar Coordinates (Latitude; Longitude)	Sample No.	Depth (m)	SiO_2 (wt.%)	Al_2O_3	Fe_2O_3 total	MgO	CaO	Na_2O	K_2O	TiO_2	P_2O_5	MnO	Cr_2O_3	LOI	TOC	S	Total
			BARMB-005	2	57.4	13.3	10.96	6.45	1.21	1.21	1.32	0.61	0.11	0.1	0.13	5.51	0.47	0.01	98.73
			BARMB-006	2.5	59.1	12.51	9.78	6.36	2.13	1.5	1.11	0.56	0.1	0.13	0.12	6.29	0.5	0.01	100.21
			BARMB-007	3	64.7	11.44	8.27	5.92	1.71	2.03	1.03	0.56	0.1	0.1	0.12	5.25	0.85	0.01	102.1
			BARMB-008	3.5	59.1	12.83	10.76	6.47	1.84	1.36	1.2	0.58	0.11	0.1	0.13	5.86	0.73	0.01	101.11
			BARMB-009	4	61.6	12.6	9.77	5.97	1.73	1.67	1.19	0.58	0.11	0.1	0.12	5.82	0.82	0.01	102.13
		25°43'51.7"S; 31°04'18.4"E	MoodG2G		72.4	13.56	3.23	1.96	0.37	4.5	2.11	0.22	0.08	0.02		1.64	0.1		100.17
			MoodG17		60.2	14.11	9	5.44	0.46	1.64	3.32	0.66	0.12	0.21		5	0.14	0.02	100.31
			MoodG32		59.4	15.81	8.92	5.54	0.64	2.43	2.22	0.68	0.11	0.11		4.18	0.31	0.04	100.36
			Mood877		65.9	13.82	6.49	3.4	0.68	3.76	1.82	0.52	0.11	0.06		3.36	0.25	0.02	100.23
			Mood880		56.4	15.9	11.93	5.31	0.28	2.36	2.43	0.75	0.13	0.11		4.27	0.13	0.03	100.04
			Mood881		53.6	10.1	22.3	4.14	1.52	1.64	1.74	0.46	0.1	0.5		3.84	0.68	0.05	100.74
			MS7		60.7	13.23	11.02	5.82	0.51	1.06	3.45	0.59	0.11	0.25		3.24	0.06	0.01	100.02
			MS8		60.3	13.41	8.82	5.47	1.8	1.58	3.55	0.63	0.13	0.27		3.92	0.39	0.04	100.34
			MS4		64.4	11.42	9.46	4.58	1.28	1.28	3.03	0.55	0.1	0.15		3.74	0.49		100.44
			MS1		51.5	20.08	9.7	4.3	1.71	3.44	6.48	0.91	0.13	0.17		1.39	0.26		100.08
			MS2		49.2	6.06	36.1	3.1	0.31	0.8	2.04	0.24	0.06	0.5		1.51	0.03		99.98

Table A. 2. Trace element concentrations of the Fig Tree and Moodies groups' marine shales.

Group	Formation	Collar Coordinates (Latitude; Longitude)	Sample No.	As (ppm)	Rb	Ba	Sr	Pb	Cs	Co	Cr	Cu	Ni	V	Sc	Zn	Ga	Zr	Nb	Hf
Fig Tree	Sheba	25° 42' 52.308" S; 31° 8' 18.276" E	BARBFC-001	45	41	210	81	8.6	3	101	868	54	375	117	31	97	15	133	9	3.6
			BARBFC-002		31	167	105	10	3	33	706	53	293	97	13	95	12	111	6	2.9
			BARBFC-003		31	195	82	9.8	3	32	741	53	334	104	14	99	12	111	7	3.2
			BARBFC-004		30	198	75	9.9	3	34	744	58	354	100	15	103	13	109	7	2.9
			BARBFC-005		29	159	103	9.3	3	28	711	55	308	101	14	100	12	107	7	2.7
			BARBFD-001	31	66	302	30	5.7		112	973		391	162	33		17	106	10	2.8
			BARBFD-002	13	77	325	38	6.1		98	960		320	148	31		16	119	10	3
			BARBFD-003	20	78	324	32	6.1		113	983		361	169	32		16	107	10	2.9
			BARBFD-004	25	72	310	31	6.5		103	972		365	166	32		16	106	9	2.8
			BARBFD-005	13	63	266	36	6.3		92	881		294	138	29		14	109	9	2.9
			BARBFD-006	34	69	296	30	5.2		111	953		381	162	30		16	103	9	2.8
			BARBFD-007	22	76	305	33	6.2		105	997		335	161	30		16	111	9	2.9

Group	Formation	Collar Coordinates (Latitude; Longitude)	Sample No.	As (ppm)	Rb	Ba	Sr	Pb	Cs	Co	Cr	Cu	Ni	V	Sc	Zn	Ga	Zr	Nb	Hf
		25°44'00.2"S; 31°04'26.4"E	FS1		98	369	29	7	2	7	56	22	62	28	5	10	16	162	9	4.4
			FS3		176	1477	9.2	7.7	3	5.7	147	27	59	29	7	38	29	255	22.3	7.9
			FS15		42	219	68.7	8.3	3	45.2	949	61	462	175	25	134	17	90	8	2.6
			FS16		67	332	44.6	12.3	4	111	961	98	460	146	20	118	17	119	8.7	3.2
			FS17		47	249	41.2	3.6	3	36.3	1129	45	484	199	28	167	22	99	8.7	2.4
			FS18		169	620	27.2	6.9	8	45.2	1277	68	588	210	29	130	24	96	8.8	2.4
			FS19		158	471	18.9	2.2	7	46.2	1253	56	593	200	29	158	23	96	8.4	2.8
Moodies Group	Clutha	25° 42' 23.4" S; 31° 9' 56.592" E	BARBMA-001	5	30	235	142	10.2		119	629		198	83	22		11	138	8	3.5
			BARBMA-002		51	274	23	6.6	4	48	1013	66	543	179	26	176	19	83	8	2.3
			BARBMA-003	19	54	295	25	5		101	1041		482	184	31		18	111	10	3.1
			BARBMA-004	16	45	287	24	4.7		104	1004		452	178	29		15	98	9	2.5
			BARBMA-005	16	54	301	29	5.3		138	1073		490	188	29		18	102	10	2.7
			BARBMA-006	12	46	239	103	10		88	770		302	119	23		13	105	8	2.8
			BARMB-001	8	31	269	121	9.6		137	704		256	110	23		12	111	8	3.0
			BARMB-002	5	42	234	91	16.8		93	768		267	105	23		13	153	10	3.8

Group	Formation	Collar Coordinates (Latitude; Longitude)	Sample No.	As (ppm)	Rb	Ba	Sr	Pb	Cs	Co	Cr	Cu	Ni	V	Sc	Zn	Ga	Zr	Nb	Hf
			BARMB-003	4	46	228	87	15.2		120	821		274	111	22		14	154	10	3.9
			BARMB-004		46	251	44	7.4	3	47	852	78	385	140	20	122	16	105	7	2.9
			BARMB-005	4	52	269	47	6.2		116	916		369	149	26		15	120	9	3.3
			BARMB-006	6	45	247	87	7.9		102	803		324	127	24		14	116	9	3
			BARMB-007	4	39	229	97	11.7		125	810		276	115	22		14	152	10	3.6
			BARMB-008	7	50	247	62	8.8		109	858		328	135	24		14	120	9	3.2
			BARMB-009	4	47	248	71	10.1		99	850		314	128	24		14	139	9	3.7
		25°43'51.7"S; 31°04'18.4"E	MoodG2G		113	193	73.4	4.6	6	10	55	2	68	19		26	12.7	120	8.6	3.3
			MoodG17		124	309	41.9	4.4	7.9	39	777	32	294	152	20	71	20	140	11.6	3.8
			MoodG32		102	286	82.3	6.9	6.7	43	798	73	347	145	21	104	19.1	137	10.3	3.4
			Mood877		82	256	82.3	7.2	3.9	25	411	37	164	79	11	62	16.2	161	9.9	4.5
			Mood880		102	420	50.8	3.8	4.7	55	889	79	408	170	23	120	16.9	122	9.3	3.2
			Mood881		73	468	68.4	10.6	5.6	35	596	65	225	113	13	94	12.6	92	6.2	2.9
			MS7		144	392	45.2	3.4	12.8	41.3	610	58	269	126	17	59	16.9	124	8.2	3.4
			MS8		123	334	62.3	4.9	9.7	38.2	687	99	257	123	19	51	17.3	124	10.1	3.3
			MS4		143	975	77.7	5.7	6.7	41.7	1549	8.7	348	106	16	57	13.2	155	8.4	3.9

Group	Formation	Collar Coordinates (Latitude; Longitude)	Sample No.	As (ppm)	Rb	Ba	Sr	Pb	Cs	Co	Cr	Cu	Ni	V	Sc	Zn	Ga	Zr	Nb	Hf
			MS1		235	919	203	17.4	8.6	31.1	1175	13.2	410	183	21	54	32.9	206	14.5	5.5
			MS2		96	541	36.5	8.8	7.5	23.2	549	11.6	169	66		75	6.8	59	4.3	1.5

Group	Formation	Collar Coordinates (Latitude; Longitude)	Sample No.	Ta	Tl	Mo	Sb	Sn	Th	U	W	Y	La	Ce	Pr	Nd	Sm	Eu	Gd	Tb	Dy	Ho	Er	Tm	Yb	Lu
Fig Tree	Sheba	25° 42' 52.308" S; 31° 8' 18.276" E	BARBFC-001	0.9		1.41	1.23	3.	6.6	1.5		19	22	40	4.42	17	3.4	0.9	3.3	0.53	3.44	0.7	2.02	0.32	2.09	0.31
			BARBFC-002	0.8		0.8		3	5.6	1.3	1	13	19	34	3.8	13.9	3.2	0.8	2.9	0.5	2.8	0.6	2	0.3	1.4	0.2
			BARBFC-003	0.8		1.3		4	6.4	1.4	1	14	20	37	4	14.6	2.9	0.7	2.7	0.5	2.9	0.6	1.7	0.3	1.5	0.3
			BARBFC-004	0.8		1.8		3	6	1.4	1	14	20	35	3.8	14.9	3.2	0.8	2.9	0.5	2.8	0.6	1.7	0.3	1.8	0.2
			BARBFC-005	0.7		1.5		3	5.8	1.4	0.5	14	19	35	3.9	14.4	3.1	0.7	2.9	0.5	3	0.6	1.8	0.3	1.7	0.2
			BARBFD-001	0.86		1.27	1.09		5.2	1.6		20	21	39	4.34	17.5	3.5	0.9	3.8	0.55	3.54	0.76	2.05	0.31	1.94	0.28

Group	Formation	Collar Coordinates (Latitude; Longitude)	Sample No.	Ta	Tl	Mo	Sb	Sn	Th	U	W	Y	La	Ce	Pr	Nd	Sm	Eu	Gd	Tb	Dy	Ho	Er	Tm	Yb	Lu
			BARBFD-002	0.92		0.83	0.89		5.8	1.5		18	19	36	4.11	15.9	3.5	0.9	3.6	0.53	3.31	0.69	2.02	0.29	2.04	0.31
			BARBFD-003	0.96		0.91	0.97		5.3	1.5		21	23	42	4.58	18.9	4	1	4.2	0.64	4.05	0.83	2.32	0.34	2.15	0.33
			BARBFD-004	0.94		0.91	1.08		5.2	1.4		20	22	40	4.54	17.6	3.9	0.9	3.9	0.58	3.65	0.79	2.27	0.33	2.17	0.32
			BARBFD-005	0.92		0.85	0.78		6	1.3		17	15	30	3.31	13.3	2.9	0.7	3.4	0.5	3.32	0.66	1.84	0.29	1.85	0.27
			BARBFD-006	0.91		1.36	1.03		5.4	1.4		19	21	39	4.3	17.3	3.6	0.9	3.8	0.56	3.51	0.7	1.99	0.31	2.03	0.31
			BARBFD-007	0.92		0.73	0.94		5.6	1.5		20	20	38	4.22	16.6	3.5	0.8	3.7	0.54	3.52	0.72	2	0.31	2	0.31
		25°44'00.2"S; 31°04'26.4"E	FS1	0.9	1.08	1.2		4	11.1	2.9	1	21	27	48	5.1	19.1	4.3	1.1	5.2	0.8	4	0.7	2	0.4	2	0.3
			FS3	2.2	1.19	1.3		9	26.9	7.7		57	78	162	18.1	66	13.8	2	11	1.9	10.9	2.4	5.9	1	6.8	1.1
			FS15	0.7	0.33	1		3	4.7	1.9		26	28	53	5.7	20.6	4.8	1.2	4.6	0.7	4.5	1	2.5	0.5	2.9	0.5
			FS16	0.8	0.3	1.3		3	4.9	1.7	2	19	18	36	3.8	15.1	3.5	0.8	3.3	0.6	3.1	0.7	2	0.4	2.2	0.4
			FS17	0.8	0.2	0.3		4	5.2	1.6	1	21	24	47	5.4	17.7	4.8	1.2	4.4	0.7	4	0.9	2.4	0.4	2.5	0.3
			FS18	0.8	0.64	0.6		4	4.7	1.5	2	22	26	52	6	21.6	4.8	1.4	3.8	0.7	4.1	0.9	2.4	0.3	2.9	0.3
			FS19	0.7	0.58	0.1		3	5.4	1.3	1	22	27	50	5.8	20.8	4.2	1.2	4.6	0.6	3.9	0.8	2.1	0.3	2.4	0.3
Moodies Group	Clutha	25° 42' 23.4" S; 31° 9' 56.592" E	BARBMA-001	0.86		1.35	0.47		7.8	1.8		18	23	41	4.51	16.8	3.1	0.8	3.2	0.51	3.18	0.66	1.8	0.29	1.89	0.29
			BARBMA-002	0.8		1		5	4.9	1.5	1	19	20	36	4.3	18.5	4	0.9	3.5	0.6	3.7	0.7	2.1	0.4	2.2	0.3

Group	Formation	Collar Coordinates (Latitude; Longitude)	Sample No.	Ta	Tl	Mo	Sb	Sn	Th	U	W	Y	La	Ce	Pr	Nd	Sm	Eu	Gd	Tb	Dy	Ho	Er	Tm	Yb	Lu
			BARBMA-003	0.97		1.51	0.83		5.1	1.4		25	21	39	4.56	18.3	3.9	1.1	4.1	0.66	3.95	0.83	2.39	0.38	2.34	0.37
			BARBMA-004	0.9		1.48	0.74		5.3	1.4		22	20	37	4.23	17.4	3.7	1	4.1	0.62	3.89	0.78	2.34	0.37	2.29	0.34
			BARBMA-005	1		1.41	0.9		5.4	1.5		23	21	41	4.68	19.3	4.4	1.1	4.1	0.62	4.01	0.84	2.4	0.37	2.43	0.38
			BARBMA-006	0.79		2.18	0.68		6.6	1.6		19	21	39	4.36	17.4	3.6	0.9	3.6	0.54	3.52	0.69	1.88	0.3	2.02	0.29
			BARMB-001	0.82		1.71	0.58		5.4	1.3		18	18	33	3.8	14.6	3.3	0.8	3.2	0.53	3.27	0.71	1.92	0.29	2.01	0.3
			BARMB-002	0.93		1.58	0.78		8.9	2		16	27	48	5.29	19.6	3.7	0.9	3.3	0.53	3.11	0.66	1.91	0.28	1.87	0.27
			BARMB-003	1		2.84	0.76		8.6	2.1		16	26	47	4.95	19.1	3.6	0.9	3.2	0.48	3.02	0.64	1.77	0.28	1.88	0.29
			BARMB-004	0.8		1		4	5.6	1.5	1	16	18	35	4	15.7	3.5	0.9	2.9	0.5	3.1	0.7	1.8	0.4	2	0.3
			BARMB-005	0.89		1.36	0.89		6.4	1.4		21	19	37	4.14	16.7	3.6	0.9	3.8	0.54	3.46	0.69	1.97	0.29	2.09	0.34
			BARMB-006	0.81		1.45	1.17		5.8	1.3		20	18	34	3.88	16.2	3.3	0.9	3.4	0.57	3.14	0.67	1.96	0.3	1.96	0.3
			BARMB-007	0.94		1.72	0.68		7.7	1.8		18	24	43	4.72	18.4	3.3	0.9	3.6	0.51	3.28	0.63	1.78	0.28	1.76	0.26
			BARMB-008	0.8		1.25	0.75		6.1	1.3		20	17	32	3.69	15	3.4	0.9	3.4	0.53	3.33	0.71	2.07	0.31	2	0.3
			BARMB-009	0.92		1.3	0.68		7.1	1.6		19	22	41	4.59	18	3.7	1	3.5	0.53	3.49	0.71	2.1	0.33	2.14	0.32

Group	Formation	Collar Coordinates (Latitude; Longitude)	Sample No.	Ta	Tl	Mo	Sb	Sn	Th	U	W	Y	La	Ce	Pr	Nd	Sm	Eu	Gd	Tb	Dy	Ho	Er	Tm	Yb	Lu
		25°43'51.7"S; 31°04'18.4"E	MoodG2G	1	0.26	0.1		3	8.2	2.5		8.3	22.7	44	4.5	14.4	2.8	0.6	2.4	0.4	1.7	0.3	0.9	0.2	1	0.1
			MoodG17	1	0.24	1		4	7	2	2	21.3	25.7	51	5.7	21.4	5.4	1	4.1	0.6	4	0.8	2.3	0.4	2.5	0.3
			MoodG32	1.1	0.32	1.2		3	6.6	2	2	21.5	26.4	52	5.5	21.3	5.7	1.3	4.3	0.7	3.7	0.9	2.3	0.4	2	0.4
			Mood877	1	0.21	0.6		3	7	2.3	2	15.7	23.6	47	4.9	19	3.7	0.8	2.7	0.5	2.8	0.6	1.7	0.3	1.5	0.2
			Mood880	1.1	0.3	1.5		5	6.2	1.6	3	19.7	25.8	51	5.7	22.9	4.9	1.2	4.4	0.5	3.9	0.8	2.2	0.3	2.2	0.3
			Mood881	0.6	0.24	0.9		3	4.5	1.4		14.3	18.8	36	4.1	14.4	3.4	0.8	2.7	0.5	2.3	0.4	1.4	0.2	1.6	0.2
			MS7	1	0.39	0.7		3	6.2	1.4		19.9	22	41	4.9	17.2	3.8	0.8	3.3	0.5	3.4	0.6	2.2	0.3	2.2	0.3
			MS8	1	0.29	1.3		3	5.9	1.7	2	17.7	22	44	4.8	17.9	4	1.1	3.5	0.5	3.3	0.7	1.8	0.3	1.9	0.3
			MS4	1	0.35	0.9		3	7	1.7	1	15	22	43	4.4	16.7	3.4	0.9	3.1	0.4	2.4	0.5	1.5	0.2	1.7	0.3
			MS1	1	1	0.6		5	10.8	2.9		27.8	37	60	7.4	27.2	5.5	1.4	4.4	0.7	4.3	0.9	3	0.4	2.8	0.4
			MS2	1	0.25	0.9		2	3	0.7		15.1	14	23	2.7	9.3	2.5	0.5	2.8	0.3	2.3	0.5	1.3	0.2	1	0.2

Group	Formation	Collar Coordinates (Latitude; Longitude)	Sample No.	Au	Ir	Os	Pd	Pt	Rh	Ru
Fig Tree	Sheba	25° 42' 52.308" S; 31° 8' 18.276" E	BARBFC-001	4	0.25	0.25	2	2	0.25	2
			BARBFC-002	7	0.25	0.25	3	3	0.25	2
			BARBFC-003	19	0.25	0.25	2	3	0.25	1
			BARBFC-004	8	0.25	0.25	2	3	0.25	1
			BARBFC-005	10	0.25	0.25	2	2	0.25	1
			BARBFD-001	2	0.25	0.25	4	4	0.25	2
			BARBFD-002	2	0.25	0.25	3	3	0.25	2
			BARBFD-003	3	0.25	0.25	5	5	0.25	2
			BARBFD-004	3	0.25	0.25	4	5	0.25	2
			BARBFD-005	3	0.25	0.25	3	3	0.25	2
			BARBFD-006	3	0.25	0.25	4	4	0.25	2
			BARBFD-007	2	0.25	0.25	4	4	0.25	2

Group	Formation	Collar Coordinates (Latitude; Longitude)	Sample No.	Au	Ir	Os	Pd	Pt	Rh	Ru
		25°44'00.2"S; 31°04'26.4"E	FS1							
			FS3							
			FS15	1			4.5	4.9		
			FS16	9			3.5	4.4		
			FS17	4			6.3	8.1		
			FS18	3			5.7	8.7		
			FS19	3			5.3	6.9		
Moodies Group	Clutha	25° 42' 23.4" S; 31° 9' 56.592" E	BARBMA-001	2	0.25	0.25	2	2	0.25	2
			BARBMA-002	3	0.25	0.25	5	6	0.25	1
			BARBMA-003	3	0.25	0.25	5	5	0.25	3
			BARBMA-004	3	0.25	0.25	5	5	0.25	3
			BARBMA-005	5	0.25	0.25	5	5	0.25	2
			BARBMA-006	3	0.25	0.25	3	3	0.25	1
			BARMB-001	5	0.25	0.25	2	3	0.25	2

Group	Formation	Collar Coordinates (Latitude; Longitude)	Sample No.	Au	Ir	Os	Pd	Pt	Rh	Ru
			BARMB-002	3	0.25	0.25	2	2	0.25	2
			BARMB-003	3	0.25	0.25	2	2	0.25	1
			BARMB-004	10	0.25	0.25	4	4	0.25	1
			BARMB-005	2	0.25	0.25	3	5	0.25	3
			BARMB-006	3	0.25	0.25	3	4	0.25	2
			BARMB-007	4	0.25	0.25	2	2	0.25	1
			BARMB-008	5	0.25	0.25	3	3	0.25	2
			BARMB-009	2	0.25	0.25	3	3	0.25	1
		25°43'51.7"S; 31°04'18.4"E	MoodG2G	2			0.5			
			MoodG17	6			5.3	3.9		
			MoodG32	6			3.5	3.8		
			Mood877	2			1.6	1.5		
			Mood880	4			6.1	4.5		
			Mood881	4			3.4	3.1		

Group	Formation	Collar Coordinates (Latitude; Longitude)	Sample No.	Au	Ir	Os	Pd	Pt	Rh	Ru
			MS7	1			3.8	5.2		
			MS8	2			3.6	4.6		
			MS4				2.7	4.6		
			MS1	1			4	6.4		
			MS2				1.6	3.1		

Table A. 3. Major element concentrations of the Witwatersrand Supergroup marine shales.

Group	Formation	Collar Coordinates (Latitude; Longitude)	Sample No.	Depth (m)	SiO_2 (Wt.%)	Al_2O_3	Fe_2O_3 total	MgO		CaO	Na_2O	K_2O	TiO_2	P_2O_5	MnO	Cr_2O_3	LOI	TOC	S	Total
			PAAS[+]		64.80	16.90	5.66	2.86		3.36	1.14	3.97	0.70	0.13	0.06	0.02				99.60
West Rand Group	Orange Grove		D14*		53.52	27.68	4.84	0.20		0.01	0.55	5.07	1.19	0.14		0.00	6.01			99.21
	Parktown - Brixton		MED-10*		57.84	14.02	16.51	5.33		0.02	0.05	1.49	0.53	0.02	0.03	0.00	4.18			100.02
			MED-11*		47.72	7.25	31.70	4.02		0.12	0.13	0.16	0.24	0.03	0.47	0.00	5.79			97.63
			MED-12*		65.32	11.71	13.40	4.36		0.02	0.02	0.86	0.47	0.02	0.10	0.00	3.52			99.80
			C-71*		40.98	7.85	42.64	2.64		0.03	0.20	1.36	0.27	0.08	0.70	0.00	2.64			99.39
	Promise		MED-13*		48.45	11.11	25.15	4.69		0.94	0.27	1.50	0.38	0.10	3.44	0.00	2.66			98.69
			MED-14*		44.06	8.48	31.84	5.12		0.91	0.40	1.30	0.28	0.08	0.38	0.00	4.40			97.25
			MED-15*		42.09	9.61	33.24	4.23		0.57	0.06	1.65	0.31	0.11	3.44	0.01	3.59			98.91
	Roodepoort Formation		MED-17*		55.32	12.77	19.13	6.49		0.17	0.01	0.02	0.53	0.11	0.07	0.01	4.76			99.39
			MED-18*		53.92	13.98	17.20	7.02		0.68	0.03	0.67	0.60	0.09	0.09	0.01	5.34			99.63
			C-75*		59.33	17.51	11.04	3.99		0.14	0.22	3.09	0.78	0.12	0.05	0.01	3.82			100.10
			AA0098*		58.82	19.97	7.02	5.00		0.22	1.12	2.33	0.90	0.04	0.06	0.01	4.82			100.31
			AA0101*		57.79	20.78	7.02	5.03		0.20	1.48	2.28	0.97	0.05	0.06	0.00	4.81			100.47
Central Rand Group	Booysens Formation		MEE-5#		55.75	19.44	6.73	6.14		0.97	1.21	3.62	0.62	0.09	0.05	0.01	4.50			99.13
			MEE-27#		54.01	15.67	7.80	11.20		1.70	1.04	1.05	0.50	0.09	0.08	0.01	6.25			99.40
			MEE-32*		52.45	18.39	8.80	11.49		0.23	0.13	1.35	0.64	0.13	0.15	0.01	6.36			100.13
			SJ-3-2*		53.64	15.84	8.52	12.21		1.37	1.27	0.74	0.61	0.09	0.06	0.01	5.78			100.14

Group	Formation	Collar Coordinates (Latitude; Longitude)	Sample No.	Depth (m)	SiO_2 (Wt.%)	Al_2O_3	Fe_2O_3 total	MgO		CaO	Na_2O	K_2O	TiO_2	P_2O_5	MnO	Cr_2O_3	LOI	TOC	S	Total
			SJ-3-4*		52.40	18.82	7.93	9.94		0.91	1.41	2.48	0.60	0.09	0.05	0.01	5.36			100.00
	Kimberly Formation (K-8)		MEE-14*		64.26	19.58	6.98	2.80		0.07	0.27	1.77	0.74	0.06	0.06	0.00	3.52			100.11
			MEE-23*		62.31	27.15	0.51	0.43		0.10	1.42	2.76	0.92	0.60		0.02	4.18			100.40
			MEE-34*		59.36	26.10	6.58	1.55		0.03	0.18	0.94	0.97	0.06	0.03	0.01	4.35			100.16
			MED-1*		63.13	23.64	3.36	0.61		0.06	0.68	4.82	0.90	0.06		0.01	3.27			100.54
			MED-7*		64.22	28.09	0.76	0.46		0.18	0.26	0.61	0.78	0.60		0.00	5.17			101.13
West Rand Group	Parktown-Brixton (East Rand Goldfield-	26° 31' 23.898" S; 28° 23' 49.5744" E	H01 09		62.97	12.98	11.42	3.22		0.03	0.02	1.98	0.57	0.49	0.03	0.10	5.04			98.85
			H04 13		62.42	13.40	12.63	2.85		0.01	0.03	3.02	0.53	0.07	0.22	0.06	3.90			99.14
			H05 01		50.69	11.60	27.69	2.58		0.01	0.02	2.19	0.44	0.05	0.26	0.07	3.90			99.50
			H09 10		65.14	13.17	8.33	5.36		0.01	0.05	2.01	0.81	0.09	0.05	0.26	4.06			99.34
	Palmietfontein (Klerksdorp Goldfield-Heidelberg)	26° 57' 11.124" S; 26° 40' 22.044" E	JP6		57.23	20.18	6.61	4.56		0.62	1.17	3.71	0.73	0.10	0.01	0.13	3.97			99.02
			JP7		59.86	16.00	8.54	5.07		1.16	1.13	2.10	0.64	0.10	0.01	0.14	3.46			98.21
			JP8		60.73	14.42	11.77	5.25		1.11	0.50	1.53	0.62	0.10	0.01	0.16	3.83			100.03
			JP9		56.53	11.43	22.00	3.61		0.99	1.20	1.89	0.45	0.05	0.01	0.07	1.84			100.07
			JP10		55.87	15.06	15.58	4.73		0.92	0.72	1.83	0.96	0.11	0.01	0.10	0.11			96.00
	Palmietfontein (East Rand Goldfield-Heidelberg)	26° 11' 42.432" S; 28° 24' 43.128" E	G13 11		75.88	6.49	6.64	6.75		0.41	0.01	0.02	0.24	0.01	0.11	0.13	3.63			100.32
			G15 14		52.85	11.20	22.70	2.66		0.35	0.02	1.03	0.40	0.01	0.03	0.05	5.92			97.22
			G16 01		59.20	11.53	19.90	2.83		0.03	0.05	1.90	0.44	0.02	0.03	0.05	3.96			99.94
			PWR		57.36	12.56	6.03	6.53		5.42	0.37	1.93	0.64	0.06	0.11	0.16	7.50			98.67
			G04 13		62.42	13.40	12.63	2.85		0.01	0.03	3.02	0.53	0.07	0.22	0.06	3.90			99.14

Group	Formation	Collar Coordinates (Latitude; Longitude)	Sample No.	Depth (m)	SiO_2 (Wt.%)	Al_2O_3	Fe_2O_3 total	MgO		CaO	Na_2O	K_2O	TiO_2	P_2O_5	MnO	Cr_2O_3	LOI	TOC	S	Total
			G05 01		50.69	11.60	27.69	2.58		0.01	0.02	2.19	0.44	0.05	0.26	0.07	3.90			99.50
			G09 10		65.14	13.17	8.33	5.36		0.01	0.05	2.01	0.81	0.09	0.05	0.26	4.06			99.34
	Roodepoort (East Rand Goldfield)	26° 29' 26.3472" S; 28° 25' 41.7108" E	PCS-36		57.57	14.90	12.62	5.74		0.67	0.03	2.81	0.65	0.10	0.09	0.11	4.47			99.76
			PCS-25		73.04	9.66	6.67	4.32		0.40	1.37	0.64	0.34	0.01	0.05	0.07	2.59			99.16
			PCS-26		89.48	5.32	1.36	0.97		0.14	0.05	1.55	0.11	0.01	0.02	0.11	1.09			100.21
			PCS-31		56.13	15.05	13.63	6.82		0.11	0.03	2.02	0.66	0.06	0.07	0.10	4.77			99.45
			PCS-32		57.30	14.47	14.37	5.71		0.47	0.07	1.95	0.64	0.09	0.07	0.10	4.62			99.86
			PCS-1		58.60	23.84	3.76	1.58		0.03	0.19	6.78	1.09	-	0.02	0.21	3.83			99.93
			PCS-2		60.68	22.41	5.55	2.28		0.02	0.16	5.91	1.02	0.02	0.04	0.20	3.70			101.99
			PCS-4		53.79	13.84	20.40	5.79		0.15	0.01	0.45	0.65	0.09	0.17	0.11	3.43			98.88
			PCS-8		53.81	12.74	20.98	5.65		0.28	0.01	0.43	0.54	0.07	0.17	0.09	4.58			99.35
			PCS-11		57.11	11.07	19.43	5.22		0.35	0.01	0.22	0.50	0.09	0.17	0.09	4.24			98.50
			PCS-16		55.62	14.39	16.14	6.40		0.17	0.02	1.64	0.65	0.09	0.09	0.10	4.65			99.96
			PCS-13		48.36	8.67	9.52	14.11		6.94	0.01	0.01	0.35	0.01	0.15	0.29	10.74			99.16
			PCS-18		51.78	13.57	21.26	6.54		0.25	0.01	0.59	0.59	0.11	0.09	0.10	4.99			99.88
	Roodepoort (Klerksdorp Goldfield)	26° 58' 26.724" S; 26° 40' 58.044" E	JP1		63.42	12.88	6.23	5.36		2.84	1.64	1.52	0.60	0.08	0.01	0.13	2.62			97.33
			JP2		65.67	12.90	6.62	5.72		1.51	1.60	1.43	0.65	0.07	0.01	0.19	3.22			99.59
			JP3		67.97	14.80	4.92	2.79		1.41	0.21	3.90	0.38	0.08	0.01	0.01	2.79			99.27
			JP4		71.20	11.63	5.07	3.54		1.70	2.56	1.28	0.44	0.05	0.01	0.11	1.89			99.48
			JP5		46.43	9.79	29.23	3.81		1.64	1.17	0.41	0.39	0.09	0.14	0.08	5.44			98.62

Group	Formation	Collar Coordinates (Latitude; Longitude)	Sample No.	Depth (m)	SiO_2 (Wt.%)	Al_2O_3	Fe_2O_3 total	MgO		CaO	Na_2O	K_2O	TiO_2	P_2O_5	MnO	Cr_2O_3	LOI	TOC	S	Total
	Roodepoort (Central Rand and East Rand Goldfield)	26° 18' 51.012" S; 28° 28' 44.508" E	UG/01		67.16	17.25	4.55	1.98		0.05	0.20	4.13	0.77	0.06	0.04	0.15	3.26			99.60
			UG/02		70.34	12.99	7.12	2.63		0.04	0.10	2.39	0.56	0.03	0.05	0.10	3.46			99.81
			UG/03		65.31	12.98	11.15	4.05		0.08	0.07	1.56	0.66	0.06	0.09	0.11	3.90			100.02
			UG/04		62.00	13.41	12.51	5.06		0.09	0.05	1.26	0.62	0.06	0.11	0.08	4.37			99.62
			UG/05		74.60	10.28	3.92	3.58		0.93	0.09	1.89	0.46	0.05	0.08	0.07	3.75			99.70
			UG/06		76.31	8.64	3.11	3.19		2.10	0.07	1.61	0.30	0.03	0.10	0.07	4.33			99.86
			UG/07		66.00	12.18	8.18	3.95		0.03	0.11	2.26	1.53	0.04	0.07	0.55	4.79			99.69
			UG/08		94.49	3.78	0.69	0.37		0.02	0.06	1.00	0.07	0.01	0.01	0.01	0.80			101.31
			UG/09		72.15	11.39	5.79	3.80		0.07	0.05	2.34	0.55	0.05	0.04	0.16	3.30			99.69
			UG/10		66.71	10.03	8.84	6.33		0.60	0.01	1.01	0.87	0.10	0.07	0.32	4.99			99.88
			UC/01		61.83	14.75	11.50	4.50		0.11	0.09	1.78	0.70	0.09	0.09	0.15	4.28			99.87
			UC/02		59.28	15.37	11.89	5.98		0.06	0.08	1.73	0.72	0.04	0.10	0.14	4.93			100.32
			UA/01		54.05	15.09	21.11	3.22		0.29	0.04	0.74	0.66	0.21	0.09	0.12	4.39			100.01
			UA/02		56.85	13.04	19.08	4.42		0.04	0.02	0.29	0.60	0.05	0.11	0.11	4.82			99.43
			UA/03		62.51	14.70	10.37	5.22		0.15	0.08	2.00	0.66	0.05	0.08	0.12	4.37			100.31
			UA/04		66.50	9.97	5.38	5.09		4.88	0.06	1.24	0.51	0.04	0.11	0.12	7.36			101.26
	Roodepoort (Carletonville Goldfield-West	26° 21' 47.808" S; 27° 28' 9.336" E	UNG001	-	56.79	22.99	11.85	3.10		0.10	0.22	2.15	0.75	0.12	0.07	0.06	0.98	0.08	0.32	99.58
			UNG002	0.20	54.44	23.79	8.94	3.14		0.09	0.42	3.87	0.71	0.09	0.03	0.06	1.73	0.09	1.14	98.54
			UNG003	0.40	55.51	22.17	9.59	3.24		0.09	0.37	3.39	0.63	0.07	0.03	0.05	1.69	0.12	1.30	98.25
			UNG004	0.60	57.06	20.60	12.37	4.63		0.11	0.18	1.86	0.67	0.11	0.05	0.06	1.00	0.12	0.52	99.34

Group	Formation	Collar Coordinates (Latitude; Longitude)	Sample No.	Depth (m)	SiO_2 (Wt.%)	Al_2O_3	Fe_2O_3 total	MgO		CaO	Na_2O	K_2O	TiO_2	P_2O_5	MnO	Cr_2O_3	LOI	TOC	S	Total
			UNG005	0.80	57.05	22.97	12.36	2.82		0.07	0.18	1.86	0.77	0.11	0.08	0.07	0.99	0.07	0.28	99.68
	Roodepoort (Carletonville Goldfield-East Driefontein mine)	26° 25' 8.184" S; 27° 30' 4.32" E	D5P03463-001	6.00	58.28	15.63	12.11	5.32		1.11	0.01	2.64	0.73	0.11	0.06	0.10	4.66	0.20	0.01	100.97
			D5P03463-002	7.00	50.36	13.37	14.14	5.50		6.32	0.01	1.57	0.66	0.12	0.17	0.11	8.67	1.40	0.01	102.40
			D5P03463-003		55.21	15.35	15.53	6.22		0.75	0.12	1.93	0.69	0.16	0.07	0.10	5.07	0.15	0.02	101.37
			D5P03463-004	9.00	52.63	15.41	15.03	6.10		2.46	0.01	1.96	0.69	0.14	0.09	0.10	6.11	0.52	0.01	101.26
			D5P03463-005	10.00	53.92	15.21	16.55	6.56		0.83	0.01	1.58	0.68	0.19	0.07	0.11	5.17	0.10	0.01	100.98
			D5P03463-006	11.00	53.72	14.79	15.69	6.31		1.77	0.01	1.67	0.70	0.15	0.08	0.10	5.48	0.33	0.01	100.81
			D5P03463-007	12.00	48.57	12.72	13.52	4.86		10.34	0.11	0.57	1.38	0.21	0.34	0.02	4.84	0.15	0.01	97.64
			D5P03463-008	13.00	54.77	15.05	15.06	5.58		2.10	0.01	2.09	0.71	0.10	0.08	0.10	5.52	0.42	0.01	101.59
			D5P03463-009	14.00	55.62	15.40	13.80	5.71		0.55	0.01	2.29	0.75	0.14	0.05	0.11	4.58	0.06	0.01	99.07
			D5P03463-010	15.00	57.14	16.08	12.33	5.71		0.98	-	2.92	0.74	0.10	0.06	0.11	4.80	0.18	0.01	101.13
			D5P03463-011	16.00	56.29	15.63	12.54	5.37		1.81	0.01	2.57	0.74	0.11	0.07	0.10	5.42	0.38	0.01	101.04
			D5P03463-012	17.00	51.16	13.27	19.03	5.94		2.24	0.01	0.72	0.56	0.11	0.09	0.09	5.82	0.48	0.01	99.53
			D5P03463-013	18.00	50.88	12.31	20.74	7.44		2.24	0.01	0.43	0.53	0.10	0.11	0.08	5.93	0.44	0.01	101.25

Group	Formation	Collar Coordinates (Latitude; Longitude)	Sample No.	Depth (m)	SiO_2 (Wt.%)	Al_2O_3	Fe_2O_3 total	MgO		CaO	Na_2O	K_2O	TiO_2	P_2O_5	MnO	Cr_2O_3	LOI	TOC	S	Total
			D5P03463-014	19.00	50.94	13.14	19.65	6.37		2.39	0.01	0.48	0.56	0.10	0.10	0.09	6.08	0.55	0.01	100.46
			D5P03463-015	20.00	53.69	14.25	18.22	6.22		0.53	0.01	1.13	0.61	0.16	0.07	0.10	4.81	0.03	0.01	99.83
			D5P03463-016	21.00	51.66	13.22	16.64	5.64		4.06	0.01	1.12	0.60	0.09	0.12	0.09	7.06	0.98	0.01	101.30
			D5P03463-017	22.00	52.19	13.18	19.03	6.31		2.16	0.01	0.76	0.57	0.12	0.10	0.09	5.60	0.13	0.01	100.24
			D5P03463-018	23.00	53.23	13.72	18.77	5.93		1.57	0.01	0.91	0.59	0.14	0.08	0.09	3.81	0.27	0.01	99.13
			D5P03463-019	24.00	52.73	12.41	20.18	6.28		2.17	0.01	0.49	0.56	0.10	0.10	0.09	5.88	0.44	0.01	101.42
			D5P03463-020	25.00	49.10	12.30	17.78	5.33		3.90	0.01	0.58	0.53	0.08	0.11	0.08	7.09	0.83	0.01	97.73
			D5P03463-021	26.00	53.70	13.28	17.83	5.56		2.10	0.01	0.95	0.59	0.12	0.08	0.10	5.80	0.42	0.01	100.54
			D5P03463-022	27.00	53.05	12.76	19.56	5.74		2.22	0.10	0.72	0.58	0.14	0.10	0.09	5.80	0.51	0.12	101.49
			D5P03463-023	28.00	53.38	12.70	18.75	5.70		1.76	0.01	0.58	0.53	0.10	0.08	0.08	5.44	0.34	0.01	99.45
			D5P03463-024	29.00	50.49	12.73	18.76	5.65		4.20	0.12	0.77	0.60	0.19	0.12	0.09	7.42	0.95	0.10	102.19
			D5P03463-025	30.00	55.30	15.43	14.27	5.88		0.98	0.01	2.19	0.74	0.15	0.06	0.10	5.56	0.43	0.01	101.11
			D5P03463-026	31.00	53.97	13.64	17.66	5.76		1.51	0.10	1.17	0.61	0.13	0.08	0.09	5.48	0.62	0.05	100.86
			D5P03463-027	57.00	50.41	12.62	16.52	5.41		5.24	0.17	0.88	0.55	0.10	0.12	0.08	7.77	1.16	0.01	101.03

Group	Formation	Collar Coordinates (Latitude; Longitude)	Sample No.	Depth (m)	SiO_2 (Wt.%)	Al_2O_3	Fe_2O_3 total	MgO		CaO	Na_2O	K_2O	TiO_2	P_2O_5	MnO	Cr_2O_3	LOI	TOC	S	Total
			D5P03463-028	58.00	54.15	13.67	18.05	5.71		1.08	0.26	1.19	0.60	0.14	0.08	0.09	5.11	0.23	0.10	100.46
			D5P03463-029	59.00	54.64	14.34	17.76	5.89		0.46	0.01	1.39	0.61	0.12	0.06	0.09	4.56	0.03	0.01	99.97
			D5P03463-030	60.00	53.88	13.65	18.65	5.76		0.92	0.01	0.95	0.59	0.10	0.07	0.09	4.85	0.14	0.01	99.66
			D5P03463-031	61.00	52.53	13.44	15.87	6.04		1.39	0.01	1.10	0.61	0.11	0.08	0.09	5.26	0.25	0.01	96.78
			D5P03463-032	62.00	56.06	13.67	16.47	6.30		0.53	0.31	1.08	0.62	0.11	0.07	0.09	4.83	0.11	0.02	100.27
			D5P03463-033	63.00	52.76	14.04	15.47	6.13		2.19	0.01	1.37	0.63	0.14	0.08	0.10	5.85	0.43	0.01	99.21
			D5P03463-034	64.00	53.92	13.84	16.31	6.32		1.19	0.09	1.13	0.62	0.12	0.08	0.09	5.32	0.35	0.01	99.37
			D5P03463-035	65.00	54.31	14.21	17.43	6.80		0.66	0.01	0.97	0.61	0.11	0.07	0.09	5.35	0.07	0.01	100.70
			D5P03463-036	66.00	54.04	14.03	16.85	6.65		1.14	0.01	1.06	0.65	0.10	0.08	0.09	5.53	0.19	0.01	100.43
			D5P03463-037	67.00	54.21	15.04	13.61	5.60		2.49	0.01	2.15	0.70	0.14	0.10	0.10	5.84	0.51	0.01	100.50
			D5P03463-038	68.00	48.30	13.05	15.81	5.69		6.39	0.17	1.26	0.62	0.13	0.16	0.09	8.86	1.45	0.18	102.16
			D5P03463-039	69.00	54.03	13.26	14.64	6.70		2.91	0.01	1.63	0.63	0.11	0.10	0.09	6.15	0.64	0.01	100.91
			D5P03463-040	70.00	53.77	13.33	16.12	5.99		1.24	0.01	1.09	0.60	0.11	0.08	0.09	5.04	0.21	0.01	97.69
			D5P03463-041	71.00	51.01	13.15	15.90	5.69		4.99	0.01	1.21	0.61	0.14	0.15	0.09	7.81	1.07	0.01	101.84

Group	Formation	Collar Coordinates (Latitude; Longitude)	Sample No.	Depth (m)	SiO_2 (Wt.%)	Al_2O_3	Fe_2O_3 total	MgO		CaO	Na_2O	K_2O	TiO_2	P_2O_5	MnO	Cr_2O_3	LOI	TOC	S	Total
			D5P03463-042	72.00	54.99	12.97	18.98	6.42		1.53	0.12	0.58	0.60	0.16	0.11	0.11	5.37	0.32	0.16	102.42
			D5P03463-043	73.00	51.08	12.65	20.54	8.00		1.36	0.01	0.51	0.58	0.12	0.11	0.09	5.50	0.26	0.01	100.82
			D5P03463-044	74.00	54.62	14.56	17.11	6.70		0.42	0.01	1.31	0.65	0.12	0.08	0.10	4.88	0.02	0.01	100.58
			D5P03463-045	75.00	57.46	14.46	14.48	6.16		0.63	0.01	1.70	0.68	0.12	0.07	0.10	4.74	0.08	0.01	100.69
			D5P03463-046	76.00	55.77	13.55	18.51	6.60		0.17	0.09	0.71	0.60	0.12	0.09	0.09	4.73	0.02	0.12	101.17
			D5P03463-047	77.00	54.56	12.87	18.03	7.46		0.66	0.01	1.01	0.59	0.14	0.09	0.09	4.70	0.10	0.01	100.32
			D5P03463-048	78.00	54.37	10.66	10.30	4.48		8.73	0.65	1.00	0.49	0.08	0.24	0.08	9.86	1.99	0.10	103.03
			D5P03463-049	79.00	53.36	12.48	15.62	5.70		4.40	0.16	1.00	0.58	0.11	0.14	0.10	7.34	0.98	0.05	102.02
			D5P03463-050	80.00	53.53	13.57	18.04	6.40		1.33	0.01	0.90	0.60	0.13	0.10	0.10	5.39	0.23	0.01	100.33
			D5P03463-051	81.00	52.78	14.54	16.88	6.18		1.20	0.01	1.42	0.63	0.01	0.08	0.09	5.33	0.21	0.01	99.37
			D5P03463-052	82.00	51.97	12.90	18.68	6.35		0.44	0.01	0.53	0.57	0.11	0.09	0.09	4.95	0.03	0.01	96.72
			D5P03463-053	82.91	49.92	12.43	17.07	5.58		5.35	0.22	0.79	0.59	0.12	0.17	0.09	8.12	1.22	0.12	101.79
	Roodepoort (Carletonville Goldfield-	26° 20' 51.036" S; 27° 29'	E1E-000001	3303.73	53.51	12.81	15.21	5.69		3.92	0.21	1.08	0.58	0.08	0.14	0.09	6.98		0.42	100.71
			E1E-000002	3304.00	52.38	13.72	17.78	6.27		0.82	0.01	0.98	0.60	0.06	0.09	0.09	5.14		0.84	98.76

Group	Formation	Collar Coordinates (Latitude; Longitude)	Sample No.	Depth (m)	SiO_2 (Wt.%)	Al_2O_3	Fe_2O_3 total	MgO		CaO	Na_2O	K_2O	TiO_2	P_2O_5	MnO	Cr_2O_3	LOI	TOC	S	Total
			E1E-000003	3304.50	51.42	13.02	17.84	6.07		2.20	0.08	0.77	0.59	0.09	0.12	0.09	6.07		0.34	98.69
			E1E-000004	3305.00	53.13	12.95	16.07	5.87		2.98	0.15	0.99	0.58	0.08	0.13	0.09	6.43		0.14	99.58
			E1E-000005	3306.17	53.87	11.57	12.96	5.09		6.57	0.41	1.00	0.54	0.10	0.19	0.09	8.60		0.49	101.45
	Roodepoort (Carletonville Goldfield-Driefontein surface borehole)	26° 20' 51.036" S; 27° 29' 20.76" E	E1G-000001	3895.65	53.19	13.20	15.95	5.86		3.12	0.13	1.12	0.59	0.07	0.12	0.09	6.52		0.10	100.07
			E1G-000002	3896.00	51.70	12.96	18.26	6.21		1.32	0.05	0.65	0.58	0.10	0.10	0.09	5.51		0.19	97.71
			E1G-000003	3896.20	56.62	14.01	16.50	6.38		0.40	0.05	1.21	0.64	0.12	0.08	0.10	4.74		0.14	100.96
			E1G-000004	3896.60	54.10	12.00	14.65	5.88		4.60	0.27	1.00	0.55	0.11	0.16	0.09	7.30		0.38	101.09
			E1G-000005	3896.80	55.21	12.55	14.99	5.84		3.47	0.27	0.98	0.57	0.11	0.14	0.09	6.66		0.14	101.02
			E1G-000006	3897.00	52.95	13.46	17.20	6.16		1.72	0.06	0.98	0.59	0.08	0.10	0.09	5.66		0.01	99.07
			E1G-000007	3897.17	54.80	12.73	15.74	6.11		2.82	0.20	0.98	0.58	0.11	0.13	0.09	6.23		0.13	100.65
Central Rand Group	Booysens (Welkom Goldfield-Beatrix mine)	28° 15' 35.748" S; 26° 47' 4.776" E	BOOYWG-011	3.00	63.64	23.76	1.09	0.26		0.39	0.70	4.76	0.94	0.04	0.01	0.08	4.56		0.01	100.24
			BOOYWG-012	4.00	60.65	25.77	0.80	0.27		0.41	0.59	5.14	1.07	0.10	0.01	0.08	6.00		0.01	100.90
			BOOYWG-013	5.00	51.63	12.60	15.60	5.92		2.00	<NWG	1.69	0.56	0.23	0.08	0.08	6.23		0.01	96.63
			BOOYWG-014	6.00	62.08	24.27	0.98	0.32		0.40	0.49	4.85	0.96	0.09	0.01	0.08	5.96		0.01	100.50

Group	Formation	Collar Coordinates (Latitude; Longitude)	Sample No.	Depth (m)	SiO_2 (Wt.%)	Al_2O_3	Fe_2O_3 total	MgO		CaO	Na_2O	K_2O	TiO_2	P_2O_5	MnO	Cr_2O_3	LOI	TOC	S	Total
			BOOYWG-015	7.00	62.30	27.80	1.39	0.35		0.43	0.76	5.41	1.17	0.12	0.01	0.08	2.00		0.01	101.83
			BOOYWG-016	8.00	64.56	22.69	2.79	0.33		0.37	0.45	4.35	0.95	0.07	0.56	0.09	3.96		0.01	101.16
			BOOYWG-017	9.00	68.82	21.15	1.64	0.31		0.60	0.47	4.19	0.95	0.04	0.02	0.09	2.90		0.01	101.18
			BOOYWG-019	11.00	65.03	17.52	7.15	0.33		0.06	0.08	2.96	0.72	0.01	2.20	0.09	3.96		0.01	100.11
			BOOYWG-020	12.00	63.03	17.42	7.13	0.30		0.61	0.36	4.15	0.81	0.01	2.35	0.09	3.92		0.01	100.18
	Booysens (Western Areas Goldfield-Cooke section, Zuurbekom)	26° 18' 32.148" S; 27° 44' 12.048" E	Z1637-001A	1485.22	51.66	12.55	7.68	8.83		7.41	0.47	0.97	0.42	0.09	0.10	0.12	9.92	1.59	0.06	101.87
			Z1673-002A	1485.80	47.83	19.32	9.41	11.65		1.09	0.25	2.81	0.68	0.11	0.11	0.20	6.69	0.10	0.05	100.30
			Z1637-003A	1486.10	46.10	20.58	9.32	11.59		1.05	0.33	3.26	0.69	0.09	0.10	0.18	6.65	0.08	0.04	100.06
			Z1637-004A	1486.40	55.82	15.20	8.07	9.70		1.95	0.23	2.04	0.52	0.08	0.10	0.15	6.28	0.34	0.04	100.52
			Z1637-005A	1486.70	45.40	18.54	11.01	13.36		1.23	0.21	1.91	0.67	0.07	0.13	0.22	7.39	0.15	0.08	100.37
			Z1637-006A	1487.00	50.04	17.12	9.77	12.73		0.90	0.24	1.66	0.61	0.07	0.12	0.19	6.73	0.08	0.02	100.28
			Z1637-007A	1487.30	49.62	17.43	9.83	12.98		0.82	0.38	1.62	0.61	0.06	0.12	0.19	6.59	0.05	0.02	100.32
			Z1637-008A	1487.60	50.19	16.82	9.44	12.28		1.45	1.03	1.18	0.60	0.07	0.11	0.18	6.79	0.19	0.02	100.35
			Z1637-009A	1487.90	52.94	15.84	8.52	11.17		1.97	1.34	0.88	0.58	0.08	0.10	0.18	6.50	0.29	0.01	100.40

Group	Formation	Collar Coordinates (Latitude; Longitude)	Sample No.	Depth (m)	SiO_2 (Wt.%)	Al_2O_3	Fe_2O_3 total	MgO		CaO	Na_2O	K_2O	TiO_2	P_2O_5	MnO	Cr_2O_3	LOI	TOC	S	Total
			Z1637-010A	1488.20	54.33	15.74	8.29	10.78		1.60	1.29	1.09	0.57	0.06	0.10	0.17	6.05		0.03	100.10
			Z1637-011A	1488.50	54.87	15.44	8.40	10.78		1.51	1.29	0.96	0.57	0.09	0.10	0.17	5.89	0.17	0.03	100.27
			Z1637-012A	1488.80	56.79	15.18	7.74	9.93		1.46	1.84	0.75	0.56	0.05	0.09	0.16	5.45	0.16	0.03	100.19
			Z1637-013A	1489.10	53.41	15.98	8.75	11.28		1.39	1.25	1.01	0.58	0.10	0.10	0.17	6.03	0.15	0.02	100.22
			Z1637-014A	1489.40	53.00	16.37	8.86	11.37		1.24	1.37	1.08	0.59	0.09	0.10	0.18	5.85	0.11	0.03	100.24
			Z1637-015A	1489.70	49.94	17.62	9.46	12.20		1.05	1.18	1.34	0.62	0.12	0.11	0.18	6.25	0.08	0.04	100.19
			Z1637-016A	1490.00	51.73	16.89	9.25	11.83		1.04	1.44	1.08	0.60	0.09	0.11	0.17	5.82	0.07	0.04	100.16
			Z1637-017A	1490.30	52.32	16.35	9.10	11.61		1.17	1.30	1.09	0.57	0.06	0.10	0.17	6.09	0.12	0.05	100.10
			Z1637-018A	1490.60	52.86	16.68	8.83	11.20		1.17	1.41	1.25	0.58	0.11	0.10	0.17	5.68	0.11	0.06	100.21
			Z1637-019A	1490.90	54.01	16.42	8.58	10.78		1.12	1.53	1.15	0.59	0.10	0.10	0.17	5.50	0.09	0.06	100.20
			Z1637-020A	1491.20	52.04	17.40	8.94	11.07		1.02	1.44	1.45	0.59	0.09	0.10	0.17	5.67	0.07	0.08	100.13
			Z1637-021A	1491.50	53.29	17.21	8.45	10.40		1.18	1.60	1.42	0.60	0.10	0.09	0.16	5.46	0.10	0.07	100.13
			Z1637-022A	1491.80	52.06	17.32	8.92	10.95		1.04	1.40	1.50	0.61	0.11	0.10	0.17	5.75	0.07	0.08	100.08
			Z1637-023A	1492.10	52.56	17.44	8.75	10.65		0.99	1.29	1.64	0.60	0.11	0.10	0.16	5.58	0.05	0.09	100.01

Group	Formation	Collar Coordinates (Latitude; Longitude)	Sample No.	Depth (m)	SiO_2 (Wt.%)	Al_2O_3	Fe_2O_3 total	MgO		CaO	Na_2O	K_2O	TiO_2	P_2O_5	MnO	Cr_2O_3	LOI	TOC	S	Total
			Z1637-024A	1492.40	52.47	17.47	8.70	10.70		1.10	1.50	1.57	0.60	0.11	0.10	0.16	5.53	0.09	0.07	100.17
			Z1637-025A	1492.70	54.64	16.76	8.17	10.03		1.09	1.61	1.47	0.60	0.10	0.09	0.16	5.28	0.07	0.09	100.16
			Z1637-026A	1493.00	52.74	17.52	8.59	10.51		0.99	1.58	1.56	0.61	0.09	0.10	0.16	5.54	0.06	0.05	100.10
			Z1637-027A	1493.30	54.45	17.17	8.04	9.83		0.97	1.84	1.57	0.62	0.09	0.09	0.15	5.14	0.04	0.07	100.07
			Z1637-028A	1493.60	53.72	17.34	8.32	10.02		0.89	1.68	1.68	0.61	0.06	0.09	0.15	5.20	0.03	0.15	99.94
			Z1637-029A	1493.90	51.85	18.42	8.46	10.19		0.97	1.55	2.00	0.64	0.08	0.09	0.16	5.36	0.05	0.13	99.95
			Z1637-030A	1494.20	51.51	18.53	8.41	10.12		1.15	1.70	2.02	0.62	0.10	0.09	0.16	5.45	0.09	0.14	100.09
			Z1637-001B	1538.21	52.05	19.20	8.23	9.32		0.96	0.46	3.06	0.65	0.11	0.08	0.15	5.62	0.14	0.13	100.16
			Z1637-002B	1538.81	52.38	19.33	8.07	8.99		0.85	0.47	3.22	0.65	0.15	0.08	0.14	5.41	0.11	0.15	100.00
			Z1637-003B	1539.11	50.11	19.22	8.58	9.48		1.65	0.37	3.06	0.63	0.14	0.09	0.15	6.05	0.32	0.25	100.10
			Z1637-004B	1539.41	51.94	18.55	8.65	9.42		1.11	0.37	2.85	0.63	0.14	0.09	0.15	5.74	0.17	0.21	100.02
			Z1637-005B	1539.71	52.05	19.20	8.31	9.32		0.72	0.37	3.12	0.66	0.12	0.09	0.15	5.61	0.09	0.21	100.02
			Z1637-006B	1540.01	51.46	17.86	7.41	8.19		3.49	0.17	3.09	0.60	0.11	0.10	0.14	7.17	0.75	0.21	100.75
			Z1637-007B	1540.31	51.87	19.53	8.16	9.14		0.83	0.27	3.27	0.70	0.14	0.09	0.14	5.53	0.12	0.20	99.99

Group	Formation	Collar Coordinates (Latitude; Longitude)	Sample No.	Depth (m)	SiO_2 (Wt.%)	Al_2O_3	Fe_2O_3 total	MgO		CaO	Na_2O	K_2O	TiO_2	P_2O_5	MnO	Cr_2O_3	LOI	TOC	S	Total
			Z1637-008B	1540.61	48.52	19.56	7.66	8.37		3.24	0.13	3.73	0.68	0.12	0.09	0.14	7.15	0.67	0.30	100.36
			Z1637-009B	1540.91	54.56	20.72	8.05	8.90		0.72	0.13	3.91	0.70	0.13	0.08	0.13	1.51	0.05	0.22	99.81
			Z1637-010B	1541.21	53.50	21.40	7.95	8.91		0.97	0.12	4.05	0.73	0.13	0.08	0.14	1.64	0.10	0.19	99.91
			Z1637-011B	1541.51	54.74	19.28	7.97	9.05		1.90	0.12	3.34	0.68	0.09	0.09	0.15	2.15	0.34	0.18	100.08
			Z1637-012B	1541.81	48.89	20.97	9.02	10.28		2.64	0.19	3.46	0.69	0.08	0.10	0.17	2.68	0.49	0.36	100.02
	Booysens (Welkom Goldfield-Saaiplaas mine, Dagbreek)	27° 58' 7.068" S; 26° 46' 45.696" E	EDPC 1.1	1.11	67.11	22.17	2.17	0.89		0.09	0.41	2.61	0.72	0.02	< 0.03	0.06	3.66			99.91
			EDPC 1.2	3.03	65.71	21.84	2.83	1.19		0.09	0.40	2.95	0.72	0.03	< 0.03	0.05	3.69			99.50
			EDPC 1.3	9.55	68.18	19.13	3.96	1.37		0.05	0.49	2.77	0.57	0.04	< 0.03	0.06	3.32			99.94
			EDPC 1.4	14.81	68.73	16.86	5.68	1.83		0.04	0.36	2.66	0.47	0.02	< 0.03	0.07	3.14			99.86
			EDPC 1.5	31.06	69.34	16.01	5.75	1.75		0.03	0.41	2.95	0.42	0.02	< 0.03	0.05	2.95			99.68
			EDPC 1.6	32.12	67.00	17.32	6.20	1.97		0.03	0.42	3.16	0.50	0.02	0.04	0.06	3.16			99.88
			EDPC 2.1	0.58	72.96	19.77	0.86	0.26		0.06	0.19	2.16	0.44	0.03	< 0.03	0.03	3.17			99.93
			EDPC 2.2	4.73	74.64	16.22	2.39	0.32		0.05	0.18	2.07	0.37	0.03	< 0.03	0.03	3.22			99.52
			EDPC 2.3	6.63	76.15	16.65	1.22	0.37		0.06	0.21	2.35	0.40	0.02	< 0.03	0.04	2.64			100.11
			EDPC 2.4	9.58	60.09	19.47	12.19	2.44		0.02	-	0.96	0.57	0.02	0.23	0.08	3.62			99.69
			EDPC 2.5	11.98	98.16	0.41	1.07	0.16		0.01	-	0.04	0.01	< 0.01	< 0.03	0.00	0.07			99.93

Group	Formation	Collar Coordinates (Latitude; Longitude)	Sample No.	Depth (m)	SiO_2 (Wt.%)	Al_2O_3	Fe_2O_3 total	MgO		CaO	Na_2O	K_2O	TiO_2	P_2O_5	MnO	Cr_2O_3	LOI	TOC	S	Total
			EDPC 3.1	1.16	69.87	21.88	0.84	0.28		0.06	0.16	2.09	0.64	0.05	< 0.03	0.05	3.63			99.55
			EDPC 3.2	2.48	72.80	20.32	0.73	0.23		0.05	0.16	1.91	0.47	0.03	< 0.03	0.03	3.25			99.98
			EDPC 3.3	8.98	66.83	21.43	3.01	1.05		0.08	0.23	2.85	0.69	0.03	< 0.03	0.05	3.60			99.85
			EDPC 3.4	23.60	62.64	18.57	9.61	2.24		0.04	0.15	2.11	0.65	0.03	0.10	0.09	3.47			99.70
			EDPC 3.5	25.48	57.49	15.33	16.88	4.04		0.02	-	0.54	0.51	0.02	0.11	0.08	4.34			99.36
			EDPC 4.1	1.19	66.70	21.52	1.71	0.56		0.13	1.25	3.78	0.63	0.02	< 0.03	0.05	3.19			99.54
			EDPC 4.2	3.07	64.19	22.10	3.45	0.98		0.12	1.11	3.76	0.64	0.03	< 0.03	0.06	3.29			99.73
			EDPC 4.3	9.22	70.81	16.94	4.50	1.13		0.08	0.76	2.94	0.31	0.03	< 0.03	0.02	2.66			100.18
			EDPC 4.4	23.06	61.94	15.20	10.51	5.02		0.05	0.21	1.57	0.59	0.02	0.10	0.09	4.15			99.45
	Booysens (Welkom Goldfield-Geduld mine, Dagbreek)	27° 57' 31.068" S; 26° 47' 18.096" E	UT 2.1	1.15	67.93	22.38	1.80	0.79		0.03	0.26	1.99	0.64	0.02	0.03	0.05	3.84			99.76
			UT 2.2	3.50	66.21	21.89	2.99	1.26		0.04	0.36	2.64	0.68	0.03	0.03	0.05	3.79			99.97
			UT 2.3	5.85	66.11	21.51	3.24	1.36		0.02	0.40	2.92	0.67	0.03	0.03	0.05	3.60			99.94
			UT 2.4	7.10	61.36	19.14	9.56	2.70		0.03	0.25	2.61	0.62	0.03	0.03	0.05	3.58			99.96
			UT 2.5	7.66	56.27	20.85	11.68	3.34		0.02	0.24	2.53	0.67	0.03	0.10	0.09	4.15			99.97
	Booysens (Welkom Goldfield-, Welkom division of Western	27° 56' 55.068" S; 26° 46' 6.096" E	MB 6.1	0.01	65.16	23.59	2.92	1.31		0.04	0.15	1.53	0.78	0.02	0.03	0.08	4.41			100.02
			MB 6.2	2.06	65.72	22.73	2.90	1.30		0.04	0.21	2.15	0.69	0.03	0.03	0.03	4.14			99.97
			MB 6.3	15.85	62.23	20.08	7.61	2.74		0.03	0.18	1.87	0.58	0.03	0.05	0.07	4.30			99.77
			MB 6.4	19.04	64.49	20.08	6.03	2.00		0.03	0.21	2.18	0.68	0.02	0.03	0.07	4.02			99.84
			MB 6.5	19.33	62.76	26.01	1.71	0.81		0.04	0.31	3.21	0.77	0.02	0.03	0.08	4.34			100.09

Group	Formation	Collar Coordinates (Latitude; Longitude)	Sample No.	Depth (m)	SiO_2 (Wt.%)	Al_2O_3	Fe_2O_3 total	MgO		CaO	Na_2O	K_2O	TiO_2	P_2O_5	MnO	Cr_2O_3	LOI	TOC	S	Total
			MB 6.6	19.53	65.34	23.94	2.33	1.02		0.04	0.18	1.69	0.83	0.02	0.03	0.08	4.42			99.92
			MB 6.7	19.72	65.44	23.73	2.63	1.23		0.05	0.15	1.56	0.74	0.02	0.03	0.07	4.48			100.13
	Booysens (Klerksdorp Goldfield-Strathmore)	26° 57' 47.124" S; 26° 40' 58.044" E	M 6.1	33.10	70.11	14.14	7.37	2.09		0.02	0.25	2.40	0.37	0.02	0.03	0.03	2.92			99.75
			M 6.2	58.43	69.56	15.41	4.96	1.74		0.61	0.38	3.04	0.65	0.03	0.03	0.05	3.39			99.85
			M 6.3	85.75	60.29	16.60	9.06	4.95		0.82	0.21	2.14	0.63	0.07	0.07	0.14	4.92			99.90
			M 6.4	101.19	64.84	15.65	7.26	3.14		1.04	0.16	2.46	0.53	0.07	0.07	0.08	4.40			99.70
			M 6.5	101.89	53.24	17.86	13.23	5.93		0.57	0.15	1.71	0.58	0.06	0.11	0.12	5.66			99.22
			M 6.6	102.33	64.16	13.92	8.25	3.53		1.98	0.28	1.86	0.50	0.07	0.10	0.08	4.96			99.69
			M 7.1	26.01	69.25	14.02	4.84	1.85		2.22	0.49	2.55	0.33	0.02	0.06	0.05	4.40			100.08
			M 7.2	30.07	62.35	18.00	7.38	3.27		0.32	0.46	3.09	0.60	0.02	0.05	0.13	4.18			99.85
			M 7.3	31.95	63.93	16.27	6.89	3.01		1.22	0.43	2.71	0.55	0.07	0.06	0.08	4.52			99.74
			M 7.4	37.95	62.60	15.69	7.17	3.26		1.70	0.42	2.57	0.45	0.04	0.09	0.07	5.65			99.71
			M 7.5	47.08	64.10	18.07	6.15	2.70		0.22	0.57	3.22	0.65	0.11	0.03	0.11	3.79			99.72
			M 7.6	51.57	67.42	17.06	4.77	1.99		0.33	0.62	3.27	0.65	0.14	0.03	0.07	3.38			99.73
	Booysens (Klerksdorp Goldfield-Vaal Reefs mine, Strathmore)	26° 57' 11.124" S; 26° 40' 22.044" E	V 2.1	29.98	70.26	14.97	4.72	1.67		0.78	0.45	2.93	0.45	0.02	0.03	0.04	3.74			100.06
			V 2.2	44.78	64.00	16.27	6.84	2.94		1.28	0.34	2.58	0.55	0.06	0.04	0.11	4.81			99.82
			V 2.3	45.84	60.70	15.16	9.47	4.31		1.39	0.28	1.89	0.60	0.07	0.11	0.16	5.52			99.66
			V 2.4	47.96	65.04	15.97	5.71	2.79		1.44	0.42	2.95	0.46	0.07	0.06	0.08	5.15			100.14
			V 2.5	51.39	63.35	17.42	6.61	2.95		0.71	0.37	2.98	0.55	0.09	0.04	0.09	4.61			99.77
			V 2.6	51.66	62.64	17.62	7.41	3.43		0.22	0.37	2.82	0.58	0.09	0.03	0.13	4.23			99.57

Group	Formation	Collar Coordinates (Latitude; Longitude)	Sample No.	Depth (m)	SiO_2 (Wt.%)	Al_2O_3	Fe_2O_3 total	MgO		CaO	Na_2O	K_2O	TiO_2	P_2O_5	MnO	Cr_2O_3	LOI	TOC	S	Total
	Booysens (Klerksdorp Goldfield)	26° 57' 11.124" S; 26° 40' 22.044" E	DN2-1	1823.00	58.50	14.70	6.97	8.20		2.16	1.50	0.80	0.44	0.05	0.06	0.13	5.36		0.01	98.88
			DN2-2	1825.00	61.40	17.50	5.87	5.10		1.03	2.10	2.25	0.52	0.07	0.04	0.06	3.44		0.09	99.47
			DN2-3	1827.00	55.50	19.20	6.73	5.60		2.44	1.60	3.08	0.59	0.06	0.10	0.07	4.99		0.10	100.06
			DN2-4	1829.00	56.90	18.20	6.40	5.40		2.08	1.40	2.97	0.57	0.07	0.08	0.08	4.80		0.08	99.03
			DN2-5	1830.00	53.70	19.80	7.19	6.40		1.59	1.50	3.07	0.58	0.10	0.08	0.09	4.93		0.07	99.10
			DN2-6	1832.00	55.40	18.10	6.17	5.60		3.21	1.30	3.03	0.55	0.08	0.08	0.08	5.79		0.06	99.45
			DN2-7	1835.00	56.10	18.60	6.20	5.80		1.89	1.30	3.20	0.60	0.12	0.10	0.08	4.95		0.05	98.99
			DN2-8	1837.00	55.80	18.90	6.64	6.00		1.88	1.10	3.23	0.61	0.09	0.06	0.09	4.97		0.04	99.41
			DN2-9	1839.00	56.90	19.30	6.31	6.00		1.03	1.10	3.47	0.58	0.07	0.02	0.08	4.37		0.07	99.30
			DN2-10	1841.00	56.20	19.00	7.21	6.80		0.85	1.00	3.18	0.62	0.07	0.08	0.09	4.56		0.04	99.70
			DN2-11	1843.00	56.00	19.10	7.11	6.70		0.69	0.90	3.40	0.67	0.04	0.06	0.10	4.47		0.04	99.28
			DN2-12	1846.00	54.70	18.90	7.03	6.60		1.70	1.00	3.19	0.60	0.07	0.06	0.09	5.15		0.05	99.14
			DN2-13	1848.00	55.00	19.90	7.35	6.80		0.72	0.70	3.71	0.65	0.05	0.06	0.10	4.70		0.04	99.78
			DN2-14	1853.00	55.50	19.00	7.35	7.30		0.66	0.80	3.35	0.65	0.05	0.06	0.10	4.82		0.04	99.68
			DN2-15	1855.00	54.60	18.30	8.46	8.00		0.66	0.70	2.80	0.71	0.04	0.08	0.14	5.04		0.10	99.63
			DN2-16	1857.00	60.80	15.80	6.42	6.90		1.08	1.10	2.12	0.64	0.07	0.12	0.12	4.54		0.06	99.77
			DN2-17	1858.00	56.80	15.30	7.74	9.30		1.43	0.90	1.17	0.62	0.05	0.10	0.16	5.47		0.04	99.08
			DN2-18	1862.00	58.90	14.10	6.94	8.70		2.29	0.90	1.02	0.57	0.04	0.08	0.15	5.87		0.05	99.61
			DN2-19	1864.00	55.60	15.30	7.85	9.71		2.15	0.80	1.22	0.59	0.03	0.10	0.16	6.16		0.18	99.85
			DN2-20	1866.00	53.60	15.30	8.68	12.10		1.20	0.60	0.92	0.60	0.04	0.10	0.19	6.20		0.02	99.55

Group	Formation	Collar Coordinates (Latitude; Longitude)	Sample No.	Depth (m)	SiO_2 (Wt.%)	Al_2O_3	Fe_2O_3 total	MgO		CaO	Na_2O	K_2O	TiO_2	P_2O_5	MnO	Cr_2O_3	LOI	TOC	S	Total
			DN2-21	1868.00	54.80	14.80	8.02	10.90		1.95	0.50	0.90	0.59	0.03	0.06	0.18	6.47		0.02	99.22
			DN2-22	1870.00	54.10	51.10	8.76	11.70		1.25	0.50	0.94	0.61	0.05	0.12	0.19	6.13		0.01	135.46
			DN2-23	1874.00	63.80	12.70	5.62	7.73		1.77	1.40	0.67	0.51	0.04	0.06	0.13	4.82		0.02	99.27
			DN2-24	1879.00	53.90	14.60	8.81	12.60		0.87	0.40	0.67	0.59	0.05	0.09	0.20	6.35		0.02	99.15
			DN2-25	1882.00	55.40	14.70	8.50	11.70		1.03	0.70	0.83	0.61	0.04	0.14	0.19	5.84		0.01	99.69
			DN2-26	1887.00	52.60	15.10	8.65	11.40		1.92	0.60	1.09	0.59	0.07	0.13	0.19	6.63		0.01	98.98
			DN2-27	1891.00	56.00	14.30	7.51	9.83		2.68	0.80	1.00	0.55	0.04	0.10	0.16	6.48		0.04	99.49
	Booysens (Evander Goldfield)	26°28'21.1"S; 29°05'42.2"E	439-2#		50.87	17.81	12.85	7.64		0.10	0.90	1.30	0.63	0.09	0.14	0.17	7.64	0.29		100.43
			439-3#		54.18	18.52	9.86	6.58		0.09	0.17	2.08	0.60	0.10	0.12	0.17	6.65	0.22		99.34
			615-7#		57.00	19.86	7.54	5.45		0.14	0.49	2.51	0.81	0.09	0.04	0.18	5.99	0.24		100.34
			615-8#		54.24	22.67	6.41	4.62		0.21	0.63	3.46	0.92	0.14	0.03	0.17	5.86	0.29		99.65
			615-9#		55.13	21.37	7.13	4.97		0.13	0.53	3.01	0.85	0.09	0.03	0.17	6.10	0.26		99.77
			730-4#		50.87	19.22	11.37	7.43		0.11	0.17	1.87	0.72	0.08	0.06	0.17	7.48	0.26		99.81
			730-5#		51.09	18.94	10.87	7.75		0.12	0.14	1.70	0.75	0.08	0.08	0.16	7.33	0.24		99.25
	Booysens (Central Rand Goldfield)	26°13'28.1"S; 27°59'31.4"E	UR1140#		59.89	13.67	9.77	7.05		0.84	0.09	0.88	0.55	0.06	0.16	0.17	5.84	0.72		99.69
			GV2-28#		52.59	15.84	14.18	7.27		0.12	0.03	0.67	0.59	0.09	0.23	0.18	7.31	0.28		99.38
			MEE-24#		58.79	19.95	7.07	5.12		0.50	0.72	2.87	0.55	0.10	0.07	0.06	4.41			100.21
			MEE-33#		54.35	16.59	8.95	11.16		0.68	0.10	0.87	0.57	0.24	0.12	0.23	6.35			100.21

Table A. 4. Trace element concentrations of the Witwatersrand Supergroup marine shales.

Group	Formation	Collar Coordinates (Latitude; Longitude)	Sample No.	As (ppm)	Rb	Ba	Sr	Pb	Cs	Co	Cr	Cu	Ni	V	Sc	Zn	Ga	Zr	Nb	Hf
West Rand Group	Orange Grove		D14*		240	313	92	12.0		572	8		77	278	48.00			239	13.00	8.8
	Parktown - Brixton		MED-10*		40	99	17	9.3		619	29		360	130	18.00			141	12.00	4.4
			MED-11*		22	50	5	2.4		436	21		243	70	11.00			55	4.70	1.6
			MED-12*		32	155	7	10.0		543	29		459	122	12.00			106	6.10	2.9
			C-71*		93	226	5			284	21		84	94	10.00			54	4.30	1.4
	Promise		MED-13*		112	403	33	8.2		395	25		282	105	11.00			91	5.50	2.1
			MED-14*		113	293	27	4.9		388	27		274	87	11.00			64	5.00	1.7
			MED-15*		122	623	21	2.7		510	36		238	101	16.00			64	5.40	2.0
	Roodepoort Formation		MED-17*		3	6	7	8.0		794	43		322	154	24.00			115	7.00	3.9
			MED-18*		34	150	19	8.9		686	43		403	161	19.00			146	8.40	4.4
			C-75*		121	349	15	6.7		1112	48		365	210	28.00			141	9.20	4.2
			AA0098*		98	423	103	20.0		690	51		338	165	24.00			143	11.00	3.9
			AA0101*		96	439	117	16.0		840	34		325	179	27.00			169	12.00	4.8
Central Rand Group	Booysens Formation		MEE-5#		144	776	95	17.0		806	44		441	166	21.00			132	9.30	4.1
			MEE-27#		42	275	78	14.0		1528	77		582	167	27.00			94	5.70	3.6
			MEE-32*		54	499	35	19.0		1060	56		620	216	25.00			103	8.00	2.8
			SJ-3-2*		32	299	108	9.7		1384	62		547	185	27.00			97	5.70	2.9
			SJ-3-4*		118	771	100	13.0		1209	68		457	191	26.00			101	6.30	3.3

Group	Formation	Collar Coordinates (Latitude; Longitude)	Sample No.	As (ppm)	Rb	Ba	Sr	Pb	Cs	Co	Cr	Cu	Ni	V	Sc	Zn	Ga	Zr	Nb	Hf
	Kimberly Formation (K-8)		MEE-14*		68	443	38	15.0		770	25		517	165	22.00			212	11.00	7.5
			MEE-23*		120	626	133	31.0		750	123		386	141	30.00			158	11.00	5.0
			MEE-34*		36	156	51	17.0		765	52		419	235	27.00			181	13.00	5.6
			MED-1*		165	450	110	24.0		724	85		547	204	25.00			203	15.00	5.8
			MED-7*		23	162	72	21.0		532	23		141	152	19.00			211	12.00	7.3
West Rand Group	Parktown-Brixton (East Rand	26° 31' 23.898" S; 28° 23' 49.5744" E	H01 09		114	239	11			34	691	83.00	283	107	15.00	107	16.00	234		10.0
			H04 13		182	763	11			25	443	11.00	164	96	15.00	44	17.00	130		9.2
			H05 01		138	600	10			28	460	38.00	194	108	16.00	52	16.00	115		7.2
			H09 10		79		23			25	1765		343	140			15.00	115		6.9
	Palmietfontein (Klerksdorp Goldfield-	26° 57' 11.124" S; 26° 40' 22.044" E	JP6		119	1085	117	2.0		40	900	61.00	252	187	21.00	97	21.00	158	4.00	
			JP7		82	608	120	11.0		36	935	46.00	258	135	18.00	98	19.00	130	2.00	
			JP8		58	407	64	13.0		32	1125	42.00	316	100	15.00	77	16.00	107	5.00	
			JP9		105	437	189	2.0		20	478	41.00	186	67	14.00	55	13.00	111	12.00	
			JP10					12.0		32	710	85.00	232	123	17.00	90	17.00	168	6.00	
	Palmietfontein (East Rand Goldfield-Heidelberg)	26° 11' 42.432" S; 28° 24' 43.128" E	G13 11		1	648	10			44	868	141.00	807	93	12.00	180	6.80	368	5.00	
			G15 14		63	15	21			27	312	29.00	158	79	19.00	58	16.00	58	3.10	
			G16 01		112	489	11			29	364	39.00	247	96	14.00	53	15.00	105	7.30	
			PWR		75	423	87			53	1110	66.00	332	135	23.00	104	15.00	156	5.80	
			G04 13		182	763	11			25	443	11.00	164	96	15.00	44	17.00	130	9.20	
			G05 01		138	600	10			28	460	38.00	194	108	16.00	52	16.00	115	7.20	

Group	Formation	Collar Coordinates (Latitude; Longitude)	Sample No.	As (ppm)	Rb	Ba	Sr	Pb	Cs	Co	Cr	Cu	Ni	V	Sc	Zn	Ga	Zr	Nb	Hf
			G09 10		79		23			25	1765		343	140			15.00	115	6.90	
	Roodepoort (East Rand Goldfield)	26° 29' 26.3472" S; 28° 25' 41.7108" E	PCS-36		108	775	9			42	719	45.00	317	155	25.00	85	19.00	142	6.90	
			PCS-25		24	141	88			29	462	22.00	151	63	9.00	61	10.00	101	4.20	
			PCS-26		494	377	77			61	786	46.00	305	231	4.00	123	5.40	484	0.10	
			PCS-31		78	439	8			39	674	32.00	306	150	23.00	86	18.00	132	8.20	
			PCS-32		78		16			41	674		278	148			18.00	125	7.00	
			PCS-1		221	749	16			73	1410	13.00	281	276	40.00	20	28.00	190	12.00	
			PCS-2		190	660	13			48	1370	11.00	332	227	42.00	28	26.00	170	10.00	
			PCS-4		17	93	4			40	781	13.00	334	142	22.00	98	17.00	154	8.70	
			PCS-8		20	118	7			34	642	16.00	286	127	19.00	106	17.00	132	7.40	
			PCS-11		10	64	7			31	599	47.00	242	123	18.00	102	15.00	126	7.90	
			PCS-16		72	346	25			37	671	19.00	308	148	23.00	79	19.00	136	7.00	
			PCS-13		-		221			74	1970		428	140			8.50	33		
			PCS-18		26		7			39	683		289	144			17.00	127	7.60	
	Roodepoort (Klerksdorp Goldfield)	26° 58' 26.724" S; 26° 40' 58.044" E	JP1		67	417	217	14.0		45	876	61.00	298	143	16.00	88	14.00	136	3.00	
			JP2		55	360	180	9.0		43	1290	64.00	352	123	16.00	88	14.00	130	2.00	
			JP3		182	1125	209	24.0		6	56	10.00	20	19	6.60	104	21.00	506	17.00	
			JP4		52	333	273	13.0		30	780	44.00	205	89	12.00	61	11.00	99	2.00	
			JP5					21.0		21	530	32.00	215	67	16.00	63	11.00	137	1.00	
	Roo dep	26° 18' 51. 012'	UG/01		131		30			29	1055	46.00	236	168		77		122	8.00	

Group	Formation	Collar Coordinates (Latitude; Longitude)	Sample No.	As (ppm)	Rb	Ba	Sr	Pb	Cs	Co	Cr	Cu	Ni	V	Sc	Zn	Ga	Zr	Nb	Hf
			UG/02		76		16			54	660	85.00	384	125		100		115	7.00	
			UG/03		51		11			56	776	77.00	409	142		139		132	8.00	
			UG/04		40		10			31	559	64.00	415	78		144		140	8.00	
			UG/05		65		26			30	456	56.00	186	66		77		212	6.00	
			UG/06		54		37			23	475	34.00	140	48		63		105	3.00	
			UG/07		79		18			89	3760	180.00	449	130		183		1115	22.00	
			UG/08		31		7			6	67	9.00	26	11		33		44		
			UG/09		83		9			37	1080	30.00	359	105		101		183	7.00	
			UG/10		39		15			58	2200	133.00	570	134		134		353	10.00	
			UC/01		58		15			46	998	49.00	363	159		122		133	9.00	
			UC/02		57		13			47	933	35.00	391	173		142		90	9.00	
			UA/01		23		9			54	824	47.00	304	173		122		143	10.00	
			UA/02		11		5			47	769	38.00	313	129		117		128	9.00	
			UA/03		70		16			43	804	57.00	294	137		87		151	8.00	
			UA/04		44		48			39	853	66.00	279	88		87		152	6.00	
	Roodepoort (Carletonville	26° 21' 47.808" S; 27° 28' 9.336" E	UNG001		69	368	54	10.7	1.80	29	435	18.20	192	165	23.00	90	25.10	154	10.70	3.9
			UNG002		127	683	87	17.8	3.00	62	407	12.40	228	145	22.00	74	28.00	137	11.50	3.7
			UNG003		106	576	75	19.6	2.30	47	367	12.80	230	129	19.00	79	23.60	90	9.50	2.8
			UNG004		59	319	51	8.0	1.70	31	404	15.60	200	127	17.00	115	23.80	146	10.50	4.0
			UNG005		60	320	51	8.4	1.50	26	453	70.40	196	175	24.00	85	25.80	147	11.20	4.1

Group	Formation	Collar Coordinates (Latitude; Longitude)	Sample No.	As (ppm)	Rb	Ba	Sr	Pb	Cs	Co	Cr	Cu	Ni	V	Sc	Zn	Ga	Zr	Nb	Hf
	Roodepoort (Carletonville Goldfield-East Driefontein mine)	26° 25' 8.184" S; 27° 30' 4.32" E	D5P03463-001	3	117	639	36	8.6		81	688		256	146	27.58		15.80	162	10.71	4.3
			D5P03463-002	3	65	496	184	4.5		79	744		257	128	24.43		13.15	156	8.67	4.3
			D5P03463-003		70	415	27	9.6	3.90	40	674	50.70	307	162	23.00	87	17.60	130	7.90	3.5
			D5P03463-004	2	82	515	64	6.2		83	698		274	156	27.50		15.75	156	10.02	4.4
			D5P03463-005	15	62	404	26	5.2		78	735		277	162	29.35		15.60	154	10.14	4.1
			D5P03463-006	7	66	453	44	2.1		82	708		266	159	27.08		14.75	158	9.96	4.1
			D5P03463-007	21	19	330	213	12.4		84	117		65	209	28.53		15.83	246	12.05	6.2
			D5P03463-008	16	76	551	52	4.0		104	658		284	153	26.18		14.73	145	10.12	4.0
			D5P03463-009	3	95	586	18	1.8		78	731		282	166	27.30		16.10	172	10.65	4.5
			D5P03463-010	5	135	752	32	6.1		118	730		273	165	26.60		17.85	170	11.30	4.7
			D5P03463-011	15	104	697	52	3.4		80	689		250	154	25.25		15.55	162	10.68	4.3
			D5P03463-012	6	24	211	59	1.5		82	628		226	136	23.98		12.53	145	9.31	3.8
			D5P03463-013	3	16	133	61	1.8		114	580		220	124	22.18		12.20	137	8.97	3.6
			D5P03463-014	13	15	132	62	1.8		88	585		228	124	22.05		12.23	140	8.93	4.0

Group	Formation	Collar Coordinates (Latitude; Longitude)	Sample No.	As (ppm)	Rb	Ba	Sr	Pb	Cs	Co	Cr	Cu	Ni	V	Sc	Zn	Ga	Zr	Nb	Hf
			D5P03463-015	7	41	300	14	1.2		65	666		242	143	25.08		14.10	141	9.16	3.8
			D5P03463-016	5	46	340	105	2.2		74	630		211	127	22.55		13.55	158	9.07	4.4
			D5P03463-017	5	28	226	57	1.7		93	616		222	129	22.89		12.79	145	8.94	4.0
			D5P03463-018	2	34	295	44	1.6		106	647		232	131	23.40		13.13	150	9.32	4.1
			D5P03463-019	2	17	155	58	1.5		108	589		200	127	22.08		11.55	140	8.18	3.8
			D5P03463-020	3	21	217	113	1.8		72	554		197	115	20.45		11.65	142	8.96	4.0
			D5P03463-021	3	35	312	56	1.5		113	657		225	133	23.55		12.65	142	8.77	3.8
			D5P03463-022		21	144	52	2.5	1.70	41	611	72.50	264	133	18.00	88	13.90	112	6.30	3.4
			D5P03463-023	2	19	166	43	1.3		72	551		209	122	23.90		11.95	133	8.16	3.5
			D5P03463-024		27	217	100	2.6	1.90	37	610	9.70	259	135	18.00	84	14.40	108	7.10	3.1
			D5P03463-025	7	83	544	27	2.0		83	701		261	164	27.65		15.45	150	9.54	4.2
			D5P03463-026	2	43	315	39	2.0	1.10	58	625	79.40	252	139	22.14	44	14.23	128	7.85	3.6
			D5P03463-027	2	33	359	165	1.9		76	514		199	105	19.48		11.75	147	9.13	3.9
			D5P03463-028		48	405	35	2.0	2.70	37	638	245.10	274	138	19.00	86	15.60	118	7.40	3.4

Group	Formation	Collar Coordinates (Latitude; Longitude)	Sample No.	As (ppm)	Rb	Ba	Sr	Pb	Cs	Co	Cr	Cu	Ni	V	Sc	Zn	Ga	Zr	Nb	Hf
			D5P03463-029	3	59	557	14	1.2		75	618		235	141	24.88		14.60	147	7.99	4.0
			D5P03463-030	3	33	320	24	1.3		106	585		208	132	23.28		12.73	141	8.62	3.9
			D5P03463-031	1	38	268	38	7.3		112	639		229	132	22.03		13.20	143	8.63	4.0
			D5P03463-032		37	220	24	5.3	2.60	38	640	84.90	282	134	17.00	92	14.60	118	7.10	3.3
			D5P03463-033	1	53	354	61	8.0		110	662		236	145	24.85		14.18	142	8.85	3.9
			D5P03463-034	1	40	267	36	5.7	0.65	83	637	21.23	243	136	21.79	23	13.79	138	8.43	3.8
			D5P03463-035	1	32	226	20	2.4		73	607		226	135	23.28		13.20	150	9.13	4.1
			D5P03463-036	1	41	244	33	3.7		75	633		237	132	22.08		14.28	158	8.98	4.3
			D5P03463-037	8	94	779	63	2.0		118	667		263	157	24.75		15.38	143	9.15	3.8
			D5P03463-038		49	476	172	5.7	3.00	42	624	41.00	276	132	18.00	78	14.90	129	7.10	3.9
			D5P03463-039	4	61	422	86	8.1		76	642		212	128	22.10		13.23	171	9.37	4.7
			D5P03463-040	3	44	413	35	2.3		122	611		243	128	21.45		13.60	152	9.09	4.0
			D5P03463-041	2	51	834	168	2.1		80	627		236	134	23.03		13.05	139	8.65	3.6
			D5P03463-042		21	263	45	1.5	1.80	40	746	111.50	310	134	19.00	89	15.70	112	7.00	3.2

Group	Formation	Collar Coordinates (Latitude; Longitude)	Sample No.	As (ppm)	Rb	Ba	Sr	Pb	Cs	Co	Cr	Cu	Ni	V	Sc	Zn	Ga	Zr	Nb	Hf
			D5P03463-043	4	20	287	41	1.0		97	645		253	135	23.35		12.68	136	8.86	3.8
			D5P03463-044	1	49	660	14	0.9		114	659		263	152	25.65		14.50	161	10.18	4.4
			D5P03463-045	1	74	819	20	1.5		122	711		272	147	23.95		14.75	154	9.64	4.3
			D5P03463-046		27	317	10	1.2	2.10	41	628	58.40	293	138	19.00	90	14.90	118	6.80	3.0
			D5P03463-047	3	38	545	24	1.9		107	642		248	139	23.53		12.78	135	8.61	3.6
			D5P03463-048		39	420	190	3.4	2.20	27	531	53.40	229	108	13.00	54	11.10	95	5.10	2.9
			D5P03463-049		42	602	121	2.5	2.50	33	683	71.20	280	128	17.00	75	13.70	114	6.70	3.4
			D5P03463-050	2	33	527	45	1.2		112	678		243	142	24.55		13.50	133	8.52	3.4
			D5P03463-051	2	51	467	34	1.2		104	620		225	149	25.08		13.70	143	9.64	4.1
			D5P03463-052	5	17	239	11	1.0		118	599		222	127	22.10		12.05	140	8.84	3.8
			D5P03463-053		37	562	170	3.0	2.70	38	628	25.20	271	126	17.00	77	12.90	115	7.80	3.3
	Roodepoort (Carletonville	26° 20' 51.036" S; 27° 29' 20.76" E	E1E-000001	1	41	504	97	2.1	1.18	69	628	31.15	244	132	19.91	32	13.00	121	7.49	3.5
			E1E-000002	3	34	353	22	1.1		111	610		223	138	23.59		12.88	141	9.24	3.9
			E1E-000003	3	29	384	68	1.7	0.90	89	612	8.40	238	130	20.90	26	12.61	132	8.62	3.7

Group	Formation	Collar Coordinates (Latitude; Longitude)	Sample No.	As (ppm)	Rb	Ba	Sr	Pb	Cs	Co	Cr	Cu	Ni	V	Sc	Zn	Ga	Zr	Nb	Hf
			E1E-000004	2	37	444	74	1.8	0.84	82	621	22.25	238	132	20.75	23	12.85	127	7.93	3.6
			E1E-000005	-	40	511	155	3.0	2.35	30	607	62.30	255	118	15.00	65	12.40	105	5.90	3.2
	Roodepoort (Carletonville Goldfield-Driefontein surface borehole)	26° 20' 51.036" S; 27° 29' 20.76" E	E1G-000001	1	43	504	81	1.9	1.13	72	638	31.15	247	135	20.68	33	13.31	126	7.94	3.6
			E1G-000002	4	23	311	40	1.3	0.45	103	606	4.20	230	129	21.50	13	12.33	136	8.73	3.7
			E1G-000003	1	50	568	15	1.4	1.05	81	670	29.20	283	143	21.48	45	14.83	136	8.22	3.6
			E1G-000004	1	40	522	111	2.6	1.57	55	619	41.53	252	125	17.84	43	12.53	115	6.80	3.3
			E1G-000005	0	39	457	82	2.1	1.73	51	612	45.63	264	128	17.83	58	13.34	116	6.73	3.2
			E1G-000006	2	36	434	47	1.3	0.29	101	631	7.79	233	138	22.91	8	13.06	134	8.62	3.7
			E1G-000007	1	38	466	68	2.0	1.28	66	619	33.71	258	131	19.37	43	13.22	121	7.27	3.3
Central Rand Group	Booysens (Welkom Goldfield-Beatrix mine)	28° 15' 35.748" S; 26° 47' 4.776" E	BOOYWG-011	105	114	711	158	5.1		123	569		108	140	25.00		17.54	606	15.60	13.2
			BOOYWG-012	107	117	732	160	5.3		124	576		112	142	26.29		19.95	605	16.70	14.7
			BOOYWG-013	107	118	739	160	5.2		123	579		113	142	26.87		20.81	605	17.15	15.0
			BOOYWG-014	107	118	741	160	5.3		124	579		114	143	27.07		21.07	605	17.09	15.2
			BOOYWG-015	107	118	745	161	5.3		124	581		114	143	27.17		21.41	605	17.35	15.4

Group	Formation	Collar Coordinates (Latitude; Longitude)	Sample No.	As (ppm)	Rb	Ba	Sr	Pb	Cs	Co	Cr	Cu	Ni	V	Sc	Zn	Ga	Zr	Nb	Hf
			BOOYWG-016	108	120	755	161	5.4		124	584		116	144	28.09		22.72	604	17.70	16.2
			BOOYWG-017	108	120	754	162	5.6		124	584		115	144	27.58		22.35	604	17.80	16.1
			BOOYWG-019	107	121	761	160	4.7		122	587		117	145	28.60		23.40	603	18.50	15.9
			BOOYWG-020	108	119	749	163	5.8		126	582		116	144	28.10		22.40	604	16.80	16.5
	Booysens (Western Areas Goldfield-Cooke section, Zuurbekom)	26° 18' 32.148" S; 27° 44' 12.048" E	Z1637-001A		51	335	202	7.9	2.90	37	817	11.40	379	129	20.00	146	14.10	74	4.40	2.1
			Z1673-002A		143	986	66	3.5	6.40	61	1347	4.20	674	202	31.00	170	22.10	108	7.30	3.0
			Z1637-003A		157	1102	70	2.6	6.70	56	1258	8.10	665	200	30.00	219	22.60	113	7.40	3.2
			Z1637-004A		95	684	59	2.6	4.40	49	1056	18.00	546	152	24.00	205	16.60	81	5.30	2.2
			Z1637-005A		91	652	54	3.0	4.50	64	1484	27.90	777	195	31.00	264	21.30	97	7.00	2.9
			Z1637-006A		76	568	51	3.1	3.30	57	1323	5.10	725	179	29.00	194	18.70	89	6.10	2.5
			Z1637-007A		75	532	58	2.0	3.90	52	1333	1.20	713	184	29.00	198	19.90	85	6.10	2.4
			Z1637-008A		52	366	115	6.6	2.50	55	1258	1.30	642	170	26.00	187	18.00	91	5.70	2.8
			Z1637-009A		40	272	157	2.9	1.80	58	1225	5.40	653	160	25.00	144	17.30	90	5.80	2.5
			Z1637-010A		48	333	147	3.8	2.50	56	1197	9.20	627	152	24.00	176	17.10	89	5.80	2.3

Group	Formation	Collar Coordinates (Latitude; Longitude)	Sample No.	As (ppm)	Rb	Ba	Sr	Pb	Cs	Co	Cr	Cu	Ni	V	Sc	Zn	Ga	Zr	Nb	Hf
			Z1637-011A		37	272	150	3.8	2.30	54	1196	11.90	630	168	24.00	150	18.50	89	5.40	2.6
			Z1637-012A		30	212	202	7.5	1.90	49	1063	9.00	556	135	21.00	151	14.70	97	5.60	2.9
			Z1637-013A		44	295	144	6.2	2.50	54	1162	10.60	642	159	25.00	140	18.20	85	5.50	2.5
			Z1637-014A		45	316	148	12.6	2.50	57	1202	10.60	646	171	26.00	169	18.90	92	5.80	2.6
			Z1637-015A		59	422	125	6.8	3.10	58	1257	14.10	678	188	28.00	182	19.90	96	6.00	2.2
			Z1637-016A		44	303	135	12.3	2.50	62	1196	15.50	653	171	28.00	166	19.70	88	5.70	2.8
			Z1637-017A		44	307	122	9.3	2.20	55	1187	21.50	659	159	26.00	169	17.60	78	5.40	2.2
			Z1637-018A		54	373	135	7.3	2.90	54	1165	20.30	632	171	26.00	182	19.00	85	5.80	2.4
			Z1637-019A		48	358	143	4.8	2.90	53	1132	35.00	603	156	25.00	173	17.70	93	6.00	2.9
			Z1637-020A		62	455	132	4.3	3.10	55	1147	37.70	624	176	26.00	182	18.80	90	6.10	2.6
			Z1637-021A		64	460	149	3.3	3.40	51	1093	41.00	578	167	25.00	164	17.80	93	6.10	2.5
			Z1637-022A		63	459	154	5.1	5.70	54	1146	26.40	609	169	26.00	198	18.30	89	5.90	2.4
			Z1637-023A		70	526	145	4.8	5.40	55	1128	21.40	607	175	25.00	219	18.80	91	6.10	2.6
			Z1637-024A		66	476	159	9.6	4.40	52	1097	25.60	605	167	26.00	172	18.70	92	6.40	2.6

Group	Formation	Collar Coordinates (Latitude; Longitude)	Sample No.	As (ppm)	Rb	Ba	Sr	Pb	Cs	Co	Cr	Cu	Ni	V	Sc	Zn	Ga	Zr	Nb	Hf
			Z1637-025A		64	454	156	5.7	3.60	52	1083	29.90	577	168	26.00	187	19.70	101	6.00	2.8
			Z1637-026A		66	478	142	5.3	3.80	53	1067	28.70	589	162	24.00	207	18.20	92	6.10	2.4
			Z1637-027A		65	491	159	4.6	3.90	54	1045	46.30	552	154	24.00	181	19.40	105	6.50	3.0
			Z1637-028A		71	508	150	4.8	4.60	54	1027	42.70	571	163	23.00	192	18.90	89	6.20	2.4
			Z1637-029A		85	652	148	4.9	4.90	52	1076	46.50	578	183	26.00	207	21.30	91	6.60	2.5
			Z1637-030A		86	642	160	4.2	4.60	52	1063	54.50	550	174	26.00	241	20.90	94	6.20	2.3
			Z1637-001B		120	790	58	12.9	5.20	54	1012	55.80	538	186	27.00	153	22.10	99	7.30	2.9
			Z1637-002B		125	822	57	8.5	5.20	53	948	88.70	517	169	27.00	153	20.70	100	7.00	3.1
			Z1637-003B		125	767	80	20.1	5.70	65	1060	89.90	636	178	28.00	231	20.40	99	7.40	2.9
			Z1637-004B		113	732	54	8.0	4.80	48	1008	58.60	551	175	26.00	177	21.80	93	7.30	2.6
			Z1637-005B		123	824	51	9.6	5.10	53	1032	49.70	537	193	28.00	183	22.70	101	7.30	2.8
			Z1637-006B		123	832	174	13.9	5.30	54	979	72.10	509	163	25.00	219	18.10	98	6.60	2.8
			Z1637-007B		128	860	46	9.5	5.40	50	968	60.60	529	182	27.00	220	21.30	105	7.60	3.2
			Z1637-008B		147	962	128	13.8	6.50	50	955	63.20	510	185	27.00	237	20.10	106	7.50	3.1

Group	Formation	Collar Coordinates (Latitude; Longitude)	Sample No.	As (ppm)	Rb	Ba	Sr	Pb	Cs	Co	Cr	Cu	Ni	V	Sc	Zn	Ga	Zr	Nb	Hf
			Z1637-009B		149	968	41	12.3	6.20	52	900	57.30	472	175	25.00	164	20.80	106	7.30	2.8
			Z1637-010B		155	1034	50	11.0	6.80	52	929	63.00	501	188	27.00	193	23.00	123	8.00	3.4
			Z1637-011B		125	840	81	21.3	5.00	55	1040	60.00	552	168	26.00	178	18.30	96	6.90	2.7
			Z1637-012B		127	887	122	45.0	5.30	59	1193	52.10	647	183	28.00	216	22.60	101	7.50	2.7
	Booysens (Welkom Goldfield-Saaiplaas mine, Dagbreek)	27° 58' 7.068" S; 26° 46' 45.696" E	EDPC 1.1		107	450	50	7.9	6.90	11	391	49.00	59	116	18.00	40		161	7.00	
			EDPC 1.2		119	483	56	11.0	3.10	34	369	52.00	162	93	16.00	125		110	6.10	
			EDPC 1.3		127	524	57	9.5	4.90	14	439	65.00	83	120	18.00	40		147	9.00	
			EDPC 1.4		87	511	30	7.8	4.00	31	480	49.00	236	88	15.00	152		163	8.80	
			EDPC 1.5		81	580	30	25.0	3.20	31	366	27.00	162	80	12.00	66		206	7.10	
			EDPC 1.6		90	600	30	9.6	3.30	44	429	34.00	186	95	14.00	73		144	6.10	
			EDPC 2.1		37	303	16	39.0	2.70	5	237	24.00	22	71	13.00	21		152	7.50	
			EDPC 2.2		81	297	30	25.0	2.90	47	229	30.00	58	78	12.00	19		206	7.10	
			EDPC 2.3		90	271	30	9.6	2.70	11	246	30.00	31	22	11.00	16		144	6.10	
			EDPC 2.4		37	171	16	39.0	3.70	59	572	17.00	402	120	17.00	171		152	7.50	
			EDPC 2.5		2	9	2	26.0	2.40	1	18	2.00	15	3	0.70	7		3		
			EDPC 3.1		82	272	32	10.0	4.20	8	367	34.00	30	109	18.00	13		168	12.00	
			EDPC 3.2		74	258	27	6.6	2.70	4	227	18.00	15	68	11.00	6		130	8.60	
			EDPC 3.3		108	402	38	21.0	3.90	12	317	32.00	60	111	16.00	42		244	12.00	

Group	Formation	Collar Coordinates (Latitude; Longitude)	Sample No.	As (ppm)	Rb	Ba	Sr	Pb	Cs	Co	Cr	Cu	Ni	V	Sc	Zn	Ga	Zr	Nb	Hf
			EDPC 3.4		80	315	27	17.0	< 3.6	55	597	16.00	345	106	18.00	137		314	8.70	
			EDPC 3.5		19	85	11	19.0	< 4	56	526	36.00	599	99	15.00	279		162	5.90	
			EDPC 4.1		152	722	128	17.0	9.20	11	337	41.00	65	108	17.00	16		196	11.00	
			EDPC 4.2		148	710	119	15.0	8.80	16	442	45.00	94	118	19.00	40		222	9.20	
			EDPC 4.3		116	599	81	23.0	6.20	13	165	9.90	108	55	9.20	52		97	4.10	
			EDPC 4.4		61	573	32	42.0	< 3.7	47	606	22.00	295	105	17.00	158		218	6.30	
	Booysens (Welkom Goldfield-Geduld mine, Portions)	27° 57' 31.068" S; 26° 47' 18.096" E	UT 2.1		84	359	31	9.0	2.80	5	334	29.00	57	104	15.00	34		182	12.00	
			UT 2.2		110	493	39	11.0	4.30	14	373	47.00	71	112	17.00	57		242	12.00	
			UT 2.3		121	548	44	13.0	4.80	14	366	51.00	90	110	18.00	50		220	10.00	
			UT 2.4		104	533	29	15.0	5.40	73	574	50.00	302	127	20.00	115		207	8.50	
			UT 2.5		102	505	30	19.0	< 3.8	79	622	53.00	391	138	20.00	138		202	9.00	
	Booysens (Welkom Goldfield-, Welkom division of Western Holdings Portions)	27° 56' 55.068" S; 26° 46' 6.096" E	MB 6.1		62	238	30	30.0	< 3	12	540	28.00	90	133	20.00	40		269	12.00	
			MB 6.2		87	340	38	11.0	4.60	14	420	48.00	74	119	18.00	44		321	9.70	
			MB 6.3		75	307	32	11.0	4.00	27	488	34.00	287	122	18.00	149		155	8.30	
			MB 6.4		86	357	36	16.0	5.20	45	459	4.30	240	109	16.00	105		340	9.60	
			MB 6.5		129	476	49	8.0	4.00	9	574	2.30	59	135	21.00	22		198	11.00	
			MB 6.6		67	257	30	9.0	< 2.9	12	540	42.00	78	131	19.00	28		308	12.00	
			MB 6.7		64	238	30	13.0	3.30	11	513	36.00	84	129	19.00	36		215	12.00	
	Booysens (Vaal Reefs Mine)	26° 57' 47.124" S; 26° 40'	M 6.1		117	559	42	27.0	3.40	28	214	41.00	162	63	11.00	149		146	4.70	
			M 6.2		146	784	75	53.0	4.50	33	331	112.00	112	88	14.00	108		279	8.90	

Group	Formation	Collar Coordinates (Latitude; Longitude)	Sample No.	As (ppm)	Rb	Ba	Sr	Pb	Cs	Co	Cr	Cu	Ni	V	Sc	Zn	Ga	Zr	Nb	Hf
			M 6.3		98	610	46	55.0	3.60	51	986	92.00	414	142	24.00	138		183	6.60	
			M 6.4		79	240	38	38.0	3.10	13	572	29.00	91	142	21.00	40		354	15.00	
			M 6.5		73	466	41	17.0	3.90	48	841	21.00	404	148	21.00	205		93	7.50	
			M 6.6		117	709	60	25.0	3.50	30	550	42.00	218	103	18.00	161		154	7.30	
			M 7.1		121	711	109	21.0	3.70	23	328	31.00	159	68	12.00	81		80	4.10	
			M 7.2		139	881	94	20.0	3.50	42	870	19.00	303	129	19.00	138		146	7.40	
			M 7.3		123	779	91	24.0	3.50	36	581	45.00	233	107	18.00	122		169	6.90	
			M 7.4		122	728	82	31.0	3.50	28	462	18.00	235	87	13.00	102		85	7.30	
			M 7.5		142	968	119	23.0	3.50	33	773	55.00	299	122	17.00	169		172	8.90	
			M 7.6		143	962	107	60.0	3.30	32	500	27.00	188	107	16.00	76		270	6.90	
	Booysens (Klerksdorp Goldfield-Vaal Reefs mine,	26° 57' 11.124" S; 26° 40' 22.044" E	V 2.1		143	845	75	24.0	3.20	19	266	42.00	100	78	13.00	79		122	5.90	
			V 2.2		124	687	53	50.0	5.00	34	757	76.00	277	125	16.00	138		123	6.30	
			V 2.3		84	581	73	48.0	3.70	49	1120	89.00	490	137	21.00	140		148	6.70	
			V 2.4		139	867	82	16.0	3.40	27	519	28.00	218	94	15.00	94		118	6.00	
			V 2.5		139	883	81	14.0	3.40	38	617	12.00	293	132	19.00	154		158	6.30	
			V 2.6		132	837	75	16.0	3.50	43	918	50.00	431	145	21.00	139		144	6.30	
	Booysens (Klerksdorp	26° 57' 11.124" S; 26° 40' 22.044" E	DN2-1	33	51	268	171	11.0	-	25	872	9.00	419	95	40.00	123	2.00	107	1.00	
			DN2-2	18	103	531	183	3.0	-	17	430	35.00	194	98	20.00	85	1.00	158	9.00	
			DN2-3	21	103	713	140	4.0		27	507	57.00	221	79	31.00	100	17.00	141	10.00	
			DN2-4	21	123	710	133	6.0		13	524	41.00	232	106	29.00	95	8.00	147	8.00	

Group	Formation	Collar Coordinates (Latitude; Longitude)	Sample No.	As (ppm)	Rb	Ba	Sr	Pb	Cs	Co	Cr	Cu	Ni	V	Sc	Zn	Ga	Zr	Nb	Hf
			DN2-5	21	125	671	106	1.0		21	600	39.00	269	122	29.00	114	8.00	151	7.00	
			DN2-6	17	122	680	129	3.0		19	520	36.00	220	109	32.00	101	9.00	144	6.00	
			DN2-7	20	129	677	111	6.0		18	565	45.00	252	110	39.00	98	11.00	163	9.00	
			DN2-8	23	127	673	108	1.0		19	587	48.00	251	111	35.00	110	26.00	167	10.00	
			DN2-9	21	137	689	99	14.0		20	581	36.00	254	110	32.00	102	10.00	169	9.00	
			DN2-10	19	127	656	89	15.0		19	609	45.00	279	126	30.00	131	16.00	150	10.00	
			DN2-11	25	128	695	78	4.0		18	679	55.00	259	129	24.00	115	10.00	166	10.00	
			DN2-12	18	119	640	79			24	622	43.00	281	122	30.00	117	11.00	139	11.00	
			DN2-13	18	134	722	68	4.0		20	686	50.00	276	127	33.00	119	22.00	161	12.00	
			DN2-14	1	129	669	62			21	717	70.00	290	123	35.00	114	11.00	154	9.00	
			DN2-15	15	125	658	59			28	936	66.00	366	138	40.00	130	8.00	137	6.00	
			DN2-16	20	97	519	84	12.0		27	802	57.00	329	124	29.00	118	13.00	136	7.00	
			DN2-17	18	66	368	89	9.0		31	1081	65.00	461	145	38.00	133		129	10.00	
			DN2-18	2	59	315	98	1.0		30	1008	49.00	437	116	39.00	97	3.00	118	5.00	
			DN2-19	14	67	349	19	1.0		35	1113	45.00	485	128	42.00	102	4.00	114	8.00	
			DN2-20	16	58	304	53	11.0		35	1334	42.00	575	166	43.00	107	3.00	97	3.00	
			DN2-21	18	52	299	73	6.0		28	1201	41.00	500	138	49.00	111		100	3.00	
			DN2-22	19	55	336	55	9.0		38	1278	50.00	548	162	50.00	112	8.00	102	7.00	
			DN2-23	17	45	232	136	7.0		26	905	50.00	387	96	27.00	82		129	10.00	
			DN2-24	25	44	284	43	7.0		28	1374	39.00	613	163	51.00	116	1.00	99		

Group	Formation	Collar Coordinates (Latitude; Longitude)	Sample No.	As (ppm)	Rb	Ba	Sr	Pb	Cs	Co	Cr	Cu	Ni	V	Sc	Zn	Ga	Zr	Nb	Hf
			DN2-25	21	48	313	54	4.0		35	1274	49.00	571	155	55.00	105	7.00	99	3.00	
			DN2-26	28	68	364	66	7.0		35	1287	44.00	544	165	52.00	112		103	6.00	
			DN2-27	29	58	361	86	4.0		38	1124	43.00	476	139	48.00	96		115	4.00	
	Booysens (Evander Goldfield)	26°28'21.1"S; 29°05'42.2"E	439-2#		50	258	21			49	1160	49.00	570	189	28.00	120		107	5.30	
			439-3#		78	408	33			56	1160	43.00	572	179	28.00	96		95	7.20	
			615-7#		99	399	76			73	1215	57.00	558	191	30.00	84		153	9.20	
			615-8#		98	505	95			84	1170	125.00	610	228	36.00	84		139	9.80	
			615-9#		116	473	84			75	1160	45.00	561	201	32.00	77		143	7.70	
			730-4#		68	298	28			74	1175	53.00	629	192	28.00	124		114	6.70	
			730-5#		64	299	26			47	1125	46.00	563	193	29.00	121		121	9.20	
	Booysens (Central Rand Goldfield)	26°13'28.1"S; 27°59'31.4"E	UR1140#		33	278	17			67	1170	32.00	507	121	23.00	140		134	4.50	
			GV2-28#		25	205	9			62	1215	39.00	654	170	25.00	172		105	7.20	
			MEE-24#		121	630	133	12.0	4.80	23	425		393	145	12.00			156	9.00	
			MEE-33#		36	301	42	24.0	3.00	67	1561		681	189	28.00			110	7.50	

Group	Formation	Collar Coordinates (Latitude; Longitude)	Sample No.	Ta	Tl	Mo	Sb	Sn	Th	U	W	Y	La	Ce	Pr	Nd	Sm	Eu	Gd	Tb	Dy	Ho	Er	Tm	Yb	Lu
			PAAS+						14.6	3.1		27	38	80	8.83	33.9	5.6	1.1	4.7	0.77	4.68	0.99	2.85	0.41	2.82	0.43
West Rand Group	Orange Grove		D14*	1.50					14.0	3.7		61	84	159			13.0	3.1		1.70					5.20	0.82
	Parktown - Brixton		MED-10*	0.87					7.2	4.7		23	20	38			3.6	0.8		0.55					2.20	0.37
			MED-11*	0.30					2.6	0.6		15	13	26			2.3	0.6		0.31					1.40	0.23
			MED-12*	0.46					3.2	1.3		17	15	32			2.5	0.6		0.35					1.20	0.24
			C-71*	0.32					2.9	0.7		18	12	22			2.3	0.5		0.17					1.30	0.18
	Promise		MED-13*	0.47					3.7	0.6		22	15	31			3.1	0.7		0.40					1.50	0.27
			MED-14*	0.39					2.9	0.6		19	13	26			2.5	0.6		0.32					1.30	0.19
			MED-15*	0.48					4.0	0.8		19	16	34			3.2	0.8		0.40					1.70	0.27
	Roodepoort Formation		MED-17*	0.51					4.2	1.0		23	25	49			4.6	1.2		0.62					2.90	0.47
			MED-18*	0.64					4.8	0.6		25	23	47			4.5	1.0		0.62					2.70	0.41
			C-75*	0.72					4.3	1.2		42	27	57			5.3	1.2		0.90					3.00	0.43
			AA0098*	0.71					5.5	2.3		23	38	79			6.0	1.3		0.74					2.30	0.30
			AA0101*	0.85					6.1	2.0		24	36	75			5.9	1.4		0.77					2.50	0.38
Central Rand Group	Booysens Formation		MEE-5#	0.84					6.0	1.8		28	32	63			5.5	1.4		0.68					2.20	0.36
			MEE-27#	0.50					3.9	0.9		19	18	37			3.9	1.2		0.48					2.00	0.34
			MEE-32*	0.54					4.2	0.8		27	24	50			5.3	1.2		0.66					2.00	0.30
			SJ-3-2*	0.46					3.1	1.0		23	17	38			3.8	0.9		0.40					1.80	0.31
			SJ-3-4*	0.56					4.6	1.3		30	23	50			4.7	1.2		0.52					2.10	0.31

Group	Formation	Collar Coordinates (Latitude; Longitude)	Sample No.	Ta	Tl	Mo	Sb	Sn	Th	U	W	Y	La	Ce	Pr	Nd	Sm	Eu	Gd	Tb	Dy	Ho	Er	Tm	Yb	Lu
	Kimberly Formation (K-8)		MEE-14*	1.10					8.9	4.0		36	49	89			6.8	1.3		0.96					4.00	0.60
			MEE-23*	1.20					11.0	4.3		24	65	124			11.0	2.8		1.60					4.30	0.70
			MEE-34*	1.10					11.0	3.8		52	53	110			9.2	2.0		1.50					4.80	0.70
			MED-1*	1.30					9.4	4.1		40	47	98			7.3	1.6		1.10					3.70	0.60
			MED-7*	1.30					12.0	7.1		43	66	125			8.7	1.5		1.20					4.70	0.72
West Rand Group	Parktown-Brixton (East Rand Goldfield-Heidelberg)	26° 31' 23.898" S; 28° 23' 49.5744" E	H01 09							2.2		19														
			H04 13							0.2		21														
			H05 01									16														
			H09 10							1.5																
	Palmietfontein (Klerksdorp Goldfield-Heidelberg)	26° 57' 11.124" S; 26° 40' 22.044" E	JP6						4.0		28.00															
			JP7						2.0		16.00															
			JP8						7.0		16.00															
			JP9						2.0		15.00															
			JP10						12.0		24.00															
	Palmietfontein (East Rand Goldfield-Heidelberg)	26° 11' 42.432" S; 28° 24' 43.128" E	G13 11							0.6	66.00															
			G15 14								15.00															
			G16 01								17.00															
			PWR								23.00															
			G04 13							0.2	21.00															
			G05 01								16.00															

Group	Formation	Collar Coordinates (Latitude; Longitude)	Sample No.	Ta	Tl	Mo	Sb	Sn	Th	U	W	Y	La	Ce	Pr	Nd	Sm	Eu	Gd	Tb	Dy	Ho	Er	Tm	Yb	Lu
			G09 10							1.5																
	Roodepoort (East Rand Goldfield)	26° 29' 26.3472" S; 28° 25' 41.7108" E	PCS-36							0.2	22.00															
			PCS-25																							
			PCS-26								53.00															
			PCS-31								22.00															
			PCS-32																							
			PCS-1							13.0	17.00															
			PCS-2							1.6	17.00															
			PCS-4								21.00															
			PCS-8							1.0	22.00															
			PCS-11								24.00															
			PCS-16								21.00															
			PCS-13																							
			PCS-18																							
	Roodepoort (Klerksdorp Goldfield)	26° 58' 26.724" S; 26° 40' 58.044" E	JP1						10.0		16.00															
			JP2						3.0		18.00															
			JP3						22.0		69.00															
			JP4						7.0		10.00															
			JP5						17.0		6.00															
	Roodepoort (Cast	26° 18'	UG/01								20.00															

Group	Formation	Collar Coordinates (Latitude; Longitude)	Sample No.	Ta	Tl	Mo	Sb	Sn	Th	U	W	Y	La	Ce	Pr	Nd	Sm	Eu	Gd	Tb	Dy	Ho	Er	Tm	Yb	Lu
			UG/02								17.00																
			UG/03								22.00																
			UG/04								21.00																
			UG/05								15.00																
			UG/06								12.00																
			UG/07								37.00																
			UG/08								5.00																
			UG/09								17.00																
			UG/10								26.00																
			UC/01								18.00																
			UC/02								18.00																
			UA/01								29.00																
			UA/02								18.00																
			UA/03								19.00																
			UA/04								18.00																
	Roodepoort (Carletonville Goldfield-West Driefontein mine)	26° 21' 47.808" S; 27° 28' 9.336" E	UNG001	0.90	0.67	1.10		3.00	7.8	2.8	2.00	28	38	77	8.70	30.6	6.5	1.4	5.3	1.00	4.90	1.00	2.90	0.40	2.50	0.40
			UNG002	1.10	1.26	1.30		3.00	9.9	2.6	2.00	24	53	105	11.40	39.1	8.0	1.8	5.9	0.90	4.60	0.90	2.60	0.40	2.60	0.30
			UNG003	1.00	1.07	1.10		2.00	8.7	2.2	2.00	21	51	99	11.00	38.3	7.6	1.6	5.4	0.90	5.00	0.80	2.20	0.40	2.30	0.30
			UNG004	0.90	0.60	1.20		3.00	8.0	2.3	2.00	21	43	86	9.60	33.9	6.7	1.5	4.6	0.80	4.10	0.70	2.10	0.40	2.10	0.30
			UNG005	0.90	0.54	1.10		3.00	7.8	2.2	2.00	30	39	78	8.60	32.3	6.9	1.5	5.9	1.10	6.40	1.10	3.30	0.50	3.40	0.40

Group	Formation	Collar Coordinates (Latitude; Longitude)	Sample No.	Ta	Tl	Mo	Sb	Sn	Th	U	W	Y	La	Ce	Pr	Nd	Sm	Eu	Gd	Tb	Dy	Ho	Er	Tm	Yb	Lu
	Roodepoort (Carletonville Goldfield-East Driefontein mine)	26° 25' 8.184" S; 27° 30' 4.32" E	D5P03463-001	0.85		1.30	0.53		4.9	1.4		23	23	45	5.05	21.3	4.3	1.0	4.2	0.66	4.22	0.82	2.57	0.39	2.51	0.39
			D5P03463-002	0.72		1.10	0.48		4.4	1.1		25	26	49	5.91	24.2	5.2	1.4	5.0	0.78	4.94	0.99	2.86	0.41	2.89	0.42
			D5P03463-003	0.80		1.00			5.0	1.3	2.00	22	24	48	5.60	22.2	4.7	1.1	4.2	0.80	4.00	0.90	2.80	0.40	2.50	0.60
			D5P03463-004	0.86		1.34	0.85		5.7	1.2		27	26	51	5.91	24.7	5.1	1.3	5.1	0.78	5.20	1.06	3.00	0.48	3.39	0.48
			D5P03463-005	0.90		1.26	1.67		5.4	1.2		33	30	59	7.02	28.3	6.0	1.5	6.4	0.94	6.24	1.23	3.50	0.51	3.45	0.47
			D5P03463-006	0.85		1.28	0.42		5.2	1.2		28	23	45	5.34	21.9	4.4	1.1	4.8	0.77	5.02	1.06	2.94	0.46	3.10	0.46
			D5P03463-007	0.78		1.32	0.11		6.6	1.2		42	34	62	7.40	31.6	7.9	4.0	8.0	1.20	7.92	1.51	4.43	0.63	4.26	0.61
			D5P03463-008	0.85		1.34	0.51		5.2	1.2		24	23	45	5.32	20.8	4.0	1.1	4.6	0.68	4.49	0.94	2.69	0.42	2.90	0.42
			D5P03463-009	0.93		1.28	0.48		5.6	1.2		27	27	52	5.99	24.4	4.8	1.0	4.9	0.75	5.01	1.10	2.96	0.47	3.17	0.46
			D5P03463-010	1.03		19.30	0.94		5.6	1.3		24	29	56	6.39	25.3	5.2	1.0	4.5	0.69	4.63	0.95	2.87	0.41	2.93	0.41
			D5P03463-011	0.90		1.71	0.76		5.4	1.3		25	25	49	5.86	24.0	4.8	1.1	4.5	0.68	4.51	0.96	2.70	0.40	2.82	0.47
			D5P03463-012	0.80		0.89	0.47		5.0	1.0		25	22	42	5.12	20.1	4.2	1.2	4.5	0.69	4.83	0.96	2.73	0.41	2.73	0.42
			D5P03463-013	0.81		1.00	0.45		4.4	1.0		24	21	39	4.66	19.4	4.1	1.2	4.3	0.65	4.48	0.91	2.50	0.38	2.59	0.36
			D5P03463-014	0.79		0.94	0.52		4.6	1.1		24	20	39	4.68	19.1	4.2	1.2	4.1	0.63	4.48	0.90	2.65	0.41	2.65	0.42

Group	Formation	Collar Coordinates (Latitude; Longitude)	Sample No.	Ta	Tl	Mo	Sb	Sn	Th	U	W	Y	La	Ce	Pr	Nd	Sm	Eu	Gd	Tb	Dy	Ho	Er	Tm	Yb	Lu
			D5P03463-015	0.81		1.10	0.56		4.9	1.1		27	24	47	5.46	23.1	4.9	1.4	5.4	0.83	5.21	1.13	3.00	0.45	3.13	0.50
			D5P03463-016	0.80		1.04	0.46		4.9	1.2		26	25	48	5.78	23.2	5.0	1.2	4.8	0.75	4.91	1.02	2.86	0.42	2.85	0.45
			D5P03463-017	0.80		1.06	0.48		4.7	1.1		25	22	43	5.05	20.9	4.5	1.2	4.5	0.71	4.66	0.96	2.72	0.41	2.78	0.43
			D5P03463-018	0.79		1.18	0.43		4.9	1.2		26	22	42	4.93	20.2	4.4	1.1	4.4	0.73	4.72	0.97	2.84	0.43	2.96	0.43
			D5P03463-019	0.78		1.10	0.45		4.8	1.0		23	22	41	4.80	20.3	4.3	1.1	3.8	0.64	4.15	0.85	2.47	0.39	2.50	0.40
			D5P03463-020	0.75		0.95	0.42		4.8	1.0		23	22	42	5.10	21.1	4.1	1.2	4.2	0.70	4.35	0.88	2.44	0.38	2.72	0.41
			D5P03463-021	0.80		1.01	0.52		4.8	1.1		25	22	41	4.91	19.9	4.4	1.2	4.5	0.70	4.75	0.96	2.79	0.42	2.89	0.42
			D5P03463-022	0.60		0.80		3.00	3.7	1.1	1.00	17	18	37	4.30	17.7	3.7	1.1	3.6	0.60	3.60	0.70	2.10	0.40	2.40	0.30
			D5P03463-023	0.79		0.83	0.41		4.8	1.0	-	23	22	41	4.92	20.0	3.9	1.1	4.0	0.63	4.19	0.86	2.65	0.37	2.45	0.37
			D5P03463-024	0.70		0.80		2.00	3.8	1.2	1.00	20	16	31	3.80	16.3	3.9	0.9	4.3	0.60	4.00	0.90	2.40	0.40	2.30	0.40
			D5P03463-025	0.92		1.28	0.39		5.2	1.2		26	20	40	4.81	20.3	4.5	1.0	4.6	0.74	4.82	1.01	2.96	0.44	3.01	0.48
			D5P03463-026	0.75		0.93	0.20	1.50	4.4	1.1	0.75	21	20	39	4.71	19.3	4.2	1.0	4.1	0.67	4.00	0.82	2.48	0.40	2.59	0.36
			D5P03463-027	0.73		1.24	0.43		4.4	1.1		23	20	38	4.83	19.5	4.4	1.1	4.0	0.62	3.91	0.84	2.38	0.36	2.45	0.37
			D5P03463-028	0.70		0.80		3.00	4.1	1.2	2.00	18	20	40	4.80	19.2	4.6	1.0	4.1	0.70	3.40	0.70	2.20	0.40	2.50	0.30

Group	Formation	Collar Coordinates (Latitude; Longitude)	Sample No.	Ta	Tl	Mo	Sb	Sn	Th	U	W	Y	La	Ce	Pr	Nd	Sm	Eu	Gd	Tb	Dy	Ho	Er	Tm	Yb	Lu
			D5P03463-029	0.87		0.97	0.56		5.1	1.1		25	23	45	5.36	21.9	4.5	1.2	4.4	0.67	4.35	0.92	2.65	0.39	2.59	0.43
			D5P03463-030	0.88		0.99	0.44		4.8	1.1		24	21	39	4.68	18.1	3.8	1.0	3.8	0.62	4.05	0.90	2.51	0.37	2.38	0.38
			D5P03463-031	0.83		1.26	0.68		4.5	1.0		22	22	41	4.90	19.4	4.1	1.0	4.2	0.64	4.29	0.90	2.42	0.36	2.40	0.39
			D5P03463-032	0.70		0.80		4.00	3.9	1.2	2.00	16	19	37	4.30	16.7	3.6	0.9	3.4	0.60	3.70	0.70	2.00	0.30	2.10	0.30
			D5P03463-033	0.86		1.65	0.86		5.1	1.2		27	24	46	5.48	22.0	4.8	1.2	4.9	0.72	4.85	0.99	2.86	0.44	2.85	0.45
			D5P03463-034	0.82		1.17	0.57	1.00	4.7	1.1	0.50	22	21	41	4.92	19.6	4.2	1.0	4.2	0.66	4.32	0.87	2.48	0.38	2.50	0.39
			D5P03463-035	0.90		0.95	0.74		5.1	1.1		25	21	41	4.99	20.2	4.2	1.0	4.4	0.66	4.46	0.90	2.64	0.42	2.64	0.40
			D5P03463-036	0.91		1.21	0.63		4.9	1.1		22	21	40	4.86	19.3	4.1	1.0	4.0	0.61	3.98	0.85	2.42	0.36	2.50	0.36
			D5P03463-037	0.84		1.28	0.53		4.9	1.1		24	23	44	5.28	21.2	3.9	1.0	4.5	0.68	4.21	0.96	2.70	0.41	2.71	0.41
			D5P03463-038	0.70		0.90		4.00	4.1	1.0	2.00	22	27	53	6.00	24.6	5.8	1.1	4.5	0.80	4.50	0.90	2.70	0.40	2.70	0.30
			D5P03463-039	0.84		1.18	0.69		5.0	1.2		25	24	46	5.59	22.2	4.8	1.1	4.7	0.70	4.63	0.95	2.72	0.42	2.87	0.43
			D5P03463-040	0.86		1.16	0.48		4.9	1.1		23	19	38	4.54	18.5	3.9	1.1	4.0	0.61	4.03	0.85	2.47	0.39	2.50	0.38
			D5P03463-041	0.73		1.03	0.39		4.9	1.1		28	25	48	5.80	23.6	5.0	1.5	5.4	0.80	5.05	0.98	2.89	0.46	3.00	0.44
			D5P03463-042	0.70		0.80		7.00	3.7	1.3	2.00	23	17	35	4.20	17.1	3.6	1.2	4.5	0.70	4.50	1.00	2.90	0.40	2.60	0.40

Group	Formation	Collar Coordinates (Latitude; Longitude)	Sample No.	Ta	Tl	Mo	Sb	Sn	Th	U	W	Y	La	Ce	Pr	Nd	Sm	Eu	Gd	Tb	Dy	Ho	Er	Tm	Yb	Lu
			D5P03463-043	0.82		1.09	0.83		4.7	1.1		26	21	41	4.91	20.8	4.3	1.1	4.6	0.73	4.74	0.96	2.69	0.42	2.88	0.44
			D5P03463-044	1.05		1.58	0.76		5.7	1.2		26	23	45	5.29	21.2	4.5	1.1	4.7	0.71	4.65	0.98	2.90	0.44	3.04	0.45
			D5P03463-045	0.97		1.40	0.61		5.3	1.2		24	21	43	4.94	20.2	4.1	1.0	3.9	0.66	4.37	0.90	2.59	0.41	2.64	0.40
			D5P03463-046	0.70		0.80		4.00	4.3	1.1	3.00	17	19	38	4.50	18.9	4.1	1.0	3.7	0.50	3.60	0.70	2.10	0.30	2.10	0.40
			D5P03463-047	0.82		1.24	0.62		4.7	1.1		26	19	37	4.59	18.4	4.0	1.1	4.5	0.68	4.50	0.97	2.76	0.41	2.66	0.40
			D5P03463-048	0.60		0.60		4.00	2.6	1.0	1.00	14	13	27	3.20	12.5	3.3	0.8	3.0	0.50	2.80	0.60	1.60	0.30	1.70	0.20
			D5P03463-049	0.60		0.90		4.00	3.8	1.3	2.00	19	19	38	4.70	17.8	4.0	1.0	3.5	0.60	4.00	0.80	2.30	0.40	2.20	0.30
			D5P03463-050	0.84		1.21	0.73		4.9	1.0		27	21	40	4.89	20.4	4.3	1.1	4.4	0.74	4.82	0.98	2.81	0.43	2.85	0.43
			D5P03463-051	0.93		1.17	0.75		5.2	1.1		23	18	35	4.07	16.2	3.6	0.9	4.0	0.67	4.27	0.86	2.69	0.40	2.76	0.43
			D5P03463-052	0.85		1.13	3.52		4.9	1.0		26	22	44	5.15	21.0	4.4	1.1	4.3	0.68	4.44	0.97	2.61	0.39	2.74	0.39
			D5P03463-053	0.70		0.80		3.00	4.1	1.1	1.00	19	19	38	4.90	18.4	3.9	1.0	3.8	0.60	4.20	0.80	2.30	0.40	2.40	0.30
	Roodepoort (Carletonville Goldfield-Driefontein surface borehole)	26° 20' 51.036" S; 27° 29' 20.76" E	E1E-000001	0.74		0.97	0.37	2.00	4.1	1.1	0.75	21	18	35	4.21	16.7	3.8	0.9	3.7	0.63	3.97	0.81	2.35	0.38	2.38	0.34
			E1E-000002	0.89		1.15	2.13		5.1	1.1		24	20	40	4.61	18.6	4.0	1.0	4.1	0.67	4.36	0.91	2.65	0.40	2.75	0.41
			E1E-000003	0.81		1.03	1.88	1.00	4.7	1.1	0.33	23	21	41	4.88	19.3	4.1	1.0	4.1	0.65	4.33	0.89	2.52	0.40	2.63	0.37

Group	Formation	Collar Coordinates (Latitude; Longitude)	Sample No.	Ta	Tl	Mo	Sb	Sn	Th	U	W	Y	La	Ce	Pr	Nd	Sm	Eu	Gd	Tb	Dy	Ho	Er	Tm	Yb	Lu
			E1E-000004	0.78		1.02	1.07	1.43	4.4	1.1	0.54	22	19	37	4.40	17.6	3.9	1.0	3.9	0.64	4.09	0.85	2.43	0.39	2.48	0.36
			E1E-000005	0.60		0.75		4.00	3.2	1.2	1.50	17	16	32	3.95	15.2	3.7	0.9	3.3	0.55	3.40	0.70	1.95	0.35	1.95	0.25
	Roodepoort (Carletonville Goldfield-Driefontein surface borehole)	26° 20' 51.036" S; 27° 29' 20.76" E	E1G-000001	0.76		1.02	0.55	1.86	4.4	1.2	0.82	21	18	36	4.34	17.1	3.8	1.0	3.8	0.63	4.08	0.83	2.44	0.39	2.45	0.36
			E1G-000002	0.83		1.08	2.70	0.50	4.8	1.1	0.17	24	22	43	5.01	20.1	4.3	1.1	4.2	0.66	4.39	0.93	2.57	0.40	2.68	0.38
			E1G-000003	0.84		1.10	0.31	2.00	4.8	1.1	1.50	20	20	40	4.72	19.6	4.1	1.0	3.8	0.58	3.98	0.80	2.35	0.35	2.37	0.40
			E1G-000004	0.67		0.91	0.21	2.67	3.7	1.1	1.00	20	17	34	4.16	16.2	3.8	1.0	3.7	0.59	3.77	0.79	2.22	0.37	2.19	0.30
			E1G-000005	0.70		0.85	0.13	3.17	3.9	1.1	1.63	18	17	35	4.15	16.8	3.8	0.9	3.5	0.54	3.54	0.72	2.07	0.33	2.09	0.33
			E1G-000006	0.84		1.12	1.34	0.50	4.8	1.1	0.19	24	20	39	4.58	18.6	4.0	1.0	4.1	0.68	4.37	0.90	2.61	0.40	2.68	0.40
			E1G-000007	0.74		0.95	0.37	2.33	4.1	1.1	1.19	20	18	36	4.27	17.3	3.9	1.0	3.8	0.58	3.79	0.78	2.24	0.35	2.25	0.35
Central Rand Group	Booysens (Welkom Goldfield-Beatrix mine)	28° 15' 35.748" S; 26° 47' 4.776" E	BOOYWG-011	1.55		4.84	1.08		14.0	5.8		26	43	73	8.44	32.4	5.5	1.4	5.4	0.74	4.58	1.05	2.97	0.47	3.50	0.56
			BOOYWG-012	1.65		5.13	1.12		14.1	6.0		26	43	71	8.61	31.7	5.8	1.5	5.4	0.76	4.60	1.07	3.05	0.47	3.57	0.56
			BOOYWG-013	1.71		5.25	1.16		14.2	6.2		26	42	73	8.33	32.6	5.4	1.5	5.5	0.73	4.58	1.04	2.96	0.47	3.48	0.57
			BOOYWG-014	1.71		5.33	1.17		14.3	6.2		26	44	73	8.65	32.0	5.7	1.5	5.3	0.76	4.58	1.07	3.00	0.47	3.54	0.55
			BOOYWG-015	1.72		5.33	1.16		14.3	6.2		26	42	74	8.36	32.7	5.3	1.4	5.5	0.73	4.57	1.04	2.93	0.47	3.46	0.56

Group	Formation	Collar Coordinates (Latitude; Longitude)	Sample No.	Ta	Tl	Mo	Sb	Sn	Th	U	W	Y	La	Ce	Pr	Nd	Sm	Eu	Gd	Tb	Dy	Ho	Er	Tm	Yb	Lu
			BOOYWG-016	1.78		5.58	1.22		14.5	6.4		27	45	69	8.87	30.7	6.2	1.5	5.3	0.79	4.62	1.09	3.16	0.48	3.67	0.57
			BOOYWG-017	1.76		5.41	1.15		14.3	6.3		27	44	75	8.74	32.5	5.5	1.4	5.1	0.77	4.55	1.07	2.92	0.46	3.49	0.53
			BOOYWG-019	1.87		5.63	1.31		14.7	6.5		27	45	62	9.00	28.9	7.0	1.6	5.4	0.81	4.70	1.11	3.40	0.49	3.86	0.60
			BOOYWG-020	1.72		5.70	1.21		14.6	6.4		26	41	73	7.98	33.0	5.2	1.5	5.8	0.69	4.60	1.02	2.95	0.47	3.44	0.59
	Booysens (Western Areas Goldfield-Cooke section, Zuurbekom)	26° 18' 32.148" S; 27° 44' 12.048" E	Z1637-001A	0.40	0.35	0.90		2.00	2.8	1.0	1.00	15	17	35	4.30	15.7	3.3	0.9	2.9	0.50	3.00	0.60	1.60	0.30	1.60	0.20
			Z1673-002A	0.70	1.01	1.70		3.00	5.3	1.5	2.00	23	28	59	7.10	27.0	6.0	1.2	4.6	0.80	4.80	0.90	2.50	0.40	2.50	0.40
			Z1637-003A	0.60	1.18	1.90		2.00	5.3	1.6	3.00	23	29	61	6.90	27.3	5.7	1.1	4.8	0.80	4.70	0.90	2.40	0.40	2.60	0.40
			Z1637-004A	0.50	0.74	1.20		2.00	4.0	1.2	2.00	18	20	42	4.90	18.5	4.1	0.7	3.2	0.70	3.40	0.70	2.20	0.30	1.80	0.30
			Z1637-005A	0.50	0.69	1.40		2.00	4.1	1.2	2.00	21	24	50	6.20	21.3	5.2	1.0	4.2	0.80	4.00	0.80	2.40	0.40	2.40	0.30
			Z1637-006A	0.50	0.57	1.50		2.00	3.6	1.2	2.00	18	20	42	5.00	20.0	4.4	0.7	4.0	0.60	3.50	0.70	2.10	0.40	2.00	0.30
			Z1637-007A	0.50	0.56	1.70		2.00	4.0	1.2	2.00	19	20	42	5.00	18.3	4.2	0.8	4.0	0.70	3.50	0.70	2.20	0.40	2.00	0.30
			Z1637-008A	0.50	0.38	1.40		2.00	3.8	1.1	2.00	18	18	39	4.80	16.2	3.7	1.0	3.5	0.70	3.40	0.70	2.10	0.30	2.00	0.30
			Z1637-009A	0.50	0.29	1.20		2.00	3.4	1.0	2.00	18	20	41	4.70	17.0	3.9	1.0	3.4	0.70	3.60	0.70	2.00	0.30	2.00	0.30
			Z1637-010A	0.60	0.36	1.30		1.00	3.1	1.1	2.00	18	19	39	4.50	16.4	4.1	1.1	3.4	0.60	3.50	0.70	2.10	0.30	2.00	0.30

Group	Formation	Collar Coordinates (Latitude; Longitude)	Sample No.	Ta	Tl	Mo	Sb	Sn	Th	U	W	Y	La	Ce	Pr	Nd	Sm	Eu	Gd	Tb	Dy	Ho	Er	Tm	Yb	Lu
			Z1637-011A	0.50	0.32	1.30		2.00	3.5	1.2	2.00	17	19	39	4.70	16.7	3.9	1.3	3.3	0.60	3.40	0.70	1.90	0.30	1.70	0.30
			Z1637-012A	0.50	0.22	1.30		2.00	3.3	1.1	2.00	17	17	35	4.10	15.3	4.0	1.2	3.0	0.50	3.20	0.60	1.60	0.30	1.60	0.30
			Z1637-013A	0.50	0.35	1.50		2.00	3.4	1.1	2.00	17	19	38	4.50	17.5	4.2	1.0	3.3	0.60	3.30	0.70	2.20	0.40	1.90	0.30
			Z1637-014A	0.50	0.32	1.50		2.00	3.7	1.1	2.00	19	20	41	4.80	18.5	3.8	1.2	3.1	0.70	3.70	0.70	2.30	0.30	1.90	0.30
			Z1637-015A	0.60	0.43	1.60		2.00	4.0	1.2	2.00	21	21	44	5.10	20.9	5.3	1.1	4.0	0.70	4.00	0.80	2.40	0.30	2.10	0.30
			Z1637-016A	0.50	0.38	1.50		2.00	3.8	1.1	2.00	19	20	41	4.90	18.7	4.0	1.1	3.8	0.60	4.20	0.70	2.30	0.40	2.10	0.30
			Z1637-017A	0.50	0.35	1.30		2.00	3.6	1.1	1.00	18	20	41	5.00	18.4	3.6	0.9	3.2	0.70	3.50	0.70	2.30	0.30	1.70	0.30
			Z1637-018A	0.60	0.40	1.50		1.00	3.8	1.2	2.00	19	20	42	5.00	20.4	4.0	1.1	3.9	0.60	3.80	0.70	2.20	0.30	2.40	0.30
			Z1637-019A	0.50	0.36	1.50		2.00	3.7	1.1	1.00	18	19	41	5.00	18.2	3.9	1.3	3.2	0.70	3.40	0.70	1.90	0.40	2.10	0.30
			Z1637-020A	0.50	0.52	1.50		1.00	4.0	1.2	2.00	19	20	42	4.90	18.5	4.3	1.2	3.8	0.70	3.80	0.70	2.10	0.30	2.00	0.30
			Z1637-021A	0.50	0.52	1.50		2.00	3.9	1.2	2.00	19	21	42	5.40	19.5	4.9	1.0	3.7	0.70	3.80	0.70	2.30	0.40	1.80	0.30
			Z1637-022A	0.50	0.53	1.30		3.00	3.9	1.2	2.00	19	21	43	4.90	18.5	4.5	1.2	3.5	0.60	3.70	0.70	2.10	0.30	2.00	0.30
			Z1637-023A	0.50	0.60	1.70		2.00	4.1	1.2	2.00	20	21	44	5.00	19.1	4.7	1.3	3.6	0.60	4.00	0.70	2.30	0.40	2.10	0.30
			Z1637-024A	0.50	0.48	1.40		2.00	4.3	1.2	2.00	19	21	43	5.10	18.7	3.7	1.0	3.9	0.70	3.90	0.70	2.30	0.40	2.10	0.30

Group	Formation	Collar Coordinates (Latitude; Longitude)	Sample No.	Ta	Tl	Mo	Sb	Sn	Th	U	W	Y	La	Ce	Pr	Nd	Sm	Eu	Gd	Tb	Dy	Ho	Er	Tm	Yb	Lu
			Z1637-025A	0.50	0.48	1.40		2.00	4.0	1.3	2.00	18	21	45	5.20	18.7	3.8	1.1	3.7	0.70	4.00	0.70	2.00	0.40	1.90	0.30
			Z1637-026A	0.60	0.51	1.70		2.00	4.1	1.2	2.00	19	20	42	5.00	18.6	4.1	1.3	3.9	0.60	3.80	0.70	2.00	0.30	2.10	0.30
			Z1637-027A	0.50	0.52	1.70		2.00	4.3	1.3	2.00	19	22	45	5.20	20.1	4.6	1.2	3.6	0.70	3.90	0.70	2.20	0.30	2.10	0.30
			Z1637-028A	0.50	0.56	1.40		2.00	3.9	1.2	2.00	17	21	42	5.00	18.4	4.0	1.1	3.4	0.60	3.80	0.60	1.90	0.40	2.00	0.30
			Z1637-029A	0.60	0.69	1.60		3.00	4.6	1.3	2.00	21	23	49	5.60	21.6	5.3	1.1	4.5	0.70	4.20	0.80	2.30	0.40	2.20	0.30
			Z1637-030A	0.60	0.70	1.70		2.00	4.7	1.3	2.00	22	24	49	5.90	21.0	5.0	1.3	4.3	0.80	4.20	0.80	2.40	0.40	1.80	0.30
			Z1637-001B	0.60	1.02	1.90		2.00	5.5	1.5	2.00	23	26	54	6.70	23.1	5.8	1.5	4.3	0.80	4.40	0.90	2.50	0.40	2.50	0.40
			Z1637-002B	0.60	1.11	1.70		2.00	5.3	1.5	2.00	23	25	54	6.30	23.3	5.7	1.3	4.3	0.70	4.50	0.90	2.60	0.40	2.20	0.40
			Z1637-003B	0.60	1.07	1.70		2.00	5.0	1.5	3.00	24	25	51	6.10	23.4	5.4	1.6	4.7	0.80	5.20	0.90	2.70	0.40	2.30	0.30
			Z1637-004B	0.60	0.97	1.60		3.00	5.1	1.4	2.00	31	32	60	7.10	27.3	6.9	2.1	6.3	1.10	6.30	1.10	3.10	0.40	2.90	0.40
			Z1637-005B	0.70	1.07	1.70		2.00	5.4	1.6	2.00	22	40	80	8.90	33.3	6.8	1.7	4.9	0.80	4.30	0.80	2.60	0.40	2.20	0.30
			Z1637-006B	0.60	1.02	1.50		2.00	4.8	1.4	2.00	18	18	42	4.90	17.3	4.3	1.0	3.8	0.60	3.30	0.70	2.00	0.30	1.90	0.30
			Z1637-007B	0.70	1.11	1.70		1.00	5.4	1.5	2.00	20	16	37	4.70	16.3	4.2	1.0	3.7	0.70	4.40	0.80	2.40	0.40	2.40	0.30
			Z1637-008B	0.70	1.21	1.90		2.00	5.9	1.7	2.00	32	56	111	12.90	49.4	11.2	1.3	7.2	1.20	7.00	1.10	3.30	0.40	3.30	0.40

Group	Formation	Collar Coordinates (Latitude; Longitude)	Sample No.	Ta	Tl	Mo	Sb	Sn	Th	U	W	Y	La	Ce	Pr	Nd	Sm	Eu	Gd	Tb	Dy	Ho	Er	Tm	Yb	Lu
			Z1637-009B	0.80	1.33	1.80		2.00	5.2	1.4	3.00	19	13	28	3.20	13.1	3.2	0.8	3.1	0.60	3.40	0.70	2.50	0.30	2.20	0.30
			Z1637-010B	0.70	1.39	2.10		2.00	5.4	1.6	3.00	24	22	46	5.60	21.2	4.8	0.9	4.4	0.80	4.80	0.90	3.00	0.50	3.10	0.30
			Z1637-011B	0.60	1.12	1.80		2.00	5.3	1.5	2.00	20	27	52	6.00	23.4	5.0	1.1	4.4	0.70	3.80	0.80	2.30	0.30	2.20	0.30
			Z1637-012B	0.70	1.08	1.90		3.00	5.5	1.6	2.00	27	29	58	6.60	25.4	5.9	1.7	5.0	0.90	5.40	1.00	2.90	0.50	2.50	0.30
	Booysens (Welkom Goldfield-Saaiplaas mine, Dagbreek)	27° 58' 7.068" S; 26° 46' 45.696" E	EDPC 1.1			2.30			7.4	1.6		12	31	60		29.0										
			EDPC 1.2			1.60			4.9	0.5		8	36	62		25.0										
			EDPC 1.3			2.30			5.9	0.1		10	44	89		36.0										
			EDPC 1.4			1.90			6.7	3.7		15	25	49		21.0										
			EDPC 1.5			2.00			7.6	6.0		15	25	47		21.0										
			EDPC 1.6			3.80			5.9	1.2		13	28	50		20.0										
			EDPC 2.1			5.10			7.9	1.9		17	31	61		29.0										
			EDPC 2.2			2.00			7.6	6.0		15	38	72		34.0										
			EDPC 2.3			3.80			5.9	1.2		13	21	37		19.0										
			EDPC 2.4			5.10			7.9	1.9		17	35	65		28.0										
			EDPC 2.5			3.70			0.5	1.2		1	2	3		2.0										
			EDPC 3.1			3.30			6.2	1.7		18	50	101		46.0										
			EDPC 3.2			3.60			4.4	1.3		19	30	55		25.0										
			EDPC 3.3			5.20			8.1	2.5		19	37	76		35.0										

Group	Formation	Collar Coordinates (Latitude; Longitude)	Sample No.	Ta	Tl	Mo	Sb	Sn	Th	U	W	Y	La	Ce	Pr	Nd	Sm	Eu	Gd	Tb	Dy	Ho	Er	Tm	Yb	Lu
			EDPC 3.4			5.00			14.0	2.9		20	33	61		26.0										
			EDPC 3.5			6.10			8.0	1.5		10	37	72		26.0										
			EDPC 4.1			3.80			8.4	3.0		12	28	54		26.0										
			EDPC 4.2			4.00			8.0	1.0		13	34	68		30.0										
			EDPC 4.3			3.80			6.7	0.7		9	20	36		18.0										
			EDPC 4.4			5.30			9.2	< 1.9		11	31	62		30.0										
	Booysens (Welkom Goldfield-Geduld mine, Dagbreek)	27° 57' 31.068" S; 26° 47' 18.096" E	UT 2.1			3.30			8.5	1.5		9	29	57		24.0										
			UT 2.2			3.30			11.0	2.2		15	32	66		30.0										
			UT 2.3			3.10			11.0	2.2		13	45	88		38.0										
			UT 2.4			5.40			7.6	0.4		20	31	57		25.0										
			UT 2.5			5.20			8.7	1.2		16	46	87		37.0										
	Booysens (Welkom Goldfield-, Welkom division of Western Holdings, Dagbreek)	27° 56' 55.068" S; 26° 46' 6.096" E	MB 6.1			3.90			10.0	3.9		15	28	54		26.0										
			MB 6.2			2.90			11.0	1.4		19	40	74		33.0										
			MB 6.3			4.00			6.4	0.6		13	51	101		38.0										
			MB 6.4			3.60			14.0	2.4		20	37	74		31.0										
			MB 6.5			3.70			8.8	4.2		8	26	59		29.0										
			MB 6.6			3.20			12.0	2.5		12	27	50		25.0										
			MB 6.7			4.00			9.1	2.4		11	27	54		26.0										
	Booysens (Klerksdorp Goldfield-Strathmore)	26° 57' 47.124" S;	M 6.1			4.20			16.0	0.7		9	39	71		26.0										
			M 6.2			3.90			27.0	5.1		18	64	120		46.0										

Group	Formation	Collar Coordinates (Latitude; Longitude)	Sample No.	Ta	Tl	Mo	Sb	Sn	Th	U	W	Y	La	Ce	Pr	Nd	Sm	Eu	Gd	Tb	Dy	Ho	Er	Tm	Yb	Lu
			M 6.3			4.80			6.0	0.6		17	26	51		26.0										
			M 6.4			4.60			16.0	4.0		19	28	62		29.0										
			M 6.5			6.90			5.8	3.9		34	43	86		39.0										
			M 6.6			4.40			8.1	1.0		14	36	68		31.0										
			M 7.1			3.50			3.3	1.7		13	22	41		19.0										
			M 7.2			14.00			5.3	0.1		15	31	64		30.0										
			M 7.3			4.00			7.7	2.5		15	25	45		22.0										
			M 7.4			3.70			3.2	0.1		15	18	33		18.0										
			M 7.5			4.50			6.7	0.5		35	68	134		60.0										
			M 7.6			4.30			9.6	21.0		16	24	48		23.0										
	Booysens (Klerksdorp Goldfield-Vaal Reefs mine, Strathmore)	26° 57' 11.124" S; 26° 40' 22.044" E	V 2.1			3.30			6.7	0.9		10	25	49		23.0										
			V 2.2			3.60			3.3	3.3		24	11	18		8.9										
			V 2.3			4.10			6.4	1.0		23	29	53		27.0										
			V 2.4			3.20			4.1	0.2		12	18	35		18.0										
			V 2.5			4.50			10.0	0.7		18	31	58		29.0										
			V 2.6			4.10			9.3	0.9		17	31	57		28.0										
	Booysens (Klerksdorp Goldfield)	26° 57' 11.124" S; 26° 40' 22.044" E	DN2-1						9.0			2	5													
			DN2-2						14.0			16	17	45												
			DN2-3						16.0			11	15	20												
			DN2-4						15.0			10	17	31												

Group	Formation	Collar Coordinates (Latitude; Longitude)	Sample No.	Ta	Tl	Mo	Sb	Sn	Th	U	W	Y	La	Ce	Pr	Nd	Sm	Eu	Gd	Tb	Dy	Ho	Er	Tm	Yb	Lu
			DN2-5						20.0			16	16	14												
			DN2-6						5.0			16	11	5												
			DN2-7						15.0	7.0		13	20	46												
			DN2-8						14.0			17	10	13												
			DN2-9						11.0	4.0		16	24	32												
			DN2-10						9.0			14	8	27												
			DN2-11						22.0	14.0		20	15	26												
			DN2-12						17.0			18	7	50												
			DN2-13						13.0			21	15	35												
			DN2-14						10.0			16	24	35												
			DN2-15						21.0	14.0		22	14	27												
			DN2-16						16.0			21	13	33												
			DN2-17						17.0	6.0		20	14	33												
			DN2-18						8.0			14	14	50												
			DN2-19						12.0	5.0		20	8	28												
			DN2-20						12.0			13	7	19												
			DN2-21									15	9	3												
			DN2-22						5.0			18	4	7												
			DN2-23						5.0			14	9	14												
			DN2-24						10.0	4.0		17	7													

Group	Formation	Collar Coordinates (Latitude; Longitude)	Sample No.	Ta	Tl	Mo	Sb	Sn	Th	U	W	Y	La	Ce	Pr	Nd	Sm	Eu	Gd	Tb	Dy	Ho	Er	Tm	Yb	Lu
			DN2-25						8.0	11.0		16	3	20													
			DN2-26						9.0	14.0		21	6	4													
			DN2-27						11.0	5.0		16	18	17													
	Booysens (Evander Goldfield)	26°28'21.1"S; 29°05'42.2"E	439-2#						3.1			21														
			439-3#						5.2			21														
			615-7#						6.3			25														
			615-8#						4.9			30														
			615-9#						7.1			25														
			730-4#						4.5			22														
			730-5#						4.9			23														
	Booysens (Central Rand Goldfield)	26°13'28.1"S; 27°59'31.4"E	UR1140#						5.9			12														
			GV2-28#						3.1			20														
			MEE-24#						4.7	1.9		23	23	41													
			MEE-33#						4.2	1.8		27	26	51													

Group	Formation	Collar Coordinates (Latitude; Longitude)	Sample No.	Au	Ir	Os	Pd	Pt	Rh	Ru
	Roodepoort (Carletonville Goldfield-West Driefontein mine)	26° 21' 47.808" S; 27° 28' 9.336" E	UNG001	43.00			5.50	4.50		
			UNG002	83.00			5.10	3.70		
			UNG003	94.00			5.00	3.40		
			UNG004	23.00			3.90	3.00		
			UNG005	35.00			5.10	4.90		
	Roodepoort (Carletonville Goldfield-East Driefontein mine)	26° 25' 8.184" S; 27° 30' 4.32" E	D5P03463-001	0.50	0.25	0.25	5.00	4.00	0.25	1.00
			D5P03463-002	2.00	0.25	0.25	5.00	4.00	0.25	1.00
			D5P03463-003	0.50	0.25	0.25	5.00	5.00	0.25	2.00
			D5P03463-004	0.50	0.25	0.25	5.00	5.00	0.25	3.00
			D5P03463-005	6.00	0.25	0.25	6.00	6.00	0.25	2.00
			D5P03463-006	2.00	0.25	0.25	5.00	4.00	0.25	2.00
			D5P03463-007	5.00	0.25	0.25	5.00	5.00	0.25	1.00
			D5P03463-008	13.00	0.25	0.25	5.00	4.00	0.25	1.00
			D5P03463-009	2.00	0.25	0.25	5.00	4.00	0.25	2.00
			D5P03463-010	6.00	0.25	0.25	4.00	4.00	0.25	2.00

Group	Formation	Collar Coordinates (Latitude; Longitude)	Sample No.	Au	Ir	Os	Pd	Pt	Rh	Ru
			D5P03463-011	1.00	0.25	0.25	5.00	4.00	0.25	2.00
			D5P03463-012	6.00	0.25	0.25	4.00	4.00	0.25	3.00
			D5P03463-013	2.00	0.25	0.25	4.00	4.00	0.25	2.00
			D5P03463-014	4.00	0.25	0.25	4.00	5.00	0.25	3.00
			D5P03463-015	4.00	0.25	0.25	5.00	4.00	0.25	2.00
			D5P03463-016	4.00	0.25	0.25	5.00	4.00	0.25	2.00
			D5P03463-017	2.00	0.25	0.25	5.00	4.00	0.25	2.00
			D5P03463-018	2.00	0.25	0.25	4.00	4.00	0.25	3.00
			D5P03463-019	3.00	0.25	0.25	4.00	4.00	0.25	2.00
			D5P03463-020	4.00	0.25	0.25	4.00	3.00	0.25	2.00
			D5P03463-021	3.00	0.25	0.25	4.00	4.00	0.25	2.00
			D5P03463-022	5.00	0.25	0.25	4.00	4.00	0.25	3.00
			D5P03463-023	9.00	0.25	0.25	4.00	4.00	0.25	2.00
			D5P03463-024	2.00	0.25	0.25	4.00	4.00	0.25	2.00

Group	Formation	Collar Coordinates (Latitude; Longitude)	Sample No.	Au	Ir	Os	Pd	Pt	Rh	Ru
			D5P03463-025	2.00	0.25	0.25	4.00	4.00	0.25	2.00
			D5P03463-026	18.00	0.25	0.25	4.00	4.00	0.25	1.00
			D5P03463-027	11.00	0.25	0.25	4.00	4.00	0.25	1.00
			D5P03463-028	9.00	0.25	0.25	5.00	4.00	0.25	2.00
			D5P03463-029	2.00	0.25	0.25	6.00	4.00	0.25	3.00
			D5P03463-030	2.00	0.25	0.25	4.00	4.00	0.25	2.00
			D5P03463-031	0.50	0.25	0.25	5.00	5.00	0.25	2.00
			D5P03463-032	0.50	0.25	0.25	4.00	4.00	0.25	4.00
			D5P03463-033	0.50	0.25	0.25	5.00	4.00	0.25	2.00
			D5P03463-034	26.00	0.25	0.25	4.00	4.00	0.25	2.00
			D5P03463-035	0.50	0.25	0.25	4.00	4.00	0.25	3.00
			D5P03463-036	0.50	0.25	0.25	4.00	4.00	0.25	2.00
			D5P03463-037	5.00	0.25	0.25	4.00	4.00	0.25	2.00
			D5P03463-038	2.00	3.00	0.25	4.00	3.00	0.25	1.00

Group	Formation	Collar Coordinates (Latitude; Longitude)	Sample No.	Au	Ir	Os	Pd	Pt	Rh	Ru
			D5P03463-039	2.00	0.25	0.25	5.00	4.00	0.25	1.00
			D5P03463-040	2.00	0.25	0.25	4.00	4.00	0.25	2.00
			D5P03463-041	1.00	0.25	0.25	5.00	4.00	0.25	1.00
			D5P03463-042	3.00	0.25	0.25	4.00	4.00	0.25	2.00
			D5P03463-043	2.00	0.25	0.25	4.00	4.00	0.25	2.00
			D5P03463-044	0.50	0.25	0.25	5.00	4.00	0.25	1.00
			D5P03463-045	0.50	0.25	0.25	4.00	4.00	0.25	2.00
			D5P03463-046	3.00	0.25	0.25	4.00	3.00	0.25	1.00
			D5P03463-047	4.00	0.25	0.25	5.00	4.00	0.25	2.00
			D5P03463-048	0.50	0.25	0.25	3.00	3.00	0.25	2.00
			D5P03463-049	2.00	0.25	0.25	4.00	3.00	0.25	1.00
			D5P03463-050	3.00	0.25	0.25	4.00	4.00	0.25	2.00
			D5P03463-051	2.00	0.25	0.25	4.00	4.00	0.25	2.00
			D5P03463-052	4.00	0.25	0.25	5.00	4.00	0.25	2.00

Group	Formation	Collar Coordinates (Latitude; Longitude)	Sample No.	Au	Ir	Os	Pd	Pt	Rh	Ru
			D5P03463-053	2.00	0.25	0.25	4.00	4.00	0.50	2.00
	Roodepoort (Carletonville Goldfield-Driefontein surface borehole)	26° 20' 51.036" S; 27° 29' 20.76" E	E1E-000001	17.00	0.25	0.25	4.00	4.00	0.25	2.00
			E1E-000002	24.00	0.25	0.25	4.00	4.00	0.25	1.00
			E1E-000003	44.00	0.25	1.00	5.00	4.00	0.25	1.00
			E1E-000004	8.00	0.25	0.25	5.00	4.00	0.25	2.00
			E1E-000005	18.00	0.25	0.25	4.00	4.00	0.25	2.00
	Roodepoort (Carletonville Goldfield-Driefontein surface borehole)	26° 20' 51.036" S; 27° 29' 20.76" E	E1G-000001	4.00	0.25	0.25	5.00	5.00	0.25	1.00
			E1G-000002	81.00	0.25	1.00	4.00	4.00	1.00	2.00
			E1G-000003	7.00	0.25	1.00	5.00	5.00	0.25	1.00
			E1G-000004	7.00	0.25	0.25	5.00	4.00	0.25	1.00
			E1G-000005	7.00	0.25	1.00	5.00	4.00	0.25	2.00
			E1G-000006	8.00	0.25	0.25	5.00	4.00	0.25	1.00
			E1G-000007	5.00	0.25	1.00	5.00	5.00	0.25	2.00
Central Rand Group	Booysens (Welkom Goldfield-Beatri	28° 15' 35.748" S; 26° 47' 4.776'	BOOYWG-011	7.00	0.25	0.25	4.00	4.00	0.25	2.00

Group	Formation	Collar Coordinates (Latitude; Longitude)	Sample No.	Au	Ir	Os	Pd	Pt	Rh	Ru
			BOOYWG-012	7.00	0.25	0.25	4.00	4.00	0.25	1.00
			BOOYWG-013	6.00	0.25	0.25	4.00	4.00	0.25	1.00
			BOOYWG-014	7.00	0.25	0.25	5.00	4.00	0.25	1.00
			BOOYWG-015	9.00	0.25	0.25	5.00	4.00	0.25	1.00
			BOOYWG-016	19.00	0.25	0.25	4.00	4.00	0.25	2.00
			BOOYWG-017	19.00	0.25	0.25	5.00	4.00	0.25	1.00
			BOOYWG-019	25.00	0.25	0.25	4.00	4.00	0.25	2.00
			BOOYWG-020	22.00	0.25	0.25	5.00	4.00	0.25	2.00
	Booysens (Western Areas Goldfield-Cooke section, Zuurbekom)	26° 18' 32.148" S; 27° 44' 12.048" E	Z1637-001A	4.00			7.80	6.80		
			Z1673-002A	3.00			9.70	7.70		
			Z1637-003A	2.00			11.50	8.30		
			Z1637-004A	2.00			9.60	6.80		
			Z1637-005A	2.00			12.80	9.10		
			Z1637-006A	1.00			9.40	8.20		

Group	Formation	Collar Coordinates (Latitude; Longitude)	Sample No.	Au	Ir	Os	Pd	Pt	Rh	Ru
			Z1637-007A	1.00			10.20	7.40		
			Z1637-008A	2.00			9.80	8.70		
			Z1637-009A	2.00			7.00	6.50		
			Z1637-010A	1.00			7.50	7.50		
			Z1637-011A	1.00			7.20	6.80		
			Z1637-012A	3.00			7.00	6.60		
			Z1637-013A	2.00			7.00	6.30		
			Z1637-014A	2.00			9.40	8.90		
			Z1637-015A	1.00			7.90	7.80		
			Z1637-016A	2.00			9.80	9.00		
			Z1637-017A	1.00			8.90	7.30		
			Z1637-018A	2.00			9.60	8.40		
			Z1637-019A	2.00			8.90	7.40		
			Z1637-020A	2.00			9.80	7.90		

Group	Formation	Collar Coordinates (Latitude; Longitude)	Sample No.	Au	Ir	Os	Pd	Pt	Rh	Ru
			Z1637-021A	2.00			8.20	7.50		
			Z1637-022A	2.00			8.60	7.30		
			Z1637-023A	4.00			8.80	7.20		
			Z1637-024A	3.00			8.70	8.40		
			Z1637-025A	3.00			9.70	8.30		
			Z1637-026A	3.00			11.80	10.20		
			Z1637-027A	2.00			12.40	8.80		
			Z1637-028A	2.00			8.60	7.10		
			Z1637-029A	2.00			11.50	8.80		
			Z1637-030A	3.00			11.00	9.40		
			Z1637-001B	2.00			9.40	9.40		
			Z1637-002B	3.00			9.80	8.80		
			Z1637-003B	4.00			11.70	11.40		
			Z1637-004B	3.00			8.40	8.40		

Group	Formation	Collar Coordinates (Latitude; Longitude)	Sample No.	Au	Ir	Os	Pd	Pt	Rh	Ru
			Z1637-005B	3.00			10.00	9.00		
			Z1637-006B	3.00			9.40	8.60		
			Z1637-007B	2.00			8.90	8.70		
			Z1637-008B	5.00			12.90	11.20		
			Z1637-009B	3.00			10.30	9.50		
			Z1637-010B	3.00			9.20	9.30		
			Z1637-011B	3.00			10.90	9.30		
			Z1637-012B	3.00			11.90	10.10		

Table A. 5. Major element concentrations of the Black Reef Formation marine shales.

Formation	Collar Coordinates (Latitude; Longitude)	Sample No.	Depth (m)	SiO_2 (wt.%)	Al_2O_3	Fe_2O_3 total	MgO	CaO	Na_2O	K_2O	TiO_2	P_2O_5	MnO	Cr_2O_3	LOI	TOC	S	Total
Black Reef Formation marine shale	26° 24' 4.1688" S; 27° 23' 6.54" E	E1H-000001	1462.43	60.9	17.63	7.47	5.04	0.79	0.01	4.93	0.87	0.01	0.18	0.05	4.96	1.10	0.04	104.01
		E1H-000002	1464.00	70.6	13.54	5.02	3.14	0.66	0.01	3.55	0.71	0.05	0.12	0.05	3.33	0.52	0.01	101.35
		E1H-000003	1468.00	66.1	14.96	6.26	4.30	0.60	0.01	4.25	0.79	0.07	0.15	0.06	4.33	0.89	0.01	102.78
		E1H-000004	1472.18	68.5	13.12	5.62	3.72	0.58	0.01	3.78	0.74	0.01	0.13	0.05	3.89	0.67	0.08	100.98

Table A. 6. Trace element concentrations of the Black Reef Formation marine shales.

Formation	Collar Coordinates (Latitude; Longitude)	Sample No.	As (ppm)	Rb	Ba	Sr	Pb	Cs	Co	Cr	Cu	Ni	V	Sc	Zn	Ga	Zr	Nb	Hf
Black Reef Formation marine shale	26° 24' 4.1688" S; 27° 23' 6.54" E	E1H-000001	28	131	158	6	1.7	0	111	364	0	118	139	23.5		15	211	11	5.4
		E1H-000002	34	117	146	6	1.7	0	137	358	0	110	128	23.1		14	239	11	6
		E1H-000003	24	150	177	6	1.7	0	91	385	0	131	156	24.7		18	192	11	5
		E1H-000004	30	119	146	5	1.6	0	119	346	0	109	128	22.4		14	216	10	5.4

Formation	Collar Coordinates (Latitude; Longitude)	Sample No.	Ta	Tl	Mo	Sb	Sn	Th	U	W	Y	La	Ce	Pr	Nd	Sm	Eu	Gd	Tb	Dy	Ho	Er	Tm	Yb	Lu
Black Reef Formation marine shale	26° 24' 4.1688" S; 27° 23' 6.54" E	E1H-000001	1.00		2.01	0.80		5.9	2.3		21	22	39	4.36	17.1	3.4	1.1	3.5	0.55	3.69	0.78	2.41	0.35	2.60	0.43
		E1H-000002	1.01		1.89	1.39		5.7	2.3		19	19	34	3.62	14.2	2.9	1.1	3.2	0.51	3.47	0.73	2.27	0.33	2.43	0.42
		E1H-000003	1.03		2.21	0.25		6.3	2.5		23	25	46	5.27	20.7	3.9	1.2	4.0	0.61	4.08	0.87	2.65	0.39	2.87	0.45
		E1H-000004	0.96		1.87	1.05		5.6	2.2		19	24	43	4.86	19.0	3.7	1.2	3.8	0.58	3.92	0.83	2.55	0.37	2.76	0.45

Formation	Collar Coordinates (Latitude; Longitude)	Sample No.	Au	Ir	Os	Pd	Pt	Rh	Ru
Black Reef Formation marine shale	26° 24' 4.1688" S; 27° 23' 6.54" E	E1H-000001	3	0.25	0.25	9	6	0.25	2
		E1H-000002	2	0.25	0.25	9	5	0.25	2
		E1H-000003	2	0.25	0.25	9	6	0.25	1
		E1H-000004	6	0.25	0.25	10	5	0.25	1

Table A. 7. Major element concentrations of the Pretoria Group marine shales.

Group	Formation	Collar Coordinates (Latitude; Longitude)	Sample No.	Depth (m)	SiO_2 (wt.%)	Al_2O_3	Fe_2O_3 total	MgO	CaO	Na_2O	K_2O	TiO_2	P_2O_5	MnO	Cr_2O_3	LOI	TOC	S	Total
Upper Pretoria Group	Silverton	26° 18' 44.2548" S; 27° 38' 38.0688" E	DP22-00001	189	56.6	19.73	8.31	2.12	1.49	2	4.69	1.04	0.15	0.04	0.01	3.40	0.39	0.02	99.98
			DP22-00002	195	55.2	19.81	8.47	2.29	1.54	2.37	4.95	1.16	0.14	0.05	0.02	3.26	0.42	0.02	99.73
			DP22-00003	200	55.8	20.00	8.62	2.18	1.39	2.06	4.78	1.05	0.16	0.04	0.02	3.40	0.38	0.03	99.93
			DP22-00004	210	56.9	20.93	8.53	1.96	1.09	1.38	4.37	0.92	0.16	0.03	0.02	3.70	0.36	0.01	100.40
			DP22-00005	220	58	21.5	8.53	1.74	0.9	0.67	4.15	0.78	0.19	0.03	0.02	3.99	0.92	0.09	101.48
			DP22-00006	230	58.9	21.95	8.07	1.61	0.69	0.36	3.93	0.75	0.16	0.02	0.02	4.06	0.88	0.06	101.48
			DP22-00007	247	56.5	20.56	8.50	2.03	1.21	1.58	4.57	0.97	0.16	0.04	0.02	3.6	0.88	0.13	100.74
			DP22-00008	250	57.1	21.1	8.45	1.92	1.06	1.24	4.35	0.91	0.16	0.03	0.02	3.75	1.18	0.13	101.38
			DP22-00009	257	57.6	21.2	8.50	1.83	0.98	0.98	4.26	0.84	0.17	0.03	0.02	3.84	0.19	0.01	100.52
			DP23-00001	220	57.8	20.6	8.65	1.71	0.95	0.69	4.25	0.69	0.22	0.02	0.02	4.05	0.42	0.01	100.11
			DP23-00002	225	58.5	23.4	7.98	1.57	0.53	0.11	3.64	0.79	0.14	0.02	0.02	4.26	0.40	0.01	101.42
			DP23-00003	230	58.7	21	8.97	1.71	1.01	0.5	4.33	0.72	0.24	0.03	0.02	3.95	0.32	0.01	101.47
			DP23-00004	234	60.6	21.9	6.79	1.42	0.31	0.15	3.61	0.71	0.08	0.02	0.02	4.04	0.33	0.01	99.90

Group	Formation	Collar Coordinates (Latitude; Longitude)	Sample No.	Depth (m)	SiO_2 (wt.%)	Al_2O_3	Fe_2O_3 total	MgO	CaO	Na_2O	K_2O	TiO_2	P_2O_5	MnO	Cr_2O_3	LOI	TOC	S	Total
Lower Pretoria Group			DP22-00010	513	58.2	21.5	8.24	1.72	0.84	0.7	4.12	0.8	0.17	0.03	0.03	3.94	0.32	0.03	100.62
			DP22-00011	520	50.9	18.83	7.18	1.53	0.74	0.66	3.61	0.72	0.14	0.02	0.05	3.42	0.20	0.03	88.02
			DP22-00012	530	60.9	19.34	8.22	1.7	1.31	1.2	3.79	0.69	0.19	0.03	0.02	3.68	0.26	0.01	101.33
			DP22-00013	600	54.2	19.95	8.2	2.32	1.58	2.32	5.2	1.23	0.13	0.04	0.01	3.32	0.11	0.01	98.57
			DP22-00014	615	54.7	19.89	8.5	2.35	1.57	2.49	5.08	1.21	0.13	0.05	0.01	3.21	0.1	0.01	99.30
			DP22-00015	625	55.6	19.69	8.88	2.38	1.51	2.67	4.83	1.15	0.13	0.06	0.01	3.09	0.1	0.01	100.02
			DP23-00005	340	59.1	20.47	8.52	1.86	1.02	0.66	3.9	0.81	0.17	0.03	0.02	3.90	0.18	0.11	100.79
			DP23-00006	416	61.5	16.85	8.48	2.45	1.58	1.33	3.38	1.03	0.1	0.06	0.02	3.34	0.62	0.01	100.79
			DP23-00007	421	61.8	16.38	8.76	2.5	1.55	1.66	2.79	0.78	0.2	0.06	0.02	3.15	0.19	0.01	99.81
			DP23-00008	500	59.8	19.22	8.92	1.2	0.35	0.03	4.5	1.15	0.25	0.06	0.02	5.13	0.2	0.01	100.85
			DP23-00009	503	52.1	9.99	11.9	8.48	10.77	1.44	0.94	0.8	0.09	0.18	0.02	2.46	0.71	0.01	99.84
			DP23-00010	588	52.2	9.95	11.87	8.56	10.93	1.56	0.94	0.82	0.09	0.18	0.12	2.25	0.27	0.01	99.69
			DP23-00011	599	59.5	7.37	11.06	1.22	0.68	0.01	0.22	0.21	0.09	0.02	0.11	1.96	0.24	0.01	82.74
			DP23-00012	631	58.7	15.06	9.51	1.16	0.36	0.01	2.77	0.56	0.28	0.01	0.01	3.04	0.06	0.01	91.51

Group	Formation	Collar Coordinates (Latitude; Longitude)	Sample No.	Depth (m)	SiO_2 (wt.%)	Al_2O_3	Fe_2O_3 total	MgO	CaO	Na_2O	K_2O	TiO_2	P_2O_5	MnO	Cr_2O_3	LOI	TOC	S	Total
			DP23-00013	642	58.4	22.8	8.65	1.61	0.4	0.05	3.34	0.7	0.09	0.03	0.02	4.17	0.26	0.01	100.51
			DP23-00014	727	58.4	22.8	8.65	1.61	0.4	0.05	3.34	0.7	0.2	0.03	0.03	4	0.44	0.01	100.64
			DP23-00015	748	58.8	16.98	9.47	1.40	0.46	0.03	2.42	0.54	0.17	0.02	0.04	3.29	0.4	0.03	94.03

Table A. 8. Trace element concentrations of the Pretoria Group marine shales.

Group	Formation	Collar Coordinates (Latitude; Longitude)	Sample No.	As (ppm)	Rb	Ba	Sr	Pb	Cs	Co	Cr	Cu	Ni	V	Sc	Zn	Ga	Zr	Nb	Hf
Upper Pretoria Group	Silverton	26° 18' 44.2548" S; 27° 38' 38.0688" E	DP22-00001	26	338	849	162	57.3		94	98		48	123	23.8		31	398	23	10.7
			DP22-00002	23	313	794	145	46.8		93	111		48	126	22.3		30	330	22	8.9
			DP22-00003	24	315	808	137	44.8		98	115		49	129	22.6		31	315	22	8.5
			DP22-00004	22	283	768	128	40.6		102	124		48	129	21.9		29	278	22	7.5
			DP22-00005	17	223	623	102	30.5		87	112		41	112	18.22		24	200	18	5.5
			DP22-00006	14	199	540	87	22.5		78	119		39	113	17.61		22	160	17	4.4
			DP22-00007	17	190	580	91	24.8		84	119		40	113	18.3		21	166	17	4.4
			DP22-00008	18	183	617	100	25.7		78	113		38	110	18.22		20	167	15	4.5
			DP22-00009	15	178	561	94	20.6		74	112		36	110	18.88		19	184	16	4.9
			DP23-00001	11	278	697	102	19.4		68	123		43	128	18.90		25	148	16	4.1
			DP23-00002	20	224	619	103	21.9		109	165		54	140	20.78		30	174	23	4.7
			DP23-00003	23	275	738	107	43.1		117	137		49	143	20.85		27	149	18	4.1
			DP23-00004	15	178	603	100	28.8		105	149		44	126	20.35		24	201	22	5.5

Group	Formation	Collar Coordinates (Latitude; Longitude)	Sample No.	As (ppm)	Rb	Ba	Sr	Pb	Cs	Co	Cr	Cu	Ni	V	Sc	Zn	Ga	Zr	Nb	Hf
Lower Pretoria Group			DP22-00010	14	157	537	105	16.6		73	205		47	127	20.98		17	173	14	4.5
			DP22-00011	15	158	608	134	17		86	327		67	164	26.2		19	186	15	4.9
			DP22-00012	13	240	592	142	46.9		79	123		45	126	20.23		24	184	15	5.2
			DP22-00013	25	401	895	156	55.6		78	92		46	125	24.98		34	451	25	12.1
			DP22-00014	35	387	970	175	67		110	92		53	126	25.4		35	504	26	13.1
			DP22-00015	30	325	939	174	59.7		111	85		47	115	24.8		32	453	24	12.3
			DP23-00005	24	189	629	104	26.8		100	129		43	126	20.5		22	197	17	5.2
			DP23-00006	10	217	500	94	14		59	150		43	141	24.2		23	247	23	6.6
			DP23-00007	40	241	1059	145	43.4		122	111		48	129	24.3		23	231	16	5.9
			DP23-00008	20	178	842	162	26.2		61	122		40	116	19.53		20	176	13	4.8
			DP23-00009	2	251	305	56	6.1		95	142		38	149	25.6		23	267	25	7
			DP23-00010	9	31	493	183	6.2		101	798		125	245	34.4		12	104	6	2.7
			DP23-00011	9	33	520	196	6.5		93	758		127	241	34.2		13	107	6	2.7
			DP23-00012	43	11	43	14	10.3		128	72		26	91	13.28		8	201	7	5.1

Group	Formation	Collar Coordinates (Latitude; Longitude)	Sample No.	As (ppm)	Rb	Ba	Sr	Pb	Cs	Co	Cr	Cu	Ni	V	Sc	Zn	Ga	Zr	Nb	Hf
			DP23-00013	64	164	511	60	6.9		94	136		37	148	18.83		18	195	16	5
			DP23-00014	28	208	540	90	39.2		112	171		54	134	18.88		26	172	21	4.6
			DP23-00015	27	140	539	113	18		101	289		62	157	24		18	182	14	5

Group	Formation	Collar Coordinates (Latitude; Longitude)	Sample No.	Ta	Tl	Mo	Sb	Sn	Th	U	W	Y	La	Ce	Pr	Nd	Sm	Eu	Gd	Tb	Dy	Ho	Er	Tm	Yb	Lu
Upper Pretoria Group	Silverton	26° 18' 44.2548" S; 27° 38' 38.0688" E	DP22-00001	2.16		3.81	1.05		25.7	6.9		58	79	139	14.81	56.8	11.1	2	10.8	1.71	11.41	2.3	6.48	1	6.66	0.95
			DP22-00002	2.2		3.25	1.1		25.1	6.5		49	71	127	13.56	51.8	10	1.8	9.4	1.46	9.54	1.92	5.43	0.83	5.56	0.8
			DP22-00003	2.26		3.08	1.12		25.5	6.5		48	70	125	13.41	51.5	10	1.8	9.4	1.45	9.33	1.88	5.35	0.82	5.47	0.78
			DP22-00004	2.31		2.77	1.15		25.3	6.2		42	66	117	12.63	48.3	9.2	1.6	8.4	1.28	8.17	1.65	4.73	0.71	4.76	0.68
			DP22-00005	1.98		1.96	1		21.3	5.1		30	52	93	10.04	38.5	7.2	1.3	6.4	0.96	5.97	1.2	3.44	0.52	3.44	0.5
			DP22-00006	1.92		1.34	0.93		19.8	4.3		23	45	82	8.85	33.6	6.1	1.2	5.1	0.74	4.5	0.89	2.58	0.38	2.61	0.38
			DP22-00007	1.85		2.15	1.02		19.3	4.1		23	43	80	8.65	32.7	6	1.1	5	0.72	4.49	0.89	2.55	0.37	2.56	0.37

Group	Formation	Collar Coordinates (Latitude; Longitude)	Sample No.	Ta	Tl	Mo	Sb	Sn	Th	U	W	Y	La	Ce	Pr	Nd	Sm	Eu	Gd	Tb	Dy	Ho	Er	Tm	Yb	Lu
			DP22-00008	1.65		2.49	0.9		17.6	3.8		23	41	76	8.31	31.6	5.8	1.1	4.9	0.73	4.63	0.9	2.56	0.37	2.58	0.38
			DP22-00009	1.66		2.63	0.75		17.4	3.3		24	41	76	8.34	31.5	5.8	1.1	4.9	0.73	4.76	0.93	2.64	0.38	2.7	0.4
			DP23-00001	1.97		2.47	0.66		20.9	5.6		26	47	89	9.83	37.8	7.3	1.4	6.5	0.9	5.19	1.02	2.94	0.43	2.84	0.44
			DP23-00002	2.59		1.23	1.78		26.2	5.7		26	58	103	11.	41.3	7.4	1.5	5.8	0.78	4.56	0.89	2.68	0.4	2.8	0.4
			DP23-00003	2.09		0.94	1.28		22.6	5.7		26	51	94	10.19	40	7.4	1.3	6.3	0.9	5.06	1.05	2.9	0.4	2.87	0.4
			DP23-00004	2.65		1.29	1.25		26	5.5		27	56	98	10.49	39.5	6.9	1.3	5.3	0.8	5.31	1.02	2.96	0.44	2.96	0.43
Lower Pretoria Group			DP22-00010	1.37		2.65	0.62		14.7	2.7		23	35	67	7.43	28.3	5.4	1.1	4.7	0.71	4.58	0.9	2.52	0.36	2.57	0.39
			DP22-00011	1.42		2.78	0.7		15.4	2.9		26	37	71	7.93	30.4	5.9	1.3	5.2	0.8	5.11	1.01	2.83	0.4	2.85	0.43
			DP22-00012	1.70		1.58	1.21		19.1	5.5		22	50	93	9.95	37.3	6.1	1.4	5.3	0.72	4.71	0.89	2.44	0.35	2.43	0.39
			DP22-00013	2.32		3.28	1		27.3	7.7		67	86	153	15.83	61.6	12.7	2.1	12.5	2.01	13.2	2.64	7.23	1.16	7.8	1.09
			DP22-00014	2.37		5.38	1.09		28.3	7.4		75	91	160	17.35	65.5	13.2	2.2	12.9	2.07	14.23	2.9	8.38	1.26	8.59	1.19
			DP22-00015	2.28		5.01	0.9		28	6.9		68	88	152	16.13	62.8	12.2	2.1	12.4	2.06	13.53	2.78	7.89	1.24	7.82	1.15
			DP23-00005	1.87		19.93	1.32		20.3	4.7		25	45	83	9.14	34.9	6.6	1.3	5.5	0.81	5.07	0.99	2.83	0.41	2.88	0.42
			DP23-00006	2.15		1.48	0.51		21.8	2.7		28	52	98	10.41	38.4	6.8	1.4	5.5	0.83	5.44	1.07	3.15	0.46	3.36	0.51

Group	Formation	Collar Coordinates (Latitude; Longitude)	Sample No.	Ta	Tl	Mo	Sb	Sn	Th	U	W	Y	La	Ce	Pr	Nd	Sm	Eu	Gd	Tb	Dy	Ho	Er	Tm	Yb	Lu
			DP23-00007	1.56		8.82	1.4		18.7	5		33	43	83	9.63	36.5	7.2	1.4	6.8	1	6.56	1.28	3.55	0.49	3.32	0.49
			DP23-00008	1.23		2.79	0.86		15	3.8		25	42	78	8.81	33.9	6.5	1.4	5.1	0.86	5.57	0.99	2.8	0.41	3.01	0.45
			DP23-00009	2.36		1.56	0.31		23	2.3		30	52	100	10.72	41	7.6	1.4	6.4	0.91	5.79	1.25	3.5	0.5	3.69	0.57
			DP23-00010	0.65		1.30	0.54		7.3	2		20	18	34	4.12	17.1	3.6	1	4	0.63	3.93	0.8	2.04	0.29	1.9	0.28
			DP23-00011	0.65		0.88	0.64		7.3	2.1		22	20	36	4.40	18	4	1.1	3.9	0.62	3.88	0.76	2.24	0.31	2.08	0.31
			DP23-00012	0.84		123	2.17		11.7	4.8		15	15	30	3.46	14.5	3.8	0.8	3.7	0.52	3.02	0.6	1.79	0.26	1.82	0.3
			DP23-00013	1.70		8.12	1.47		19.6	6.3		20	48	92	9.91	36.5	6	1.2	4.5	0.66	4.13	0.78	2.34	0.37	2.55	0.41
			DP23-00014	2.41		3.41	2.51		25.3	6		30	55	103	10.93	41.7	7.7	1.4	6.5	0.92	5.89	1.11	3.13	0.44	3.18	0.46
			DP23-00015	1		19	1		16	4		24	37	70	8	30	6	1	5	1	5	1	3	0	3	0

Group	Formation	Collar Coordinates (Latitude; Longitude)	Sample No.	Au	Ir	Os	Pd	Pt	Rh	Ru
Upper Pretoria Group	Silverton	26° 18' 44.2548" S; 27° 38' 38.0688" E	DP22-00001	5	0.25	0.25	2	2	0.25	1
			DP22-00002	2	0.25	0.25	2	2	0.25	1
			DP22-00003	2	0.25	0.25	1	2	0.25	0.25
			DP22-00004	1	0.25	0.25	1	1	0.25	0.25
			DP22-00005	3	0.25	0.25	2	2	0.25	3
			DP22-00006	2	0.25	0.25	2	2	0.25	2
			DP22-00007	3	0.25	0.25	3	3	0.25	1
			DP22-00008	4	0.25	0.25	2	2	0.25	0.25
			DP22-00009	2	0.25	0.25	1	1	0.25	0.25
			DP23-00001	1	0.25	0.25	2	1	0.25	0.25
			DP23-00002	1	0.25	0.25	2	2	0.25	0.25
			DP23-00003	3	0.25	0.25	1	1	0.25	0.25
			DP23-00004	2	0.25	0.25	2	2	0.25	0.25
Lower Pretoria Group			DP22-00010	7	0.25	0.25	1	1	0.25	2

Group	Formation	Collar Coordinates (Latitude; Longitude)	Sample No.	Au	Ir	Os	Pd	Pt	Rh	Ru
			DP22-00011	2	0.25	0.25	1	1	0.25	2
			DP22-00012	1	0.25	0.25	1	1	0.25	2
			DP22-00013	2	0.25	0.25	2	1	0.25	4
			DP22-00014	3	0.25	0.25	1	1	0.25	0.25
			DP22-00015	3	0.25	0.25	1	1	0.25	0.25
			DP23-00005	1	0.25	0.25	0.25	0.25	0.25	0.25
			DP23-00006	-	0.25	0.25	2	1	0.25	1
			DP23-00007	2	0.25	0.25	1	1	0.25	0.25
			DP23-00008	2	0.25	0.25	1	1	0.25	1
			DP23-00009	-	0.25	0.25	2	1	0.25	0.25
			DP23-00010	2	0.25	0.25	9	4	0.25	1
			DP23-00011	3	0.25	0.25	9	4	0.25	1
			DP23-00012	2	0.25	0.25	0.25	0.25	0.25	0.25
			DP23-00013	1	0.25	0.25	1	1	0.25	0.25

Group	Formation	Collar Coordinates (Latitude; Longitude)	Sample No.	Au	Ir	Os	Pd	Pt	Rh	Ru
			DP23-00014	2	0.25	0.25	3	3	0.25	1
			DP23-00015	2	0.25	0.25	2	3	0.25	

Appendix A. 2. Mineral chemistry of chlorite.

Sample No	(%)[SiO_2	TiO_2	Al_2O_3	Cr_2O_3	FeO	MnO	MgO	CaO	Na_2O	K_2O	Fe_2O_3(c)	FeO(c)](%)	(apfu)[Si]
013a-chl-1	24.443	0.077	21.091	0.026	30.961	0.088	11.663	0.006	0.01	0.017	0.3353	30.6593	2.6359
013a-chl-2	24.173	0.054	20.7	0.236	30.49	0.078	11.551	0.024	0.015	0.034	0.1736	30.3338	2.6395
013b-chl-1	23.87	0.094	21.522	0.056	30.515	0.116	11.088	0.047	0.015				2.6066
013b-chl-2	24.381	0.159	22.116	0.108	30.699	0.107	11.654	0.004					2.5983
013c-chl-1	24.338	0.946	21.646	0.156	30.251	0.107	11.317	0.032	0.017	0.034			2.6033
013c-chl-2	24.071	0.091	21.333	0.212	30.666	0.106	11.26	0.013	0.002	0.041			2.6163
013d-chl-1	25.604	0.119	20.3	0.137	29.677	0.113	10.805	0.016	0.006	0.011			2.7898
013d-chl-2	23.833	0.064	21.201	0.129	30.562	0.12	11.019	0.019	0.021	0.01			2.6163
013d-chl-3	24.265	0.086	20.99	0.158	29.921	0.16	11.745	0.003	0.005				2.641
013d-chl-4	24.53	0.054	21.259	0.011	30.544	0.094	11.678	0.018	0.022	0.001			2.6455
013d-chl-5	23.815	0.055	22.208	0.114	30.881	0.164	10.996	0.027	0.02	0.059			2.5736
013d-chl-6	23.743	0.078	22.166	0.154	31.211	0.162	10.895	0.029	0.017	0.059	0.0038	31.2076	2.566
013e-chl-1	23.993	0.061	21.682	0.157	30.259	0.13	11.496	0.025	0.017	0.035			2.5996
013e-chl-2	24.161	0.051	21.166	0.108	30.612	0.142	11.626	0.024	0.014	0.052	0.3343	30.3112	2.6182
013e-chl-3	24.202	0.063	22.025	0.136	30.953	0.113	11.025	0.007	0.119	0.022			2.6033
013e-chl-4	23.877	0.067	21.542	0.095	30.777	0.129	11.244	0.009	0.007	0.014	0.3077	30.5002	2.5953
013e-chl-5	25.355	0.213	21.001	0.131	29.93	0.089	10.983	0.028	0.025	0.024			2.7335
013a-chl-3	23.864	0.167	21.917	0.107	31.084	0.107	11.053	0.022	0.001		0.0411	31.047	2.5808
013a-chl-4	23.773	0.082	21.538	0.27	30.681	0.157	11.058	0.018	0.014	0.002	0.0418	30.6434	2.5922
013a-chl-5	23.887	0.039	21.908	0.069	30.412	0.112	11.298	0.001	0.009	0.005			2.5918
013b-chl-3	24.315	0.077	20.895	0.219	30.887	0.126	11.714	0.01	0.002		0.6476	30.3043	2.6266
013b-chl-4	23.438	0.069	21.314	0.162	30.844	0.163	10.932	0.037	0.017	0.015	0.5512	30.348	2.5765
013b-chl-5	23.872	0.059	21.457	0.268	30.878	0.147	11.306		0.003	0.007	0.5676	30.3673	2.5886
Cl_Ph-WS2-24	27.245	0.102	24.326	0.014	27.531	0.351	11.578	0.055	0.098	0.135			2.7543
013c-chl-3	23.867	0.093	21.681	0.011	30.966	0.089	11.189	0.013	0.026	0.036	0.2138	30.7737	2.59
013c-chl-4	24.168	0.071	20.792	0.098	29.967	0.11	11.494		0.002				2.6515
013c-chl-5	24.048	0.071	21.692	0.034	30.546	0.149	11.31		0.008				2.6072
014a-chl-a	23.991	0.115	21.875		30.602	0.068	11.341	0.041	0.013	0.023			2.5945
014a-chl-a	24.554	0.065	21.193	0.088	29.813	0.099	11.852	0.015	0.01	0.034			2.6543
014a-chl-3	24.406	0.079	21.252	0.216	30.187	0.135	11.745	0.03	0.005	0.021			2.6349
014a-chl-4	24.2	0.039	21.512	0.024	29.863	0.089	11.407	0.038	0	0.002			2.6342
014a-chl-5	23.953	0.058	21.866	0.126	30.657	0.108	11.319	0.057	0.019	0.022			2.5896
014b-chl-1	24.174	0.076	21.289	0.118	30.729	0.126	11.393	0.044	0.013				2.6218
014b-chl-2	24.172	0.079	21.546	0.162	30.547	0.132	11.619	0.062	0.004	0.016	0.0535	30.4989	2.6066
014b-chl-3	23.701	0.066	21.905	0.016	30.308	0.142	10.906	0.008	0.018				2.5924
014b-chl-4	23.642	0.101	21.857	0.036	30.787	0.118	10.988	0.05	0.011	0.013	0.0233	30.7661	2.5772
014b-chl-5	23.686	0.071	21.122	0.224	30.666	0.152	11.071	0.022	0.007	0.018	0.316	30.3817	2.6003
014c-chl-1	23.821	0.064	21.97	0.023	30.721	0.14	10.981	0.06	0.011	0.006			2.5879

Sample No	(%)[SiO_2	TiO_2	Al_2O_3	Cr_2O_3	FeO	MnO	MgO	CaO	Na_2O	K_2O	Fe_2O_3(c)	FeO(c)](%)	(apfu)[Si]
014c-chl-2	23.822	0.064	22.49	0.185	30.438	0.09	11.005	0.209	0.02	0.013			2.5673
014d-chl-1	24.773	0.029	21.305	0.037	29.785	0.133	11.997	0.015	0.021	0.026		29.785	2.6626
014d-chl-2	24.051	0.052	21.999	0.129	30.299	0.087	11.047	0.03		0.014			2.6072
014d-chl-3	23.93	0.04	21.991	0.031	30.76	0.137	11.173	0.128	0.009	0.038			2.587
014d-chl-4	24.257	0.06	21.942	0.025	30.172	0.176	11.35	0.013		0.05			2.6169
Cl_Ph-WS3-4	25.892	0.059	20.888	0.005	26.644	0.247	13.134	0.03	0.081	0.08			2.7663
025a-chl-1	21.134	9.356	19.12	0.138	28.52	0.074	9.436	0.038	0.006	0.021			2.3053
025a-chl-2	24.062	0.113	20.693	0.23	31.553	0.152	10.949	0.07	0.015	0.021	0.232	31.3443	2.6281
025a-chl-3	23.79	0.139	21.406	0.187	31.605	0.139	10.623	0.045	0.023		0.0243	31.5831	2.5956
025a-chl-4	23.827	0.073	21.518	0.132	31.52	0.102	11.009	0.065			0.5261	31.0466	2.5841
025a-chl-5	24.492	0.036	21.206	0.185	31.549	0.162	11.552	0.005			0.7078	30.9121	2.6223
025b-chl-1	23.909	0.134	20.947	0.18	30.748	0.104	10.966	0.003	0.015	0.003		30.748	2.6267
025b-chl-2	24.241	0.022	21.973	0.194	32.269	0.075	10.536	0.089	0.015	0.024			2.6011
025b-chl-3	24.282	0.081	21.757	0.207	31.155	0.157	10.639	0.004	0.124				2.6237
025c-chl-1	23.321	0.083	21.439	0.227	30.891	0.142	10.487	0.01	0.03	0.025	0.0122	30.88	2.5792
025c-chl-2	23.947	0.258	21.157	0.232	31.437	0.177	10.807	0.024	0.007	0.015		31.437	2.6079
025c-chl-3	24.358	0.014	20.671	0.007	31.033	0.144	11.101	0.045	0.018	0.016			2.6644
025d-chl-1	23.5	0.266	22.04	0.109	31.058	0.192	10.439	0.061	0.007	0.015			2.5648
025d-chl-2	23.826	0.108	21.201	0.188	31.394	0.138	10.767	0.048	0.012	0.038	0.0632	31.3372	2.6049
025e-chl-1	24.475	0.065	20.946		31.227	0.115	11.359	0.105	0.02	0.022			2.6486
025e-chl-2	23.919	0.794	21.594	0.037	31.895	0.099	10.677	0.118	0.013	0.026			2.5743
025e-chl-3	23.907	0.061	21.953	0.033	31.773	0.151	10.739	0.098		0.02	0.0107	31.7634	2.5828
025f-chl-1	23.731	0.105	21.622	0.077	31.655	0.115	10.521	0.032	0.016	0.018	0.0003	31.6547	2.5905
025f-chl-2	24.268	0.108	21.138		31.376	0.185	11.059	0.04	0.027	0.023			2.6331
025f-chl-3	24.16	0.053	21.294	0.073	31.295	0.104	10.961	0.02	0.014	0.012			2.6266
026a-chl-1	24.544	0.093	21.266	0.078	30.505	0.189	12.146	0.025	0.011	0.001	0.5108	30.0454	2.6246
026a-chl-2	23.777	0.04	20.698	0.191	30.201	0.14	11.231	0.025	0.005	0.018	0.1737	30.0447	2.6282
026a-chl-3	23.81	0.065	21.465	0.159	30.535	0.166	11.412		0.012	0.031	0.4959	30.0888	2.5888
026a-chl-4	23.925	0.064	22.548	0.064	30.897	0.16	11.379	0.078	0.002	0.042	0.0436	30.8578	2.5578
026b-chl-1	24.517	0.081	20.909	0.277	30.615	0.157	11.9	0.01	0.009	0.009	0.3516	30.2986	2.6386
026b-chl-2	23.538	0.079	22.193	0.018	30.298	0.082	11.008	0.002	0.013	0.01			2.5687
026b-chl-3	24.287	0.062	21.535	0.039	30.02	0.151	11.71	0.022		0.037			2.6252
026d-chl-1	24.113	0.102	21.329	0.187	30.192	0.114	11.708	0.019	0.031	0.013	0.0499	30.1471	2.6132
026d-chl-2	24.085	0.027	21.543	0.187	30.218	0.096	11.6	0.005	0.01	0.007	0.0573	30.1664	2.6098
026d-chl-3	24.29	0.141	20.854	0.14	30.207	0.109	11.785	0.025	0.025	0.011	0.0121	30.1961	2.64
026d-chl-4	23.397	0.049	21.418	0.083	30.156	0.146	10.879	0.054	0.028	0.014		30.156	2.5897
026g-chl-1	25.315	0.094	22.736	0.042	30.007	0.102	11.13	0.02	0.323	0.063		30.007	2.6615
027a-chl-1	26.879	0.08	22.564	0.071	26.813	0.091	10.326	0.012	1.792	0.055			2.8181
027a-chl-2	23.135	0.041	21.975	0.015	29.325	0.111	11.186	0.027	0.008				2.5598

Sample No	(%)[SiO_2	TiO_2	Al_2O_3	Cr_2O_3	FeO	MnO	MgO	CaO	Na_2O	K_2O	Fe_2O_3(c)	FeO(c)](%)	(apfu)[Si]
027a-chl-3	23.67	0.083	21.979		29.37	0.096	11.809	0.03	0.017	0.018	0.0241	29.3483	2.5761
027a-chl-4	24.343	0.065	20.943	0.081	29.665	0.14	12.321	0.018		0.015	0.4764	29.2364	2.6336
027a-chl-5	24.464	0.055	20.91		28.855	0.111	12.514	0.013	0.019	0.027		28.855	2.6569
027b-chl-1	24.137	0.012	21.766	0.225	29.048	0.09	11.828	0.035	0.039	0.036			2.6167
027b-chl-2	27.017	0.079	21.038	0.178	29.085	0.101	11.864	0.011	0.078	0.024		29.085	2.8279
027b-chl-3	24.508	0.061	21.498	0.225	29.296	0.177	12.203	0.033	0.033	0.031			2.6331
027b-chl-4	26.447	0.085	22.935	0.087	27.238	0.105	11.17	0.006	0.535	0.034			2.7686
027b-chl-5	24.391	0.059	21.607	0.298	28.47	0.118	12.077	0.015	0.02	0.029			2.6391
027c-chl-1	24.196	0.064	21.826	0.061	29.442	0.122	11.824	0.018	0.021				2.615
027c-chl-2	24.402	0.053	21.769	0.131	29.073	0.133	12.089	0.027	0.031	0.015		29.073	2.6271
027c-chl-3	24.353	0.045	21.178	0.218	29.306	0.158	12.427	0.006	0.02	0.017	0.2263	29.1024	2.6275
027c-chl-4	24.416	0.043	21.805	0.185	29.677	0.159	12.083	0.028	0.017	0.014			2.6156
027c-chl-5	24.679	0.045	20.931	0.114	28.654	0.131	12.58	0.006	0.031			28.654	2.6695
027d-chl-1	24.169	0.104	21.536	0.159	29.129	0.163	12.078	0.005	0.04			29.129	2.6168
027d-chl-2	24.886	0.088	21.618	0.14	29.014	0.099	12.525	0.007	0.022	0.02			2.6525
027d-chl-3	25.167	0.087	22.382	0.11	29.181	0.14	11.584	0.024	0.469	0.033			2.66
027d-chl-4	24.673	0.104	20.269	0.044	29.004	0.145	12.412	0.011	0.012	0.011			2.6923
027d-chl-5	24.286	0.061	21.479	0.371	29.552	0.129	11.942	0.013	0.024	0.036			2.6202
027e-chl-1	24.366	0.079	22.186	0.255	29.409	0.113	12.124	0.007	0.014	0.028			2.6005
027e-chl-2	25.71	0.066	22.205	0.163	27.373	0.159	10.663	0.014	0.81	0.005			2.7541
006a-chl-1	24.196	0.118	22.262		28.398	0.161	12.626	0.127		0.043			2.5899
006a-chl-2	24.149	0.023	22.511	0.049	28.485	0.157	12.629	0.074					2.5799
006a-chl-3	24.183	0.039	22.13	0.149	28.683	0.138	12.59	0.105	0.004	0.017			2.5899
006a-chl-4	24.418	0.071	21.561	0.14	28.739	0.152	12.681	0.27	0.018	0.034			2.6171
006b-chl-1	24.597	0.041	21.711	0.112	28.111	0.141	13.033	0.241					2.627
006b-chl-2	24.099	0.062	22.274	0.077	28.543	0.133	12.543	0.373	0.013				2.5783
006b-chl-4	24.308	0.033	21.637	0.076	27.949	0.134	12.85	0.205	0.02				2.62
006b-chl-5	24.397	0.149	21.409	0.029	28.571	0.155	12.668	0.17					2.6275
006b-chl-6	23.702	0.063	21.979	0.07	28.778	0.12	12.454	0.218			0.0388	28.7431	2.564
006c-chl-2	24.38	0.07	21.5	0.17	27.942	0.14	12.721	0.52	0.009	0.01			2.6236
006c-chl-3	24.257	0.02	21.748	0.088	28.227	0.116	12.615	0.261	0.002	0.022			2.6143
006c-chl-4	24.143	0.057	21.265	0.093	27.897	0.106	12.662	0.388	0.171				2.6211
006c-chl-6	24.771	0.054	21.066	0.077	28.266	0.109	12.485	0.422	0.008				2.6726
006d-chl-2	24.79	0.059	22.059	0.244	27.258	0.077	12.411	0.018	0.21	0.018			2.6584
006d-chl-3	26.551	0.079	20.475	0.446	27.456	0.168	14.23	0.022	0.053	0.026			2.7667
006d-chl-4	27.687	0.102	23.6	0.273	25.011	0.135	11.527	0.011	0.88	0.016			2.8363
006d-chl-5	26.021	0.066	19.726	0.063	27.601	0.11	13.751		0.013				2.7856
006d-chl-8	26.454	0.105	22.687	0.202	25.823	0.141	11.745	0.017	0.9	0.043			2.7731
005a-chl-2	24.797	0.036	22.513	0.108	28.173	0.201	13.1	0.018	0.023	0.029			2.6123

Sample No	(%)[SiO_2	TiO_2	Al_2O_3	Cr_2O_3	FeO	MnO	MgO	CaO	Na_2O	K_2O	Fe_2O_3(c)	FeO(c)](%)	(apfu)[Si]
005a-chl-3	23.648	0.06	21.565	0.137	28.008	0.155	12.37		0.021	0.02		28.008	2.5926
005a-chl-5	24.706	0.083	21.546	0.108	27.985	0.144	12.971	0.016	0.026	0.028			2.6469
005a-chl-6	24.447	0.024	21.354	0.381	27.674	0.122	13.122	0.023	0.033	0.029			2.6324
005a-chl-7	23.655	0.003	21.639	0.169	28.015	0.051	12.571		0.011	0.006	0.2986	27.7463	2.5851
005b-chl-1	24.24	0.099	22.37	0.06	27.914	0.128	12.842	0.013	0.016	0.007			2.593
005e-chl-2	24.266	0.039	21.957	0.022	28.209	0.13	12.702	0.03	0.01	0.022			2.6107
005f-chl-1	25.608	0.049	21.202	0.153	26.923	0.096	12.593	0.015	0.027	0.038			2.7495
006apy-chl-2	24.333	0.08	21.604	0.116	28.681	0.119	12.716	0.038	0.011	0.006		28.681	2.6162
06b-chl-1	24.247		22.069		28.291	0.141	12.727	0.238					2.6009
05aoty-chl-1	24.843	0.053	22.385	0.17	27.903	0.142	13.093		0.085	0.013			2.6228
05-chl-4	28.062	0.1	20.399	0.231	26.867	0.104	12.438		0.011				2.938
00ung-chl-1	23.136	0.014	26.031	0.127	25.251	0.076	12.739	0.008	0.058	0.013			2.4407
013a-chl-1	24.443	0.077	21.091	0.026	30.961	0.088	11.663	0.006	0.01	0.017	0.3353	30.6593	2.6359
013a-chl-2	24.173	0.054	20.7	0.236	30.49	0.078	11.551	0.024	0.015	0.034	0.1736	30.3338	2.6395
013b-chl-1	23.87	0.094	21.522	0.056	30.515	0.116	11.088	0.047	0.015				2.6066
013b-chl-2	24.381	0.159	22.116	0.108	30.699	0.107	11.654	0.004					2.5983
013c-chl-1	24.338	0.946	21.646	0.156	30.251	0.107	11.317	0.032	0.017	0.034			2.6033
013c-chl-2	24.071	0.091	21.333	0.212	30.666	0.106	11.26	0.013	0.002	0.041			2.6163
013d-chl-1	25.604	0.119	20.3	0.137	29.677	0.113	10.805	0.016	0.006	0.011			2.7898
013d-chl-2	23.833	0.064	21.201	0.129	30.562	0.12	11.019	0.019	0.021	0.01			2.6163
013d-chl-3	24.265	0.086	20.99	0.158	29.921	0.16	11.745	0.003	0.005				2.641
013d-chl-4	24.53	0.054	21.259	0.011	30.544	0.094	11.678	0.018	0.022	0.001			2.6455
013d-chl-5	23.815	0.055	22.208	0.114	30.881	0.164	10.996	0.027	0.02	0.059			2.5736
013d-chl-6	23.743	0.078	22.166	0.154	31.211	0.162	10.895	0.029	0.017	0.059	0.0038	31.2076	2.566
013e-chl-1	23.993	0.061	21.682	0.157	30.259	0.13	11.496	0.025	0.017	0.035			2.5996
013e-chl-2	24.161	0.051	21.166	0.108	30.612	0.142	11.626	0.024	0.014	0.052	0.3343	30.3112	2.6182
013e-chl-3	24.202	0.063	22.025	0.136	30.953	0.113	11.025	0.007	0.119	0.022			2.6033
013e-chl-4	23.877	0.067	21.542	0.095	30.777	0.129	11.244	0.009	0.007	0.014	0.3077	30.5002	2.5953
013e-chl-5	25.355	0.213	21.001	0.131	29.93	0.089	10.983	0.028	0.025	0.024			2.7335
013a-chl-3	23.864	0.167	21.917	0.107	31.084	0.107	11.053	0.022	0.001		0.0411	31.047	2.5808
013a-chl-4	23.773	0.082	21.538	0.27	30.681	0.157	11.058	0.018	0.014	0.002	0.0418	30.6434	2.5922
013a-chl-5	23.887	0.039	21.908	0.069	30.412	0.112	11.298	0.001	0.009	0.005			2.5918
013b-chl-3	24.315	0.077	20.895	0.219	30.887	0.126	11.714	0.01	0.002		0.6476	30.3043	2.6266
013b-chl-4	23.438	0.069	21.314	0.162	30.844	0.163	10.932	0.037	0.017	0.015	0.5512	30.348	2.5765
013b-chl-5	23.872	0.059	21.457	0.268	30.878	0.147	11.306		0.003	0.007	0.5676	30.3673	2.5886
Cl_Ph-WS2-24	27.245	0.102	24.326	0.014	27.531	0.351	11.578	0.055	0.098	0.135			2.7543
013c-chl-3	23.867	0.093	21.681	0.011	30.966	0.089	11.189	0.013	0.026	0.036	0.2138	30.7737	2.59
013c-chl-4	24.168	0.071	20.792	0.098	29.967	0.11	11.494		0.002				2.6515
013c-chl-5	24.048	0.071	21.692	0.034	30.546	0.149	11.31		0.008				2.6072

Sample No	(%)[SiO_2	TiO_2	Al_2O_3	Cr_2O_3	FeO	MnO	MgO	CaO	Na_2O	K_2O	Fe_2O_3(c)	FeO(c)](%)	(apfu)[Si]
014a-chl-a	23.991	0.115	21.875		30.602	0.068	11.341	0.041	0.013	0.023			2.5945
014a-chl-a	24.554	0.065	21.193	0.088	29.813	0.099	11.852	0.015	0.01	0.034			2.6543
014a-chl-3	24.406	0.079	21.252	0.216	30.187	0.135	11.745	0.03	0.005	0.021			2.6349
014a-chl-4	24.2	0.039	21.512	0.024	29.863	0.089	11.407	0.038		0.002			2.6342
014a-chl-5	23.953	0.058	21.866	0.126	30.657	0.108	11.319	0.057	0.019	0.022			2.5896
014b-chl-1	24.174	0.076	21.289	0.118	30.729	0.126	11.393	0.044	0.013				2.6218
014b-chl-2	24.172	0.079	21.546	0.162	30.547	0.132	11.619	0.062	0.004	0.016	0.0535	30.4989	2.6066
014b-chl-3	23.701	0.066	21.905	0.016	30.308	0.142	10.906	0.008	0.018				2.5924
014b-chl-4	23.642	0.101	21.857	0.036	30.787	0.118	10.988	0.05	0.011	0.013	0.0233	30.7661	2.5772
014b-chl-5	23.686	0.071	21.122	0.224	30.666	0.152	11.071	0.022	0.007	0.018	0.316	30.3817	2.6003
014c-chl-1	23.821	0.064	21.97	0.023	30.721	0.14	10.981	0.06	0.011	0.006			2.5879
014c-chl-2	23.822	0.064	22.49	0.185	30.438	0.09	11.005	0.209	0.02	0.013			2.5673
014d-chl-1	24.773	0.029	21.305	0.037	29.785	0.133	11.997	0.015	0.021	0.026		29.785	2.6626
014d-chl-2	24.051	0.052	21.999	0.129	30.299	0.087	11.047	0.03		0.014			2.6072
014d-chl-3	23.93	0.04	21.991	0.031	30.76	0.137	11.173	0.128	0.009	0.038			2.587
014d-chl-4	24.257	0.06	21.942	0.025	30.172	0.176	11.35	0.013		0.05			2.6169
Cl_Ph-WS3-4	25.892	0.059	20.888	0.005	26.644	0.247	13.134	0.03	0.081	0.08			2.7663
025a-chl-1	21.134	9.356	19.12	0.138	28.52	0.074	9.436	0.038	0.006	0.021			2.3053
025a-chl-2	24.062	0.113	20.693	0.23	31.553	0.152	10.949	0.07	0.015	0.021	0.232	31.3443	2.6281
025a-chl-3	23.79	0.139	21.406	0.187	31.605	0.139	10.623	0.045	0.023		0.0243	31.5831	2.5956
025a-chl-4	23.827	0.073	21.518	0.132	31.52	0.102	11.009	0.065			0.5261	31.0466	2.5841
025a-chl-5	24.492	0.036	21.206	0.185	31.549	0.162	11.552	0.005			0.7078	30.9121	2.6223
025b-chl-1	23.909	0.134	20.947	0.18	30.748	0.104	10.966	0.003	0.015	0.003		30.748	2.6267
025b-chl-2	24.241	0.022	21.973	0.194	32.269	0.075	10.536	0.089	0.015	0.024			2.6011
025b-chl-3	24.282	0.081	21.757	0.207	31.155	0.157	10.639	0.004	0.124				2.6237
025c-chl-1	23.321	0.083	21.439	0.227	30.891	0.142	10.487	0.01	0.03	0.025	0.0122	30.88	2.5792
025c-chl-2	23.947	0.258	21.157	0.232	31.437	0.177	10.807	0.024	0.007	0.015		31.437	2.6079
025c-chl-3	24.358	0.014	20.671	0.007	31.033	0.144	11.101	0.045	0.018	0.016			2.6644
025d-chl-1	23.5	0.266	22.04	0.109	31.058	0.192	10.439	0.061	0.007	0.015			2.5648
025d-chl-2	23.826	0.108	21.201	0.188	31.394	0.138	10.767	0.048	0.012	0.038	0.0632	31.3372	2.6049
025e-chl-1	24.475	0.065	20.946		31.227	0.115	11.359	0.105	0.02	0.022			2.6486
025e-chl-2	23.919	0.794	21.594	0.037	31.895	0.099	10.677	0.118	0.013	0.026			2.5743
025e-chl-3	23.907	0.061	21.953	0.033	31.773	0.151	10.739	0.098		0.02	0.0107	31.7634	2.5828
025f-chl-1	23.731	0.105	21.622	0.077	31.655	0.115	10.521	0.032	0.016	0.018	0.0003	31.6547	2.5905
025f-chl-2	24.268	0.108	21.138		31.376	0.185	11.059	0.04	0.027	0.023			2.6331
025f-chl-3	24.16	0.053	21.294	0.073	31.295	0.104	10.961	0.02	0.014	0.012			2.6266
026a-chl-1	24.544	0.093	21.266	0.078	30.505	0.189	12.146	0.025	0.011	0.001	0.5108	30.0454	2.6246
026a-chl-2	23.777	0.04	20.698	0.191	30.201	0.14	11.231	0.025	0.005	0.018	0.1737	30.0447	2.6282
026a-chl-3	23.81	0.065	21.465	0.159	30.535	0.166	11.412		0.012	0.031	0.4959	30.0888	2.5888

Sample No	(%)[SiO_2	TiO_2	Al_2O_3	Cr_2O_3	FeO	MnO	MgO	CaO	Na_2O	K_2O	Fe_2O_3(c)	FeO(c)](%)	(apfu)[Si]
026a-chl-4	23.925	0.064	22.548	0.064	30.897	0.16	11.379	0.078	0.002	0.042	0.0436	30.8578	2.5578
026b-chl-1	24.517	0.081	20.909	0.277	30.615	0.157	11.9	0.01	0.009	0.009	0.3516	30.2986	2.6386
026b-chl-2	23.538	0.079	22.193	0.018	30.298	0.082	11.008	0.002	0.013	0.01			2.5687
026b-chl-3	24.287	0.062	21.535	0.039	30.02	0.151	11.71	0.022		0.037			2.6252
026d-chl-1	24.113	0.102	21.329	0.187	30.192	0.114	11.708	0.019	0.031	0.013	0.0499	30.1471	2.6132
026d-chl-2	24.085	0.027	21.543	0.187	30.218	0.096	11.6	0.005	0.01	0.007	0.0573	30.1664	2.6098
026d-chl-3	24.29	0.141	20.854	0.14	30.207	0.109	11.785	0.025	0.025	0.011	0.0121	30.1961	2.64
026d-chl-4	23.397	0.049	21.418	0.083	30.156	0.146	10.879	0.054	0.028	0.014		30.156	2.5897
026g-chl-1	25.315	0.094	22.736	0.042	30.007	0.102	11.13	0.02	0.323	0.063		30.007	2.6615
027a-chl-1	26.879	0.08	22.564	0.071	26.813	0.091	10.326	0.012	1.792	0.055			2.8181
027a-chl-2	23.135	0.041	21.975	0.015	29.325	0.111	11.186	0.027	0.008				2.5598
027a-chl-3	23.67	0.083	21.979	0	29.37	0.096	11.809	0.03	0.017	0.018	0.0241	29.3483	2.5761
027a-chl-4	24.343	0.065	20.943	0.081	29.665	0.14	12.321	0.018	0	0.015	0.4764	29.2364	2.6336
027a-chl-5	24.464	0.055	20.91	0	28.855	0.111	12.514	0.013	0.019	0.027		28.855	2.6569
027b-chl-1	24.137	0.012	21.766	0.225	29.048	0.09	11.828	0.035	0.039	0.036			2.6167
027b-chl-2	27.017	0.079	21.038	0.178	29.085	0.101	11.864	0.011	0.078	0.024		29.085	2.8279
027b-chl-3	24.508	0.061	21.498	0.225	29.296	0.177	12.203	0.033	0.033	0.031			2.6331
027b-chl-4	26.447	0.085	22.935	0.087	27.238	0.105	11.17	0.006	0.535	0.034			2.7686
027b-chl-5	24.391	0.059	21.607	0.298	28.47	0.118	12.077	0.015	0.02	0.029			2.6391
027c-chl-1	24.196	0.064	21.826	0.061	29.442	0.122	11.824	0.018	0.021				2.615
027c-chl-2	24.402	0.053	21.769	0.131	29.073	0.133	12.089	0.027	0.031	0.015		29.073	2.6271
027c-chl-3	24.353	0.045	21.178	0.218	29.306	0.158	12.427	0.006	0.02	0.017	0.2263	29.1024	2.6275
027c-chl-4	24.416	0.043	21.805	0.185	29.677	0.159	12.083	0.028	0.017	0.014			2.6156
027c-chl-5	24.679	0.045	20.931	0.114	28.654	0.131	12.58	0.006	0.031			28.654	2.6695
027d-chl-1	24.169	0.104	21.536	0.159	29.129	0.163	12.078	0.005	0.04			29.129	2.6168
027d-chl-2	24.886	0.088	21.618	0.14	29.014	0.099	12.525	0.007	0.022	0.02			2.6525
027d-chl-3	25.167	0.087	22.382	0.11	29.181	0.14	11.584	0.024	0.469	0.033			2.66
027d-chl-4	24.673	0.104	20.269	0.044	29.004	0.145	12.412	0.011	0.012	0.011			2.6923
027d-chl-5	24.286	0.061	21.479	0.371	29.552	0.129	11.942	0.013	0.024	0.036			2.6202
027e-chl-1	24.366	0.079	22.186	0.255	29.409	0.113	12.124	0.007	0.014	0.028			2.6005
027e-chl-2	25.71	0.066	22.205	0.163	27.373	0.159	10.663	0.014	0.81	0.005			2.7541
006a-chl-1	24.196	0.118	22.262		28.398	0.161	12.626	0.127		0.043			2.5899
006a-chl-2	24.149	0.023	22.511	0.049	28.485	0.157	12.629	0.074					2.5799
006a-chl-3	24.183	0.039	22.13	0.149	28.683	0.138	12.59	0.105	0.004	0.017			2.5899
006a-chl-4	24.418	0.071	21.561	0.14	28.739	0.152	12.681	0.27	0.018	0.034			2.6171
006b-chl-1	24.597	0.041	21.711	0.112	28.111	0.141	13.033	0.241					2.627
006b-chl-2	24.099	0.062	22.274	0.077	28.543	0.133	12.543	0.373	0.013				2.5783
006b-chl-4	24.308	0.033	21.637	0.076	27.949	0.134	12.85	0.205	0.02				2.62
006b-chl-5	24.397	0.149	21.409	0.029	28.571	0.155	12.668	0.17					2.6275

Sample No	(%)[SiO_2	TiO_2	Al_2O_3	Cr_2O_3	FeO	MnO	MgO	CaO	Na_2O	K_2O	Fe_2O_3(c)	FeO(c)](%)	(apfu)[Si]
006b-chl-6	23.702	0.063	21.979	0.07	28.778	0.12	12.454	0.218			0.0388	28.7431	2.564
006c-chl-2	24.38	0.07	21.5	0.17	27.942	0.14	12.721	0.52	0.009	0.01			2.6236
006c-chl-3	24.257	0.02	21.748	0.088	28.227	0.116	12.615	0.261	0.002	0.022			2.6143
006c-chl-4	24.143	0.057	21.265	0.093	27.897	0.106	12.662	0.388	0.171				2.6211
006c-chl-6	24.771	0.054	21.066	0.077	28.266	0.109	12.485	0.422	0.008				2.6726
006d-chl-2	24.79	0.059	22.059	0.244	27.258	0.077	12.411	0.018	0.21	0.018			2.6584
006d-chl-3	26.551	0.079	20.475	0.446	27.456	0.168	14.23	0.022	0.053	0.026			2.7667
006d-chl-4	27.687	0.102	23.6	0.273	25.011	0.135	11.527	0.011	0.88	0.016			2.8363
006d-chl-5	26.021	0.066	19.726	0.063	27.601	0.11	13.751		0.013				2.7856
006d-chl-8	26.454	0.105	22.687	0.202	25.823	0.141	11.745	0.017	0.9	0.043			2.7731
005a-chl-2	24.797	0.036	22.513	0.108	28.173	0.201	13.1	0.018	0.023	0.029			2.6123
005a-chl-3	23.648	0.06	21.565	0.137	28.008	0.155	12.37		0.021	0.02		28.008	2.5926
005a-chl-5	24.706	0.083	21.546	0.108	27.985	0.144	12.971	0.016	0.026	0.028			2.6469
005a-chl-6	24.447	0.024	21.354	0.381	27.674	0.122	13.122	0.023	0.033	0.029			2.6324
005a-chl-7	23.655	0.003	21.639	0.169	28.015	0.051	12.571		0.011	0.006	0.2986	27.7463	2.5851
005b-chl-1	24.24	0.099	22.37	0.06	27.914	0.128	12.842	0.013	0.016	0.007			2.593
005e-chl-2	24.266	0.039	21.957	0.022	28.209	0.13	12.702	0.03	0.01	0.022			2.6107
005f-chl-1	25.608	0.049	21.202	0.153	26.923	0.096	12.593	0.015	0.027	0.038			2.7495
006apy-chl-2	24.333	0.08	21.604	0.116	28.681	0.119	12.716	0.038	0.011	0.006		28.681	2.6162
06b-chl-1	24.247		22.069		28.291	0.141	12.727	0.238					2.6009
05aoty-chl-1	24.843	0.053	22.385	0.17	27.903	0.142	13.093		0.085	0.013			2.6228
05-chl-4	28.062	0.1	20.399	0.231	26.867	0.104	12.438		0.011				2.938
00ung-chl-1	23.136	0.014	26.031	0.127	25.251	0.076	12.739	0.008	0.058	0.013			2.4407

Appendix A. 3. Brief history of geostatistics and its application to unmineralised marine shales.

Geostatistics encompasses a range of fields that would never have occurred had it not been for the pioneers of science, mathematics and philosophy such as John Napier, a Scottish mathematician and clergyman who was responsible for the introduction of the Napierian logarithms. Back in 1607 he devised a methodology of representing any number as a base rose to a power. These simplified mathematical calculations significantly, reducing complicated multiplication and division functions to simple addition and subtraction, a method used to this day in modern computing. Geostatistics originated in South Africa over 70 years ago to provide more efficient ore evaluation techniques for gold mines. It has developed into a branch of statistics covering a wide range of earth related applications – e.g. ore valuation, environmental, petroleum, agriculture, forestry, marine, rainfall forecasting. The data for all these applications have the special common feature of a 2D or 3D spatial structure, which can be modelled and used to improve the standard of data interpretations. Data for evaluation is always limited, from original widely spaced surface boreholes during mineral resources exploration, to regularly space confined to exposed ore faces during mining. Herbert Sichel (Statistician at the University of Witwatersrand, South Africa) in the 1940s made great advances in the areas of both theoretical and applied geostatistics after he noticed that certain distributions could be normalised by taking the Napierian logarithms and in certain cases adding a constant (Sichel, 1947). He developed the Sichel-t estimator for the log-normal distribution's t-statistic. He also made great leaps in the area of the generalised inverse Gaussian distribution which became known as the Sichel distribution (Sichel, 1947). Following the work of Sichel, Danie Krige (Mining Engineer at the University of Witwatersrand, South Africa) in the early 1950s incorporated spatial dynamics with statistical theory and inferred that there was a relationship between disparate samples, their distances, and direction between them (Krige, 1951). This although done on an empirical basis provided the necessary principle for a mathematical formalism. In the 1960s, Georges Matheron (Mathematician at Paris school of mines, France) mathematically formalised Danie Krige's empirical system and named it in honour of him as Kriging (Matheron, 1963). Matheron defined geostatistics, as the application of the formalism of random functions to the reconnaissance and estimation of natural phenomena (Matheron, 1963). Sample elemental concentration, for example, is a regionalised variable because it is distributed throughout a space. The variability of the concentration throughout that space is described by a function called the 'variogram.' Through a process known as 'kriging,' samples and the variogram are used to estimate the mean concentration of a point, area, or volume.

Kriging provides the best estimate of the mean value of a regionalised variable (Krige, 2000). It provides the Best Linear Unbiased Estimator (BLUE) of the grade or concentration. During kriging, each sample is assigned a sample weight. The weighted samples are then linearly combined to give the best estimate. It is the 'best' estimate because the procedure minimises the expected error between the estimated mean concentration and the true concentration. Sample weights are calculated such that the variance of the estimate is a minimum. That variance can be calculated using the sample positions and the variogram function. Having the estimation variance is extremely useful because it allows the user to explore the risk of the estimate (Morgan, 2005).

In both mineralised and unmineralised samples, gold and PGE contents are highly variable with positively skew distributions of the general lognormal type. This usually result in sample blocks (drillcores or chip samples) with low gold and PGE concentrations being under-valued, and those with high concentrations being over-valued. In the context of this study, geostatistics was used to eliminate conditional biases which were introduced by grade variability within the same stratigraphic unit of each studied marine shale. Below is a custom designed excel spreadsheet that was used to calculate the mean and log variance of the studied marine shales gold and PGE contents.

Au (ppb)	LN(ppb +B)
1	0.09531018
3	1.13140211
7	1.96009478
92	4.52287494
7	1.96009478
5	1.62924054
4	1.41098697
12	2.49320545
1	0.09531018
2	0.74193734
2	0.74193734
5	1.62924054
4	1.41098697
100	4.60616968
2	0.74193734
2	0.74193734
3	1.13140211
5	1.62924054
8	2.09186406
9	2.20827441
6	1.80828877

Domain		
Barb		
log mean	**log variance**	**B**
1.6562731	3.639178701	0.1

1	0

Estimate of mean

32

Arithmetic mean

13

Use this one

Figure A. 1. Outlier calculation custom-designed spreadsheet.

References cited only in Appendix A.2

Krige, D.G., 1951. A statistical approach to some basic mine valuation problems on the Witwatersrand. Journal of the Chemical, Metallurgical and Mining Society of South Africa. pp. 119–139.

Krige, D.G., 2000. Half a century of geostatistics from a South African perspective. In: Kleingeld, W.J., Krige, D.G. (Eds) Geostats 2000 Cape Town: Proceedings of the sixth International Geostatistics Congress held in Cape Town, South Africa, April 2000. 1, pp. 3–11.

Matheron, G., 1963. Principles of geostatistics. Economic Geology, 58, 1246–1266.

Morgan, C.J., 2005. Analysing spatial data via geostatistical methods. MSc thesis, University of Witwatersrand, Johannesburg, South Africa.

Sichel, H.S., 1947. An experimental and theoretical investigation of bias error in mine sampling with special reference to narrow gold reefs. Trans. Inst. Min. Metall. London, 56, pp. 403–443.

Appendix A. 4. Mass transfer calculation results for profile from upper contact into shale unit of Roodepoort Formation. Abbreviations: ΔCi/Ci0 = Gain/Loss relative to Ci0 and Δci = Gain/Loss in wt. % or ppm.

Sample	UNG005	UNG001	$\Delta C_i/C_i^0$	ΔC_i	UNG005	UNG002	$\Delta C_i/C_i^0$	ΔC_i	UNG005	UNG003	$\Delta C_i/C_i^0$	ΔC_i
	Unaltered	Chloritised			Unaltered	Sericitised			Unaltered	Less Sericitised		
SiO_2 (Wt. %)	57.05	56.79	0.00	-0.26	57.05	54.44	-0.05	-2.61	57.05	55.51	-0.03	-1.54
TiO_2	0.77	0.75	-0.03	-0.02	0.77	0.71	-0.08	-0.06	0.77	0.63	-0.18	-0.14
Al_2O_3	22.97	22.99	0.00	0.02	22.97	23.79	0.04	0.82	22.97	22.17	-0.03	-0.80
Fe_2O_3	12.36	11.85	-0.04	-0.51	12.36	8.94	-0.28	-3.42	12.36	9.59	-0.22	-2.77
MnO	0.08	0.07	-0.13	-0.01	0.08	0.03	-0.63	-0.05	0.08	0.03	-0.63	-0.05
MgO	2.82	3.10	0.10	0.28	2.82	3.14	0.11	0.32	2.82	3.24	0.15	0.42
CaO	0.07	0.10	0.43	0.03	0.07	0.09	0.29	0.02	0.07	0.09	0.29	0.02
Na_2O	0.18	0.22	0.22	0.04	0.18	0.42	1.33	0.24	0.18	0.37	1.06	0.19
K_2O	1.86	2.15	0.16	0.29	1.86	3.87	1.08	2.01	1.86	3.39	0.82	1.53
P_2O_5	0.11	0.12	0.09	0.01	0.11	0.09	-0.18	-0.02	0.11	0.07	-0.36	-0.04
S	0.28	0.32	0.14	0.04	0.28	1.14	3.07	0.86	0.28	1.30	3.64	1.02
Cs (ppm)	1.5	1.8	0.20	0.30	1.5	3.0	1.00	1.50	1.5	2.3	0.53	0.80
Rb	60	69	0.14	8	60	127	1.11	67	60	106	0.76	46
Ba	320	368	0.15	48	320	683	1.14	363	320	576	0.80	256
Sr	51	54	0.05	3	51	87	0.71	36	51	75	0.48	24
Pb	8.4	10.7	0.27	2.30	8.4	17.8	1.12	9.40	8.4	19.6	1.33	11.20
Cr	453	435	-0.04	-18	453	407	-0.10	-46	453	367	-0.19	-86
Ni	196	192	-0.02	-3	196	228	0.16	32	196	230	0.18	35
V	175	165	-0.06	-10	175	145	-0.17	-30	175	129	-0.26	-46
Sc	24.0	23.0	-0.04	-1.00	24.0	22.0	-0.08	-2.00	24.0	19.0	-0.21	-5.00
Ga	25.8	25.1	-0.03	-0.70	25.8	28.0	0.09	2.20	25.8	23.6	-0.09	-2.20
Zn	85	90	0.06	5	85	74	-0.13	-11	85	79	-0.07	-6
U	2.2	2.8	0.27	0.60	2.2	2.6	0.18	0.40	2.2	2.2	0.00	0.00
Zr	147	154	0.05	7	147	137	-0.07	-10	147	90	-0.39	-57
Hf	4.1	3.9	-0.05	-0.20	4.1	3.7	-0.10	-0.40	4.1	2.8	-0.32	-1.30
Y	30	28	-0.06	-2	30	24	-0.18	-5	30	21	-0.30	-9
Nb	11.2	10.7	-0.04	-0.50	11.2	11.5	0.03	0.30	11.2	9.5	-0.15	-1.70
Ta	0.9	0.9	0.00	0.00	0.9	1.1	0.22	0.20	0.9	1.0	0.11	0.10
Th	7.8	7.8	0.00	0.00	7.8	9.9	0.27	2.10	7.8	8.7	0.12	0.90
Tl	0.5	0.7	0.24	0.13	0.5	1.3	1.33	0.72	0.5	1.1	0.98	0.53
La	39	38	-0.03	-1	39	53	0.35	14	39	51	0.30	12
Ce	78	77	-0.01	-1	78	105	0.35	27	78	99	0.28	22
Pr	8.6	8.7	0.01	0.10	8.6	11.4	0.33	2.80	8.6	11.0	0.28	2.40
Nd	32	31	-0.05	-2	32	39	0.21	7	32	38	0.19	6
Sm	6.9	6.5	-0.06	-0.40	6.9	8.0	0.16	1.10	6.9	7.6	0.10	0.70
Eu	1.5	1.4	-0.07	-0.10	1.5	1.8	0.20	0.30	1.5	1.6	0.07	0.10
Gd	5.9	5.3	-0.10	-0.60	5.9	5.9	0.00	0.00	5.9	5.4	-0.08	-0.50
Tb	1.1	1.0	-0.09	-0.10	1.1	0.9	-0.18	-0.20	1.1	0.9	-0.18	-0.20

Dy	6.4	4.9	-0.23	-1.50	6.4	4.6	-0.28	-1.80	6.4	5.0	-0.22	-1.40
Ho	1.1	1.0	-0.09	-0.10	1.1	0.9	-0.18	-0.20	1.1	0.8	-0.27	-0.30
Er	3.3	2.9	-0.12	-0.40	3.3	2.6	-0.21	-0.70	3.3	2.2	-0.33	-1.10
Tm	0.5	0.4	-0.20	-0.10	0.5	0.4	-0.20	-0.10	0.5	0.4	-0.20	-0.10
Yb	3.4	2.5	-0.26	-0.90	3.4	2.6	-0.24	-0.80	3.4	2.3	-0.32	-1.10
Lu	0.4	0.4	0.00	0.00	0.4	0.3	-0.25	-0.10	0.4	0.3	-0.25	-0.10

Appendix A. 5. Sources of Nickel in the studied marine shales.

Below are the calculations applied to provide the likely source of Ni in the studied marine shales as described in section 7.3, Nickel provenance discussion.

Table A. 9. Ni in Archaean Rock Proportion Composition (Condie, 1993).

Concentration (ppm)	Archaean Basalt	Archaean Komatiite	Archaean TTG	Archaean felsic volcanic rocks	Archaean Andesite	Archaean Granite
Ni	190	1700	13	18	100	12

Table A. 10. Rock Proportions Mixture Model.

Archaean sediment-source mixing calculations	Basalt-komatiite mixture (85:15)	Archaean Granite	Archaean TTG
Mixture 1	35%	45%	20%
Mixture 2	60%	25%	15%
Mixture 3	50%	40%	10%

Table A. 11. Average Ni Composition from sediment mixture.

Average Ni Composition from sediment mixture	Basalt-komatiite mixture: Ratio B:K = 85:15	Archaean Granite	Archaean TTG
Ni (ppm)	417	12	13

Table A. 12. Source rock mixture model scenarios.

Source sediments Mixture model	Ni Concentration based on Source Rock Mixture Models
[1] Mixture 1: Ni (ppm) [Ratio-BK:G:TTG-35:45:20]	154
[2] Mixture 2: Ni (ppm) [Ratio-BK:G:TTG-60:25:15]	255
[3] Mixture 2: Ni (ppm) [Ratio-BK:G:TTG-50:40:10]	214

% Ni from the hinterland	100.00000%	60.00000%	20.00000%	1.00000%
Mixture 1: Ni (ppm)	153.77500	92.26500	30.75500	1.53775
Mixture 2: Ni (ppm)	254.85000	152.91000	50.97000	2.54850
Mixture 2: Ni (ppm)	214.35000	128.61000	42.87000	2.14350

Table A. 13. Calculations parameters/assumptions.

Palaeo-marine Ni concentration (Archaean dissolved Ni)			
Archaean Ni Concentration	400	nm	
Archaean Ni Concentration	4E-07	M	
Ni Molar Mass	58.6934	g/mol	
Archaean Ni Concentration	0.002348	ppm	highest in the Archaean
Change in Palaeo-marine Ni concentration to near modern marine water concentration			
Archaean Ni Concentration	200	nm	
Archaean Ni Concentration	2E-07	M	
Archaean Ni Concentration	0.001174	ppm	Dramatic decline between 2.7 and 2.5 Ga

Calculations Parameters/Assumption			1
Average Ni in Archaean shale (Condie, 1993)	221	g/t	[a]
Kaapvaal Craton Catchment area (Frimmel, 2016 35th IGC)	1.00E+05	km^2	[b]
Density of Archaean marine water (Kasting et al., 2006)	1.03	g/cm^3	[c]
Rain Precipitation (Estimate)	1	m/a rain	[d]
Amount of Water Based on Density of 1.03 g/cm^3	1.03E+05	t water	2
Amount of water per annum	1.03E+11	t water/annum	[e]
Amount of water in my	1.03E+14	t water/my	[f]
Total Tons of Ni in Archaean shales[Based on average of 221 ppm]	2.28E+10	tons Ni/my	[g]

Table A. 14. Time required to accumulate Ni from source rocks.

% Absorbed into shales from source rocks	100.00000%	60.00000%	20.00000%	1.00000%
Mixture 1: Ni (tons)	1.58E+10	9.50E+09	3.17E+09	1.58E+08
Mixture 1: Time Required (myr) to accumulate >2.28 X10^10 (myr)	1.44	2.40	7.19	143.72
Mixture 2: Ni (tons)	2.62E+10	1.57E+10	5.25E+09	2.62E+08
Mixture 2: Time (myr) Required to accumulate >2.28 X10^10 (myr)	0.87	1.45	4.34	86.72
Mixture 3: Ni (tons)	2.21E+10	1.32E+10	4.42E+09	2.21E+08
Mixture 3: Time (myr) Required to accumulate >2.28 X10^10	1.03	1.72	5.16	103.10

Coded Scientific Notation				
Mixture 1: Time Required to accumulate >2.28 X10^10 (myr)	1.4x10^E+0	2.4x10^E+0	7.1x10^E+0	1.4x10^E+2
Mixture 2: Time Required to accumulate >2.28 X10^10 (myr)	8.6x10^E-1	1.4x10^E+0	4.3x10^E+0	8.6x10^E+1
Mixture 3: Time Required to accumulate >2.28 X10^10 (myr)	1.0x10^E+0	1.7x10^E+0	5.1x10^E+0	1.0x10^E+2
Average Time (myr) Required to Leach Ni from the Hinterland into Shale	1.1x10^E+0	1.8x10^E+0	5.5x10^E+0	1.1x10^E+2